

NASA Contractor Report 199830

Research Reports—1995 NASA/ASEE Summer Faculty Fellowship Program

G.R. Karr, C.R. Chappell, F. Six, L.M. Freeman, Editors

Contract NGT-01-008-021
Prepared for Marshall Space Flight Center

February 1996

TABLE OF CONTENTS

- I. Antar, Basil N.
The University of Tennessee Space Institute
Bubble Formation in Microgravity
- II. Bales, John W.
Tuskegee University
Triangulation Methods for Automated Docking
- III. Fork, Richard L.
The University of Alabama in Huntsville
Optical Amplifiers for Coherent Lidar
- IV. Marshall, Karen Benn
Oakwood College
The Development, Assessment, and Validation of Virtual Reality for Human
Anatomy Instruction
- V. Bernstein, Edward L.
Alabama A&M University
Modeling Aluminum-Lithium Alloy Welding Characteristics
- VI. Bucinell, Ronald B.
Union College
Damage Accumulation in Closed Cross-Section, Laminated, Composite Structures
- VII. Bunton, Patrick H.
Austin Peay State University
Particulate Electron Beam Weld Emission Hazards in Space
- VIII. Carlisle, W.H.
Auburn University
Web Interfaces to Relational Databases
- IX. Chang, Kai H.
Auburn University
The Feasibility Study and Evaluation of Applying Expert System Techniques to the
Mission Operations for the AXAF-I Spacecraft
- X. Chu, Tsuchin Philip
Southern Illinois University at Carbondale
Non-Destructive Evaluation of Composites

- XI. Drueding, Thomas W.
Boston University
Investigation of Ion-Beam Machining Methods for Replicated X-Ray Optics
- XII. Elrod, David A.
The University of Alabama in Huntsville
Large Deflection Analysis of a Tension-Foil Bearing
- XIII. Feikema, Douglas A.
The University of Alabama in Huntsville
Atomization characteristics of Swirl Injector Sprays
- XIV. Gerhardt, Rosario A.
The Georgia Institute of Technology
Characterization of Zinc Selenide Single Crystals
- XV. Gross, R. Steven
Auburn University
Residual Life Assessment of the SSME/ATD HPOTP Turnaround Duct (TAD)
- XVI. Gudimetla, V.S. Rao
Oregon Graduate Institute
Relativity Effects for Space-Based Coherent Lidar Experiments
- XVII. Harrison, Harry C.
Capitol College
Static Measurement of the Thickness of the Ablative Coating of the Solid Rocket Boosters
- XVIII. Hartfield, Jr., Roy
Auburn University
Thermodynamic Measurements in a High Pressure Hydrogen-Oxygen Flame
Using Raman Scattering from a Broadband Excimer Laser
- XIX. Hochstein, John I.
The University of Memphis
Computational Modeling of Magnetically Actuated Propellant Orientation
- XX. Howard, Thomas G.
Northwest-Shoals Community College
SXI Mirror Characterization

- XXI. Ierkic, V., H. Mario
University of Puerto Rico-Managuez
VLF Long-Range Lightning Location Using the Arrival Time Difference
Technique (ATD)
- XXII. Jones, Kenneth M.
North Carolina A&T State University
Modeling of Micro Thrusters for Gravity Probe B
- XXIII. Kennedy, W.J.
Clemson University
Preliminary Work Toward the Development of a Dimensional Tolerance Standard
for Rapid Prototyping
- XXIV. Kineke, Jack
Centre College
Development of Software for the MSFC Solar Vector Magnetograph
- XXV. Lebo, George R.
University of Florida
Extending the JOVE Program Through Undergraduate Research
- XXVI. Lo, Chor Pang
University of Georgia
Thermal Signatures of Urban Land Cover Types: High-Resolution Thermal
Infrared Remote Sensing of Urban Heat Island in Huntsville, Alabama.
- XXVII. Losure, Nancy S.
Mississippi State University
The Search for Materials to Mitigate Spacecraft Charging
- XXVIII. Lyne, James Evans
The University of Tennessee
Protein Crystallization Studies
- XXIX. Mahanta, Kamala
State University of New York College at Oneonta
Development of a Material Property Database on Selected Ceramic Matrix
Composite Materials
- XXX. Maier, Mark W.
University of Alabama in Huntsville
Development of the SEASIS Instrument for SEDSAT

- XXXI. Main, John A.
Vanderbilt University
ISSA/TSS Power Preliminary Design
- XXXII. Matthys, Donald R.
Marquette University
Linearization of an Annular Image by Using a Diffractive Optic
- XXXIII. Morris, Jon D.
University of Florida
Marketing and Communications Plan
- XXXIV. Mazzoleni, Andre P.
Texas Christian University
Analysis, Design, and Testing of High Pressure Waterjet Nozzels
- XXXV. Olsen, Eugene A.
The University of Alabama in Huntsville
Reinvention/Reengineering of Business and Technical Processes
- XXXVI. Palazzolo, Alan B.
Texas A&M University
Impeller Leakage Flow Modeling for Mechanical Vibration Control
- XXXVII. Pearson, Earl F.
Western Kentucky University
Design of a Nonlinear, Thin-Film Mach-Zehnder Interferometer
- XXXVIII. Phillips, James A.
California Institute of Technology
Development of a Low-Cost Virtual Reality Workstation for Training and Education
- XXXIX. Prasthofer, Thomas
Albany College of Pharmacy
Using Naturally Occurring Polysaccharides to Align Molecules with Nonlinear Optical Activity
- XL. Romine, Peter L.
Florida International University
Welding Rework Data Acquisition and Automation

- XL I. Rosmait, Russell L.
Pittsburg State University
Technology Readiness Levels and Technology Status for Selected Long
Term/High Payoff Technologies on the RLV Program
- XLII. Schonberg, William P.
The University of Alabama in Huntsville
Pressure Wall Hole Size and Maximum Tip-To-Tip Crack Length Following
Orbital Debris Penetration
- XLIII. Schreur, Barbara
Texas A&M University-Kingville
The Shuttle Main Engine: A First Look
- XLIV. Smith, Willard A.
Tennessee State University
An Analyses of CD-ROM Technology for Spacelink
- XLV. Solakiewicz, Richard
Chicago State University
A Geometrical Result Regarding Time-of-Arrival Lightning Location
- XLVI. Spencer, Dwight C.
Mississippi Delta Community College
Was the MSSTA II Mission Successful?
- XLVII. Talia, George E.
The Wichita State University
Role of the Micro/Macro Structure of Welds in Crack Necleation and Propagation
in Aerospace Aluminum-Lithium Alloy
- XLVIII. Tawfik, Hazem H.
State University of New York at Farmingdale
Mathematical Modeling of the Gas and Powder Flow in the (HVOF) Systems to
Optimize Their Coatings Quality
- XLIX. Taylor, Charles R.
Pacific University
Orbital Debris Removal Using Ground-Based Lasers
- L. Temple, Enoch C.
Alabama A&M University
Statistical Optimization of Shearography Inspections

- LI. Thornburg, Hugh J.
Mississippi State University
Adaptive Grid Methods for RLV Environment Assessment and Nozzle Analysis
- LII. Treise, Debbie
University of Florida
Creating New Opportunities for Communicating About Space Science
- LIII. Trivoli, George W.
Jacksonville State University
Technology Transfer Metrics: Measurement and Verification of Date/Reusable Launch Vehicle Business Analysis
- LIV. Wang, Francis C.
Alabama A&M University
Non-Linear Resonance of Fluids in a Crystal Growth Cavity
- LV. Wang, Jai-Ching
Alabama A&M University
Effect of Melt-Solid Interface Shape on Lateral Compositional Distribution of Unidirectionally Solidified II-VI Semiconducting Alloys
- LVI. Wang, Peter Hor-Ching
Alabama A&M University
A Convertor and User Interface to Import CAD Files Into Worldtoolkit Virtual Reality Systems
- LVII. Wells, B. Earl
The University of Alabama in Huntsville
Development of the Command Data System and Ground Software for the SEDSAT-1 Microsatellite
- LVIII. Williams, George O.
Calhoun Community College
Capillary Electrophoresis: Imaging of Electroosmotic and Pressure Driven Flow Profiles in Fused Silica Capillaries
- LIX. Wohlman, Richard A.
Western Carolina University
A Technique for Determining Cloud Free vs Cloud Contaminated Pixels in Satellite Imagery

LX. Woodbury, Keith A.
 University of Alabama
 Thermal Analysis of HGFQ Using FIDAP: Solidification Front Motion

1995

NASA/ASEE SUMMER FACULTY FELLOWSHIP PROGRAM

MARSHALL SPACE FLIGHT CENTER
THE UNIVERSITY OF ALABAMA IN HUNTSVILLE

BUBBLE FORMATION IN MICROGRAVITY

Prepared By:	Basil N. Antar
Academic Rank:	Professor
Institution and Department:	The University of Tennessee Space Institute Engineering Science and Mechanics
NASA/MSFC:	
Office:	Space Science Laboratory
Division:	Microgravity Science and Applications
Branch:	Biophysics
MSFC Colleague:	Dale M. Kornfeld

1. Introduction

Almost all of the experiments dealing with protein crystal growth and with growth of crystals from solution require complicated fluid handling procedures such as filling of containers with liquids, mixing of solutions and stirring of liquids. Such procedures can be accomplished in a straight forward manner when performed under terrestrial conditions in the laboratory. However, in the low gravity environment in space such as on board the Space Shuttle or Earth orbiting space station, these procedures are no longer straight forward. Under terrestrial conditions, liquids are normally positioned below the gas due to the buoyancy effects of Earth's gravity. Consequently any gas bubbles that are entrained into the liquid during a fluid handling procedure will eventually migrate towards the top of the vessel where they can be removed. In a low gravity environment any folded gas bubble tend to remain within the liquid bulk due to the absence of the buoyancy force resulting from the diminished gravity.

An extensive experimental program was initiated for the purpose of understanding the mechanisms leading to bubble generation during fluid handling procedures in a microgravity environment. Several key fluid handling procedures typical for PCG experiments were identified for analysis in that program. Experiments were designed to specifically understand how such procedures can lead to bubble formation. The experiments were then conducted aboard the NASA KC-135 aircraft which is capable of simulating a low gravity environment by executing a parabolic flight attitude. However, such a flight attitude can only provide a low gravity environment of approximately $10^{-2}g_0$ for a maximum period of 30 seconds. Thus all of the tests conducted for these experiments were designed to last no longer than 20 seconds.

Several experiments were designed to simulate some of the more relevant fluid handling procedures during protein crystal growth experiments. These include submerged liquid jet cavitation, filling of a cubical vessel, submerged surface scratch, attached drop growth, liquid jet impingement, and geysering experiments. To date, four separate KC-135 flight campaigns were undertaken specifically for performing these experiments. However, different experiments were performed on different flights.

Some of these experiments have been thoroughly analyzed elsewhere including the the vessel filling experiment, the surface scratch experiment and the submerged liquid jet cavitation experiment. The results from these tests are found in Antar and Kornfeld (1995). Below we describe some of the other experiments including the jet impingement, the attached drop growth, and the geysering experiments.

2. Jet Impingement Experiment

This experiment was designed to investigate the spread mechanism of a liquid jet over a solid surface upon impacting the surface. Jet impingement is a fluid handling procedure that may develop during filling of a vessel when the inflow rate is very high.

It is obvious that the liquid spread over the solid surface resulting from a jet impact in low gravity environment is entirely different from a similar incident under terrestrial conditions. In a terrestrial laboratory the spread mechanism depends very strongly on the orientation of both the jet and the solid surface. Such dependence on geometry is absent in low gravity environment. Another objective of this experiment was to delineate the conditions under which some of the impacted liquid rebounds from the solid surface in the form of droplets that subsequently fold gas bubbles into the liquid bulk.

The test cell for this experiment comprised of a plexiglas cubical box with the dimensions of 2.5 cm on each side. A hole was drilled at the center of one of the cube faces, through which a hypodermic needle was inserted. The needle end was positioned at a set predetermined distance from the opposite wall. The liquid jet in each test of this experiment was established by injecting liquid through the hypodermic needle. The impact of the jet on the opposite face of the cube and the subsequent accumulation and spread of the liquid on the wall was visually recorded using high speed motion picture camera. The liquid flow rate was achieved using a syringe pump with a preset flow rate setting.

The objective of this experiment was to understand the mechanism of jet impact on a solid wall and the subsequent form of liquid spreading for different jet exit velocities, different liquids and different liquid jet lengths. Two hypodermic needle sizes were used in the tests with 0.16 cm and 0.12 cm ID. Three test liquid types were used for this experiment; distilled water, and a mixture of water with 10% PEG, 20% PEG, and 30 % PEG, respectively. Four different jet lengths were tested 0.5 cm, 1.0 cm, 1.5 cm and 2.0 cm. Flow rates of 20, 30, 40 and 50 ml/min were tested corresponding to jet exit velocities of 25, 30, 40, 45, 60, and 74 cm/sec.

Each test was initiated after the low gravity portion of the aircraft flight parabola was attained by activating the pump and the camera. Most of the tests had a liquid injection period no longer than 5 seconds. Each test was completed during the low gravity period of the parabola. Normally one test was conducted during a single parabola. Also every test was performed at least twice, once with a dry wall initial conditions and another with a wet wall initial conditions. For each test one of the four variables, namely, the flow rate, the needle diameter, the test liquid type, or the jet length was varied while the rest of the parameters were kept the same. This experiment was performed in the second and third KC-135 flights campaigns which took place during June 20 - 24, 1994 and January 30 - February 3, 1995.

The results of the tests for this experiment show that the liquid will always accumulate at the jet impact point with the solid wall. The accumulating liquid took the form of a hemispherical dome with its cap at the jet end and the flat surface against the solid wall. As further liquid is injected, the dome expanded radially increasing both its base and its tip. This form of liquid accumulation was consistent regardless of the jet

exit velocity, the jet diameter, or the type of test liquid used. The liquid spread over the solid surface was manifested, in this case, through an expansion of the base of the liquid dome in the radial direction. This was the accumulation configuration observed whenever the wall was dry.

When the liquid jet impacted a wet wall the liquid spreading configuration varied from test to test depending on the shape of the original liquid film on the solid wall prior to the jet impact. In this case the liquid meandered along the wet region of the wall after some liquid mass accumulated at the stagnation region. However, the liquid meandered only after it acquired some mass and when gravity perturbations were present. In other words the accumulating liquid mass was very unstable to small disturbances when the wall was wet. The meandering liquid mass took very interesting forms and shapes which are not the subject of this experiment. No splattering of liquid was ever observed for all jet exit velocities tested in this experiment.

The flow of the liquid over the solid surface was extremely interesting forming unusual patterns that can only be observed under low gravity conditions. One of the most common patterns observed was the motion of the hemispherical dome along the wet path of the wall as also the merging of accumulating liquid volume with existing volume shapes in the container. The resulting liquid configuration took different shapes depending on the material it merged with. In certain instances the hemispherical drop merged with a horizontally flat gas/liquid interface. This pattern evolved as the liquid accumulated from the jet impact on the wall spread and collided with another liquid in the container was partially filled with liquid. In other instances when the test chamber was empty the hemispherical drop evolved into a quarter spherical at the intersection of two walls of the test chamber.

3. Attached Drop Growth Experiment

The purpose of this experiment is to investigate the growth process of a drop attached to a solid surface as liquid is continuously added to the drop. The growth process of the attached drop includes in this case the development of the drop geometry with increasing liquid mass as well as the variation of the liquid/solid contact angle as the drop spreads along the solid surface.

All of the tests for this experiment were conducted by injecting liquid through a hole drilled into a solid surface. The liquid drop was formed by injecting liquid through the hole. The drop subsequently was allowed to remain attached to the surface. The test cell for this experiment comprised of a plexiglas cube of 2.5 cm per side. The hole was drilled at the center of one of the cube faces. The liquid was supplied to the drop using a hypodermic needle attached from the other side of the wall. Four different needle sizes were used for injecting the liquid; 0.16, 0.12, 0.084, and 0.058 cm ID, respectively. Five liquid injection flow rates were used resulting in liquid exit velocities ranging from 1.66 cm/sec to 92.4 cm/sec, depending on the needle diameter. Also, four different

liquid types were used in these tests including distilled water, distilled water solution with 10% PEG, 20% PEG, and 30% PEG, respectively. The growth of the drop was recorded visually using high speed movie camera and film.

Each test in this experiment was initiated by injecting liquid through the orifice in the solid surface at a constant flow rate. The variation of the shape of the drop was recorded visually as additional liquid is injected. Each test was conducted during the low gravity portion of the flight parabola. The liquid flow rates, the test liquid and the pore size were varied for each individual test.

There were 20 different completed successful tests for this experiment over the second and third KC-135 flight campaigns. In all of the tests for which the liquid exit velocity was greater than 40 cm/sec, the liquid issued from the orifice in the form of a jet and consequently a liquid drop did not form at the orifice. For all of the tests in which the liquid exit velocity was less than 40cm/sec a drop formed and developed in almost the same manner for all of the tests except in three cases. In the majority of the tests the liquid drop took an almost perfect hemispherical domed shape immediately upon exiting the orifice with a flat surface against the solid wall . The drop was attached to the orifice in all of these cases and was positioned centrally at that location. As further liquid is added to the drop, the drop expanded radially retaining its hemispherical shape. However, in one test for which the conditions were: 0.16 cm orifice diameter, 4.98 cm/sec for the exit velocity, and 30% PEG test liquid, the hemispherical dome flattened out to a disc covering the orifice as the liquid mass increased beyond a specific value.

In the remaining three cases, for which the orifice diameter and exit velocity were: 0.16cm and 2.49cm/sec; 0.12cm and 2.95 cm/sec; and 0.12cm and 4.3cm/sec, respectively, the liquid took an almost perfect spherical shape upon exiting the orifice with the drop being attached to the orifice. The spherical drop expanded radially with increased injection of the test liquid which was distilled water in all of the three cases. However, the spherical shape became unstable as further liquid was added and subsequently the drop shape changed to a hemispherical dome. The cause of this shape instability could either be due to the effects of the residual gravity or to the increased mass of the drop. The specific cause of this instability could not be identified since that test run was conducted without the benefit of the accelerometer readings being visible simultaneously with the photograph.

No attempt has yet been made at measuring the variation of the solid/liquid contact angle as a function of the advancing liquid front during the growth of the drop. The following general conclusion can be drawn from this experiment. At very low exit velocities, i.e. less than 5 cm/sec the attached liquid drop took a spherical shape. For higher exit velocities a hemispherical domed shape drop was consistently observed.

4. Geysering Experiment

The purpose of the series of tests for this experiment was to validate the critical Weber number criteria at which the free surface is broken by the geysering phenomenon. Previous low gravity experiments have suggested a critical Weber number value of 1.5. The value for the critical Weber number for the geysering experiment were explored by varying the values of some of the parameters that enter into the definition of the Weber number, namely

$$We = \frac{\rho U^2 d}{\sigma}$$

For a specific liquid composition in which σ and ρ have fixed values, only the liquid expulsion velocity U and the exit nozzle diameter can be varied in order to cover the desired range of values for the Weber number. The liquid injection velocity U was varied by changing the fill flow rate through the pump speed. The inlet nozzle diameter d was varied by using different diameter injection needles. A test matrix was constructed for performing a number of tests in this experiment comprising of four liquid injection rates and two injection needle diameters. The values for these parameters were chosen such that they enveloped the empirically determined critical Weber number value of $We = 1.5$. Also since surface tension plays a major role in all free surface phenomena in low gravity environment, three different liquid mixtures were used. The test liquid used in this case was distilled water and water with 10%, 20%, and 30% PEG. This last test item was intended to support the PCG experiments in which water base is used with added surfactants.

The test cell used for the geysering experiment was the same as the one used for the attached drop growth experiment described in section 3. In fact all of the tests for the geysering experiment were performed immediately after completing the drop growth experiment tests by adding more test liquid into the test cell at the end of that experiment. The geysering experiment tests were performed by injecting liquid through the nozzle at a predetermined constant flow rate. The nozzle in all of the tests was covered with a liquid layer of a predetermined depth. The free surface of the liquid layer was observed to determine whether or not, as well as the extent, in which the liquid jet was able to break the free surface. the observations were recorded visually using high speed camera and film.

5. References

Antar, B. N. and M. Kawaji (1995) Bubble Generation During Low Gravity Fluid Handling Procedures. AIAA Paper No. AIAA-95-0898.

1995

NASA/ASEE SUMMER FACULTY FELLOWSHIP PROGRAM

**MARSHALL SPACE FLIGHT CENTER
THE UNIVERSITY OF ALABAMA IN HUNTSVILLE**

TRIANGULATION METHODS FOR AUTOMATED DOCKING

Prepared by: John W. Bales, Ph. D.

Academic Rank: Associate Professor

Institution and Department: Tuskegee University
Department of Mathematics

NASA/MSFC:

Directorate: Science and Engineering
Laboratory: Astrionics
Division: Avionics Simulation
Branch: Orbital Systems and Robotics

MSFC Colleague: Fred Roe, Jr.

Introduction

An automated docking system must have a reliable method for determining range and orientation of the passive (target) vehicle with respect to the active vehicle. This method must also provide accurate information on the rates of change of range to and orientation of the passive vehicle. The method must be accurate within required tolerances and capable of operating in real time.

The method being developed at Marshall Space Flight Center employs a single TV camera, a laser illumination system and a target consisting, in its minimal configuration, of three retro-reflectors. Two of the retro-reflectors are mounted flush to the same surface, with the third retro-reflector mounted to a post fixed midway between the other two and jutting at a right angle from the surface. For redundancy, two additional retro-reflectors are mounted on the surface on a line at right angles to the line containing the first two retro-reflectors, and equally spaced on either side of the post. (Figure 1) The target vehicle will contain a large target for initial acquisition and several smaller targets for close range.

There are other target configurations which might provide information on range and orientation [for example see Ref. 1, or see the cross-ratio of projective geometry, Ref. 2]. However, these configurations fail to provide reliable estimates of target yaw--the angle at which the target tilts away from the line of sight. With one of the three retro-reflectors mounted to a center post aligned (ideally) with the line of sight, reliable estimates of yaw angles may be computed.

This report will detail the mathematics required in the computation of accurate range and orientation measurements for a target configured as in Figure 1.

Detector Hardware Components

The target detector consists of a TV camera, frame grabber and associated computer. The camera contains a lens which focuses an image of the target onto an image plane. Located in the image plane is a rectangular array of individual photo-detectors called "picture elements" or "pixels". The amount of light falling on each individual pixel can be measured and digitized into a number of "grey levels" (in the case of a black and white image). The number of grey levels is typically a power of two, with 256 being the highest number of grey levels commonly used, and 2 being the least. The frame grabber is a digital device which takes successive "snapshots" of the image coming from the camera and stores these "frames" in a block of memory accessible to the associated computer. The computer is programmed to detect the target in the frame and compute the range and orientation of the target, and the related velocities.

Geometric Model of the Imaging System

For the purpose of analysis, the lens of the camera is modelled as a pinhole. In a pinhole camera, every object is in focus, regardless of its distance from the camera. For actual lenses, only objects at a given distance, determined by the lens equation, are in perfect focus. Points at other distances from the camera are imaged as "blur circles" whose diameters are proportional to the distance of the point from the ideal distance and to the lens diameter while inversely proportional to the focal length of the lens. The target detection system being developed, however, uses the centroids of detected images. In a statistical sense, the centroid of such an image should be the same whether or not it is in perfect focus. Thus, for purposes of geometrical analysis, the pinhole model is adequate.

While the image plane lies behind the lens at a distance f equal to the focal length of the lens, an imaginary *projected* image plane may lie at any distance behind or in front of the lens. For ease of illustration, a projected image plane is frequently used. We will use a projected image plane lying a distance f in *front* of the lens (Figure 2). A right-handed xyz coordinate system is used, with the positive x -axis extending from C through the center of the projected image plane, and with the positive y and z -axes extending vertically upward and horizontally to the right, respectively.

Determination of Target Range

In Figure 3, C denotes the geometrical center of the lens, P'_1, P'_2 , and P'_3 represent the retro-flectors in the target, and P_1, P_2 , and P_3 represent the respective images in the image plane. The symbols $\vec{P}_1, \vec{P}_2, \vec{P}_3, \vec{P}'_1, \vec{P}'_2$, and \vec{P}'_3 represent the vectors from C to the respective points on the target and on the image plane. The vector components of \vec{P}_1, \vec{P}_2 , and \vec{P}_3 are, respectively, $\langle f, a_1, b_1 \rangle, \langle f, a_2, b_2 \rangle$, and $\langle f, a_3, b_3 \rangle$. The magnitudes of the vectors \vec{P}_1, \vec{P}_2 , and \vec{P}_3 , representing the distances to the retro-reflectors, are r_1, r_2 , and r_3 , respectively. The fixed distance from retro-reflector 1 (on the center post) to retro-reflectors 2 and 3 is D . The fixed distance between retro-reflectors 2 and 3 is L . The height of the center post is H . The angle between vectors \vec{P}_1 and \vec{P}_2 is θ_{12} . The angle between vectors \vec{P}_1 and \vec{P}_3 is θ_{13} . The angle between vectors \vec{P}_2 and \vec{P}_3 is θ_{23} .

The coordinates of \vec{P}_1, \vec{P}_2 , and \vec{P}_3 are determined directly from the output of the imaging system. The angles θ_{12}, θ_{13} , and θ_{23} are determined by the relations

$$\cos \theta_{12} = \frac{\vec{P}_1 \cdot \vec{P}_2}{\|\vec{P}_1\| \|\vec{P}_2\|}$$

$$\cos \theta_{13} = \frac{\vec{P}_1 \cdot \vec{P}_3}{\|\vec{P}_1\| \|\vec{P}_3\|}$$

$$\cos\theta_{23} = \frac{\vec{P}_2 \cdot \vec{P}_3}{\|\vec{P}_2\| \|\vec{P}_3\|}$$

Using the Law of Cosines, it is seen that

$$\begin{aligned} r_1^2 + r_2^2 - 2r_1r_2 \cos\theta_{12} &= D^2 \\ r_1^2 + r_3^2 - 2r_1r_3 \cos\theta_{13} &= D^2 \\ r_2^2 + r_3^2 - 2r_2r_3 \cos\theta_{23} &= L^2 \end{aligned}$$

In general, a set of three quadratic equations in three variables can have as many as eight distinct solutions. In this case, however, there are at most four solutions where all values of the variables are positive, since, if (r_1, r_2, r_3) is a solution, then so is $(-r_1, -r_2, -r_3)$. In point of fact, there are never more than three distinct all positive solutions. Three solutions occur when $\theta_{12} = \theta_{13}$. If $\theta_{12} \neq \theta_{13}$, then there are only two distinct solutions in which all three variables are positive. In either case, only one of the solutions has the reflector on the center post pointed toward the camera. The other solutions represent situations where the center post points away from the camera. Since such a target orientation would be undetectable, such a solution may be discarded.

In fact, the method of solution used by Marshall Space Flight Center avoids the necessity of computing all solutions and then rejecting some. It is assumed that the image of the point halfway between P'_1 and P'_3 (the base of the center reflector post) would lie at the point halfway between the images of those points in the image plane. While this assumption is not true, it is a good approximation in the case of the correct solution, and a bad approximation for the spurious solutions. Using an iterative routine (the Newton-Rafson method), the initial guess is improved upon until the system converges to the correct solution. The iterative routine also computes the pitch, roll and yaw of the target. This information, along with the range to the target, is updated and the corresponding rates of change are computed. All range, orientation and rate of change information is then passed along to the guidance routines so that necessary course corrections can be computed for the docking maneuver.

Alternate Solution Method

While the method described above is sufficient, the following method is presented for possible comparison of speed or accuracy.

Assuming that $\theta_{12} \geq \theta_{13}$, Figure 4 represents the target geometry relative to the camera, with C representing the camera, and P'_1, P'_2 , and P'_3 representing the three retro-reflectors on the target. The segment P'_1A is perpendicular to CP'_2 . The segment P'_2D is perpendicular to CP'_3 . The segment P'_3B is perpendicular to CP'_1 . Then

$CP'_2 = CA + P'_2A$. Likewise, $CP'_3 = CD + DP'_3$, and $CP'_1 = CB - P'_1B$. Using right triangle trigonometry, and using D and L as defined in the previous section, these three equations may be rewritten as follows:

$$r_2 = r_1 \cos \theta_{12} + \sqrt{D^2 - r_1^2 \sin^2 \theta_{12}}$$

$$r_3 = r_2 \cos \theta_{23} + \sqrt{L^2 - r_2^2 \sin^2 \theta_{23}}$$

$$r_1 = r_3 \cos \theta_{13} - \sqrt{D^2 - r_3^2 \sin^2 \theta_{13}}$$

To solve for r_1 , r_2 , and r_3 , one makes an initial guess that $r_1 = \left(\frac{L}{2}\right) \cot\left(\frac{\theta_{23}}{2}\right)$, then iterates the equations. If $\theta_{12} < \theta_{13}$, then the 2s and 3s in the above equations should be reversed.

References

1. "Marking parts to aid robot vision", J. W. Bales and L. K. Barker, NASA Technical Paper 1819, NASA-Langley Research Center 1981
2. Geometric Computation for Machine Vision, K. Kanatani, Clarendon Press, 1993

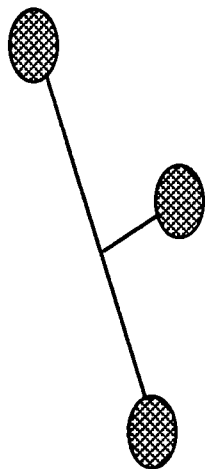


Figure 1: Three-reflector target configuration

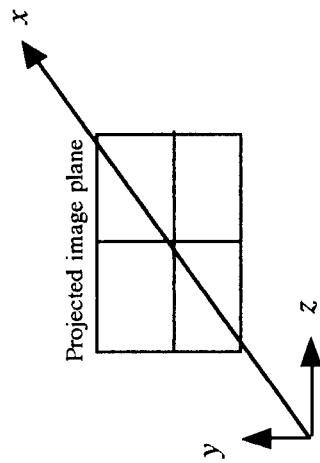


Figure 2: Camera Coordinate System

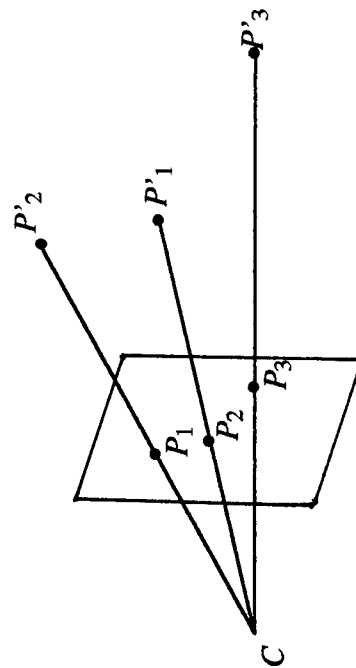


Figure 3: Projection of target onto image plane

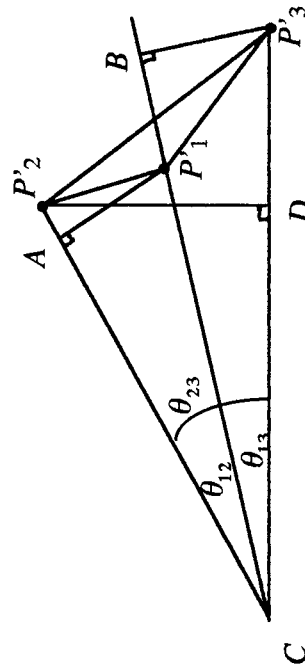


Figure 4: Target geometry for range solution

1995

NASA/ASEE SUMMER FACULTY FELLOWSHIP PROGRAM

**MARSHALL SPACE FLIGHT CENTER
THE UNIVERSITY OF ALABAMA IN HUNTSVILLE**

OPTICAL AMPLIFIERS FOR COHERENT LIDAR

Prepared by:	Richard Fork, Ph.D.
Academic Rank:	Professor Electrical & Computer Engineering
Institution and Department:	University of Alabama in Huntsville Electrical & Computer Engineering
NASA/MSFC:	
Laboratory:	Astrionics
MSFC Colleague:	Michael J. Kavaya, Ph.D.

Optical Amplifiers for Coherent Lidar

R.L. Fork and A. Ghobrial
University of Alabama in Huntsville
Huntsville, AL 35899

Abstract

We examine application of optical amplification to coherent lidar for the case of a weak return signal (a number of quanta of the return optical field close to unity). We consider the option that has been explored to date, namely, incorporation of an optical amplifier operated in a linear manner located after reception of the signal and immediately prior to heterodyning and photodetection. We also consider alternative strategies where the coherent interaction, the nonlinear processes, and the amplification are not necessarily constrained to occur in the manner investigated to date. We include the complications that occur because of mechanisms that occur at the level of a few, or one, quantum excitation. Two factors combine in the work to date that limit the value of the approach. These are: (a) the weak signal tends to require operation of the amplifier in the linear regime where the important advantages of nonlinear optical processing are not accessed , (b) the linear optical amplifier has a -3dB noise figure (SN_{out}/SN_{in}) that necessarily degrades the signal. Some improvement is gained because the gain provided by the optical amplifier can be used to overcome losses in the heterodyned process and photodetection. The result, however, is that introduction of an optical amplifier in a well optimized coherent lidar system results in, at best, a modest improvement in signal to noise. Some improvement may also be realized on incorporating more optical components in a coherent lidar system for purely practical reasons. For example, more compact, lighter weight, components, more robust alignment, or more rapid processing may be gained. We further find that there remain a number of potentially valuable, but unexplored options offered both by the rapidly expanding base of optical technology and the recent investigation of novel nonlinear coherent interference phenomena occurring at the single quantum excitation level. Key findings are: (1) insertion of linear optical amplifiers in well optimized conventional lidar systems offers modest improvements, at best , (2) the practical advantages of optical amplifiers, especially fiber amplifiers, such as ease of alignment, compactness, efficiency, lightweight, etc., warrant further investigation for coherent lidar, (3) the possibility of more fully optical lidar systems should be explored, (4) advantages gained by use of coherent interference of optical fields at the level of one, or a few, signal quanta should be explored, (5) amplification without inversion, population trapping, and use of electromagnetic induced transparency warrant investigation in connection with coherent lidar, (6) these new findings are probably more applicable to earth related NASA work, although applications to deep space should not be excluded, and (7) our own work in the Ultrafast Laboratory at UAH along some of the above lines of investigation, may be useful.

1. Introduction

Both ground based and airborne laser radar systems are being explored and developed for wind velocity measurements. The measurements provided by these systems yield essential information needed, e.g., for space shuttle launches and aircraft flights. Timeliness of the information may have life and death consequences. A real time global wind profile; however, remains a challenge beyond the reach of current technology.

We focus here on strategies that need to be addressed if a goal, such as real time global wind profiling, is to be realized. In particular we examine the problem of optimizing the acquisition of information under circumstances where quantum properties, coherent interference, and nonlinear interactions of the signal, reference fields, and the transmission medium may be important. Space based technology tends to require maximally efficient performance and it is reasonable to expect that space based wind sensing will be no exception.

Addition of an optical amplifier to a coherent lidar system deserves exploration. Optical amplifiers have had a powerful and positive impact on emerging optical information transmission and handling systems. A fundamental problem is encountered, however, in the manner used to date in applying optical amplifiers to coherent lidar. Optical amplifiers are traditionally most effective if used in conjunction with nonlinear processes before a signal has been reduced to the level of a few quanta. By using an optical amplifier after reception and immediately prior to detection we limit our options. In particular, optical amplifiers used at the level of a few quanta tend to introduce spontaneous emission noise in ways that are difficult to avoid. On the other hand the nature of lidar applications makes it difficult to introduce the optical amplifier at any other point in the system.

In essence we consider two approaches: (1) conventional, where the optical amplifier is introduced into an existing coherent lidar system where a return signal of a few quanta is to be amplified immediately prior to photodetection, and (2) non conventional, where we allow more novel and more distributed use of amplification, coherent interference, and nonlinear optical processes including excitation levels of one or a few quanta. In the former case we find some practical advantages, but little opportunity for revolutionary progress. In the latter case we find no immediate practical advantages, but do find a potential for more revolutionary progress in coherent lidar. These non-conventional strategies, interestingly, make contact with vigorous and rapidly emerging new fields and new technology.

1.1 Signal to noise considerations

Conventional coherent lidar already uses optical interactions in a powerful and effective manner. The signal, heterodyned against a local optical oscillator is, in essence, noiselessly amplified. For an ideal system coherent detection provides a 3dB advantage over direct detection. The frequency shift of the return signal is also made easily detectable since the heterodyne process modulates the resulting photocurrent at the difference frequency between the initial and return signals. Linear optical amplifiers, on the other hand, introduce a 3 dB noise penalty. In addition access to optimum performance of the linear optical amplifier can be expected to require spectral filtering and temporal gating of the return signal to avoid further unnecessary degradation of signal to noise arising from excess spontaneous emission.

The most obvious advantage of the linear optical amplifier used for a weak return signal is that of overcoming the losses that occur between the output of the amplifier and the conversion of the photons in the return signal to electrical current in the photodetector.

Typical sources of such losses are quantum and heterodyne efficiencies less than unity, and any other losses that occur after exit of the signal from the optical amplifier and before conversion to photoelectrons. In general, we see the principal value of the optical amplifier as used in experimental work to date as compensating these losses at the receiver.

1.2 Optical signal processing issues other than signal to noise considerations

Aside from issues of signal to noise performance emerging optical technology may offer improvements to state of the art coherent lidar systems. Diode pumped optical fiber amplifiers offer advances in compact, robust, efficient, lightweight easily aligned technology. Cladding pumped amplifiers offer very high average power while maintaining highly coherent wavefronts. Fiber amplifiers can also assist in achieving and maintaining robust alignment of wavefronts. More fully optical coherent lidar systems may eventually offer more rapid processing. Recent advances in fiber grating techniques may provide a means for spectrally resolving a return signal with sufficient resolution and efficiency to allow frequency shift resolution for wind sensing that is more fully optical. Other advantages not yet perceived may emerge since this field is still evolving in substantial ways.

1.3 Novel strategies

In general, we find a proliferation of new optical technology and substantial new work and ideas regarding coherent nonlinear interactions where quantum phenomena can be important. While we cannot guarantee substantial benefit to coherent lidar, the richness of the technology and the vigorous new experimental and theoretical work appear to warrant a "back to the drawing board" examination of coherent lidar and systems that perform functions similar to coherent lidar. In essence we note the physical mechanisms that make coherent lidar effective are coherent interaction and nonlinear mixing that operate in a useful manner at excitation levels of one, or a few, quanta of the radiation field. Novel combinations of these mechanisms may work to advantage.

If we relax the condition that improvement be sought only by inserting a linear optical amplifier at the receiver of a conventional coherent lidar more options emerge. One direction of interest appears to be that of using interference of quantum states at low where nonlinear processes also have significant consequence. New physical phenomena occur and new options are accessed. Electromagnetically induced transparency (EIT) [1],[2] and optical amplification without inversion [3] are two recent areas of vigorous research that warrant investigation. Our own work in this area may be of significance.[18]

2. Conventional and non-conventional approaches

There are essentially two paths that can be followed, one relatively conventional and the other non-conventional. We explore both options. The conventional path appears to offer modest, but readily implemented improvements. The non-conventional path appears to offer more possibilities for revolutionary advances, but with a correspondingly lower probability of near term working systems. Both paths appear to warrant consideration.

2.1 Introduction of optical amplifiers into conventional lidar systems

As regards background on existing coherent lidar there are a number of good recent publications that examine topics of current interest and provide references to earlier work.. Frehlich [4], [5] and Kavaya [5] have investigated the signal to noise and heterodyne efficiency of coherent heterodyne laser radar under the Fresnel approximation and general

conditions. This includes spatially random fields, refractive turbulence, monostatic and bistatic configuration, detector geometry and targets. Frehlich has compared the performance of 2 and 10 micron coherent lidar systems [6]. Hawley et al [7] investigate the performance of the coherent launch-site atmospheric wind sounder (CLAWS), a Nd:YAG based coherent lidar operating at 1.06 micron with 1-J energy per pulse. Salisbury [8],[9] has performed a combined calculational and experimental test of a system that incorporates a neodymium doped fiber preamplifier, and Baker et al [10] have written a general analysis of the lidar measurement of winds from space with an emphasis on the CO₂ laser at 10 microns originally proposed for the Laser Atmospheric Wind Sounder (LAWS).

Experimentally oriented studies, such as those of Salisbury[9], Rahm [11] and Morley [16] find improvement on introducing optical amplifiers to existing coherent lidar systems; however, their findings do not appear to be in contradiction to the above interpretation of the improvement. In general, the basic conclusion seems to be that, a system that departs significantly from ideal performance can be correspondingly improved by adding an optical amplifier; however, a well designed coherent lidar can at best experience modest improvements. Other important practical benefits, such as those gained by: alignment of wave fronts, robust alignment of pump and probe, and light weight, compact character of components are discussed to a limited extent.

The general problem of signal to noise in coherent heterodyne and direct detection systems has been analyzed by a number of authors e.g., Agrawal [12]. Theoretical analyses of optical amplifiers, Caves [13], Bondurant [14] assign a noise figure of -3 dB to optical amplifiers for incoherent signals and -6 dB to optical amplifiers for coherent signals. There also appears to be general agreement that improvement by the product of the reciprocal of the heterodyne efficiency and the quantum efficiency can be argued for in a fundamental manner [12],[8]. In essence photons that are lost in the detection process before excitation of a photoelectron occurs cause a degradation in the signal to noise. This degradation of signal can be avoided by introduction of an amplifier that is located at the receiver, but positioned before the photodetection and heterodyne mixing, but at the price of introducing spontaneous emission noise.

The conclusions concerning conventional use of optical amplifiers for coherent lidar are: (1) the heterodyne step in coherent lidar is a powerful technique for sensing return signals containing a few quanta, (2) the possibility of some modest improvement in signal to noise may be realized on introduction of an optical amplifier (3) This improvement is attributable to compensation for losses occurring after amplification and prior to detection. (4) without some substantial change in strategy this approach is unlikely to cause revolutionary improvements in a well designed existing coherent lidar, (5) practical advantages such as, more robust alignment, more efficient pumping, better wavefront quality, more compact technology, lighter weight, and opportunities for more fully optical and faster signal processing may be realized, aside from signal to noise considerations.

2.2 Non-conventional strategies

The non-conventional strategies do not appear to be easily addressed; however, attention appears warranted. We approach the task by dividing the discussion into four parts: (1) Novel preparation and transmission of the emitted signal, (2) novel amplification and processing of the return signal, (3) novel detection and (4) novel interactive generation-transmission-reception strategies.

2.2.1 Novel preparation and transmission of the emitted signal: There is new science and technology of electromagnetically induced transparency (EIT) that is vigorous and promises potential breakthroughs. Proper preparation of an optical signal for a given

medium can result in a nonlinearly induced transparency. The applications to NASA would tend to be found where the lidar signal propagates through media that would normally be lossy or distorting. Reduced diffraction and hence enhanced signal may be found under some circumstances. The physical phenomena is not trivial, but results from interference effects at the single quantum excitation level that can drastically alter the propagation of an electromagnetic field through otherwise lossy and distorting media. The current experimental work relates primarily to laboratory efforts, e.g., metal vapors in a highly controlled environment, or, in our work, to cooled solid state samples. Legitimate questions can be raised as to whether this technology will ever be of practical interest to NASA. On the other hand, the progress in laboratory demonstration and in theoretical mastery of this interesting phenomena are impressive. Possible breakthroughs may occur in high signal rate optical communications technology or in sensing between space and ground through otherwise obscuring media. There is also separate work on diffractionless beams that might be followed, but in the opinion of the PI this latter work does not appear promising [17].

2.2.2 Novel amplification and processing of the return signal

There is an active field addressing techniques for reducing quantum noise in amplifiers. These techniques usually offer an improvement by decreasing noise in a given quadrature and increasing noise in an (unused) conjugate quadrature. We have not seen an obvious strategy of clear value to NASA, but we similarly do not see cause to rule out strategies of this kind.

An approach that might be of some interest would be that of spectrally resolving the signal return prior to detection in a manner that does not discard any signal prematurely. This might be done, for example, using emerging fiber grating array technology. Fiber grating arrays provide high spectral resolution, high efficiency, compact and lightweight components, rugged alignment, and contact with rapidly developing, relatively low cost, communication technology.

We note also the recent successful operation of synthetic aperture optical detection. While this technique is currently only used for ground based observation of satellites it represents a novel technology. This approach appears more useful for enhancing spatial resolution than for improving signal gathering efficiency, but warrants attention.

2.2.3 Novel Detection techniques

Noiseless amplification is not limited to heterodyne strategies. Bondurant, e.g., describes a system where the noise figure of an amplifier is reduced to zero [11]. There, intense beams in a Mach-Zehnder interferometer are designed to balance in such a way that a weak signal in an on-off keying arrangement can be amplified, in principle, with no increase in noise. This example has not been proven experimentally, but it helps make the case that noiseless amplification at the level of a few signal quanta may be a more general phenomena than previously thought. Other schemes for noise figure improvement have been discussed and some improvement demonstrated, as in nonlinear fiber loops. Here squeezing is used to reduce the noise in a particular quadrature.

In our own work we see evidence of nonlinear processes playing a role at the level of single quantum excitations. The main point here is that there appears to be considerable reason to expect improvements in signal detection near the single quantum level by using coherent interference and nonlinear processes. An approach of this kind could provide significant gains and should not be ruled out. At the same time these techniques should not be relied on in the short term since they are demanding of realization, and application to a

problem of practical interest to NASA could be long in maturing. Applications in the atmosphere are more demanding than current laboratory experiments. The fluctuations of the atmosphere and the long distances used in lidar may render the electromagnetic induced transparency techniques that work in a laboratory setting ineffective for lidar. On the other hand, very substantial DoD funding is directed at this set of problems and a prime motivation for that funding is the possibility of enhanced transmission through the atmosphere.

A third relatively unconventional theme is that of a more fully optical lidar system. The incoming signal might be frequency resolved using fiber gratings prior to amplification and a spectrally selective, temporally gated, and nonlinear optical amplifier used in place of current rf and microwave technology. This approach could, in principle, provide faster processing and could be as good or better as regards signal to noise ratio. This is an area where the path is not obvious, but research effort could be warranted.

2.2.4 Interactive generation, transmission and detection

A last area is that of interactive generation, transmission and detection that includes coherent interference, single quantum phenomena, nonlinear processes, and amplification in a relatively distributed interactive manner over the entire signal path. Because light propagates rapidly, there is an opportunity to use optical means to sense the optical path and then modify the generated signal, and possibly the detection scheme, so as to optimize the sensing process in more holistic manner. Electromagnetic induced transparency has shown some advantages in this regard. A control signal sent along with a second signal has demonstrated that otherwise distorting and lossy mechanisms can be significantly reduced. This is a complex, but active and promising area. Our best guess is that improvements that can be adapted to NASA applications are unlikely in the immediate future; however, close attention to this field is warranted.

3. Conclusions

Our essential conclusions are: (1) incorporation of an optical amplifier in existing lidar systems as a preamplifier for weak return signals offers some modest improvements, but is unlikely to result in major breakthroughs, (2) recent work that predicts, and in some cases finds, modest improvement for coherent lidar through application of optical amplifiers appears substantially correct, but the improvement tends to arise from overcoming flaws in the existing technology rather than from a fundamental advantage, (3) if the roles of optical amplification, coherent interference, nonlinear signal processing, use of novel optical technology, are viewed broadly, interesting opportunities emerge, (4) this latter work is at a relatively early stage of development and is probably best viewed as an area of basic research to be pursued and monitored, rather than exploited in the short term. (5) Our own work on electromagnetically induced transparency at the level of one, or a few quanta bears some relevance and warrants following.

We, in particular, wish to thank Michael Kavaya, Farzin Amzajerian, and Gary Spiers for numerous discussions and large amounts of resource material. This work task was well posed and has provided a valuable and stimulating experience.

References

[1] "Normal modes for electromagnetically induced transparency", S.E. Harris, Physical Review Letters **72** (January 1994) pp 52-5.

- [2] "Preparation energy for electromagnetically induced transparency", S.E. Harris and Zhen-Fei Lou, *Physical Review A* **52** (August 1995) pp R928-31
- [3] " Degenerate Quantum-Beat Laser: Lasing without inversion and inversion without lasing", Marlan O. Scully, *Physical Review Letters* **62** (June 1989) pp 2813-6
- [4] "Heterodyne efficiency for a coherent laser radar with diffuse or aerosol targets," R.G. Frehlich, *Journal of Modern Optics* **41** (No. 11), 2115-2129.
- [5] "Coherent laser radar performance for general atmospheric refractive turbulence," R.G. Frehlich and M.J. Kavaya, *Applied Optics* **30** (December 1991) pp 5325-52.
- [6] "Comparison of 2- and 10um coherent Doppler lidar performance," R. Frehlich, *Journal of Atmospheric and Oceanic Technology*, **12** (April 1995) pp 415-20.
- [7] "Coherent launch-side atmospheric wind sounder: theory and experiment," J. G. Hawley, R. Targ, S. W. Henderson, C. P. Hale, M. J. Kavaya, D. Moerder, *Applied Optics* **32** (August 1993) pp 4557-68.
- [8] "Sensitivity improvement of a 1-um ladar system incorporating an optical fiber preamplifier," M. S. Salisbury, P. F. McManamon, B. D. Duncan, *Optical Engineering* **32** (November 1993) pp 2671-80.
- [9] "Optical-fiber preamplifiers for ladar detection and associated measurements for improving the signal-to-noise ratio," M. S. Salisbury, P. F. McManamon, B. D. Duncan, *Optical Engineering* **33** (December 1994) pp 4023-32.
- [10] "Lidar-measured winds from space: A key component for weather and climate prediction," W.E. Baker, et al, *Bulletin of the American Meteorological Society* **76** (June 1995) pp 869-88.
- [11] "Performance of an optical detector preamplifier," S. Rahm, *Optics Letters* **18** (September 1993) pp 1559-60.
- [12] "Fiber-Optic Communication Systems", Govind P. Agrawal, Wiley series in microwave and optical engineering, 1992
- [13] "Quantum limits on noise in linear amplifiers," C.M. Caves, *Physical Review D*, **26** (October 1982) pp 1817-39.
- [14] "Quantum noise properties of a nonlinear amplifier," R.S. Bondurant, *Physical Review Letters* **71** (September 1993) pp 1709-1710.
- [15] "Recent advances in high power semiconductor laser diodes", David F. Welch (tutorial) OSA annual meeting (September 1995)
- [16] " Enhancement of coherent laser radar performance by predetection amplification ", R.J. Morley, H.J. Baker, D.R. Hall, M. Harris, and J.M. Vaughan
- [17] " Localized transmission of electromagnetic energy ", R. W. Ziolkowski *Physical Review A* **39** (February 1989) pp2005-33.
- [18] Manuscript in preparation.

Background References: I. Detection:

"Noise in homodyne and heterodyne detection," H.P. Yuen, V.W.S. Chan, *Optics Letters* **8** (March 1983), pp 177-9.

"Sensitivity enhancement using coherent heterodyne detection," G. Lachs, S.M. Zaidi, A.K. Singh, *Journal of Lightwave Technology* **12** (June 1994) pp 1036-41.

"Quantum noise and excess noise in optical homodyne and heterodyne receivers," J.H. Shapiro, MIT, report under NRL contract N0014-81-K-0662.

"Performance of a 2um coherent Doppler lidar for wind measurements," R. Frehlich, S.M. Hannon, S. W. Henderson, *Journal of Atmosphere and Oceanic Technology*, **11** (December 1994) pp 1517-1528.

"Optimal local oscillator field for a monostatic coherent laser radar with a circular aperture," R. Frehlich, *Applied Optics* **32** (August 1993) pp 4569-4577.

"Speckle characteristics of atmospherically backscattered laser light," J.H. Churnside, H.T. Yura, *Applied Optics* **22** (September 1983) pp 2559-2565.

"Performance of Mean-frequency estimators for Doppler radar and lidar," R.G. Frehlich and M.J. Yadlowsky, *Journal of Atmospheric and Oceanic Technology* **11** (October 1994) pp 1217-20.

"Coherent versus incoherent lidar detection at 2.09 um," J.A. Overbeck, M.B. Mark, S.H. McCracken, P.F. McManamon, B.D. Duncan, *Optical Engineering* **32** (November 1993) pp 2681-9.

"Cramer-Rao bound for Gaussian random processes and applications to radar processing of atmospheric signals," R. Frehlich, *IEEE Transactions on Geoscience and Remote Sensing* **31** (November 1993) pp 1123-31.

"Doppler lidar atmospheric wind sensors: a comparative performance evaluation for global measurement applications from earth orbit," R.T. Menzies, *Applied Optics* **25** (August 1986) pp 2546-2553.

II. Optical Amplifiers

"Laser-amplifier gain and noise", R. Loudon and Harris, *Physical Review A* **48**, (July 1993) pp 681-701

"Optical Amplification: Current Status and Future Trends," M. Federighi and F. Di Pasquale, *SPIE* **2450** (March 1995) pp 110-120.

"Measuring and modifying the spontaneous emission rate of erbium near an interface," E. Snoeks, A. Lagendijk, A. Polman, *Physical Review Letters* **74** (March 1995) pp 2459-62.

"Efficient erbium-doped fiber amplifiers incorporating an optical isolator," M.N. Zervas, R.I. Laming, D.N. Payne, *IEEE JQE*, **31** (March 1995) pp 472-80.

"Performance evaluation of EDFA preamplified receivers taking into account intersymbol interference," L. F.B. Ribeiro, J. R.F. Da Rocha, J. L. Pinto, *Journal of Lightwave Technology* **13** (February 1995) pp 225-31.

"Quantum Noise Reduction in Optical Amplification," Z.Y. Ou, S.F. Pereira, H.J. Kimble, Physical Review Letters, **70** (May 1993) pp 3239-3242.

"High-sensitivity two-stage erbium-doped fiber preamplifier at 10 Gb/s," R.I. Laming, A.H. Gnauck, C.R. Giles, M.N. Zervas, D.N. Payne, IEEE Photonics Technology Letter **4** (December 1992) pp 1348-50.

"Quantum nondemolition measurement of the photon number via the optical Kerr effect," N. Imoto, H.A. Haus, Y. Yamamoto, Physical Review A **32** (October 1985) pp 2287-92.

"Near-quantum optimum receivers for the phase-quadrature coherent-state channel," R.S. Bondurant, Optics Letters **18** (November 1993) pp 1896-8.

"Laser detector preamplifier for CO₂ lasers," promotional literature provided August 1987 by Pulse Systems, Inc., of Los Alamos, N.M. to attendees of Aspen Coherent Laser Radar Conference.

III. Actual detection systems/experiments

"Considerations and calculations concerning the application of an optical amplifier as an output amplifier and preamplifier," F. Malota, European Space Agency translation ESA-TT-1004 (September 1986).

"Pre-detection amplification using a multifold CO₂ laser gain cell," R.J. Morley, D.R. Hall, H.J. Baker, Proceedings of the 7th Conference on Coherent Laser Radar Applications and Technology, FA6 (July 19-23, 1993).

"Optical fiber preamplifiers for lidar detection and associated signal to noise ratio improvement measurements," M.S. Salisbury, P. F. McManamon, B. D. Duncan, unpublished manuscript, Feb. 7, 1994.

"Discrete spectral peak estimation in incoherent backscatter heterodyne lidar. I: Spectral accumulation and the Cramer-Rao lower bound," B.J. Rye, R. M. Hardesty, IEEE Transactions on Geoscience and Remote Sensing, **31** (January 1993) pp 16-27.

"Doppler lidar atmospheric wind sensor: reevaluation of a 355-nm incoherent Doppler lidar," D. Rees and I.S. McDermid, Applied Optics **29** (October 1990) pp 4133-44.

"Sensitivity and signal to noise ratio improvement of a one micron lidar system incorporating a neodymium doped optical fiber preamplifier," M. S. Salisbury, Electro-optics Techniques Section, Wright-Patterson AFB, Ohio; final report for period August 1991 to November 1993.

"Analysis of measurements for solid state laser remote lidar system," F. Amzajerdian, Center for Applied Optics, University of Alabama in Huntsville, submitted to NASA/MSFC, contract no. NAS8-38609, June 1, 1993-September 31, 1994.

"Improvement of a CO₂ Doppler lidar with an optical detector preamplifier," S. Rahm, C. Loth, FA5, 7th Conference on Coherent Laser Radar Applications and Technology, July 19-23, 1993.

"Lidar aerosol backscatter measurements: systematic modeling and calibration error considerations," M. J. Kavaya, R. T. Menzies, Applied Optics **24** (November 1985) pp 3444-53.

1995

NASA/ASEE SUMMER FACULTY FELLOWSHIP PROGRAM

**MARSHALL SPACE FLIGHT CENTER
THE UNIVERSITY OF ALABAMA IN HUNTSVILLE**

**THE DEVELOPMENT, ASSESSMENT AND VALIDATION
OF VIRTUAL REALITY FOR
HUMAN ANATOMY INSTRUCTION**

Prepared By:

Karen Benn Marshall, M.S.

Academic Rank:

**Instructor/Director
Allied Health Program**

Institution and Department:

**Oakwood College
Department of Chemistry,
Biochemistry & Allied Health**

NASA/MSFC:

**Laboratory:
Division:
Branch:**

**Mission Operations
Operations Engineering
Crew Systems Engineering**

MSFC Colleague:

Joseph P. Hale

INTRODUCTION

Virtual reality is the computer graphics creation of an environment which allows its participants to physically interact with objects within an electronic environment. A virtual reality applications program has been under development at the Marshall Space Flight Center (MSFC) since 1989. The MSFC VR systems consist of VPL Research, Inc. EyePhones (Models 1 and LX), DataGloves and software (Swivel 3D, Body Electric and ISAAC), Polhemus Isotrak and Fastrak spatial tracking systems, two Macintosh IIfx computers and two Silicon Graphics Incl. graphics computers (4D/310VGX and 4D/320VGXB). In addition, MSFC is now utilizing WorldToolKit software. The objectives of the MSFC VR applications program are to develop, assess, validate and utilize VR in hardware development, operations development and support, mission operations training and science training.

This research project seeks to meet the objective of science training by developing, assessing, validating and utilizing VR as a human anatomy training medium. Current anatomy instruction is primarily in the form of lectures and usage of textbooks. In ideal situations, anatomic models, computer-based instruction, and cadaver dissection are utilized to augment traditional methods of instruction. At many institutions, lack of financial resources limits anatomy instruction to textbooks and lectures. However, human anatomy is three-dimensional, unlike the one-dimensional depiction found in textbooks and the two-dimensional depiction found on the computer. Virtual reality allows one to step through the computer screen into a 3-D artificial world.

The primary objective of this project is to produce a virtual reality application of the abdominopelvic region of a human cadaver that can be taken back to the classroom. The hypothesis is that an immersive learning environment affords quicker anatomic recognition and orientation and a greater level of retention in human anatomy instruction. The goal is to augment not replace traditional modes of instruction.

RESEARCH PLAN

Previous work, in the summer of 1994, resulted in the creation of a static three-dimensional model of the abdominopelvic region of a human cadaver utilizing RB2 Swivel software, creation of the behavioral relationship between objects in the virtual environment via Body Electric software and establishment of the communications between the two software packages- RB2 Swivel and Body Electric. RB2 Swivel is a 3D modeling tool that runs on the Macintosh in which the appearance and structure of virtual worlds are built. Body Electric, which also runs on the Macintosh, brings the world to life by associating dynamic behaviors with the static Swivel objects. The software that renders the model in action is called Isaac. It runs on fast graphic computers, such as the Silicon Graphics. In real time, Body Electric modifies the whole condition of the world based on information from the physical world and internal process. Still in real-time (up to 30 times a second) Body Electric then sends the newly changed information to Isaac, which renders each object according to the updates received. By utilizing RB2 Swivel, the human body and the organs of the abdominopelvic region were created. These organs were the intestines, liver, gallbladder, stomach, spleen, pancreas, right kidney and left kidney. This 3-dimensional model is currently run on expensive graphic computers utilizing Polhemus Fastrak spatial tracking sensors.

This three-dimensional model has now been modified utilizing WorldToolKit (WTK) for Windows, a library of C functions. WTK has given considerable application

development power to the model. WTK allows the user to utilize an IBM compatible PC, head mounted display unit and joystick to interact with the virtual environment. This modification allows greater usability and will allow application usage in the classroom at a moderate cost.

The modification of the VR training medium consisted of hardware and software components of the WTK development system. These components included the host computer, WTK library, C compiler, RB2 Swivel, IPhoto Plus and 3D Studio software packages, standard mouse and joystick. With these components, one can do all the basic operations necessary to construct and use a virtual world application, including 3-D model creation, image or "texture" capture and editing, application development, and interaction with the finished program. This application development process was interactive and is shown below:

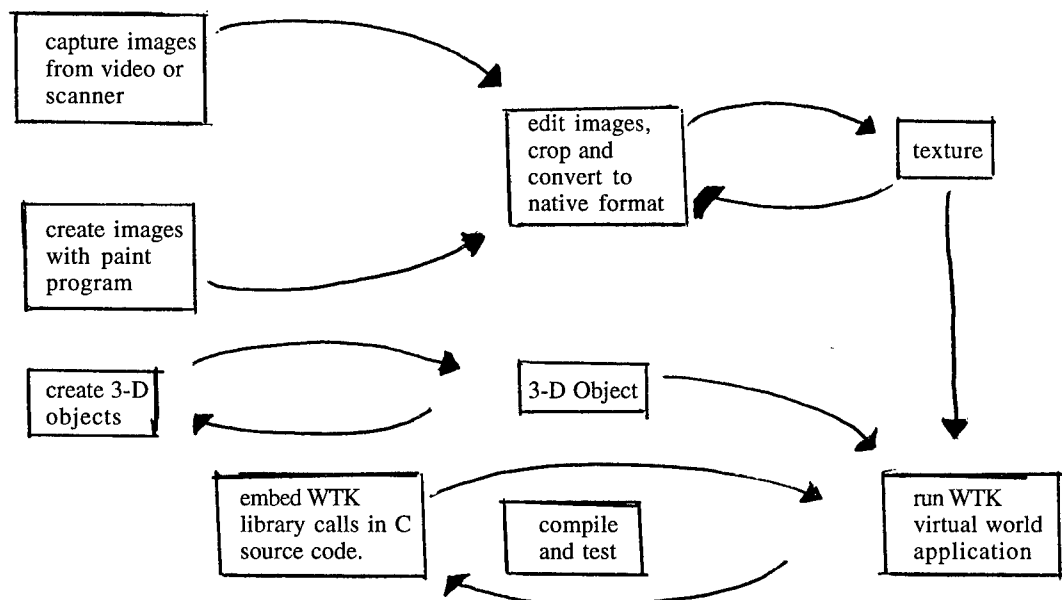


Figure 1. WTK Application Development Process

The 3-dimensional abdominopelvic organs and human body were created utilizing RB2 Swivel and 3D Studio software packages. Photo images of these organs were captured, edited and converted to native form utilizing IPhoto Plus Paint program. The 3-dimensional human body and organs were then loaded into the WorldToolkit Program for Windows as DXF files. WTK library calls were embedded in C source code. The information was compiled and tested. The 3-dimensional virtual reality human cadaver now runs utilizing the WTK virtual world application.

The VR application system as implemented will run on a Pentium PC. The commercial software required is WorldToolKit for Windows. WTK is platform independent and active in supporting new peripherals. In addition, WTK demos can be used to create virtual applications with very little modification. Currently, there are approximately twenty (20) demos on version 2.02. The C code language requirements are simple to master. Examples are included that one can easily cut and paste.

CONCLUSION

In conclusion, the continued development, assessment and validation of virtual reality as a tool for human anatomy instruction will determine if and to what extent an artificial computer graphics simulation of the human body augments traditional modes of instruction. Modification of the current system using WTK has given considerable application development power and will allow greater usability of the model in the classroom at a moderate cost.

Future goals include the expansion of the human cadaver virtual reality model to include all organs, texture mapping, acoustics and haptic and forcefeedback.

ACKNOWLEDGEMENTS

I would like to thank my MSFC Colleague, Joseph Hale, for his support and guidance. In addition, I would like to thank Mark Blasingame and Rick Moseley for their technical assistance in the development of this project.

REFERENCES

1. Benn, Karen. 'The Assessment of Virtual Reality for Human Anatomy Instruction', *Final Report, Contract NASA - CR 196533*, October 1994, p IV-1-4.
2. Burdea, Grigore and Philippe Coiffet. Virtual Reality Technology New York: John Wiley & Sons, Inc., 1994.
3. Durlach, Nathaniel I. and Anne S. Mavor, ed. Virtual Reality:Scientific and Technological Challenges. Washington, D.C.: National Academy Press, 1995.
4. Larijani, L. Casey. The Virtual Reality Primer. New York: McGraw-Hill, Inc., 1994.
5. Roehl, Bernie. Playing God: Creating Virtual Worlds with REND386. California: Waite Group Press, 1994.

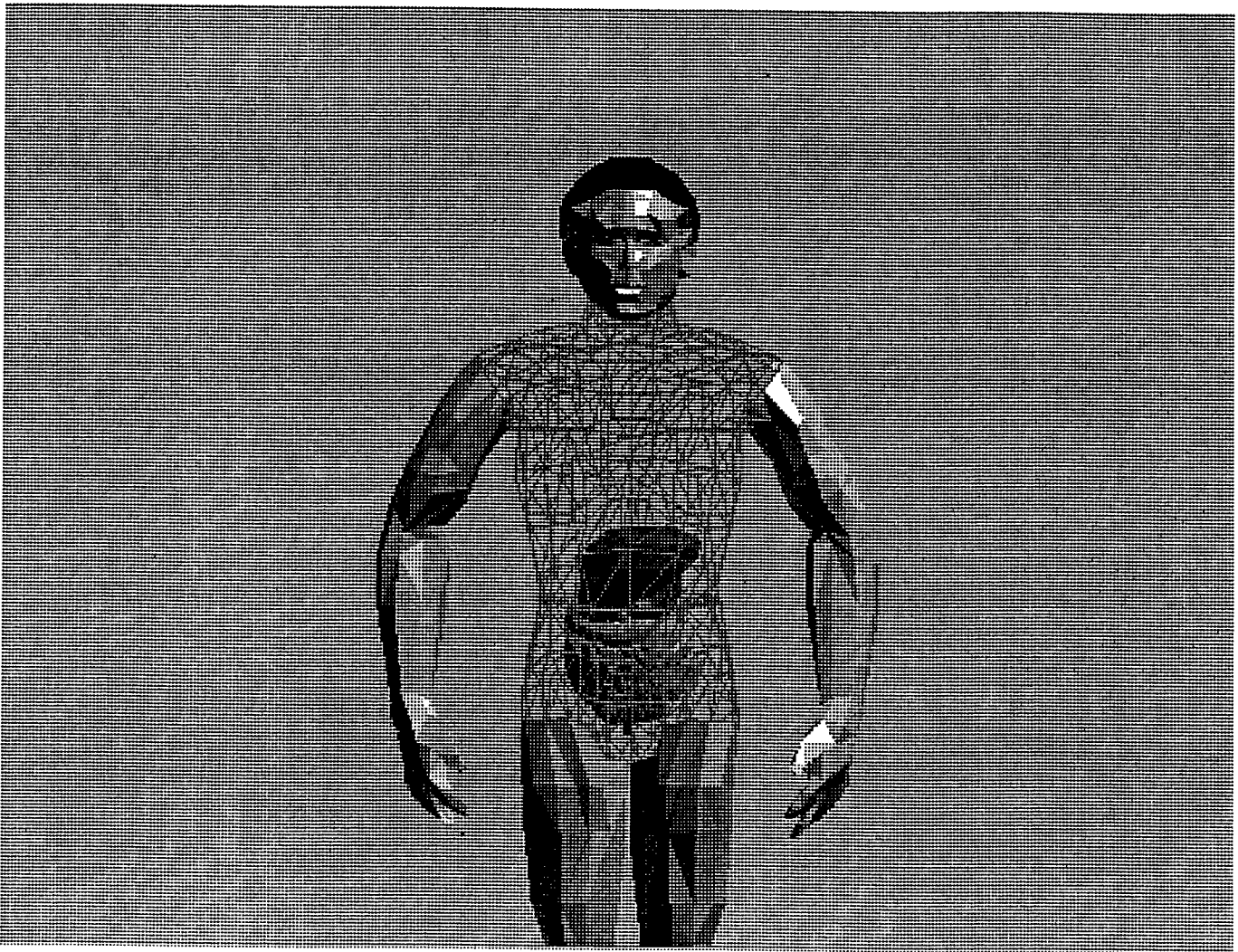


Figure 2 Virtual Cadaver

1995

NASA/ASEE SUMMER FACULTY FELLOWSHIP PROGRAM

**MARSHALL SPACE FLIGHT CENTER
THE UNIVERSITY OF ALABAMA**

MODELING ALUMINUM-LITHIUM ALLOY WELDING CHARACTERISTICS

Prepared by:	Edward L. Bernstein
Academic Rank:	Assistant Professor
Institution and Department:	Alabama A&M University Department of Engineering Technology
NASA/MSFC:	
Laboratory:	Materials and Processes
Division:	Metallic Materials and Processes
Branch:	Metallurgy Research
MSFC Colleague:	Arthur C. Nunes, Jr.

INTRODUCTION

The occurrence of microfissures - small cracks at grain boundaries at temperatures near solidus - has been observed in various metals as a result of the welding process. Aluminum-lithium alloy seems to be particularly susceptible. These defects may take several forms: delaminations in the parent next to the weld fusion line, fusion line cracks through the thickness of the plate, and fissures in the weld material itself. These defects are shown in Figure 1.

Each type of defect is associated with strain in a direction perpendicular to the orientation of the cracks. The susceptibility of a metal to microfissuring is a function of a number of variables, including grain size, heat treatment, material composition, and previous welding history. There does not appear to be a reliable method for prediction of the onset of microfissuring.

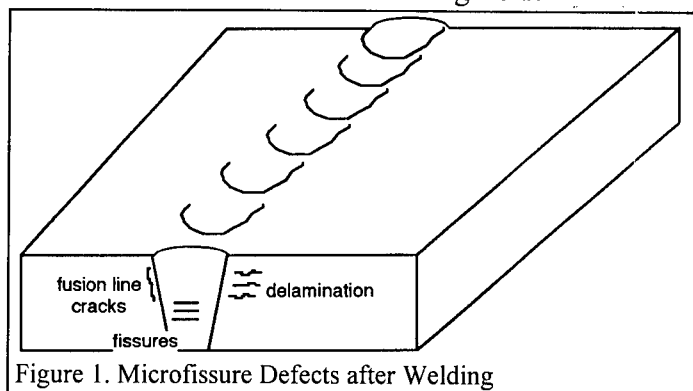


Figure 1. Microfissure Defects after Welding

A theory was developed (Nunes, Ref. 1) in an attempt to explain the onset of microfissures. The theory proposes that microfissuring will occur when three factors are considered: the value of a critical isothermal hot-cracking strain ϵ_c as a function of temperature; a history of plastic strain in the vicinity of the weld, arising from the temperature field produced by the welding heat input into the plate; and a theory of cumulative damage, analogous to Miner's theory of fatigue prediction. This theory depends on the calculation of a damage measure D defined as

$$D = \sum \frac{\Delta \epsilon_p}{\epsilon_c} \quad (1)$$

where $\Delta \epsilon_p$ is the increase in plastic strain resulting from the heating of the material adjacent to the weld. When D reaches a value of unity, microfissuring is expected to occur. A computer model based on the elements of this theory showed a promising correlation with experimental results.

This purpose of this project was to develop a finite element model of the heat-affected zone in the vicinity of a weld line on a plate in order to determine an accurate plastic strain history. The resulting plastic strain increments calculated by the finite element program were then to be used to calculate the measure of damage D . It was hoped to determine the effects of varying welding parameters, such as beam power, efficiency, and weld speed, and the effect of different material properties on the occurrence of microfissuring. The results were to be compared first to the previous analysis of Inconel 718, and then extended to aluminum 2195.

TEMPERATURE DISTRIBUTION

Plastic strains which are believed to lead to the onset of microfissuring develop due to the action of tensile strains in the weld heat-affected zone during the period when this region cools down, while the environment continues to heat up and expand. The region of temperatures in which this effect occurs is a relatively small band adjacent and parallel to the weld line. In order

to accurately model the steep thermal gradients in this region, it was necessary to calculate the temperature distribution to determine the size of this significant area on the plate.

The flow of heat in a plate in the vicinity of a weld has been represented as a moving line source (Rosenthal, Ref. 2) by the equation

$$T - T_0 = - \frac{P_2}{2\pi k d} e^{-\frac{v}{2\alpha} x} K_0\left(\frac{v}{2\alpha} r\right) \quad (2)$$

where $T - T_0$ = temperature above ambient, P_2 = net welding beam power applied to plate, k = thermal conductivity, α = thermal diffusivity, v = velocity of line source, x = distance from line source along weld line, r = radial distance from line source = $\sqrt{x^2 + y^2}$, K_0 = modified Bessel function of second kind and zero order, and d = thickness of plate

The coordinate system used for the analysis is shown in figure 2. The origin is taken at the center of the plate at the point of the heat source. The weld line is along the x-axis, the y-axis represents the distance perpendicular to the weld line at the top surface of the plate, and the z-axis is directed through the thickness of the plate.

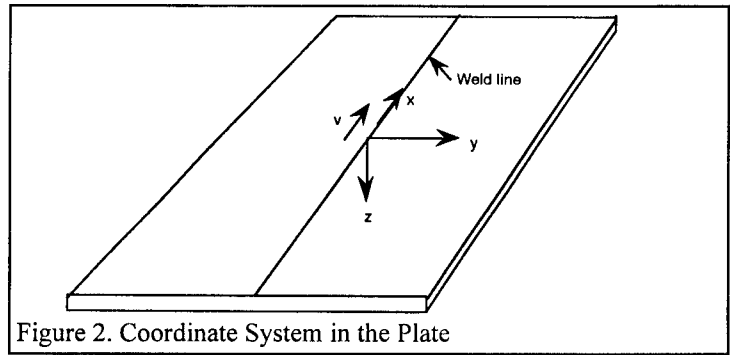


Figure 2. Coordinate System in the Plate

Equation (2) was then evaluated to locate the region of the plate in which rising temperatures cause tensile strains resulting in plastic deformation.

ANALYSIS OF INCONEL 718

Microfissuring of Inconel 718 was analyzed in reference 1. Microfissuring was predicted

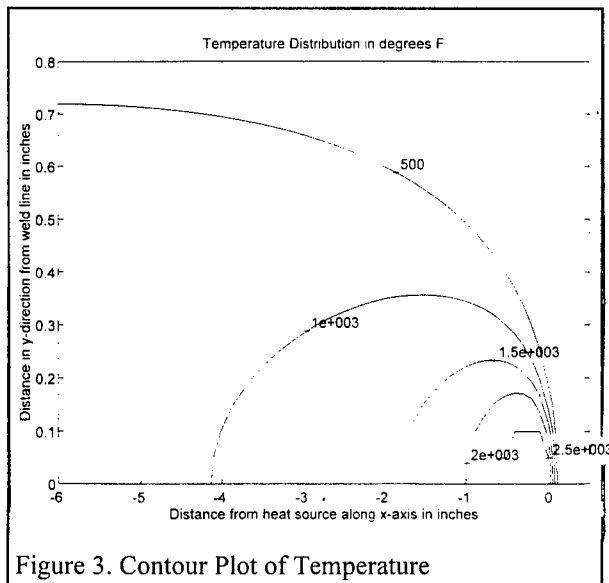


Figure 3. Contour Plot of Temperature

for a power level of 1.7 kW and a welding speed of 7 inches per minute. The same material and welding parameters were examined in the present analysis for comparison. Properties used in equations (1) were $k = 1.61 \times 10^{-4}$ kW/(in 2 ·°F), $\alpha = 0.2977$ in 2 /min, $v = 7$ in./min, and $P_2 = 1.41$ kW. The net power P_2 was calculated using an overall power transfer efficiency estimated at 83%. A temperature distribution was calculated for this case. The results of this calculation are shown in figure 3, as contour lines of constant temperature. Temperatures are also shown in figure 4 in the form of a time history along the line $x = 0$, by setting $x = vt$ at times $x = 0$,

1,2,5,30, and 60 seconds. These illustrations show that the significant temperature ranges occur within a distance of 0.4 inches of the center weld line, and within 4 inches of the heat source along the direction of the weld. This area was then chosen for the construction of the finite element model.

The material properties for Inconel 718 were based on reference 3. A maximum melting temperature of 2500 °F was used. The modulus of elasticity, coefficient of thermal expansion, and yield stress vary with temperature. Poisson's ratio was 0.3.

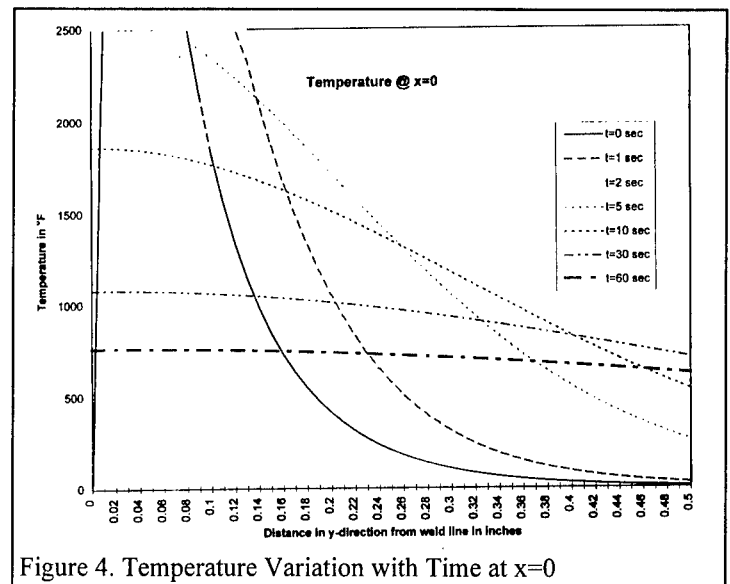


Figure 4. Temperature Variation with Time at $x=0$

MODELING PROCEDURE

The ADINA finite element program was used for the structural modeling. This program allows the specification of temperature-dependent material properties, nonlinear elastic-plastic stress-strain relationships, large deformations, and the ability to progressively accumulate values of plastic strain over a series of time-stepped temperature loadings. An eight-node solid element

was used to construct the model, with 16 elements along the x-direction, ten elements in the y-direction, and three elements through the thickness. A symmetric weld line was assumed along the center line of the plate, and symmetry also assumed at the center plane of the plate, allowing one-quarter of the plate to be modeled by using suitable boundary conditions. The IDEA-S program was used for node and element generation and analysis of results. In order to accurately specify the rapidly varying temperature range, the size of elements was graduated outward from the location of the heat source by a factor of 15. When specifying the

material properties, it was not possible to set the elastic modulus and yield stress equal to zero at the melt temperature, but rather to 0.03% of the maximum value. The strain-hardening modulus was assumed to be 10% of the elastic modulus. The model is illustrated in figure 5.

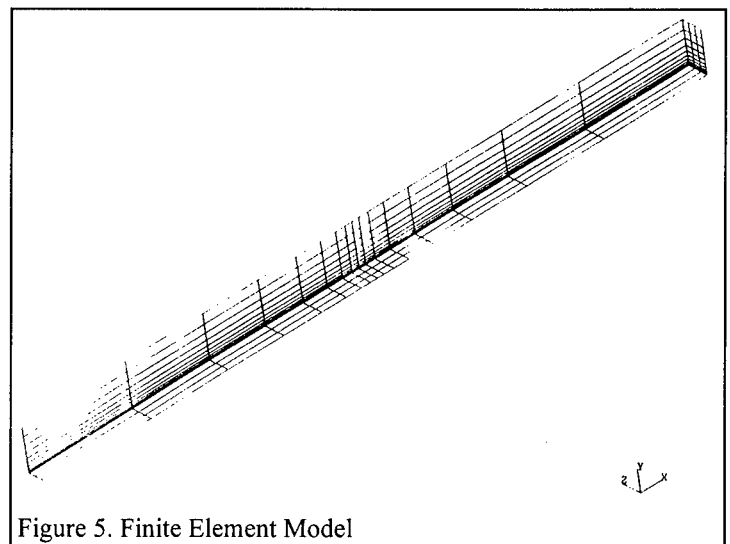


Figure 5. Finite Element Model

RESULTS OF THE FINITE ELEMENT ANALYSIS

The accumulated plastic strains that resulted from the passage of the temperature field along the plate were calculated. The quantities of interest are the strains ϵ_{pzz} associated with

delamination microfissures parallel to the plate surface (see figure 1). The maximum plastic strains occurred at the nodes located at 0.083 in below the top surface of the plate. Figure 6 shows the strains at $x = 0$ for each load step varying along the transverse (y) direction distance from the weld. The magnitudes of the plastic strains range up to 0.014 in./in.

The computation of the damage D from equation 1 was performed by calculating the increase in plastic strain $\Delta\epsilon_{pzz}$ associated with each thermal load step. Each of these increments is then divided by the temperature at that node associated with the thermal load. The result of this calculation is the contribution to the total damage D caused at that load step. In order to perform this calculation, a value for the critical hot-cracking strain ϵ_c was calculated from the expression in reference 1:

$$\epsilon_c = 0.002\sqrt{2}e^{\frac{(T-2475)^2}{2058}} \quad (3)$$

where T is the temperature in $^{\circ}\text{F}$.

A logarithmic plot of ϵ_c is shown in figure 7. This figure reveals that for the material selected for analysis, temperatures that vary more than 150 $^{\circ}\text{F}$ from the melt temperature are associated with extremely large critical strains. Since these critical strains appear in the denominator of the damage term $\frac{\Delta\epsilon_{pzz}}{\epsilon_c}$, the plastic strain increments that are associated with such temperatures make a negligibly small contribution to the total damage D .

A sample calculation was performed to estimate the damage D at a distance of $y = 0.12$ in from the centerline of the weld. This value was selected because it includes the region with significant temperature variation contributing to the total damage. The values used for plastic strain increments $\Delta\epsilon_{pzz}$ and temperature T were interpolated from the results of the analysis. After the summation in equation (1) was performed, a damage value of $D = 1.22$ was found. Since this value is greater than one, the occurrence of microfissures is indicated in this case.

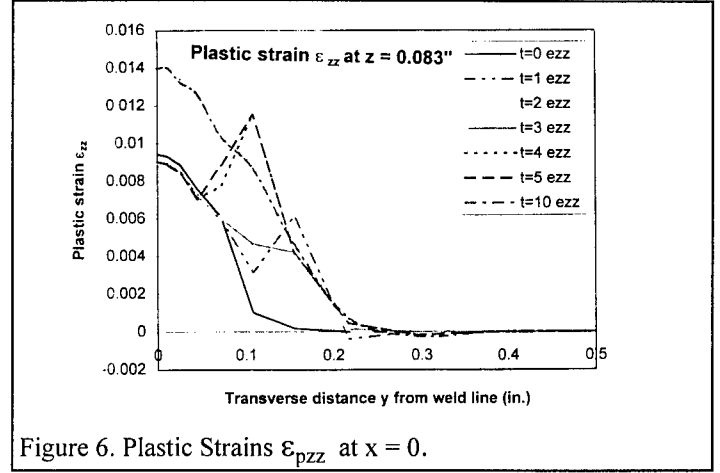


Figure 6. Plastic Strains ϵ_{pzz} at $x = 0$.

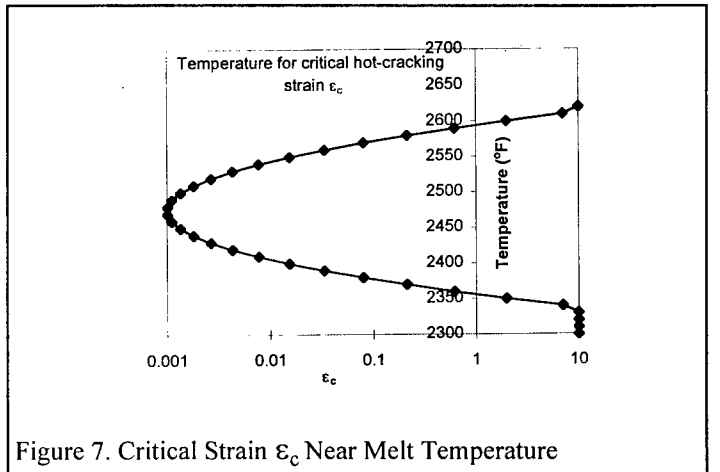


Figure 7. Critical Strain ϵ_c Near Melt Temperature

CONCLUSIONS

This project succeeded in modeling plastic strain in the vicinity of a weld on a plate. Although a range of welding parameters, namely beam power and speed, were not analyzed, due to time limitations, the procedures used in this report could be applied to produce a more general study of the effect of these quantities on incremental plastic strain and the resulting predicted damage measure. They could also apply to other materials, such as aluminum-lithium alloy 2195.

The solution procedure could be made more efficient and parametric analysis done more easily if a combined thermal and structural finite element analysis were performed. This approach could be taken with the ADINA-T program which has thermal modeling capability.

The finite element approach may not be the best way to verify the damage theory of microfissuring. The great variation in stiffness within the structure, due to the mechanical properties near the melt temperature, are likely to cause convergence problems in achieving a solution. Although these problems were overcome in the present analysis by changing the solution technique, there is no guarantee that this would always be possible.

Another difficulty is the fact that the area of the structure is quite small in which the temperature range both produces an increasing plastic strain, and is also so close to the melt temperature that there is a noticeable contribution to the accumulated damage. The small size of this region requires that the finite element mesh be finely graduated so that the temperature variation from node to node is not too large. This effect may well require that the model for each case that is studied must be remeshed and a separate analysis performed.

The small size of the critical area in which the damage will accumulate might be used to construct an approximate analytical expression, valid in a small range of temperatures and distance, which would allow a simplified solution. The resulting expression could then be analyzed to see the effects of varying the weld parameters. A solution of this type would be a more valuable tool and could be used by designers of welding procedures to predict which techniques would result in welds free of microfissures.

ACKNOWLEDGMENTS

The author thanks Art Nunes for his guidance and instruction in the science of welding, Doug Wells for his time spent in assisting with the computer skills required, and Preston McGill for suggestions on usage of ADINA.

REFERENCES

1. Nunes, A., "Interim Report on Microfissuring of Inconel 718," *NASA TM-82531*, NASA George C. Marshall Space Flight Center, June 1983
2. Rosenthal, D., "The Theory of Moving Sources of Heat and Its Application to Metal Treatments," *Transactions of the ASME*, Vol. 68, 1946
3. "Inconel Alloy 718," *Product Handbook*, Inco Alloys International, 1985

1995

NASA/ASEE SUMMER FACULTY FELLOWSHIP PROGRAM

**MARSHALL SPACE FLIGHT CENTER
THE UNIVERSITY OF ALABAMA**

**DAMAGE ACCUMULATION IN CLOSED CROSS-SECTION,
LAMINATED, COMPOSITE STRUCTURES**

Prepared By:	Ronald B. Bucinell, Ph.D, P.E.
Academic Rank:	Assistant Professor
Institution and Department	Union College, Schenectady, NY 12308 Department of Mechanical Engineering

NASA/MSFC:

Laboratory:	Materials and Processes
Division:	Nonmetallic Materials and Processes
Branch:	Polymers and Composites

MSFC Colleague:	Alan T. Nettles
-----------------	-----------------

INTRODUCTION

The need for safe, lightweight, less expensive, and more reliable launch vehicle components is being driven by the competitiveness of the commercial launch market. The United States has lost 2/3 of the commercial launch market to Europe. As low cost Russian and Chinese vehicles become available, the US market share could be reduced even further. This international climate is driving the Single Stage To Orbit (SSTO) program at NASA. The goal of the SSTO program is to radically reduce the cost of safe, routine transportation to and from space with a totally reusable launch vehicle designed for low-cost aircraft-like operations. Achieving this goal will require more efficient uses of materials. Composite materials can provide this program with the material and structural efficiencies needed to stay competitive in the international launch market place.

In satellite systems the high specific properties, design flexibility, improved corrosion and wear resistance, increased fatigue life, and low coefficient of thermal expansion that are characteristic of composite materials can all be used to improve the overall satellite performance. Some of the satellites that may be able to take advantage of these performance characteristics are the Tethered Satellite Systems (TOSCIFER, AIRSEDS, TSS2, SEDS1, and SEDS2), AXAF, GRO, and the next generation Hubble Space Telescope. These materials can also be utilized in projects at the NASA/MSFC Space Optics Technology and System Center of Excellence.

The successful implementation of composite materials requires accurate performance characterization. Materials characterization data for composite materials is typically generated using flat coupons of finite width. At the free edge of these coupons the stress state is exacerbated by the presence of stiffness and geometric discontinuities. The exacerbated stress state has been shown to dominate the damage accumulation in these materials and to have a profound affect on the material constants. Space structures typically have closed cross-sections, absent of free edges. As a result, composite material characterization data generated using finite width flat specimens does not accurately reflect the performance of the composite materials used in a closed cross-section structural configuration.

Several investigators have recognized the need to develop characterization techniques for composite materials in closed cross-sectioned structures [1-3]. In these investigations test methods were developed and cylindrical specimens were evaluated. The behavior of the cylindrical specimens were observed to depart from behavior typical of flat coupons. However, no attempts were made to identify and monitor the progression of damage in these cylindrical specimens during loading. The identification and monitoring of damage is fundamental to the characterization of composite materials in closed cross-section configurations. In the study reported here, a closed cross-sectioned test method was developed to monitor damage progression in 2 in. diameter cylindrical specimens and 1.5 in. finite width flat coupons subjected to quasi-static, tensile, loading conditions. Damage in these specimen configurations was monitored using pulse echo ultrasonic, acoustic emission, and X-ray techniques.

In the remainder of this report the specimen configuration and test method are describes, the non-destructive evaluation techniques are summarized, and the preliminary results discussed. Because the efforts being reported on here are part of a larger characterization study, the larger

characterization study will also be described. This report will conclude with a summary of the progress made on this study.

CLOSED CROSS-SECTION SPECIMEN AND FIXTURE DESCRIPTION

The investigation into the characterization of closed cross-sectioned composite material structures utilizes both flat, finite width, coupons and cylindrical specimens as seen in Figure 1. Two laminate stacking sequences are used in the fabrication of these specimens, $[\pm 45/90/0]_s$ and $[\pm 45/0/90]_s$. These laminate stacking sequences are chosen because they isolate the effects of the Mode I and II interlaminar damage initiation and propagation mechanisms during static and fatigue loading [4].

The finite width specimens were manufactured using 0.005 in thick AS4/3501-6 prepreg tape and a standard cure cycle. The end tab material is a Spalding G-10 fiber glass sheet that is attached to the coupon using Newport NB102 film adhesive. The Tube specimens were manufactured using 0.01 in AS4/3501-6 towpreg tape supplied by Fiberite Corporation and a standard cure cycle. The end-tab material is Fiberite MXB 7701/7781 glass/epoxy cloth that is co-cured with the cylindrical specimens.

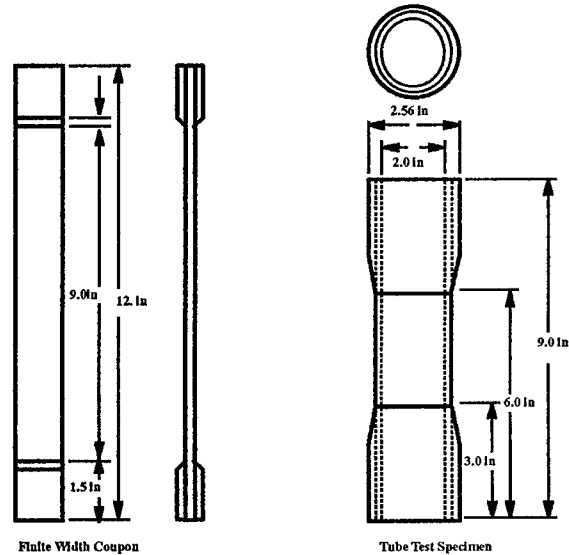


Figure 1: Test specimen configurations used in damage investigation.

Tube testing has yet to be standardized or widely accepted in the composites community, therefore, a test fixture to test the tube was designed and fabricated for this testing program at Union College. The test fixture is seen in Figure 2 attached to the 100 Kip load frame at the NASA Marshall Space Flight Center. The fixture uses mechanical jaws inside the housing, seen enclosing the test specimen in Figure 2, to grip the specimen. Both the top and bottom housings have 4 independent, concentric, grip sections that are hand tightened by threaded studs to a torque of 100 ft-lbs. To prevent the tubes from being crushed by this loading, an expanding collet insert is placed in the top and bottom of the tube end tab region to support the inner wall of the tube.

TEST MATRIX AND DAMAGE MONITORING TECHNIQUES

The evaluation in this study focuses on the accumulation of damage under quasi static tensile loading conditions. Both tube and finite width coupons were utilized in order to make a comparison between the damage accumulation characteristics in these two structural geometries. Damage was monitored using a gated pulse echo ultrasonic, acoustic emission, and x-ray techniques.

Five finite width coupons for each of the laminate geometries were tested in this study. The coupons were loaded to 70% , 90%, and 100% of their ultimate strength. At each of these load level the specimen was removed from the test fixture and impregnated with a dye penetrant and x-rayed. These x-rays were used to monitor the damage accumulation. Data generated as a result of these experiments compared favorably with previous studies [5,6]

The test matrix for the tubes is much more extensive than the finite width specimens because of the scant amount of data on damage progression in composite tubes. Twenty four tubes were tested in each of the previously described laminate configurations. Four tubes of each type were loaded to 60%, 70%, 80%, 90%, 95%, and 100% of the ultimate strength of the tubes. Prior to the testing each tube, an ultrasonically inspection was made in order to identify flaws in the tubes that were not related to the loading. The tubes were also ultrasonically inspected after each of the load levels in order to determine if this technique could be used to monitor damage progression. The acoustic emission sensor pictured in Figure 2 was attached to one specimen at each of the load levels to monitor the acoustic signature of the damage progression. After the tubes reached their designated load level, the tubes were cut axially into two halves, impregnated with a dye penetrent, and x-rayed. This technique allowed the coupon and tube damage progression data to be directly compared. This technique also aided in the interruption of the ultrasonic and acoustic emission data.

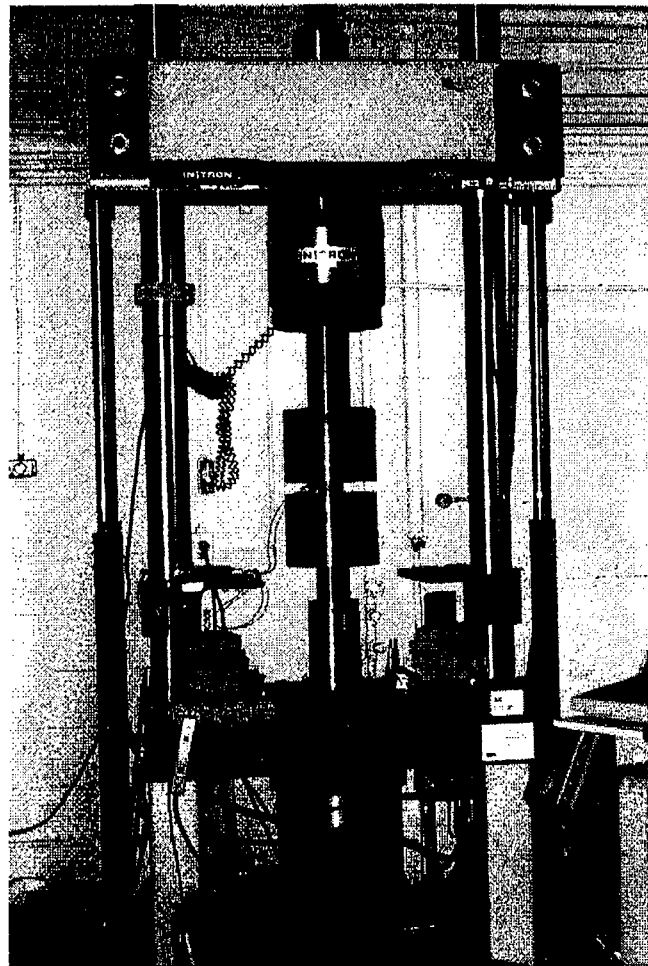


Figure 2: Load frame and test fixture used in the evaluation of the 2 in diameter composite tube specimens.

PRELIMINARY RESULTS

The ten week term for this project barely provided enough time to perform all of the designated testing and inspection described above. Thus, reflection on the data generated has yet to commence. However, some preliminary results do look interesting.

Radiographic images of the damage progression in the flat coupons show several damage types that proceed failure of the coupon. The damage includes transverse cracks in the 90°

layers, splitting in the 45° layers, and interlaminar delamination between layers. The radiographic images of the tube only indicate the presence of transverse cracking in the 90° layers. This was expected since interlaminar delamination is typically a free edge phenomenon. The constraint of the cylindrical geometry could be constraining the 45° layer from straining in a fashion that would lead to transverse cracking.

The only other preliminary data comes from direct observation. Both the flat coupon and tube specimens were very audible during testing. Both specimen geometries exhibited a unique set of sounds that appear to be related to fiber failure, bundle failure, and matrix cracking. The observations of these sounds were recorded during the testing. It is hoped that the inspection techniques used will help to positively identify the source of these sounds.

SUMMARY AND FUTURE WORK

The work performed this summer is the initial phase of a much larger composite materials characterization effort. To maximize the efficiency of composite materials, it is necessary to characterize the progression of damage during the life of the material in a given structure. The onset of damage can be a result of static and fatigue loads, impact events, thermal loading, etc. The anisotropic and heterogeneous nature of the material complicates the analytical evaluation of a composite structure. Since the geometric flexibility of composite materials provides the designer with an infinite number of material configurations, much work is still needed to build the analytical tools to design and evaluate composite structures.

REFERENCES

1. Andrews, K.B., Fatigue Damage Accumulation and Property Degradation in Flat Versus Cylindrical Specimens, Masters Thesis, Texas A&M University, Department of Civil Engineering, 1992.
2. Groves, S.E., "Characterizing the Failure of Composite Structures," LLNL Thrust Area Annual Report, 1990
3. Norman, T.L., Civelek, T.S., Prucz, J., "Fatigue of Quasi-Isotropic Composite Cylinders Under Tension-Tension Loading," Journal of Reinforced Plastics and Composites, 11(1992), pp. 1286-1301.
4. Bucinell, R.B., "Formation of free-edge delamination in graphite/epoxy laminates subjected to static and fatigue loading, Proceedings of the JANNAF Composite Motor Case Subcommittee Meeting, May 17-18, 1989.
5. Bucinell, R.B., Wang, A.S.D., "A stochastic model for fatigue delamination growth in laminates subjected to constant amplitude loading, " Proceedings of the Applied Mechanics and Engineering Science Conference, Berkeley, CA, (1988)

6. Bucinell, R.B., Wang, A.S.D., "Delamination crack growth in fatigue loaded laminated composite materials," Proceedings of the 23rd Annual Meeting of the Society of Engineering Science, Buffalo, NY, (1986)

1995

NASA/ASEE SUMMER FACULTY FELLOWSHIP PROGRAM

**MARSHALL SPACE FLIGHT CENTER
THE UNIVERSITY OF ALABAMA IN HUNTSVILLE**

PARTICULATE ELECTRON BEAM WELD EMISSION HAZARDS IN SPACE

Prepared By:	Patrick H. Bunton, Ph.D.
Academic Rank	Assistant Professor
Institution and Department:	Austin Peay State University Department of Physics
NASA/MSFC:	
Office:	Materials and Processes
Division:	Metallic Materials and Processes
Branch:	Metallurgical Research
MSFC Colleague(s)	Arthur Nunes, Ph.D. Carolyn Russell

Introduction

The electron-beam welding process is well adapted to function in the environment of space. The Soviets were the first to demonstrate welding in space in the mid-1980's. Under the auspices of the *International Space Welding Experiment (ISWE)*, an on-orbit test of a Ukrainian designed electron-beam welder (the Universal Hand Tool or "UHT") is scheduled for October of 1997. The potential for sustained presence in space with the development of the international space station raises the possibility of the need for construction and repair in space. While welding is not scheduled to be used in the assembly of the space station, repair of damage from orbiting debris or meteorites is a potential need. Furthermore, safe and successful welding in the space environment may open new avenues for design and construction. The safety issue has been raised with regard to hot particle emissions (spatter) sometimes observed from the weld during operations. On earth the hot particles pose no particular hazard, but in space there exists the possibility for burn-through of the space suit which could be potentially lethal. Contamination of the payload bay by emitted particles could also be a problem.

Experimental Evidence and Parameters of the Problem

Experiment has suggested a correlation between metal gas content and sparking during electron beam welding.¹ When dissolved gas was intentionally introduced to a metal by an unshielded tungsten-arc weld, particle emissions were observed during electron-beam welding of the same region. Furthermore, anecdotal evidence suggests that the presence of dissolved volatiles in targets decreases the quality of films formed by electron-beam evaporation. The presence of hydrogen contamination has also been reported to be associated with sparking during welding and hydrogen is known to be a source of porosity during welding.² Data from the international space welding experiment contamination tests suggest a correlation between butt welding and sparking. One possible interpretation is that butting two metal plates together forms little pockets of contaminants due to the surface roughness at the interface. Residual surface contaminants such as machine oil may vaporize during heating thus forming gas bubbles in the advancing weld pool.

The UHT is not intended to operate in the keyhole formation power density regime more common of electron beam welding. Keyholing should be avoided so that the beam does not pass through the sample and impinge another surface. According to The Physics of Welding³ a power density of order 10^{10} W/m² is needed for keyhole formation. Assuming a voltage of 8 kV and current of 100 mA for the UHT yields a power of 800 W. Hence the beam would have to be focussed to a diameter of about 0.32 mm to expect keyhole formation. However, other circumstances may alter this; for example, we observed keyhole formation in a hydrogenated sample of 304 stainless at an energy density that did not produce a keyhole in the normal material.

Four possible mechanisms of spatter are discussed. Experimental results on electron beam welding of 5456 aluminum, 304 stainless steel, and Ti-6Al-4V titanium are then presented. Finally, the results are discussed in light of the potential mechanisms.

A. Spatter by Recoil Pressure

Spatter may occur due to the impulse applied to the surrounding fluid when the small volume above the gas pore quickly vaporizes. The presence of a pore near the melt surface within the irradiated area results in increased local heating. Energy that otherwise would have been conducted away is trapped by the low thermal conductivity of the pore. The increased temperature results in enhanced vaporization above the pore. The recoil force of the vaporizing particles pushes against the melt rather like a piston forcing emission of fluid as shown in figure 1. At sufficiently high beam energy, such vaporization could occur even in the absence of a pore and drilling results.⁴

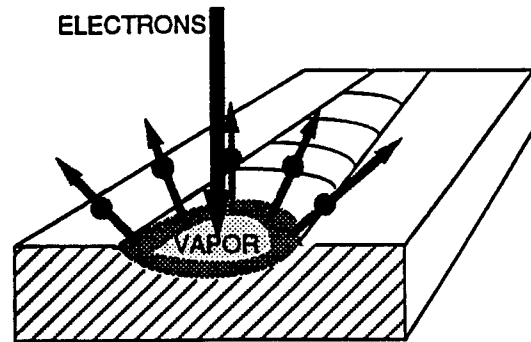


Figure 1: Vapor-pressure-induced spatter. Vapor pressure acts like a piston forcing liquid from the melt.

B. Spatter by Snapping Open of a Pore

One possible source of spatter is the snapping open or "popping" of a pore at the surface as shown in figure 2. Using an assumed geometry, we calculated the change in surface area for a bursting pore. Recall that surface energy is generally proportional to surface area. Our results indicated that using surface energy alone, only very tiny masses could be removed corresponding to particle diameters of order fifty microns assuming all of the mass goes into one drop. It seems more likely that the emitted material would break up into several smaller drops resulting in emission of a ring of smaller droplets.

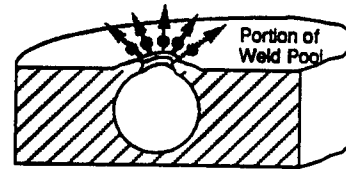


Figure 2: Snapping open or bursting of a bubble could lead to emission of a ring of small droplets.

C. Spatter by Collapse of the Pore

Particles may also be emitted by the collapse of a pore after it bursts. The sequence of events is described in figure 3. After the pore snaps open (emitting small droplets as discussed above), one may be left with a cavity in the surface. The cavity collapses due to surface tension and the inertia of the fluid moves mass away from the surface. The drop breaks away and the surface is returned to its initial state. We modeled this process as follows. The initial surface area is taken to be the area of the cavity after the pore snaps open. The final surface area is taken to be that of the emitted drop plus the area surface necessary to restore the surface to its undisturbed state. The surface energy times the change in surface area is the energy available. This approach neglects the initial loss of surface area upon the opening up of the pore. We assume that this energy is already lost to small spatter (as discussed in B) and fluid motion before the closer process begins. Under these

assumptions and assuming the radius of the initial pore is r_1 , the change in surface area upon emission is $3\pi r_1^2$ and the available surface energy is the surface energy times that. In a perfectly efficient process, this could just eject (zero speed) a particle of radius $0.866r_1$. To get what we hope is a more reasonable estimate of the resultant particle emission we assumed that one half of the energy went into particle ejection and the remaining into motion in the melt. Under this assumption the maximum radius (zero speed) of an emitted particle would be $0.612r_1$. This maximum radius corresponds to emission with zero kinetic energy. If instead we assume one fourth of the available energy goes into kinetic energy and one fourth goes into surface energy (with the remaining one half still lost to the melt), then the radius of the emitted particle would be $0.433r_1$. In this scenario the speed of the emitted particle would be

$$v = 3.7 \sqrt{\gamma/\rho r_1}.$$

By way of example, a pore of radius $250 \mu\text{m}$ in pure aluminum would lead to emission of a particle of $108 \mu\text{m}$ radius with speed 4.3 m/s .

D. Spatter by Change in Beam Focus

An experiment was performed prior to this work where the electron beam focus was changed during the course of a weld in one inch thick aluminum. A sudden change in focus from the bottom of the plate to 25% higher led to the formation of a hole in the surface several millimeters in diameter.

Experimental Results on Electron Beam Welds

The UHT was not available so a Hamilton-Zeiss electron beam welder was used for the performance of the following welds.

5456 Aluminum

The degree of sparking in bead-on-plate welding of 5456 aluminum depended on the focus with more sparking at tighter focus. With a sufficiently defocused beam a regime was found where sparking occurred at about one spark per eight inch weld (40kV, 10 mA and 10 in/min). Operating in this regime, a sheared butt joint showed a few sparks. Intentionally roughed joints showed more sparks. A very rough butt joint was prepared with a film of oil on half its length. Sparking was enhanced in the oil region. This may be ascribed to the oil vaporizing and forming pores in the melt. Another butt joint was prepared with various sized center punch holes along the faying surface. The

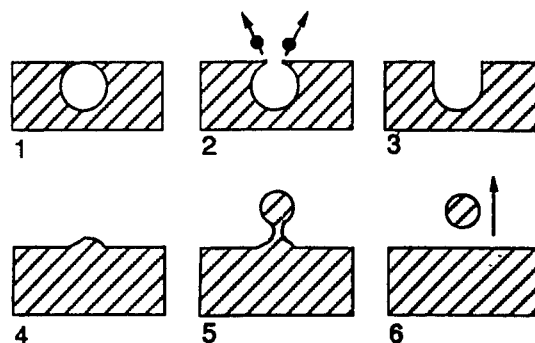


Figure 3: The bursting of a pore at the weld-pool surface may leave a cavity in the surface. The collapse of such a cavity could lead to emission of a drop as sketched.

joint alternated about every other inch between center punch holes and undamaged material. Our hope was that the holes would become pores in the melt. Half the plate had the holes just below the surface and the other half had holes deeper in the material. The half with the holes near the surface sparked more than the half with the holes below the surface; however, the sparks did not completely correlate with the hole locations.

304 Stainless Steel

Bead-on-plate welds of 304 stainless resulted in little sparking even at very high key-holing energy densities. A milled smooth butt joint emitted a few tiny sparks and one larger one. A rough butt joint emitted lots of small sparks; however, the welder reported that the surface appeared different with the presence of what he termed mill scale so some difference besides just edge roughness may have been involved.

It is known that the presence of hydrogen in a metal can lead to weld porosity. Plates of stainless were impregnated with hydrogen by heating in a hydrogen atmosphere. A normal stainless plate and a hydrogenated one were simultaneously mounted in vacuum for welding. The normal stainless did not spark at all while the hydrogenated material sparked dramatically. Additionally, the hydrogenated sample keyholed at the same power density where the normal sample did not. This was repeated at lower power density where the hydrogenated material did not keyhole, and the hydrogenated material still sparked considerably. Since the hydrogenated material also had a thick oxide layer, a non-hydrogenated sample was prepared with a surface oxide using a torch in air. The oxidized but otherwise normal 304 stainless did not spark.

Ti-6Al-4V Titanium

A bead-on-plate weld of titanium produced no sparks. An attempted rough butt weld produced at least one spark, but we had difficulty getting the puddle to bridge the gap and consistently fuse.

Conclusions

Vapor-pressure driven expulsion of liquid tentatively fits well with the observations. The presence of pores would thermally insulate the surface resulting in vaporization of material above the pore. The vapor pressure (more properly, the recoil pressure of the evaporating particles) pushes on the liquid expelling some of it. Recall that aluminum seemed to spark more readily than steel or titanium. This may be accounted for by the higher boiling temperatures of steel and titanium as compared to aluminum. While it was not part of this study, previous work has indicated that 2219 aluminum sparks less readily than 5456 aluminum. The 5456 contains magnesium which would result in higher vapor pressures at lower temperatures. Hydrogen is known to lead to porosity, so this mechanism is consistent with the sparking from hydrogen as well. We observed both emission of single droplets and emission of "sprays" of droplets that could perhaps be identified with emission of a ring of droplets that one would expect from this mechanism. Butt welds may entrap volatile material. The volatile material could possibly result in pore formation and/or increase the vapor pressure beyond its normal value for the pure material. Still, we cannot conclusively rule out

contributions from the other proposed mechanisms or perhaps even mechanisms which we have not yet considered.

Finally, a few observations of some potential concern follow. Hitting a previous tack weld which had been made in vacuum resulted in sparking. There were indications that sparks were more likely at the start or finish of a weld. When the weld begins by climbing up over the edge of the plate, the energy density on the metal at the edge is increased due to the change in angle of exposure to the beam. This may sometimes account for the increased sparking at the beginning; however, there may have been cases of increased sparking when the beam was first turned on even when not climbing over the edge. The change of surface area exposed to the beam because of angle of exposure could also play a role in sparking from butt welds. This might further predict sparking in cases of undulations of the molten pool surface. Sparks resulted when the beam was cutting a channel. The possibility exists that sparking could occur from the weld root when welding in the keyhole regime. Finally, contamination on the surface from the electron beam hitting the fixture prior to the start of the weld may have contributed to sparking.

Acknowledgements: Thanks to Craig Wood for performing the electron beam welds. Thanks to George Talia of Wichita State University for performing the metallography on an emergency stop in a VPPA weld.

References

1. C. Russell, A. Nunes, and R. Carruth, "Characterization of the Molten Weld Pool Produced by Electron Beam for the International Space Welding Experiment," Materials and Processes Laboratory, George C. Marshall Space Flight Center, National Aeronautics and Space Administration, internal report (May 25, 1995).
2. D. G. Howden and D. R. Milner, "Hydrogen Absorption in Arc Melting," British Welding Journal (June, 1963) 304-316; G. R. Salter, "Hydrogen Absorption in Arc Welding," British Welding Journal (June, 1963) 316-325; R. A. Woods, "Porosity and Hydrogen Absorption in Aluminum Welds, Welding Res. Supp. (Mar., 1974) 97-s - 108-s.
3. The Physics of Welding, 2nd ed., ed. J. F. Lancaster, (Pergamon Press, NY, 1986)307-309.
4. C. L. Chan and J. Mazumder, "One-dimensional steady-state model for damage by vaporization and liquid expulsion due to laser-material interaction," J. Appl. Phys. **62** (11) (1987) 4579-4586.

1995

NASA/ASEE SUMMER FACULTY FELLOWSHIP PROGRAM

**MARSHALL SPACE FLIGHT CENTER
THE UNIVERSITY OF ALABAMA IN HUNTSVILLE**

WEB INTERFACES TO RELATIONAL DATABASES

Prepared By: W. H. Carlisle, Ph.D.
Academic Rank: Associate Professor
Institution and Department: Auburn University
Department of Computer Science and Engineering

NASA/MSFC

Office: Program Development
Division: Advanced Systems and Technology
Branches: Advanced Concepts Office,
Space Science and Applications

Office: Science and Engineering Astrionics Laboratory
Divisions: Avionics Simulation Division, Software Division
Branches: Computer Systems Engineering,
Requirements and Technology

MSFC Colleague(s): Vance Houston & Dan O'Neil, MSFC Colleague
Les Johnson, MSFC Colleague
Steve Jones, Ron Newby, MSFC Colleague
Brandon Dewberry, MSFC Colleague

This reports on a project to extend the capabilities of a Virtual Research Center (VRC)¹ for NASA's Advanced Concepts Office. The work was performed as part of NASA's 1995 Summer Faculty Fellowship program and involved the development of a prototype component of the VRC -- a database system that provides data creation and access services within a room of the VRC. In support of VRC development, NASA has assembled a laboratory containing the variety of equipment expected to be used by scientists within the VRC. This laboratory consists of the major hardware platforms, SUN, Intel, and Motorola processors and their most common operating systems UNIX, Windows NT, Windows for Workgroups, and Macintosh. The SPARC 20 runs SUN Solaris 2.4, an Intel Pentium runs Windows NT and is installed on a different network from the other machines in the laboratory, a Pentium PC runs Windows for Workgroups, two Intel 386 machines run Windows 3.1, and finally, a PowerMacintosh and a Macintosh IIsi run MacOS.

Summer Activities Overview

The project's completion will provide a World Wide Web interface into a database system, the Advanced Concepts Information System (ACIMS). Initial activities consisted of network installations and software configurations within the laboratory so that all systems would be Web clients. One client system within the laboratory, the Windows NT machine, was installed on a different network (138.115.xx.xxx) from the other systems (128.158.xx.xxx). Additionally a Mosaic web server was installed on both the NT and on the SUN/SPARC 20 machines. To support software development on the SUN/Solaris machine, the gnu C compiler, a Perl interpreter, and mSQL -- a public domain (for nonprofit institutions) database server, were retrieved from the network and installed on the SUN. During this time planning activities of the project were conducted. This involved investigations into current Web interfaces to database systems, and the installation of one such system for testing. None of the existing systems was as desired for the VRC system, and consequently a prototype system consisting of the mSQL database and Web pages that query and insert information into this database was implemented. Both C and Perl CGI scripts were written to interface the Web to the database server. The following sections present in more detail the information associated with this overview.

An Interface to the Virtual Research Laboratory: The World Wide Web

The World Wide Web (WWW)² has become the de facto standard for sharing resources over the Internet, largely because web browsers are freely available for the most common hardware platforms and their operating systems.³ The WWW provides the opportunity to share images, video, audio, etc., and extensions to the server standards now allow for clickable script execution. Soon to be available are animation⁴ and virtual navigation capabilities.^{5 6} Within the Web the VRC seeks to provide access to information associated with the Advanced Concepts Office. To understand how the Web can provide information to clients we first discuss how the WWW functions.

How the World Wide Web Works

The WWW acts with clients and servers. Clients request pages (screens) via an address called a Uniform Resource Locator (URL). This address contains not only information location but also specifies the way (protocol) in which communication is to be conducted. The most common communication protocol used by Web clients is Hypertext Markup Language (HTML). Requests are sent to a hypertext protocol server program (http). The client expects that a server will return text containing "markup," that provides formatting information as defined by the HTML language.⁷ The client, upon receiving the document, formats and presents it to the user. The power of the HTML languages is that other URLs can be part of the format (hypertext links). To support easy navigation the client software tracks the mouse. When clicked over the presentation of a URL link, another server request is generated.

Servers simply wait for client requests on the network, and return requested pages to the clients. Although this mechanism is the foundation for the World Wide Web, it is not sufficiently powerful to allow the server to itself become a client of other services such as a database server. For this capability it is necessary that a URL cause a server to execute a program and return the results of execution to the client. Such capabilities are provided by extensions such as the Common Gateway Interface (CGI).⁸ For this service, a client requests a URL that is a program in a special directory of the server. The server recognizes that requests to this directory are programs and runs the requested program. The client also sends information to the server that is required as input to the server programs, and so the first function of server programs is to retrieve any further information that was sent by the client, decode it, and then run the program. The client is expecting an acceptable type of document as a return, generally HTML, so the final function of the script is to generate an HTML document and return this document to the client.

As mentioned in the overview above, CGI server software for a Windows NT⁹ and a SUN Workstation¹⁰ were installed. Although the SUN system will be the primary server for the laboratory, it was desirable to experiment with the NT operating system and compare its capabilities with those of UNIX on the SUN. The laboratory's NT machine is installed on a more secure CAD/CAM network. This network will not allow external clients, but machines on this network can be a client of other networks. This installation allows inter-network experimentation, but restricted the NT server testing to the CSD/CAM network. Client software was installed on all hardware in the laboratory. Initially the web server was the public domain HTTPD, but the Netscape¹¹ software that was purchased for the laboratory arrived, was installed, and replaced the SUN server and the clients on all machines in the laboratory. Netscape provides the user authentication that is desired for access to some components of the database.

Interfacing Web Clients and Database Servers with CGI Scripts

Several different groups have built Web database servers using CGI scripts for servers. Gsql¹² was one of the first such software systems. This software allows the user to specify details required to form an SQL language database query. The CGI script parses an SQL specification file to create a form that is presented to the client. With client input, the script

builds a database query, then calls a database backend program to retrieve the information from the database. The script then builds a text (not HTML) return of the information. Another example of using CGI scripts to access a database server is an example system built by Oak Ridge National Labs to make a database of textile and apparel manufacturers and their capabilities available over the World Wide Web to the apparel industry (experimental site)¹³. This system is special purpose for the application, but provides a good example of how web interfaces to database systems can be built. The European Southern Observatory generated software (WDB)¹⁴ to make Hubble Space Telescope information (ST-ECF science data archive) available to the scientific community. The WDB system is a general purpose database interface, that is, not tied to a particular database, and so was investigated for its applicability to the ACIMS.

Although the interface between the WWW client and a HTTPD server is well defined, there is no standard for interfacing a database client with a database server (although efforts in this direction are being made). Currently each database system has its own separate database interface protocol, and the choice of the database determines the CGI program.

Since the http server must become a client of a database server, HTTP servers are implemented more easily within multitasking operating systems such as UNIX and Windows NT. Although the database systems for Windows NT are cheaper, they generally have their roots in DOS and cannot handle multiple clients who wish to access the database. Only the UNIX database systems having their roots in mainframe systems support the distributed database management that is desired for a networked system. Within UNIX the most common database systems are Sybase¹⁵, Oracle¹⁶, Informix¹⁷, Ingres and mSQL. The Oak Ridge software system and ESO system targeted Sybase as the database server. The gsql software targeted Oracle. Oracle was chosen for the final version of the ACIMS database, and while awaiting arrival of software to support a C or Perl interface to Oracle, an mSQL database system was installed on the SUN system. mSQL is a small, public domain, and open source database system.¹⁸

After installation of the mSQL software, a prototype database was built. The tables in this database are shown in the appendix. This database would allow for experimentation with the Web database server system known as WDB, an investigation into its possible use for the ACIMS, and experimentation with other CGI-script interfaces to database systems.

WDB

In order to experiment with the WDB system it was necessary to first install and configure the Perl¹⁹ programming language and an associated Perl interface to the mSQL database system. This interface is called Msql.²⁰ Then the WDB software was installed. This software is similar to gsql in that it uses a single CGI script (WDB) for each query. In order to have a page associated with different tables in the database, the wdb script reads a page specification, and then builds an HTML page for the client to query the database according to the specification. The script then accepts a query, and builds a return to the client based on the results of the database query. WDB also provides software that can automatically generate a

specification from a database table. The prototype mSQL database and the script provided by WDB were used to generate a specification. The query page built by wdb from this specification is found in the Appendix. WDB is a powerful tool and could be modified to serve the purposes of the ACIMS. However, this would require interfacing WDB with Oracle. Efforts in this direction are being addressed by others. But it would still be awkward within WDB to make the user interface that which was desired for the ACIMS, so while awaiting ORACLE interface software (PRO*C) and license verifications from Oracle, a prototype system was built to illustrate the ACIMS interface. The HTML pages were designed by Dan O'Neil.

ACIMS Prototype Investigations and Experiments

C based CGI-scripts were written to interface mSQL with the HTML pages designed by Dan O'Neil. CGI scripts are generally written in C or in Perl, so the public domain gnu C compiler²¹ was downloaded and installed on the SUN system. The HTML initial page, presented to the user, is shown in the appendix. Based on the user's selection of radio and toggle buttons an SQL query of the mSQL database is presented to the database server. The server determines but does not return the database lookup information to the client. After the initial query, the client makes the C function calls to retrieve the resulting information, inserts this information within HTML markup, and sends the results back to the web client. For the initial test, the information was returned as an HTML table as shown in the Appendix.

To experiment with adding information to the database, Dan O'Neil designed pages to support insertion into tables. A CGI program was written in C to take the information provided by the "Concepts" page and add it to the Concept table in the database. The programs that were written were experimental, and prototypical. The Oracle based production system will require new CGI scripts, since each database system has its unique interface routines. The prototype system did, however, confirm that the user interface is as desired, and no further work was done with mSQL.

Conclusions and Future Work

Work will now proceed with installing software to interface with the ORACLE system at MSFC. Following this, scripts can be written to interact with the HTML pages designed by Dan O'Neil for ACIMS. Only one choice will remain, and this will be to decide whether the CGI scripts will be in the Perl programming language or in C. C will perhaps be the quicker choice, since the use of Perl would require installation of a Perl to ORACLE interface (such as ORAPERL). Currently, most programmers of CGI scripts prefer to use the Perl programming language. To illustrate the differences in C and Perl CGI scripts, an example of a script performing a query of the prototype mSQL database was written in Perl.

Acknowledgements

The author would like to acknowledge the help and support of those he has met this summer. Whenever something was needed, Steve was there to figure out how we could get it. Whenever I felt as if I was catching up, Dan O was generating new ideas from Washington. Behind the scenes, Dan O, Les, and Vance are making the concept of the VRC succeed, and in the trenches are Dan O, Brandon, and Ron, who will make the idea of a distributed and collaborative engineering environment known as the Virtual Research Center work with their enthusiasm for new and experimental systems, their abilities at integrating these ideas into a Web based environment, and their commitment to put in whatever time is necessary to get the job done. Additional thanks go to others "on the hall," i.e. Drew, Dan M, Joey, who helped me with questions and installations, and the rest, too many to mention, whose friendliness, hospitality and juggling instructions made the summer fun.

REFERENCES

- ¹ <http://nova.msfc.nasa.gov>
- ² <http://www.w3.org>
- ³ <http://www.ncsa.uiuc.edu/SDG/Software/Mosaic/NCSAMosaicHome.HTML>
- ⁴ <http://www.SUN.com>
- ⁵ <http://www.ncsa.uiuc.edu/General/VRMS/VRMLHome.HTML>
- ⁶ http://home.netscape.com/assist/net_sites/HTML_extensions.HTML
- ⁷ <http://www.ncsa.uiuc.edu/General/Internet/www/HTMLQuickRef.HTML>
- ⁸ <http://hoohoo.ncsa.uiuc.edu/CGI/overview.HTML>
- ⁹ <ftp://emwac.ed.ac.uk/pub/https/https>
- ¹⁰ <ftp://SUNsite.unc.edu/packages/infosystems/WWW.servers>
- ¹¹ <http://home.netscape.com>
- ¹² <http://ncsa.uiuc.edu/SDG/People/jason/pub/gsql/starthere.HTML>
- ¹³ <http://avalon.epm.ornl.gov/Dama2>
- ¹⁴ <http://arch-http.hq.eso.org/bfrasmus/wdb/wdb.HTML>
- ¹⁵ <http://www.sybase.com>
- ¹⁶ <http://www.oracle.com>
- ¹⁷ <http://www.informix.com>
- ¹⁸ <ftp://ftp.Bond.edu.au/pub/Minerva/msql>
- ¹⁹ <ftp://prep.ai.mit.edu/pub/gnu/sparc-SUN-solaris2/gnu>
- ²⁰ <ftp://franz.www.TU-Berlin.DE/pub/perl>
- ²¹ <ftp://prep.ai.mit.edu/pub/gnu/sparc-SUN-solaris2/gnu>

APPENDIX

Database = acims

Table
Concepts
Missions
People
Concept_Workforce

Table = Concepts

Field	Type	Length	Not Null	Key
Concept_Id	int	4	Y	Y
Concept_Name	char	50	Y	N
Description	char	128	N	N

Table = Missions

Field	Type	Length	Not Null	Key
Mission_Id	int	4	Y	Y
Mission_name	char	50	Y	N
Description	char	128	N	N

Table = People

Field	Type	Length	Not Null	Key
Contact_Id	int	4	Y	Y
Firstname	char	50	N	N
LastName	char	50	Y	N

Table = Concept_Workforce

Field	Type	Length	Not Null	Key
Concept_Id	int	4	N	N
Contact_Id	int	4	N	N

Prototype mSQL database

Concept Query Form

Please enter qualifiers in the fields below and press the '**Search**' button.

<input checked="" type="checkbox"/> Concept ID..... :	<input type="text"/>
<input checked="" type="checkbox"/> Concept Name..... :	<input type="text"/>
<input checked="" type="checkbox"/> System Level..... :	<input type="text"/>
<input checked="" type="checkbox"/> Description..... :	<input type="text"/>
<input checked="" type="checkbox"/> Operating Principle :	<input type="text"/>
<input checked="" type="checkbox"/> History..... :	<input type="text"/>
<input checked="" type="checkbox"/> Benefits..... :	<input type="text"/>
<input checked="" type="checkbox"/> Technical Issues... :	<input type="text"/>
<input checked="" type="checkbox"/> Assumed Infra..... :	<input type="text"/>

☐ Use full-screen output even if more than one row is returned.

Return max rows.

<input type="button" value="Search"/>	<input type="button" value="Reset"/>	<input type="button" value="Help"/>	<input type="button" value="Home"/>
---------------------------------------	--------------------------------------	-------------------------------------	-------------------------------------

wdb 1.3a1 - 3-Mar-1994 Send comments to bfrasmus@eso.org

Query form built by WDB

Available Tables (Select One)	Search Refinement (Optional)
<input checked="" type="radio"/> Concepts	<input type="radio"/> People
<input type="radio"/> Missions	<input type="radio"/> References
<input type="radio"/> Technology	<input type="radio"/> Parameters
<input type="radio"/> Programs	<input type="radio"/> Requirements
	<input type="radio"/> None
Keyword: <input type="text"/>	Keyword: <input type="text"/>

<input type="button" value="Reset Query"/>	<input type="button" value="Submit Query"/>
--	---

Last Modified on: June 28, 1995

HTML page to query ACIMS

RESULTS

Concept Name	Description
Mag Lifter	A tube, filled with an inert gas contains a guideway for a sled carrying a launch vehicle
Tether Lunar Transfer	Platforms use tethers to swing payloads from one orbit to another

Results of the query "SELECT * FROM CONCEPTS"
generated by previous HTML page

RESULTS

Concept_Name	LastName
Mag Lifter	Daughtery
Mag Lifter	Rather
Tether Lunar Transfer	Anderson
Tether Lunar Transfer	Daughtery
Tether Lunar Transfer	Rather

Results of a "join" of People and Concepts

Concepts

[Reference][Requirements][Personnel][Parameters]

Concept Name:

Description:

Operating Principles:

History:

Assumed Infrastructure:

Benefits:

Technical Issues:

Concept Level	<input checked="" type="radio"/> System of Systems	<input type="radio"/> System	<input type="radio"/> Subsystem	<input type="radio"/> Component
---------------	--	------------------------------	---------------------------------	---------------------------------

Cancel	Done
--------	------

July 12, 1995

HTML page to input into Concepts table.
Page generates SQL "INSERT INTO CONCEPT (Concept_ID, ..)"

1995

NASA/ASEE SUMMER FACULTY FELLOWSHIP PROGRAM

**MARSHALL SPACE FLIGHT CENTER
THE UNIVERSITY OF ALABAMA IN HUNTSVILLE**

**THE FEASIBILITY STUDY AND EVALUATION OF APPLYING EXPERT
SYSTEM TECHNIQUES TO THE MISSION OPERATIONS FOR THE
AXAF-I SPACECRAFT**

Prepared by: Kai H. Chang
Academic Rank: Associate Professor
Institution and Department: Auburn University
Department of Computer Science and Engineering

NASA/MSFC:

Office: Mission Operations
Division: Operations Engineering
Branch: Operations Development

MSFC Colleague(s): Richard McElyea
Mark Rogers

THE FEASIBILITY STUDY AND EVALUATION OF APPLYING EXPERT SYSTEM TECHNIQUES TO THE MISSION OPERATIONS FOR THE AXAF-I SPACECRAFT

1. INTRODUCTION

Advanced X-ray Astrophysics Facility - Imaging (AXAF-I) is a spacecraft for X-ray emitting sources observation and has been tentatively scheduled for a space shuttle launch in late 1998 at the Kennedy Space Center. Its main objectives are "to determine the nature of astronomical objects ranging from normal stars to quasars, to understand the nature of the physical processes which take place in and between astronomical objects, and to add to our understanding of the history and evolution of the universe." [AXAF1] The AXAF-I will have an expected five year life time for the science mission phase. During the science mission phase, the monitoring and management operation of the flight and ground systems is personnel intensive, requiring system experts on duty around the clock. The purpose of the expert system presented in this report is intended to reduce the level of expertise, training, and personnel requirement for the mission operation.

The telemetry data from the spacecraft can be divided into two categories: the science observation data and the engineering status data. The science data contains the outputs from the X-ray sensing devices and will be forwarded to the AXAF-I Science Center for interpretation; while the engineering status data will be monitored by the Operation Control Center (OCC) for the operation diagnosis of the spacecraft. The expert system is designed to assist the operation controllers at the OCC to perform the daily mission operations.

Since there are hundreds of engineering telemetry data points and the interpretation of the telemetry depends on many factors, e.g., sun or eclipse, the monitoring of the AXAF-I is not a trivial task. In this phase of expert system development, the focus has been limited to the engineering data interpretation, i.e., warnings will be provided to the operation controllers to signal any anomaly. The system is hosted in a Silicon Graphics Indigo-2 workstation running the IRIX operating system. The expert system tool used is the G2 system from Gensym [Gensy].

2. AXAF-I DESCRIPTION

The major components of the AXAF-I include a spacecraft, an X-ray telescope, and a science instrument module (SIM) [AXAF1]. The spacecraft contains six subsystems that provide the necessary services to the telescope and the SIM. The telescope consists of a 10 meter optical bench, a high resolution mirror assembly, and the related optical support hardware. The SIM contains four X-ray sensing devices with different spectrum range capabilities.

For the monitoring and management purposes, sensors are installed throughout the spacecraft to provide the component status information. There are two types of sensors, analog (i.e., numeric) and bilevel (i.e., on/off). Since the number of sensors is in the order of hundreds and complex relationships exist among the sensor readings, the discussion of

this paper will focus on the Electrical Power System (EPS) of the spacecraft to provide a clear presentation. At the time of this expert system development, the EPS contains 17 analog telemetry outputs and 28 bilevel telemetry outputs. Most of the analog telemetry outputs concern with voltages and currents; while most of the bilevel outputs concern with the status of components, like on/off and enabled/disabled. The number and the type of sensors in the EPS are still evolving. For this reason, the expert system must be able to accommodate future changes.

One major factor affects the functioning of the EPS is the sun/eclipse status. In the sun, the solar arrays provide all the power for the operation needs and maintain the full charge of the batteries. During eclipse, the batteries will provide the power. The number of eclipses is limited throughout the operation lifetime of the AXAF-I (<160) and most eclipses will be less than 2 hours long [AXAF2]. The switching of relays in the EPS is controlled by an on-board computer.

3. STRUCTURE DESIGN OF THE EXPERT SYSTEM

The entities involved in the AXAF-I monitoring and management operations must be first identified. The entities include (1) object class definitions, (2) physical objects, (3) rules, (4) telemetry variables, (5) valid ranges for telemetry variables, and (6) user-controlled simulation biases. In the G2 environment, a "workspace" hierarchy [Gensy] has been created for each entity. The G2 object and workspace hierarchies possess the common features available in most object-oriented programming languages [Wang]. By using the separate entity hierarchies, the definitions of entities and the creation of classes and instances become manageable.

3.1 Object Class Definition

An object class defines the properties (or attributes) of physical subsystems or components that have common features. For example, the AXAF-OBJECT class is defined as the top level class and all subsystems and objects inherit features from this class. One level down the hierarchy, a subclass named EPS-COMPONENT is defined for the major components of the EPS.

3.2 Physical Objects

Each physical object is an instance of an object class. It is used to represent a single or a collection of components. A single component object (called primitive object), e.g., BATTERY-1 and SOLAR-ARRAY, contains all of its related telemetry readings. An object representing a collection of components (called compound object), e.g., EPS, contains the integrated status (determined by the rules) of the compound object. Each primitive and compound object is represented by an icon. The color of an icon is used to indicate the status of an object. For example, under normal operation status, the original icon color is displayed. When a warning is signaled for an object, its icon color may be changed to red. When a compound object is clicked upon, a subworkspace containing the icons of its components will be popped out. The user may continue the process of traversing down the hierarchy by clicking on the desired components. However, when a primitive object is clicked upon, a subworkspace containing all of its real-time telemetry

readings will be popped out. By this selective observation, the user will be able to focus on an appropriate level of monitoring.

A system level physical object workspace is given in Figure 1. In this figure, under normal status, each major subsystem has a green icon. When a subsystem or object is signaled for a warning, its icon color will be changed to red. In addition, a sun icon is shown in this workspace. When the AXAF-I is under the sun, the sun icon color is orange; while in eclipse, the color is gray. For simulation purpose, two buttons are provided to the user for the sun or eclipse selection. Figure 2 shows the top-level components of the EPS subsystem and Figure 3 shows the telemetry readings subworkspace of BATTERY-1.

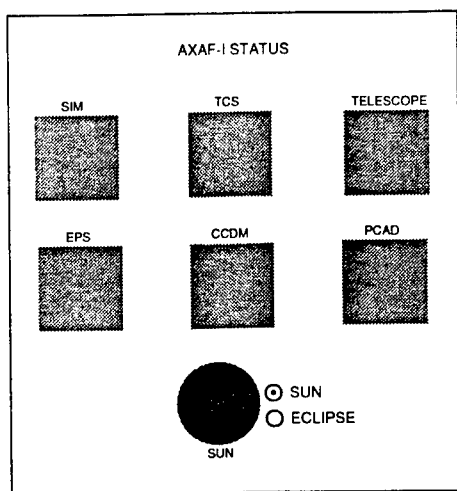


Figure 1 System level physical object workspace

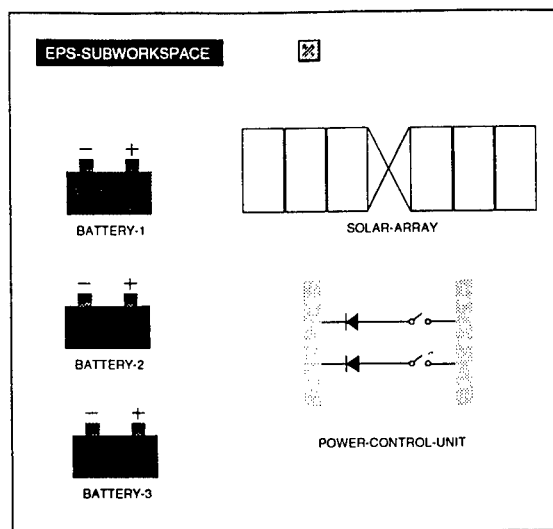


Figure 2 EPS workspace

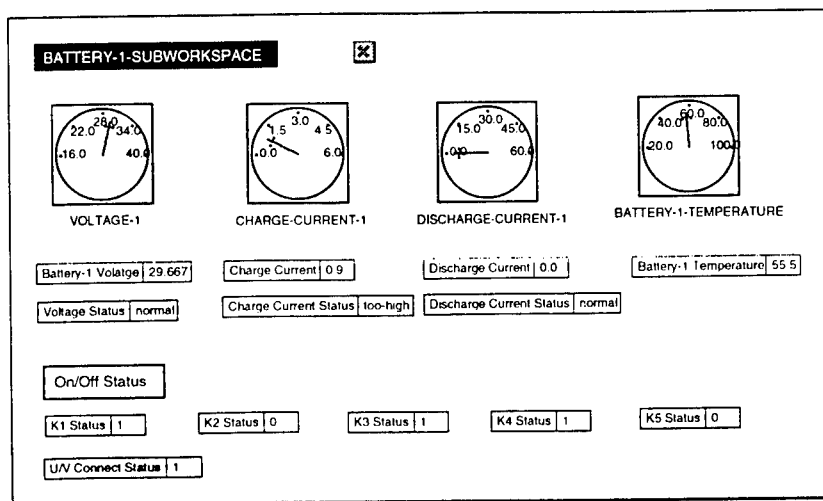


Figure 3 Telemetry readings workspace for BATTERY-1

3.3 Rules

The rules determine when a telemetry reading is out of range and when to signal a warning. A range checking rule typically requires information on the operation mode, e.g., sun/eclipse, the valid ranges of telemetries, and the actual telemetries to reach a conclusion. The (partial) table of a range checking rule for the BATTERY class is given in Figure 4 as an example. It can be seen that G2 provides a natural-language like rule syntax [Gensy].

```
For any battery whenever the charge-current of the battery
receives a value and when the value of the charge-current >
the Batt-charge-current-sun-k5-off-max of battery-limits and
the state of sun = 1 and the k5-status of the battery = 0
then conclude that the charge-current-status of the battery
is too-high
```

Figure 4 The battery CHECKING-FOR-CHARGE-CURRENT-TOO-HIGH-WHEN-SUN-K5-OFF rule

3.4 Telemetry Variables

Every telemetry reading processed by the prototype must be defined in the G2 environment. The reason is that different telemetries may need different treatments. For example, some telemetries should cause forward chaining immediately after its reception; while other telemetries should be accessed only when a backward chaining has requested them. The telemetries of AXAF-I are defined as *variables* in G2. They are organized in a hierarchy as well. The top level class of the variable is AXAF-VAR which is a subclass of the system-defined QUANTITATIVE VARIABLE. Subclasses are then defined for voltage, current, temperature, etc. In this prototype, all telemetries are individually simulated using formulas.

3.5 Valid Ranges for Telemetry Variables

Each telemetry reading has a valid range in a specific operating mode. Instead of specifying these ranges along with the telemetry variable definitions, they are defined and specified in a table. This arrangement provides easiness to locating a desired range and performing modification - especially when multiple modifications are needed.

3.6 User-Controlled Simulation Biases

These are the values that will be added in the telemetry simulation formulas. For example, on a slide, the user can slide the pointer to a desired value; while on the radio buttons, the user can simply click on the desired button.

4. CONCLUSION

The described prototype has demonstrated the feasibility of applying expert system techniques to the mission operations monitoring. Several findings are listed in the follows.

Hierarchical design: The hierarchical structure design for the object and telemetry definitions and the workspaces provide a conceptually clear framework for the prototype. It not only provides a reasonable way to specify the entity attributes and relationships, but also makes the system development and testing very efficient. This design also allows the user to choose the appropriate monitoring levels for different components which reduces the mental reasoning burden of the user.

System flexibility: In addition to the demonstration of feasibility, the prototype has also shown the flexibility to the system modification. Specification changes can be easily updated by editing the rules or the attributes of the related tables. This feature is extremely important in this system because the detailed specifications of AXAF-I are still evolving. This flexibility is mainly attributed to the hierarchical design and the G2 environment.

Graphical user interface: The powerful graphics capabilities of the Silicon Graphics workstation and the G2 environment have made the mission operations monitoring more pleasant. By using the combination of rule-based reasoning, status display colors, and different icon designs, the user can easily identify the status of any system components. The labor intensive telemetry observation task is now accomplished by the expert system. This leaves the user time to perform other more meaningful tasks.

G2 environment: During the course of the design, development, and testing of this prototype, G2 has been confirmed to be a powerful expert system development tool. Most of the positive features mentioned above are directly related to the G2 capabilities. Its natural language like rule syntax is easy to construct; while the attribute tables associated with objects and workspaces provide efficient way to describe the domain and configurate the relationships among entities. Another important feature of G2 is the built-in *modes*. Under different modes, the environment would provide different access capabilities. For example, under the operator mode, the user can only perform monitoring tasks; none editing or system parameter observation capability is allowed. While under the administrator mode, the user would have the authority to perform any necessary changes. Although G2 is proved to be a powerful tool, the learning curve to achieve proficient understanding of the tool can be long and costly. The standard training course of G2 should be a requirement for most project development team members using the G2 environment.

5. REFERENCES

- [AXAF1] Advanced X-ray Astrophysics (AXAF) - Mission Operation Plan, AMO-1010, Mission Operations laboratory, George C. Marshall Space Flight Center, NASA, April 1994.
- [AXAF2] Electrical Power Subsystem - AXAF-I Preliminary Design Audit Presentation Package, TRW Space & Electronics Group, September 9, 1994.
- [Gensy] G2 Reference Manual, Version 3.0, Gensym Corporation, July 1992.
- [Wang] Wang, Paul S., C++ with Object-Oriented Programming, PWS Publishing Company, 1994.

**1995
NASA/ASEE SUMMER FACULTY FELLOWSHIP PROGRAM**

**MARSHALL SPACE FLIGHT CENTER
THE UNIVERSITY OF ALABAMA IN HUNTSVILLE
NON-DESTRUCTIVE EVALUATION OF COMPOSITES**

Prepared by:	Tsuchin Philip Chu, Ph.D.
Academic Rank:	Associate Professor
Institution and Department:	Southern Illinois University at Carbondale Department of Mechanical Engineering and Energy Processes
NASA/MSFC:	
Laboratory:	Material and Processes
Division:	Engineering Physics
Branch:	Non-Destructive Evaluation
MSFC Colleague:	Sam Russell, Ph.D.

INTRODUCTION

The composite materials have been used in aerospace industries for quite some time. Several non-destructive evaluation (NDE) methods have been developed to inspect composites in order to detect flaws, matrix cracking, and delamination. These methods include ultrasonics, acoustic emission, shearography, thermography, X-ray, and digital image correlation. The NDE Branch of Marshall Space Flight Center has recently acquired a thermal imaging NDE system. The same system has been used at NASA Langley Research Center for detecting disbonds [1,2].

In order to compare different NDE methods, three carbon/carbon composite panels were used for experiment using ultrasonic C-scan, shearography, and thermography methods. These panels have teflon inserts to simulate the delamination between plies in a composite panel. All three methods have successfully located the insert. The experiment and results are presented in the following sections.

EXPERIMENT

Three [0, +/-45, 90]_s carbon/carbon composite panels with teflon inserts were used for this experiment. The size of each panel is 76 mm (3 inches) square. Each panel is fabricated with eight plies of standard T-300, 8 harness, satin weave carbon/carbon laminates which have a per ply thickness of 0.29 mm (0.0115 inches). Teflon inserts between two adjacent plies were used to simulate delamination in the composite panels. Three different configurations of inserts are listed in Table 1. The teflon tape insert is one half ply thick (0.145 mm, 0.00575 inches).

Table 1. Description of Sample Configurations

Sample #	Sample Code	Insert Size	Between Ply #
1	D7&8D1/4	6.35mm (0.25")	7 and 8
2	D7&8D1/2	12.7mm (0.5")	7 and 8
3	D6&7D1/2	12.7mm (0.5")	6 and 7

Ultrasonic C-Scan

A 20 MHz, 6.35 mm (0.25 inch) transducer was used to inspect sample #3 (12.7 mm square insert between 6th and 7th plies). The center area of 45.7 mm (1.8 inch) square was scanned with a rate of 12.7 mm (0.5 inches) per second. The teflon tape insert was detected. Efforts have also been made to determine the depth of the

insert by locating the signals from the insert. However, the attempts were not successful due to the facts that the panel was too thin and the insert was too close to one of the surface.

Electronic Laser Shearography

All three samples were evaluated by this method. The back surface (8th ply) of each panel was coated with white powder to eliminate the glare. Each panel was placed in front of the electronic shearography NDE system. A thermal couple was attached to the surface away from the camera. The laser speckle images were sheared in the horizontal (x) direction. The panel was then excited with a heat gun to raise the temperature of the surface to above 93 C (200 F). The shearograms produced clearly showed the locations of the inserts in terms of the variation of the fringe patterns at the center of each panel.

Thermography

A halogen lamp was first used as the heat source. The results were not satisfactory. A heat gun was then used to provide a constant heat flux while the thermal images were digitized by the thermal imaging system. The heat was transferred from the first ply surface to the eighth ply surface which was facing the camera. The digitized thermal images were carefully studied. By selecting the proper median temperature and increments, the inserts appeared as dark areas at the center of each panel. An image analysis software was then used to enhance these images and the simulated delamination were classified.

RESULTS AND DISCUSSION

The ultrasonic C-scan produced the best result for detecting the shape and location of the inserts as shown in Figure 1. However, this method is not portable and requires water for sound transmission. The shearography showed the general location of the insert in each panel. Two shearograms of the panels with inserts embedded between 6th and 7th plies and 7th and 8th plies, respectively, are shown in Figure 2. Notice that the shape of the fringe patterns are quite different between these two shearograms. This is because the depth of the inserts are different by one ply of the laminate. The thermography method gave a very good indication of the size, shape and the location of each insert. Figure 3 shows a typical thermal image of the panel. The edge of the area representing the delamination is not very clear. With the aid of image processing, a better representation can be obtained.

CONCLUSIONS

Ultrasonic C-scan, shearography, and thermography are very powerful NDE tools in detecting flaws, cracks, and delamination of composites. The three

carbon/carbon composite panels with the teflon tape inserts provided samples for comparing these methods. All three methods could determine the locations of the inserts without difficulties. The ultrasonic and thermography system could also identify the general shape of the inserts although the edges were not clear. The shearograms indicated the changes of the surface slopes. When the delamination occurs closer to the surface, the fringe patterns tend to become more complex due to the deformation of the thin laminate. Both shearography and thermography NDE systems are portable and easy to use. However, it requires training and experience to effectively use the systems for detecting flaws in materials.

ACKNOWLEDGMENT

The author would like to thank Dr. Sam Russell for his support and encouragement of this project. The author would also like to thank Mr. Michael Suits and Mr. Mat Lansing for the help in using the NDE systems.

REFERENCES

1. W.P. Winfree and P.H. James, "Thermographic Detection of Disbonds," *Proceedings of the 35th ISA International Instrumentation Symposium*, pp. 183-188, 1989.
2. W.P. Winfree, et. al., "Thermographic Detection of Disbonds in Rivetted Lap Joints," *Proceedings of the 37th ISA International Instrumentation Symposium*, pp. 1097-1105, 1991.

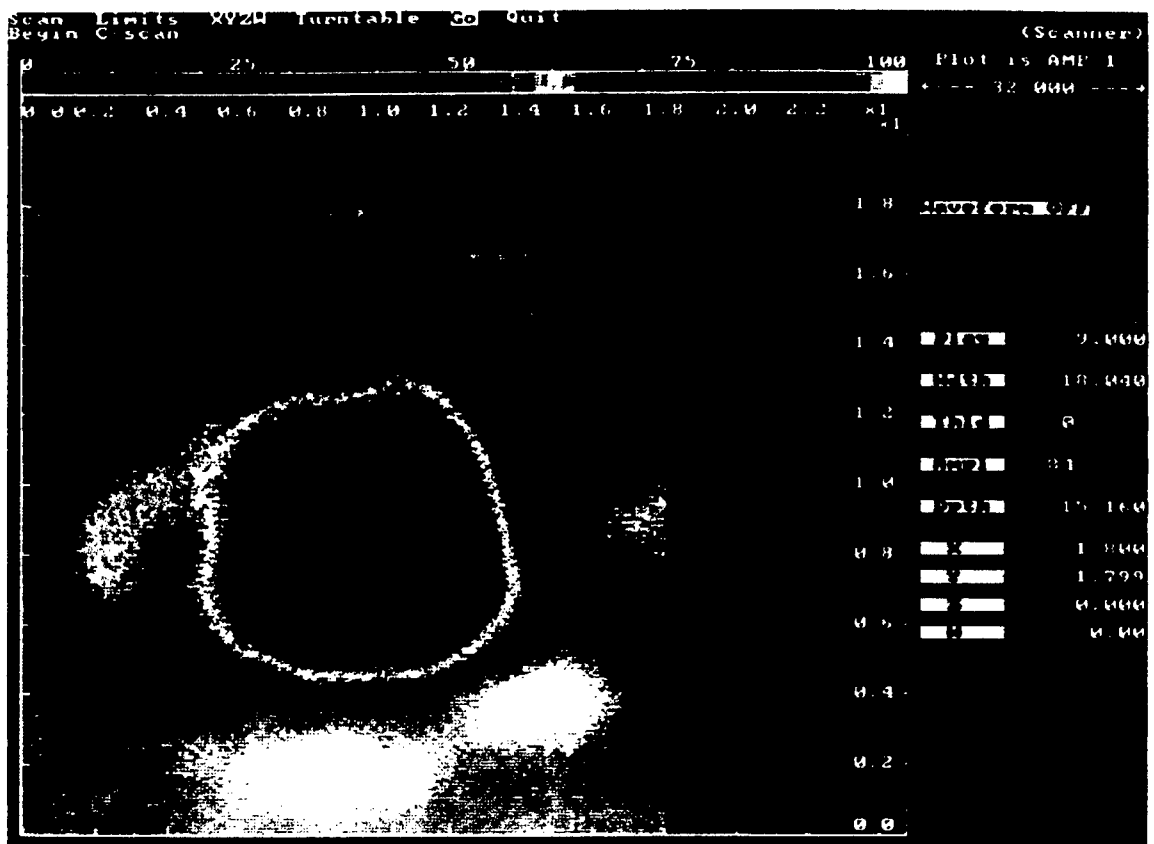
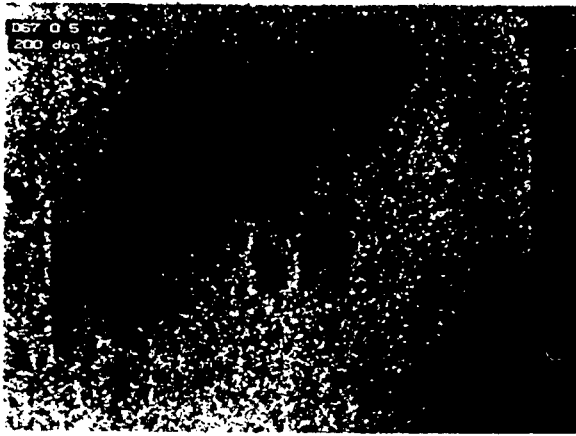
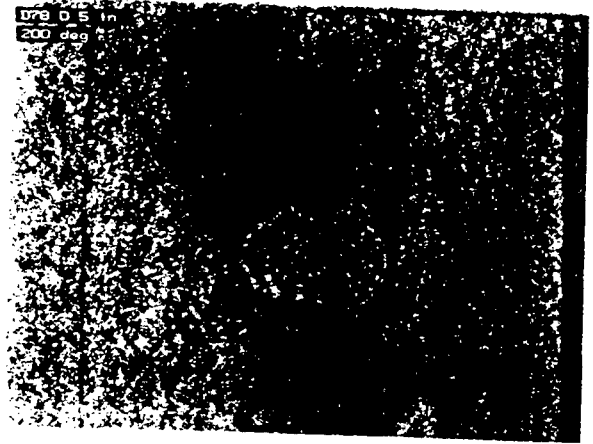


Figure 1. Ultrasonic C-Scan Image of Sample D6&7D1/2



D6&7D1/2



D7&8D1/2

Figure 2. Shearograms Showing the Simulated Delaminations

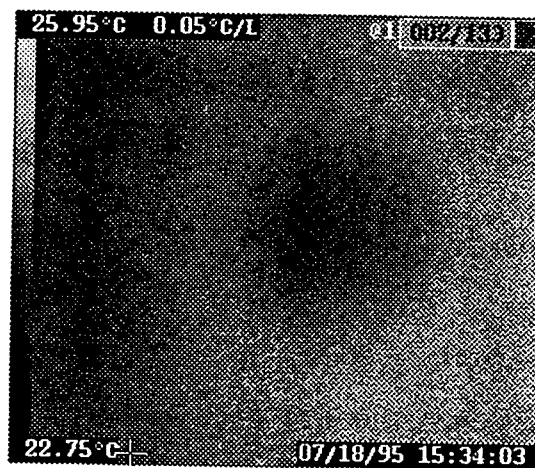


Figure 3. Thermal Image of Sample D7&8D1/2

1995 NASA/ASEE SUMMER FACULTY FELLOWSHIP PROGRAM

**MARSHALL SPACE FLIGHT CENTER
THE UNIVERSITY OF ALABAMA IN HUNTSVILLE**

**INVESTIGATION OF ION-BEAM MACHINING METHODS FOR
REPLICATED X-RAY OPTICS**

Prepared By: Thomas W. Drueding

Institution: Boston University
Aerospace and Mechanical Engineering Department

NASA/MSFC:

Office: Astrionics Laboratory
Division: Optics and Radio Frequency
Branch: Optical Fabrication

MSFC Colleagues: James W. Bilbro
Robert W. Rood

INVESTIGATION OF ION-BEAM MACHINING METHODS FOR REPLICATED X-RAY OPTICS

1. Introduction

The final figuring step in the fabrication of an optical component involves imparting a specified contour onto the surface. This can be expensive and time consuming step. The recent development of ion beam figuring provides a method for performing the figuring process with advantages over standard mechanical methods. Ion figuring has proven effective in figuring large optical components [1-7].

The process of ion beam figuring removes material by transferring kinetic energy from impinging neutral particles. The process utilizes a Kaufman type ion source, where a plasma is generated in a discharge chamber by controlled electric potentials [8]. Charged grids extract and accelerate ions from the chamber. The accelerated ions form a directional beam. A neutralizer outside the accelerator grids supplies electrons to the positive ion beam. It is necessary to neutralize the beam to prevent charging workpieces and to avoid bending the beam with extraneous electro-magnetic fields. When the directed beam strikes the workpiece, material sputters in a predictable manner. The amount and distribution of material sputtered is a function of the energy of the beam, material of the component, distance from the workpiece, and angle of incidence of the beam. The figuring method described here assumes a constant beam removal, so that the process can be represented by a convolution operation. A fixed beam energy maintains a constant sputtering rate. This temporally and spatially stable beam is held perpendicular to the workpiece at a fixed distance. For non-constant removal, corrections would be required to model the process as a convolution operation. Specific figures (contours) are achieved by rastering the beam over the workpiece at varying velocities. A unique deconvolution is performed, using series-derivative solution[9] developed for the system, to determine these velocities.

The two main advantages of the ion machining process are that it is non-contacting and highly predictable. The non-contact nature eliminates the problems of tool wear and edge effects encountered in most standard polishing techniques. The process also avoids rib structure print through and warping due to loading stresses on the workpiece. Holding beam parameters constant ensures beam stability, and results in a predictable and highly deterministic removal process. This allows for rapid convergence of the process to required specifications, resulting in a significant time and cost savings.

Early work on the ion figuring of optical components was performed by Gale [10]. This work was expanded at the University of New Mexico by Wilson, et. al. [5-7]. The initial experiments involved figuring of 30 cm fused silica, Zerodur and copper optics with a 2.54 cm ion beam source. Allen, et. al. developed an ion figuring system for large optics at Eastman Kodak [1-4]. The Kodak Ion Figuring System (IFS) is capable of processing

components up to 2.5 m by 2.5 m using several ion sources of up to 15 cm diameter. Other current research is being carried out at Oak Ridge National Laboratory. Their system is capable of figuring up to a 60 cm size component [11].

The new Precision Ion Machining System (PIMS) research facility at NASA's Marshall Space Flight Center is currently focused on the figuring of small (≈ 10 cm diameter) optics using a 3 cm ion source. The initial experiments were performed figuring 8 cm diameter fused silica and chemical vapor deposited SiC. These experiments confirmed the effectiveness of the system[12]. Issues of concern in ion beam figuring process include; beam stability, the surface properties of the workpiece, workpiece heating, and dwell function computation. Beam stability effects the predictability and accuracy of the removal process, while workpiece surface properties and heating influence the effectiveness of the process. The effects on the surface roughness are reported in earlier work[13].

2. Precision Ion Machining System

The PIMS machining apparatus itself is constructed around a surplus sputtering vacuum chamber. Fitted inside the chamber is a 3 cm, Kaufman filament type ion source driven by a programmable power supply. A computer controlled translation stage is fitted to the floor of the chamber, below the ion source. The workpiece holder is placed on the translation stage that provides translations and rotations of the workpiece. The motion of the system as well as the ion source power supply is controlled by a 80386 based personal computer. In the configuration, the workpiece is moved and the ion beam source is held in a fixed position above the workarea. The system is shown in the computer model of Figure 1.

The surface contour measurements are taken using a ZYGO Mark IVxp interferometer with a 4 inch aperture. For computing rastering parameters, the surface map is transferred to a personal computer. Surface roughness measurements are taken using a WYKO 3-D optical profilometer. The sample workpieces are circular and 80.0 mm in diameter.

The Precision Ion Machining System was successful in figuring 8 cm diameter fused silica and chemical vapor deposited SiC samples[12]. A 1 cm aperture was used for correcting a near flat, fused silica sample. Small apertures are useful for making finer corrections on optical components, but they are limited by the reduce volumetric removal rate. Subsequent iterations failed to improve surface contours because of an apparent non-constant removal caused because insufficient area was covered by the ion beam. Non of the workpieces experienced significant increases in surface roughness.

Any removal method, such as ion figuring, which has a Gaussian profile will suffer from a variation in removal from the edge of a workpiece to the center. To prevent the variation, removal must take place beyond the workpiece itself. In previous experiments,

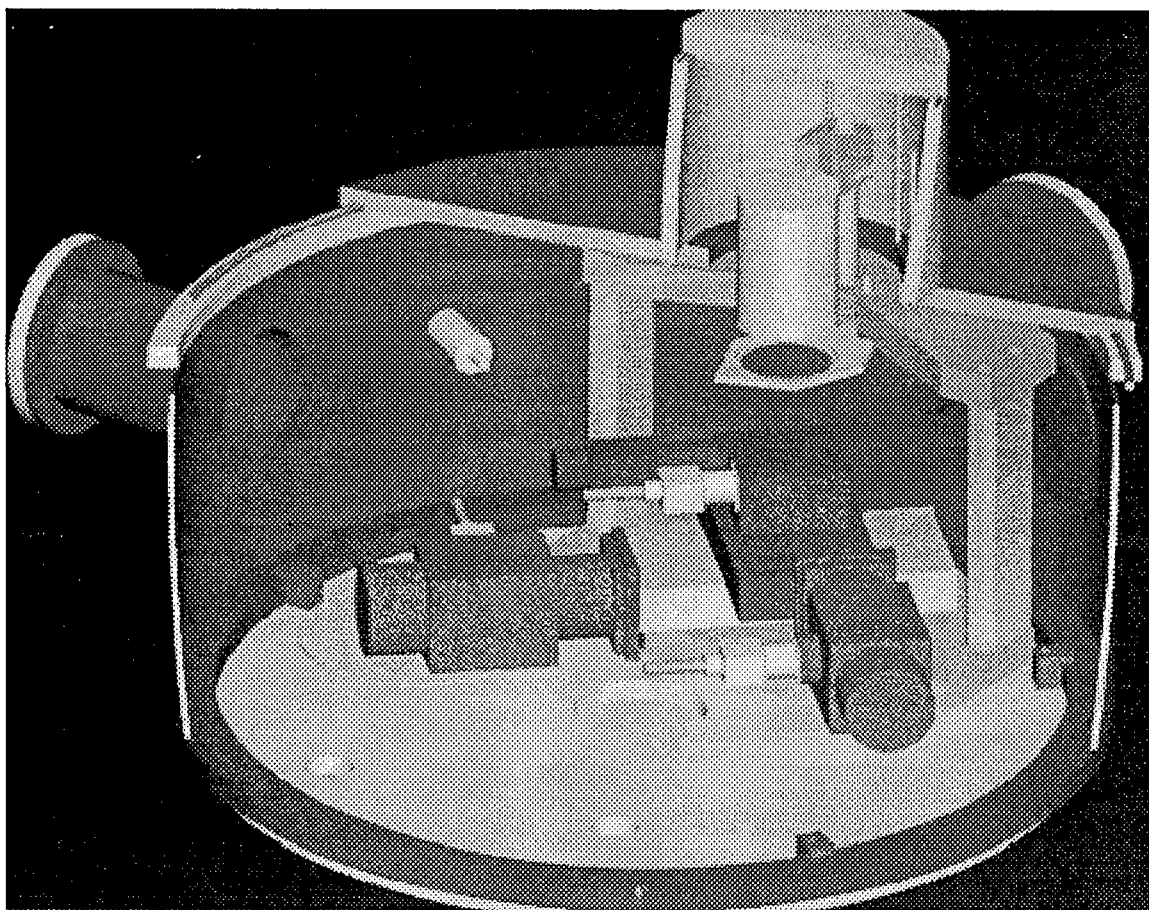


Figure 1 Solid model of the ion figuring system components. The ion source is supported on two posts above the translation and rotation stage assembly. These components are housed in a 1 meter diameter, cylindrical vacuum chamber.

we chose limits that were too small, resulting in the removal variation. The limits were chosen in an effort to reduce machining time, as an increase in machining limits results in a proportionally larger amount of area to be machined and thus a longer machining time. However, this decrease in time was accompanied by an decrease in accuracy, and also prevented us from improving a workpiece over successive iterations. This summer experiments were performed using appropriate limits. This resulted in effective iterations of the process. An initial flat fused silica sample with a deviation of 1088 nm rms, was figure to 271 nm rms in the first iteration, and then corrected to 114 nm rms in the subsequent iteration.

3. Plans for X-Ray Replication Optics

Future projects involve implementing ion-beam machining techniques in the fabrication of x-ray optics[14]. Ion-beam machining is proposed as a method for the final figuring of a mandrel for replicating optics. This will require significantly expanding the capabilities of the Precision Ion Machining System, currently in operation at the Optical Fabrication Branch. Advanced x-ray telescopes consist of a large number of nested

cylindrical mirror shells with the reflecting surface on the inside of each shell. Replicated x-ray mirrors are produced by electroforming a thin shell optic over a figured polished mandrel. The mandrel is diamond turned electroless nickel over an aluminum substrate. The electroformed mirror shell is made from pure nickel deposited in a state of minimum stress. A cryo separation technique is used to remove the mirror from the mandrel. Since a large number of x-ray mirrors are used in an x-ray telescope, a large number of mandrels must be produced, and is important to develop precise and cost-effective methods for manufacturing these mandrels. It has been demonstrated that ion-beam figuring is an effective method for final figuring of normal incidence optics[1-7,12]. We propose these methods be extended and the Precision Ion Machining System be expanded to assist in fabricating grazing incidence optics. By investigating the effectiveness of this technique we plan to demonstrate that ion-beam machining is an important new technology in the production of x-ray optics.

The Precision Ion Machining System can be expanded to handle small cylindrical workpieces. This will require a large vacuum chamber, and modification of the translation system, to hold the mirror mandrel. New computational (deconvolution) and control methods for machining cylindrical workpieces will be developed, based on previous research for figuring near-normal incidence optics. Operating parameters that will be determined include: the ion-beam removal rate and shape; effects on the resulting surface finish and translation motor tolerances. The relative effectiveness of ion-beam machining process with respect to current methods must be test by figuring sample mandrels.

4. Conclusions

The Precision Ion Machining System at NASA's Marshall Space Flight Center was reconstructed and tested. A new graphical control interface was developed for the system. Experiments were performed using corrections to a previous problem with removal variations, cause by insufficient machining range. This resulted in effective iterations of the process. An initial flat fused silica sample with a deviation of 1088 nm rms, was figure to 271 nm rms in the first iteration, and then corrected to 114 nm rms in the subsequent iteration. Initial plans were also developed for expanding the system for assisting in the fabrication of replicated x-ray optics.

5. References

- 1 Lynn N. Allen, John J. Hannon, and Richard W. Wambach. "Final surface error correction of an off-axis aspheric petal by ion figuring," *Advances in Fabrication and Metrology for Optics and Large Optics*, SPIE, 1543, 1991.
- 2 Lynn N. Allen and Robert E. Kiem. "An ion figuring system for large optics fabrication," *Current Developments in Optical Engineering*, SPIE, 1168, 1989.

- 3 Lynn N. Allen, Robert E. Kiem, and Timothy S. Lewis. "Surface error correction of a Keck 10m telescope primary segment by ion figuring," *Advances in Fabrication and Metrology for Optics and Large Optics*, SPIE, 1531, 1991.
- 4 Lynn N. Allen and H. W. Romig. "Demonstration of an ion figuring process," *Advances in Fabrication and Metrology for Optics and Large Optics*, SPIE, 1333, 1990.
- 5 S. R. Wilson. "Ion beam figuring of optical surfaces," Master's thesis, University of New Mexico, 1987.
- 6 S. R. Wilson and J. R. McNeil. "Neutral ion beam figuring of large optical surfaces," *Current Developments in Optical Engineering*, SPIE, 818:320-323, 1987.
- 7 S. R. Wilson, D. W. Riecher, and J. R. McNeil. "Surface figuring using neutral ion beams," *Advances in Fabrication and Metrology for Optics and Large Optics*, SPIE, 966:74-81, 1988.
- 8 H. R. Kaufman, P. D. Reader and G. C. Isaacson, "Ion Sources for Ion Machining Applications," *AIAA Journal*, 15(6): 843-847, June 1977.
- 9 T. W. Drueding, T. G. Bifano, and S. C. Fawcett. "Contouring Algorithm for Ion Figuring," *Precision Engineering*, January 1995, 17(1).
- 10 A. J. Gale, "Ion Machining of Optical Components", Optical Society of America Annual Meeting Conference Proceedings, November, 1978.
- 11 Charles L. Carnal, C. M. Egert, and Kathy W. Hylton. "Advanced matrix-based algorithm for ion beam milling of optical components", presented at the *Society of Photo-Optical Instrumentation Engineers*, 1992 International Symposium on Optical Applied Science and Engineering, 1992.
- 12 T. W. Drueding, S. C. Fawcett, S. R. Wilson, and T. G. Bifano. "Ion Beam Figuring of Small Optical Components", *Optical Engineering*, December 1995, 34(12).
- 13 S. C. Fawcett, T. W. Drueding, and T. G. Bifano, "Neutral Ion Figuring of CVD SiC", *Optical Engineering*, 33(3):967-974, March 1994.
- 14 M. Ghigo, O. Citterio, P. Conconi, R. Loi, and F. Mazzoleni. "Perspectives of ion-beam polishing of mandrels for x-ray replication optics", *X-Ray and Extreme Ultraviolet Optics*, SPIE, 2515:56-62, 1995

1995

NASA/ASEE SUMMER FACULTY FELLOWSHIP PROGRAM

**MARSHALL SPACE FLIGHT CENTER
THE UNIVERSITY OF ALABAMA IN HUNTSVILLE**

LARGE DEFLECTION ANALYSIS OF A TENSION-FOIL BEARING

Prepared By:	David A. Elrod, Ph. D.
Academic Rank:	Assistant Professor
Institution and Department:	The University of Alabama in Huntsville Mechanical and Aerospace Engineering Department
NASA/MSFC:	
Laboratory:	Propulsion
Division:	Component Development
Branch:	Turbomachinery
MSFC Colleague:	Henry P. Stinson

INTRODUCTION

The rolling element bearings (REB's) which support many turbomachinery rotors offer high load capacity, low power requirements, and durability. Two disadvantages of REB's are:

- rolling or sliding contact within the bearing has life-limiting consequences; and
- REB's provide essentially no damping.

The REB's in the Space Shuttle Main Engine (SSME) turbopumps must sustain high static and dynamic loads, at high speeds, with a cryogenic fluid as lubricant and coolant. The pump end ball bearings limit the life of the SSME high pressure oxygen turbopump (HPOTP). Compliant foil bearing (CFB) manufacturers have proposed replacing turbopump REB's with CFB's. CFB's work well in aircraft air cycle machines, auxiliary power units, and refrigeration compressors. In a CFB, the rotor only contacts the foil support structure during start up and shut down. CFB damping is higher than REB damping. However, the load capacity of the CFB is low, compared to a REB. Furthermore, little stiffness and damping data exist for the CFB. A rotordynamic analysis for turbomachinery critical speeds and stability requires the input of bearing stiffness and damping coefficients.

The two basic types of CFB are the tension-dominated bearing (Figure 1) and the bending-dominated bearing (Figure 2). Many investigators have analyzed and measured characteristics of tension-dominated foil bearings, which are applied principally in magnetic tape recording. The bending-dominated CFB is used more in rotating machinery. Recently, a new tension-foil bearing configuration has been proposed for turbomachinery applications.

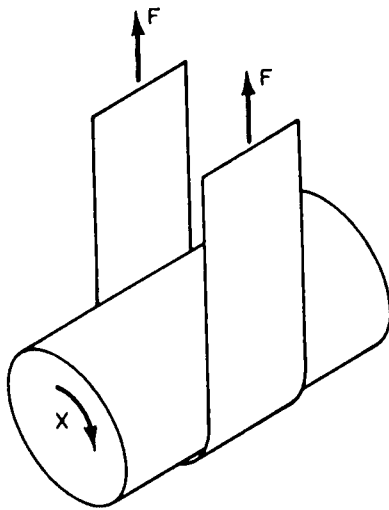


Figure 1. Tension-dominated foil bearing

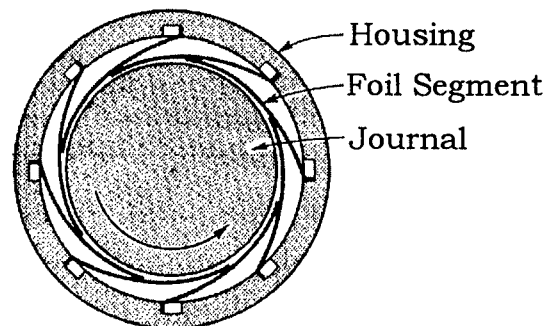


Figure 2. Bending-dominated foil bearing

Previous foil bearing models have included a plate analysis for the foil in which small deflections are assumed. If the deflection of a plate is greater than about 20% of the plate thickness, a large deflection analysis should be used [1]. In a tension foil bearing, the foil deflection may be several times the foil thickness. The goal of the present work is to develop bench-mark ANSYS finite element analyses of a uniformly loaded plate, and a FORTRAN code for the large deflection analysis of a tension-foil bearing. In this report, results of ANSYS finite element analyses of a thin plate under uniform load are presented. Progress on the development of the FORTRAN code are also presented.

THEORY

Von Karman's equations for the transverse deflection w of a plate under a transverse pressure load are [1]

$$\frac{\partial^4 F}{\partial x^4} + 2 \frac{\partial^4 F}{\partial x^2 \partial y^2} + \frac{\partial^4 F}{\partial y^4} = E \left[\left(\frac{\partial^2 w}{\partial x \partial y} \right)^2 - \frac{\partial^2 w}{\partial x^2} \frac{\partial^2 w}{\partial y^2} \right] \quad (1)$$

$$\frac{Eh^3}{12(1-\nu^2)} \left(\frac{\partial^4 w}{\partial x^4} + 2 \frac{\partial^4 w}{\partial x^2 \partial y^2} + \frac{\partial^4 w}{\partial y^4} \right) = q + h \left(\frac{\partial^2 F}{\partial y^2} \frac{\partial^2 w}{\partial x^2} + \frac{\partial^2 F}{\partial x^2} \frac{\partial^2 w}{\partial y^2} - 2 \frac{\partial^2 F}{\partial x \partial y} \frac{\partial^2 w}{\partial x \partial y} \right) \quad (2)$$

In equations (1) and (2), the xy directions are in the plane of the plate, h is the plate thickness, E and ν are Young's modulus and Poisson's ratio, and q is the transverse pressure. F is called the "Airy stress function", and is related to the normal and shear loads per unit length, Q_x , Q_y , and Q_{xy} by:

$$Q_x = h \frac{\partial^2 F}{\partial y^2} \quad Q_y = h \frac{\partial^2 F}{\partial x^2} \quad Q_{xy} = -h \frac{\partial^2 F}{\partial x \partial y} \quad (3)$$

The von Karman equations account for the in-plane loading and deflections which occur when a plate is loaded by an external transverse pressure. If the transverse deflection is less than 20% of the plate thickness, the in-plane loads and deflections are neglected, and equations (1) and (2) are replaced by the "small deflection" equation:

$$\frac{Eh^3}{12(1-\nu^2)} \left(\frac{\partial^4 w}{\partial x^4} + 2 \frac{\partial^4 w}{\partial x^2 \partial y^2} + \frac{\partial^4 w}{\partial y^4} \right) = q \quad (4)$$

Previously, the finite difference approach was used to program equation (4) for small deflection analyses of a foil. A finite difference template set up to represent the equation was modified at the edges to model clamped conditions on two ends of the foil, a free edge along the length of the foil, and a line of symmetry at the mid-width of the foil. An iterative solution technique was used.

In order to apply the finite difference technique to solve the von Karman equations, one would solve for the plate deflections iteratively assuming the Airy stress function is zero, use the deflection solution to solve iteratively for the Airy stress function, and continue to iterate

until the solutions for deflections and Airy stress function converge. In addition, modeling the boundary conditions is more difficult for the solution of von Karman's equations than for the small deflection equation. As a result, the finite element approach was chosen as the numerical method for the large deflection analysis.

In a finite element analysis of a continuous structure, the structure is subdivided into smaller parts called "elements", which are connected at points called "nodes". Each element is represented by a stiffness matrix, which relates forces and displacements at the nodes. The stiffness matrix is a function of the element stress/strain state. For small deflections, a first order approximation for strain is adequate. For large deflections, the solution is iterative and the stiffness matrix must be modified to include additional terms in the strain approximation, and to include "stress stiffening": the in-plane stresses carry some of the transverse load.

ANSYS MODELS

Before beginning the FORTRAN code development, the ANSYS finite element program was used to model a foil under a uniform pressure load. The elastic quadrilateral shell element, Stif63, was used to model the plate. This element can be used to model stress stiffening and large deflection effects. A 2 inch long, 1 inch wide, 0.01 inch thick Inconel foil was modeled. Since a uniform load is assumed, two lines of symmetry exist. The ANSYS models are for one fourth of the foil, with 50 square elements, and clamped and free boundary conditions.

Figure 3 is a plot of maximum displacement predictions for the uniformly loaded Inconel foil. The three lines plotted are the results of ANSYS large deflection analyses, ANSYS small deflection analyses, and small deflection finite difference analyses. The small deflection analysis results agreed within 5% at all nodes in the models. The small deflection and large deflection results begin to differ at less than 0.5 psi uniform load. At 10 psi, the maximum deflection predicted by the large deflection analysis is less than 20% of that predicted by the small deflection analyses. The predictions of the finite element program which is described in the next section will be compared to the ANSYS results in figure 3.

FINITE ELEMENT MODEL

The finite element program described in this section is similar in structure to the PLASTOSHELL program in reference [2]. Many elements used to model the deflection of a plate under a transverse load have proven too stiff when the plate modeled is very thin and the deflection is large. As a result, Hughes and Cohen [3] developed the "heterosis" element, which is used in the present analysis. The element has nine nodes: four corner nodes, four mid-side nodes, and a center node.

AFOIL, the FORTRAN code for the large displacement analysis of a tension-foil bearing, is an 800 line, double precision program. Presently, AFOIL includes the following subroutines:

- INPUT - reads the problem description from a file;

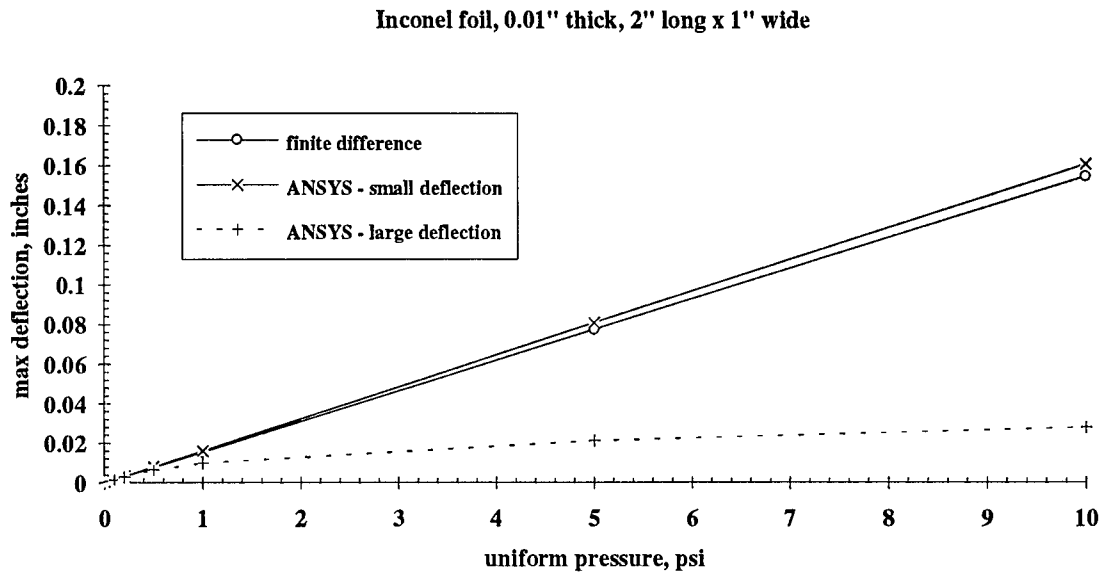


Figure 3. Finite difference/ANSYS comparisons

- ZERO - initializes vectors and matrices;
- ELAS - generates the elasticity matrix for the foil;
- MESH - identifies the location of element nodes;
- BGL - reads the pressure input from a file, sets up the linear and nonlinear parts of the strain/displacement matrix $[B]$, and computes the nodal loads due to pressure;
- SHAPE - evaluates the shape functions used to compute $[B]$ and the nodal loads;
- BFILL - fills $[B]$;
- BOUNDS - fixes the boundary conditions, two clamped ends, one free edge, and one line of symmetry;
- STIFF - computes the stiffness matrix for each element;
- FRONT - solves for the displacements using the frontal technique [4];
- RESID - computes reaction forces and residual forces for a convergence check;
- CONV - checks for convergence of the iterative process; and
- OUT - writes the results to an output file.

Presently, AFOIL runs, but computes incorrect deflections. It appears that the problem is in the FRONT subroutine. If the problem continues despite debugging efforts, a slower Gaussian elimination method will be substituted for the frontal technique.

CONCLUSIONS

ANSYS models of a thin foil under uniform transverse pressure indicate the importance of using a nonlinear large deflection analysis for computing the foil deflections. An 800 line, double precision FORTRAN computer program, AFOIL, has been developed for the analysis of the foil in a tension-foil bearing. However, debugging of AFOIL is not complete. The

solution technique may be changed if debugging of the frontal subroutine does not correct the current problem.

REFERENCES

- [1] Szilard, Rudolph, 1974, *Theory and Analysis of Plates: Classical and Numerical Methods*, Prentice Hall, Englewood Cliffs, NJ.
- [2] Hinton, E. and Owen, D. R. J., 1984, *Finite Element Software for Plates and Shells*, Pineridge Press Limited, Swansea, U.K.
- [3] Hughes, T. J. R., and Cohen, Martin, 1978, "The 'Heterosis' Finite Element for Plate Bending," *Computers and Structures*, Vol. 9, pp 445-450.
- [4] Hinton, E. and Owen, D. R. J., 1977, *Finite Element Programming*, Academic Press, London.

1995

NASA/ASEE SUMMER FACULTY FELLOWSHIP PROGRAM

**MARSHALL SPACE FLIGHT CENTER
THE UNIVERSITY OF ALABAMA IN HUNTSVILLE**

ATOMIZATION CHARACTERISTICS OF SWIRL INJECTOR SPRAYS

Prepared By:	Douglas A. Feikema, Ph.D.
Academic Rank:	Assistant Professor
Institution and Department:	The University of Alabama in Huntsville Department of Mechanical and Aerospace Engineering Propulsion Research Center
NASA/MSFC:	
Laboratory:	Propulsion
Division:	Motor Systems
Branch:	Combustion Physics
MSFC Colleagues:	Richard Eskridge Chris Dobson

INTRODUCTION

Stable combustion within rocket engines is a continuing concern for designers of rocket engine systems. The swirl-coaxial injector has demonstrated effectiveness in achieving atomization and mixing, and therefore stable combustion. Swirl-coaxial injector technology is being deployed in the American RL10A rocket design and Russian engine systems already make wide spread use of this technology. The present requirement for swirl injector research is derived from NASA's current Reusable Launch Vehicle (RLV) technology program. This report describes some of the background and literature on this topic including drop size measurements, comparison with theoretical predictions, the effect of surface tension on the atomization process, and surface wave characteristics of liquid film at the exit of the injector.

BACKGROUND AND LITERATURE

High frequency combustion instabilities in liquid-propellant rocket engines are considered the most destructive and continues to challenge the designer due to the complex interactions of turbulent combustion processes ^{1, 2}. The periodic combustion within the chamber results in pressure oscillations and often periodic flow of propellant. Historically, these instabilities have been reduced by joining baffle plates to the injector face which serve to damp the coupled, unsteady combustion and oscillating propellant flow. These effects can result in periodic atomization of the liquid propellants which include fluctuations in drop size, local mixture fraction of combustible mixture, and position of the flame front. Such changes within the reaction zone are important since they affect wall heating and chamber pressure. The approach selected to better understand these high pressure combustion phenomenon is to test single injector elements inside a windowed combustion chamber where detailed measurements and flow visualization can be conducted. Prior to making high pressure measurements, atmospheric atomization studies are made for diagnostic purposes as well as to validate computer models.

The objective of this study was to investigate some properties of atomization provided by pressure-swirl type injectors. The parameters which affect the atomization process have been extensively reported ^{3, 4, 5, 6, 7, 8}. Atomization is a process whereby a volume of liquid is transformed into a large number of small drops ⁹. The principle aim is to produce a high ratio of surface area to mass of the liquid phase which promotes high evaporation rates and more rapid combustion. Means of controlling the drop size is important in this application and is understood by examination of the mechanisms by which the liquid sheets breakup ¹⁰. The fundamental principle for the disintegration of a liquid involves increasing the surface area of the sheet until it becomes unstable and disintegrates. Disintegration of the liquid sheet is promoted by turbulence in the liquid flow prior to exiting the injector, and by the action of aerodynamic forces ¹¹, and is opposed by the viscosity and surface tension forces of the liquid sheet ⁷. For the swirl injector considered in this study a conical sheet ³ forms upon exiting the injector body and previous drop size measurements ⁴ and theory ¹⁰ suggest that the thickness of the liquid sheet is important in predicting the drop size in the atomized liquid.

The present effort attempts to investigate some parameters important for the atomization of a liquid propellant simulant injected with a swirl, hollow-cone injector operating at atmospheric pressure. Optical measurements within these environments have proven to be invaluable tools in quantifying the physical environment of two phase flows. The effort reported herein attempts to investigate the role of the injected liquid film and surface tension on the atomization process and resulting drop size.

EXPERIMENTAL METHODS

The single element injector test facility utilized during the course of the laboratory investigations has been previously developed and described ⁴. The major features of the system include six pressurized

accumulators which are first filled with water and then pressurized with compressed air. These accumulators can deliver approximately six gallons of water at constant delivery pressures up to 500 psia. A transparent, acrylic, swirl injector element has been characterized which has been previously designed to examine the internal flow environment in the central posts of tangential-entry, swirl injector elements typical of those used in liquid propellant rockets³. Several such injectors have been tested and analyzed³ for their internal geometry and measurements were made of the axial pressure distribution, the shape of the air core formed in the post, the velocity profile in the liquid film, and the near exit spatial mass flow distribution of the spray cone. The H-3, I-9 injector from this group was selected for the effort. The injector element was calibrated and later operated at plenum stagnation pressures of 75 to 85 psig (90 to 100 psia) where the water mass flow rate was 1.1 to 1.2 lbm/s (499 to 544 gm/s). Under these conditions the injector could be operated for approximately 40 seconds.

Optical measurements of the exiting liquid film just before exiting the injector were made to investigate the wave structure of the water/air interface. A Questar QM1 magnifying microscope with a large working distance was used along with a synchronized 1 ms strobe to record the flow of the water film. The time resolved images were stored on standard video with the use of CIDTEC (Model: CID2710) street camera. The video was digitized into a image processing software package and the two dimensional wave structure was represented as a curve. Fourier analysis of this wave was completed in order to determine if dominant wave lengths exist.

RESULTS AND DISCUSSION

Drop size measurements⁴ and breakup mechanism¹⁰

At the exit of the injector a rotating, annular, cross-sectional, liquid sheet exits at a measured mean thickness of 635 μm and axial velocity of approximately 35 m/s (Ref. 3). The turbulence intensity in the axial direction of the liquid film was measured to be 10%. As the liquid sheet leaves the injector body the radial momentum of the fluid induced by the tangential entry ports at the entrance of the post causes the liquid sheet to move radially outward and enhance the breakup of the sheet into ligaments and eventually drops. At the injector exit waves are formed due to disturbances resulting in local thickening and thinning of the conical sheet normal to the sheet propagation direction. The thickened regions sever from the sheet into rings which then break apart into ribbons and ligaments. The ribbons and ligaments then breakup into drops by the Rayleigh mechanism and interactions with other drops. This mechanism applies only for the case when the atomizing liquid is below the supercritical pressure, where surface tension plays an important role. Above the supercritical pressure the surface tension becomes zero and is believed to have little or no effect upon the atomization process; however, little information is available to either confirm or deny this statement.

Previous measurements⁴ have shown that the largest individual drops are found in the dense spray region and the maximum individual drop sizes measured were 1670 μm and appear consistent with the measured mean exit liquid film thickness at the injector exit of 635 μm ³ which is in agreement with the value presently measured. It is important to point out that the maximum drop size is 2.6 times the measured exiting liquid sheet thickness. It also is interesting to note that a liquid jet which breakups purely due to the Rayleigh mechanism is 1.89 times the jet diameter⁸ even though the mechanism for breakup of the conical sheet is physically much different. The mechanism proposed by York et al.¹⁰ resulted in a method for estimating the mean drop size for conical sheets produced by pressure-swirl,

$$D_d = 2.13(t_s \cdot \lambda^*)^{1/2} \quad (1)$$

hollow cone atomizers. In Eqn. 1, t_s , is the sheet thickness at the injector exit and λ^* is the wavelength corresponding to the maximum growth rate. In estimating the wavelength corresponding to the maximum growth rate they define two Weber numbers as:

$$We_1 = \frac{\rho_A \cdot U_R^2 \cdot t_s}{\sigma_L} \quad We_2 = \frac{\rho_A \cdot U_R^2 \cdot \lambda^*}{\sigma_L} \quad (2)$$

These parameters are dependent upon the gas/liquid density ratio ρ_A/ρ_L . The various parameters as they relate to the present conditions are shown in Table 1. The calculated wavelength corresponding to the maximum growth rate, λ^* , is predicted to be 464 μm . The predicted mean diameter after Eqn. 1 is 1150 μm which is in qualitative agreement with the measured maximum diameter (1670 μm) but is larger than the arithmetic mean diameter, D_{10} , (330 μm). It is proposed that the measured mean diameter is smaller than predicted by Eqn. 1 since the break-up mechanism of York et al., does not account for drop collisions and aerodynamic breakup effects.

Table 1 Parameters used in Eqns. 1 and 2

ρ_A (kg/m ³)	ρ_L (kg/m ³)	U_R (m/s)	σ_L (kg/s ²)	μ_L (kg/m/s)	We ₁	We ₂
1.2	1000	35	0.0717	8.5×10^{-4}	13.0	9.5

Effects of Surface Tension:

Surface tension is a force or pressure exerted along a liquid/gas interface which results from the difference of the cohesive intermolecular forces present in the liquid and gas. The action of surface tension on the atomization process has two important effects. In the initial stages surface tension opposes the development of surface distortions into ligaments and the formation of drops from the ligaments, but it assists in the final stages of disruption⁶. Figure 1 and 2 show the surface tension of liquid hydrogen¹² and oxygen¹³ respectively. Above the critical conditions the surface tension becomes zero. The use of surfactants in atomization phenomenon is common in many applications since low concentrations of the surfactant can greatly change the surface forces at a liquid/gas interface. However, use of surfactants to study rocket atomizers is impracticable since the adsorption of surfactants is slow and the liquid breaks up initially as if no surfactant is present⁷.

Water Film Surface Wave Characteristics

Figure 4 shows an instantaneous digitized image of the water film thickness at the exit of the injector. The thickness agrees with the measurements previously reported³. Figure 5 shows the Fast Fourier Transform (FFT) of the measured wave in Figure 4. Several such FFT's have been constructed for many different realizations at the same location and they all have the same form as Figure 5. The FFT's show that long wavelength water waves at low frequencies are dominant. Other frequencies exist but none appear dominant. This supports the hypothesis that the surface is chaotic suggesting that the turbulence in the liquid film determines the surface wave structure.

CONCLUSIONS

The following conclusions can be drawn from this summer's results:

- 1) The York mechanism is in qualitative agreement with drop size measurements.
- 2) The present liquid film thickness measurements agree with previous measurements³.
- 3) The liquid film is statistically flat as verified by the video images and the FFT.

- 4) The dominant frequency/wavelength of the surface wave at the liquid/gas interface corresponds a low frequency or long wavelength disturbance. Turbulence appears to determine the wave structure.

ACKNOWLEDGMENT

The author gratefully acknowledges the assistance of and discussions with Richard Eskridge, Chris Dobson, Michael Lee, Dolf Mills, and John Hutt of the Combustion Physics Branch in connection with the summer faculty program.

REFERENCES

1. Oefelein, J.C. and Yang, V., "Comprehensive Review of Liquid-Propellant Combustion Instabilities in F-1 Engines", *Journal of Propulsion and Power*, Vol. 9, No. 5, Sept. - Oct. 1993.
2. Sutton, G. P., *Rocket Propulsion Elements: An Introduction to the Engineering of Rockets*, Sixth Edition, John Wiley and Sons Inc., pp. 268 - 279, 1992.
3. Hutt, J.J., McDaniels, D.M., Smith, A.W., "Internal Flow Environment of Swirl Injectors", AIAA 94-3262, submitted to Journal, Indianapolis, IN, 1994.
4. Feikema, D.A., Eskridge, R, and Hutt, J.J., "Structure of a Non-Evaporating Swirl Injector Spray", submitted to journal, March, 1993.
5. Rahman, A.A., Pal, S., and Santoro, R.J., "Swirl Coaxial Atomization: Cold-Flow and Hot-fire Experiments", AIAA 95-0381, 33rd Aerospace Sciences Meeting and Exhibit, Reno, Jan., 1995.
6. Griffen, E., and Muraszew, A., *The Atomization of Liquid Fuels*, Chapman and Hall, 1953.
7. Dombrowski, N. and Fraser, R.P., "A Photographic Investigation into the Disintegration of Liquid Sheets", *Philos. Trans. R. Soc. London Ser. A, Math. Phys. Sci.*, Vol. 247, No. 924, 1954, pp. 101 - 130.
8. Lefebvre, A. H., *Atomization and Sprays*, Hemisphere Publishing Corporation, 1989.
9. Mansour, A. and Chigier, N., "Dynamic Behavior of Liquid Sheets", *Phys. Fluids A*, 3 (12), pp. 2971 - 2980, 1991.
10. York, J.L., Stubbs, H.E., Tek, M.R., "The Mechanism of Disintegration of Liquid Sheets", *Trans. ASME*, Vol. 75, pp. 1279 - 1286, 1953.
11. Wu, P.-K. and Faeth, G.M., "Aerodynamic Effects on Primary Breakup of Turbulent Liquids", *Atomization and Sprays*, Vol. 3, pp. 265 - 289, 1993.
12. McCarty R.D. and Weber, L. A., "Thermophysical Properties of Parahydrogen from the Freezing Liquid Line to 5000 R for Pressures to 10,000 psia", *NBS Technical Note 617*, 1972.
13. McCarty R.D. and Weber, L. A., "Thermophysical Properties of Oxygen from the Freezing Liquid Line to 600 R for Pressures to 5,000 psia", *NBS Technical Note 384*, 1971.

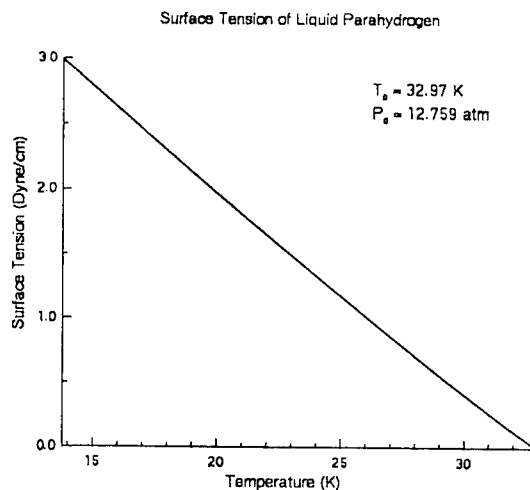


Figure 1 Surface Tension Liquid Hydrogen, Pressure Corresponds to the Saturation Pressure.

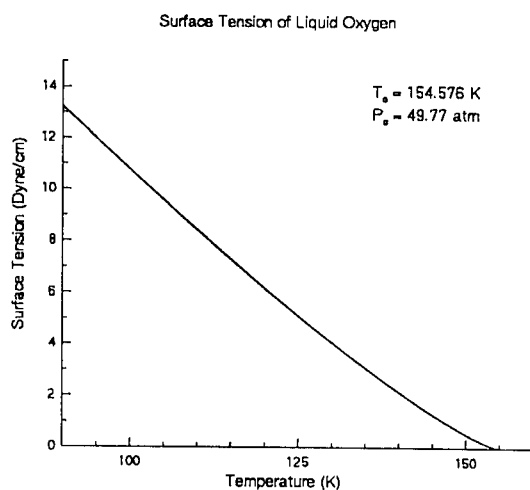


Figure 2 Surface Tension Liquid Oxygen, Pressure Corresponds to the Saturation Pressure.

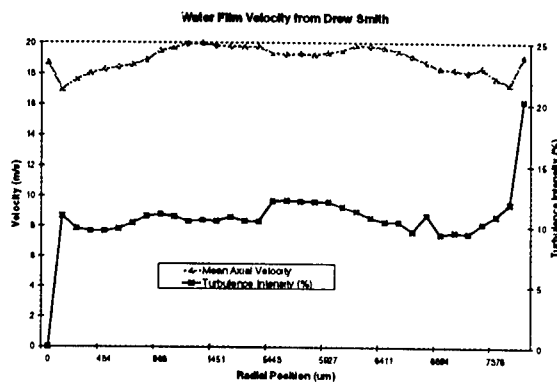


Figure 3 LDV Measured Mean Axial Velocity and Turbulence Intensity Across the Film Thickness 0.22 inches from the Injector Exit. (Conditions Different from the present)

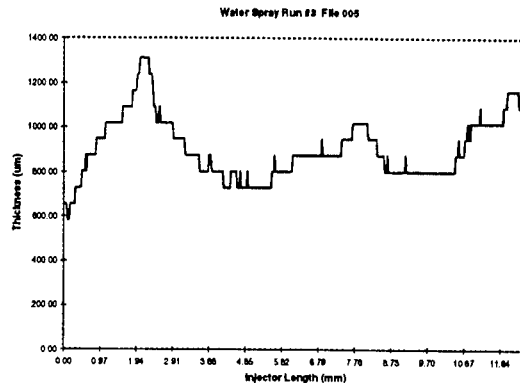


Figure 4 Instantaneous Two-Dimensional Surface Wave Thickness at the Injector Exit.

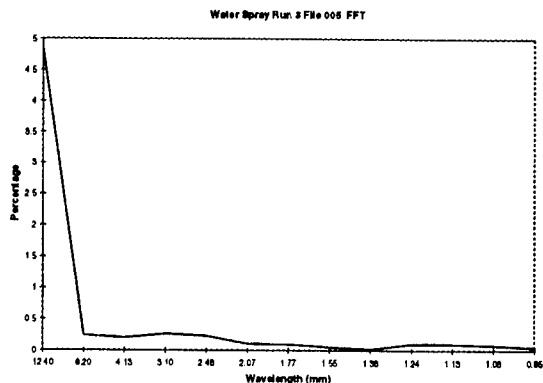


Figure 5 Fast Fourier Transform of the Water Wave Shown in Figure 4 (Wave Length decreases from right to left).

1995

NASA/ASEE SUMMER FACULTY FELLOWSHIP PROGRAM

**MARSHALL SPACE FLIGHT CENTER
THE UNIVERSITY OF ALABAMA IN HUNTSVILLE**

CHARACTERIZATION OF ZINC SELENIDE SINGLE CRYSTALS

Prepared By:	Rosario A. Gerhardt, Eng.Sc.D.
Academic Rank:	Associate Professor
Institution and Department:	The Georgia Institute of Technology School of Materials Science and Engineering
NASA/MSFC:	
Office:	Space Sciences Lab
Division:	Microgravity
Branch:	Crystal Growth and Solidification
MSFC Colleagues:	S.L. Lehoczky, Ph.D. Ching-Hua Su, Ph.D. Curtis Banks Martin Volz, Ph.D.

INTRODUCTION

ZnSe single crystals of high quality and low impurity levels are desired for use as substrates in optoelectronic devices. This is especially true when the device requires the formation of homoepitaxial layers[1]. While ZnSe is commercially available, it is at present extremely expensive due to the difficulty of growing single crystal boules with low impurity content and the resultant low yields. Many researchers[2-6] have found it necessary to heat treat the crystals in liquid Zn in order to remove the impurities, lower the resistivity and activate the photoluminescence at room temperature.

The physical vapor transport method (PVT) has been successfully used at MSFC to grow many single crystals of II-VI semiconducting materials including ZnSe[7]. The main goal at NASA has been to try to establish the effect of gravity on the growth parameters. To this effect, crystals have been grown vertically upwards or horizontally. Both (111) and (110) oriented ZnSe crystals have been obtained via unseeded PVT growth. Preliminary characterization of the horizontally grown crystals has revealed that Cu is a major impurity and that the low temperature photoluminescence spectra is dominated by the copper peak. The ratio of the copper peak to the free exciton peak is being used to determine variations in composition throughout the crystal[8].

It was the intent of this project to map the copper composition of various crystals via photoluminescence first, then measure their electrical resistivity and capacitance as a function of frequency before proceeding with a heat treatment designed to remove the copper impurities. However, equipment difficulties with the photoluminescence set up, having to establish a procedure for measuring the electrical properties of the as-grown crystals and time limitations made us re-evaluate the project goals. Vertically grown samples designated as ZnSe-25 were chosen to be measured electrically since they were not expected to show as much variation in their composition through their cross-section as the horizontally grown samples.

EXPERIMENTAL DETAILS

(1) Sample surface preparation

ZnSe crystals are very brittle and handling them requires much care. Samples were lapped manually on SiC paper, washed and then attached to glass platens using paraffin wax. Samples were then lapped on both sides using the Logitech Lapping and Polishing Equipment. Lapping was done with 9 micron alumina particles. Polishing was accomplished with 0.3 micron alumina particles suspended in 12.5% sodium hypochlorite solution diluted 50:50 with water. Chemomet Buehler paper was used for the polishing steps.

(2) Photoluminescence Measurements

The sample was placed in a cryostat and held at a temperature of $T=1.4$ K. An Ar ion laser from Coherent Inc. run at 364nm with 10mW was used to excite photoluminescence from the sample. A Spex spectrometer was used to collect the PL intensity data. The spectrometer was run at a voltage of 1730 and its slits were set at 0.18, 0.22 and 0.18.

(3) Electrical contacts

Electrical contacts were placed on the samples using 5/9 pure indium. The method employed does not require heating of the indium, instead it consists of depositing extremely thin sequential layers of indium until a good contact has been established. Gold wires were used to attach samples to the measuring equipment. At least 4 contacts were placed on each sample.

(4) Electrical resistivity measurements

Samples were placed in the Hall measurement cryostat set up. Van der Pauw[9] resistivity measurements of the as-grown crystals of ZnSe-25 using the established Keithley 220 Current Source and Keithley 181 Nanovoltmeter were not possible because their resistivity was beyond the capabilities of those instruments. Instead of the Keithley 181 Nanovoltmeter, a Keithley 617 Electrometer was used. Changes to the Hall measurements computer program were made in order to run the new configuration automatically. Many measurements were carried out manually in order to establish the correct waiting times and to be sure that measurements would be made in the ohmic regime.

(5) Capacitance measurements

Samples were measured as a function of frequency, ac voltage signal and superimposed dc bias voltage. The equipment used was a Hewlett-Packard LCR Meter Model 4275A. A short computer program was written in order to collect C-V measurements. The Keithley 617 was used as the dc bias voltage source in this case.

(6) Heat treatment of the samples

Samples were heat treated in closed quartz ampoules. Samples were originally surrounded by Zn powder and subsequently heated above the melting point of Zn and held at that temperature for 48 hours.

RESULTS AND DISCUSSION

The resistivity of the as-grown ZnSe-25 samples is so large that very long waiting times are required in order to let the sample reach equilibrium. The Keithley 617 is capable of giving resistance values directly using only two contacts. Values between individual contact pairs varied from 17 to 42 gigaohms. In order to make van der Pauw measurements, it was necessary to establish whether contacts were ohmic. Figure 1 displays the voltage vs. current curve obtained using the 220 current source and the 617 as a voltmeter. Waiting times between points shown were only 10 minutes. Under other circumstances, waiting periods needed to be as long as 45 minutes. The fairly linear behavior seen in this figure demonstrates that behavior of the sample is ohmic below 8 nanoamps. The deviations at higher currents may actually be due to limitations of the current source rather than non-ohmic behavior of the samples. Based on this information, a current of 3 nanoamps was used to measure the resistivity. The limitations of the current source were again noticeable when resistivity measurements as a function of temperature(200-400K) were taken. Values did not seem to change with temperature very much. The resistivity of the ZnSe-25 sample at 300K, using the van der Pauw method, was calculated to be 3.0×10^9 (ohm-cm).

Capacitance measurements were first made as a function of frequency. The frequencies of the LCR meter used range from 10 kHz to 10 MHz. This instrument is designed to measure samples with impedances of 10 megaohms or less, therefore obtaining data that can be ascribed to the sample itself is a challenging task. Nevertheless, since impedance of a capacitor in series is given by $1/\omega C$, some useful data may be obtained as the frequency of the measurement is increased. On the other hand, inductive losses may dominate at the highest frequencies. Figure 2 shows a capacitance vs. log frequency plot taken at a constant ac voltage of 0.1. As might be expected because of the length of the leads, the data above 1 MHz shows inductive behavior (showing a decreasing value of capacitance which reaches negative values at the highest frequencies). In order to make sure that these values are not genuinely due to the sample, capacitance measurements were taken at a fixed frequency of 4 MHz and the ac voltage was varied from 0.1 to 1.0 volts. Both capacitance and dissipation factor demonstrated that the inductive behavior nearly disappears at higher levels of ac voltages. In order to avoid short circuiting through the instrument at lower frequencies or being dominated by inductive losses at the higher frequencies, a frequency of 400 kHz was picked for conducting the C-V measurements. It should be mentioned that each pair of contacts was measured independently and that values of capacitance obtained ranged from 35 fF to 240 fF. Measurements were taken at temperatures ranging from 15K to 300K. Virtually no temperature dependence could be detected.

The C-V measurements were taken at room temperature with as low an ac signal as needed to prevent short circuiting through the LCR meter. The superimposed dc bias voltage was varied from -10 to +10 in 100 mV steps. As is expected for an insulating sample, no dependence upon dc bias voltage was found. Figure 3 displays the $1/C^2$ vs Bias voltage curve. The heat treated sample is expected to show a dependence on bias voltage which may then be used to calculate the number of carriers present[10].

Prior to subjecting the electrically measured sample to a heat treatment to lower its resistivity, photoluminescence measurements were taken. Figure 4 depicts the photoluminescence spectrum at wavenumbers between 22000 and 22700 cm^{-1} . Three major features are seen. They are the peaks at 22592.5, 22445.5 and 21900 cm^{-1} . The first peak is ascribed to the free exciton peak while the other two are presumably related to the copper impurities[11]. It should be noted that it has been observed that the sample surface condition affects the magnitude of the peaks, although it appears that it affects them all equally[12]. It is expected that the ratio of the first to the second peak will increase dramatically after the heat treatment.

CONCLUSIONS

This project provided this investigator with the opportunity to learn about some of the activities in the microgravity division and work with single crystals of technological importance for optoelectronics. In particular, the exposure to the photoluminescence and semiconductor polishing and etching will be very useful for this investigator's future research projects. At the same time, her expertise with insulating materials was crucial for

establishing the proper procedures for measurement of the electrical resistivity and capacitance measurements of the as grown ZnSe-25 crystals. The resistivity of these crystals at room temperature was determined to be 3×10^9 ohm-cm. CV measurements confirmed the highly insulating nature of these crystals by showing no bias voltage dependence. Since all data reported was obtained by borrowing equipment from other branches, it is recommended that the crystal growth and solidification branch purchase a Keithley 617 electrometer for both the resistivity as well as the C-V measurements. This equipment is versatile in that it can be used to measure resistance directly, as a voltage source, a voltmeter and also as a current meter (as low as 1×10^{-15} amps). It should be added that in order to use the 617 to its fullest capability and allow measurement of resistances higher than a few gigaohms, additional hardware changes will be needed. The LCR meter used to obtain the capacitance values (HP4275A) has to be used with care as discussed in the results section. A single frequency capacitance meter better capable of measuring higher impedance samples can be obtained from Boonton Electronics or Andeen-Hagerling. However, the HP4275A will work well with lower resistivity semiconducting crystals.

Acknowledgements

The author would like to thank the following MSFC colleagues for their contributions to this project: Don Gillis, for showing me the proper procedures for polishing and etching II-VI single crystals; Charles Sisk, for showing me how to put electrical contacts via the cold indium method and loaning me the HP4275A LCR meter; Victoria Coffey, for loaning me the Keithley 617 Electrometer and related cables; Bill Witherow, for loaning me an optical aperture and answering questions concerning the PL set up. In addition, the following people deserve special thanks for all their help and support: Curtis Bahr, Shirley Buford, Jeffrey Wang, Ernestine Cothran, Teresa Shurtz and Gerald Karr.

REFERENCES

1. J. Nishizawa, K. Itoh, Y. Okuno and F. Sakurai, *J.Appl.Phys.* 57(6)2210(1985).
2. Y.S. Park, C.R. Geesner and B.K. Shin, circa 1973.
3. M.E. Ozsam and J. Woods, *Appl.Phys.Lett.* 25[9] 489(1974).
4. R.J. Robinson and Z.K. Kun, *Appl.Phys.Lett.* 27[2] 74(1975).
5. D.M. Chiu, *J.Phys.D: Appl.Phys.* 16, 2281 (1983).
6. A.N. Krasnov, Yu N. Purtov, Yu F. Vaksman and V.V. Serdyuk, *J.Cryst.Growth* 125, 373(1992).
7. Ching-Hua Su and Yi-Gao Sha, Book Chapter entitled "Growth of Wide Band Gap II-VI Compound Semiconductors by Physical Vapor Transport", in press.
8. M.P. Volz and Ching-Hua Su, preliminary Cu compositional analysis of ZnSe-15 crystals, June 1994.
9. ASTM Designation: F76-86: Measuring Resistivity and Hall Coefficient and Determining Hall Mobility in Single-Crystal Semiconductors.
10. S.Z. Fujita, T. Tojyo, T. Yoshizawa and S.G. Fujita, *J.Elect. Matls.* 24[3] 137 (1995).
11. G. Jones and J. Woods, *J. Lumin.* 9, 389(1974).
12. Analysis of PL data taken by M.P. Volz under various surface conditions.

Voltage vs. Current

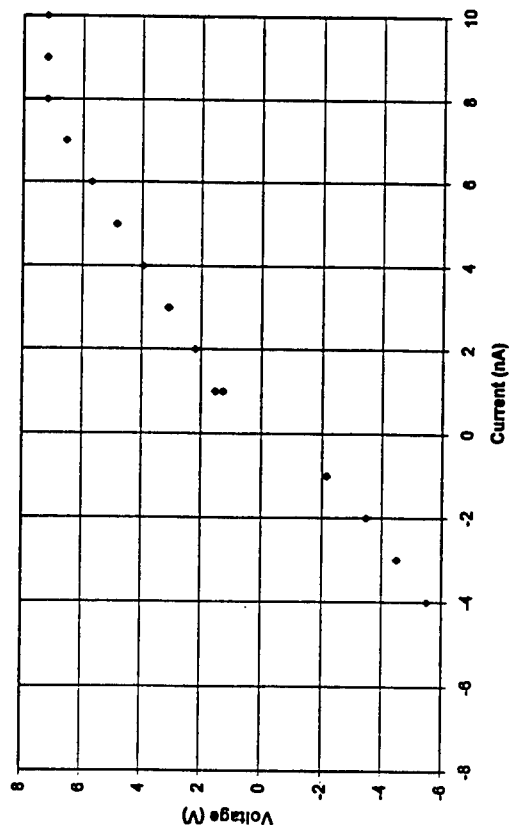


Figure 1

Capacitance vs. Log Frequency

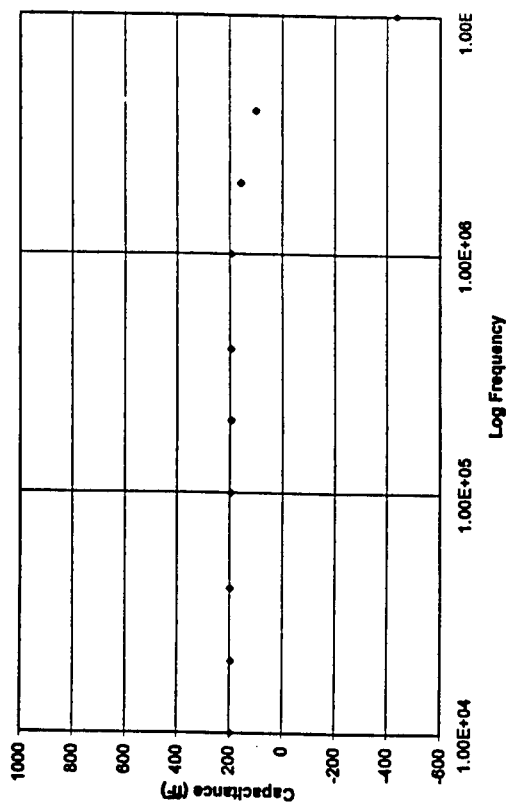


Figure 2

$1/C^2$ vs. Bias Voltage

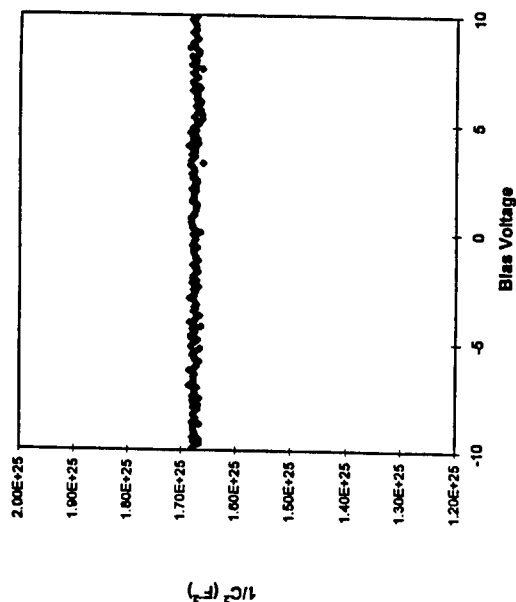


Figure 3

642100 25H1C0R2.SPT xms25;.18-.22,.18;1738;1844

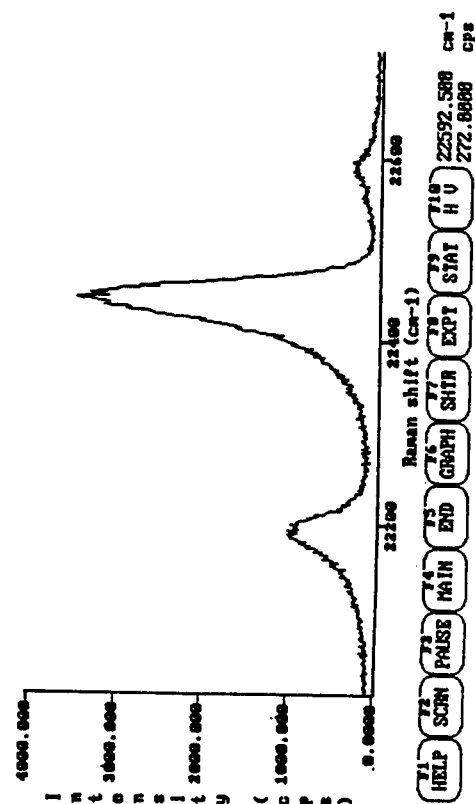


Figure 4

RESIDUAL LIFE ASSESSMENT OF THE SSME/ATD HPOTP
TURNAROUND DUCT (TAD)

Prepared By: R. Steven Gross

Academic Rank: Assistant Professor

Institution and Department: Auburn University
Department of Aerospace Engineering

NASA/MSFC:

Laboratory: Structures and Dynamics
Division: Structural Analysis
Branch: Thermostructural Analysis

MSFC Colleague: David Herda

INTRODUCTION

Many of the life-limiting structural problems encountered in high-temperature aircraft and rocket engines result from thermal fatigue behavior. It has been known for over a hundred years that temperature gradients within a structure produces internal stresses. These thermally induced stresses can be as large or larger than the internal stresses generated by the application of external mechanical loads to the structure. Most aircraft and many rocket engines are reusable designs which must be able to withstand cyclic thermal and mechanical stress excursions associated with engine startup and shutdown. For these reusable designs, low cycle thermal fatigue is the life-limiting failure process for certain engine components.

A large body of analytical and experimental work has been produced over the last 50 years concerning the low cycle thermal fatigue behavior of metals. Halford [1] provides a historical review of work in this area starting in the early 1950's and extending into the late 1980's. The field of engineering fracture mechanics grew parallel with this field of low cycle thermal fatigue. From an engineering standpoint, these two fields merge once the component has been exposed to sufficient thermal stress cycles to allow for formation of a discernible crack or cracks.

This paper is concerned with the prediction of the low cycle thermal fatigue behavior of a component in a developmental (ATD) high pressure liquid oxygen turbopump (HPOTP) for the Space Shuttle Main Engine (SSME). This component is called the Turnaround Duct (TAD). The TAD is a complex single piece casting of MAR-M-247 material. Its function is to turn the hot turbine exhaust gas (1200⁰ F hydrogen rich gas steam) such that it can exhaust radially out of the turbopump. In very simple terms, the TAD consists of two rings connected axially by 22 hollow airfoil shaped struts with the turning vanes placed at the top, middle, and bottom of each strut. The TAD is attached to the other components of the pump via bolts passing through 14 of the 22 struts. Of the remaining 8 struts, four are equally spaced (90⁰ interval) and containing a cooling tube through which liquid hydrogen passes on its way to cool the shaft bearing assemblies. The remaining 4 struts are empty. One of the pump units in the certification test series was destructively examined after 22 test firings. Substantial axial cracking was found in two of the struts which contain cooling tubes. None of the other 20 struts showed any sign of internal cracking. This unusual low cycle thermal fatigue behavior within the two cooling tube struts is the focus of this study.

The fatigue and fracture analysis described in this report closely follows work performed by Sakon et al., [2] on thermally shocked steam turbine pump casings. The investigation procedure follows the outline given below.

- A. Establish an approximate analytical relationship between the J-integral for a cracked body under deformation-controlled loading and the strain-based intensity factor K_e .
- B. Use a linear finite element analysis (FEA) of the TAD structure to determine the cyclic stress behavior of the "cracked" region. This FEA did not model the crack(s) and only standard solid elements were employed to represent the geometry.
- C. Determine the functional form of the cyclic J-integral (ΔJ) in terms of the elliptical crack dimensions using the information from steps (A) and (B).
- D. Employ the experimental crack growth data for the MAR-M-247 material to establish the differential crack growth equation

$$da/dN = f(\Delta J). \quad (1)$$

- E. Numerically solve the ordinary, first order, nonlinear, differential equation (1) for the crack length "a" as a function of the number of thermal cycles "N".

ANALYSIS

A. Estimation of Cyclic J-Integral (ΔJ)

A number of investigators [3-4] have examined the use of the strain-based intensity factor to estimate the J-integral value when small scale yielding is occurring in the vicinity of the crack. Sakon and Kaneko [3] proposed that the value of J for the inelastic situation can be approximated by the elastic J-integral, J_e , for a deformation-controlled problem, such as thermal fatigue. They compared elastic and inelastic J-integral values for several cracked plate specimen geometry's using the FEM to substantiate the $J=J_e$ approximation.

Since the elastic form of the J-integral has been assumed for this problem, the relationship $J_e = K_I^2/E$ may be employed to convert the problem from one of finding the functional form of ΔJ to one of finding the functional form for ΔK , the cyclic stress intensity factor.

B. Linear Finite-Element Analysis of the TAD

As part of the TAD design process, the pump designers at the Pratt and Whitney Division of United Technologies developed a 3-D ANSYS finite element model of a 1/22nd section of the TAD. This initial model consisted of 39,720 tetrahedral (10 noded) elements and 66,639 nodes (=200,000 DOF). Essentially symmetric mechanical and thermal loading conditions on the TAD allowed for the construction of a smaller 1/44th segment model with symmetric boundary conditions.

This 1/44th segment model was used to perform the thermal and structural analyses of the TAD. A transient thermal analysis was done covering the standard Service Life mission at the 109% power level. The highest temperature gradients within the TAD structure were observed to occur during quick acceleration from 0% to the 109% power level and during steep deceleration from the 65% power level to engine shutdown. Steady state operation at the 109% power level produces low thermal gradients within the TAD structure and, hence, low thermal stresses.

Examination of the transient thermal analysis results by Pratt and Whitney engineers lead to the identification of two acceleration time points and two deceleration time points where the temperature gradients peaked within various locations of the TAD structure. Linearly elastic structural analyses were performed at each of these four time points to determine the TAD internal stress and strain state. This stress (strain) information is necessary to establish the cyclic stress (strain) history experienced by the TAD structure during the Service Life mission.

"Hoop" stress (σ_H) contours acting on the centerline of the strut were constructed for the four time points of interest. Based on these stress contours and the observed fracture behavior, two possible crack "paths" are considered for fracture analysis. The distribution of the "hoop" stress along each of the assumed crack paths was extracted from the FEM results for all four of the time points. The stress range experienced by a given point, A, along the crack path is the difference between the acceleration and deceleration hoop stress values at point A. Since there are two acceleration and two deceleration time points, four stress range combinations are possible:

$$\Delta\sigma_H^1 = \sigma_H^{7703} - \sigma_H^{7203}$$

$$\Delta\sigma_H^2 = \sigma_H^{7705} - \sigma_H^{7203}$$

$$\Delta\sigma_H^3 = \sigma_H^{7703} - \sigma_H^{7205}$$

$$\Delta\sigma_H^4 = \sigma_H^{7705} - \sigma_H^{7205}$$

for each crack path. The largest stress range for any point along crack path #1 is produced by the stress difference created from time points 7705 (deceleration) and 7205 (acceleration). This behavior is true for the other three crack paths and from this point onward in the analysis, the stress range employed to calculate the cyclic stress intensity value, ΔK , is that given by $\Delta\sigma_H = \sigma_H^{7705} - \sigma_H^{7205}$, for all four crack paths.

C. Functional Form of ΔK in Terms of Cyclic Stress Range and Crack Dimensions

The cyclic stress intensity factor, ΔK can be calculated from the cyclic stress range, $\Delta\sigma$, by use of a method recommended by the ASME Boiler and Pressure Vessel Code, Section XI.

$$\Delta K_I = (M_m \Delta\sigma_m + M_b \Delta\sigma_b) \sqrt{\pi a} \quad (2)$$

M_m - MEMBRANE CRACK SHAPE FACTOR

M_b - BENDING CRACK SHAPE FACTOR

$\Delta\sigma_m$ - MEMBRANE COMPONENT OF THE STRESS RANGE AT CRACK TIP

$\Delta\sigma_b$ - BENDING COMPONENT OF THE STRESS RANGE AT CRACK TIP

The membrane and bending crack shape factors functions of the crack dimensions a (depth) and c (length). The formulas for these shape factors was given by Newman in terms of a and c . From the previously determined stress range along the crack path, $\Delta\sigma$, the membrane and bending stress range components, $\Delta\sigma_m$ and $\Delta\sigma_b$, are known as functions of the crack depth a . Consequently, ΔK is now completely determined as a function of the crack depth a .

D. Experimental Determination of $h(\Delta K)$

Pratt and Whitney engineers have experimentally determined the function $h(\Delta K)$ for the MAR-M-247 material and approximated the function as

$$\log[h(\Delta K)] = C_1 \sinh(C_2 \log[\Delta K] + C_3) + C_4$$

where C_1 , C_2 , C_3 and C_4 are experimentally determined constants.

E. Solution of the Crack Growth Equation, $da/dN = h(\Delta K)$

The Crack Growth Equation is a first order, nonlinear, ordinary differential equation which was solved using the MATLAB software (Runge-Kutta, 2-3) for the crack depth $a(N)$.

CONCLUSIONS

- 1) The present analysis method cannot completely predict the low-cycle thermal fatigue cracking observed in the cooling tube struts of Unit #9.
 - a) During thermal cycling the analysis predicts periods of rapid crack growth, but the total crack length is less than that observed in service.
 - b) Prediction accuracy could be improved by defining how the hoop stress varies across the "net" section as the crack grows.
- 2) The linear elastic FEM analysis indicates that a sufficient thermal stress cycling occurs to cause substantial low-cycle crack growth, if an initial flaw exists.
- 3) More complete knowledge of the thermal environment on the interior of the strut is necessary to improve the fatigue behavior prediction.

REFERENCES

1. Halford, A. G, in *Thermal Stresses II*, edited by Richard B. Heinarski, published by North-Holland, 1987.
2. Sakon, T., Fujiharu, M., and Sada, T., in *Thermo-mechanical Fatigue Behavior of Materials*, ASTM STP 1186, 1993, pp. 239-252.
3. Sakon, T., and Kaneko, H., in *Proceedings of the Fifth International Conference on Creep of Materials*, May 18-21, 1992, pp. 227-233.
4. Rau, C. A., Jr., Gemma, A. E., and Leverant, G. R., in *Fatigue at Elevated Temperatures*, ASTM STP 520, 1973, pp 166-178.

1995

NASA/ASEE SUMMER FACULTY FELLOWSHIP PROGRAM

MARSHALL SPACE FLIGHT CENTER
THE UNIVERSITY OF ALABAMA IN HUNTSVILLE

RELATIVITY EFFECTS FOR SPACE-BASED COHERENT LIDAR EXPERIMENTS

Prepared by:	V. S. Rao Gudimetla, Ph. D.
Academic Rank:	Assistant Professor
Institution and Department:	Oregon Graduate Institute Department of Electrical Engg. and Applied Physics
NASA/MSFC:	
Laboratory:	Astrionics
Division:	Optics and RF
Branch:	Electro-optics
MSFC Colleague:	Michael J. Kavaya, Ph. D.

INTRODUCTION

An effort was initiated last year¹ in the Astrionics Laboratory at Marshall Space Flight Center to examine and incorporate, if necessary, the effects of relativity in the design of space-based lidar systems. A space-based lidar system, named AEOLUS, is under development at Marshall Space Flight Center and it will be used to accurately measure atmospheric wind profiles. Effects of relativity were also observed in the performance of space-based systems, for example in case of global positioning systems², and corrections were incorporated into the design of instruments. During the last summer, the effects of special relativity on the design of space-based lidar systems were studied in detail, by analyzing the problem of laser scattering off a fixed target when the source and a co-located receiver are moving on a spacecraft. Since the proposed lidar system uses a coherent detection systems, errors even in the order of a few microradians must be corrected for to achieve a good signal-to-noise ratio. Previous analysis assumed that the ground is flat and the spacecraft is moving parallel to the ground, and developed analytical expressions for the location, direction and Doppler shift of the returning radiation. Because of the assumptions used in that analysis, only special relativity effects were involved. In this report, that analysis is extended to include general relativity³ and calculate its effects on the design.

METHOD OF ANALYSIS AND PATH GEOMETRY

Laser Atmospheric Wind Sounder systems were described in detail elsewhere⁴. Figure 1. shows the path geometry. Initially earth is assumed to be spherical and a satellite is moving with an angular velocity of ω radians/sec at a height H above the ground. For convenience, it is assumed that the satellite is in the equatorial orbit. Our goal is to find out first the direction of a light ray from a moving source (satellite) to the stationary ground, as observed from the ground and the paths taken by the retro-reflected and diffuse rays from the ground towards the satellite as observed by a receiver adjacent to the transmitter in the moving coordinate system.

Figure 1. also shows two coordinate systems. K system is a fixed coordinate system (coordinates are x, y, z and t). K_1 system describes the satellite motion and is moving with respect to K at an angular velocity of ω radians/sec (the coordinates are x_1, y_1 and z_1). Both have a common center and an angular separation ϕ_i between them at the starting time. In the analysis, all the coordinates are converted into spherical coordinates (r, θ, ϕ) where θ is the angle. For convenience, another coordinate system K' , centered on the satellite and rotating synchronously with K_1 , is shown (the coordinates are x', y' and z') and used in the analysis.

A correct approach to analyze this problem is to consider Kerr metric which is valid in the presence of gravitational field due to spinning mass and analyze the problem of the bend of the path of a photon under this metric. A general solution to this problem is not available except for the case of large gravitational fields such as those near black holes. In addition, consideration of Schwartzchild metric (mass not spinning but stationary), shows that the correction term in the metric for space and time scales is in the order of 10^{-9} . Hence a different approach is used. First zero mass

corrections that are valid for rotational geometry were calculated following the method Ashworth and Davies⁵. Then gravitational corrections were added linearly. Such methods were used in case of GPS and corrections appear to be acceptable².

Also if A and B are two points in a rotating system, the distance between them can be used by using a radar technique (A sends a signal to B and B returns it and the distance is given by multiplying half the round trip time with the light velocity) or by finding the shortest distance between them. In the literature, both techniques are used and it appears that the former method leads to Lorentz-like transformations.

In order to set up proper coordinate transformations, consider in the rotating system two orbits, separated by a distance dR in the equatorial plane and consider two points A and B in it (Figure 2.). The system is rotating about the origin O with an angular velocity ω (measured in the fixed system K). A laser transmitter is located at a distance of R from the origin of the K_1 system (at the center of K') and a ray is sent at time t_1 by the transmitter A when it is at A_1 towards an observer B when B is at B_1 on the ground. When the ray reaches ground, A is A_2 and B is at B_2 . When B sends the ray back along the retro-reflection (or in an arbitrary) direction, assume A is at A_3 and B is B_3 . The corresponding angles and geometry are shown in Figure 2.

The corresponding coordinate transformations between the inertial and rotating coordinates are given by

$$\begin{aligned} r_1 &= r [1 - R^2 \sin^2(\theta) \omega^2 / c^2] & r &= r_1 [1 + R_1^2 \sin^2(\theta_1) \omega_1^2 / c^2] \\ \cos(\theta_1) &= \frac{\cos(\theta)}{[1 - R^2 \sin^2(\theta) \omega^2 / c^2]} & \cos(\theta) &= \frac{\cos(\theta_1)}{[1 + R_1^2 \sin^2(\theta_1) \omega_1^2 / c^2]} \\ \Phi_1 &= \frac{\Phi - \omega t}{1 - R^2 \omega^2 / c^2} & \Phi &= \frac{\Phi_1 + \omega_1 t_1}{1 + R_1^2 \omega_1^2 / c^2} \end{aligned} \quad (1)$$

In addition,

$$\omega_1 = \frac{\omega}{1 - R^2 \omega^2 / c^2} \quad \omega = \frac{\omega_1}{1 + R_1^2 \omega_1^2 / c^2} \quad (2)$$

and

$$[1 - R^2 \omega^2 / c^2] [1 + R_1^2 \omega_1^2 / c^2] = 1$$

Using the above transformations, the direction and location of at the point of incidence on the earth of a light ray, transmitted in the direction (θ_{1t}, ϕ_{1t}) , is calculated in both coordinate systems. Then the ray is retro-reflected or sent along an arbitrary direction in the fixed coordinate system of the earth and the corresponding direction and location of return are calculated in the satellite coordinate system. The results are then corrected by adding the term $1 + \chi/c^2$ for the differential space-time metric. The results will be detailed in a separate report.

GENERAL RESULTS

If ϕ_{1t} is the azimuth angle of the transmitted ray and ϕ_{1ret} is that of the returning radiation after retro-reflection at the ground, then

$$\Delta\phi = \phi_{1ret} - \phi_{1t} = \omega T_{ret} \left[1 + R^2\omega^2/C^2 + \dots \right] \quad (3)$$

where all parameters are measured in the fixed coordinate system and T_{ret} is the round trip time. The corresponding change in the azimuthal angle at the receiver is calculated by multiplying the above change with $(R_e+h)/h$ where R_e is the radius of the earth and h is the satellite altitude (Figure 3.). Similar calculations can also be done for nadir angle.

$$\cos(\theta_{1rec}) = \cos(\theta_{1t}) \left[1 - \frac{1}{2} \frac{R_1^2 \omega_1^2 \sin^2(\theta_{1t})}{C^2} + \frac{1}{2} \frac{R^2 \omega^2 \sin^2(\theta)}{C^2} + \dots \right] \quad (4)$$

After estimating the angle difference, the result is multiplied by $(R_e+h)/h$ to get the nadir angle change at the transmitter/receiver location. Another simple approach is to estimate the arc lengths and calculate as follows:

$$\tan(\Delta\theta) = \Delta\theta = \frac{\omega T_{ret} (R_e+h) \sin(\theta_{1t}) \cos(\phi_{1t})}{h} \quad (5)$$

The relative Doppler shift in frequency is given by

$$f'_0 - f_0 = \frac{1}{2} \frac{R^2 \omega^2}{C^2} + \frac{GM}{C^2} \left[\frac{1}{R_e+h} - \frac{1}{R} \right] \quad (6)$$

where the first term is due to special relativity and the second term is due to gravity. It will be shown that the relativistic changes in both the coordinate angles are small compared with the lag angles.

ADDING THE GRAVITATIONAL EFFECTS

The gravitational effects can be incorporated, by recognizing that the Schwarzschild metric is given by

$$ds^2 = (1+2\chi/c^2) c^2 dt^2 - (1-2\chi/c^2)(dr^2 + r^2 d\theta^2 + r^2 \sin^2(\theta) d\phi^2) \quad (7)$$

This modifies all the results in the above equations, by modifying the terms $R^2\omega^2/c^2$ as $R^2\omega^2/c^2 + \chi/c^2$ for the forward path and by $R^2\omega^2/c^2 - \chi/c^2$ for the return path. The results are modified accordingly.

RESULTS FOR THE PROPOSED WIND SOUNDER

AEOLUS has a proposed altitude of 350 Kilometers, an angular velocity of 7704.3 meters/sec, nadir angle of 30° , azimuth angle of 45° and wavelength of $2 \mu\text{m}$. We assume that the earth has a radius (R_e) of 6432 Kilometers. For this data, in the case of retro-reflection, the change in the azimuth angle is 74 micro radians and that in nadir is 27μ radians. For higher velocities ($v/c \geq 0.1$), the corrections could be substantial. For LAWS, backscatter may be reasonably acceptable. In case of diffuse

scattering off the ground or off aerosols, for any transmission angle, there exists a return direction, for which no compensation is required at the receiver. For AEOLUS data, this direction did not differ greatly from the retro-reflection direction (36μ radians in azimuth and 14μ radians for nadir). There are Doppler shifts due to the satellite motion and relativity. It is found that the Doppler shift due to the general relativity leads to an error of at best 1% in wind sending.

RECOMMENDATIONS

First, the analysis has to be redone, taking into consideration the gravity effect by adding the term $\frac{2\chi}{c^2}$ to the term $(1-R^2\omega^2/C^2)$ in several coordinate transformations. The above results use radar measurements. To use geodesic lines, we have to expand Kerr metric and solve the path of a photon under this field. Non-sphericity of the earth should also be accounted for.

SUMMARY

In summary, we derived several analytical results based on the theory of general relativity, useful for space-based lidar experiments. We applied our results to the proposed AEOLUS system and found out that the current design recommendations are within acceptable tolerances. The results agree, where required, with those, derived last year. Some important next steps that will improve the analysis and provide better design rules have been identified.

ACKNOWLEDGEMENTS

The author thanks Dr. Michael J. Kavaya (NASA/MSFC) for suggesting this problem and for several useful discussions. He expresses his gratitude to NASA/Marshall Space Flight Center and American Society of Engineering Education for the Summer Faculty Fellowship, which made this work possible.

REFERENCES

1. V. S. Rao Gudimetla and M. J. Kavaya: Effects of Special Relativity for Space-based Lidar Experiments, Technical Report, 1994 NASA/ASEE Summer Faculty Program, Marshall Space Flight Center, AL, to be published as a NASA Technical Memorandum.
2. B. Hoffman-Wellenhof, H. Lichtenegger, and J. Collins: Global Positioning System, Theory and Practice, Springer-Verlag, New York, 1994, pp. 117-123
3. J. Van Bladel: Relativity and Engineering (Springer-Verlag, New York 1984). This book has several references related to this work and not cited here due to page limitations.

-
- The diagram shows a top-down view of Earth and a satellite. The Earth is represented by two concentric ellipses. The center of Earth is the origin of a coordinate system with axes Z, Z_1 (vertical), X (horizontal), Y_1 (diagonal down-left), and Y (diagonal down-left). A satellite is located on a circular orbit of radius R from the center. The Earth's radius is R_e . The angle between the Z -axis and the line to the satellite is ωt . A local coordinate system (X', Y', Z') is centered on the satellite, with Z' pointing away from Earth, Y' pointing down-left, and X' pointing right. The satellite is labeled "Satellite $X_1 (X'_1)$ ".

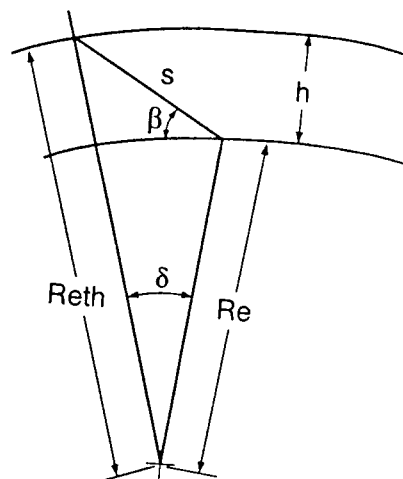


Figure 2. Radar Measurement of Distance by A (after Reference 5)

1995

NASA/ASEE SUMMER FACULTY FELLOWSHIP PROGRAM

**MARSHALL SPACE FLIGHT CENTER
THE UNIVERSITY OF ALABAMA IN HUNTSVILLE**

**STATIC MEASUREMENT OF THE THICKNESS OF THE ABLATIVE
COATING OF THE SOLID ROCKET BOOSTERS**

Prepared By: Harry C. Harrison

Academic Rank: Professor

Institution and Department: Capitol College
Department of Mathematics and Computer Engineering

NASA/MSFC:

Office: Materials and Processes Laboratory
Division: Fabrication Services Division
Branch: Process Automation & Modeling Branch

MSFC Colleagues: Wendell Colberg
Maninderpal Gill

Introduction

1. The Solid Rocket Boosters(SRBs) used to launch the Space Shuttle are coated with a layer of ablative material to prevent thermal damage when they reenter the earth's atmosphere. The coating consists of a mixture of cork, glass, and resin. A new coating(Marshall Convergent Coating, MCC-2) was recently developed that is environmentally complaint. The coating must meet certain minimum thickness standards in order to protect the SRB.
2. The coating is applied by a robot controlled nozzle that moves from the bottom to top, as the rocket part rotates on a table. Several coats are applied, building up to the desired thickness. Inspectors do a limited amount of destructive "wet" testing. This involves an inspector inserting a rod in the wet coating and removing the rod. This results in a hole that, of course, must be patched later. The material is cured and the thickness is measured. There is no real-time feedback as the coating is being applied. Although this might seem like the best way to control thickness, the problems with "blowback"(reflected material covering the sensor) are formidable, and have not been solved.
3. After the thermal coating is applied, a protective top coat is applied. The SRB part is then placed in a oven and baked to harden the surface. The operations personnel then measure the thickness of the layer using the Kaman 7200 Displacement Measuring System.. The probe is placed on the surface. One person(the inspector) reads the instrument, while another(the technician) records the thickness. Measurements are taken at one foot intervals.
4. After the measurements are taken, the number of low readings is tabulated. If more than 10% of the points fall below the minimum value, there is a design review, and the part may be stripped of coating, and a new coating is applied. There is no other analysis.

Goals

Improve the measurement process by speeding up the process, improve analysis of thickness data and to evaluate the utility of the virtual instrument concept for taking measurements

Proposed System

1. HARDWARE:

a. COMPUTER: laptop(WinBookxp) with the following characteristics:

CPU:	486DX
RAM:	8 Meg of RAM
Hard Disk:	493 Megabyte
PCMCIA:	2 type II

b. DATA ACQUISITION:

MANUFACTURER: National Instruments
MODEL: DAQCard-700
INTERFACE: PCMCIA Type II
TYPE: 12 bit ADC
CHANNELS: 16 analog/8 differential
DIGITAL: 8 inputs, 8 outputs
SPEED: 100k Samples/second
COUNTERS: 2 16 bit
CONNECTOR: CB-50(50 screw down connector)

2. SOFTWARE:

MANUFACTURER: National Instruments Corporation
PRODUCT: LabVIEW for Windows
VERSION: 3.1.1

3. PROCESS:

The operator places the sensor flush with the ablative coating surface. The instrument is based on the measurement of eddy currents. It measures induced current that is proportional to the distance between a conductive material(the metal surface of the SRB) and the sensor. A set of non-conductive ceramic disks were provided by the manufacturer for calibration of the instrument. The output is in mils, and is accurate to 1 mil. The output of the sensor was available through pins 4 and 5 in the front of the sensor. These pins were connected to pins 2 and 3 on the CB-50 connector.

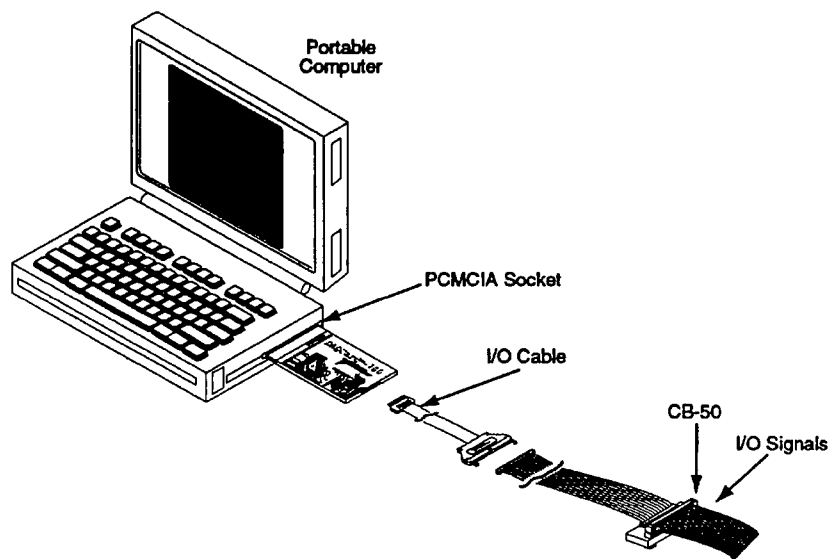


Figure 1. Sensor Connection

This figure shows how the laptop computer interfaced with the PCMCIA Card and CB-50 Connector. The PCMCIA (Personal Computer Memory Interface Association - a standards group for small credit card sized devices(not limited to memory). The DAQ card is supplied by National Instruments.

4. The Program:

The LabVIEW(Virtual Instrument Engineering Workbench) software represents several revolutionary concepts.

The first is the concept of the virtual instrument. Given the right interfaces, a general purpose computer(PC, Mac, Sun , HP, etc.) can be programmed to perform the operations of an expensive special purpose instrument or to control certain processes. The PC can be easily modified to perform a wide variety of different tasks.

The second concept is called Visual Programming. The displays and inputs are represented by pictures(icons). They are connected together using a roll of wire icon. This is similar to the flow diagrams which are second nature to engineers.

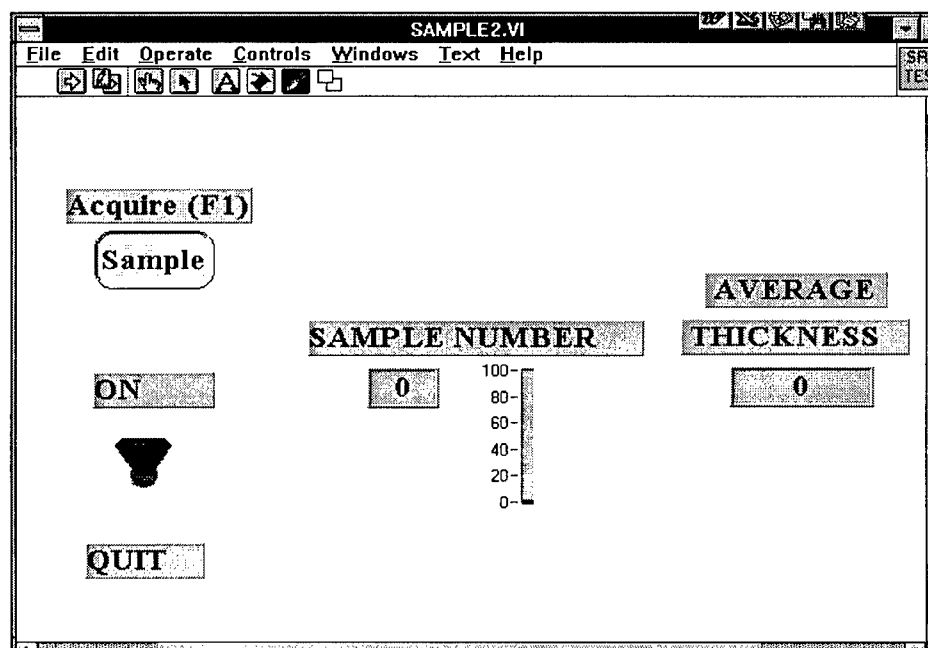


Figure 2. Instrument Panel

This diagram show the panel of the virtual instrument. The user moves the mouse to the operate icon the selects RUN. He then presses F1 when the sensor is ready to be read. A pop up menu appears that prompts him for the name of the file where the data is be stored. The sensor take 10 measurements and averages them. It writes the sequence number of the reading, along with the value of the thickness, in spreadsheet format.

In the figure below, TEST is the data acquisition VI. It is in a Loop that is executed 10 times. The values are multiplied by 1000 to convert them to mils and are fed to the Mean VI. The output of the, along with the sequence number, is written to a file in spreadsheet format (tabs between values, Return at the end of each line).

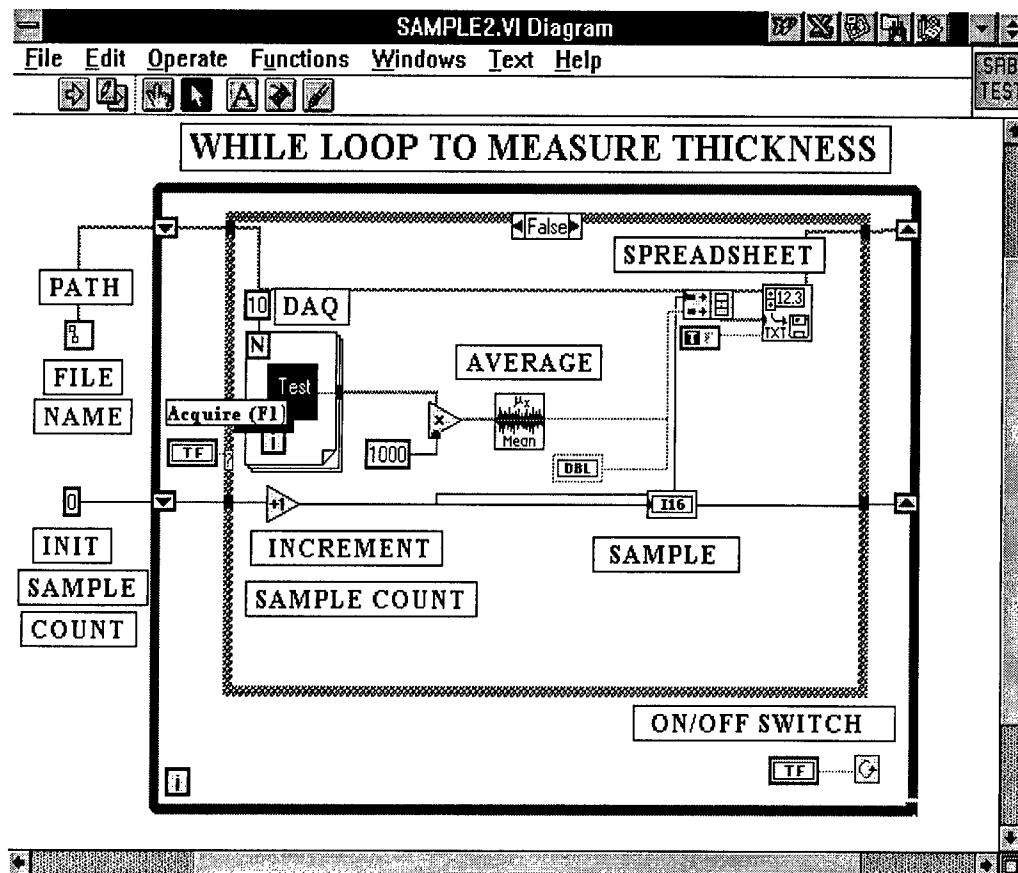


Figure 3. LabVIEW Diagram

LabVIEW Programming

The LabVIEW programs are written in a graphical language called "G". It is a pure visual language. There is no text based part, as there is in visual BASIC. Programming is done by selecting icons that stand for functions, sensors, controls, and displays. The programmer lays out a "panel" that represents the display and controls the user will see. See figure 2. The programmer then switches to the diagram view, where the functions and instruments are represented as icons. See figure 3. The programmer then connects the icons together with a wiring tool.

The data was written in spreadsheet format. The mean and standard deviation can be easily computed. The next step to convert the sequence numbers to grid coordinates (x and y) representing the surface of the SRB section. Now, the thickness could be plotted using color codes. For example, RED would indicate below minimum thickness, GREEN above

thickness. Now the entire surface could be viewed with respect to out of specification areas. The would allow the easy identification of areas that are out of specification, and indicating the need to control the application of the spray.

Conclusions

The project was completed successfully. The concept of using virtual instruments based on a lap top PC is practical and cost effective. It is widely applicable to throughout NASA. It offers significant savings compared to the use of traditional savings. Given the funding forecasts, this approach may be of greater importance than before. The use of virtual instruments should be encouraged throughout NASA.

Recommendations

The handle(gun) for the sensor needs to be fabricated, along with a trigger to activate the sensor. The concept needs to be tested at Cape Kennedy. Some user resistance might expected, as the new process may involve taking the measurements in a different order than was done previously.

The time for laptop data acquisition and instrument control has arrived. Using visual software, it fast, easy, and inexpensive to develop useful applications. A task force or committee should be formed to recommend ways that the use of this approach can be spread throughout the agency. Perhaps guidance and recommended practices need to be published. Videos and training material should be acquired at the libraries.

Bibliography

1. Acquiring Data through Windows, Andy Reinhardt, BYTE magazine, volume 17 page 63-64, Sep 1992.
2. Harley-Davidson Engineer Evaluates LabVIEW's Graphical Programming, EDN, volume 38, pages 201-204, October 28, 1993.
3. LabVIEW Graphical Programming, Gary W. Johnson, McGraw-Hill Publishing Co., 1994.
4. LabVIEW for Windows Documentation, National Instruments Corporation, 1994.
5. The PC: Prime Tool for Testing, interview with James Trunchard, President and Chairman, National Instruments, in Design News, volume 49, page 162, April 1993.

1995

NASA/ASEE SUMMER FACULTY FELLOWSHIP PROGRAM

**MARSHALL SPACE FLIGHT CENTER
THE UNIVERSITY OF ALABAMA IN HUNTSVILLE**

**Thermodynamic Measurements in a High Pressure
Hydrogen-Oxygen Flame Using Raman Scattering from a
Broadband Excimer Laser**

Prepared By:	Roy Hartfield, Jr.
Academic Rank:	Assistant Professor
Institution and Department:	Auburn University Aerospace Engineering Department
NASA/MSFC:	
Office:	Propulsion Laboratory
Division:	Motor Systems Division
Branch:	Combustion Physics Branch
MSFC Colleagues:	Richard Eskridge Chris Dobson

Thermodynamic Measurements in a High Pressure Hydrogen-Oxygen Flame Using Raman Scattering from a Broadband Excimer Laser

Introduction

Raman scattering is an inelastic molecular scattering process in which incident radiation is reemitted at a fixed change in frequency.¹ Raman spectroscopy can be used to measure the number density and temperature of the irradiated species.² The strength of the Raman signal is inversely proportional to the wavelength raised to the fourth power. Consequently, high signal to noise ratios are obtained by using ultraviolet (UV) excitation sources. Using UV sources for Raman Spectroscopy in flames is complicated by the fact that some of the primary constituents in hydrogen-oxygen combustion absorb and reemit light in the UV and these fluorescence processes interfere with the Raman signals.³ This problem has been handled in atmospheric pressure flames in some instances by using a narrowband tunable excimer laser as a source. This allows for detuning from absorption transitions and the elimination of interfering fluorescence signals at the Raman wavelengths.⁴ This approach works well in the atmospheric pressure flame; however, it has two important disadvantages. First, injection-locked narrowband tunable excimer lasers are very expensive. More importantly, however, is the fact that at the high pressures characteristic of rocket engine combustion chambers, the absorption transitions are broadened making it difficult to tune to a spectral location at which substantial absorption would not occur.

The approach taken in this work is to separate the Raman signal from the fluorescence background by taking advantage of the fact that Raman signal has nonisotropic polarization characteristics while the fluorescence signals are unpolarized. Specifically, for scattering at right angles to the excitation beam path, the Raman signal is completely polarized. The Raman signal is separated from the fluorescence background by collecting both horizontally and vertically polarized signals separately. One of the polarizations has both the Raman signal and the fluorescence background while the other has only the fluorescence signal. The Raman scatter is the difference between the signals. By choosing an appropriate optical setup, both signals can be obtained simultaneously with the same monochromator; hence, time resolved measurements are possible using this approach.

An alternative approach for using the polarization characteristics of the Raman scattering process to separate the Raman signal from the fluorescence background is to take advantage of the directional dependence of the scattering on the laser polarization. For a laser polarization in the plane formed by the laser beam and the collection path, no Raman scatter will be detected for a collection path which is perpendicular to the incident radiation. For a laser polarization perpendicular to this plane, Raman scatter can be detected; hence, the Raman signal can be separated from the fluorescence signal based on laser polarization. This process is not preferred because of the necessity of rotating the polarization of the excitation source; however, polarizing the laser source can increase the ratio of the Raman scatter to the fluorescence yield.

The accuracy of these separation techniques depends in part on the relative magnitudes of the signals being separated. Measurements conducted to date indicate that, at least in parts of the flame, the Raman scatter is of the same magnitude as the

fluorescence and measurements published in Ref. 3 indicate that, if a Krypton Fluoride (KrF) laser is used, the Raman signal is larger than the fluorescence for most flame conditions. In that case, signal to noise ratios for the extracted Raman signal can be expected to be comparable to those of the raw measurements.

The scope of the work detailed in this manuscript includes a description of the basis for the technique and a discussion of a set of measurements demonstrating the fact that the Raman scatter can be separated from the fluorescence based on polarization. This discussion is followed by a general outline for implementing the technique in a combustor.

Theory

Both Rayleigh and Raman scattering can be modeled classically as radiation from an induced oscillating dipole. The electric and magnetic fields of the incident radiation induce the oscillating dipole. When the induced dipole oscillates at the frequency of the incident radiation, the scattering, which is at the frequency of the incident radiation, is classified as Rayleigh. It is possible for the scattering process to occur with the irradiated molecule giving up or absorbing discrete amounts of energy. This process is referred to as Raman scattering and the scattered light is at a different frequency from the incident radiation; nevertheless, the oscillating dipole radiation model provides fundamental insight into the directional and polarization characteristics. Using the classical oscillating dipole model, it can be seen that for scatter in a direction perpendicular to the electric field vector of the incident radiation, the electric field vector of the scattered light will be parallel to the electric field of the incident light. A more complete theoretical description of the polarization characteristics of Raman scatter arise from quantum mechanical treatments and can be described using the Stokes parameters. The Stokes parameters for Raman scatter by a diatomic molecule are given in Ref. 1 for scattering perpendicular to the incident radiation. These Stokes parameters are complicated functions of the molecular structure and the precise evaluation of these parameters is complex; however, for scattering perpendicular to both the incident radiation polarization vector and propagation direction, two of the four Stokes parameters are zero. This indicates that the light must be polarized regardless of the precise values of the two remaining Stokes parameters. For scattering parallel to the polarization vector and perpendicular to the direction of propagation, three of the Stokes parameters are zero which indicates that no scatter will occur in this direction. (This is responsible for the second idea discussed in the introduction.)

Clearly, a measurement scheme can be designed in which the Raman signal is polarized. The fluorescence processes involve the absorption of incident energy and reemission of photons. In the absence of an external field, unless the reemission is stimulated there is no preferred direction or polarization for the emission and the fluorescence process is isotropic. Hence, discrimination between fluorescence signals and Raman scatter based on polarization is theoretically feasible. The experimental and results sections of this report detail the measurements demonstrating the practical feasibility of this idea.

The selection of a probe species for the application of Raman spectroscopy is clearly dependent on the reactants and the flame conditions. The combustor conditions for which this measurement effort is designed are LOX-rich LOX hydrogen flames at approximately 100 atm. Clearly an injection-based nonpremixed combustor will contain a substantial range

of conditions; however, some insight concerning expected species concentrations can be gained from equilibrium calculations. Figure 1 contains plots of the molecular species present in the flame conditions expected based on equilibrium calculations for a range of OF equivalence ratios. The LOX-rich regions would be to the right of unity in these plots and, since the injection ratio is substantially LOX rich, the conditions away from the immediate vicinity of the injectors would be LOX rich. Molecular oxygen and water are both present in substantial amounts for these conditions; however water is not a diatomic molecule and it cannot currently be used as a thermometric species. Hence molecular oxygen has been chosen as the probe species for the Raman measurements.

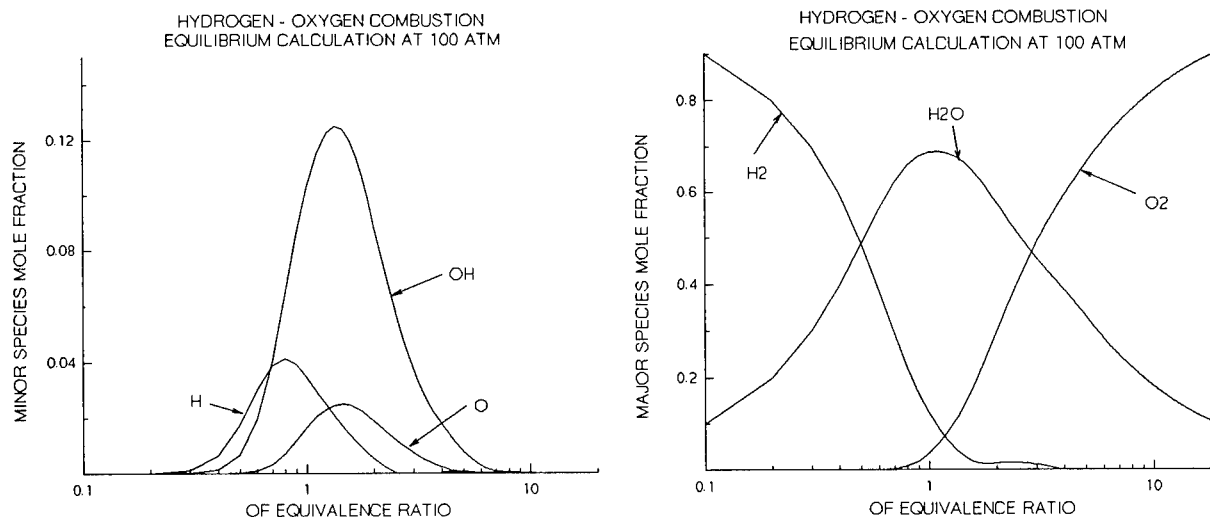


Figure 1: Species concentrations for LOX-Hydrogen combustion at 100 atm.

Experimental Setup

A schematic of the laboratory Raman scattering system is shown in Fig. 2. The Raman scattering is induced by a broadband excimer laser (Lumonics HyperEX-400) operated with Xenon Chloride. Laser power is monitored using a beam splitter and a power meter (Molecutron Model J25Hr). The line width of this laser system is approximately 0.5

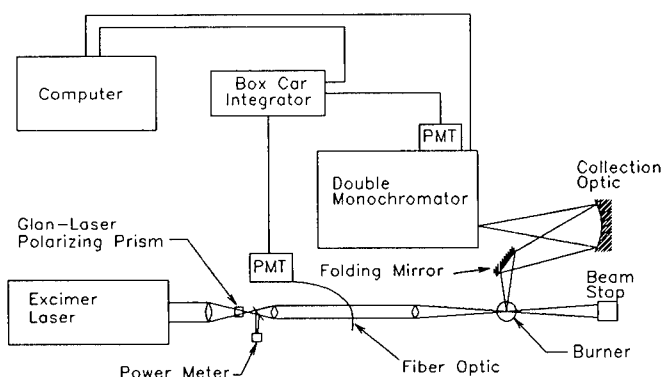


Figure 2: Schematic of UV Raman System

nm and the pulse length is approximately 10 ns. The laser beam is passed through a

telescope consisting of a 30 cm focal length lens (first) and a 20 cm focal length lens. The beam is then focused into the control volume using a 50 cm focal length lens. The scattered signal is collected and analyzed using a double monochromator (ISA JY Ramanour). The photomultiplier tube (PMT) connected to the double monochromator is a Hamamatsu R1477. The box car integrator is from SRS and is triggered using a fiberoptic and a Hamamatsu R928 PMT. The collection optic for this work is a 60 cm focal length Paraboloid. The flame is generated using a burner equipped with hydrogen ports in a central region and oxygen ports in a circular pattern surrounding the hydrogen ports.

Results

The central idea conveyed by the results obtained thus far is a demonstration of the discrimination between the Raman signal and the fluorescence signal based on polarization. The plot shown in Fig. 3 shows spectra obtained at the wavelength expected for the Raman scatter for the oxygen molecule using the XeCl excimer laser. This demonstration measurement was conducted by collecting spectra with horizontal and vertical laser polarizations rather than by discriminating between polarization in the collection path for instrumental reasons. The signals for the two polarizations and the difference between the signals are all plotted. Each of the raw signals contains the fluorescence. The signal with the vertically polarized beam also contains the Raman and the difference between the signals is the oxygen Raman scatter.

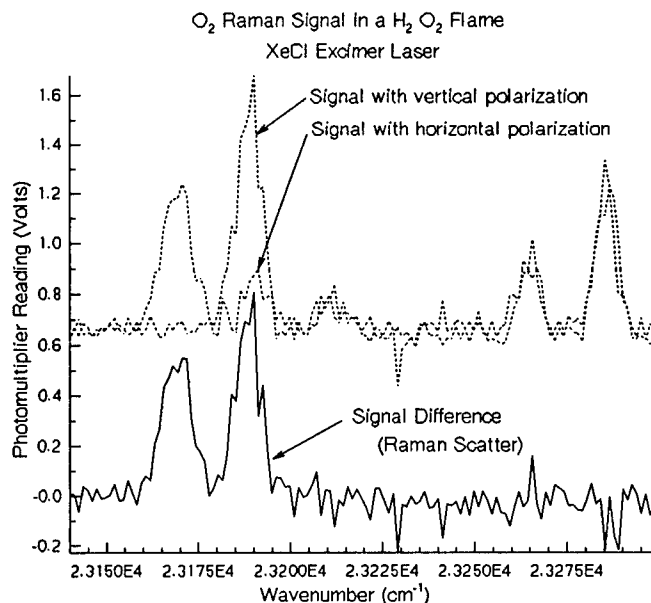


Figure 3: Raman signal separated based on laser polarization

Summary and Future Work

The measurements conducted to date have demonstrated the principle that Raman scattering signals can be separated from fluorescence signals based on polarization. The temperature and number density information will be extracted from the Raman signals

collected in the laboratory setup as a demonstration of the measurement approach. Additionally, a plan for implementing this technique in a combustor has been developed. A schematic of the optical setup proposed for the combustor measurements is shown in Fig. 4. This setup is similar to the laboratory rig with some notable exceptions. An intensified CCD array will replace the PMT to eliminate the need for scanning the monochromator and allow for single-shot measurements. A polarization separation prism will be included in the collection optics so that the Raman signal can be separated from the fluorescence without rotating the polarization of the laser beam. This too is necessary for single shot measurements. The monochromator will only pass vertically polarized light efficiently; hence a half wave plate is necessary to get the initially horizontally polarized component of the signal through the monochromator. An ellipsoidal reflecting collection optic has also been designed for use in the combustor rig.

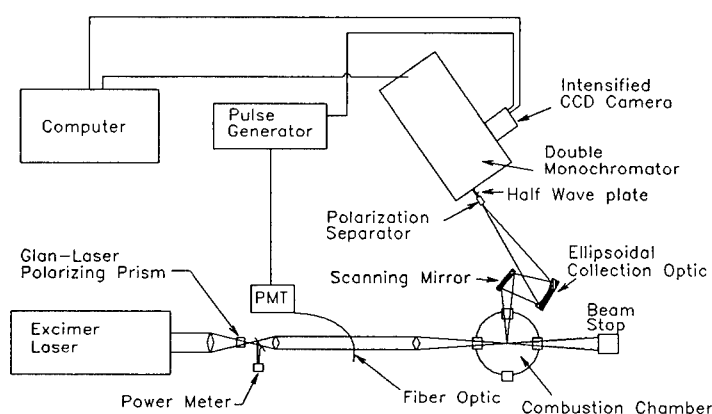


Figure 4: Schematic of Proposed Optical Setup

Acknowledgement

This document is a report on the summer faculty fellowship for Roy Hartfield; however, the author is only a small contributor offering support to the effort and suggestions concerning the polarization to an ongoing effort designed to conduct measurements of temperature and species concentration in a liquid rocket motor combustor. Chris Dobson, Richard Eskridge and Mike Lee are all principle contributors to that project.

References

1. Long, D. A., Raman Spectroscopy, McGraw-Hill International Book Company, London, 1977.
2. Lederman, S., "The Use of Laser Raman Diagnostics in Flow Fields and Combustion," Progress in Energy and Combustion Science, Vol. 3, pp. 1-34, 1977.
3. Pitz, Robert W.; Wehrmeyer, Joseph A.; Bowling, J. M.; and Cheng, Tsarng-Sheng, "Single Pulse Vibrational Raman Scattering by a Broadband KrF Excimer Laser in a Hydrogen-Air Flame," Applied Optics, Vol. 29, No. 15, May 1990, pp. 2325-2332.
4. Wehrmeyer, Joseph A.; Cheng, Tsarng-Sheng; and Pitz, Robert W., "Raman Scattering Measurements in Flames Using a Tunable KrF Excimer Laser," Applied Optics, Vol. 31, No. 10, April 1992, pp. 1495-1504.

1995

NASA /ASEE SUMMER FACULTY FELLOWSHIP PROGRAM

**MARSHALL SPACE FLIGHT CENTER
THE UNIVERSITY OF ALABAMA IN HUNTSVILLE**

**COMPUTATIONAL MODELING OF MAGNETICALLY ACTUATED PROPELLANT
ORIENTATION**

Prepared By:	John I. Hochstein, Ph.D.
Academic Rank:	Associate Professor
Institution and Department:	The University of Memphis Department of Mechanical Engineering
NASA/MSFC:	
Laboratory:	Propulsion Laboratory
Division:	Propulsion Systems
Branch:	Advanced Propulsion
MSFC Colleague:	George R. Schmidt, Ph.D.

INTRODUCTION

Unlike terrestrial applications where gravity positions liquid at the "bottom" of the tank, the location of liquid propellant in spacecraft tanks is uncertain unless specific actions are taken or special features are built into the tank. Some mission events require knowledge of liquid position prior to a particular action: liquid must be positioned over the tank outlet prior to starting the main engines and must be moved away from the tank vent before vapor can be released overboard to reduce pressure. It may also be desirable to positively position liquid to improve propulsion system performance: moving liquid away from the tank walls will dramatically decrease the rate of heat transfer to the propellant, suppressing the boil-off rate, thereby reducing overall mission propellant requirements. The process of moving propellant to a desired position is referred to as propellant orientation or reorientation.

Several techniques have been developed to positively position propellant in spacecraft tanks and each technique imposes additional requirements on vehicle design. Propulsive reorientation relies on small auxiliary thrusters to accelerate the tank. The inertia of the liquid causes it to collect in the aft-end of the tank if the acceleration is forward. This technique requires that additional thrusters be added to the vehicle, that additional propellant be carried in the vehicle, and that an additional operational maneuver be executed. Another technique uses Liquid Acquisition Devices (LAD's) to positively position propellants. These devices rely on surface tension to hold the liquid within special geometries (i.e. vanes, wire-mesh channels, start-baskets). While avoiding some of the penalties of propulsive orientation, this technique requires the addition of complicated hardware inside the propellant tank and performance for long duration missions is uncertain. The subject of the present research is an alternate technique for positively positioning liquid within spacecraft propellant tanks: magnetic fields.

The idea of using electromagnetic fields to position propellants in spacecraft tanks was studied briefly in the 1960's. Electrical fields can produce voltage differentials within the tank that pose a prohibitive safety hazard. Magnetic fields do not pose this risk. Since LOX is paramagnetic (attracted toward a magnet) and LH₂ is diamagnetic (repelled from a magnet), a nonuniform magnetic field of sufficient strength could provide a positioning force. Order-of-magnitude analyses showed that magnets based on 1960's technology were prohibitively massive and this option has remained dormant during the intervening years. Recent advances in high-temperature superconducting materials hold the promise of electromagnets with sufficient performance to support cryogenic propellant management tasks. Therefore, a recent initiative was authorized in late 1992 at NASA MSFC to assess the feasibility of using magnetic fields to positively position propellants in spacecraft tanks. The key component of this initiative is the Magnetically-Actuated Propellant Orientation (MAPO) experiment. A mixture of ferrofluid and water will be used to simulate the paramagnetic properties of LOX and the experiment will be flown on the KC-135 aircraft to provide a reduced gravity environment. The influence of a 0.4 Tesla ring magnet on flow into and out of a subscale Plexiglas tank will be recorded on video tape. The first flight is currently scheduled for late September 1995.

Given the complexity of the physical processes involved in the magnetically-actuated orientation process, it is unlikely that analytical solutions to the equations describing these processes can be obtained. While experimentation is essential in establishing basic relationships

between the process parameters, the requirement for a reduced gravity environment makes experimentation particularly expensive and time consuming. The most efficient approach to evaluating the feasibility of MAPO is to compliment the experimental program with development of a computational tool with a demonstrated ability to model the process of interest. The goal of the present research is to develop such a tool. Once confidence in its fidelity is established by comparison to data from the MAPO experiment, it can be used to assist in the design of future experiments and to study the parameter space of the process. Ultimately, it is hoped that the computational model can serve as a design tool for full-scale spacecraft applications.

MATHEMATICAL MODEL

Although the practitioner of experimental or computational fluid mechanics may have familiarity with many of the features of the research problem, it is less likely that he/she will have a strong background in the magnetic and paramagnetic aspects of the problem. The author spent considerable time and effort retrieving the background information in these areas and has collected the basic information into a single resource that it is hoped will be of value to other researchers who tackle this problem, "Magnetism and the Flow of Paramagnetic Fluids: An Introduction for the Non-Specialist." In addition to this review of the basic physics, 22 papers related to the flow of paramagnetic fluids and ferrofluids were extracted from the literature and assembled into a reference resource.

LOX and LH2 are reasonably well represented as incompressible, constant property, Newtonian fluids and therefore the flow of interest can be modeled using a modified form of the Navier-Stokes equations

$$\rho \frac{\partial \vec{V}}{\partial t} + \rho (\vec{V} \cdot \nabla) \vec{V} = -\nabla p + \mu \nabla^2 \vec{V} + \rho \vec{g} + \mu_0 (\vec{M} \cdot \nabla) \vec{H}$$

where ρ , \vec{V} , p , μ , and \vec{g} have the usual definitions of density, velocity, viscosity, and gravity, μ_0 is the permeability of free space, \vec{H} is the magnetic intensity, \vec{M} is the magnetization, and χ is the susceptibility. The last term on the right-hand side is known as the Pondermotive force and provides the coupling between the magnetic field and the fluid motion. For the flow of a paramagnetic or diamagnetic fluid, it is appropriate to assume that: the direction of the magnetization vector is always in the direction of the local magnetic field, the fluid is electrically nonconducting, and the displacement current is negligible. Given these assumptions, the expression for the Pondermotive force can be simplified to:

$$\mu_0 M \nabla H.$$

It is also reasonable to assume that the fluid behavior will be linear in the magnetic sense, reducing the expression for the Pondermotive force to the form implemented in the computational model.

$$\mu_0 \chi H \nabla H$$

In addition to the usual flow boundary conditions, the normal stress boundary condition at a gas/liquid interface is given by:

$$\Delta p = \sigma \kappa + \frac{1}{2} \mu_o \left[(\vec{M} \cdot \hat{n})_{\text{liq}}^2 - (\vec{M} \cdot \hat{n})_{\text{gas}}^2 \right]$$

where the first term is the "pressure jump" at the interface due to surface tension and the second term is the "magnetic pressure" due to the change in magnetization across the interface.

The magnetic field due to the ring magnetic will be modeled as a magnetic dipole located at the center of the ring.

$$\vec{B} = \frac{\mu_o m}{4\pi r^3} [(2 \cos \theta) \hat{e}_r + (\sin \theta) \hat{e}_\theta] = \mu_o (\vec{H} + \vec{M})$$

where \vec{B} is the magnetic flux density, m is the magnetic dipole strength, and r, θ, φ are spherical coordinates with θ measured "down" from an upright z -axis and φ is measured in the x - y plane.

COMPUTATIONAL MODEL

A computational tool for the simulation of magnetically-actuated propellant orientation must be able to solve all of equations and boundary conditions presented in the development of the mathematical model. Further, the tool must be capable of modeling the large interface deformation and mass transport associated with bulk propellant motion within the spacecraft tank. This single requirement eliminates most candidate CFD codes and identifies the RIPPLE code as uniquely well qualified to serve as the foundation for building the desired computational tool. RIPPLE was developed at the Los Alamos National Laboratory under an interagency agreement with NASA and source code is readily available. Except for the Pondermotive force term, the baseline code provides all of the required capabilities. Further, the fidelity of this code in modeling propulsive propellant reorientation has been previously demonstrated, providing strong confidence that it will serve well as a foundation for the present research.

The RIPPLE code models the transient flow of an incompressible Newtonian fluid. The flow field is discretized into finite volumes to form a nonuniform computational mesh. A staggered-grid approximation to the continuity and momentum equations produces a nonlinear system of algebraic equations that is solved using a two-step projection method. Instead of an interface tracking scheme, the VOF technique is used to follow the advection of mass through an Eulerian mesh and special donor-acceptor cell differencing is used for the VOF-function to preserve steep interface shapes. The Continuum Surface Force (CSF) model is used to represent surface tension forces producing a more robust tool than previously developed codes.

The RIPPLE code, and a supporting graphics package known as RGO, were ported to a workstation (SGI 4D/35TG) in the MSFC computational environment. The analysis code contains a sequence of subroutine calls in which each subroutine computes the contribution of a force term to momentum equation. A new subroutine, ponder, has been written to compute the contribution of the Pondermotive force and this subroutine has been inserted into the calling

sequence. Additional modifications to support the magnetic model have been accomplished including changes to the I/O subroutines and the common blocks. RGO was also modified to support the new variables introduced by the magnetic model.

TEST CASES

Several test cases have been run to evaluate the new model for the Pondermotive force. To check that the new force model interacted properly with the pressure solver, two cases were constructed in which the magnetic force was specified to be uniform in the coordinate directions, (one case in x-direction and one in y-direction). As expected, constant pressure contours are straight lines, orthogonal to the direction of the force, and equally spaced.

The second set of cases was composed of three analyses in which simple magnetic fields were imposed: $dh/dx = \text{constant}$, $dh/dy = \text{constant}$, and $dh/dx = dh/dy = \text{constant}$. The third case is also the first in which a small void region was provided to test the interaction of the magnetic model and the free surface model. The constant pressure contours predicted for the second two cases are presented in Figure 1. As expected, the constant pressure contours are straight lines orthogonal to the gradient of the magnetic field. The nonlinear dependence of the Pondermotive force on the magnetic intensity (H^2) is evident in the concentration of the constant pressure contours toward the region of high field strength, (left and lower-left corner). The deflection of the contours at the wall in the third case is an anomaly in the graphics package. The heavy contour in the upper-right corner of the third case is both a constant pressure contour and the computational prediction for the free-surface shape. As expected, these contours are coincident.

The third set of test cases sought to more rigorously test the interaction between the Pondermotive force model and the free surface/surface tension model. As a representative case, Figure 2 depicts the pressure and velocity fields predicted for the motion of an initially circular void region under the influence of a magnetic field with $dh/dx = \text{constant}$. Although there is no experimental data available for comparison to these calculations, the results seem reasonable and provide confidence that computational tool has the desired basic modeling capabilities required to simulate magnetically-actuated propellant orientation.

The final set of test cases executed this summer were an attempt to begin modeling the flows expected in the MAPO experiment. Measurements of magnetic intensity were made in the neighborhood of the ring magnet and a comparable dipole strength was computed for use in the computational simulation. A model was then constructed in which the dipole was located 0.05 m below the bottom of the tank and along the tank centerline. Given the short period available for this study, it was not possible to obtain a completely successful simulation. Although the predicted pressure contours appear to be reasonable, the velocity fields exhibit a strong vortex near the tank outlet that did not appear in any of the previous tests. Figure 3 depicts the magnetic field, pressure contours, and velocity field shortly after initiating a simplified analysis in which the tank is cylindrical, there is no surface tension, and the initial free surface is flat. As expected, the velocity field in the neighborhood of the free surface appears to be moving the interface toward an equilibrium configuration in which the fluid is higher at the left wall and lower at the right. The vortex in the lower-left corner was not expected and at present cannot be explained.

FUTURE DIRECTIONS

The preceding text describes ten weeks of effort, and, in the author's mind, comes to a sudden halt. This reflects the unfinished nature of the research effort. A reasonably difficult problem has been approached and preliminary tests indicate a good chance of success for the methods and tools developed. The next step must be an understanding of the cause of the unexpected vortex and modification of the computational model as required. Once this is accomplished, the code should be exercised on additional test cases that have been identified during the literature search for which experimental data or analytical solutions are available. The fidelity of the code should then be evaluated by comparing computational predictions to measurements from the MAPO experiment. Successful completion of this research program will produce a valuable tool that can be used for the design of additional experiments, to study the parameter space of the MAPO process, and ultimately as a design tool for full-scale spacecraft applications.

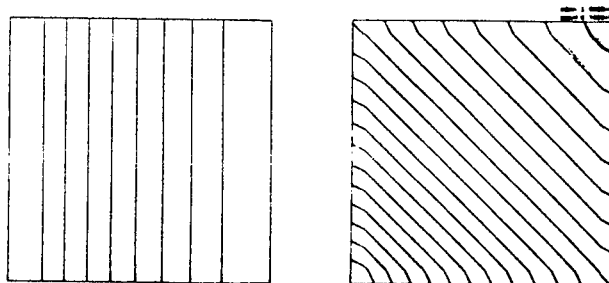


Figure 1

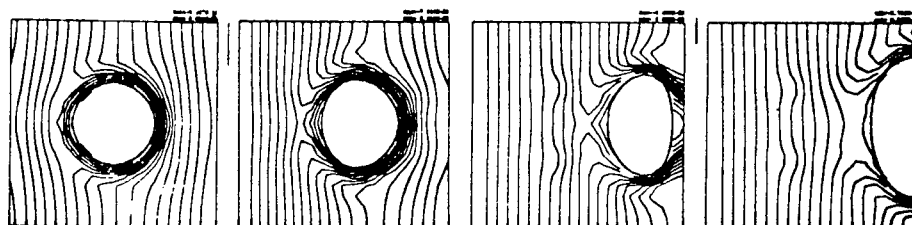


Figure 2

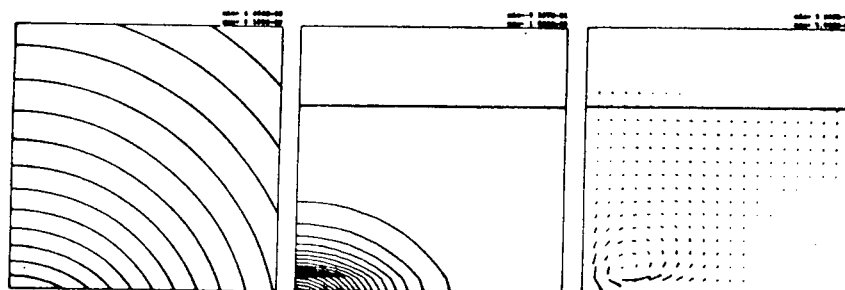
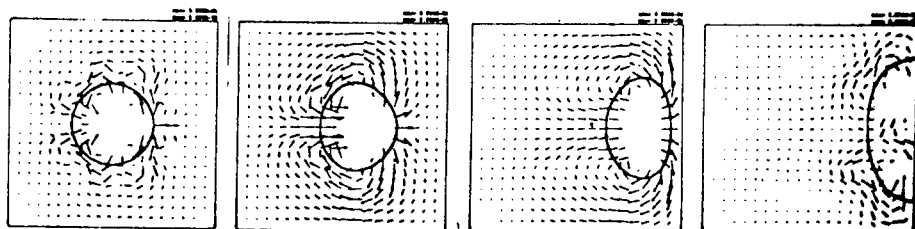


Figure 3

Log(Hmag)

Pressure

Velocity

1995

NASA/ASEE SUMMER FACULTY FELLOWSHIP PROGRAM

**MARSHALL SPACE FLIGHT CENTER
THE UNIVERSITY OF ALABAMA IN HUNTSVILLE**

SXI MIRROR CHARACTERIZATION

Prepared By: Thomas G. Howard

Academic Rank: Instructor

Institution and Department: Northwest-Shoals Community College
Electro-Optics Department

NASA/MSFC:

Laboratory: Astrionics
Division: Optics and Radio Frequency Division
Branch: Optical Fabrication Branch

MSFC Colleague: Cheryl Bankston

Introduction

The purpose of this test is to determine how well the SXI mirror will focus x-ray energy from the Sun as that will be its main function. The types of sources chosen for the test produce soft x-rays and are listed in Table 1.

<u>Wavelength</u>	<u>Energy</u>	<u>Material</u>
8.83 Å	1.41 keV	aluminum
10.0 Å	1.24 keV	magnesium
13.3 Å	0.935 keV	copper
44 Å	0.277 keV	carbon

Where: Å $\equiv 10^{-10}$ meter
 1 eV = 1.60 (10)⁻¹⁹ Joule

Table 1

Optic

The SXI project utilizes grazing incidence optics which is a very mature technology. The optic is a cylindrical glass structure with one end formed into a parabolic shape and the opposite end formed into a hyperbolic shape. The inside of the optic has a high-quality surface finish. X-ray photons are reflected first by the parabolic surface then by the hyperbolic surface to bring the energy into sharp focus in the focal plane. To increase the effective collection area, several mirrors may be nested one inside the other. However, because the SXI telescope will be directed toward a brilliant source (the Sun), only one mirror will be needed (Ramsey et al., 1994).

Detector

The Proportional Counter chosen for this test is a type of detector which came of age in the early 1950s. Basically, it consists of a fine wire (anode) in the center of a methane-filled cylinder (cathode). The anode (wire) is held at a high positive potential relative to the cathode (cylinder). This anode wire is capacitively coupled to a pre-amplifier. The cylinder has a window which is transparent to x-ray energy. When x-ray photons enter the window and are absorbed, primary electrons are emitted and drift toward the anode (wire). As these electrons approach the high potential applied to the anode, they gain additional kinetic energy from the increasing electric field sufficient to ionize the methane gas producing secondary electrons. This causes an avalanche and, in effect, momentarily "shorts out" the high voltage causing a negative-going signal to be applied to the pre-amplifier. The amplitude of this signal is proportional to the energy of the

absorbed photon. This signal is amplified and applied to a single-channel analyzer (SCA) (Decher et al., 1994).

Positioning System

A two-axis rotary table is used to remotely position the mirror inside a vacuum chamber. The detector will be positioned with a three-axis linear stage. These stages are capable of moving in steps of 1 micron (10^{-6} meter). The test will take place in a vacuum ($\sim 10^{-6}$ Torr) to simulate the telescope's operation in space. Hence the need for remote positioning.

Test Setup

Refer to Figure One. The Reference Detector and Test Detector are as described above. The Reference is physically located in the center of the mirror and provides an indication of the flux (total number of photons) arriving at the mirror. The active area of the Test Detector is partially blocked by a vertical slit and only sees the photons focused by the mirror. Comparing the number of photons per time seen by both detectors yields an appraisal of the mirror's ability to focus. Basically, one x-ray photon being detected results in one pulse out of the SCA. The computerized data acquisition system will count the pulses from both detectors and store the data for later analysis.

Test Procedures

After much painstaking alignment of the system, the Test Detector will be moved to locate the focal plan of the mirror. Then, the Test Detector will be moved perpendicular to the beam in 12 micron increments. At each increment, an observation will occur consisting of allowing the two counters to increment (counting photons) until the Reference Counter reaches a preset number. The two counter values will be saved and the Test Detector will be stepped to the next position. During this step and count process, the data acquisition system will monitor temperature, gas pressure, and physical vibration.

Summary

Upon successful completion of the mirror characterization test as well as additional testing, the SXI optic will become the heart of a space-bound telescope utilized by NOAA for predicting activity associated with the Sun such as sun spots which are a major disruption to radio communications.

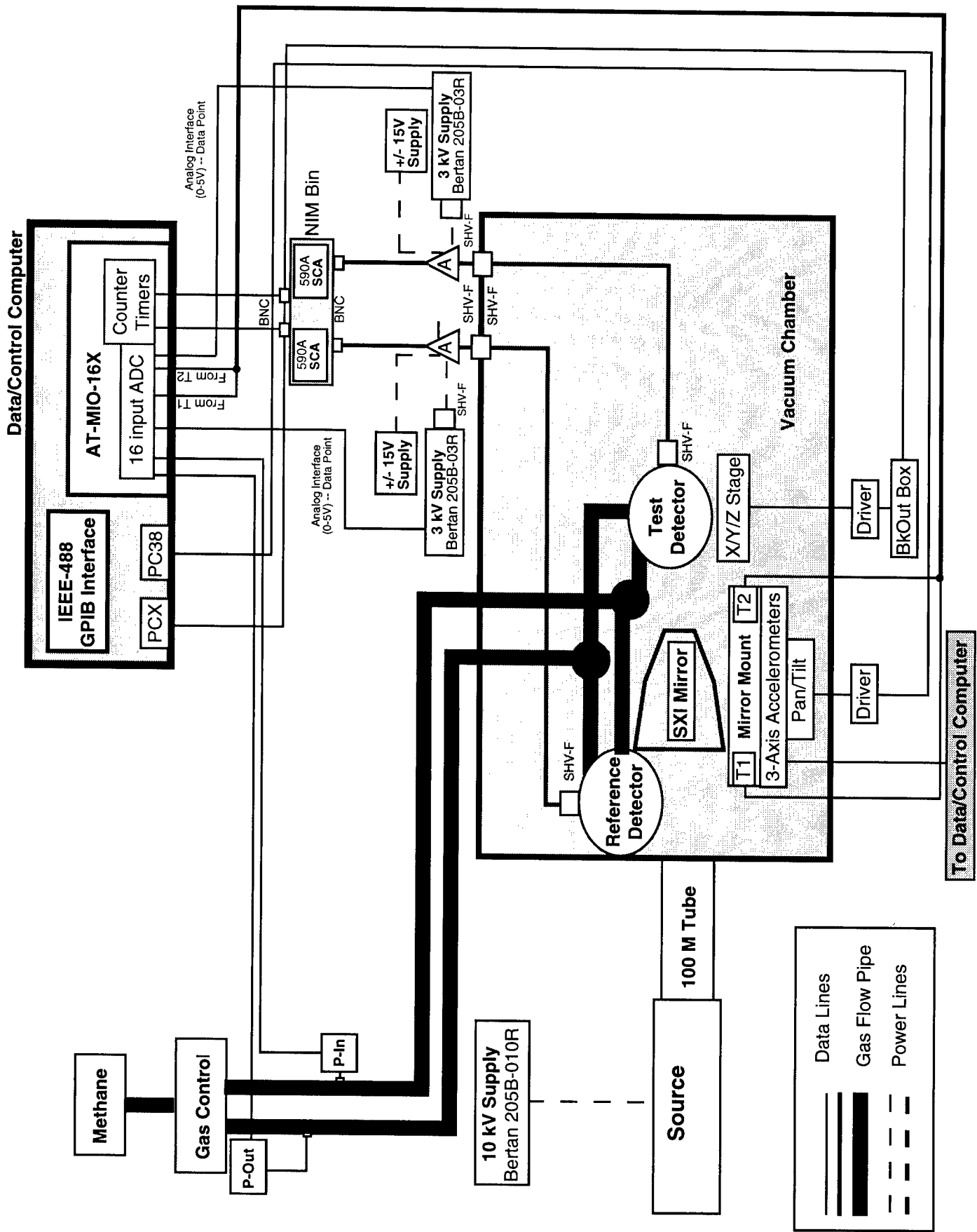


Figure One - SXI Mirror Characterization -- Data Acquisition and Control Block Diagram

References

- Decher, R., Ramsey, B. D., Austin, R.: 1994, NASA Scientific and Technical Information Program. NASA SP-517.
- Ramsey, B. D., Austin, R. A., Decher, R.: 1994, *Space Science Reviews*. 69, 139-204.

1995

NASA/ASEE SUMMER FACULTY FELLOWSHIP PROGRAM

**MARSHALL SPACE FLIGHT CENTER
THE UNIVERSITY OF ALABAMA IN HUNTSVILLE**

**VLF LONG-RANGE LIGHTNING LOCATION USING THE
ARRIVAL TIME DIFFERENCE TECHNIQUE (ATD)**

Prepared By: H. Mario Ierkic V., Ph.D.

Academic Rank: Associate Professor

Institution and Department: University of Puerto Rico-Mayagüez
Electrical and Computer Engineering Department

NASA/MSFC:

Office: Global Hydrology and Climate Center
Division: Earth System Science
Branch: Environmental Data and Hydrologic Processes

MSFC Colleague: Steven J. Goodman, Ph.D.

VLF LONG-RANGE LIGHTNING LOCATION USING THE ARRIVAL TIME DIFFERENCE TECHNIQUE (ATD)

H. Mario Ierikic V.[†], and Steven J. Goodman[‡]

[†]University of Puerto Rico-Mayagüez, and [‡]Global Hydrology and Climate Center, MSFC
August 1995

Introduction

A new network of VLF receiving systems is currently being developed in the USA to support NASA's Tropical Rain Measuring Mission (TRMM). The new network will be deployed in the east coast of the US- including Puerto Rico- and will be operational in late 1995. The system should give affordable, near real-time, accurate lightning locating capabilities at long ranges and with extended coverage (Kriz, 1995). It is based on the Arrival Time Difference (ATD) method of Lee (1986; 1990). The ground system results will be compared and complemented with satellite optical measurements gathered with the already operational Optical Transient Detector (OTD) instrument and in due course with its successor the Lightning Imaging Sensor (LIS) (Christian, et al., 1992).

Lightning observations are important to understand atmospheric electrification phenomena, discharge processes, associated phenomena on earth (e.g. whistlers, explosive Spread-F) and other planets. In addition, lightning is a conspicuous indicator of atmospheric activity whose potential is just beginning to be recognized and utilized. On more prosaic grounds, lightning observations are important for protection of life, property and services.

Lightning is observed with a variety of methods and here we focus on ground based RF techniques for the study of ground to cloud lightning. The field may be divided in close range (≤ 100 km, say) and long range (≥ 250 km) techniques. Close range measurements have used several procedures: (a). Interferometry at VHF to construct RF images of the lightning channel (Richard and Auffray, 1985), (b). Radar (or active) UHF observations of physical properties of the hot ($5000^{\circ}K$) and overdense plasma channel (William et al., 1989), (c). Magnetic Directional Finder (MDF) at VLF to establish angle of arrival and fixing via triangulation (Volland, 1995 and references therein). VLF Long range measurements include: (a) The single station Group Time Delay Difference (GDD) system (Volland, 1995), (b). Arrival Time Difference (ATD) at VLF to overcome polarization and timing errors. Arguably, the ATD offers the best prospects for accurate (sometimes to within a few kms!), efficient and inexpensive system for lightning observations at thousands of kilometers distance (Lee, 1990). It is pertinent to note that here we are mostly concerned with Cloud to Ground (CG) lightning. Other forms include cloud to cloud (encompassing intra-cloud and inter-cloud), cloud to stratosphere. The systems above are fairly insensitive to the latter types of lightning, due to the horizontal (perpendicular) polarization characteristics of the emitted radiation.

The organization of this work is as follows. First we review some basic concepts of the theory of long range VLF propagation. Second we discuss the modernized version of the ATD system as proposed by Kriz (1995). Next, we offer some comments aimed to shed some light on peculiar VHF satellite observations known as Trans-Ionospheric Pulses (TIPPs). Finally, the main conclusions are summarized.

VLF wave propagation in the earth-ionosphere waveguide

It is convenient to begin the discussion of sferics propagation in the earth-ionosphere waveguide considering first the ideal case of perfectly reflecting top (height h) and bottom walls (Budden, 1961; Wait, 1968). The waves supported by such a structure are proportional to $\sim e^{-ik(x \cos \theta \pm z \sin \theta)}$ where the positive (negative) sign preceding the z coordinate indicates upward (downward) propagation in the positive x direction. The wavevector \vec{k} lies in the x - z plane. The angle θ is measured relative to the abscissa x . The waveguide supports the combination of these two waves or $\sim \cos(kz \sin \theta) e^{-ikx \cos \theta}$. Maxwell's boundary conditions ensure that $kh \sin \theta = 2n\pi$, where n is an integer ≥ 0 . The waves above are known as *progressive plane waves*; they must be augmented with *inhomogeneous plane waves* to constitute a set of functions- or modes- whose superposition reproduces the original radiation. Inhomogeneous plane waves are captured in the description above by simply allowing that $\sin \theta > 1$. In this case we have, from $\cos \theta = \sqrt{1 - \sin^2 \theta}$, that the latter attenuate in the x direction and that evanescent waves arise even though the guide is lossless.

The theory just reviewed suffices to establish the existence of a cutoff frequency f_n for mode n . Here, $f_n = nc/2h$ with c the speed of light. A radio signal of frequency $f < f_n$ attenuates with coefficient $k\sqrt{(f_n/f)^2 - 1}$. The phase velocity v of a particular mode is given by $v = c/\sqrt{1 - (f_n/f)^2}$ and the group velocity u satisfies $uv = c^2$. Note that $v \geq c$ and $u \leq c$. This model captures some interesting observed features of atmospherics. For example, when the height h decreases from about 85 km to 65 km (due to regular day to night ionospheric changes or in response to sudden disturbances) f_n increases. This behavior agrees with diurnal or sudden absorption events measurements at frequencies near cutoff. A second example is the propagation of mode n , with $n \geq 1$, to long distances. For the sake of argument let's consider the radiation source (or lightning event) as a vertically oriented electric dipole that discharges instantaneously. (The dipole will have an infinite number of images at the top and bottom walls). The current associated with this event is a delta function whose Fourier components are equal to a constant. The time response of mode n can be calculated by re-synthesizing the frequency spectra subject to the constraint that $\omega/c \sin \theta = n\pi/h$ (Budden, 1961). The response in the time domain shows several measured characteristics: the waveform is distinctly oscillatory, the frequency diminishes with time eventually reaching the cutoff frequency, the intensity decreases due to dispersion in the waveguide.

However, the lossless model just described fails to explain several features. Notably, mode $n = 0$ has no attenuation hence it should reach the receiver as an impulse of radiation contrary to actual measurements. The theory must be improved by allowing for lossess in the walls. The new boundary condition for mode n becomes, $R(\theta)e^{-i2kh \sin \theta} = e^{-i2\pi n}$, with $R(\theta)$ an effective reflection coefficient that incorporates ionospheric and surface-of-

the earth effects. The reflection coefficients of importance here correspond to vertical (or parallel) propagation,

$$R(\theta) = \frac{\aleph^2 \sin \theta - \sqrt{\aleph^2 - \cos^2 \theta}}{\aleph^2 \sin \theta + \sqrt{\aleph^2 - \cos^2 \theta}}$$

where \aleph is the index of refraction, $\aleph^2 = \epsilon - i\sigma/\omega\epsilon_0$, with ϵ the relative permittivity of the medium, σ its conductivity, and ϵ_0 the permittivity of vacuum. The earth's surface conductivity is regarded as a constant while the ionospheric conductivity is given by, $\sigma = \epsilon_0 N e^2 / m \nu$, where N is the electron density, e and m the electron's charge and mass respectively, and ν is the collision frequency. Here the geomagnetic field has been ignored; however it can influence the reflection process by depolarizing the radiation and also, specially for equatorial paths, by introducing zonal asymmetries wherein west to east reflection coefficients are larger than east to west ones (Volland, 1995). Another simplification employed here has been to treat the ionosphere as sharply bounded. The ATD technique predictions should not be unduly influenced by these approximations.

The lossy walls model just described predicts radio atmospherics propagation fairly well. One of its main virtues is that only one mode needs to be considered for each frequency. This mode (possibly a hybrid) has been referred as the *least attenuated mode*. This special mode is introduced to allow for the re-synthesizing of Fourier components by considering only those modes (usually the zero or one) that have minimal attenuation characteristics versus frequency. Here lies the convenience of the mode theory of propagation over the ray theory. Namely, the least attenuated mode is sufficient to describe wave signatures at long distances. In contrast, ray theory requires the superposition of the line-of-sight and of the multiply-reflected rays.

The modernized ATD technique

The ATD technique is based on the estimation of the time of arrival of sferics detected over an 18 kHz bandwidth. The receiving system includes a VLF whip antenna and a GPS system to locate in time the incoming radiation. This system is complemented with two crossed loop aeriels for the estimation of angles of arrival to remove ambiguities in lightning fixing- specially useful for high flashing rates. The signals are digitized with substantial dynamic range- equivalent to 16 bits- leading to superior detection efficiencies. The measured signals are correlated with a synthetic waveform to determine time of arrival - based on the complete waveform, not just its leading part. Each station relays this parameter to a server station whose location engine uses least square fitting to establish lightning position. To our knowledge this procedure has not been documented in easily accessible form.

Each system has several carefully designed and computer controlled filters. Contaminating VLF signals (usually transmitters) are removed with the help of notch filters. The whole receiving section and the time of arrival algorithms are calibrated and tested locally with the injection of a pseudo-noise code 1023 elements wide and with 10 μ sec baud. A station is capable of inferring the relative position of the code to within 0.1 μ sec. This accuracy does not conflict with the 18 kHz bandwidth of the receiving chain.

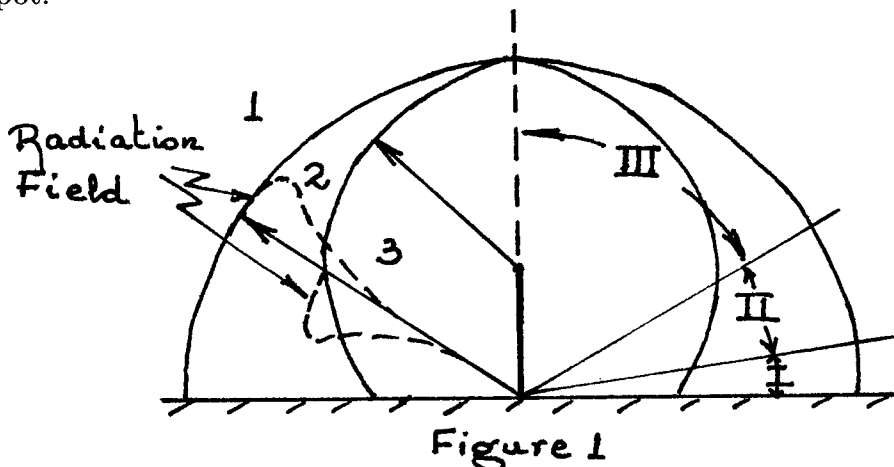
The proposed network of outstations around the east coast of the USA, linked via the Internet, should be capable of monitoring the North Atlantic area and part of the continental USA. Expected detection rates are in excess of 50 strokes per second with locations accuracies of better than 10 km (Lee, 1990; Kriz, 1995). There are plans to extend geographical coverage with the installation of more stations in the western part of Europe, the west coast of the USA, Hawaii, Australia and other locations.

On the nature of TIPP's

Recent VHF (25 to 95 Mhz) satellite observations with a multichannel receiver have documented the occasional presence of pairs of pulses of radiation $\approx 5 \mu\text{sec}$ wide separated by upto $50 \mu\text{sec}$ (Holden et al., 1995). The radiation apparently has sub-ionospheric origin because it is distinctively affected by ionospheric dispersion.

Next, we argue in favor of the hypothesis that Trans-Ionospheric Pulse Pairs may be due to ground to cloud lightning. (Note however that the arguments below may be applied to the case of cloud to cloud lightning.) Recall that the radiation emitted from thin wires effectively originates at each end of the filament (Schelkunoff, 1952; Le Vine and Meneghini, 1978 hereafter referred to as L&M). Figure 1 below shows a vertical wire aerial over the earth's surface and two spherical waves propagating outwardly. We discuss reflection effects later. The transmission line model of lightning assumes a discharge electric current waveform with a steep leading edge $\leq 5 \mu\text{sec}$ and with a gentle tail (e.g. see Fig. 1 of L&M). Note now that the steep edges translate into pulse shaped emitted radiation (see top panel of L&M's Fig. 2). The width of this pulse is given by the separation between the regions 1 and 3 in Fig. 1. The width is also determined by the length of the lightning channel and by the speed of propagation of the discharge current along the channel. In the absence of dispersion by the ionosphere the satellite's receiver would detect two bursts of radiation (one from each edge of the pulse) separated by a, of course, constant delay-independent of frequency- and equal to the width of the radiated pulse.

Coming now to the topic of reflections on the ground we suggest that reflections can be ignored. Fig. 1 shows rough estimates for the vertical reflection coefficient $R_v(\theta)$. In region III, $R_v \approx 0.6$. This value can be substantially lowered by invoking the relative roughness of the terrain at the frequencies of interest. Region II is about the Brewster's angle where $R_v \approx 0$. In region I, $R_v \approx -1$ which in turn means that there is no space wave. The surface wave on the other hand is heavily attenuated at VHF. Region I is therefore a quiet spot.



Conclusions

In conclusion we note the following points. The Arrival Time Difference technique (Lee, 1986; 1990) is probably the best method to study lightning at long ranges. We say this because ATD makes use of superior technologies (e.g. GPS, The Internet, efficient network management facilities, powerful computer hardware, data compression procedures, high performance digital equipment) and of proven lightning location algorithms. This new tool should complement nicely OTD'd and LIS's observations. We welcome ATD's capability as a research platform that should be helpful to: a). understand and improve the location engine section, b). document the diurnal and other variabilities of sferics, and c). characterize the nature of the radiation sources (e.g. channel tortuosity) and the impact on wave shapes. Finally, it is important to develop a sistematic method to determine optimum outstations sites.

On the subject of TIPP's it has been suggested that they are related to lightning and that the satellite observations of Holden et al. (1995) may be explained by taking into account the radiation by thin wires and also various propagation effects.

References

- [1] Budden, K. G., (1961) "The wave-guide mode theory of wave propagation," *Prentice Hall, Inc.*, 325pp.
- [2] Christian, H. J., R. J. Blakeslee, and S. J. Goodman, (1992) "Lightning Imaging Sensor (LIS) for the Earth Observing System," *NASA TM-4350*, 36pp.
- [3] Holden, D. N., C. P. Munson, and J. C. Devenport, (1994) "Satellite observations of Transionospheric Pulse Pairs," *Geophys. Res. Lett.*, Vol. 22, No. 8, 889-892.
- [4] Kriz S. J., (1995) "The RDI lightning detection network," *LIS/OTD Science Team Meeting, June 6-7, 1995, Huntsville, Alabama*.
- [5] Lee, A. C. L., (1986) "An experimental study of the remote location of lightning flashes using a VLF arrival time difference technique," *Quart. J. Roy. Meteor. Soc.*, 112, 203-229.
- [6] Lee, A. C. L., (1990) "Bias elimination and scatter in lightning location by the VLF arrival time difference technique," *J. Atmos. Oceanic Tech.*, 7, 719-733.
- [7] Le Vine, D. M., and R. Meneghini, (1978) "Electromagnetic fields radiated from a lightning return stroke: Application of an exact solution to Maxwell's equations," *J. Geophys. Res.*, 83, 2377-2384.
- [8] Richard, P., and G. Auffray, (1985) "VHF-UHF interferometric measurements, applications to lightning discharge mapping," *Radio Sci.*, Vol. 20 No. 2, 171-192.
- [9] Schelkunoff, S. A., (1952) "Advanced antenna theory," *John Wiley, New York*, 216pp.
- [10] Volland, H., (Ed.), (1995) "Handbook of Atmospheric Electrodynamics," *CRC Press Inc., Boca Raton, Florida*, 2 Volumes.
- [11] Wait, J. R., (1968) "EM propagation in the earth-ionosphere waveguide," *Advances in Electronics and Electron Phys.*, 25, Academic Press, 145-209.
- [12] William, E. R., and S. R. Geotis, and A. B. Bhattacharya, (1989) "A radar study of the plasma and geometry of lightning," *J. Atmos. Sci.*, Vol. 46, No. 9, 1173-1185.

1995

NASA/ASEE SUMMER FACULTY FELLOWSHIP PROGRAM

**MARSHALL SPACE FLIGHT CENTER
THE UNIVERSITY OF ALABAMA IN HUNTSVILLE**

MODELING OF MICRO THRUSTERS FOR GRAVITY PROBE B

Prepared By:	Kenneth M. Jones, Ph.D.
Academic Rank:	Assistant Professor
Institution and Department:	North Carolina A&T State University Department of Mechanical Engineering
NASA/MSFC:	
Laboratory:	Structures and Dynamics
Division:	Fluid Dynamics
Branch:	Computational Fluid Dynamics
MSFC Colleagues:	Paul K. McConnaughey, Ph.D. Alan R. Droege

INTRODUCTION

The concept of testing Einstein's general theory of relativity by means of orbiting gyroscopes was first proposed in 1959 simultaneously by Pugh[1] and Shiff[2], which lead to the development of the Gravity Probe B experiment. Einstein's theory concerns the predictions of the relativistic precession of a gyroscope in orbit around earth. According to his theory, there will be two precessions due to the warping of space-time by the earth's gravitational field. The geodetic precession in the plane of the orbit, and the frame-dragging effect, in the direction of earth rotation. For a polar orbit, these components are orthogonal.

In order to simplify the measurement of the precessions, Gravity Probe B will be placed in a circular polar orbit at 650 km, for which the predicted precessions will be 6.6 arcsec/year (geodetic) and 42 milliarcsec/year (frame-dragging). As the gyroscope precesses, the orientation of its spin-axis will be measured with respect to the line-of-sight to Rigel, a star whose proper motion is known to be within the required accuracy. The line-of-sight to Rigel will be established using a telescope, and the orientation of the gyroscope spin axis will be measured using very sensitive SQUID (Superconducting Quantum Interference Device) magnetometers. The four gyroscopes will be coated with niobium. Below 2K, the niobium becomes superconducting and a dipole field will be generated which is precisely aligned with the gyroscope spin-axis. The change in orientation of these fields, as well as the spin-axis, is sensed by the SQUID magnetometers.

In order to attain the superconducting temperatures for the gyroscopes and the SQUIDs, the experiment package will be housed in a dewar filled with liquid helium. As the liquid helium slowly boils-off from the cryogenic system of the spacecraft, the gas must be vented overboard. The resulting thrust can easily be the largest disturbance to the attitude and translational control system. In view of this, the helium could be thought of as a free propellant. Since fuel consumption can not be conserved, the boil-off helium can be vented through proportional thrusters which will control the attitude of the spacecraft by keeping the telescope pointing to Rigel within 70 milliarcseconds. It will also maintain drag-free control along the three translational axes. The drag-free control will essentially null the external disturbance forces arising from atmospheric drag, and from solar and terrestrial radiation. The principle behind drag-free control is that a proof mass inside the spacecraft is shielded from external forces, so that the proof mass follows a nearly ideal gravitational orbit, and a control system activates jets or thrusters to make the spacecraft follow the proof mass. Making the spacecraft drag-free helps in two ways: (1) it reduces gyro suspension forces which result in torques down to a level where relativistic precession can be measured, (2) it reduces errors in orbit determinations needed in analyzing relativity data.

Due to the low rate at which helium gas escapes from a well insulated helium tank, the thrusters must operate in a flow regime vastly different from conventional thruster systems. The development work by Bull[3], Chen[4] and Lee[5] at Stanford University have shown that the helium propulsion system is realistic. Wiktor[6] has worked on the implementation of ultra low flow thruster into the propulsion system for GP-B. The motivation for the present work is to obtain a better understanding of the effect that the plume has on the flow characteristics of the a thruster. A secondary purpose of this investigation is to determine the requirements for modeling the plume, since this is the first attempt at modeling this type thruster.

MODEL DESCRIPTION

Since Gravity Probe B will operate in the rarefied gas regime, traditional computational fluid dynamics cannot be used to model the nozzle flow and exhaust plume. CFD obtains solutions of the mathematical equations that model the processes. When the gas density becomes sufficiently low, the Navier-Stokes equations do not provide a valid model for the rarefied gas. The Navier-Stokes equations depend on the Chapman-Enskog theory for the shear stresses, heat fluxes and diffusion velocities as linear functions of the velocity, temperature and concentration gradients. The formulation for the Chapman-Enskog distribution incorporates the local Knudsen numbers which are the ratio of the local mean free path to the scale lengths of the velocity and temperature gradient. It has been found that errors become significant when these Knudsen numbers exceed 0.1 and continuum theory is useless when they exceed 0.2[7].

Since the Knudsen numbers for the Gravity Probe B thrusters are well above 1; the direct simulation Monte Carlo method was used to model the flow field. The DSMC method developed by G.A. Bird[8], models the gas flow by following the trajectories of a large number of simulated molecules within a region of simulated space. The basic assumption in the method is that the movement of molecules can be decoupled from the collisional process. A probabilistic rather than a deterministic method is used for calculating collisions and is therefore limited to gas flow in which the mean spacing between molecules is large compared to the diameter of the molecules. The time parameter in the model corresponds to physical time in the real flow. All calculations are unsteady, but steady flow may be obtained as the large time average of unsteady flow conditions. The basic assumptions used in the DSMC technique are the same as those in the Boltzmann equation, so that the results are equivalent to a numerical solution of the Boltzmann equation as long as the time step, the cell size and the number of simulated molecules are kept within reasonable limits. The art of setting up the problem is in defining the "reasonable" limits. A DSMC calculation is more like an experiment than a traditional analytical analysis[9].

The results presented in this study were obtained using the axisymmetric/two-dimensional G2/A3 DSMC code written by G.A. Bird [10], which has been modified to run parallel on two processors of a Convex 240 supercomputer. The code employs a variable hard sphere (VHS) model. This is essentially a hard sphere with a diameter that varies with some inverse power of the relative velocity between the molecules in the collision.

DISCUSSION OF RESULTS

The investigation was divided into three test cases: Case 1 modeled only the thruster, while Cases 2 and 3 modeled the thruster with a plume. Case 2 used a plume grid that was designed to capture the flow structure around the nozzle lip. This grid was similar to the one used by Campbell and Weaver[9] in their DSMC nozzle calculations. See Figure 2. Case 3 used a grid for the plume that was designed to capture the flow density profile as it decreases away from the exit plane as shown in Figure 1. All three cases were run at a throat Reynolds Number of 0.06. This low Reynolds Number would simulate the low flow case of helium being vented.

Cases two and three showed that the addition of the plume increased the static pressure in the thruster plenum. In addition, the plume caused the sonic line to move upstream toward the nozzle throat. On the other hand, the sonic line for the thruster without the plume was located very close to the nozzle exit. This indicates that the thruster plenum is subsonic and any downstream disturbance can affect the entire flow field. This means that the thruster region must be solved each time a new plume grid is employed.

As seen in Table 1, the addition of the plume had very little effect on the total thrust developed by the nozzle. The plume did require more molecules to reach steady state as one would expect. The calculations did show that the coarse grid used in Case 2 allowed the flow field to develop faster than the finer grid used in Case 3. This would allow the investigator to gain a feel for the flow characteristics earlier and be able to make adjustments to the grid. The plume calculations did show that the backflow region develops very slowly. Many different cell sizes and time steps were employed in this region in an attempt to develop this region, but it just took time.

CONCLUSIONS

The structure of the flow of helium through a GP-B micro thruster and into vacuum has been investigated using the Direct Simulation Monte Carlo method. Three cases, the thruster alone, and the thruster with two different plume grids have been compared. The addition of the plume to the calculations does have a definite effect on the upstream plenum flow characteristics. Therefore, the plenum section must be included in each plume calculation due to their interdependence.

REFERENCES

1. Pugh, G. H., "Proposal for a Satellite Test of the Coriolis Prediction of General Relativity," SWEG Research Memorandum No. 111, Weapons Systems Evaluation Group, Pentagon, Washington, D.C., November 12, 1959.
2. Schiff, L. I., "Motion of a Gyroscope According to Einstein's Theory of Gravitation," Proceedings of the National Academy of Sciences, 46(871), 1960.
3. Bull, J. S., "Precise Attitude Control of the Stanford Relativity Satellite," Stanford University Ph.D. Thesis, SUDAAR 452, 1973.
4. Chen, J-H, "Helium Thruster Propulsion System for Precise Attitude Control and Drag Compensation of the Gravity Probe B Satellite," Stanford University Ph.D. Thesis, SUDAAR 538, 1983.
5. Lee, K-N, "The Design of a Wide Dynamic Range Helium Thruster for Gravity Probe B," Stanford University Ph.D. Thesis, 1992.
6. Wiktor, P. J., "The Design of a Propulsion System Using Vent Gas from a Liquid Helium Cryogenic System," Stanford University Ph.D. Thesis, 1992.

6. Wiktor, P.J., "The Design of a Propulsion System Using Vent Gas from a Liquid Helium Cryogenic System," Stanford University Ph.D.Thesis, 1992.
7. Chapman, S. and Cowling, T.G., The Mathematical Theory of Non-uniform Gases, (2nd edn.), Cambridge University Press, London, (1952).
8. Bird, G. A., Molecular Gas Dynamics, Clarendon Press, Oxford, 1976.
9. Campbell, D. H. and Weaver, D. P., "Nozzle Lip Effects on Gas Expansion into Plume Backflow Region," AIAA Paper 88-0748, January, 1988.
10. Bird, G. A., The G2/A3 Program System Users Manual, version 1.3, September, 1988.

	CASE I	CASE II	CASE III
Total Thrust, N	0.36483E-05	0.36439E-05	0.36570E-05
Integrated Thrust, N	0.37004E-05	0.37029E-05	0.37095E-05
Number-Molecules	24,312	51,857	32,529
Number - Samples	100,100	88,400	37,900

Table 1. Comparison of Thrust Calculations.

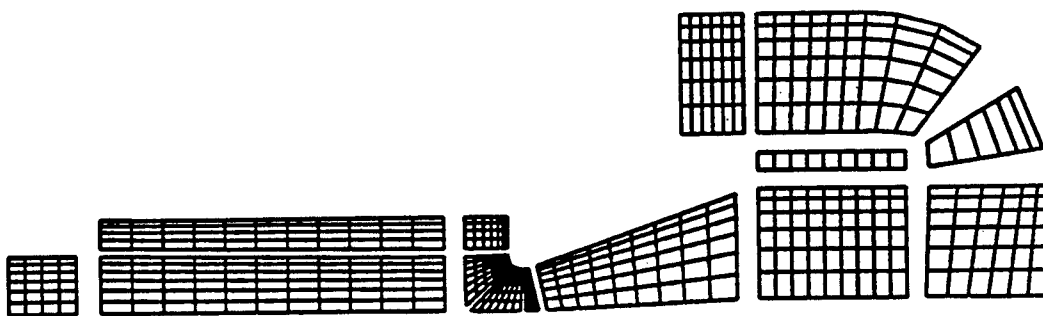


Figure 1. Grid for Case 3 Calculations

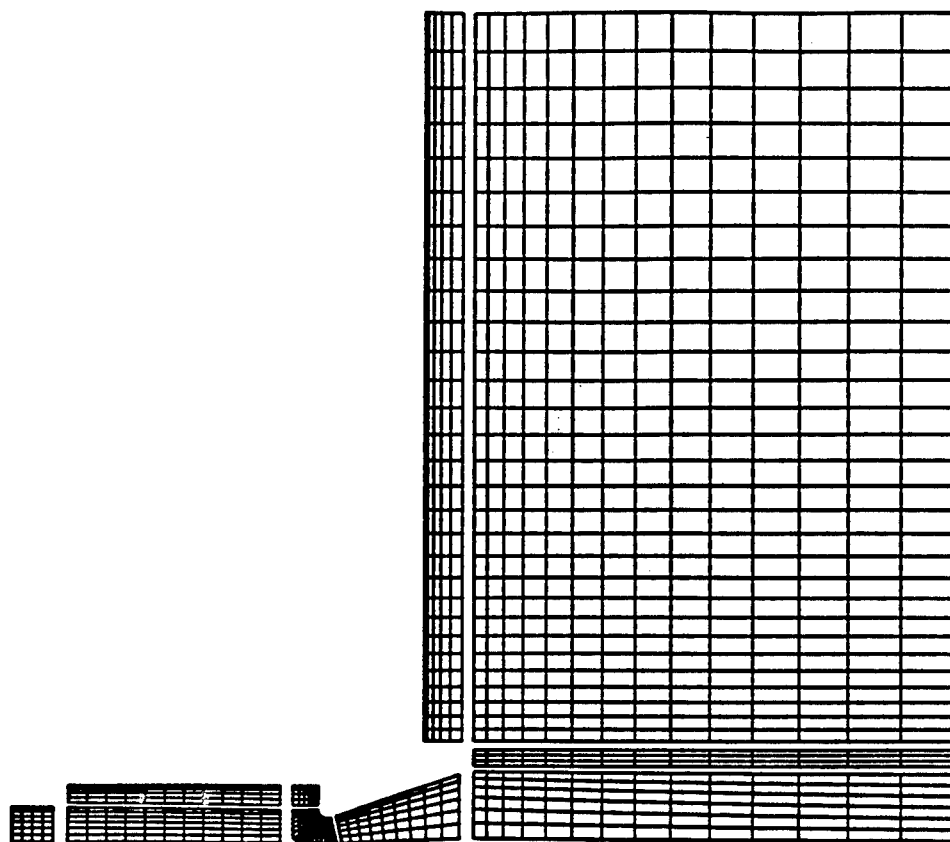


Figure 2. Grid for Case 2 Calculations.

1995

NASA/ASEE SUMMER FACULTY FELLOWSHIP PROGRAM

**MARSHALL SPACE FLIGHT CENTER
THE UNIVERSITY OF ALABAMA IN HUNTSVILLE**

**PRELIMINARY WORK TOWARD THE DEVELOPMENT OF A DIMENSIONAL TOLERANCE STANDARD
FOR RAPID PROTOTYPING**

Prepared By:	W. J. Kennedy, Ph.D., P.E.
Academic Rank:	Professor
Institution and Department:	Clemson University Department of Industrial Engineering
NASA/MSFC:	
Office:	Materials and Processes Laboratory
Division:	Non-Metallic Materials and Processes
Branch:	Ceramics and Coatings Branch
MSFC Colleague:	Floyd E. Roberts

INTRODUCTION

Rapid prototyping is a new technology for building parts quickly from CAD models. It works by slicing a CAD model into layers, then by building a model of the part one layer at a time. Since most parts can be sliced, most parts can be modeled using rapid prototyping. The layers themselves are created in a number of different ways - by using a laser to cure a layer of an epoxy or a resin, by depositing a layer of plastic or wax upon a surface, by using a laser to sinter a layer of powder, or by using a laser to cut a layer of paper. Rapid prototyping (RP) is new, and a standard part for use in comparing dimensional tolerances has not yet been chosen and accepted by ASTM (the American Society for Testing Materials). Such a part is needed when RP is used to build parts for investment casting or for direct use. The objective of this project was to start the development of a standard part by using statistical techniques to choose the features of the part which show curl - the vertical deviation of a part from its intended horizontal plane.

PROBLEM STATEMENT

Rapid prototyping has many uses. These are given in Table 1.

General use	NASA Application	Industrial Application
Visualization of a concept	Reusable Launch Vehicle (RLV)	Backup light cover (Used by BMW)
Checking fit of different parts	Space Station furnace	Texas Instruments
Models for direct use	Space Lab mockup parts	Injection molds
Molds for sand casting	None yet	Bearing housing (Reliance Electric)
Parts for investment casting	LOX resistant turbo pumps	Hip joint replacements (Clemson U.)
Functional prototypes	Wind tunnel test model	Gearbox housing (VW)

Table 1. Applications of rapid prototyping

Of these applications, only the first does not require some part accuracy. Accuracy means conformity to some standard of surface finish, linear dimension, twist, curl (hereby defined as the vertical deviation of a part from its intended horizontal plane), and the preservation of angles. Most physical standards are defined with reference to some accepted part geometry and some measurement process, but for rapid prototyping, neither a part nor a measurement process has been accepted by the American Society for Testing Materials (ASTM).

For a part to be useful as a standard, it should have at least four characteristics: (1) The geometry should be simple, so as to avoid unknown

interactions between different types of dimensional deviations (2) It should be easy to measure the part for a particular type of dimensional deviation, preferably with only two or three measurements needed per deviation type. (3) It should be made of components each designed to indicate the magnitude of the deviation of one dimensional characteristic. In particular, the ultimate part should have components to measure linear dimension accuracy (when compared with the CAD drawing), surface finish, twist, curl, and the minimum angles it is possible to build in the vertical and horizontal directions.

In addition to the characteristics described above, the author and his NASA colleague felt strongly that a part used as a standard for rapid prototyping should perform the following functions:

- (1) It should serve as a measure of accuracy for each of the dimensional parameters chosen.
- (2) It should enable vendors to achieve part accuracy by being inexpensive to manufacture and easy to measure, hence easy to use in the optimal selection of RP process parameters and materials.
- (3) It should enable a NASA branch or a company contemplating the purchase of a machine to evaluate the accuracy of different RP processes or materials.
- (4) If a complex part is to be manufactured for NASA or for a company by an organization selling RP services, manufacturing this standard part should enable NASA contractors to demonstrate process accuracy without the manufacture of the complex part.

Developing a standard part for rapid prototyping would include the design of components to measure each of the dimensional distortion types given above. In order to demonstrate a methodology for the complete part, the author and his NASA colleague concentrated on the component that would best measure curl.

DEVELOPING THE PART AND DETERMINING ITS SIGNIFICANT ATTRIBUTES

The objective of this research was to determine design elements that would show curl so that these elements could be included in a standard part for rapid prototyping. The systematic design process used to select these design elements was to choose a part with many such elements, then to vary them and determine which elements were statistically significant. The part is shown in Figure 1 below.

The components of this part were chosen using the following logic:

45 degree leg: This feature tests whether curl is additive - i.e. whether the curl at the end of the 45 degree leg is the sum of the curl in the X and Y legs. This leg was present in all parts measured.

X and Y ramps: These test whether anisotropy in component mass makes a significant difference in the curl, in either the X or Y direction. Some parts measured in this project had the X ramp, some had the Y ramp, some had both, and some had neither.

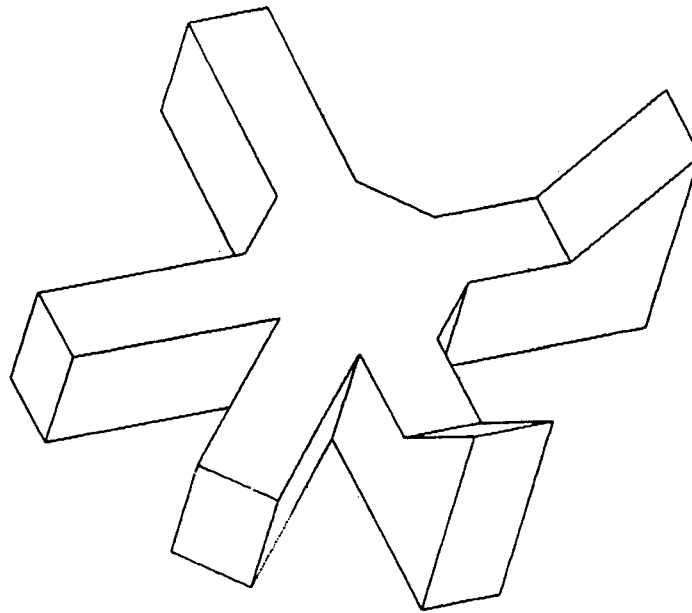


Figure 1. Geometry of test part

Radial offset: This was the distance from the center of the part to the center of the build platform of the RP device. Since some of the RP processes use lasers, and these impinge upon the build material at different angles at different parts in the build platform, it seemed reasonable that the location on the build platform might make a difference. Varying the radial offset from 0 to the corner of the platform tested whether offset from center of build platform was a significant factor.

Width: The width of a leg was varied to test whether spar width is a significant factor. The parameter varied was the horizontal aspect ratio, defined as the spar width/spar length. This parameter took on the values 0.10, 0.24, and 0.38 for test parts. When this parameter was varied, all the legs took on the same value. This procedure was also used for the thickness.

Thickness: The thickness was also varied, since it seemed likely that spar thickness was also a significant factor. For thickness, the vertical spar ratio, defined as spar thickness/spar, was given the values 0.10, 0.24, and 0.38.

An experimental design was used in which width, thickness, the radial offset, and the presence or absence of X and Y ramps were varied systematically according to a central composite experimental design similar to those discussed by Montgomery [1]. This particular design was developed by some software from BBN [2]. Twenty-seven parts were made using ABS plastic in a fused deposition modeling FDM 1500 machine made by Stratasys. Parts were measured using a dial gauge, making seven measurements of bottom curl at 6

points for each part, with the mean of the five non-extreme measurements (of the seven) being used as the data point for the experimental analysis.

CONCLUSIONS AND RECOMMENDATIONS FOR FUTURE RESEARCH

One question was that of correlation among various measures of curl. The measures used were horizontal deviations at (1) the end of the X leg adjacent to the 45 degree leg, (2) the end of the Y leg adjacent to the 45 degree leg, (3) the end of the X leg opposite the 45 degree leg, (4) the end of the Y leg opposite the 45 degree leg, (5) the end of the 45 degree leg, (6) the point on angled leg where this leg is intersected by a line through the end of the adjacent X leg and parallel to Y leg, and, (7) the maximum of all curl values. This correlation matrix is shown in Table 2. This chart shows

	X leg adj	X leg opp	Y leg adj	Y leg opp	X part way	Leg end	Max curl
X leg adj	1						
X leg opp	.01366	1					
Y leg adj	0.6991	0.6132	1				
Y leg opp	0.7982	0.3550	0.6171	1			
X part way	0.9029	0.1084	0.6818	0.7256	1		
Leg end	0.9000	0.1036	0.7756	0.6558	0.8639	1	
Max curl	0.9068	0.3645	0.8023	0.8919	0.8452	0.8515	1

Table 2. Correlations among various measures of curl

	T/L	W/L	X Ramp	Y Ramp	Offset	Intercept
X leg R ² = .665	.131 **	.032	-.0047	-.00492	.00378 *	.00265
X opp R ² = .534	.080 **	.052 *	.00491	.00307	-.00329 *	.009183
Y leg R ² = .700	.087 **	.062 *	-.00349	-.00797	.000015	.00717
Y opp R ² = .736	.148 **	-.00234	-.00656	.00270	.00054	.0124
X part R ² = .431	.0489 **	.0156	-.00461	-.00167	.001305	.002373
Leg end R ² = .665	.0813 **	.0301	-.00485	-.0104	.00181	.0185
Max curl R ² = .748	.135 **	.0139	-.0054	-.0052	.00188	.0190 *

Table 3. Regression coefficients from model. (* - Significant at $\alpha \leq .05$; ** = $\alpha \leq .01$)

that the X leg adjacent to the angled leg and the Y leg opposite to the leg are the most highly correlated with the maximum curl. A further analysis gives a correlation of 0.917 between the sum of curl in the X and Y legs and the curl in the leg between them.

A regression analysis was performed on the data, with results that are shown in Table 3. From these results, it is clear that the only factors that are statistically significant in determining the curl are the thickness - very significant - and the width - not so significant. From these results, the following conclusions can be drawn:

- Curl is most closely associated with thickness.
- Curl is associated, though less closely, with width.
- The presence or absence of X and Y ramps does not make a significant difference in the curl.
- Legs at 90 degrees from each other give curl measurements whose sum is significantly correlated to the curl of the leg half way between them, leading to the conclusion that curl is in some sense additive.

In addition to these conclusions from statistics, the build process leads any user to suspect anisotropic behavior parallel to the perpendicular sides of the build envelope. Therefore, the conclusions of this research are that the component of the final part used for a dimensional tolerance standard should include two legs at right angles, with each leg having at least the width and thickness used in this experiment, with the legs parallel to two perpendicular sides of the build platform.

Further research: To complete this study, more parts need to be made on machines other than the FDM - in particular, on machines using stereolithography, since that is the most commonly used process. The experimental design process shown here is useful and can profitably be used to design the other component of the standard part for rapid prototyping.

Acknowledgments: I would like to acknowledge the interested help and consideration given to me as to this work by my MSFC colleague, Floyd Roberts. He has been consistently encouraging and has given me a better understanding of the techniques and technical possibilities of rapid prototyping. Dr. Gerald Karr and Ms. Teresa Schurtz of his staff of the University of Alabama at Huntsville have also been most helpful.

References:

- [1] Montgomery, Douglas C. *Design and Analysis of Experiments*, Second Edition (John Wiley & Sons, New York, 1984).
- [2] BBN Software Products, *BBN/Catalyst Handbook*, Cambridge, MA, 1992.

1995
NASA/ASEE SUMMER FACULTY FELLOWSHIP PROGRAM

MARSHALL SPACE FLIGHT CENTER
THE UNIVERSITY OF ALABAMA IN HUNTSVILLE

DEVELOPMENT OF SOFTWARE FOR THE
MSFC SOLAR VECTOR MAGNETOGRAPH

Prepared By:	Jack Kineke
Academic Rank:	Associate Professor
Institution and Department:	Centre College Department of Mathematics and Science
NASA/MSFC:	
Office:	Space Science Laboratory
Division:	Physics and Astronomy
Branch:	Solar Physics
MSFC Colleague:	Dr. Mona Hagyard

The Marshall Space Flight Center Solar Vector Magnetograph is a special purpose telescope used to measure the vector magnetic field in active areas on the surface of the sun. This instrument measures the linear and circular polarization intensities (the Stokes vectors Q, U and V) produced by the Zeeman effect on a specific spectral line due to the solar magnetic field from which the longitudinal and transverse components of the magnetic field may be determined. Beginning in 1990 as a Summer Faculty Fellow in project JOVE and continuing under NASA Grant NAG8-1042, the author has been developing computer software to perform these computations, first using a DEC MicroVAX system equipped with a high speed array processor, and more recently using a DEC AXP/OSF system. This summer's work is a continuation of this development.

The existing MSFC Vector Magnetograph measures polarization intensities at points in a square array of 128×128 pixels which cover a field-of-view (FOV) of about 5 by 5 minutes of arc. At the present time, a new magnetograph is under construction which will provide considerably higher resolution, up to a maximum of 1024×2048 pixels covering a FOV of 4 by 8 arc-minutes. Initially, programs are being written to process arrays of 512×1024 pixels, later to be expanded when the full resolution of the instrument is realized.

The computation of the longitudinal and transverse components of the magnetic field is described by Hagyard et al (1982)¹. Once the Stokes vectors P_V , P_Q , and the azimuth angle ϕ are determined, the magnetic field components are then computed by evaluating polynomials in P_V and P_Q at each point of the data array. The coefficients in these polynomials are dependent on the inclination angle Ψ (angle to the line-of-sight) of the magnetic field vector at any point. The calculation is straightforward for points along the neutral line where $\Psi = 90^\circ$, but the result is less accurate for points away from the neutral line where Ψ varies from 0 to 90° . A new method was developed by Hagyard and Kineke (1995)² to calculate the magnetic field components by evaluating the polynomials at points away from the neutral line by an iterative process using an individual set of polynomial coefficients which correspond to the inclination angle of the field at each point in the array.

The software to implement the magnetic field computations by the new method is written in Interactive Data Language (IDL), which supports efficient vector and array processing capabilities. However, since the new iterative algorithm involves evaluating polynomials having coefficients which depend on Ψ , it was necessary to implement the iterative processing in external FORTRAN subroutines called by IDL, since IDL is very inefficient when a data dependency exists. Originally, the programs were developed on a MicroVAX 3600 running the VMS operating system, and reasonable execution times (~1 minute) were realized for the 128×128 pixel arrays produced by the existing magnetograph. The present effort is to migrate the IDL and FORTRAN routines to an AXP/OSF system which has considerably greater speed and memory capacity to handle the high resolution data arrays produced by the magnetograph now being assembled. A problem was encountered when it was discovered that the IDL documentation and

examples describing the calling of external subroutines on AXP/OSF systems were in error. When the software vendor (Research Systems, Inc.) provided the correct documentation, the process worked properly.

A major part of the programming effort has been directed to the development of a "user friendly" interactive graphical user interface which exploits the windowing capabilities available in the OSF1 operating system (X windows). The IDL language supports a series of "widgets" which can be manipulated to produce buttons for making selections from a set of options, sliders for the selection of a number from a given range of values, text boxes for keyboard input and a draw widget for plotting the results. In most cases, the user makes selections and chooses numerical values by means of a pointing device (mouse). In a typical execution of the IDL profile SPOT, the user first sees menus for the selection of input data files. The desired directory and files can be chosen by highlighting the selection and pressing (clicking) a mouse button. Next, the menu shown in figure 1a appears, where the user can change the constants used in the magnetic field calculations by clicking the appropriate box and entering the data from the keyboard. In addition, "YES/NO" button options are available to save the constants, save the calculated magnetic field components in output files, or plot the resulting magnetogram on the display. Clicking the "OK" button causes the profile to continue, whereupon the user sees the menu of figure 1b, where the number of iterations of the polynomial evaluation algorithm is chosen. The IDL profile then calls an external FORTRAN routine to perform the iterations, and then plots a histogram which indicates the change in the transverse and longitudinal components from one iteration to the next. If these changes are not sufficiently small, the iteration selection menu (figure 1b) can be used again to program additional repetitions. Clicking "OK" with zero iterations selected causes the program to display the plotting menu of figure 2. In this display, widget buttons are used to select the type of plot (observed, potential etc.), the plot parameters (contour levels, shear points, etc.) and the output device (X window display, laser printer, etc.). Widget sliders are used to select the limits of the area to be plotted, and a draw widget is produced on which the magnetogram plot is displayed. In the example, an active area with numerous shear points is illustrated, where the data was obtained in 1991 by a magnetograph having 128 by 128 pixel resolution. Normally, the user would run the profile and plot the magnetogram on the display, and then re-plot on a hard copy output device such as a laser printer if the data appeared valid. It should be noted that each menu has a "CANCEL" and "HELP" button. Clicking on "CANCEL" stops the program at that point, while pressing "HELP" produces a new window containing detailed instructions for the unfamiliar user. As it is now written, this IDL profile gets input data from files containing the calibrated polarization intensity ratios (differences divided by sums) described in reference (1). An IDL profile is now being developed to produce these arrays from the raw polarization intensity data produced by the magnetograph, with the ultimate goal of an integrated software package to do the complete data analysis.

Magnetograph Calibration Profile

CK	UOBAR	X2 (%)
[4.395000]	[0.0001050]	[-1.60000]
PVO	ROBAR	X3 (%)
[0.0000000]	[0.0000690]	[2.84000]

Save constants in /usr/users/kinekej/ar6659/b13439f.h? ☒ YES ☐ NO

Save B-files in /usr/users/kinekej/ar6659/? ☒ YES ☐ NO

Plot Results on Display? ☐ YES ☒ NO

Figure 1a

Magnetograph Calibration Profile

Select Number of Iterations:

☒ 0
 ☒ 2
 ☒ 3
 ☒ 4
 ☒ 5
 ☒ 6
 ☒ 7
 ☒ 8
 ☒ 9

Figure 1b

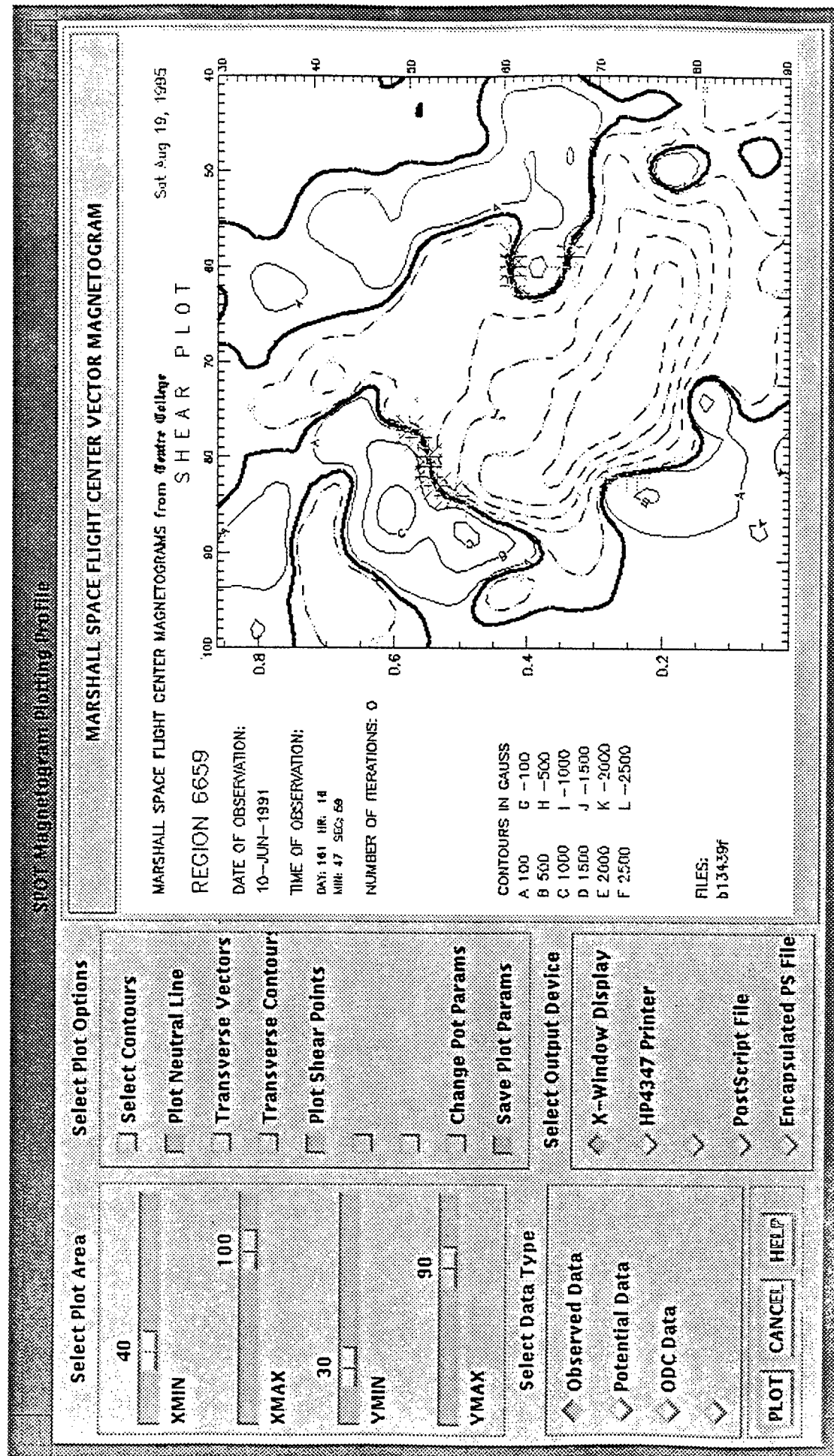


Figure 2

Clearly, the software development process for the new magnetograph is just beginning. Preliminary tests indicate that for 512×1024 pixel arrays, execution times with five iterations of the polynomial evaluation algorithm are on the order of several minutes, which is certainly quite reasonable. Considerable programming remains to be done to provide for additional calculations, such as the production of plots in the heliocentric coordinate system. The author intends to submit a new proposal to continue his work in January, 1996. The assistance and cooperation of all of the members of the staff of the MSFC Vector Magnetograph Laboratory is greatly appreciated by the author, for it made his five week visit a pleasant and intellectually stimulating experience, despite the exceptionally hot weather.

References

1. M.J. Hagyard, N.P. Cummings, E.A. West and J.E. Smith: "The MSFC Vector Magnetograph," *Solar Phys.* **1**: 31-51, 1982.
2. M.J. Hagyard and J.I. Kineke: "Improved Method for Calibrating Filter Vector Magnetographs," *Solar Phys.* **158**: 11-28, 1995.

1995

NASA/ASEE SUMMER FACULTY FELLOWSHIP PROGRAM

**MARSHALL SPACE FLIGHT CENTER
THE UNIVERSITY OF ALABAMA IN HUNTSVILLE**

**EXTENDING THE JOVE PROGRAM THROUGH
UNDERGRADUATE RESEARCH**

Prepared by:	George R. Lebo, PhD
Academic Rank:	Associate Professor
Institution and Department:	University of Florida Department of Astronomy
NASA/MSFC:	
Office:	Associate Director for Science
MSFC Colleague:	Frank Six, PhD.

EXTENDING THE JOVE PROGRAM THROUGH UNDERGRADUATE RESEARCH

My summer activities spanned several projects, the most prominent of which involved the JOVE program. Each effort will be reported under a separate heading.

I. THE JOVE PROGRAM

A. UNDERGRADUATE RESEARCH

The JOVE program was initiated in 1988 to develop NASA-related research capabilities in colleges and universities which had had little or no previous experience with NASA. Any institution which was not currently funded at more than \$100 K annually by NASA was eligible. In an open competition six universities were selected for participation in the first year. NASA supplied funds, access to its facilities and data, collaboration with its researchers and a hookup to the internet. In return the university was expected to match NASA's investment by giving its participating faculty members time off of their teaching schedules to perform research during the school year, by waiving it overhead charge and by putting up real funds to match those supplied by NASA. Each school was eligible for three years after which they were expected to seek funds from other sources. Over the span of the program more than 100 colleges and universities have participated. Fifteen have finished their eligibility.

Since one of the strong components of the program was the direct involvement of undergraduate students in active research, it was decided to develop a followon program which would provide stipends to undergraduate students at the institutions who had used up their JOVE eligibility. Though the program has not yet been completely defined, important features require that:

The University will:

1. Continue to grant the faculty member release time from the classroom during the academic year to pursue his/her research.
2. Supply housing in dormitories for students in summer programs.
3. Continue to develop new aerospace related curricula.
4. Continue to do educational outreach.
5. Waive indirect costs.
6. Match NASA's contributions toward student stipends, travel and any faculty salaries with real or like-kind funds.

NASA will supply:

1. Liason support to its laboratories and mentors.
2. Data.
3. Faculty Summer Salary.
4. Student Support.
5. Internet Link.
6. Travel.
7. Supplies, Software and Publications costs.

It is noteworthy that NSF has a program (the Research Experiences for Undergraduates program) which rather closely parallels that proposed above. A particular difference is that the REU program brings undergraduate students from smaller colleges and universities to large universities for the summer, whereas the proposed JOVE followon program would make research experiences available to undergraduates at their own institutions where the JOVE faculty members have already put research programs in place using NASA's help. The JOVE followon program could be conducted in either the school year or in the summer. A joint NASA/NSF program would serve in the best interests of both agencies inasmuch as the administration is pushing interagency collaboration. In addition NSF stands to expand its outreach because it will:

1. Reach into institutions which pride themselves primarily in providing outstanding undergraduate (rather than graduate) education. Their current REU programs are run out of the large research universities.

2. Gain access to institutions which have projects directly linked to ongoing research at NASA's ten field centers. NASA's advantage is that it has world-class research facilities whereas NSF has to rely on those in the universities.

B. PAVE

NASA's desire to transfer its technologies to the private sector now permeates all of its programs. Therefore a Partnering Venture program is now being discussed in which JOVE-like rules will be applied to small companies which do not now do much business with NASA. I participated in these discussions and prepared transparencies to be used in presentations to prospective funding sources.

C. OTHER

I participated in the preparation of materials for and helped manage the JOVE annual retreat which was held in Monterey, CA. July 5-8, 1995.

II. SPACE GRANT

One of the goals of NASA's Space Grant program is to build relationships between NASA, Industry and Space Grant Universities. Since I had participated in the formation of Space Grant's Industrial Task Force (SGITF), I was asked to present the results of the SGITF organizational meeting to the Space Grant Directors at their annual meeting which was held in Washington, DC., May 15, 1995. Two days later I addressed the Florida Higher Education Consortium at their annual meeting in St. Petersburg, FL where I discussed the Hubble Space Telescope.

III. TECHNOLOGY TRANSFER

On several occasions I have discussed NASA technologies with interested participants:

1. I spoke frequently with Jerry Mastromarino, an entrepreneur from Sarasota, FL, who is interested in forming a company which will market NASA technologies. He visualizes raising up to \$100 M to fund the completion and commercialization of up to 50 products, processes and technologies. He plans to visit the MSFC Technology Transfer office in the next few weeks. He is also very interested in developing a company to fund and commercialize NASA's Reusable Launch Vehicle (RLV) provided his first venture is successful.

2. I participated with Tony Phillips, an MSFC Summer Fellow who is attempting to commercialize educational virtual reality arcade games, in his discussions with the MSFC Technology Transfer people. I also participated in his discussions with Dr. David Powe, Director of NASA's Tri-State Education Initiative, who is interested in including Virtual Reality techniques in the classroom.

IV. LOW FREQUENCY TELESCOPE (LOFT)

Larry Scott, a University of Florida alumnus, challenged me to design a large low frequency radio telescope which could produce world-class observations. I assembled a group of astronomers; Dr. Bob Backer, University of California at Berkley; Dr. Tom Carr, University of Florida; Dr. Bill Erickson, University of Maryland and University of

Tasmania; Dr. Namir Kassim, Navy Research Laboratory; Dr. Shri Kulkarni, California Institute of Technology; Dr. George Lebo, University of Florida; and Dr. Tony Phillips, California Institute of Technology, to design such a facility. It will be a T-shaped array with legs 500 kilometers long. Each of the up to 20 array elements will be a sub-array of low frequency antennas which will cover about two acres. Mr. Scott has indicated that he is reasonably confident that he can raise from \$3 M to \$4 M from private sources for such an effort.

1995

NASA/ASEE SUMMER FACULTY FELLOWSHIP PROGRAM

**MARSHALL SPACE FLIGHT CENTER
THE UNIVERSITY OF ALABAMA IN HUNTSVILLE**

**THERMAL SIGNATURES OF URBAN LAND COVER TYPES: HIGH-RESOLUTION
THERMAL INFRARED REMOTE SENSING OF URBAN HEAT ISLAND
IN HUNTSVILLE,AL.**

Prepared By: Chor Pang Lo, Ph.D.
Academic Rank: Professor
Institution and Department: University of Georgia
Department of Geography

NASA/MSFC:

Office: Global Hydrology and Climate Center
Division: Earth Science and Applications

MSFC Colleagues: Dale A. Quattrochi, Ph.D.
Jeffrey C. Luvall, Ph.D.

Introduction

The main objective of this research is to apply airborne high-resolution thermal infrared imagery for urban heat island studies, using Huntsville, Al., a medium-sized American city, as the study area. The occurrence of urban heat islands represents human-induced urban/rural contrast, which is caused by deforestation and the replacement of the land surface by non-evaporating and non-porous materials such as asphalt and concrete. The result is reduced evapotranspiration and more rapid runoff of rain water (Carlson 1986, Kim 1992). The urban landscape forms a canopy acting as a transitional zone between the atmosphere and the land surface. The composition and structure of this canopy have a significant impact on the thermal behavior of the urban environment (Goward, 1981).

Research on the trends of surface temperature at rapidly growing urban sites in the United States during the last 30 to 50 years suggests that significant urban heat island effects have caused the temperatures at these sites to rise by 1 to 2 °C. (Cayan and Douglas 1984, Karl et al., 1988). Urban heat islands have caused changes in urban precipitation and temperature that are at least similar to, if not greater than, those predicted to develop over the next 100 years by global change models (Changnon, 1992).

Satellite remote sensing, particularly NOAA AVHRR thermal data, has been used in the study of urban heat islands (e.g., Lee 1993, Matson et al. 1978, Brest 1987, Gallo et al. 1993, Roth et al. 1989). Because of the low spatial resolution (1.1 km at nadir) of the AVHRR data, these studies can only examine and map the phenomenon at the macro-level.

The present research provides the rare opportunity to utilize 5-metre thermal infrared data acquired from an airplane to characterize more accurately the thermal responses of different land cover types in the urban landscape as input to urban heat island studies.

Data Acquisition and Processing

The thermal infrared data were acquired as Mission M424 over the greater Huntsville, Alabama area, on September 7, 1994, a clear day with less than 5 per cent of cloud cover in the sky, using the Advanced Thermal and Land Applications Sensor (ATLAS) sensor system on board a NASA Stennis LearJet. The ATLAS is a 15-channel imaging system which incorporates the bandwidth of the Landsat Thematic Mapper with additional bands in the middle reflective infrared and thermal infrared range (Table 1). All 15-channel data were acquired on the same date at two different scales: 10-metre and 5-metre spatial resolutions. To optimize the detection of warming and cooling of urban land surfaces, the image data were planned to be acquired around solar noon (noon-1:00 p.m.) and 2-3 hours after sunset. In all, starting from 11:00 a.m. local time, nine daytime flight lines were flown from an altitude of 5,000 metres to image at 10-metre resolution, and six daytime flight lines were flown from an altitude of 2,500 metres to image at 5-metre resolution. All these flight lines were repeated at night beginning at 8:30 p.m. Central Time. Color infrared aerial photography was also acquired simultaneously using a Zeiss aerial camera (with 152 mm focal length) during the daytime flights only. Ground data collection, including measurement of surface temperatures at selected sites throughout the city and the concurrent launches of radiosonde were also carried out at the time of overflight. In addition, meteorological station data were obtained from the Army at Redstone Arsenal and at Marshall Space Flight Center during overflights. Portable Ground Atmospheric Measurement System (PGAMS) was also used to collect data for atmospheric correction. Altogether over 10 gb of digital image data were obtained by the flight mission. Despite some bad data in channels 7, 8 and 9 (the mid-infrared channels) and some smears in channel 3, the overall quality of these digital data, particularly the thermal infrared data of channels 10 to 15, was judged to be very good. The CIR photography is excellent in quality, and, because of its superior spatial resolution, provides "ground truth" information against which the digital image data can be checked.

For this particular research, the focus has been on the six thermal infrared bands (Channels 10 to 15, in the spectral range from 8.20 μm to 12.2 μm) These data have recorded long wave radiation emitted by both

the natural and artificial surfaces in the city of Huntsville. The original image data recorded the radiation as digital number (DN) in 8-bit format with integer values ranging from 0 to 255. Before these image data can be used, they have to be (1) corrected for the attenuation effect of transmitting through the atmosphere (i.e., atmospheric corrections), and (2) calibrated to produce accurate temperature measurements. Atmospheric correction is achieved by applying the MODTRAN program developed by the United States Air Force Geophysics Laboratory, which estimates atmospheric transmittance and radiance for a given atmospheric path at moderate spectral resolution over an operational wavelength region of from 0.25 to 28.5 μm (Berk et al. 1989). The input data to the program for the atmospheric correction are the radiosonde data of atmospheric profiles during the ATLAS overflights. Temperature calibration of the ATLAS sensor for each channel is achieved by using onboard low and high temperature blackbodies which are referenced at the beginning and end of each scan line. With a knowledge of the emittance value for the blackbodies, Planck's equation can be used to calculate the ATLAS reference blackbody radiance for each channel of the sensor system. By combining the outputs of the MODTRAN atmospheric correction program with the high and low blackbodies temperature calibration of the ATLAS sensor system, the Earth Resources Laboratory Applications Software (ELAS) module TRADE converted the 8-bit DN of each pixel of the image data into 32-bit radiance in units of $\text{W cm}^{-2} \text{sr}^{-1} \mu\text{m}^{-1}$ (Graham et al., 1986, Luvall et al. 1990, Anderson, 1992). In this paper, to provide a better appreciation of the thermal characteristics of the land cover type, radiance is converted into irradiance, or radiant flux density incident on a surface in W m^{-2} (Monteith, 1973).

This research will make use of the high-resolution 5-metre ATLAS data only because the complexity of human activities in the urban environment requires the highest possible spatial resolution for an accurate characterization of the urban land cover's thermal responses. In view of the need to produce a false color composite image and to compute the normalized difference vegetation index (NDVI), four channels of data (# 2, 3, 6 and 13) were extracted from the five flight lines acquired in the daytime (Table 1), and one channel (#13) from the corresponding five flight lines acquired at night.

Channel 13 (9.60-10.2 μm) is the thermal band of choice mainly because after the atmospheric correction and temperature calibration procedures, Channel 13 data exhibit the best noise-equivalent temperature change (NEDT) of 0.25 $^{\circ}\text{C}$ (i.e., the temperature change across the target that would produce a signal-to-noise ratio of unity in the detector output). According to Wien's Law, the surface temperatures recordable within the waveband limits of Channel 13 are from 284 to 301 K. In other words, the waveband limits of Channel 13 display the maximum energy per unit wavelength of terrestrial radiation. Image data from the other three channels: Channel 2 (0.52-0.60 μm), the green band, Channel 3 (0.60-0.63 μm) the red band, and Channel 6 (0.76-0.90 μm), the reflected infrared band, when displayed through the appropriate blue, green, and red guns of a TV monitor as overlays, will produce a false color composite image (simulating the color infrared) which emphasizes vegetation vigor. When combined with the thermal infrared red band (channel 13) data, the false color composite image will pinpoint hot and cool objects distinctly. As for the night time imagery, images can be recorded clearly only in the six thermal bands. Channel 13 is the band of choice for the night image for comparison with its counterpart in day time. By extracting a smaller number of channels from the original 15-channel image data, the storage capacity requirement has been greatly reduced. However, each 4-channel flight line is about 125 mb data, and the single channel flight line is 25 mb. In short, the volume of image data to be dealt with in this research is large, and only a computer workstation such as Silicon Graphics equipped with optical drives and a large hard-drive capacity can process these digital image data efficiently.

Methodology

In order to make the best use of the high-resolution thermal infrared data, the characteristics of the thermal signatures of each land cover type in the city of Huntsville will be studied. With the aid of the ELAS image processing software running on the Silicon Graphics workstation, the daytime and night-time images of the city are displayed simultaneously. A key of land cover type is developed. From the displayed

images, polygons of homogeneous land cover types are manually delineated from both the daytime and night-time images. These polygons will be analyzed later for their mean radiance values and standard deviations.

Because urban heat island is related to the reduction of evapotranspiration from surface vegetation cover, it is useful to know the relationship between surface vegetation cover and water availability. Recent research has shown that normalized difference vegetation index (NDVI) is a good indicator of surface radiant temperature (Niemani and Running 1989, Gillies and Carlson, 1995). NDVI for the city of Huntsville is therefore computed from the daytime image data using the following formula:

$$NDVI = (ch6 - ch3)/(ch6 + ch3)$$

where ch3 is the red band and ch6 is the reflected infrared band of the image data. The NDVI are computed for each of the land cover polygons extracted from the daytime images.

Results of Analysis

(1) Day and Night Contrasts in Irradiance

A total of 351 pairs of polygons covering the city of Huntsville were extracted from six flight lines for 10 broad classes of land cover. The five major land cover types are: residential, agricultural, vegetation, services, and commercial. The fact that agricultural and vegetation feature so prominently indicates their intermingling with services and residential uses in the city. In comparing the day-time irradiance of these 10 broad classes of land cover, commercial, industrial and service uses of the land exhibit the highest irradiance (68-70 W m⁻²) while water, vegetation, and agriculture (in that order) show the lowest (55-58 W m⁻²). Residential uses occupy an intermediate position in irradiance (from 60-70 W m⁻²) because they are composed of buildings and tree cover in varying degrees of mixture. At night, commercial, services, and industrial land cover types cool down rapidly to very similar irradiance (45-46 W m⁻²). On the other hand, water, vegetation, and agricultural land cover types show relatively high irradiance at night (43-52 W m⁻²). Water stands out alone as the warmest land cover while agriculture is the coolest at night. All the 10 categories of land cover are cooler at night than during the day. Residential uses, which are again intermediate in position in irradiance at night (44-46 W m⁻²) show much less variation than that during the day.

(2) Relationships between NDVI and Irradiance of Land Cover Types

The value of NDVI varies from -1 to 1 indicating the amount of vegetation (biomass) that is found in the polygon. In this research, the relationship between surface temperature of the land cover type (as represented by irradiance) and the amount of vegetation (as represented by NDVI) is investigated. Very strong negative correlation exists between NDVI and the daytime irradiance of all broad land cover classes with the exception of transportation, commercial, and industrial uses of the land. NDVI is positively correlated with the irradiance of water during the day, but negatively at night. The highest negative correlation during the day is with the irradiance of transitional or vacant (-0.94), residential (-0.86), agricultural (-0.84), and vegetation (-0.74) land. At night, NDVI is only strongly and negatively correlated with the irradiance of recreation land (-0.91). The implication is that higher vegetation amount in agricultural, residential, and vacant land can bring down the surface temperatures in that land cover type. In other words, residential, agricultural, vegetation, and some vacant/transitional land uses in the city of Huntsville are conducive to lower daytime surface temperatures.

The very strong relationship between NDVI and residential and agricultural uses prompts the author to perform a linear regression analysis. For the relationship between NDVI and residential uses, the adjusted R square value is 0.73 based on 68 polygons. The linear model developed takes the following form:

$$Y_{ire} = 66.87420123 - 22.30358429 * (X_{ndvi})$$

where Y_{ire} and X_{ndvi} are irradiance and NDVI for residential land cover respectively. Similarly, for agricultural uses, the adjusted R square value is 0.70 based on 64 polygons. The linear regression equation is:

$$Y_{iag} = 62.87217884 - 13.91271856 * (X_{ndvi})$$

where Y_{iag} and X_{ndvi} are irradiance and NDVI for agricultural land cover type respectively. By using these equations, the irradiance of residential and agricultural uses can be predicted based on NDVI.

Conclusions

High-resolution thermal infrared image data acquired from the ATLAS sensor system after correction for atmospheric transmittance and path radiance followed by blackbodies temperature calibration produce radiance (or surface temperature) values in 32-bit accuracy for the study of the urban heat island effect. Thermal signatures of different land cover types in the city for day and night help to shed light on their roles in contributing to the urban heat island phenomenon. A study of the relationship between NDVI and the irradiance of each category of land cover reveals the importance of vacant, residential, agricultural, and vegetation land cover types in contributing towards lowering their surface temperatures by virtue of their association with biomass. Because of the intermingling of agricultural and vegetation land cover with commercial and services land cover inside the city, enhanced further by the topographic effect in the east, favorable conditions exist in Huntsville for the development of pockets of day-night temperature differences either between the city center and its rural periphery or between contrasting land cover types inside the city.

References

- Anderson, J.E. (1992), Determination of water surface temperature based on the use of thermal infrared multispectral scanner data, Geocarto International 3:3-8.
- Berk, A.L., Bernstein, L.S., and Robertson, D.C. (1989), MODTRAN: A Moderate Resolution Model for LOWTRAN 7, Geophysics Laboratory, Air Force Systems Command, United States Air Force, Hanscom Air Force Base, MA 01731-5000.
- Brest, C.L. (1987), Seasonal albedo of an urban/rural landscape from satellite observations, Journal of Climate and Applied Meteorology 26:1169-1187.
- Carlson, T.N. (1986), Regional-scale estimates of surface moisture availability and thermal inertia using remote thermal measurements, Remote Sensing Review 1:197-247.
- Cayan, D.R. and Douglas, A.V. (1984), Urban influences on surface temperatures in the Southwestern United States during recent decades, Journal of Climate and Applied Meteorology 23:1520-1530.
- Changnon, S.A. (1992), Inadvertent weather modification in urban areas: lessons for global climate change, Bulletin of the American Meteorological Society 73:621-627.
- Gallo, K.P., McNab, A.L., Karl, T.R., Brown, J.F., Hood, J.J., Hood, J.J., and Tarpley, J.D. (1993), The use of a vegetation index for assessment of the urban heat island effect, International Journal of Remote Sensing 14:2223-2230.
- Gillies, R.R. and Carlson, T.N. (1995), Thermal remote sensing of surface soil water content with partial vegetation cover for incorporation into climate models, Journal of Applied Meteorology 34:745-756.

- Goward, S.N. (1981), Thermal behavior of urban landscapes and the urban heat island, Physical Geography 2:19-33.
- Graham, M.H., Junkin, B.G., Kalcic, M.T., Pearson, R.W., and Seyfarth, B.R. (1986), ELAS-Earth Resources Laboratory Applications Software. Revised Jan 1986. NASA/NSTL/ERL Report No. 183.
- Karl, T.R., Diaz, H.F., and Kukla, G. (1988), Urbanization: its detection and effect in the United States climate record, Journal of Climate 1:1099-1123.
- Matson, M., McClain, E.P., McGinnis, D.F., and Pritchard, J.A. (1978), Satellite detection of urban heat islands, Monthly Weather Review 106:1725-1734.
- Kim, H.H. (1992), Urban heat island, International Journal of Remote Sensing 13:2319-2336.
- Lee, H.Y. (1993), An application of NOAA AVHRR thermal data to the study of urban heat islands, Atmospheric Environment 27B:1-13.
- Luvall, J.C. (1990), Estimation of tropical forest canopy temperatures, thermal response numbers, and evapotranspiration using an aircraft-based thermal sensor, Photogrammetric Engineering and Remote Sensing 56:1393-1401.
- Monteith, J.L. (1973), Principles of Environmental Physics, American Elsevier Publishing Company, Inc., New York, pp.14-22.
- Nemani, R.R. and Running, S.W. (1989), Estimation of regional surface resistance to evapotranspiration from NDVI and thermal-IR AVHRR data, Journal of Applied Meteorology 28:276-284.
- Nichol, J.E. (1994), A GIS-based approach to microclimate monitoring in Singapore's high-rise housing estates, Photogrammetric Engineering and Remote Sensing 60:1225-1232.
- Roth, M., Oke, T.R., and Emery, W.J. (1989), Satellite-derived urban heat islands from three coastal cities and the utilization of such data in urban climatology, International Journal of Remote Sensing 10:1699-1720.

TABLE 1: ATLAS SYSTEM SPECIFICATIONS

Channel No.	Band Width Limits (um)	NER mW/cm ² um	NEDT °C	MTF @ 2 mrad	Cooling
1	0.45-0.52	<0.008	N/A	0.5	Ambient
2	0.52-0.60	<0.004	N/A	0.5	Ambient
3	0.60-0.63	<0.006	N/A	0.5	Ambient
4	0.63-0.69	<0.004	N/A	0.5	Ambient
5	0.69-0.76	<0.004	N/A	0.5	Ambient
6	0.76-0.90	<0.005	N/A	0.5	Ambient
7	1.55-1.75	<0.05	N/A	0.5	77 °K
8	2.08-2.35	<0.05	N/A	0.5	77 °K
9	3.35-4.20	N/A	<0.3	0.5	77 °K
10	8.20-8.60	N/A	<0.2	0.5	77 °K
11	8.60-9.00	N/A	<0.2	0.5	77 °K
12	9.00-9.40	N/A	<0.2	0.5	77 °K
13	9.60-10.2	N/A	<0.2	0.5	77 °K
14	10.2-11.2	N/A	<0.2	0.5	77 °K
15	11.2-12.2	N/A	<0.3	0.5	77 °K

1995

NASA/ASEE SUMMER FACULTY FELLOWSHIP PROGRAM

**MARSHALL SPACE FLIGHT CENTER
THE UNIVERSITY OF ALABAMA IN HUNTSVILLE**

THE SEARCH FOR MATERIALS TO MITIGATE SPACECRAFT CHARGING

Prepared By: Nancy S. Losure, Ph.D.

Academic Rank: Assistant Professor

Institution and Department: Mississippi State University
Department of Chemical Engineering

NASA/MSFC:

Lab: Systems Analysis and Integration Lab
Division: Systems Definition Division
Branch: Electromagnetics Environments Branch

MSFC Colleagues: Matt B. McCollum
Steve D. Pearson

Introduction

As spacecraft orbit the earth, they encounter a variety of particles and radiation. Charged particles are common enough that a spacecraft can collect substantial charges on its surfaces. If these charges are not bled off, they can accumulate until electrostatic discharges occur between a charged surface and some lower-potential location on the craft. Electrostatic discharge (ESD) is the suspected culprit in a number of spacecraft failures, according to *Spacecraft Environment Interactions: Protecting Against the Effects of Spacecraft Charging*, (NASA Reference Publication 1354). Silverized Teflon film has become the standard heat-reflecting outer layer of spacecraft because of its flexibility, chemical inertness, and low volatiles content. However, as spacecraft are designed to operate in orbits with greater probability of accumulating enough ions and electrons to create ESD, the Teflon-based thermal control blankets are becoming a liability. Unless stringent (and sometimes burdensome) shielding measures are taken, ESD can upset delicate electronic systems by upsetting or destroying components, interfering with radio signals, garbling internal instructions, and so on. As orbits become higher and more eccentric, as electronics become more sensitive, and as fault-free operation becomes more crucial, it is becoming necessary to find a replacement for silver/Teflon that has comparable strength, flexibility and chemical inertness, as well as a much lower potential for ESD. This is a report of the steps taken toward the goal of selecting a replacement for silver/Teflon during the Summer of 1995. It is a condensation of a much larger report available on request from the author. Three tasks were undertaken. Task 1 was to specify desirable properties for thermal control blankets. The second task was to collect data on materials properties from the literature and organize into a format useful for identifying candidate materials. The third task was to identify candidate materials and begin testing.

Task 1:

The main purpose of thermal control blankets (TCB) on spacecraft is to shield the structure and components from solar energy, to mitigate thermal cycling. For this purpose, thermal control blankets should have a ratio of absorptivity to emissivity less than one. In other words, the material should absorb less heat from the sun (absorptivity) than it can radiate to space (emissivity) so that the spacecraft will not tend to heat up. As a practical matter, the lower the ratio (α/ϵ) the better, because a tendency to cool off due to a high emissivity is easy to correct with solar-powered heaters, whereas a tendency to heat up is much more difficult to correct. As a rule, highly reflective surfaces are good choices, whether mirror-bright or white. The TCB must also withstand the rigors of the space environment for the duration of the life of the spacecraft. Depending on the specific orbit of the spacecraft, the long-term effects of ultra-violet radiation (UV), gamma radiation, vacuum, thermal cycling, atomic oxygen, other charged particles, should be considered. Finally, the TCB should be chosen so as to minimize the effects of electrostatic discharge on the spacecraft as a whole. For non-polar orbits in low Earth orbit, spacecraft charging has been shown not to be a problem. However, for polar orbits, geo-stationary or geo-synchronous orbits, and for high-altitude ellipses, the potential for ESD does exist, and must be planned for. It should be emphasized here that the danger to the spacecraft does not come from the charging per se. The danger to the spacecraft is due to the ESD, which in turn is made possible by the *differential* charging of surfaces on the spacecraft. If all points on

a spacecraft could be effectively grounded, then the floating ground potential could increase to very large levels, without ESD, and so without ESD-induced electromagnetic interference (EMI). The best way to avoid ESD in a charging environment appears to be to increase the conductivity of the TCB to a level which will allow charges to be bled off to ground as voltage levels well below the ESD threshold.

Table 1 summarizes some material property requirements for the "ideal" thermal control blanket material, compared with two of the most popular materials. The ideal TCB material will be conductive, tough, lightweight, stable to UV, radiation and oxidation, will not flake, outgas or volatilize, and will allow designers to specify the alpha/epsilon ratio to suit the needs of any given mission. The first step toward finding such a material is to gather data on existing materials, and looking for significant correlations.

Table 1: Summary of desirable material properties.

Property	Teflon + silver	Kapton+Z93 white paint	Ideal Material
ESD potential	very great	tolerable	very slight
Resistivity ohm-cm	10^{16}	Kapton = 10^{14} Z93 < 10^2	< 10^8
alpha/epsilon	0.08/0.80 = 0.10	0.19/0.90 = 0.21	0.0/1.0, no change over lifetime
UV stability	stable	N/A	stable
Radiation Stability	not recommended	preferred	preferred
Atomic oxygen stability	not recommended	N/A	preferred
Contamination potential	slight	very great (paint chips)	slight to none

Task 2

The database, MATDAT was compiled to give NASA engineers a compact reference for the material properties that affect choices for spacecraft applications. Special emphasis was given to polymeric materials and thermal control coatings. Other materials were chosen for inclusion because they were already used in spacecraft, or because they were under consideration for spacecraft. In all, 43 properties for 118 materials were collected. The database contains 1056 entries, which gives an overall completion of approximately 21% so the database is far from complete. The literature is fragmentary when it comes to the properties of polymers of greatest interest to spacecraft designers, namely absorptivity and emissivity of light energy, ability to withstand vacuum, radiation and atomic oxygen bombardment, and electrical properties such as resistivity and dielectric constant. Properties which depend on surface treatment, such as emissivity, are particularly hard to find in the literature. Data on atomic oxygen and radiation tolerance are largely lacking. Filling in all the empty spaces in the database is probably neither possible nor desirable. Further effort should concentrate on those values of most importance to

the task at hand, which is designing space worthy craft. Each entry contains a material name, a property name, a property type, units and numerical value, then a reference. At the far right of the table are columns containing values in consistent SI units, to make graphing and comparisons easier. Extensive analysis of the data has already been done, and the results are discussed in the full report, available from the author or the author's colleagues, on request.

Note: Some properties are given more than once, from different sources. This serves to show the range of values reported in the literature. This should also be a warning that these numbers should be used with caution. They are good enough to be used for screening purposes, or to debate trade-offs, but any particular material should be tested *in the form in which it is going to be used*, before precise calculations can be made or relied upon.

Task 3

During the analysis of the data being collected in MATDAT, it was noticed that values given for the resistivity for polyethylene were lower than any other polymer, except 'conductive' and 'anti-stat' grades. Therefore, samples of UV stabilized film grade low density polyethylene (LDPE) film were obtained from Eastman Chemical Co. in Longview, Texas. The samples were tested for absorptivity and emissivity at the MSFC materials testing lab, and results are contained in Table 2, below. The film samples were 3 mil thick. The absorptivity of the film was measured without a mirrored back surface. The high density polyethylene sample was included for comparison. The small value of the standard deviation on all four sets shows that the tests have good repeatability. It also appears that there is little reason, based on absorptivity or emissivity to choose one of these grades over another. The absorptivity of the HDPE is only slightly better than the two grades of LDPE, and its emissivity is essentially the same.

Compared to silverized Teflon, these polyethylene samples have about double the absorptivity, and about one third of the emissivity. This does not indicate that these samples are immediate replacements for silver/Teflon, but it is worth pointing out that these PE samples were run-of-the-mill film with no special effort made to obtain clarity, and no silver backing applied. Given that the clarity of PE film is highly dependent on the rate of cooling during the film drawing process, clearer film is probably attainable. Therefore there appears to be room for improvement in the absorptivity of these PE films. As it is, the absorptivity of the PE films is about equal to the absorptivity of white thermal control paints, like Z93, at the beginning of their lives.

The values for the emissivity are another story. The emissivity of the gold/PE is only 36% of that of 5 mil thick silver/Teflon, and only 45% of that of 2 mil thick silver/Teflon. Since emissivity is so strongly dependent on surface properties, it would be worth investigating PE films of varying surface roughness. Unless the emissivity of PE films can be brought up to at least 0.7, their advantageous electrical properties will not offset their thermal disadvantage in comparison with silver/Teflon.

Table 2: Thermal properties of polyethylene samples.

Material	absorptivity	emissivity	alpha/epsilon
MgF ₂ Mirror	0.088	N/A	
High density PE	0.156	0.293	0.53
PE1-3 A	0.169	0.294	0.59
PE1-3 B	0.173	0.295	
PE1-3 C	0.174	0.293	
PE1-3 AVG.	0.172 ± 0.0026	0.294 ± 0.0010	
PE2-3 A	0.176	0.294	0.60
PE2-3 B	0.176	0.294	
PE2-3 C	0.177	0.296	
PE2-3 AVG.	0.176 ± 0.0006	0.295 ± 0.0012	
Silver/Teflon, 2 mil	0.08	0.66	0.12
Silver/Teflon, 5 mil	0.08	0.82	0.10

Conclusions.

As part of this project, a database of material properties for materials important to spacecraft was established. In all 43 properties of 118 materials were surveyed. As of the date of this report, the database is approximately 21% filled. It will not be advisable to attempt to complete the 43 by 118 matrix of property values versus materials. Instead, it is desired to use the data gathered heretofore to decide where to concentrate further data-gathering efforts. The three properties of greatest interest for identifying candidates to replace Teflon as a thermal control blanket material are the electrical resistivity, the solar absorptivity, and the emissivity. As discussed above, several other properties, including the dielectric constant and the dielectric strength seem to be of little importance to the choice of candidate materials.

Polyethylene samples were obtained from Eastman Chemical Co. in Longview Texas. Polyethylene resin seemed attractive from the literature value of 10^7 to 10^9 ohms-cm for resistivity. The samples have been undergoing testing at the MSFC materials testing lab, and preliminary results indicate that the thermal properties are not as good as those of silver/Teflon, but that further testing seems warranted.

Several gaps in the published literature of material properties were found in the course of this study. For example, electrical resistivity values are lacking for many of the thermal control paints commonly used in space, and for which the thermal properties (absorptivity and emissivity) are well documented. In general, the resistivity of polymeric materials has been published, without any data on the thermal properties.

Conductive grades of several polymers have been coming into commercial production for applications in the computer and electronics industries. These polymers deserve scrutiny as candidate materials, as they have resistivities as low as 10^3 ohms-cm. However, all of these polymers are untried in an orbital environment, and extensive testing will need to be done. In particular, there is no data on atomic oxygen and UV stability of these resins. As some anti-static additives work by absorbing water to the surface of the polymer, it is expected that these additives

should be avoided as candidate materials, because the vacuum of space will deplete the surface-bound water, and diminish the surface conductivity. It may not be common knowledge among polymer manufacturers which additives work in this manner, and so a screening test may have to be devised. This would probably consist of performing the standard test for resistivity in a vacuum environment.

Recommendations.

Electrical resistivity, solar absorptivity and emissivity seem to be the properties most valuable in screening candidate materials for thermal control blanket applications in charging environments. Values of all three properties for any single material were not available in the literature. Therefore, there is a need for the values to be generated experimentally for a variety of candidate materials.

During the course of this study, the author became aware of the commercial availability of polymer resins which have very low resistivities; on the order of 10^3 ohms-cm. These polymers should be investigated as candidates for thermal control blanket applications. Anticipated problems are UV stability, atomic oxygen stability, and retention of low resistivity in a vacuum environment.

Testing on the polyethylene film samples obtained from Eastman Chemical Co. should continue. Of particular interest is their behavior in a simulated space environment. Preliminary results indicate that thermal properties are not as good as silver/Teflon, and methods to improve them should be investigated.

Acknowledgments:

This project was undertaken with funding from the MSFC/UAH Summer Education Programs. I am grateful for their support, both monetary and professional.

Amy Hitchcock of Eastman Chemical Co. very kindly provided polyethylene film samples.

Also, I want to thank all the people who helped make my summer productive and exciting. Not only did people pitch in to bring me up to speed in such a short time, but they were willing to listen to my ideas and to perform tests. I'm sure we all learned a lot. In particular, I want to thank my sponsor Matt McCollum, and the technicians at the materials lab.

1995

NASA/ASEE SUMMER FACULTY FELLOWSHIP

**MARSHALL SPACE FLIGHT CENTER
THE UNIVERSITY OF ALABAMA IN HUNTSVILLE**

PROTEIN CRYSTALLIZATION STUDIES

Prepared By:	James Evans Lyne, M.D., Ph.D.
Academic Rank:	Assistant Professor
Institution and Department:	The University of Tennessee Mechanical and Aerospace Engineering
NASA/MSFC:	
Division:	Microgravity Science and Applications
Branch:	Biophysics and Advanced Materials
MSFC Colleague:	Daniel C. Carter, Ph.D.

1995 NASA/ASEE SUMMER FACULTY FELLOWSHIP PROGRAM

PROTEIN CRYSTALLIZATION STUDIES

JAMES EVANS LYNE

The Structural Biology laboratory at NASA Marshall Spaceflight Center uses x-ray crystallographic techniques to conduct research into the three-dimensional structure of a wide variety of proteins. A major effort in the laboratory involves an ongoing study of human serum albumin (the principal protein in human plasma) and its interaction with various endogenous substances and pharmaceutical agents. Another focus is on antigenic and functional proteins from several pathogenic organisms including the human immunodeficiency virus (HIV) and the widespread parasitic genus, *Schistosoma*. My efforts this summer have been twofold: first, to identify clinically significant drug interactions involving albumin binding displacement and to initiate studies of the three-dimensional structure of albumin complexed with these agents, and secondly, to establish collaborative efforts to extend the lab's work on human pathogens.

ALBUMIN STUDIES

Human serum albumin (HSA) is the most abundant of the plasma proteins with an average concentration in healthy individuals of 5 gm/dl. It is important in maintaining the colloid oncotic pressure and in binding an enormous variety of endogenous and exogenous ligands. Binding to HSA greatly increases the solubility of fatty acids and bilirubin in the plasma. Albumin also binds amino acids, steroids, and several metals and is implicated in the facilitated transfer of many ligands across organ-circulatory interfaces. By complexing with various pharmaceutical agents, albumin can strongly influence their therapeutic effect. In some cases, this may render agents inactive *in vivo* despite high efficacy in the absence of albumin *in vitro*.

Human albumin consists of 585 amino acids, has a molecular weight of 66,500 daltons, and contains 17 disulfide bridges. There is a high degree of homology among albumins from various species including rat, human, and bovine. The three dimensional structure of HSA was first reported by Carter et al in 1989,^{1,2} and structural studies of albumin bound to various pharmaceutical agents including aspirin, warfarin, digitoxin, AZT, and diazepam were reported in 1992.³ Albumin has long been known to have multiple binding sites, and the drugs studied thus far attached at either the IIA or IIIA site.

The displacement of endogenous and exogenous agents from albumin by the concomitant administration of certain drugs can lead to clinically significant effects. For example, in infants, sulfonamides can interfere with the binding of bilirubin to albumin, causing a higher free bilirubin concentration in the plasma and leading to its accumulation in the brain, producing kernicterus with lethargy, vomiting, seizures and, occasionally, death.⁴⁻⁶ Children who survive may suffer from cerebral palsy, mental retardation, or sensorineural hearing loss. Similar interference with bilirubin-albumin binding is known to occur with aspirin and ceftriaxone, a commonly used parenteral antibiotic.^{6,7} The displacement of warfarin from albumin by non-steroidal anti-inflammatory drugs (particularly phenylbutazone), clofibrate, and sulfonamides can potentiate its anticoagulant effect and lead to bleeding complications.⁸⁻¹¹ This is enhanced by alterations in the metabolism of warfarin induced by phenylbutazone and the sulfonamides.^{9,12,13} In other clinically significant interactions, the hypoglycemic effect of tolbutamide is increased by the concomitant administration of both sulfonamides and non-steroidals (particularly phenylbutazone).^{9,14,15} Again, the potentiation of tolbutamide's effect results both from albumin binding displacement interactions and from alterations in tolbutamide's metabolism induced by the other agents.^{9,16} Another well known interaction involves the concomitant administration of phenytoin and valproic acid, two drugs which are frequently used together in the control of seizures. The interaction of these agents involves both alterations in phenytoin metabolism and its displacement from albumin binding sites; the combined effect can lead to phenytoin toxicity if not carefully monitored. Phenytoin can also be displaced by other agents including tolbutamide and phenylbutazone. A recent report suggests the ability of phenytoin to displace warfarin from albumin resulting in acute toxicity and death.¹⁷

Drugs displaced from albumin in clinically important interactions tend to have a small volume of distribution, a low therapeutic index, and undergo restrictive elimination.¹⁰ Compounds which are present in high concentrations and are tightly protein bound such as non-steroidals, valproic acid, and sulfamethoxazole are particularly capable of displacing other agents and must be used with caution when they are given concomitantly.¹⁴

Efforts have begun to determine the three dimensional structure of albumin complexed with various compounds which are involved in clinically significant displacement interactions. Crystals of HSA bound to phenytoin, valproic acid, sulfamethoxazole, and tolbutamide have been grown from polyethylene glycol using the hanging drop and sitting drop techniques as previously described.¹ Ceftriaxone bound albumin will be crystallized in the near future. The crystals are to be used in x-ray diffraction studies to determine the three dimensional molecular structures of the albumin-ligand complexes. X-ray diffraction data collection has already begun on albumin bound to valproic acid, phenytoin, and sulfamethoxazole. Initial difference mapping indicates that valproic acid attaches in the IIIA binding site.

COLLABORATIVE STUDIES

Efforts have been made to establish collaborations which will expand the work of the Structural Biology Laboratory in the study of human pathogens. Schistosomiasis, a parasitic disease endemic in Africa, South America, and Asia, historically has been one of the most significant causes of morbidity and mortality in the world. The parasite, which is absorbed through the skin from contaminated water, is a blood fluke which, in its various forms, may cause liver and spleen enlargement, hepatic fibrosis, portal hypertension, diarrhea, and cystitis, as well as pulmonary and CNS symptoms. Although a highly efficacious curative agent is now available (praziquantal), disease control has proven very difficult because of high reinfection rates. Therefore, worldwide efforts have focused on the development of a vaccine, but none is yet available. Previous studies by the Structural Biology Lab resulted in the determination of the three-dimensional structure of the 26 kDa glutathione S-transferase from *Schistosoma japonicum*.¹⁸ Glutathione transferase has been identified by other investigators as a possible vaccine candidate for both *S japonicum* and *S*

mansoni.¹⁹ However, schistosomes possess two glutathione transferases, and a successful vaccine would probably require an immune response to both. Therefore, it is desirable that the 28 kDa GST from *S japonicum* and both GSTs from *S mansoni* be studied crystallographically. The laboratory of Dr. Kathy Davern at the Walter and Eliza Hall Institute for Medical Research in Melbourne, Australia has a long history of successful studies of schistosomal GSTs. Dr. Davern has agreed to produce these proteins by recombinant techniques and supply them to NASA as part of a collaborative agreement reached this summer. Work has already begun on the protein production, and the GSTs are expected to be available for crystallization and structural studies within approximately six weeks.

REFERENCES

- 1) Carter, D. C., Ho, X.M., Munson, S.H., Twigg, P.D., Gernert, K.M., Broom, M.B. and Miller, T.Y., *Science*, 244, 1195-1198 (1989).
- 2) Carter, D.C. and He, X.M., *Science*, 249, 302-303 (1989).
- 3) He, X.M. and Carter, D.C., *Nature*, 358, 209-215 (1992).
- 4) Silverman, W., Anderson, D., Blanc, W., et al, *Pediatrics*, 18, 614-624, (1956).
- 5) Mandell, G.L. and Sande, M.A., Chap. 49 in *Goodman and Gilman's The Pharmacologic Basis of Therapeutics*, sixth edition (eds. Gilman, A.G., Goodman, L.S., and Gilman, A.), 1106-1125 (Macmillan, New York, 1980).
- 6) Disturbances in Infants and Newborns, Chap. 189 in *The Merck Manual*, sixteenth edition (ed. Berkow, R.), 1972-2050 (Merck Research Laboratories, Rahway, N.J., 1992).
- 7) Fink, S., *Pediatrics*, 80, 873-875 (1987).
- 8) McElnay, J.C. and D'Arcy, P.F., *Drugs*, 25, 495-513, (1983).
- 9) Sellers, E.M., *Pharmacology*, 18, 225-227, (1979).
- 10) Rolan, P.E., *Br. J. Clin. Pharmac.*, 37, 125-128, (1994).

- 11) American Medical Association, *Drug Evaluations Annual 1994*.
- 12) Lewis, R.J., Trager, W.F., Chan, K.K., Breckenridge, A., Orme, M., Schary, W., *J. Clin. Invest.*, 53, 1607-1617 (1974).
- 13) O'Reilly, R.A., *New Engl J. Med.*, 302, 33-35 (1980).
- 14) Lindup, W.E., in *Progress in Drug Metabolism*, Vol. 10 (eds. Bridges, J.W., Chasseaud, L.F., and Gibson, G.G.), 141-185, (Taylor and Francis, London, 1987).
- 15) Koch-Weser, J. and Sellers, E.M., *New Engl. J. Med.*, 294, 311-316, 526-531 (1976).
- 16) Christensen, L.K., Hansen, J.M., and Kristensen, M., *Lancet ii*, 1298-1301 (1963).
- 17) Panegyres, P.K. and Rischbieth, R.H., *Postgraduate Med. J.*, 67, 98 (1991).
- 18) Lim, K., Ho, X., Keeling, K., Gilliland, G.L., Ji, X., Rucker, F., and Carter, D.C., *Protein Science*, 3, 2233-2244 (1994).
- 19) Grzych, J.M., Grezel, D., Xu, C.B., Neyrinck, J.L., Capron, M., Ouma, J.H., Butterworth, A.E., and Capron, A., *The Journal of Immunology*, 150, 527-535 (1993).

1995

**NASA / ASEE SUMMER FACULTY FELLOWSHIP PROGRAM
MARSHALL SPACE FLIGHT CENTER
THE UNIVERSITY OF ALABAMA IN HUNTSVILLE**

**Development of a Material Property Database on Selected
Ceramic Matrix Composite Materials**

Prepared by:	Kamala Mahanta, Ph. D.
Academic Rank:	Assistant Professor
Institution and Department:	State University of New York College at Oneonta Department of Physics / Astronomy

NASA / MSFC:

MSFC Colleague:	R. G. Clinton, Ph. D.
Rank:	Branch Chief
Branch:	Ceramics and Coatings
Division:	Non Metallics
Office:	Materials and Processes Laboratory

Development of a Material Property Database On Selected Ceramic

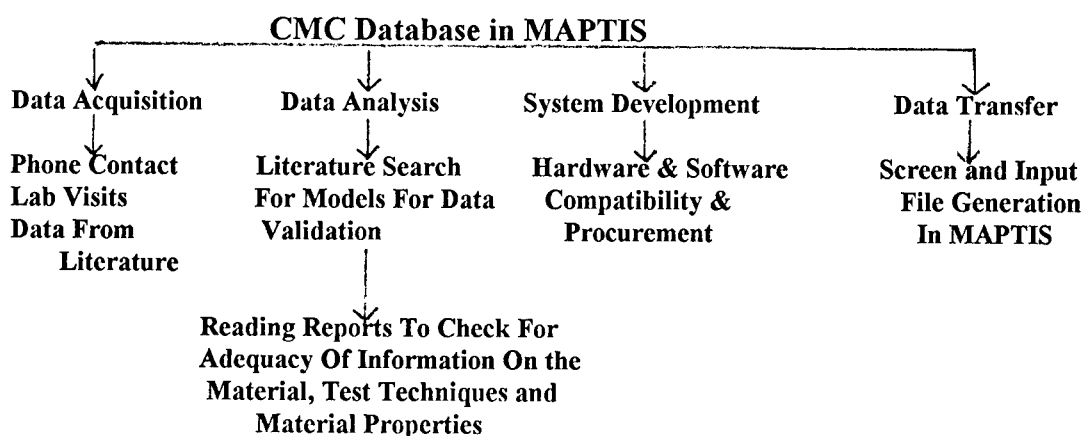
Matrix Composite Materials

Introduction:

Ceramic Matrix Composites, with fiber/whisker/particulate reinforcement, possess the attractive properties of ceramics such as high melting temperature, high strength and stiffness at high temperature, low density, excellent environmental resistance, combined with improved toughness and mechanical reliability. These unique properties have made these composites an enabling technology for thermo-mechanically demanding applications in high temperature, high stress and aggressive environments such as turbine engines, combustors, nozzles, heat exchangers, boilers, fusion reactor first wall and blanket and so on. On a broader scale, CMC's are anticipated to be applicable in aircraft propulsion, space propulsion, power and structures¹ in addition to ground based applications. However, it is also true that for any serious commitment of the material toward any of the intended critical thermo-mechanical applications to materialize, vigorous research has to be conducted for a thorough understanding of the mechanical and thermal behavior of CMC's. The high technology of CMC'S is far from being mature.

In view of this growing need for CMC data, researchers all over the world have found themselves drawn into the characterization of CMC's such as C/SiC, SiC/SiC, SiC/Al₂O₃, SiC/Glass, SiC/C, SiC/Blackglas. A significant amount of data has been generated by the industries, national laboratories and educational institutions in the United States of America. NASA/Marshall Space Flight Center intends to collect the "pedigreed" CMC data and store those in a CMC database within MAPTIS (Materials and Processes Technical Information System).

The task of compilation of the CMC database is a monumental one and requires efforts in various directions. The project started in the form of a summer faculty fellowship in 1994 and has spilled into the months that followed and into the summer faculty fellowship of 1995 and has the prospect of continuing into the future for a healthy growth, which of course depends to a large extent on how fast CMC data are generated. The 10-week long summer fellowship has concentrated, basically, on establishing the procedure for a smooth transfer of data into a CMC database on MAPTIS which is a vital part of the following broader picture of the project.



Data Acquisition:

Several major industries, national laboratories and educational institutions of America have been involved in the generation of CMC data. Some of those are:

NASA Lewis / Rocketdyne / GE / Brockmeyer and Schnittgrund² :
 Ceramic Composites for Earth-to-Orbit Engine Turbines
 DuPont Lanxide / Wright Patterson AFB³ :
 C/SiC Turbine Rotor for an Expendable Missile Engine
 WPAFB / Williams International / DuPont / Dow-Corning-Kaiser / General Atomics⁴ :
 Ceramic Composites such as HPZ/SiC, C/Si₃N₄, SiC/Al₂O₃(with SiC_p) for
 combustor components in the WR24-7 engine.
 Southern Research Institute/WPAFB⁵ :
 Ambient and Elevated Temperature behavior of C/SiC composites

In general, CMC's are being researched vigorously for applications such as Gas Turbine Engines, Hot Aerostructure, Space Based Systems, Thermal Protection Systems, Antenna Windows, Rocket Propulsion

Contacts :

Throughout the fellowship and contract, contact has been established and maintained with the following: DuPont Lanxide, Williams International, Southern Research Institute, McDonnell Douglas, Wright Patterson AFB, Dow-Corning / Kaiser, BF Goodrich, Pratt & Whitney, NASA Lewis, Oakridge Laboratory, Voight Corporation, Boeing, Northrop / Grumman, CINDAS / Purdue, General Electric, Lockheed / Martin, University of Michigan.

This effort has led to the acquisition and promise of a variety of CMC data for storage into the CMC database here at NASA/Marshall Space Flight Center. To mention a few:

1. Ceramic Composite Turbine Component Evaluation : Williams International Report

Contains information on flat panel and combustor component (combustor cover and primary plate) testing of four cmc's, namely, DuPont Lanxide fabricated HPZ/SiC (CVI) and Nicalon/Al₂O₃(SiC_p reinforced) via DIMOX, General Atomics fabricated C/Si₃N₄ via a forced flow thermal gradient CVI method and Dow-Corning/Kaiser fabricated Nicalon/SiNC via Polymer Infiltration and Pyrolysis (PIP). The data presented in the report are comprised of mechanical property tests conducted at the University of Michigan, thermal conductivity tests at Purdue University and thermal expansion tests at Harrop Industries and of as received as well as engine tested data. The report also carries information on the use of Non Destructive Techniques (NDE) such as Thermal Wave Imaging as well as stress analysis data.

2. Turbine Rotor Development Program : DuPont Lanxide Composites, Inc. Report

Presents data on a silicon carbide matrix reinforced with carbon fibers (C/SiC) generated with the objective of developing and demonstrating the technology necessary to produce a CMC turbine rotor for a missile engine. A variety of physical and mechanical data show the effect of optimum fiber structure, reinforcement unit cell size, porosity and fiber volume, oxidation protection. Information on NDE techniques as tools for the evaluation of infiltration of rotor shaped test articles (C/SiC rotor disks), identification of optimum steps between CVI cycles to machine thick CVI parts etc. have been also incorporated. Blade and disk subelements were developed for rig evaluations to address critical areas of concern for structural requirements unique to the blade root and rotor bore regions of a turbine rotor.

As is the case with any good database, it is absolutely essential to look for "pedigreed" data. With this in mind, a specific request sheet has been made available to the data suppliers. The format of the files required by MAPTIS is likely to help refine this request sheet. The question of pedigree also calls for effort in two additional directions:

- a. Evaluate the standards maintained and care taken in the experimental procedures used to generate the data. A thorough study of the reports, asking questions, and, especially, visiting labs has been found to be of considerable help.
- b. Study the current literature and extract information on how CMC's ought to behave and look for the possibility of applying any model to the data. The literature, has at times, led to useful data also.

The Data :

The data have been supplied by the data sources in the form of both graphs and tables. The reports also provide information on the specimen geometry, objectives, experimental procedures etc. which is very helpful in the assessment of the quality of the data. The biggest concern relates to the procedure for a smooth transfer of the data into the database without losing any of the original flavor.

The CMC Database in MAPTIS:

The data will, after proper formatting, be stored into MAPTIS as a CMC database. MAPTIS can read in only ASCII datafiles and cannot store scanned images. Since the incoming data is usually in the form of graphs, tables, information text, a large part of the research has involved figuring out how best to transfer data most effectively.

Information Represented By The Data:

The database will provide information regarding Data Source, Type of the CMC, Coating (both external surfaces and fiber-matrix interfaces), and Test data accompanied by information such as test technique, loading condition, temperature, environment etc. Tests are likely to be as follows:

Physical Properties : Density, Porosity

Mechanical Properties : Tension, Compression, Fracture Toughness, Fatigue, Creep/Stress Rupture, Flexure, Torsion, Impact

Thermal Properties : Specific Heat, Diffusivity, Conductivity, Thermal Expansion, Emissivity

NDE : X-Ray, Ultrasonic, Acoustic, Computed Tomography, Pulsed Thermal Wave Imaging etc. providing information on density distribution, flaw detection, ultrasonic velocity in the material etc.

Ideally, search would be possible within the database with all of these as search criteria. An overview file and a help file containing information on how to search with any of these will be available. The format of the data will be the relevant set of numbers accompanied by the information relevant to the test.

System Development :

Software and Hardware required for data input :

MAPTIS, in its present form, cannot read in graphs or images. So the following actions had to be taken:

The Digitizer :

MAPTIS requires graphs and images to be turned into ASCII files. A time consuming search of the market led to the purchase of the SUMMASKETCH II PROFESSIONAL digitizer and the supporting software called "ROCKWORKS" which contains a digitizing software. This setup converts graphs into x-y files (also x-y-z files if necessary) which is then edited using the DOS EDITOR.

The Scanner:

An additional hardware and software need has arisen in connection with the transfer of the tables supplied by the data sources. It would be impractical to type the tables into a DOS text file manually, A scanner driven by an OCR (Optical Character Reader) software has been anticipated to be the solution. During the 1995 fellowship, information has been collected on this and the purchase will be made outside of the fellowship (under the contract). The HP 3C scanner supported by the CALERA WORDSCAN OCR software has been considered to be a good configuration so far.

Visits For Data Acquisition :

During the fellowship, a trip was taken to Oakridge National Laboratory (ORNL) in Tennessee. The visit comprised of :

1. Individual discussions with the CMC research personnel

2. Tour of the Mechanical and Thermal Properties test facilities and the lab in general.
3. Collection of ORNL reports, published and unpublished data generated using ORNL fabricated CMC's as well as other recent publications of data and concept related interest.

Southern Research Institute at Birmingham, Alabama was visited during the 1994 summer fellowship and the visit was similar in format. Other intended visits are to : DuPont, Williams International, University of Michigan, NASA/Lewis, Wright-Patterson AFB.

Literature : Samples :

The following publications are likely to provide valuable information toward the selection of data for the database.

1. High Temperature Behavior of Ceramic Composites ; edited by S. V. Nair and K. Jakus; Butterworth-Heinemann, 1995.
2. Ceramics and Ceramic Matrix Composites : Flight Vehicle Materials, Structures and Dynamics, Vol. 3, edited by S. R. Levine, A. K. Noor, S. L. Venneri, 1992.

Critical Issues In Testing CMC's⁶:

Specimen Design:

Test specimens may be : Straight sided or Dog bone, cylindrical or flat. DuPont used a blade subelement (a tensile coupon) with a gage section of elliptical shape, to simulate the leading edge of the rotor blade.

Finite Element Methods can be used in the design of specific test specimens to ensure that stresses are applied where needed. However, FEM cannot have, readily incorporated into it, the very localized changes in stresses and strains resulting from changes in fiber architecture.

Gripping Scheme, Load Train Design, Heating Methods, Furnace Materials Requirements For Testing are some other issues.

Measurement Techniques :

Temperature: Thermocouples (limit 1650⁰C) and Optical Pyrometers (non-contacting, no temperature limit ; but do not work well at mildly elevated temperatures) - SRI use both. ASTM standards are available for calibrating temperature measuring equipment.

Strain: Strain Gauges, Laser Dimension Sensors, Clip on extensometers and Quartz Rod (or other high temperature rod) extensometer . The choice depends on specimen geometry, the test geometry and conditions as well as the degree of precision required.

Strain Gauges: adequate for room temperature measurements; but not so for mildly elevated temperature.

Laser Dimension Sensors and Clip on Extensometers : do not have the required precision.

High Temperature Rod Extensometers : are to be focused on. The specimen deformation can be transferred to the contact rods via pin holes, grooves and grooved paint, all three of which work equally satisfactorily under conditions appropriate for them. The choice depends upon the specimen (whether it is coated) and the temperature of the test (the paint can creep).

Commercially available extensometers and their thermal limits are:

Water Cooled Extensometers : upto 500⁰C

Quartz Rod Extensometers : upto 1000⁰C

Capacitance Extensometers : upto 1600⁰C

Bending moment being a major concern, strain should be measured on more than one side of the specimen. This is made necessary by the fact that specimens are heterogeneous and may be bent or warped

as a result of the manufacturing or fabrication process and cannot be corrected by machining or grinding due to other testing constraints.

At Oakridge Lab, they have acquired capacitance extensometers; however, the measurements are made only on one side of the specimen.

Control Variables : Temperature, Heating Rate, Environment, Load and Loading Rate.

Effort will be made to tag the data with this kind of information as far as possible.

Research Data : The literature search has made available data on some of the less studied properties and incorporating those into the database may be beneficial to facilitating interlaboratory comparison for the discerning of the testing reproducibility and limitations, material behavior and its variability for Ceramic Composites.

Example : Research Data on Interface Behavior :

The stress-strain behavior and damage tolerance of Ceramic Composites are significantly influenced by the strength of the fiber-matrix interface. This makes the characterization of the interfaces and their properties (co-efficient of friction, residual clamping stress, residual axial stress and debond stress) in continuous fiber reinforced ceramics an essential part of CMC characterization.

The forces between the fibers and the matrix in a CMC can be modified by introducing interphases (such as Nicalon fibers coated with carbon and SiC using polypropylene and a mixture of methyltrichlorosilane and H_2) that protect the fiber during processing. Fiber pushout tests with variation in coating thickness yields information on changes in fiber bonding and sliding characteristics⁸. The summary of the results of the tests reported in ref⁸ shows the following :

1. The interfacial shear stress for a SiC(Nicalon)/Graphite/SiC CFCC decreases when the thickness of the fiber-matrix interphase layer increases from 0.03e-06m to 1.2e-06m.
2. The co-efficient of friction decreases with increasing coating thickness.

Similarly, the CMC database could contain information on environmental effects on crack growth in CMC's as crack velocity versus applied stress intensity measured in different environments⁹.

REFERENCES

1. Ceramics and Ceramic Matrix Composites : Flight -Vehicle Materials, Structures, and Dynamics - Assessment and Directions , Vol 3 : edited by S. R. Levine, A. K. Noor, S. L. Venneri, ASME, 1992.
2. T. P. Herbell and A. J. Eckel : "Composites in High Speed Turbines for Rocket Engines", NASA/Lewis Report
3. DuPont Report, October, 1994, "C/SiC Turbine Rotor Development Program"
4. Williams International Report, April, 1995, "Ceramic Composite Turbine Engine Component Evaluation"
5. Southern Research Institute Report, August, 1990, "Physical, Mechanical, and Thermal Properties of Two RCI Graphite/Silicon Carbide 2D Composite Materials at Room and Elevated Temperatures".
6. High Temperature Mechanical Behavior of Ceramic Composites : edited by S. V. Nair and K. Jakus, Butterworth-Heinemann, 1995.
7. Understanding ORACLE : J. T. Perry and J. G. Lateer, Sybex, 1989.
8. E. Lara-Curzio, M. K. Ferber, and R. A. Lowden: "The Effect of Fiber Coating Thickness on the Interfacial Properties of a Continuous Fiber Ceramic Matrix Composite", Ceram. Eng. Sci. Proc. , 15, 5 (1994) 989-1000.
9. C. H. Henager, Jr., R. H. Jones : "Environmental Effects on Elevated Temperature Subcritical Crack Growth of SiC/SiC Composites", presented at the meeting on "Critical Issues in the Development of High Temperature Structural Materials", March 7 - March 12, 1993, Kailua-Kona, Hawaii.

1995

NASA/ASEE Summer Faculty Fellowship Program

Marshall Space Flight Center

The University of Alabama in Huntsville

Development of the SEASIS Instrument for SEDSAT

Prepared By: Mark W. Maier, Ph.D.
Academic Rank: Assistant Professor
Institution and Department: University of Alabama in Huntsville
Department of Electrical and Computer Engineering
NASA/MSFC:
Office: Program Development
Division:
Branch:
MSFC Colleague: Charles C. Rupp

Project Goals and Summary

July 1997 is the target date for the combined SEDS tether and SEDSAT mission. In this mission a small satellite (the SEDSAT) will be deployed on a 20 kilometer tether from the Space Shuttle. The tether will deploy in an unreel and braking profile that will be used to "slingshot" the SEDSAT at the end of the tether into a higher orbit with a three year expected lifetime. The SEDSAT will carry out a variety of experiments during and after tether deployment.

1. Measure and record accelerations experienced at the end of the tether.
2. Record panoramic imagery through the SEASIS instrument that will allow reconstruction of the three axis orientation history of the SEDSAT during portions of tether deployment.
3. Record imagery during tether cut and recoil to reveal tether recoil dynamics.

After the tether has been cut at both the shuttle and SEDSAT end the SEDSAT will enter a post tether mission phase. During the post tether mission the objectives are:

1. Downlink all recorded tether data.
2. Measure SEDSAT attitude in real-time and attitude stabilize the satellite with the SEASIS telephoto lens pointing earthward.
3. Record imagery of the Earth and atmosphere across the visible spectrum in response to ground command.
4. Serve as an amateur radio relay satellite.

As the list makes clear, the SEASIS instrument plays a central role in many of the SEDSAT objectives. When this faculty fellowship began in May, 1995, the SEASIS instrument had been worked on for several years under the leadership of its student principal investigator, Ms. Cheryl Bankston. However, since Ms. Bankston graduation a year previously very little progress had been made on the instrument. At that time a considerable body of design work had been completed and much of the hardware had been procured, but very little had been assembled or tested. The optical design was largely complete, but very little fabrication had been done. A considerable portion of the electronic design had been done, but essentially no elements had been fabricated. There were doubts about the electronic design because of the unusual processor (effectively mandated by the projects funding vehicle). Almost software design or development had been done.

During the course of the fellowship we have developed a detailed set of requirements, design, interface, and planning documents. The new graduate fellow SEASIS team members (Mr. Robert Hillman and Ms Amy Houts) have nearly completed development of a prototype unit. A final decision on flying the SEASIS instrument as part of the mission will await demonstration of the prototype (which is not scheduled until the end of August, 1995), but we believe that the instrument can be completed on schedule at acceptable risk.

Mission Objectives for SEASIS

Two SEASIS experiment objectives are key: take images that allow three axis attitude determination and take multi-spectral images of the earth. During the tether mission it is also desirable to capture images for the recoiling tether from the endmass perspective (which has never been observed). SEASIS must store all its imagery taken during the tether mission until the earth downlink can be established. SEASIS determines attitude with a panoramic camera and performs earth observation with a telephoto lens camera. Camera video is digitized, compressed, and stored in solid state memory. These objectives are addressed through the following architectural choices:

1. A camera system using a Panoramic Annular Lens (PAL). This lens has a 360 deg. azimuthal field of view by a ± 45 degree vertical field measured from a plan normal to the lens boresight axis. It has been shown in Mr. Mark Steadham's UAH M.S. thesis that his

camera can determine three axis attitude anytime the earth and one other recognizable celestial object (for example, the sun) is in the field of view. This will be essentially all the time during tether deployment.

2. A second camera system using telephoto lens and filter wheel. The camera is a black and white standard video camera. The filters are chosen to cover the visible spectral bands of remote sensing interest.
3. A processor and mass memory arrangement linked to the cameras. Video signals from the cameras are digitized, compressed in the processor, and stored in a large static RAM bank. The processor is a multi-chip module consisting of a T800 Transputer and three Zoran floating point Digital Signal Processors. This processor module was supplied under ARPA contract by the Space Computer Corporation to demonstrate its use in space.

SEASIS System Design

When the faculty fellowship began many aspects of the SEASIS design were effectively frozen. The basic two camera structure with PAL and telephoto lenses was fixed. Among the most important frozen elements was the selection of the SCC-100 processor. The processor had been selected in conjunction with ARPA support for the program. In retrospect, there could have been happy choices. Replacement of the processor was actively considered, but interface design and lack of funding for an alternative were dominant factors.

The principal goal during the fellowship has been to complete the design requirements and supervise the assigned students to the point that NASA can be given a reasonable assurance of flight readiness for July, 1997. To that end we have produced a complete set of requirements, design, interface, and development plan documents. Those documents are included with this report as appendices. A key element of the development plan is demonstration of an end-to-end prototype by September 1, 1995. At the time of this writing (August 4, 1995) that prototype is still in development.

Hardware Architecture

The SEASIS hardware architecture is shown in figure 1. Figure 1 shows the division of the SEASIS into its principal modules and their physical interfaces. The SEASIS processor board contains an SCC-100 processor module, boot hardware, and some of the digitizer interface hardware. Transputer links from the SCC-100 are used for most of the I/O. Video data is digitized in the Weber digitizer and passes into the SCC-100 through its shared memory interface. Images are stored in the mass memory, which is accessed through the second SCC-100 memory port. A full companion architecture flow diagram is provided in the referenced appendices.

SEASIS Hardware Development

Three major hardware development efforts have been carried out by the student investigators for SEASIS during the fellowship period.

1. Mr. Robert Hillman has designed and fabricated the camera control electronics. The interface implemented by this unit is documented (principally from the software point of view) in the SEASIS interface document included as an appendix. This design uses an Altera erasable programmable logic device (EPLD) reduce the projected four camera control boards to one. A secondary advantage to this design is that it is "self-documenting" in the sense that the Altera schematic capture files are used to directly program the chip leaving no latitude for on board hardware changes that don't get updated on the schematic.

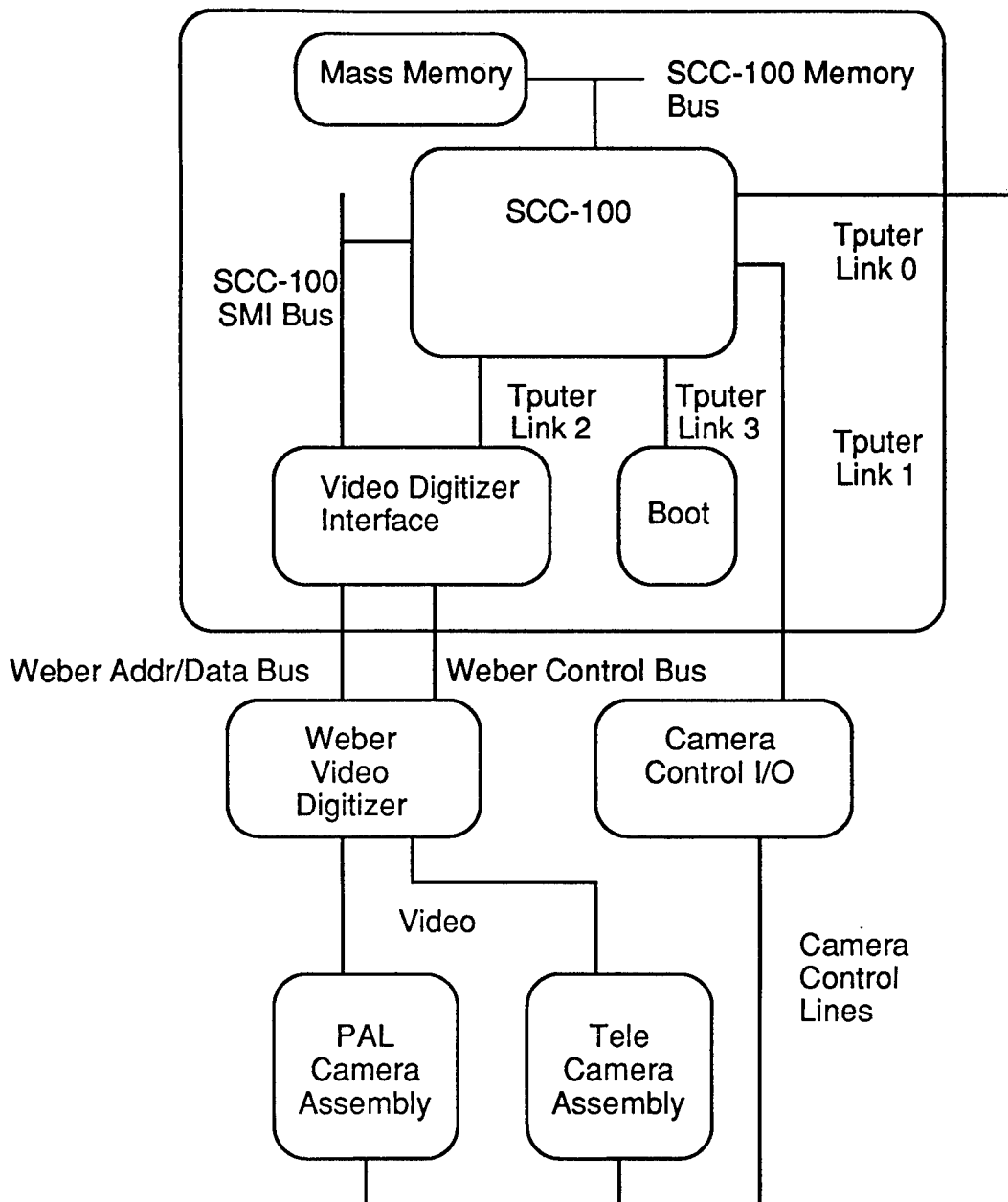


Figure 1: SEASIS architecture interconnect diagram. Processor I/O is predominantly done through Transputer links. Several specialized interfaces are necessary for experiment control and data acquisition.

2. Mr. Hillman has also fabricated a video interface board transfer control codes and digitized video to and from the Weber video digitizer.
3. Ms. Amy Houts has fabricated a breadboard version of the PAL lens camera for use in the prototype and for integrity testing. This unit includes the filters and transfer lenses.

One issue we believe has been effectively resolved is the radiation resistance of the Altera EPLD's. An Altera application note states that resistance above 10krads is achieved when input voltages are maintained below 5 volts. This would be adequate, at least for the tether portion of the mission. The lifetime dose is expected to be 14krads.

Software Architecture and Release Plan

Because of the significant schedule constraints, we have developed a phases software release plan oriented to early delivery of software with minimum mission functionality. The SEASIS can fly as long as it can support the tether mission. If software to support post-tether operations is not available when the satellite is sealed, this is acceptable. Post-tether mission software can be uplinked after the tether mission.

Our baseline software release plan defines 5 release levels. Two are developmental, two are considered flight objectives, and the last is more of a wish list for on-orbit operations. Detailed functional requirements for each release level are given in the SEASIS Systems Requirements Document. Final requirements for each level are defined in the document version of the same number. Requirements for higher numbered versions are assumed preliminary. The currently defined release levels are:

Release 0.2

This will be a prototype oriented release. It will implement a minimum loop of power-up, fixed rate imagery collection, and image transfer to the host. This release is targeted to run on the SCC-100 engineering prototype unit provided by Space Computer Corporation.

Release 0.7

This release will incorporate all functionality required to perform the tether mission and allow software reloading. It will differ from the 1.0 release in that its image analysis and compression algorithms will be of the simplest type and will not be optimized for the SCC architecture. The 0.7 release level could be flown, though it would not collect as much useful data.

Release 1.0

This release is the baseline primary mission flight software. All primary mission designated functions are included and the image algorithm have been modified to run on the SCC 100 architecture efficiently.

Release 2.0

This release is the baseline post-tether mission software package. The major changes are the inclusion of real-time attitude estimation to close the attitude stabilization loop through the CDS and earth imaging software. The earth imaging software uses the telephoto lens and filter system to collect multi-spectral data on the earth and its atmosphere.

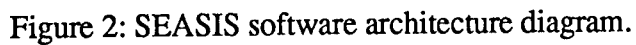
Release 3.0

This release is only loosely defined. Possible features are managing the mass memory as a RAM disk accessible to the CDS and advanced image processing and compression algorithms.

The SEASIS 0.7/1.0 software architecture is shown in figure 2. The system is comprised of two primary tasks. One task communicates with the CDS, receiving commands and sending data for downlink. the other task is the primary functional task and coordinates all imaging control and processing. Both tasks make use of the Transputer specific channel module for I/O and intertask communication.

Conclusions

The SEASIS experiment planned for SEDSAT is a highly challenging development project for a University student team. Its scientific, engineering, and educational payoffs, however, are consistent with the challenge, and the development risks are manageable. The plan developed under this fellowship is, in my judgment, feasible for the available team at reasonable risk. But in the absence of a working prototype (which is not scheduled for another month, it is impossible to give a firm go-ahead decision. I recommend the situation be revisited as scheduled for a final decision.



Appendix A: SEASIS System Requirements Document
Appendix B: SEASIS System Development Plan
Appendix C: SEASIS Software Design Document
Appendix D: SEASIS Interface Document

1995

NASA/ASEE SUMMER FACULTY FELLOWSHIP PROGRAM

**MARSHALL SPACE FLIGHT CENTER
THE UNIVERSITY OF ALABAMA AT HUNTSVILLE**

ISSA/TSS POWER PRELIMINARY DESIGN

Prepared By:	John A. Main, Ph.D.
Academic Rank:	Research Assitant Professor
Institution and Department:	Vanderbilt University Department of Mechanical Engineering
NASA/MSFC:	
Office:	Preliminary Design
Division:	Systems Engineering
Branch:	Systems Analysis
MSFC Colleagues:	Melody Herrmann Les Johnson

Introduction A projected power shortfall during the initial utilization flights of the International Space Station Alpha (ISSA) has prompted an inquiry into the use of the Tethered Satellite System (TSS) to provide station power. The preliminary design of the combined ISSA/TSS system is currently underway in the Preliminary Design Office at the Marshall Space Flight Center. This document focusses on the justification for using a tether system on space station, the physical principles behind such a system, and how it might be operated to best utilize its capabilities.

Concept The basic components of a simple DC generator are a magnet of some type and a conductive wire. Moving the wire through the magnetic field causes forces to be applied to the electric charges in the conductor, and thus current is induced to flow. This simple concept is the idea behind generating power with space-borne tether systems. The function of the magnet is performed by the earth's magnetic field, and orbiting a conductive tether about the earth effectively moves the tether through the field.

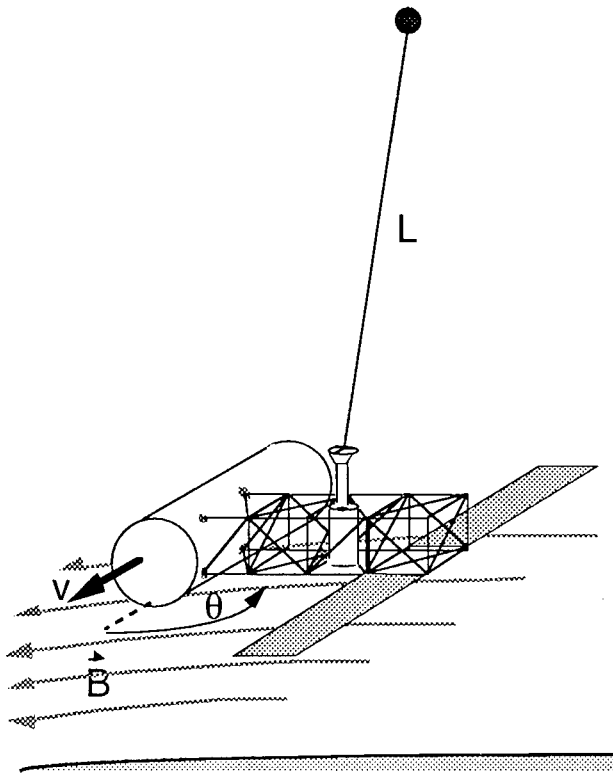


Figure 1. Generation of a potential difference in a tether moving through the earth's magnetic field.

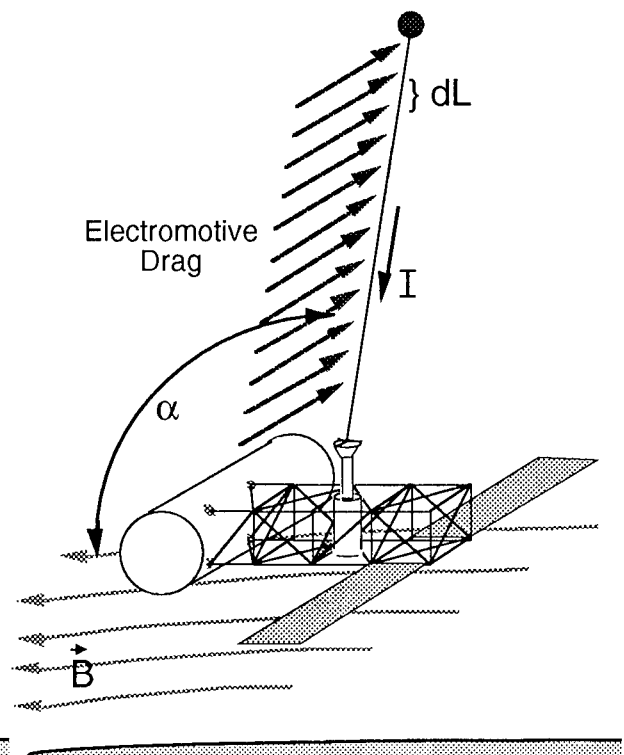


Figure 2. The electromotive drag due to generation of power with a tether.

Dragging a conductor through a magnetic field will create a potential in the conductor according to¹

$$\vec{V} = (\vec{v} \times \vec{B}) \cdot \vec{L} \quad (1)$$

where V is the electric potential generated, v is the velocity of the tether, B the magnetic field vector, and L the tether length vector.

It is fairly reasonable in the case of a near-equatorial, low-earth, circular orbit to assume that B and L are mutually perpendicular. In this case equation (1) simplifies to

$$V = vBL\sin(\theta) \quad (2)$$

where θ is the angle between the B -field and the velocity vector.

Assuming nominal values for orbit altitudes, velocities, and magnetic fields in low earth orbit a potential of approximately 200 V/km can be generated in a conductive tether.² This value can vary widely due to variations in the earth's magnetic field, however, so potentials as high as 250 V/km and as low as 75 V/km should be expected in any given orbit.

The laws of thermodynamics state that you do not get something for nothing, and that is as true here as anywhere. The energy that is being extracted from the tether as electric power must come from somewhere, and it turns out that electric power extracted from an orbiting tether will cause a net drag on the tether, thus slowing the orbital velocity and lowering kinetic energy.

This drag force is directly proportional to the amount of current flowing through the tether according to

$$\vec{F} = I \int d\vec{L} \times \vec{B} \quad (3)$$

where F is the total drag force on the tether and I is the current flow.

In the case of a straight tether equation (3) simplifies to

$$F = ILB\sin(\alpha) \quad (4)$$

where α is the angle between the B -field and the tether vector.

It is interesting to note in equation (3) that the direction of the force is dependent upon the direction of the current. This emphasizes one of the unique capabilities of space-borne tether systems: if power is being generated from the tether, then, logically, the drag force acts to slow the system, but if current is pumped through the tether in the opposite direction, an accelerating force is applied. This means that a conductive tether is not just a generating system. Its true function is as an energy exchange mechanism between electric power and system kinetic energy. An application of this exchange mechanism would be in a system where there was an additional power generation capability, say solar panels. In periods when the solar panels cannot supply the needed power to the orbiting spacecraft the tether could be used in generating mode to fill the gap, thus decelerating the spacecraft. When the solar panels are generating excess power, power that would otherwise be burned up and radiated to space, that power would instead be pumped through the tether and used to accelerate the spacecraft. Use of a tether system in this fashion could reduce overall propellant requirements for reboosting the space station, decrease the amount of heat that must be rejected from a primary power source, and increase the overall efficiency of the primary power source since excess power is stored as kinetic energy, not wasted.

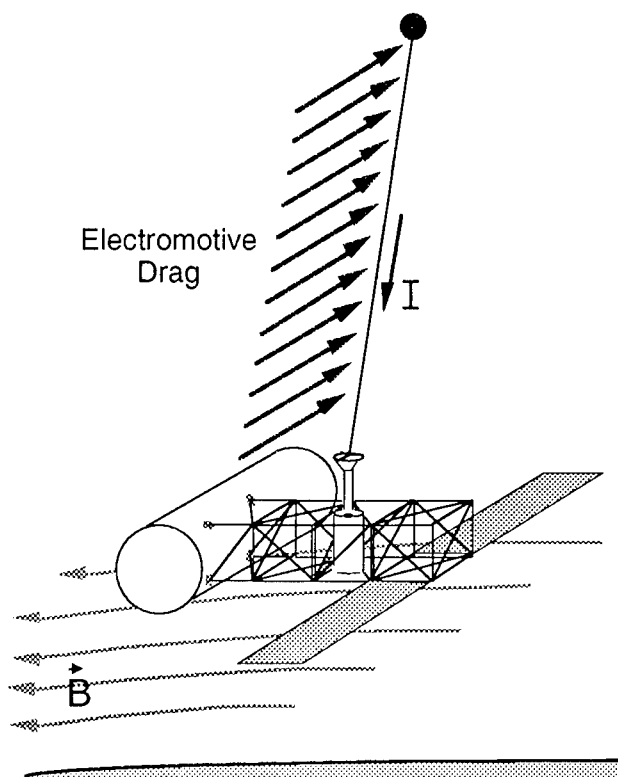


Figure 3. Current flow direction during power generation produces a net drag.

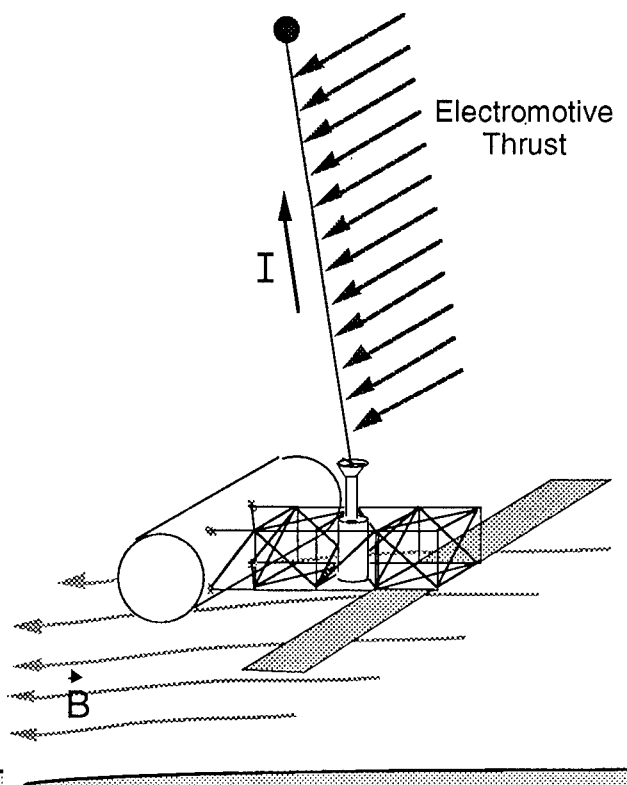


Figure 4. Pumping current in the reverse direction will produce an accelerating force.

Performance Predictions The current design of the ISSA tether power system calls for a 5 km #6 aluminum tether which will have a 250 kg endmass that includes a plasma contactor. A 5 km tether in LEO would be expected to generate a nominal potential difference of approximately 1 kV, with voltages ranging between 380 V and 1.25 kV.

Losses in the system will come from electrical resistance in the tether, plasma contactor losses, and conversion losses. It is unclear at this point what the conversion losses will be, as those will be very method dependent. A 5 km #6 aluminum wire has a resistance of approximately 10Ω , so if 5 amps are flowing the tether losses would amount to 50 V. Budgeting an additional loss of 15 volts to the plasma contactor leaves 935 V nominal left for station use. At 5 amps this amounts to a 4.7 kW power supply!

Of course, this power generation will induce a drag force on the station that will have to be countered with additional reboost if the thrusting capability of the tether is not utilized. Assuming a nominal field strength for earth at LEO of 30×10^{-6} Tesla, the force acting on the tether due to the generation of 4.7 kW of power is

$$F_{Elec} = (5\text{amps})(5\text{km})(30 \times 10^{-6} \text{ Tesla}) = 0.750\text{N} \quad (5)$$

where F_{Elec} is an electromotive drag in this case. An additional drag of 0.04 N will also be present with this tether design due to aerodynamic drag.³ Unlike the electromotive forces, this will always be a decelerating force.

The electromotive drag force (F_{Elec}) at 4.7 kW represents an impulse loss to the station of 2700 N-s/hr, but only while the power system is running. Assuming the reboost propellant is hydrazine ($I_{sp}=300$ s) this will necessitate burning 0.918 kg of extra fuel for every hour the system is in operation. The aerodynamic forces, on the other hand, will be present whenever the tether is reeled out. The aerodynamic force represents an impulse loss of 144 N-s/hr, which results in a fuel requirement of 0.05 kg/hr.

Figures 5 and 6 are included to aid in the calculation of the extra fuel required for a given mission. Figure 5 shows the extra fuel needed as a function of the length of time the tether will be reeled out, and Figure 6 shows the extra fuel necessary as a function of the length of time the power system is running at nominal. Adding these two values will yield the total extra fuel required for a given mission.

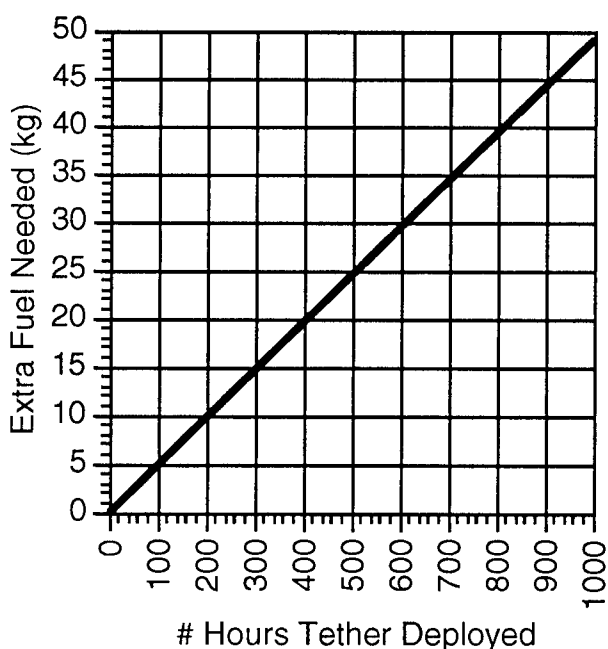


Figure 5. Extra fuel required as a function of tether deployment time.

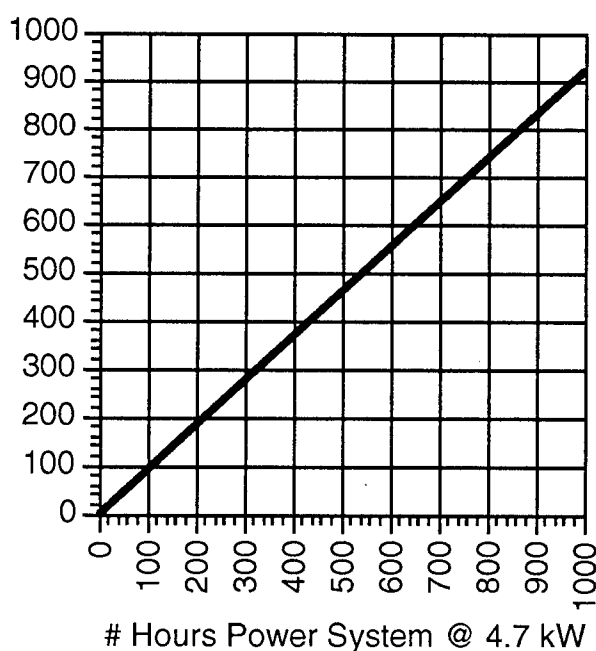


Figure 6. Extra fuel required as a function of the duration of power system operation.

Fuel Cell Trade An important point to address in this study is whether or not there is another available system that can abate the temporary power shortfall in the ISSA faster/better/cheaper than the TSS tether system. One possible alternative for providing this kind of temporary power is a hydrogen-oxygen fuel cell. Table 1 shows a trade study comparing the cost and fuel requirements of the TSS power system as compared to a fuel cell capable of providing the same level of power (4.7 kW nominal).

The cost of the TSS system modified to generate power on the space station is TBD. The deployer hardware is available from the TSS-1 mission, but the electrical interface exists only in concept at this time. The cost of an orbiter fuel cell, basically the only one available, comes in at about \$8 million.⁴

The fuel weight for the required for the TSS power system is calculated from the results of the previous section. Note that it assumes that excess power is not pumped through the tether to

reboost the station. The mass of hydrogen and oxygen required (0.372 kg/kW-hr) to run an equivalent fuel cell is based on a fuel cell efficiency of 75%.⁵ Note that, by weight, the fuel requirement for the tether system is about half that required by an equivalent fuel cell. This ratio will become even more favorable if excess power is pumped through the tether to reboost the station.

Table 1. Tether Power - Fuel Cell Trade.

<u>Tether - Fuel Cell Trade</u>		
Power Source	Equipment Cost	Fuel Requirement Running at 4.7 kW
5 km #6 AL Tether	Cost of Tether & Power Conditioner (TBD)	0.968 kg/hr (hydrazine)
Orbiter Fuel Cell	~\$8 Million	1.748 kg/hr (hydrogen/oxygen)

Additional Benefits Perhaps the greatest benefit of using the TSS tether system to generate power would come after the power generation phase were over. The ISSA would then have an absolutely unique facility for atmospheric research. The possibilities for a downward deployed tether are extremely exciting and include 3-D mapping of the upper atmosphere, two-body dynamics and control experiments, examination of auroral structure, controlling μ -gravity on station for materials experiments, and examining antenna behavior in the magnetoplasma. These applications alone justify the addition of a tether facility to the ISSA, the added benefit here is that the system can be used to abate an already serious station power shortage.

Conclusions This short report represents a very top-level look at the possibility of using a tether on the ISSA to abate the projected power shortfall. No showstoppers were encountered, although the treatment of the design is admittedly very shallow and the amount of extra fuel needed does become large as the power generation time rises. The results of this study indicate that there are strong reasons for including a tether facility like TSS on the ISSA both for power generation and general science. The fact that both of these issues can be addressed with one facility makes the case for pursuing this concept very strong.

Acknowledgments The author gratefully acknowledges the assistance of a number of individuals in Program Development at the Marshall Space Flight Center, some of whom are noted in the reference section. In addition, Chris Rupp of MSFC provided valuable insight and much of the material that this study is based upon.

References

1. Tethers in Space Handbook, Second Edition.
2. Presentation by J. McCoy, Johnson Space Flight Center, at the Marshall Space Flight Center, 6/15/95.
3. Conversation with Jim McCarter, Marshall Space Flight Center.
4. Conversation with Don Williams, Marshall Space Flight Center.
5. Batteries and Energy Systems, C.L. Mantell, Second Edition, McGraw-Hill.

1995

NASA SUMMER FACULTY FELLOWSHIP PROGRAM

**MARSHALL SPACE FLIGHT CENTER
THE UNIVERSITY OF ALABAMA IN HUNTSVILLE**

LINEARIZATION OF AN ANNULAR IMAGE BY USING A DIFFRACTIVE OPTIC

Prepared By:	Donald R. Matthys, Ph. D.
Academic Rank:	Professor
Institution and Department:	Marquette University, Milwaukee, WI Department of Physics
NASA/MSFC:	
Office:	Astrionics
Division:	Optics and Radio Frequency
Branch	Optical Design
MSFC Colleague	Helen J. Cole, Ph. D.

Linearization of an Annular Image by Using a Diffractive Optic

In 1984, Dr. Pal Greguss of Hungary patented a side-viewing panoramic viewing system which consists of a single piece of glass with spherical surfaces which produces a 360 degree view of the region surrounding the lens which extends about 25 degrees in front of the lens and 20 degrees behind it. This belt-shaped region is imaged into an annular shaped virtual image within the lens; by using a standard lens as a transfer lens, this virtual image can be placed onto an optical sensor (film, camera, detector, eye) as a real image. Earlier efforts to obtain panoramic viewing go back at least to 1878 when Mangin obtained a patent for such a system. However, all of the earlier systems were either complex designs with many lenses, or blocks with non-spherical surfaces, or produced images of very poor quality. Thus almost all imaging of interior walls of cavities or panoramic views were obtained by using traditional lenses and simply rotating the system about an axis. Greguss' system is simple, easy to fabricate, and produces images of good quality. Another useful property of the lens is that it is essentially afocal, *i.e.*, images stay in focus for objects located right next to the lens as well as for objects located far away from the lens.

The lens designed by Greguss produced a panoramic view in an annular shaped image, and so the lens was called a PAL (panoramic annular lens). The physical shape of the PAL is shown in Figure 1, which also shows a few rays from a cylindrical wall surrounding the PAL and coaxial with it. Note that the central region of the PAL is not used and that sections of the front and back sides of the lens are coated and used as mirrors. These mirrored surfaces are shown in Figure 1 as thick heavy lines. Note also the location of the virtual image within the lens and the use of a transfer lens to produce a real image.

Figure 2 shows a different view of the PAL inside a cylindrical cavity and indicates how the final image is shaped like an annulus. The images produced by this system are of necessity distorted, since a curved surface (cavity wall) cannot be represented on a flat surface (real image) without introducing some distortion. However, the distortion is relatively minor, and viewers of the image have no difficulty interpreting it. Indeed, the image is of sufficient quality to allow standard holographic interferometric and electronic speckle pattern interferometric measurements of minute displacements of the cavity surface.

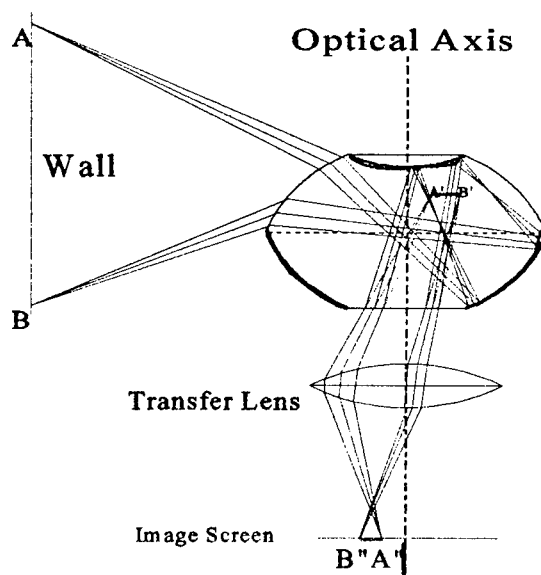


Figure 1. Ray diagram for a PAL located within a cylinder, showing the virtual image transferred to a screen by a lens.

When applying these traditional measurements to PAL images, it is found advantageous to linearize the annular image, *i.e.*, to transform the annulus into a rectangle which looks like the belt shaped region of the imaged cavity wall as if it were opened flat. This can easily be done with a computer and such a linearized image can be produced within about 40 seconds on current microcomputers. However, this process requires a frame-grabber and a computer, and is not real-time.

Therefore, it was decided to try to perform this linearization optically by using a diffractive optic. The final image would then be obtained in real time and requires no additional equipment.

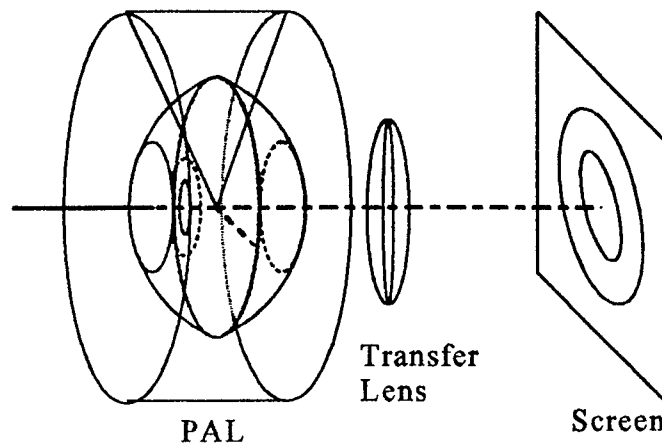


Figure 2. Another view of a PAL showing how the annular image is produced.

Generally, control and modification of images is done by using refractive elements, traditional lenses which produce phase changes into the spatial light distribution constituting the image. These systems are well understood and their operation is controlled by Snell's law as presented in introductory physics courses: $n_1 \sin\theta_1 = n_2 \sin\theta_2$. Gratings have rarely been used for imaging purposes because the light coming from any point of the image and impinging on the grating is divided into several discrete beams or orders according to the standard grating equation: $a \sin\theta = m\lambda$, where a is the spacing of the grating and m is the order of the output. Since this division of the input was rarely desired, gratings were almost never used in imaging applications. However, it was known that by properly adjusting the phase changes introduced by the grating, specifically making the changes continuous rather than discrete, the incoming optical energy could be concentrated with high efficiency into a single order; gratings that were designed this way were called *blazed* gratings. Still, it was not clear that variable gratings which could modify the complex light distribution of an image in a controlled way could be fabricated. Nonetheless, the development of holographic gratings and the utilization of machinery designed for the microelectronics industry seemed to suggest that diffractive as well as refractive lenses could be designed and produced.

A major difference between the two types of lenses is that refractive lenses can produce a wide range of smoothly varying phase changes, while diffractive lenses usually only produce phase changes up to 2π radians, and these changes tend to be discrete. Although a range of 2π radians is sufficient for controlling the direction of a wave front, and if the phase change introduced by a grating could be made continuous, efficient diffractive lenses would be possible, it is quite challenging to produce gratings with complex and smooth phase changes, although it can be done with very expensive equipment such as electron beam lithographic machines. It was soon found that more standard equipment such as that used for microlithography in the electronics industry could be used to produce approximations to a continuous phase change. With a single design

mask, the continuous phase could be approximated modulo 2π with stepwise changes. A single mask allowed 2 levels in the approximation, two masks allowed 4 levels, three masks 8 levels, and four masks 16 levels. With the higher number of masks came much higher efficiency: a two level approximation gave only about 30 per cent efficiency, while 16 levels could give over 95 per cent efficiency.

Thus diffractive lenses of high efficiency could be used for transforming images if methods for introducing a variable grating spacing to match the varying phase shifts needed could be devised.

Designs were quickly found for the production of simple diffractive lenses that could compensate for some of the aberrations of traditional lenses, and the new diffractive elements offered additional advantages in weight and use of material; indeed, in some cases the desired gratings could be cut right into the surface of the refractive lens the new lens was to complement.

However, the design of complex systems for producing diffractive elements that might perform unique functions unobtainable from traditional lenses is more challenging. In the project described in this report, an annular image was to be modified into a rectangular image, and the distortions in the annular image compensated. A formalism to determine the phase map required to change the geometric characteristics of the original image had to be developed. Assuming the original image in the x-y plane was covered with a variable grating, the location of each point in the image was to be mapped to some point in the u-v plane. Limiting the discussion to one dimension, assuming the small angle approximation $\theta = \sin \theta = \tan \theta$, applying the grating equation $a \sin \theta = \lambda$ where a is the grating spacing, and expressing quantities in terms of spatial frequencies, gives $\theta = \lambda/a = (2\pi/k)/(2\pi/q)$ where q is the angular spatial frequency of the grating in radians/distance. Since the link between phase and spatial frequency is given by $q = d\phi/dx$, examination of Figure 3 shows that the phase map $\phi(x) = (k/d)[\int u(x) dx - x^2/2]$. The last term in this equation describes the phase shift introduced by a simple refractive lens and so will be dropped and replaced physically by a lens of focal length $f = d$.

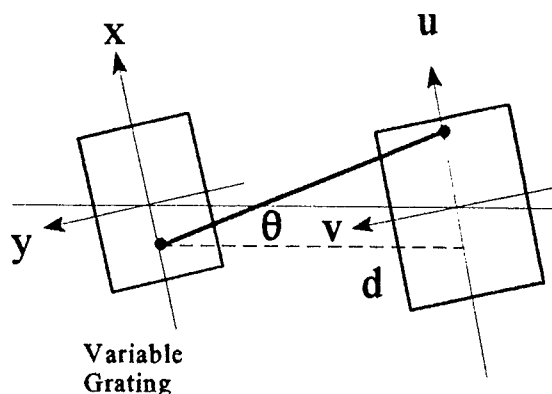


Figure 3. Transformation of a point in the x-y plane to a point in the u-v plane; $u = f(x)$, the two planes are separated by d , and it is desired to determine the grating frequency q which will produce the necessary angle θ .

Going to two dimensions is straightforward, and for the case under study the transformations are $u(x,y) = x_0 \ln ([x^2 + y^2]^{1/2})$ and $v(x,y) = x_0 \operatorname{atan}(y/x)$, where x_0 is an arbitrary scale factor having the dimension of length. The application of these transforms is shown in Figure 4 and the desired phase function is $\phi(x,y) = (kx_0/d) \{ \ln ([x^2 + y^2]^{1/2}) - y \operatorname{atan}(y/x) - x \}$. Once the requisite mathematical formalism has been found, it is put into a computer, the phase map is generated, the desired contours of fixed phase are determined, and a fracturing algorithm is applied to produce the desired phase mask for the transformation. The procedure used to fracture the data is shown in Figure 5. In Figure 5 an arbitrary point P1 is chosen on the contour curve and its gradient is found, which then gives the normal and the tangent lines to the contour curve. Another arbitrary point P2 is then chosen and its gradient found. When the intersection P3 is found for the two tangent lines through P1 and P3, the error between P3 and the contour value is measured. If this is smaller than the allowed maximum error, point P2 is moved further away and the process is repeated. If the error is too large, P2 is moved closer. The width of the rectangles is determined by moving down the perpendicular to the contour line until the phase change desired is attained. This process is repeated for each pair of contour lines specifying a zone. When the appropriate zones over the phase map have all been fractured and filled by the rectangles, the resulting list of rectangles is fed to a photolithographic machine which actually produces the desired phase mask

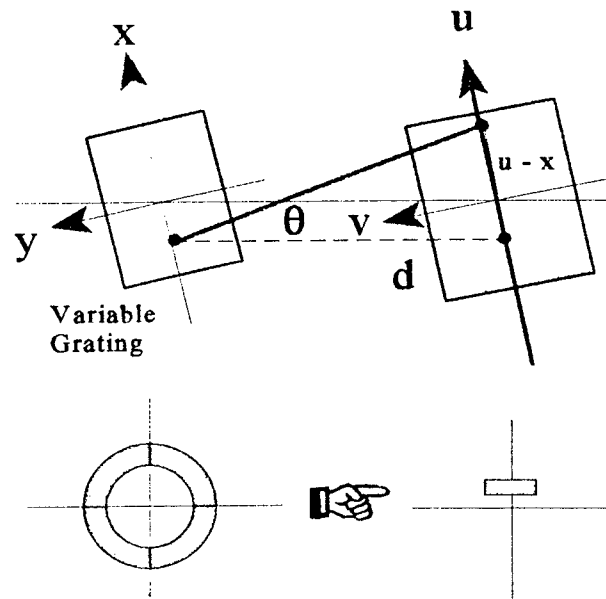


Figure 4. Diagram showing a log-polar transformation, where the coordinate transforms are $u(x,y) = x_0 \ln ([x^2 + y^2]^{1/2})$ and $v(x,y) = x_0 \operatorname{atan}(y/x)$. The upper figure shows the geometric relationships and the lower figure shows the effect of the transform on the annular image.

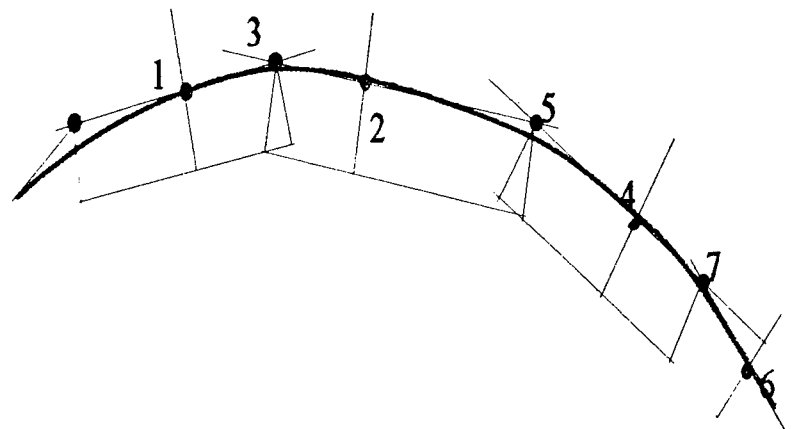


Figure 5. Diagram showing how the region defined by specified curved contour lines is approximated by rectangles.

for the diffractive optic. This mask is used to expose a properly prepared substrate and the mask pattern is etched into the substrate to actually produce the desired diffractive optic.

Once the diffractive optic has been produced, the setup shown in Figure 6 is used to produce the modified image. Since the diffractive element has no imaging power and the light into it must be collimated, the image to be transformed is placed on an LCD display which essentially presents it as a transparency to the incoming light. After going through the image, the light passes through the diffractive optic and a focussing lens which produce an image at $f = d$ from the lens. This image is very small since the LCD screen is less than two inches high and the scaling factor is between 0.2 and 0.4. Also, since there is only a single two level diffractive element, the efficiency is very low (about 30 per cent). Finally, the low resolution of the TV display blurs the image. In sum, the final transformed image is of very poor quality. If it is really desired to produce a sharp image, then an element of at least eight levels should be made, and an LCD display of at least 300 by 300 pixels should be used. Recall that for this project the real goal was to develop the algorithms for fracturing the zones defined by the mapping transformation, and to actually produce the binary optic in an appropriate setup. These goals were both obtained.

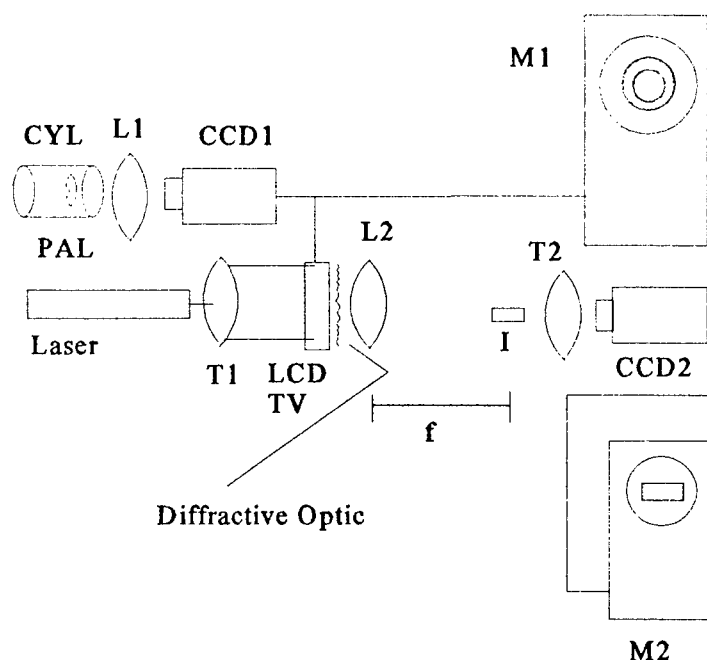


Figure 6. Layout for viewing the log-polar transformation. CYL cylindrical pipe; PAL panoramic lens; L1, L2 lenses; T1, T2 telescope expanders; M1, M2 monitors; I real image; CCD1, CCD2 cameras; f design focal length of diffractive optic. Monitor 1 shows annular image from PAL, monitor 2 shows image after transformation.

Bibliography

1. Matthys, Gilbert, Greguss, "Endoscopic Measurement using Radial Metrology with Digital Correlation", *Optical Engineering* **30** (10), 1455-1460, 1991.
2. Swanson, G.J., "Binary Optics Technology: Theory and Design of Multi-Level Diffractive Optical Elements", Lincoln Laboratory, Massachusetts Institute of Technology, Technical Report 854, August 14, 1989.
3. Saleh, Freeman, "Optical Transformations", in *Optical Signal Processing*, ed. by J. Horner. Academic Press 1987.

1995

**NASA/ASEE SUMMER FACULTY FELLOWSHIP
PROGRAM**

MARSHALL SPACE FLIGHT CENTER

MARKETING AND COMMUNICATIONS PLAN

Prepared By:

Jon D. Morris

Academic Rank:

Associate Professor

Institution and Department:

University of Florida
Department of Advertising

NASA/MSFC:

Laboratory:

Technology Transfer Office

MSFC Colleague:

Harry Craft

Marketing and Communications Plan
MSFC Tec Transfer Office
July 14, 1995

Marketing Objectives

To increase the number problem statements by 20 % for the 1996?

To gain support from industry, government leaders, and the general public for the Technology Transfer and the Marshall Technology Transfer Office.

Strategies

Product

1. Sell the services of the technology office to industry. Those services include:

A. Expert consultations in several important industry related technological areas including:

Materials

Manufacturing

Coatings

Insulation

Etc.....more

(SEE Attached Product List)

Up to 40 hours of engineering consultation for each technical inquiry at no cost

B. NASA inventions available for licensing

COSMIC: Computer programs from NASA adapted for commercial use

C. Information and access; nationwide technology transfer network

D. Cooperate projects to modify space technology

E. Dual Use Technology

F. CARS

Price

The pricing strategy includes:

- 40Hr rule
- Project Costs
- Development cost

Place

Primary

The primary geographic areas for MSFC are:

Alabama, Arkansas, Florida, Georgia, Kentucky,
Louisiana, North Carolina, South Carolina, Tennessee,
West Virginia

Secondary

The rest of the United States and other countries including areas of
previous problem statement activity, including:
(Selection was made using data to locate states with the most TTA
activity in the last year; see attached)

California
Canada
Illinois
Indiana
Mississippi
New Jersey
New York
Ohio
Pennsylvania
Texas

Promotion

Focus on companies in the following SIC Codes---

Manufacturing
Materials

Cars and TTA

Focus on Service and connections with labs, contractors, KSC,
Stennis, STAC other Technology Centers, other NASA Centers

Integrated Marketing Promotions

Target Audience:

1. Engineers and Plant Managers particularly in Manufacturing and Materials based companies, in the Southeast Region.
2. Same group Nationally
3. General Public, Business and Civic Leaders.

Objectives

1. Create an image/logo for NASA Technology Transfer Office at Marshall that reflects the efforts at Marshall and presents a point of differentiation from other Tech Transfer offices both inside and outside NASA.
2. Establish a plan for reaching the constituents/audience in:
Alabama, Arkansas, Florida, Georgia, Kentucky,
Louisiana, North Carolina, South Carolina, Tennessee,
West Virginia Arkansas, Louisiana, Alabama, Tennessee, Kentucky,
Georgia, North Carolina, South Carolina, North Carolina, West Virginia.

Secondary areas: California, Canada, Illinois, Indiana,
Mississippi, New Jersey, New York, Ohio, Pennsylvania,
Texas.
3. Establish a plan to introduce State reps to possible clients in each state.
4. Create a process for disseminating information regionally and nationally about technology transfer breakthroughs.
5. Establish an interactive method for inquires about Tech Transfer services and Data Bases.

Strategies

1. Differentiate the Marshall/Southeast Region Technology Transfer office from from other TecTransfer Offices by establishing a new, industry friendly identity and theme. (SEE ATTACHMENT) This new signature can be used in conjunction with the current NASA logo and should be referred to as a "office identifier" rather than a logo. Using the new identifier will help distinguish the Marshall Office from other government and non-government technology transfer offices. In addition the new identifier is more memorable and descriptive of the services that are offered. It conveys a positive direction and positions the Tec Office as an active participant not just a source of data.

Advertising

2. Use ads in national trade publications to convey the capabilities of the Tec Transfer Office to the target audience. The publications selection process will be discussed in the advertising media planning.
3. Use direct mail and local/regional publications where available to introduce and support state representatives. (See Attached). Each PE visit to a state that includes a presentation before a group should be preceded by a mailout identifying the PE, the subject of the presentation, and a method for response.
4. Use direct mail to relate recent intra-state "success stories" to industry executives within the state.

Public Relations

5. Implement a NASA Technology Fair at the Kennedy Space Center press site for each Shuttle launch. The Fair, needs a name, and should highlight one, two or three good success stories. The plan should focus on transfers that have come from NASA, that are not widely known and that make interesting stories for both print and electronic media. A Project Selection and Implementation Committee should be established to direct and manage the Tech Fair (SEE attached KSC site visit report).
6. Implement a Media Relations Plan that is both beneficial and reasonable (SEE attached handout by Kathy Jordan of Tec-Masters). Establish a process that can be implemented when success stories or special events warrant. Care should be taken to clearly identify sources that are likely to be interested in specific topics or levels of significance. This is an opportunity to establish an ongoing relationship.

Events Marketing

7. Trade shows continue to be an important part of the promotion mix. Each show should be evaluated on established criteria. Many of these shows require advanced promotion by direct mail, show programs or allied magazines. Invitations in advance will prepare the audience for the booth. This advance publicity will lead to more problem statements by priming the audience to ask questions at the show.

Speeches and Presentations

8. Develop a speakers bureau to provide speakers for various presentations. Although several presentations have been developed, there needs to be a process for assisting the speaker and facilitating presentations. A laptop computer and video projector would improve the flexibility and overall capability of the

presentations, although care should be taken in selecting the package. Some of the projectors work far better than others.

Specialty Material

9. Use specialty material as "leave behinds" and as trade show material. This will help to produce top of mind awareness for the Tec Transfer Office. The material should be: a. attractive, b. useful or valuable, c. high quality, d. long lasting, e. innovative (possibly related to NASA technology), f. enduring

Response material

10. Create coordinated response folders and videotapes to be sent to companies that request information. All packages should include material that is directed to that company's specific problem as well as general information about the MSFC technology transfer program. The packages should be designed to make responding easy.

The current videos are too instructional, predictable and military sounding. In the future, videos should focus on the inherent excitement of the Tec Office product success and attempt to spark interest and imagination. A good place to start would be the Wednesday TAB meetings. Recording some of the discussions in the meetings will interest viewers in the process and demonstrate the kind of expertise that is assembled just to consider a project or problem. The discussions in the TAB meetings are interesting, sometimes entertaining and often novel.

Internet/Space Link/ Home Page.

11. Develop an improved association with the Space Link and begin placing success stories on the Tech Transfer Home Page. At Space Link, the Tech Transfer office should a) establish a system for monitoring and updating the current 'success story' material now being featured, and b) establish a direct link from Space Link to the Tech Transfer home page, so that those that enter the system through Space Link can interact with Tech Office data bases such as the patent catalogue.

12. Establish a list of success stories on the Tech Office Home Page. Those stories could be catalogued with several key words so that interested parties that want more information can receive response packages mentioned above, in electronic form. Although the present need for this service is limited, it will become more valuable as companies improve their computer systems and as new employees come onboard.

13. Establish "patent search" capabilities through the home page. If the service is advertised it would make patent searching easy for those that have computer and internet capabilities. A Patent Search Home Page Button should be created.

Internal Marketing

14. Develop a House Newsletter to be used to improve relationships with Labs, contractors and NASA personnel. This would be a forum for presenting information and incentives and will improve the relationship between all parties. This effort should not replace the current presentations but should be a supplement to them.

15. In addition, Special Incentives would help to improve productivity and moral. The key to a successful Tec Office operation is completing Problem Statements in a proficient and timely manner. Any incentive that is permitted under Center guidelines will help.

Creative Materials

Objectives

1. To differentiate the Marshall/Southeast Region Technology Transfer office from other Tech Transfer Offices by establishing a new, industry friendly identity and theme.

Strategy

The name and slogan are: ***NASA Solutions***
 Bringing Space Age Technology Down to Earth

The addition to the logo might look something like this.

NASA Solutions

MSFC Technology Transfer Office

Bringing Space Age Technology Down to Earth
800-USA-NASA

Rationale

The value of the new identifier is: it conveys an active participation by NASA and links the Space Program to the Tec Office. It will improve the visibility of the services provided by the office, among all three target audiences. It will help to differentiate the MSFC office from other tech transfer offices by establishing a unique name. The theme helps to demonstrate that contemporary knowledge from the space program that can be shared to solve real life problems.

Objective

2. Use ads in national trade publications to convey the capabilities of the Tech Transfer Office to the target audience. The publications selection process will be discussed in the media planning section.

Strategy

The ads will focus on: 1. introducing the program, 2. emphasizing the services, 3. reporting the successes, and 4. presenting the cost structure. Later ads should focus success stories.

The ads should make it easy to contact the office while stressing NASA's commitment to timely quality service. Headlines should be written to peak industry interest and provoke thought. Visuals should be simple to but easy to follow, and give the target a quick look at the services. Each ad should focus on a different aspect of NASA Solutions' services. (SEE ATTACHED ADS)

After the initial industry wide coverage, specific industries should be targeted. Survey data and 'problem statement' tracking should be used to pinpoint the industry with the greasiest potential (SEE Media Strategy).

Objective

3. Use direct mail and local/regional publications where available to introduce and support state representatives.
4. Use direct mail to relate recent intra-state "success stories" to industry executives within the state.

Strategy.

Ads featuring a photo, background information, and the telephone number of the state representative should be sent to companies within the state. If the PE is making a presentation in a specific city, one page announcements should be sent to the surrounding industries.

In addition, PEs should be encourage to use the industry data base (SEE Media Section) to inform companies within their state of recent developments, i.e. noteworthy tech transfers to industries in their state. To promote unity the format for the ad/mailer should closely follow the design of the ads for the national publications ads (SEE Attached Example).

This regional campaign is designed to build confidence in the state reps (PE) and to acquaint industries with the local service provided by the Technology Transfer Office. In addition, national ads can be mailed to designated industries within the states. Each company in the state can be identified by SIC code and interest.

Rationale

The state ads/ mailers support the work in the regional area and provide a method for each state rep to exercise control over promotional material within their territory. While the national ads inform industries nationwide about NASA Solutions, the state ads directly address businesses in the Marshall assigned region. This affords the Tec Office the ability to focus attention on the mandated area and on the areas with the greatest potential for response.

Media Plan

Objective

1. To reach 20% of the three target audiences nationwide, and
2. To convey the capabilities of the Transfer Office to 50% of those reached.

Strategy

Use ads in national trade publications that have been selected by SIC code. From the preliminary survey data, most respondents read publications within their specific industry (i.e. Appliance Manufacturing, or Plastics Engineering) while some read industry-wide publications (Design News). A list of specific publications, rate information, and other data about the magazine can be found in the three volume set, of the SRDS books. (One copy of each has been given to the Tec Office by the Uof Florida.) These books are published every month and are available at the following address:

SRDS Business Publications Advertising Source
1700 Higgins Road
Des Plaines, IL 60018
708-375-5000

Information about the service has been included with this report (SEE Attached).

Flow Chart

A flow chart of media insertions and events should be developed. (SEE attached example). This flow chart is a schedule of activity and presents at a glance the entire media plan for the year at a glance. Also, a Production Report (SEE attached example) should be developed to help track the progress of material development.

Objective

3. To reach 20% of the three target audiences statewide, to convey the capabilities of the Transfer Office, to introduce the state reps and to distribute information of local interest.

Strategy

Use a data base of industries by state to reach the engineers and plant managers. The Harris Publishing Company produces a book (which some PEs have) and a database by state of manufacturers. Their list is developed in conjunction with the Chamber of Commerce, or the development office in each state, and the data is verified every year by Harris. (SEE a description of the service included with this report). Also, a demo disk is available. A copy of Select Your Best Prospects a Demo for Louisiana, is available from Liz Rodgers.

The data base also should be used to announce tradeshow presentations. For example, Chicago area industries could be assembled into a mailing list for the 2005 trade show.

DATA Bases by state from:
Harris Publishing
2057 Aurora Road
Twinsburg, Ohio 44087-1999
800-888-5900 Fax 216-963-6355
Contact: Bill Jones x2270
Title: Manufacturers Directories by State on Disc

Specialty Advertising

1. Use specialty material as "leave behinds" and as trade show material. This will help to produce top of mind awareness for the Tec Transfer Office. The material should be: a. attractive, b. useful or valuable, c. high quality, d. long lasting, e. innovative (possibly related to NASA technology), f. enduring.

Pens

NASA Solutions
Write us your problems
1-800-USA-NASA

Other give-away items worth investigating are: Computer Mouse Pads, Screen Savers, and Hand Rests. In addition, a luggage tag maker to be used at tradeshow. These will endure the office name to the prospects.

FUTURE AREAS OF INTEREST

Reaching Children (See Childrens' Magazine)

Virtual Reality Project

Reaching Children
Virtual Reality

1995

**NASA/ASEE SUMMER FACULTY FELLOWSHIP
PROGRAM**

MARSHALL SPACE FLIGHT CENTER

**ANALYSIS, DESIGN AND TESTING
OF HIGH PRESSURE WATERJET NOZZLES**

Prepared By: Andre P. Mazzoleni

Academic Rank Assistant Professor

Institution and Department Texas Christian University
Department of Engineering

NASA/MSFC:

Laboratory: Materials and Processes
Division: Fabrication Services Division
Branch: Process Automation and Modeling

MSFC Colleagues: Eutiquio Martinez
David Hoppe

Preface

This report summarizes research conducted by the author as a Summer Faculty Fellow for the Hydroblast Research Cell at Marshall Space Flight Center (MSFC) in 1995. The project is a continuation of work done at MSFC as a Faculty Fellow in 1994 [3] and has consisted of identifying and investigating the basic properties of rotating, multijet, high pressure water nozzles, and how particular designs and modes of operation affect such things as stripping rate, standoff distance and completeness of coverage. The study involved computer simulations, an extensive literature review, and experimental studies of different nozzle designs.

Introduction

The Hydroblast Research Cell at MSFC is both a research and a processing facility. The cell is used to investigate fundamental phenomena associated with waterjets as well as to clean hardware for various NASA and contractor projects. In the area of research, investigations are made regarding the use of high pressure waterjets to strip paint, grease, adhesive and thermal spray coatings from various substrates. Current industrial methods of cleaning often use ozone depleting chemicals (ODC) such as chlorinated solvents, and high pressure waterjet cleaning has proven to be a viable alternative [6, 7]. Standard methods of waterjet cleaning use hand held or robotically controlled nozzles. The nozzles used can be single-stream or multi-jet nozzles, and the multijet nozzles may be mounted in a rotating head or arranged in a fan-type shape.

We consider in this paper the use of a rotating, multijet, high pressure water nozzle which is robotically controlled. This method enables rapid cleaning of a large area, but problems such as incomplete coverage (e.g. the formation of "islands" of material not cleaned) and damage to the substrate from the waterjet have been observed. In addition, current stripping operations require the nozzle to be placed at a standoff distance of approximately 2 inches in order to achieve adequate performance. This close proximity of the nozzle to the target to be cleaned poses risks to the nozzle and the target in the event of robot error or the striking of unanticipated extrusions on the target surface as the nozzle sweeps past. Two key motivations of this research are to eliminate the formation of "coating islands" and to increase the allowable standoff distance of the nozzle.

Nomenclature

For definitions of commonly used waterjet technology terms, see [3].

Coverage

The main factors affecting coverage are the sweep rate, the number of orifices and the placement of these orifices on the nozzle. We summarize here the analysis of these factors as found in [3].

The angular velocity of the nozzle necessary for full coverage decreases as the number of orifices increases. However, since there is a maximum flow rate associated with a given pump, there is a limit to the number of orifices of a given diameter that can be added.

From [3] we have a formula for the maximum number of orifices that can be placed on a nozzle for a given flow rate, pressure and orifice exit diameter. If F = flow rate, A = cross sectional area of orifice exit, v = exit velocity of waterjet, d = exit diameter of orifice, p = pump pressure, p_a = atmospheric pressure, ρ = density of water and n = number of orifices, then $n \leq \frac{4F}{\pi d^2} \sqrt{\frac{\rho}{2(p-p_a)}}$, where c_v is an experimentally determined constant called the velocity coefficient which is usually between 0.9 and 0.95 [6]. For a conservative assessment of n , we set $c_v = 1$. Thus if $F = 13 \text{ gpm} = 50 \text{ in}^3/\text{sec}$, $p = 36,000 \text{ psi}$, and $d = .019 \text{ in}$, we have $n \leq 6.36$ (i.e. $n \leq 6$). Once the number of orifices for the nozzle is chosen, the effect of different placements can be studied, and in [3] we show that the optimum arrangement for cleaning applications is to arrange the orifices at an equal distance from the center of the nozzle with equal angular spacing (see Fig.1). Then, if the minimum trace width of all the orifices is denoted by w_t , sweep rate and angular velocity must satisfy the relation $\omega \geq \frac{2\pi v_0}{nw_t}$ if we are to have complete coverage [6]. For example, if $n = 6$, $w_t = 0.5 \text{ mm}$ and $v_0 = 30 \text{ mm}$, then we require $\omega \geq 20\pi \text{ rad/sec}$ for complete coverage.

The preceding analysis assumes that the centerline of the nozzle is aligned perpendicular to the target which is assumed flat as shown in Fig.1. A precise characterization of the jet shape is necessary to determine the trace width w_t . For practical purposes, a chart showing trace width w_t as a function of standoff distance for various operating pressures can be determined experimentally. We note here that the influence of gravity on the jet must also be accounted for, although this effect will be negligible for short jets.

Computer Simulation

A computer program consisting of a collection of *MATLAB* "m-files" (see Ref. [4]) has been written to assist operators of the Hydroblast Research Cell in selecting the fastest possible sweep rate allowed for a given set of system parameters. In addition to this operational computer program, Computational Fluid Dynamics (CFD) analysis has been initiated as a means of evaluating different nozzle and orifice designs.

Orifice Geometry and Jet Compactness

A liquid jet issuing into the air has a structure [6] which consists of a core surrounded by a layer of droplets (Fig.2). Increasing the core length increases the standoff distance we can use in cleaning operations. (Increased standoff distances are desirable, as discussed in the "Introduction".) We call the region of the jet which contains a core the "compact" region of the jet. Many papers have studied the effect of various orifice designs on jet compactness [1, 2, 5, 8]. Once a basic shape for the internal profile of the orifice is chosen, one can attempt to maximize the core length of the jet produced by varying the internal parameters of the orifice. For this study, two basic orifice geometries (see Figs.3a and 3b), both with exit diameters of 0.018 inches, were selected after an extensive literature search for orifice designs which yield highly compact jets. (Further details of these geometries will be presented in a future report.) To start the process of optimizing these designs, the effect of various L/D ratios on jet compactness was studied experimentally, as discussed in the next section.

Testing Procedures

The methods chosen for evaluating different orifice designs were stripping tests, high-speed video, high-speed film, still photography and pressure measurements. (We note here that filming high-speed waterjets requires extremely bright lighting conditions.) For the stripping test, 24 inch by 24 inch panels coated with MCC (Marshall Convergent Coating) were used as targets and stripping ability was determined at various standoff distances and water pressures. A test figure was designed for measuring the pressure delivered by the waterjet to the target (see Fig.4). (Fabrication of the fixture was not completed in time to use this summer.) As seen in the figure, water strikes a target disk and imparts a force, which is then transmitted through a lever to the load cell. By adjusting the position of the support, we can change the sensitivity of the system. By measuring the force on targets of different diameters, we can determine the force acting on thin annular regions at various radial distances. By dividing the force by the area of these regions, we can obtain pressure as a function of radial distance from the center of the jet. These measurements can then be made at several different standoff distances. This system is a low-cost alternative to measuring pressure via a pressure transducer which is placed directly in the path of the jet [5].

Results

Due to necessary repairs and refurbishments of the Hydroblast Research Cell equipment during the author's stay at MSFC, it was only possible to do preliminary testing on the orifice designs described in the section on "Orifice Geometry and Jet Compactness". These preliminary results consist of a qualitative assessment of the relative ability of the orifices to strip MCC from panels. The water pressure supplied to the orifices during the tests was 15,000 psi. From best to worst, the orifices were judged as follows: A6, B6, B3, A3, A0, B0, B1, A1. (The letters refer to the nozzle type and the numbers refer to the L/D ratio (see Figs.3a and 3b).) It is interesting that when we compare the orifices of each type with respect to L/D ratios, we obtain the following rankings: A6, A3, A0, A1 and B6, B3, B0, B1. Note that for both designs, $L/D = 6$ gives the best result and $L/D = 1$ gives the worst result. It is stressed here that these results are preliminary and conclusive results await further testing.

Current Research

In addition to the eight orifice designs discussed above, eleven more were designed and fabricated this summer. As of the writing of this report, only limited testing of these designs had been completed, so no results are reported here. We do note, however, that preliminary studies indicate that some of these new orifice designs may provide an order of magnitude increase in the standoff distances that can be achieved with current waterjet cleaning systems.

Summary

Basic properties of rotating, multijet, high pressure water nozzles have been outlined. An orifice configuration which enables complete coverage during cleaning has been identified. A computer program has been written to assist operators of the Hydroblast Research Cell in

selecting sweep rates for a given set of system parameters. CFD analysis has been initiated. Orifice geometries likely to produce highly compact jets have been designed and fabricated. Preliminary tests of these orifices have been conducted and indicate that some of these designs may provide an order of magnitude increase in the standoff distances that can be achieved with current waterjet cleaning systems.

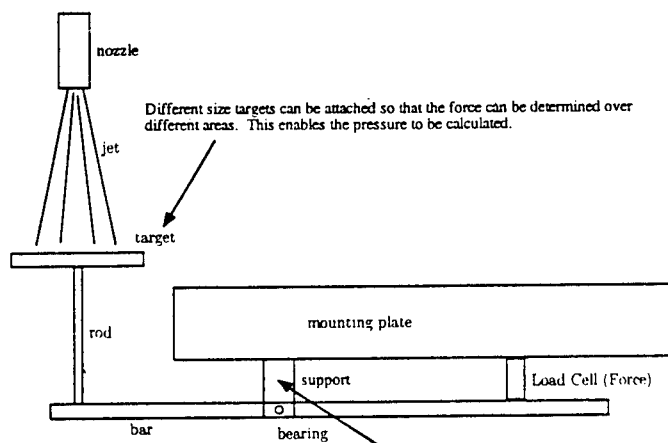
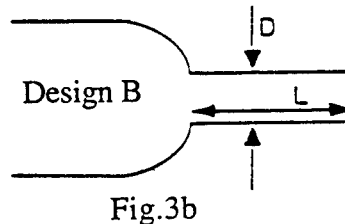
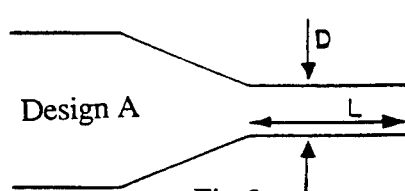
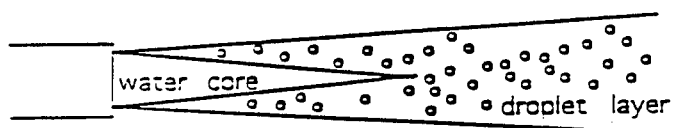
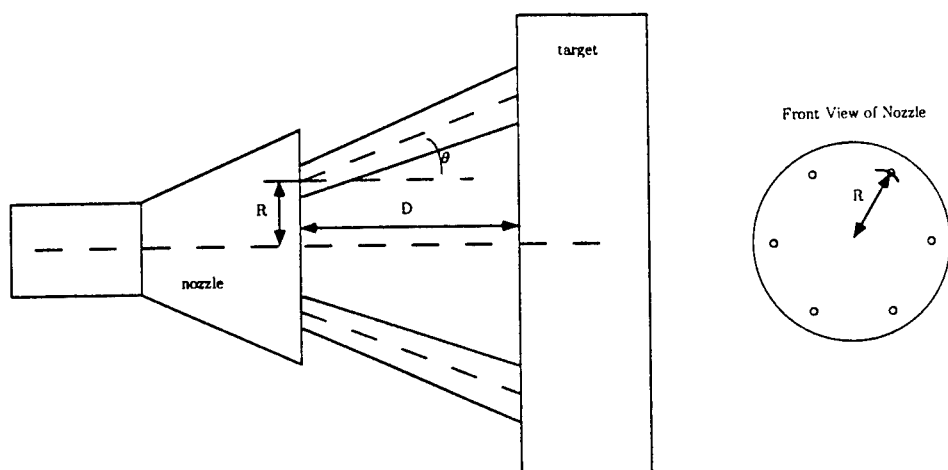
Acknowledgments

The author would like to thank Eutiquio Martinez and David Hoppe for all of their help and for sponsoring this research. The author would also like to thank Wendell Colberg, Steve Burlingame, Paul Gill and John Ransburgh of MSFC, Paul Page of USBI, and Gary Stiger and David Jellison of Intergraph for their assistance over the past two summers. Considerable thanks are also due Gerry Karr, Mike Freeman, Frank Six, Sandy Cothren, Teresa Shurtz, and Symmetris Jefferson of the Summer Education Programs Office for making the Summer Faculty Fellowship Program such an enriching experience.

References

- [1] R. Kobayashi, T. Arai and Y. Masuki, "Water Jet Nozzle Geometry and Its Effect On Erosion Process of Metallic Material", *5th American Water Jet Conference*, August 29-31, 1989, Toronto Canada, pp.59-68.
- [2] S. J. Leach and G. L. Walker, "The Application of High Speed Liquid Jets to Cutting", *Phil. Trans. Roy. Soc. (London)*, Vol. 260, Series A, pp. 295-308.
- [3] A. P. Mazzoleni, "Design of High Pressure Waterjet Nozzles", Report XXIX for the 1994 Summer Faculty Fellowship Program at Marshall Space Flight Center, Huntsville, AL.
- [4] *MATLAB-High-Performance Computation Software*, The Mathworks Inc., 24 Prime Park Way, Natick, MA 01760
- [5] M. J. McCarthy and N. A. Molloy, "Review of the Stability of Liquid Jets and the Influence of Nozzle Design", *The Chemical Engineering Journal*, Vol. 7, 1974, pp.1-20.
- [6] P. J. Singh, J. Munoz and W. L. Chen, "Ultra-High Pressure Waterjet Removal of Thermal Spray Coatings", *Jet Cutting Technology*, Kluwer, 1992, pp.461-480.
- [7] J. M. Sohr and M. L. Thorpe, "Stripping of Thermal Spray Coatings with Ultra High Pressure Water Jet", *28th Annual Aerospace/Airline Plating & Metal Finishing Forum and Exposition*, San Diego, CA, 1992, paper 920939.
- [8] P. F. Thorne and C. R. Theobald, "The Effect of Nozzle Geometry on the Turbulent Structure of Water Jets - A Photographic Study", *Fourth International Symposium on Jet Cutting Technology*, Canterbury, England, 1978, paper A4.

Figures



1995

NASA/ASEE SUMMER FACULTY FELLOWSHIP PROGRAM

MARSHALL SPACE FLIGHT CENTER
THE UNIVERSITY OF ALABAMA IN HUNTSVILLE

REINVENTION/REENGINEERING OF BUSINESS AND TECHNICAL PROCESSES

Prepared By:	Eugene A. Olsen, Ph.D.
Academic Rank:	Associate Professor
Institution and Department:	The University of Alabama in Huntsville Department of Management and Marketing
NASA/MSFC:	
Office:	Technology Transfer Office
Division:	Process Management Office
MSFC Colleague(s):	Harry G. Craft Robert C. McAnnally

INTRODUCTION

The changing marketplace as evidenced by global competition is requiring American organizations to rethink, regroup, and redesign their processes. The umbrella of total quality management (TQM) includes many quality methods, techniques, tools, and approaches. There is no right way for every situation or circumstance. Adaptability and experimentation of several tools is necessary. Process management when properly applied can lead to continuous quality improvements. But some processes simply need to be discarded and new ones developed. This reengineering often results in vertical compression and job redesign and restructuring. Work activities must be designed around processes, not processes around work activities. Reengineering and process management do not stand alone--they support each other. Senior executive leadership and empowerment of workers at all organizational levels is vital for both short-term and long-term success.

TOTAL QUALITY MANAGEMENT

Total quality management is a roadway with many stops along the way. These stops are in effect variations of many approaches, methods, techniques, and procedures now being used by organizations throughout the world. Japan has been at the forefront of quality for many years with tremendous success. The application of quality within the U.S. is fairly recent. And with the introduction of ISO 9000 by the European community, quality has gained new interest and converts. Total quality management (TQM) is often described in many ways. Regardless of the description it is a structured, systematic process geared towards meeting the customer's expectations in both quality and price. It is a means to an end, with the end being the long-term success of the organization.

Eighty-eight percent of executives believe that employee involvement is critical to the success in improving productivity, yet only 38 percent of workers indicate they are involved (empowered) and given the opportunity in decision making. Organizational improvement demands a shared perspective and involvement creates motivation which in turn creates innovation leading to improvements (Simmerman 1994, pp. 87-88). "An ineffective organization is like a wagon with square wheels" (Simmerman 1994, p. 87). Leaders must develop teams for only through team work does the organization improve.

Corporate leaders are making total quality management a part of the corporate American fabric. As of 1991, 93 percent of manufacturing companies and 69 percent of service companies have made quality management a strategic part of their operations

(Olian, Rynes 1991, p. 303). TQM is not just another tool or technique but a very powerful management system and philosophy. It realigns and thus recommit the organization's focus towards meeting its customers' demands. As a result, the organizational culture and often structure are changed to maintain this customer focus. Input and feedback from customers is essential for aligning the perceptions between them and management (Babbar 1992, p. 39).

Over the years, a number of variations or approaches of TQM have been developed by experts such as Demming, Crosby, Duran, and Joiner. These different approaches share certain characteristics which often include: (1) the primary objective of focusing on meeting customers' expectations in terms of both quality and price; (2) an absolute emphasis by top management is essential and required for TQM to be successful; (3) a vigorous emphasis on improving work processes with decisions being made based on verifiable data; (4) vertical deployment throughout the organization with a focus on ensuring that everyone is keenly aware of fundamental organizational objectives; (5) true empowerment of employees by eliminating barriers and obstacles so that they can fully focus on meeting customers' (both internal and external) expectations; and (6) creating a cultural environment where quality is recognized as the primary value with the further understanding that quality is a progressive process focusing on continuous improvement (Olian, & Rynes 1991, pp. 304-306; Merron 1994, pp. 51-54; Ehrenberg, & Stupak 1994, pp. 79-80).

PROCESS MANAGEMENT

Process management has become one of the most widely used TQM approaches. It focuses on the work processes considering both internal and external customers and suppliers. A process can be defined as those activities that add value applied to transform inputs into outputs, e.g., products and services. The transformation process should result in an output that has greater value than its input(s). This transformation process exists regardless of the type or nature of work and the environment, manufacturing or service.

For process management to be successful, Melan described six crucial steps: (1) establish ownership of the process; (2) establish workflow boundaries; (3) define the process; (4) establish control points; (5) implement measurements; and (6) take corrective action (Melan 1989, pp. 398-401).

REENGINEERING

Reengineering or rightsizing is a radical method of improvement for any organization. This in-depth process involves totally redesigning business processes. The technique requires management to take the building blocks of the organization, its basic functions, and restructure them in a way that will benefit the company as a whole. Companies such as AT&T, American Express, GTE, and PepsiCo have all successfully used this process to assist them in becoming major competitors within their business markets. Reengineering places enormous value on considering customer needs and in the ability of the "reengineered" firm to fulfill these needs. Unfortunately, often times reengineering does lead to some reduction in the organization's work force. However, the motivations behind these reductions are quite different compared to those of downsizing. By eliminating non-value added activities, or reducing the production process to the essential elements for completing the job, companies see a dramatic increase in productivity. Ultimately, the organization minimizes "unproductive overhead" and production inefficiencies which will result in a "fatter" bottom line or increased profits (Hammer 1994, p. 46). According to James Champy, chairman of CSC Consulting Group, "just moving [a company's] performance 10% or 20% won't do it [anymore]." For this reason, reengineering assists many companies in maintaining their competitive edge by reestablishing their market position.

Champy recommends that each organization answer three important questions to obtain optimum results from reengineering efforts. First, before management begins the reengineering procedure, they must identify the purpose and overall focus of the company. Next, they should establish what organizational culture is present. Lastly, the organization must determine what production processes need to be altered to achieve the desired results. Along with these three things, management must continually reassess organizational objectives to stay focused on reengineering efforts. Contrary to downsizing, which is merely a one-time reaction to market instability, reengineering is an ongoing process.

Downsizing is clearly a financially driven method of cutting operating expenditures, but reengineering is a "participative approach" that reorganizes itself to meet customer needs and in doing so, increases profitability (Davidson, Dickson, & Trice 1993, p. 11). Reengineering is a beneficial approach to strategic management which requires a constant reassessment of the organization's mission and long-term goals. It promotes a "shared" vision of the future of the organization supported by management and well communicated to employees of the organization. By

communicating to employees and allowing them to participate in the redesign of the organization, they develop a "bond" or personal commitment to the organization.

CONCLUSIONS

Quality efforts must continue if organizations are going to adapt themselves to meeting customers' expectations in an ever changing global marketplace. Whether they employ some variation of process management or reengineering or some supportive combination thereof, the roadway will be littered with obstacles, failures, rewards, and successes. These obstacles, failures, rewards, and successes then become the pillars for integrating quality efforts into the organizational culture.

Strong and positive leadership by senior management is critical and essential to success. They must not only walk-the-talk but the vision of the future must be shared by all, management and employees. Total quality rests in total understanding of what the objectives are and why they are important to the organization. Without total understanding and commitment, change does not occur. Change must become the norm and ally, not something to be feared.

ACKNOWLEDGMENT

The author would like to acknowledge his NASA colleagues Harry G. Craft and Robert C. McAnnally for their outstanding leadership and personal support in the accomplishment of my faculty fellowship duties at MSFC. Their encouragement made this summer effort a most valuable professional learning experience for me. I wish to commend Harry and Bob for their initiative in formulating the Process Improvement team, of which this author was a member, and in developing the internal metrics project, which I also was a part of. The outcome of these two measures should greatly contribute to the short-term and long-term success of MSFC. I also want to extend individual thanks to my other Process Improvement team members, Rosa M. Kilpatrick, Don Whirley, Larry Lechner, Conrad Jackson, and Kevin McDaris. Their consideration and cooperation allowed me to feel as a special member of the group at Marshall. Lastly, I want to express my appreciation to Mrs. Brenda Lyle of the Process Management Office who has been an invaluable resource for information, documents, and all around administrative help.

REFERENCES

- Babbar, S. A dynamic model for continuous improvement in the management of service quality. International Journal of Operations and Production Management. 12(2), 38-48.
- Davidson, D., Dickson, D., and Trice, Jr. (1993). Rightsizing for success. Business Forum. 18(1&2), 10-12.
- Ehrenberg, R. H., and Stupak, R. J. (1994). Total quality management: Its relationship to administrative theory and organizational behavior in the public sector. Public Administration Quarterly. 43(3), 75-98.
- Hammer, M. (1994). Reengineering is not hocus-pocus. Across the Board. 31(8), 45-47
- Melan, E. H. (1989). Process management: A unifying framework for improvement. National Productivity Review. 8(4), 395-406.
- Merron, K. A. (1994). Creating TQM organizations. Quality Progress. 12(1), 51-54.
- Olian, J. D., and Rynes, S. L. (1991). Making total quality management work: Aligning organizational processes, performance measures and stakeholders. Human Resource Management. 30(3), 303-333.
- Simmerman, S. J. (1994). The square wheels of organizational development. Quality Progress. 12(10), 87-89.

1995

NASA/ASEE SUMMER FACULTY FELLOWSHIP PROGRAM

MARSHALL SPACE FLIGHT CENTER
THE UNIVERSITY OF ALABAMA IN HUNTSVILLE

IMPELLER LEAKAGE FLOW MODELING FOR MECHANICAL VIBRATION CONTROL

Prepared By: Alan B. Palazzolo, Ph.D

Academic Rank: Associate Professor

Institution and Department: Texas A&M University
Mechanical Engineering

NASA/MSFC:

Office: Structures & Dynamics Laboratory
Division: Control System
Branch: Mechanical Systems Control

MSFC Colleague(s): Steve Ryan, Ph.D

INTRODUCTION

HPOTP and HPFTP vibration test results have exhibited transient and steady characteristics which may be due to impeller leakage path (ILP) related forces. For example, an axial shift in the rotor could suddenly change the ILP clearances and lengths yielding dynamic coefficient and subsequent vibration changes. ILP models are more complicated than conventional-single component-annular seal models due to their radial flow component (coriolis and centrifugal acceleration), complex geometry (axial/radial clearance coupling), internal boundary (transition) flow conditions between mechanical components along the ILP and longer length, requiring moment as well as force coefficients. Flow coupling between mechanical components results from mass and energy conservation applied at their interfaces. Typical components along the ILP include an inlet seal, curved shroud, and an exit seal, which may be a stepped labyrinth type. Von Pragenau (MSFC) has modeled labyrinth seals as a series of plain annular seals for leakage and dynamic coefficient prediction. These multi-tooth components increase the total number of "flow coupled" components in the ILP.

Childs' (1987) developed an analysis for an ILP consisting of a single, constant clearance shroud with an exit seal represented by a lumped flow-loss coefficient. This same geometry was extended to include compressible flow by Nhai The Cao and Childs (1993). The latter reference did not discuss dynamic coefficients, presumably due to their highly non-quadratic results for impedance vs whirl frequency. These "resonances" appear in both references and are reported to be caused by the centrifugal acceleration term of the path momentum equations. Test impedances measured by Guizburg (1995) at Cal Tech (1992) do not contain the resonances and appear quite apt to be accurately described by quadratic functions of whirl frequency.

The objective of the current work is to:

- (a) Supply ILP leakage-force-impedance-dynamic coefficient modeling software to MSFC engineers. The initial model will be based on incompressible/compressible bulk flow theory.
- (b) Design the software to model a generic geometry ILP described by a series of components lying along an arbitrarily directed path.
- (c) Validate the software by comparison to available test data, CFD and bulk models.
- (d) Develop a hybrid CFD-bulk flow model of an ILP to improve modeling accuracy within practical run time constraints.

RESULTS

A. Theory

The governing equations consisted of continuity (mass conservation), momentum and equation of state (thermophysical properties). The momentum equations were obtained from the cylindrical coordinate Navier-Stokes equations by imposing:

- (a) The kinematic constraint of uniform (rectangular) velocity profiles through the film thickness.
- (b) Zero pressure gradient through the film thickness.
- (c) Velocity components perpendicular to flow path are zero.
- (d) The perpendicular to the flow path intersects stator and rotor at equal distances ($\pm H/2$).

Time and circumferential derivatives are set to zero to obtain the steady state (zeroeth order) differential equation. The primitive constitutive and clearance variables (u, w_s, p, q, m, h) are expressed as sums of their steady state values plus their perturbation values. The latter resulting from infinitesimally small, circular, cylindrical and conical whirl orbits. Cancellation of second order terms provides the governing P.D.E.'s for the perturbation variables ($u_1, w_s, p_1, q_1, \text{ and } m_1$). The P.D.E.'s are transformed to O.D.E.'s by separating out their harmonic time and circumferential dependencies. Both zeroeth and first order problems are solved as nonlinear and linear, two point boundary value problems, respectively. Runge Kutta 4th order numerical integration is employed in both problems. Internal transition conditions of mass, energy and angular momentum conservation are imposed at the interfaces between individual components in the ILP.

Forces and moments perturbation eccentricity and angle, i.e. impedances, are determined by integrating first order pressure and shear stresses along the rotor length. Quadratic curve fits of the impedances vs whirl frequency ration yield a set of 24 independent stiffness, damping, and inertia coefficients. These dynamic coefficients or impedance functions may then be used as input to turbopump rotordynamic codes for mechanical system vibration control.

B. Examples

Various check cases were formulated to help validate the ILP modeling software. These included comparison to:

- (a) Analytical, closed form solutions for zeroeth order flow in a frictionless linear radius shroud-constant radius exit seal ILP model.

(b) Published data for dynamic coefficients of a linear-clearance tapered seal of length L . The ILP was modeled as a "constant radius" shroud of length $3L/4$ and an exit seal of length $L/4$. The radius and linear taper profile of the original seal was maintained in the ILP model.

(c) Published results of Childs' (1987) simulation of an ILP including a linear-radius profile shroud and plain annular exit seal.

The results for check case (a) show near perfect agreement as seen in Table 1. The results of check case (b) again showed near perfect agreement for leakage rate and all dynamic coefficients. The check case (c) geometry is shown in Figure 1 with parameters given in Table 2. The predicted leakage rates vs exit seal clearances showed excellent agreement with Childs' as shown in Table 3. Figure 2 shows a comparison of predicted impedances with Childs' results. Although agreement is very good for the radial impedance the tangential impedances are significantly different. The dynamic coefficients contributed by the shroud and by the seal in the ILP show fair agreement with Childs' as shown in Table 4. Discrepancies in the results may have resulted in different input data since the following parameters were not specified in Childs' model;

- * Seal Hir's constants

- * Seal inlet loss factor (assumed to be same as shroud inlet loss factor (0.1).

- * Frequency ratios used in impedance curve fit (0.5, 1.25, 2.0, used in current analysis).

- * Shroud clearance profile used by Childs (assumed to be constant at 5.8 mm).

The total coefficients for the ILP are obtained as the sums of the shroud and seal contributions in Table 4.

CONCLUSIONS

A bulk flow based computer model has been developed for obtaining ILP dynamic forces due to cylindrical and conical perturbation orbits of the shaft. These forces vary with whirl orbit frequency and are curve fit to obtain stiffness, mass, and damping coefficients. Future plans include upgrading the code to accept a more general ILP geometry, validating it against test and CFD results, and preparing a CFD based ILP code.

REFERENCES

Childs, D. W., "Fluid-Structure Interaction Forces at Pump-Impeller-Shroud Surfaces for Rotodynamic Calculation," ASME Jour. of Vibration; July, 1989, Vol. III, pp. 216-225.

Guinzburg, A., "Model Prediction and Experimental Results for the Rotordynamic Characteristics of Leakage Flows in Centrifugal Pumps," Proc. of the 10th Inter. Pump Users Sym.; pp. 41-48., 1993, Texas A&M Turbomachinery Laboratory.

Table 1. Closed form solution for frictionless flow through Shroud and Exit Wear-ring Seal

Particulars	Closed Form Solution	Current Analysis
Shroud Inlet Path Velocity, $W_s(0)$ (m/s)	0.918	0.9193
Shroud Exit Path Velocity, $W_s(L)$ (m/s)	1.361	1.3626
Shroud Inlet Pressure, $P(0)$ (N/m ²)	465,536.5	465,640.6
Shroud Exit Pressure, P (N/m ²)	26,363.2	26,420.56
Shroud Exit Swirl Velocity, $U(L)$ (m/s)	27.16	27.163
Leakage, Q (kg/s)	5.85	5.859

Table 2. Bolleter et al. Shrouded Impeller Test Results and comparison with Childs (1989)

Input Data :

$\Delta P = 0.466 \text{ MPa}$	Working Fluid: Water	$\rho = 1000 \text{ kg/m}^3$	$\mu = 1.3 \text{E-}03 \text{ Pa-s}$
Shrd Inlet Loss, $\xi = 0.1$ Seal Inlet Loss, $\xi = 0.1$	Shroud: $C_i = C_o = 5.8 \text{ mm}$ Seal: $C_i = C_o = 0.36 \text{ mm}$	Speed, $N = 2000 \text{ rpm}$	Shrd. Length $L_s = 64 \text{ mm}$ $dr/ds = -0.89$ Seal Length $l_{sl} = 33 \text{ mm}$
Shrd. Inl Dia = 175 mm Seal Inl Dia = 118 mm	Preswirl, $\gamma = 0.5$	Shroud $n_s, m_s = 0.079, -0.25$ Seal $n_s, m_s = 0.079, -0.25$	Shroud $n_s, m_s = 0.079, -0.25$ Seal $n_s, m_s = 0.079, -0.25$

Table 3. Comparison of Leakage (kg/s) with Childs (1989) for various Wear-ring seal clearances

Wear-ring seal Clearance (in mm)	Childs	Current Analysis
0.36	4.03	3.886
0.54	6.241	6.425
0.72	8.432	8.594

Table 4 ILP Dynamic Coefficients

<u>Shroud</u>			<u>Seal</u>	
<u>Coefficient</u>	<u>Current</u>	<u>Childs</u>	<u>Current</u>	<u>Childs</u>
K	64,472. n/m	60,050 n/m	1,870,000 n/m	612,000.
k	196,724. n/m	199,700 n/m	1,340,000 n/m	463,000.
C	951. N.s./m	1,200. N.s./m	7329. N.s./m.	3356.
c	105. N.s./m	682 N.s./m	440. N.s./m.	79.
M	1.09 Kg.	2.51 Kg.	3.08 Kg.	.311
m	-.715 Kg.	0.01 Kg.	-1.3 Kg.	.08

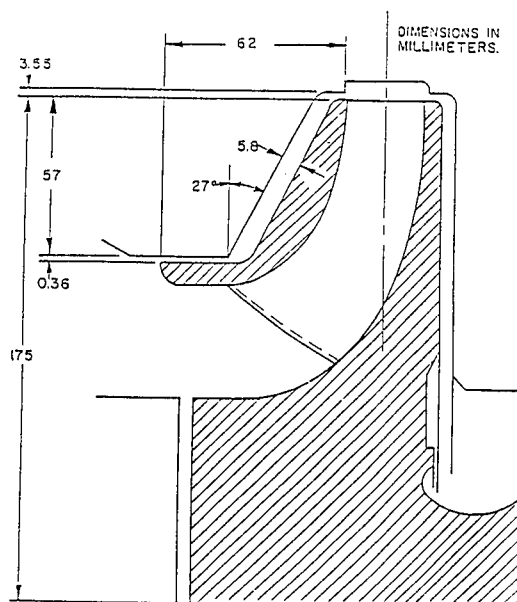


Figure 1. Example impeller; Bolleter

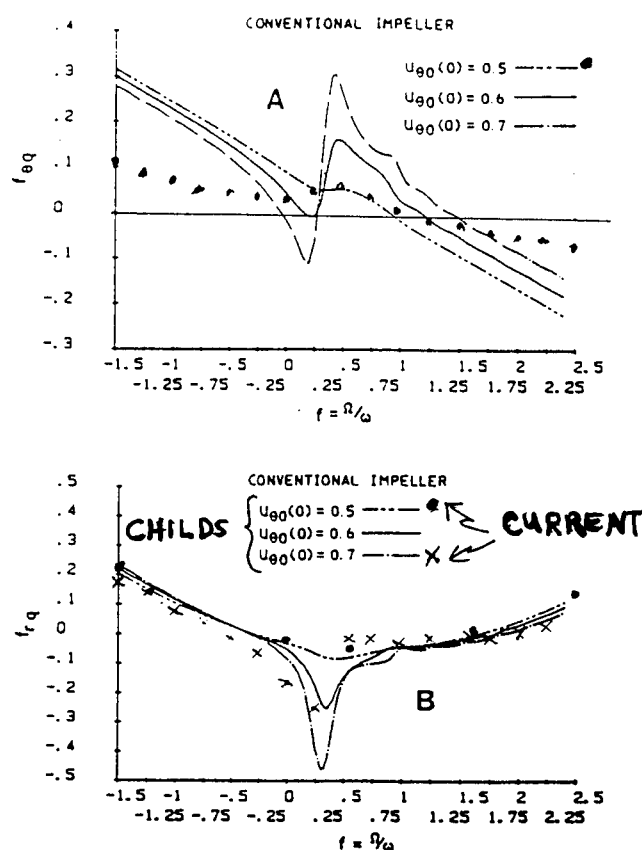


Figure 2. Nondimensional force coefficients for the conventional impeller
(a) tangential-force coefficient, (b) radial-force coefficient

1995

NASA/ASEE SUMMER FACULTY FELLOWSHIP PROGRAM

MARSHALL SPACE FLIGHT CENTER
THE UNIVERSITY OF ALABAMA IN HUNTSVILLE

DESIGN OF A NONLINEAR, THIN-FILM
MACH-ZEHNDER INTERFEROMETER

Prepared By : Earl F. Pearson, Ph.D.
Academic Rank: Professor
Institution and Department: Western Kentucky University
Department of Chemistry

NASA/MSFC:

Office: Space Sciences Laboratory
Division: Microgravity Science and Applications
Branch: Biophysics and Advanced Materials

MSFC Colleague(s): Benjamin Penn, Ph.D.
Don Frazier, Ph.D.

Optical waveguides are the optical equivalent of wires in electronic circuits. An optical waveguide is a device along which or through which a beam of light is confined to travel(1-3). The confinement is accomplished by creating a narrow channel (a few micrometers in width) with an index of refraction slightly higher than that of anything surrounding it. Assuming a glass substrate and single mode of 1.06 micron light, the change in the index of refraction between the channel and the surrounding substrate required for confinement of a light beam is about 0.01.

When two channel waveguides are placed close together, the "tail" of the light in the input channel will overlap the "tail" of light in the other channel and power will be exchanged back and forth between the two channels. As light originally focussed into channel 1 moves along the directional coupler, some of its energy is transferred into channel 2 until at some distance (called the 3db length) its power is reduced to 50% of the original power and the other 50% will reside in channel 2. At twice this distance, (called the coupling length) all of the original power input into channel 1 will be resonating in channel 2. At twice the coupling length, all the power will have returned to channel 1 and this switching back and forth continues until the light beam reaches the end of the directional coupler.

The coupling length is determined by the index of refraction, the change in the index of refraction inside the channel, the wavelength of the light and the spacing between the channels. The performance of waveguide directional couplers depends critically on the construction parameters especially film uniformity and design length. Waveguide directional couplers can be used to split a beam of light into a number of output channels and to control the relative intensity in each channel. However, they can not be used to change the total output power (switch power on and off). These considerations together with the unpredictable or unstudied influence on the properties resulting from the use of nonlinear materials make the directional coupler less attractive for initial fundamental studies.

Interference between two light beams can be used to switch output on through constructive interference and to turn output off through destructive interference. Interference between two light beams can also be used to multiplex or demultiplex signals carried at slightly different wavelength(4).

A Mach-Zehnder interferometer consists of a 3db splitter to create the two separate beams, an optical path difference to control the interference between the two beams and another 3db coupler to reconstruct the output signal. The performance of each

of its components has been investigated by Najafi, et. al.(5). Since an optical path difference is required for its function, the performance of a Mach-Zehnder interferometer is not very sensitive to construction parameters.

An optical path difference can be produced by creating a physical path difference by making one arm of the interferometer longer than the other arm or by causing the index of refraction to be different in one of the arms if they are the same length.

In addition the wavelength cutoff caused by its component waveguide parts, a Mach-Zehnder interferometer will pass wavelengths (constructive interference) which will fit evenly into the optical path difference. (The optical path difference = index * difference in length of the two arms.) Wavelengths which are halfway between any two wavelengths passed by the interferometer will be completely blocked due to destructive interference.

At any fixed wavelength, the intensity may be switched on or off by varying the index of refraction of the material composing the two arms. The index of refraction may be varied by varying the voltage of an electric field penetrating the arms of the interferometer(6), or by heating one arm of the interferometer(7). The interference may also be observed in an interferometer made of nonlinear materials by changing the intensity of light resonating in the two arms of the interferometer if the arms are of different lengths or if the light intensity is not split equally between them.

In designing an interferometer for this work, the following considerations must be observed:

1. The interferometer is to be made of phthalocyanine or polydiacetylene thin films.
2. In order to avoid thermal effects which are slower, the wavelength chosen must not be absorbed in either one or two photon processes.
3. The wavelength chosen must be easily generated (laser line.)
4. The spacing between the interferometer arms must be large enough to allow attachment of external electrodes.
5. The vapor deposition apparatus can accept disks no larger than 0.9 inches.
6. The design must allow multiple layer coating in order to determine the optimum film thickness or to change to another substance.

A symmetrical Mach-Zehnder interferometer which meets each of these requirements is illustrated in Figure 1.

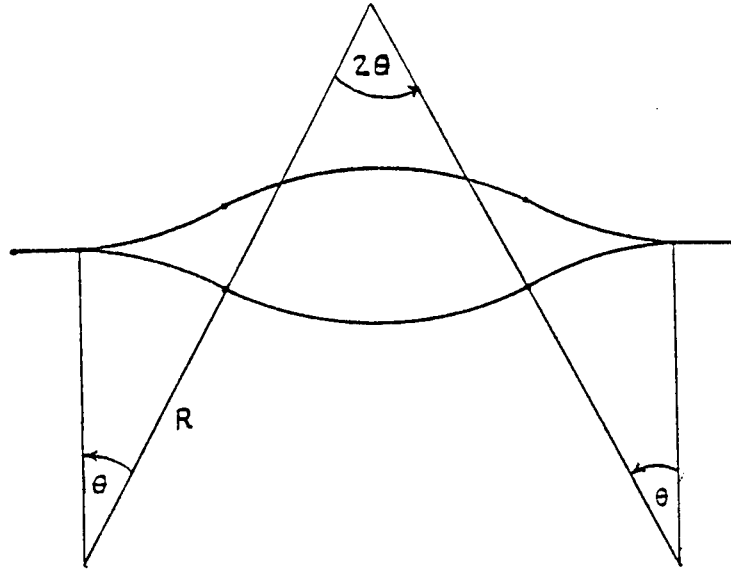


Figure 1

Each arm of the interferometer is composed of six(6) segments two short linear segments (0.05 inches) for input and output coupling, two adjacent concave outward circular arcs and two concave inward circular arcs in the middle. Each arc is the same length and has the same radius of curvature (40 mm). Studies have shown that a circular arc with a radius greater than about 60 mm behaves as if it were linear with no significant additional losses(8). Such large radii lead to insufficient spacing between the arms. Small radii which separate the arms better have significant excess bending losses. A radius of 40 mm is expected to have less than 1db excess bending loss and was chosen as an appropriate compromise. The angle of bending is calculated to be 7.30 degrees of arc. The spacing between the arms is 1.30 mm and the length of each arm is 20.38 mm.

The symmetrical design of Figure 1 may not be appropriate to the experiments involving physical vapor transport. Since there is no way to attach the electrodes after vapor coating without risking damage to the delicate film, a nonsymmetrical Mach-Zehnder interferometer is more appropriate. See Figure 2.

The difference in the length of each arm has been accomplished by bending each end about the center point while requiring that every point of intersection remain a tangent point on each of the circular arcs. The radius of curvature has been kept at 40 mm. The difference in path length of the two arms achieves a maximum with a bending angle of 8.50 degrees. This results in a concave side angle (bottom of Figure 4) of 11.54 degrees and a convex side angle of 3.09 degrees. The central angles are calculated from these two angles.

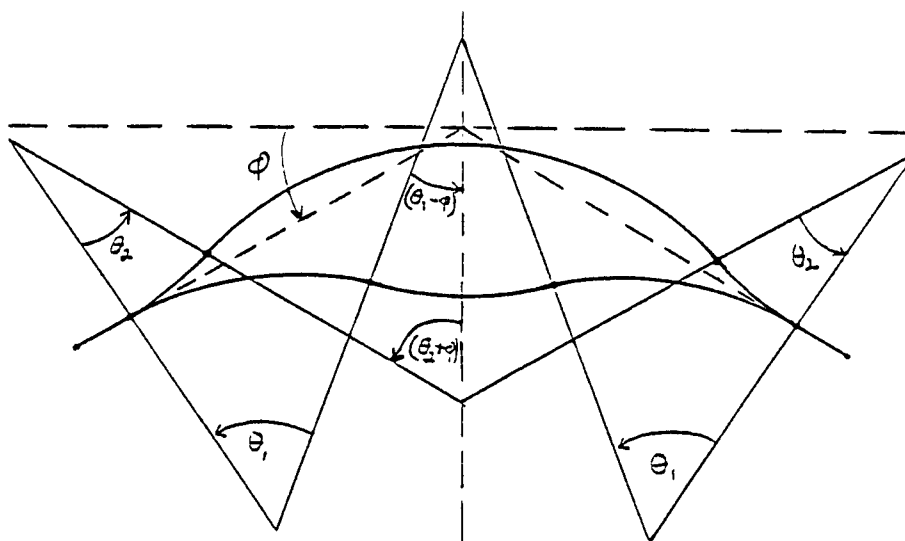


Figure 2

The master patterns will be generated using standard lithographic techniques. Photoresist is coated over a layer of gold which has been sputtered on the surface of a substrate disk. The pattern of the Mach-Zehnder interferometer is exposed on the photoresist and developed exposing the gold in the areas of the arms of the interferometer. Argon ion milling removes the gold without removing the photoresist or the gold under it which surrounds the interferometer. The unexposed photoresist is then washed away completing the fabrication of the master pattern. These master patterns can be used to create duplicate patterns for use in experimental studies. Electrodes may be attached to the gold if the electro-optical effect is to be investigated. The symmetrical pattern with attached electrodes is ideal for the polydiacetylene studies.

A more robust pattern may be generated for the unsymmetrical Mach-Zehnder interferometer using buried potassium ion channel waveguides. The technology for constructing ion-exchanged channel waveguides has been thoroughly investigated (9-13). The Mach-Zehnder interferometer can be fabricated by immersion of a duplicate of the master pattern on soda-lime glass in molten potassium nitrate. The potassium ions migrate through the openings in the pattern and exchange with sodium ions in the glass substrate. Since potassium ions are larger than sodium ions, stress birefringence is produced in the glass surface. This increases the index of refraction in the channels under the openings in the mask. By regulation of the temperature and time of immersion, the depth of the potassium channel can be adjusted to match any wavelength one wishes to guide.

The temperature and time of immersion should be adjusted to

guide at the second harmonic of the YAG laser (532 nm) but not long enough to permit guiding at the fundamental (1064 nm). The gold pattern may be removed (ion milling which would also clean and polish the surface) and the entire surface coated by vapor deposition with a phthalocyanine film. The thickness of the film should be adjusted to allow guiding at 1064 nm AT LOW INTENSITY. The entire surface should then be coated with an index-matching optical epoxy and a cover disk attached.

LITERATURE CITED

1. R. G. Hunsperger, Integrated Optics: Theory and Technology, Springer-Verlog, 1984 Chapter 12.
2. William K. Burns, "Normal Mode Analysis of Waveguide Devices. Part I: Theory", J. Lightwave. Tech nol., 1988, 6(6), 1051-7.
3. William K. Burns, "Normal Mode Analysis of Waveguide Devices. Part II: Device Output and Crosstalk", J. Lightwave Technol., 1988, 6(6), 1058-68.
4. A.Guangwen Zhang, Seppo Honkanen , Ari Tervonen, Chun-Meng Wu, and S. Iraj Najafi , "Glass integrated Optics Circuit for 1.48/1.55 and 1.30/1.55 Micron-Wavelength Division Multi-plexing and 1/8 Splitting", Appl. Opt., 1994, 33(16), 3371-74
5. I. Najafi, P. Lefebvre, J. Albert, S. Honkanen, Vahid-Shahidi and W. J. Wang, "Ion-Exchanged Mach-Zehnder Interferometers in Glass" , Appl. Opt., 1992, 31(18), 3381-83.
6. Thomas A. Tumolillo, Jr. and Paul R. Ashley, "Multilevel Registered Polymeric Mach-Zehnder Intensity Modulator Array", Appl. Phys. Lett., 1993, 62(24), 3068-70.
7. J. L. Jackel, J. J. Veselka and S. P. Lyman, "Thermally Tuned Glass Mach-Zehnder Interferometer Used as a Polarization Insensitive Attenuator", Appl. Opt., 1985, 24(5), 612-14.
8. P. Lefebvre, A. Vahid-Shahidi, J. Albert and S. I. Najafi, "Integrated Optical Mach-Zehnder Interferometers in Glass", SPIE, Integrated Optical Circuits, 1991, 1583, 221-25.
9. R. V. Ramaswamy and R. Srivastava, "Ion-Exchanged Glass Waveguides: A Review", J. Lightwave Technol., 1988, 6(6), 984-02.
10. T. Findakly, "Glass Waveguides by Ion Exchange: A Review", Opt. Eng., 1985, 24(2), 244-50 .
11. G. L. Yip and J. Albert, "Characterization of Planar Optical Waveguides by K-ion Exchange in Glass", Opt. Lett., 1985, 151-53.
12. Janet L. Jackel, " Glass Waveguides Made Using Low Melting Point Nitrate Mixtures", Appl. Opt., 1988, 27(3), 472-75.
13. Prafulla J. Masalkar, V. Venkateswara Rao and Rajpal S. Sirohi, "Design and Fabrication of Single Mode Waveguides in Glass by Inverse Ion-exchange", SPIE, Integrated Optical Circuits II, 1992, 271-76.

1995

NASA/ASEE SUMMER FACULTY FELLOWSHIP PROGRAM

**MARSHALL SPACE FLIGHT CENTER
THE UNIVERSITY OF ALABAMA IN HUNTSVILLE**

**DEVELOPMENT OF A LOW-COST VIRTUAL REALITY WORKSTATION
FOR TRAINING AND EDUCATION**

Prepared by:	James A. Phillips, Ph.D.
Academic Rank:	Senior Research Fellow
Institution and Department:	California Institute of Technology Division of Physics, Math, and Astronomy
NASA/MSFC:	
Office:	Mission Operations Laboratory
Division:	Operations Engineering
Branch:	Crew Systems Engineering
MSFC Colleague:	Joseph P. Hale, M.S., C.H.F.P.

DEVELOPMENT OF A LOW-COST VIRTUAL REALITY WORKSTATION FOR TRAINING AND EDUCATION

1. INTRODUCTION

Virtual Reality (VR) is a set of breakthrough technologies that allow a human being to enter and fully experience a 3-dimensional, computer simulated environment. A true virtual reality experience meets three criteria:

1. It involves 3-dimensional computer graphics.
2. It includes real-time feedback and response to user actions.
3. It must provide a sense of immersion.

Good examples of a virtual reality simulator are the flight simulators used by all branches of the military to train pilots for combat in high performance jet fighters. The fidelity of such simulators is extremely high -- but so is the price tag, typically millions of dollars.

Virtual reality teaching and training methods are manifestly effective, but the high cost of VR technology has limited its practical application to fields with big budgets, such as military combat simulation, commercial pilot training, and certain projects within the space program. However, in the last year there has been a revolution in the cost of VR technology. The speed of inexpensive personal computers has increased dramatically, especially with the introduction of the Pentium processor and the PCI bus for IBM-compatibles, and the cost of high-quality virtual reality peripherals has plummeted. The result is that many public schools, colleges, and universities can afford a PC-based workstation capable of running immersive virtual reality applications. My goal this summer was to assemble and evaluate such a system.

2. THE PC VIRTUAL REALITY STATION

The first point in the 3-point definition of Virtual Reality, above, involves 3D computer graphics. The rule of thumb in digital video is that an animation must run at least 15 frames/sec to appear smooth to the human eye, so I adopted 15 frames/sec as a benchmark for evaluating PC performance. I benchmarked four different PC systems using the Sense8 WorldToolKit software to render a virtual reality scene consisting of approximately 750 polygons. The results for shaded and shaded+textured polygons are tabulated below. Only the Pentium systems gave frame rates for complicated simulations that were above 15 frames/s. A comparison of the two 486-based systems shows similar frame rates despite the factor of two difference in system RAM. In fact, the 80 MHz system with only 8MB of RAM outperformed the 66 MHz system with 16 MB RAM by a factor of 1.21, almost exactly the ratio of the clock speeds. The relative frame rates of the two Pentium systems also scaled with clock speed, the 120 MHz system being about 25% faster than the 90 MHz system. (Note, however, that the 120 MHz Pentium had a 4 MB graphics board while the 90 MHz system had a 2 MB board.)

TABLE 1: PC Performance comparisons

Processor	Clock	RAM	Graphics Accelerator	Shaded frames/s	Textured frames/s
486DX	66 MHz	16 MB	Cirrus Logic w/1 MB ram	7.5	4.0
486DX	80 MHz	8 MB	Trident 9440CX w/1 MB ram	9.1	3.6
Pentium	90 MHz	32 MB	ATI Mach 64 w/2 MB ram	16.7	7.5
Pentium	120 MHz	32 MB	ATI Mach 64 w/4 MB ram	21.0	9.0

From Table 1 we see that a 90 MHz Pentium system, or better, will give adequate 3D graphics rendering performance.

The second point in the 3-point definition of Virtual Reality was real-time interaction to user input. The participant in a VR simulation must be able to navigate through the virtual world, select objects, and move them. I tested three devices for user interaction with WorldToolKit applications: a mouse, a Logitech Cyberman (6 degree-of-freedom mouse with limited tactile feedback), and a ThrustMaster joystick. I also tested the VPL DataGlove and a Spatial Systems Spaceball (6 degree-of-freedom controller) using VPL VR simulation software. For picking and moving objects, the DataGlove was by far the best. For navigation the ThrustMaster joystick was best. The mouse was unintuitive and difficult to learn as a navigation device, as was the Spaceball. The LogiTech Cyberman was awful. I tested two Cybermen and both were poorly constructed, overly sensitive, and nearly impossible to control. The simple tactile feedback feature (a pulse modulation of the controller stem triggered by hitting virtual walls or other objects) was satisfying but did not compensate for the other shortcomings of the device. In Table 2 I rate the peripherals on a scale of 1 to 10 (10 is best, 1 is worst) in two categories: "Picking" refers to the ease with which objects could be selected or grabbed with the device, and "Flying" refers to navigation through the virtual environment. The ratings are subjective, and are based on my own experience with the devices, and the experience of students aged 5 to 12 years who have tested the PC with a VR Human Cadaver application developed at the MSFC virtual reality lab.

TABLE 2: EVALUATION OF VR PERIPHERALS

Device:	Picking	Flying
Microsoft Mouse	8	3
Logitech Cyberman	5	1
VPL DataGlove	9	7
SpaceBall	6	6
ThrustMaster Joystick	N/A	9

Finally, the third point in my definition of Virtual Reality is that the experience must be immersive. Immersion means that you forget about all outside stimuli and become a

thinking, feeling part of the computer's virtual world. In theory, total immersion would include touch, smell, temperature, visual input, and sounds. In practice, it is difficult, expensive, and, fortunately, unnecessary to attack all 5 senses to produce a sense of immersion. I find that the visual cues provided by a wide-field-of-view head-mounted display in combination with 3-dimensional sound effects are sufficient to create a powerful immersive effect. The mind fills in the gaps not covered by the HMD and the 3D sound hardware.

2.1 3D SOUND FOR THE PC

3D sound technology operates on the principle that all the spatial information about a sound source is contained in its spectrum. At its source the complex Fourier spectrum of a sound is $S(f)$, where f is the frequency. The acoustic wave propagates to both ears and is filtered by reflections off the human body, primarily the head and shoulders, and the inner ear. When the sound reaches the inner ear, its complex spectrum is $T_L(\mathbf{n},f)S(f)$ in the left ear and $T_R(\mathbf{n},f)S(f)$ in the right ear; \mathbf{n} is the unit direction vector toward the sound source and T is the "transfer function." The product $T(\mathbf{n},f)S(f)$ in the frequency domain can be expressed as a convolution in the time domain $T(\mathbf{n},t)*S(t)$, and this is the basis of practical 3D sound devices.

The Alphasatron is an expansion card for the PC, sold by Crystal River Engineering, that performs the 3D sound convolution. The head-related transfer function, $T(\mathbf{n},t)$, is loaded into a digital signal processor on a Tahiti MultiSound card, and up to 16 user-defined sounds, $S(t)$, can be spatialized in real time. The cost of the system is \$750 retail, and I have successfully incorporated 3D sound effects in WorldToolKit applications using the Alphasatron.

2.2 HEAD-MOUNTED DISPLAYS

In 1994 Virtual I/O released the *iglasses!*, the first high-quality HMD for under \$1000. The *iglasses!* feature a 25 deg (H) x 9 deg (V) field of view, with 640 x 480 active matrix pixels. It weighs only 8 oz. and features a superb ergonomic design. The restricted field of view is the main limitation of this device, but for the price (\$850 retail) it can't be beat for low-cost educational applications. A far better HMD is the VR4 by Virtual Research, Inc. It features a 48 deg (H) x 30 deg (V) field of view with resolution comparable to that of the *iglasses!*. The wide field-of-view is critical for total immersion simulations, and the VR4 would be the helmet of choice except for its price tag, \$7000, which makes it impractical for most classroom situations.

Finally, I note that WorldToolKit is the software of choice for PC-based VR applications because of its support for nearly all the VR peripherals on the market today. Sense8 rapidly introduced a driver for the *iglasses!* very soon after the product was released, and third party software vendors, like Crystal River Engineering, are working to make their library calls compatible with WorldToolKit conventions.

3. CONCLUSIONS

I have assembled a low-cost virtual reality workstation for education applications using off-the-shelf technology. The least expensive system which meets all the criteria for an acceptable VR platform consists of the following:

- a 90 MHz Pentium CPU with 32 MB system RAM
- video graphics accelerator with at least 2 MB on-board RAM
- a Thrustmaster joystick for navigation
- a Microsoft mouse for object-picking
- a Virtual I/O *iglasses!* HMD with 25x9 deg field of view and 640x480 pixel resolution
- a Crystal River Engineering Alphasatron for 3D sound spatialization

The total retail cost of the system, including a 15" VGA monitor and a WorldToolKit run-time license is about \$6000. The ideal PC-based system would include a DataGlove for object-picking, but the cost would increase by 30%. A mouse, for only \$29, is a reasonable trade-off. Three years ago a system with the same capabilities would have cost at least an order of magnitude more. With prices still dropping and capabilities increasing I predict that the next year will see increasing numbers of classrooms equipped with VR workstations.

1995

NASA/ASEE SUMMER FACULTY FELLOWSHIP PROGRAM

**MARSHALL SPACE FLIGHT CENTER
THE UNIVERSITY OF ALABAMA IN HUNTSVILLE**

**USING NATURALLY OCCURRING POLYSACCHARIDES TO ALIGN
MOLECULES WITH NONLINEAR OPTICAL ACTIVITY**

Prepared By:	Thomas Prasthofer, Ph.D.
Academic Rank:	Assistant Professor of Biochemistry
Institution and Department:	Albany College of Pharmacy Department of Physical Sciences and Mathematics
NASA/MSFC:	
Office:	Life and Microgravity Sciences and Applications
Division:	Microgravity Science and Applications
Branch:	Biophysics and Advanced Materials
MSFC Colleague(s):	Donald Frazier, Ph.D. Mark S. Paley, Ph.D.

INTRODUCTION:

The Biophysics and Advanced Materials Branch of the Microgravity Science and Applications Division at Marshall Space Flight Center has been investigating polymers with the potential for nonlinear optical (NLO) applications for a number of years. Some of the potential applications for NLO materials include optical communications, computing, and switching. To this point the branch's research has involved polydiacetylenes, phthalocyanins, and other synthetic polymers which have inherent NLO properties.

The aim of the present research is to investigate the possibility of using naturally occurring polymers such as polysaccharides or proteins to trap and align small organic molecules with useful NLO properties. Ordering molecules with NLO properties enhances 3rd order nonlinear effects and is required for 2nd order nonlinear effects. Potential advantages of such a system are the flexibility to use different small molecules with varying chemical and optical properties, the stability and cost of the polymers, and the ability to form thin, optically transparent films. Since the quality of any polymer films depends on optimizing ordering and minimizing defects, this work is particularly well suited for microgravity experiments. Polysaccharide and protein polymers form microscopic crystallites which must align to form ordered arrays. The ordered association of crystallites is disrupted by gravity effects and NASA research on protein crystal growth has demonstrated that low gravity conditions can improve crystal quality.

EXPERIMENTAL APPROACH:

Ordered structures are a central theme in biological systems so nature is a logical place to look for polymers which might be used to trap and orient small organic molecules with desirable NLO properties. Cellulose and chitin are the primary structural polysaccharides found in plants and arthropods. Both polymers have been shown to produce transparent thin films from dilute suspensions *in vitro* (1-3). These films are composed of crystallites (small crystals of polymer) which self-assemble into chiral nematic ordered structures which arise from the formation of hydrogen-bonding networks between strands of polymers and between the surfaces of crystallites. Some organic molecules, para-nitroaniline (PNA) for example, possess desirable NLO properties and are capable of forming hydrogen bonds. The intent of this research is to investigate the possibility of incorporating molecules like PNA into the hydrogen bonding networks of chitin or cellulose in such a way that the PNA molecules align with each other. This would enhance the molecule's NLO properties and the result would be a chemically stable, transparent thin film which might be used for the production of NLO devices.

There are at least three ways in which one might incorporate a molecule like PNA into chitin or cellulose thin films. PNA could be trapped between crystallites as a film deposits on a surface, PNA could be trapped between strands of denatured polysaccharide during renaturation, or PNA could be chemically linked to polysaccharide chains. Thus far the experiments have been limited to the first method. Chitin or cellulose are treated with acid to leave only crystalline forms of polysaccharide intact. Dilute mixtures of the purified crystallites are then sonicated to form suspensions in the presence or absence of PNA. Clear films with and without PNA have been prepared from chitin on quartz and glass substrates. The films produced thus far have been examined using light microscopy to determine the degree of ordering and Z-scan to determine NLO X3 values. Transmission electron microscopy are underway.

The results thus far (8/1/95) are inconclusive. The chiral nematic ordering of our chitin thin films has not been clearly demonstrated. It is not clear whether the conditions for film formation require modification or if the instrument being used is adequately equipped to detect order using crossed-polars microscopy. The Z-scans performed on a number of samples do show nonlinear

absorption by chitin films containing PNA but further Z-scans using a picosecond pulsed laser are required to determine non-thermal nonlinear effects which are the values of real importance for NLO devices. Transmission electron microscopy of the films requires materials which are not currently available on site.

This work will be continued at Albany College of Pharmacy in collaboration with my colleagues at MSFC.

CONCLUSIONS:

It is still unclear whether chitin and/or cellulose thin films containing PNA can be used in the construction of NLO devices. We have made stable, transparent films of chitin both with and without PNA but further characterization is required before can evaluate the success of the project so far.

ACKNOWLEDGMENTS:

I would like to express my appreciation for the cooperation I received from my NASA colleague, Don Frazier and my USRA colleague Steve Paley. David Donovan facilitated much of my progress and worked with very little to do much. Hossin Abdeldeyem performed Z-scans on chitin films and Don Gilles performed TEM.

REFERENCES:

Revol, J.-F. and Marchessault, R.H. In vitro chiral nematic ordering of chitin crystallites. Int. J. Macromol. **15**: 329-335. 1993

Revol, J.-F., Bradford, H., Giasson, J., Marchessault, R.H., and Gray, D.G. Helicoid self-ordering of cellulose microfibrils in aqueous suspension. Int. J. Macromol. **14**: 170-172. 1992

Madeleine, M. and Guille, G. Liquid order of biopolymers in cuticles and bone. Microscopy Res. and Tech. **27**: 420-428. 1994.

1995

NASA/ASEE SUMMER FACULTY FELLOWSHIP PROGRAM

**MARSHALL SPACE FLIGHT CENTER
THE UNIVERSITY OF ALABAMA IN HUNTSVILLE**

WELDING REWORK DATA ACQUISITION AND AUTOMATION

Prepared By:	Peter L. Romine, Ph.D.
Academic Rank:	Associate Professor
Institution and Department:	Florida International University Department of Electrical and Computer Engineering
NASA/MSFC:	
Laboratory:	Materials and Processes
Division:	Metallic Materials and Processes
Branch:	Metals Processes
MSFC Colleague:	Kirby Lawless

Introduction

Aluminum-Lithium is a modern material that NASA MSFC is evaluating as an option for the aluminum alloys and other aerospace metals presently in use. The importance of aluminum-lithium is in its superior weight to strength characteristics. However, aluminum-lithium has produced many challenges in regards to manufacturing and maintenance. The solution to these problems are vital to the future uses of the shuttle for delivering larger payloads into earth orbit and are equally important to future commercial applications of aluminum-lithium. The Metals Processes Branch at MSFC is conducting extensive tests on aluminum-lithium which includes the collection of large amounts of data. This report discusses the automation and data acquisition for two processes: the initial weld and the repair. The new approach reduces the time required to collect the data, increases the accuracy of the data, and eliminates several types of human errors during data collection and entry..

The same material properties that enhance the weight to strength characteristics of aluminum-lithium contribute to the problems with cracks occurring during welding, especially during the repair/rework process. The repairs are required to remove flaws or defects discovered in the initial weld, either discovered by x-ray, visual inspection, or some other type of non-destructive evaluation. It has been observed that cracks typically appear as a result of or beyond the second repair. MSFC scientists have determined that residual mechanical stress introduced by the welding process is a primary cause of the cracking. Two obvious solutions are to either prevent or minimize the stress introduced during the welding process, or remove or reduce the stress after the welding process and MSFC is investigating both of these.

Planishing Automation

The goal this summer was to discover approaches and implement a system for automating the planishing process which is used to reduce the residual mechanical stress after the weld is made. When two pieces of aluminum-lithium are welded together, a filler material is added to the molten weld pool to compensate for the original material missing in the gap between the two parts. This is required to provide a uniform thickness in the finished part. As this molten portion cools, the mechanical forces reach an equilibrium. In the repair process this equilibrium is disturbed when only a portion of the original seam is remelted and then cooled, resulting in a deformity or shrinkage in the part along the area of the repair. In practice, cracks start to appear during and after the second repair. In the planishing process, a pneumatic hammer is used to pound the material back towards the original shape, and in so doing reducing the residual stress introduced by the repair, Figure 1. Thus allowing multiple repairs to be made without cracks.

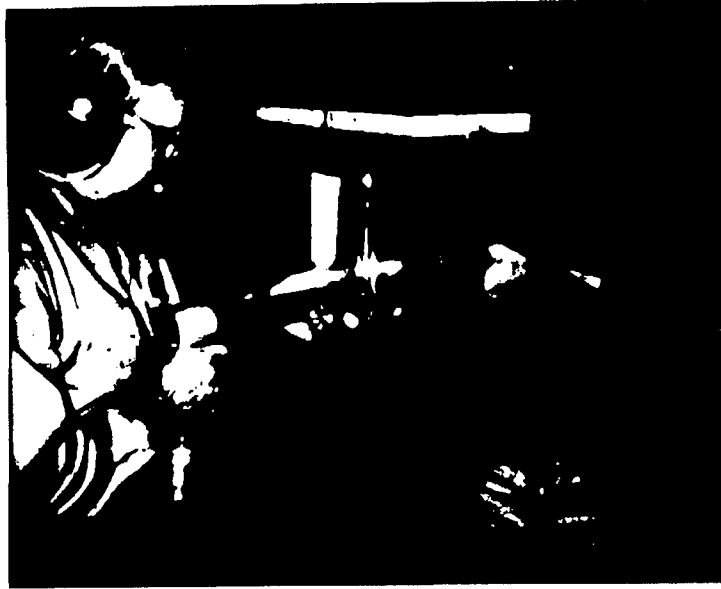


Figure 1. A pneumatic hammer is being used to planish a repair weld.



Figure 2. Measurements being taken along the repair weld.

The location and amount of distortion or shrinkage must be determined to make the planishing work. The two approaches that have been considered are by mechanical measurement and optical or image processing. The mechanical measurement method is the one currently in use and requires the welder to use calipers to make measurements along the welded seam after the original weld to determine the baseline curve, Figure 2. The number of measurements must be sufficient to illustrate the shrinkage that will appear during the subsequent repairs, typically about one measurement per inch. The measurements are hand entered into a spreadsheet for documentation, processing and plotting, Table 1.

Table 1. Measurements taken during the planishing process in an Excel sheet.

Panel ID m201				Thickness .200"		Date: 6/15/95						
Pneumatic Hammer Planishing												
2195	4043	4043										
		Face Measurement										
		-2	-1	0	1	2	3	4	5	6	7	8
Pass	Pre - Planish		2.000	1.992	1.985	1.983	1.984	1.986	1.990	1.997	2.003	
1	1" 25 PSI, (3.5 to 2.5), Gun Root		2.001	1.994	1.990	1.992	1.994	1.991	1.991	1.998	2.004	
2	4", 25 PSI, (5 to 1), Gun Root		2.003	2.002	2.003	2.003	2.002	2.001	1.999	2.001	2.004	
3	8", 25 PSI, (-1 to 7.0), Gun Face		2.007	2.008	2.008	2.008	2.007	2.007	2.007	2.008	2.009	
4												
5												
6												
7												
8												
9	Progress 3	#VALUE!	100.000	106.667	104.545	104.167	100.000	100.000	100.000	110.000	150.000	#DIV/0!
10	Progress 2	#VALUE!	42.857	66.667	81.818	83.333	78.261	71.429	52.941	40.000	25.000	#DIV/0!
Initial Weld-->-->-->			2.007	2.007	2.007	2.007	2.007	2.007	2.007	2.007	2.007	
Shrinkage		0.000	2.000	1.992	1.985	1.983	1.984	1.986	1.990	1.997	2.003	0.000
		#VALUE!	0.007	0.015	0.022	0.024	0.023	0.021	0.017	0.010	0.004	0.000
Target 90%		#VALUE!	2.006	2.006	2.005	2.005	2.005	2.005	2.005	2.006	2.007	0.000

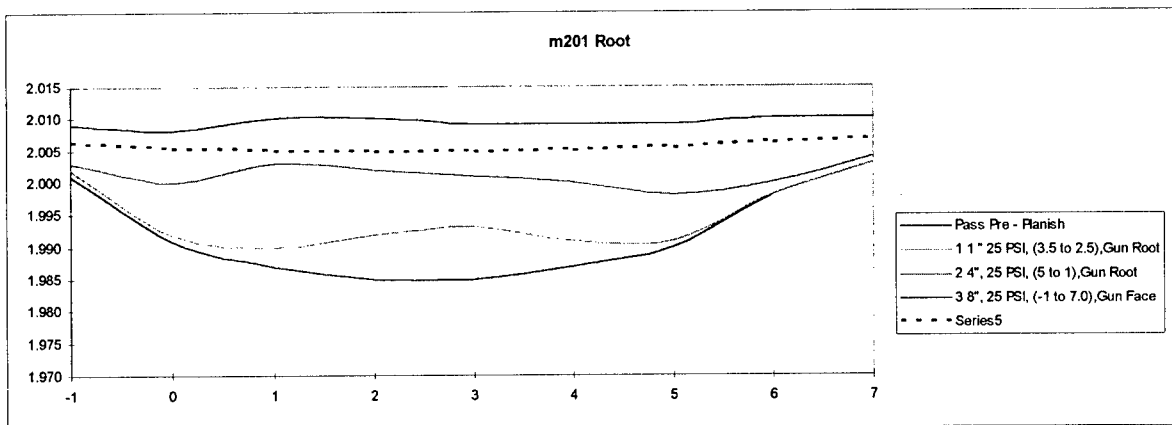


Figure 3. Recovery curves plotted to illustrate planishing progress.

Measurements are then made after each repair pass and plotted to determine the amount of shrinkage, typically from one to five repair passes. The amount and location for planishing is

then determined by visually comparing the original baseline curve to the current repair curve. The measurement process must then be repeated for each planishing phase to determine how well the shrinkage is being removed or recovered. The recovery curves are then visually compared to the desired recovery curve to determine if additional planishing is required, Figure 3.

Planishing Automation

Obviously, the total number of measurements can become very large for a repair, the use of over a hundred test points is sometimes required. This requires a lot of time and presents many opportunities for errors. The solution chosen was to utilize digital calipers and customized software to directly enter the measurements into the computer. The requirements were that the operation of the tool be intuitive enough to require minimal training for welders that might have no formal computer training or experience. Microsoft Visual Basic was chosen to implement the tool because of its rapid prototyping features for graphical user interfaces. The toolbar for the application is shown in Figure 4 and a sample data screen is shown in Figure 5.

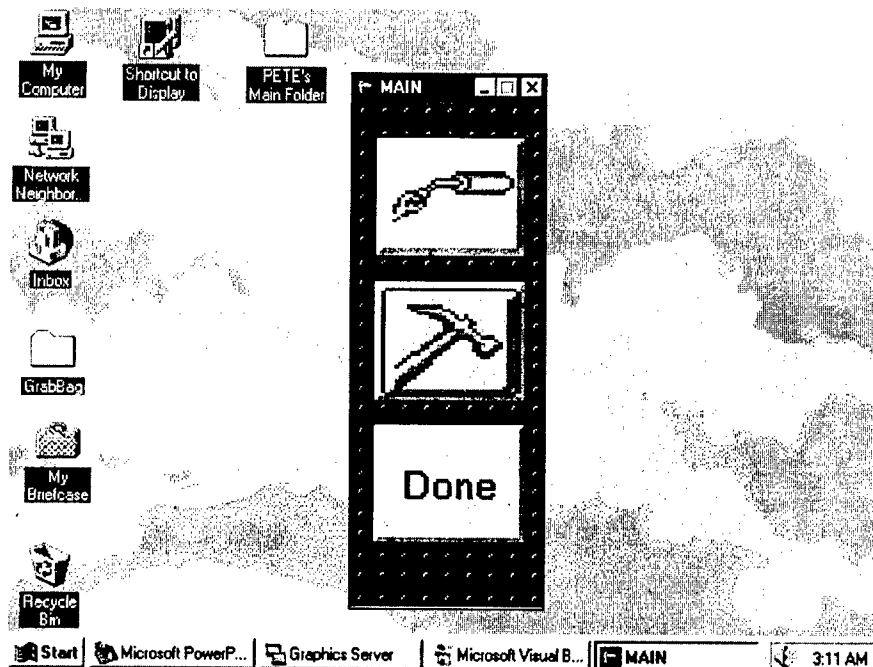


Figure 4. Opening toolbar for the planishing application.

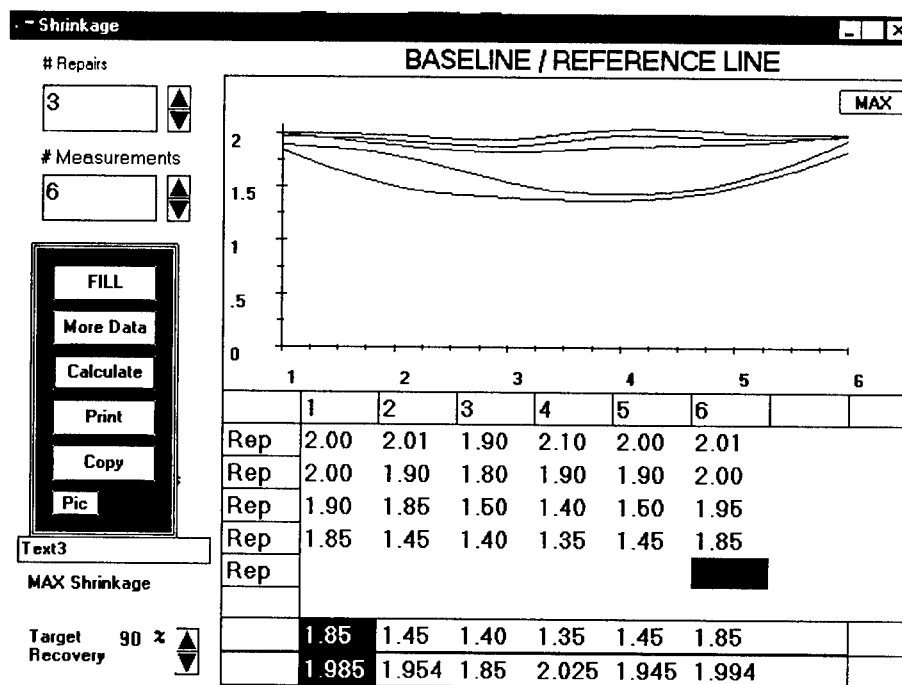


Figure 5. Sample data screen for the planishing application.

Summary and Conclusion

The idea of the planishing application tool has received a very positive response from the welding engineers and scientists. Direct entry of the shrinkage measurements into the computer will significantly reduce the time consumed by this process and eliminate most sources of error encountered during the repair and planishing process. It has been determined that a superior approach will be to embed a simplified data entry tool into an automated spreadsheet. This combination will open-up the additional analytical and presentation powers of modern spreadsheet technology that would otherwise require prohibitive programming efforts. The resulting tool can still be designed to be non-intimidating to the diverse family of welding engineers.

Other potential candidates for automation in the data acquisition and documentation processes were discovered during the summer. One of these included automating the measurement of travel speed during a manual repair weld. A voice-activated approach was considered but sufficient time was not available to implement an actual tool.

Acknowledgment

The accomplishments of this summer would not have been possible without the technical input and direction from my NASA colleague, Kirby Lawless of the Metals Processes Branch. I would also like to thank and commend all of the SFFP administrators and staff for a professionally and smoothly operated program.

1995

NASA/ASEE SUMMER FACULTY FELLOWSHIP PROGRAM

MARSHALL SPACE FLIGHT CENTER
THE UNIVERSITY OF ALABAMA IN HUNTSVILLE

TECHNOLOGY READINESS LEVELS AND TECHNOLOGY
STATUS FOR SELECTED LONG TERM/HIGH PAYOFF
TECHNOLOGIES ON THE RLV PROGRAM

Prepared By:	Russell L. Rosmait
Academic Rank:	Associate Professor
Institution and Department:	Pittsburg State University Department of Engineering Technology
NASA/MSFC:	
Office:	Engineering Cost Group
Division	Program Planning
Branch	Program Deveploment
MSFC Colleague:	Joseph W. Hamaker

Introduction

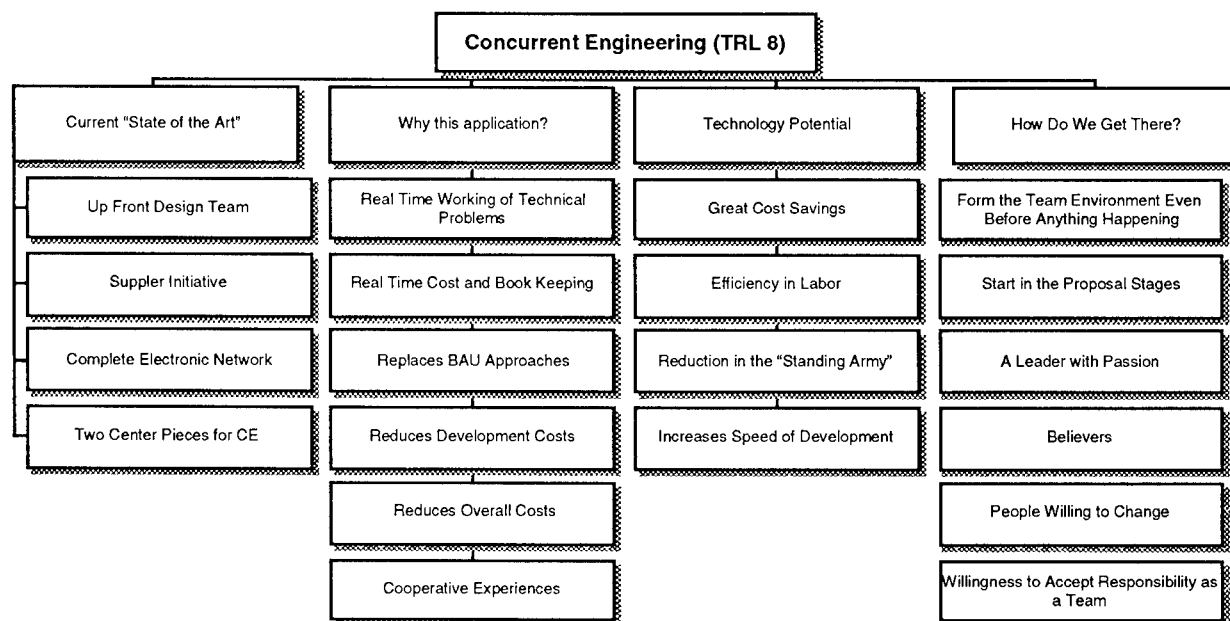
The development of a new space transportation system in a climate of constant budget cuts and staff reductions can be and is a difficult task. It is no secret that NASA's current launching system consumes a very large portion of NASA funding and requires a large army of people to operate & maintain the system. The new Reusable Launch Vehicle (RLV) project and it X programs are faced with a monumental task of making the cost of access to space dramatically lower and more efficient than NASA's current system. With pressures from congressional budget cutters and also increased competition and loss of market share from international agencies RLV's first priority is to develop a "low-cost, reliable transportation to earth orbit." (Austin 94)

One of the RLV's major focus in achieving low-cost, reliable transportation to earth orbit is to rely on the maturing of advanced technologies. The technologies for the RLV are numerous and varied. Trying to assess their current status, within the RLV development program is paramount. There are several way to assess these technologies. One way is through the use of Technology Readiness Levels (TRL's).

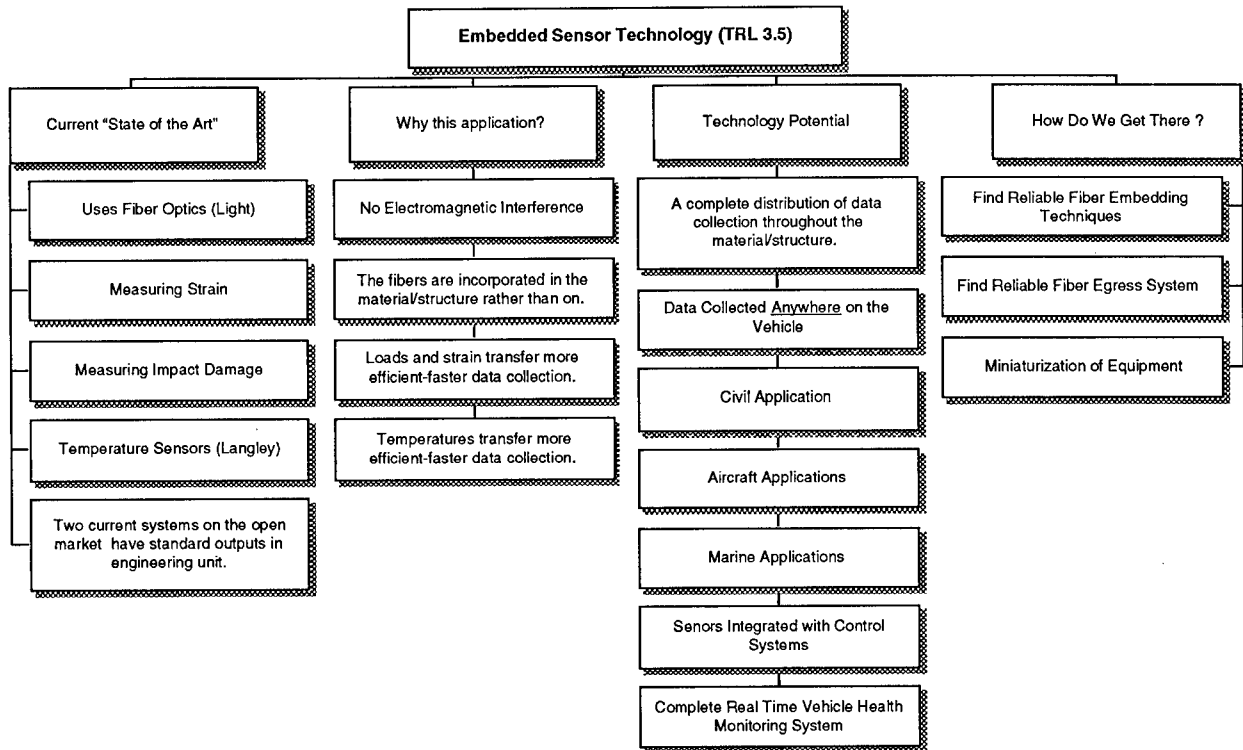
The Project

This project focused on establishing current (summer 95) worst case TRL's for six selected technologies that are under consideration for use within the RLV program. The six technologies evaluated were Concurrent Engineering, Embedded Sensor Technology, Rapid Prototyping, Friction Stir Welding, Thermal Spray Coatings and VPPA Welding.

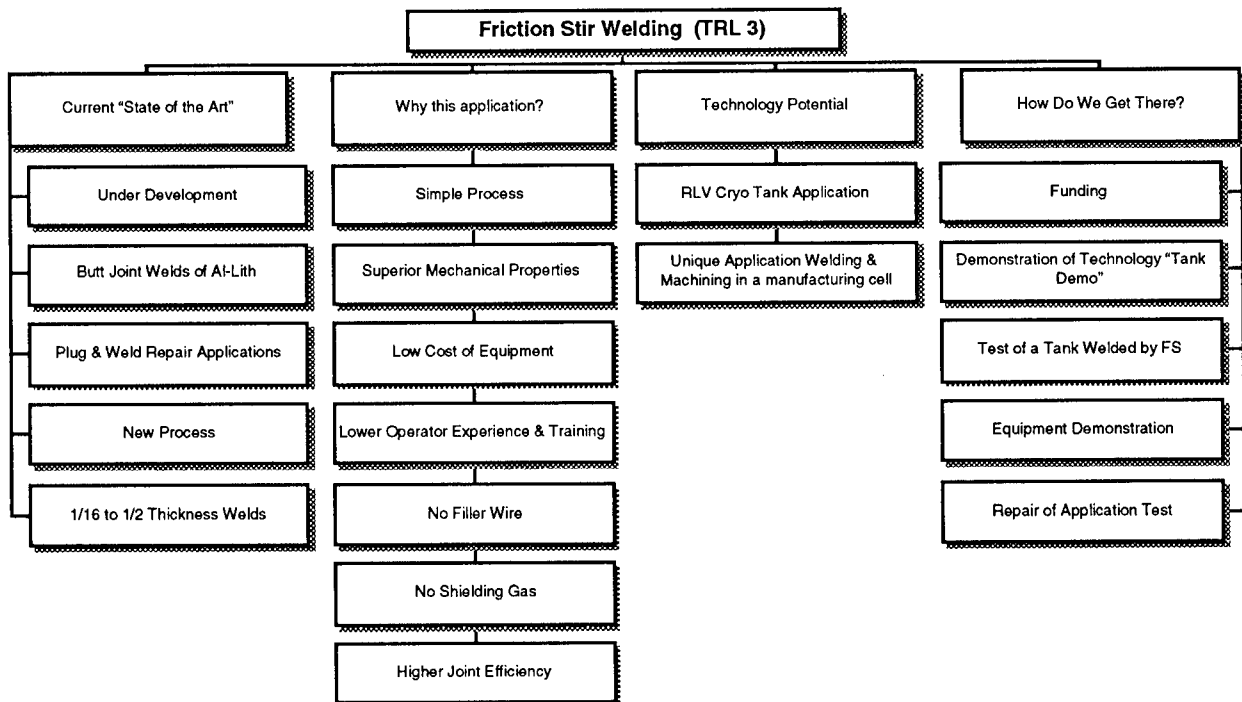
In order to establish the TRL's for these areas this project evaluated these technologies to determine there status from within four simple categories. These categories are 1) Current State of Art for the technology, 2) Why this application should be considered?, 3) The Technology Potential for the given application or technology, and 4) How Do We Get There? What needs to be accomplished to benefit from the technology. The following is a summary of the data collected. It is presented in tree chart form for ease of presentation



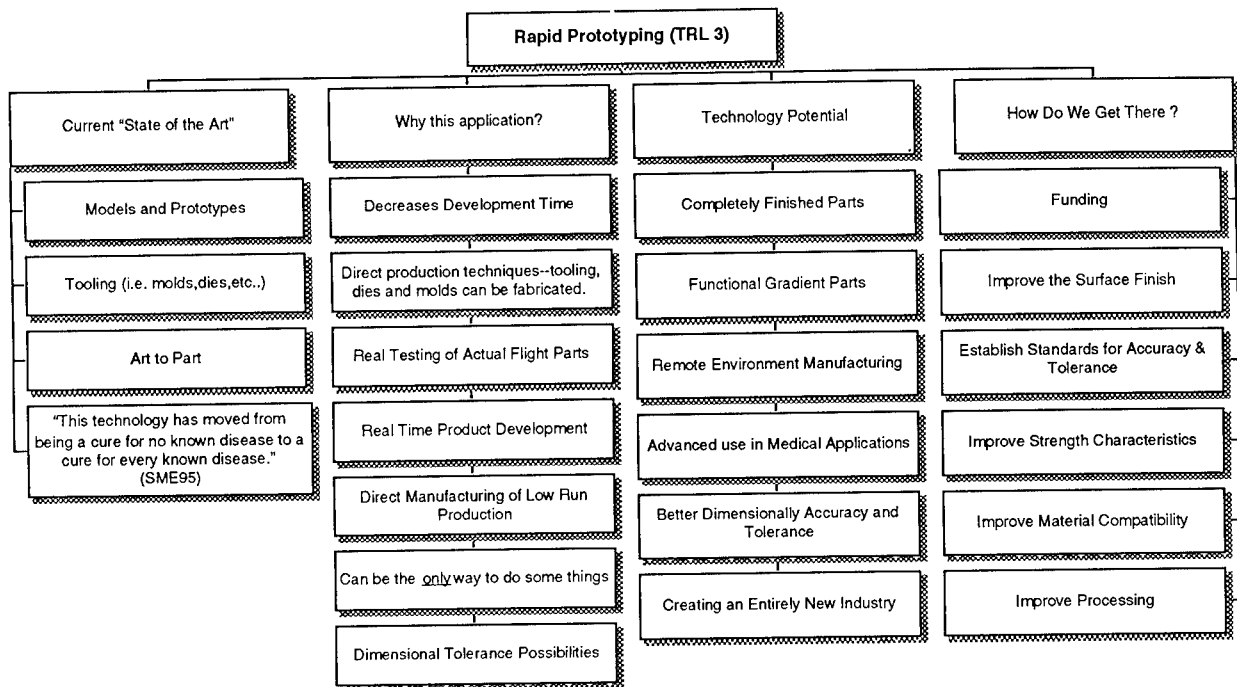
Concurrent Engineering - is a product design system/approach that integrates design personnel, manufacturing personnel and product support within the development phase of a product and transfers ideas throughout the products life cycle. The tree chart above is an overview of concurrent engineering and its potential benefit to the RLV program.



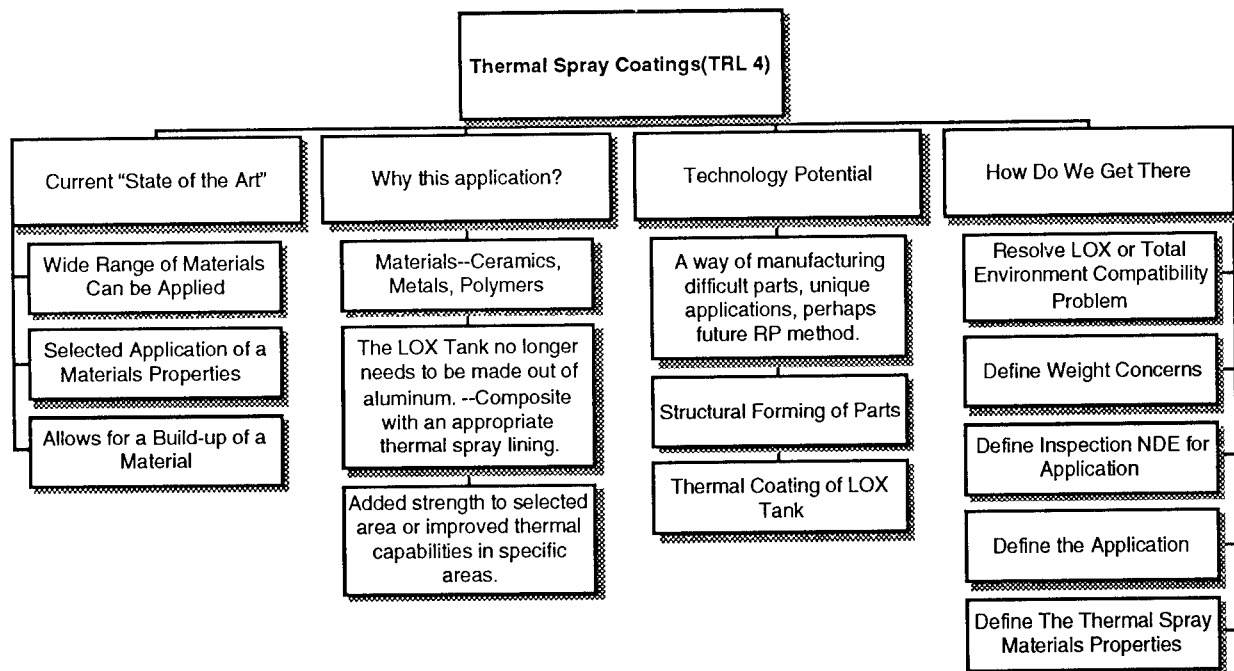
Embedded Sensor Technology is the application of fiber optic technology to filament wound composites. The fiber optics are placed with the composite where data on the product is monitored. The tree chart below gives an overall picture of the application for Embedded Sensor Technology



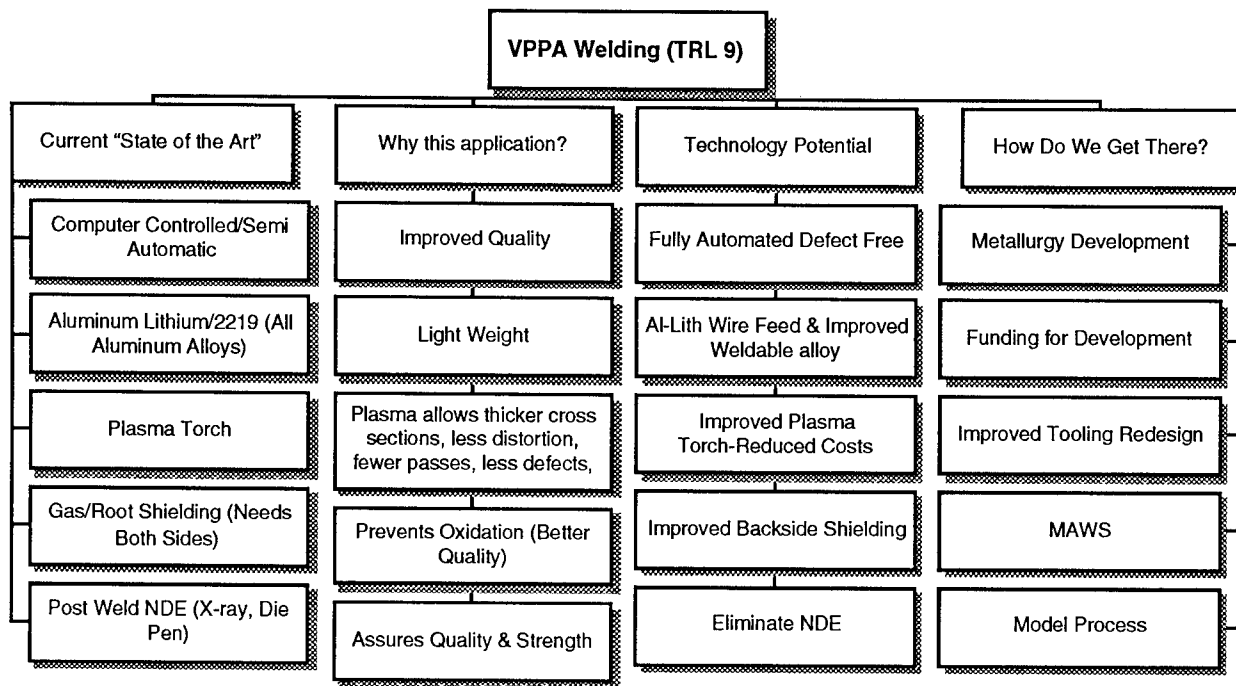
Friction Stir Welding is a new welding process that welds using heat that is generated by friction from a speciality tool as it is run along the joint that is to be welded. The process takes place using a milling machine. The joint to be welded is fixtured into the machine and the tool is run along the joint literally "stirring the metal together" with not a great deal of melting. The tree chart above shows the current status of this unique process.



Rapid Prototyping(RP) is simply, a process that takes the designers ideas from a CAD drawing and converts them directly to a visual or usable part. The process is basically the same for all the RP systems on the market today. Computer software cuts or slices the part on the screen. The RP unit then layers each slice one on top the other and builds the part. The tree chart below gives a good picture of the future for Rapid Prototyping.



Thermal Spray Coating is used to deposit metal, ceramic or a combination of materials to coating or from near net shape structures. Coating applications can include thermal resistance, wear resistance, corrosion protection and is being considered for high pressure LOX compatibility. The tree chart below gives a good picture of the future for development of Thermal Spray Coating.



VPPA Welding is the process currently being used for welding of the space shuttles' external tank. It is a proven technology but current projects are underway to improve the process. The tree chart below gives some information relating to the continued development and use of VPPA Welding.

Summary

This project looked at six technologies under consideration for the RLV project. Concurrent Engineering, Embedded Sensor Technology, Rapid Prototyping, Friction Stir Welding, Thermal Spray Coatings and VPPA Welding. The current TRL's shown were developed based on the following criteria. 1) Current State of Art for the technology, 2) Why this application, 3) The Technology Potential, and 4) How Do We Get There?

Acknowledgment

The data compiled for this project could not have been presented without the help and cooperation of the following NASA Marshall Center Employees.

Jack Macpherson	Concurrent Engineering.	PT41	544-5936
Chuck Wilkerson	Embedded Sensor Technology.	EH13	544-8834
Floyd Roberts	Rapid Prototyping.	EH34	544-1967
Jeff Ding	Friction Stir Welding.	EH25	544-2700
Frank Zimmerman	Thermal Spray Coatings.	EH25	544-4958
Carolyn Russell	VPPA Welding.	EH25	544-2705

References

- Austin, R.E. & Cook, S.A. (1994 Nov) Reusable Launch Vehicle Technology Project. Aerospace America, 32 (11) p.34-39
- Dwivedi, S.N. & Sharan, R. (1990) Concurrent Engineering Why and What?. IEEE Technical Paper, p. 142-148.
- Key, L.K. (1992) Concurrent engineering for consumer, industrial products and government systems. IEEE Transactions on Components, and Hybrids, and Manufacturing Technology, 15 (3), p. 282-287.

1995

NASA/ASEE SUMMER FACULTY FELLOWSHIP PROGRAM

**MARSHALL SPACE FLIGHT CENTER
THE UNIVERSITY OF ALABAMA IN HUNTSVILLE**

**PRESSURE WALL HOLE SIZE AND MAXIMUM TIP-TO-TIP CRACK LENGTH
FOLLOWING ORBITAL DEBRIS PENETRATION**

Prepared By:	William P. Schonberg, PhD, PE
Academic Rank:	Professor
Institution and Department:	The University of Alabama in Huntsville Civil & Environmental Engineering Dept.
NASA/MSFC Laboratory:	Structures and Dynamics
Division:	Structural Design
Branch:	Structural Development
NASA/MSFC Colleague:	Joel Williamsen, PhD

PRESSURE WALL HOLE SIZE AND MAXIMUM TIP-TO-TIP CRACK LENGTH FOLLOWING ORBITAL DEBRIS PENETRATION

William P. Schonberg
Civil & Environmental Engineering Department
University of Alabama in Huntsville

Abstract

The threat of damage from high speed meteoroid and orbital debris particle impacts has become a significant design consideration in the development and construction of long duration earth-orbiting spacecraft. Historically, significant amounts of resources have been devoted to developing shielding for such structures as a means of reducing the penetration potential of high speed on-orbit impacts. These efforts have typically focused on simply whether or not the inner (or 'pressure') walls of candidate multi-wall structural systems would be perforated. Only recently the nature and extent of pressure wall penetration damage have begun to be explored. This report presents the results of a study whose objective was to characterize the hole formation and cracking phenomena associated with the penetration of the multi-wall systems being considered for the International Space Station Alpha (ISSA).

INTRODUCTION

All long-duration spacecraft in low-earth-orbit are subject to high speed impacts by meteoroids and pieces of orbital debris. The threat of damage from such high speed impacts has become a significant design consideration in the development and construction of long duration earth-orbiting spacecraft. Historically, significant amounts of resources have been devoted to developing shielding for such structures as a means of reducing the penetration potential of high speed on-orbit impacts (see, e.g. [1-5]). These efforts have typically focused on simply whether or not the inner (or 'pressure') walls of candidate multi-wall structural systems would be perforated. Numerous studies have concluded that the level of protection afforded a spacecraft by a multi-wall structure significantly exceeds the level provided by an equal weight single wall of the same material. However, the nature and extent of pressure wall damage in the event of a penetration have only recently begun to be explored [6].

In addition to a hole, the pressure wall of a dual-wall structure impacted by a high speed particle can also experience cracking and petalling ([3,5,7]). If such cracking were to occur on-orbit, it is possible that unstable crack growth could develop and possibly lead to an unzipping of the impacted module [8]. Thus, it is imperative to be able to characterize the cracking phenomena associated with the penetration of the dual-wall systems being considered for the International Space Station Alpha (ISSA). While pressure wall cracking and petalling have been observed in several previous laboratory studies of multi-wall structures under high speed impact, a systematic characterization of cracking phenomena in the various ISSA module wall systems has yet to be performed.

This report presents the results of a study whose objective was to develop empirical models of effective hole size and maximum tip-to-tip crack length for the various multi-wall systems being developed for the ISSA. The significance of the work performed is that these models can be incorporated directly into a survivability analysis (see, e.g. [9,10]) to determine whether or not module unzipping would occur under a specific set of impact conditions. The likelihood of module unzipping over a structure's lifetime based on the environment to which it is exposed can also be determined in such an analysis. In addition, the prediction of effective hole size can be used as part of a survivability analysis to determine the time available for module evacuation prior to the onset of incapacitation due to air loss.

EXPERIMENTAL SET-UP AND DATA

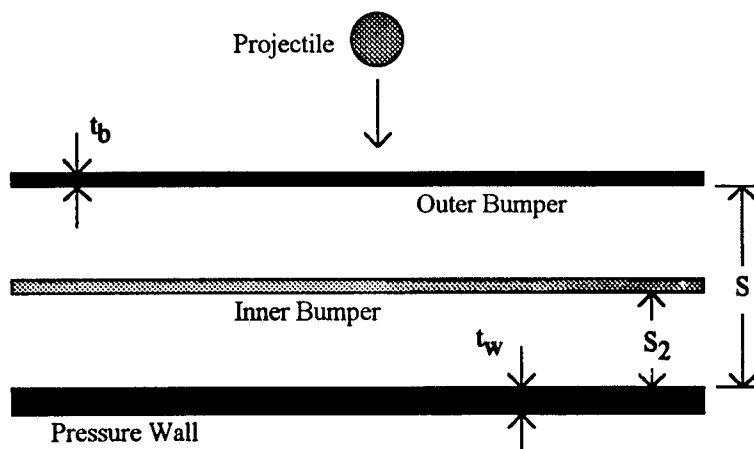


Figure 1. Hypervelocity Impact of a Multi-Wall Structure

Figure 1 shows the normal impact of a multi-wall structure impacted by a spherical projectile. In such a system, the outer and inner bumpers protect the pressure wall against perforation by causing the disintegration of the impacting projectile and the creation of a debris cloud which imparts a significantly lower impulse per unit area to the pressure wall. Table 1 contains the geometric and material parameters for the systems tested considered in this study. As noted in Table 1, 2/3-scale versions of the actual wall systems were occasionally used to

allow the modeling of such systems under the impact of projectiles that are considerably larger than those which could be tested. In addition, the types of inner bumper specified in Table 1 are defined as follows.

- Type A1,A2.....aluminum 6061-T6 panel (A1 ... 0.125 in. thick, A2 ... 0.050 in. thick;
used in 2/3 scale testing of two ESA module wall systems)
Type B.....20 layers of MLI (areal density = 0.033 gm/cm³)
Type C1.....6 layers of Nextel AF62 cloth backed with 6 layers of Kevlar 710 cloth (areal
density = 0.80 gm/cm³)
Type C2.....5 layers of Nextel AF62 cloth backed with 5 layers of Kevlar 710 cloth (areal
density = 0.66 gm/cm³)
Type C3.....4 layers of Nextel AF62 cloth backed with 4 layers of Kevlar 710 cloth (areal
density = 0.53 gm/cm³; used in 2/3 scale testing of configuration with a
Type C1 inner bumper)

We note that in Table 1, for those tests conducted at 2/3 scale, the dimensions given in Table 1 are the test specimen dimensions; actual wall system dimensions can be obtained by multiplying the values given for the 2/3 scale tests by 3/2. The conditions of impact were chosen to simulate orbital debris impact of light-weight long-duration space structures as closely as possible and still remain within the realm of experimental feasibility. Kessler, et al. [11] state that the average density for orbital debris particles smaller than 1 cm in diameter is approx. 2.8 gm/cm³, which is similar to that of aluminum. Therefore, aluminum 1100-0 was used as the projectile material in all of the tests.

Table 1. System Configuration Parameters

WALL TYPE	SCALE	OUTER BUMPER MAT'L	t _b (in)	INNER BUMPER TYPE	S (in)	S ₂ (in)	PRESSURE WALL MAT'L	t _w (in)
US NODE	F	6061-T6	0.050	B	4.5	2.25	2219-T87	0.160
US LAB CYLINDER	F	6061-T6	0.050	B	4.5	2.25	2219-T87	0.188
ESA LAB CYLINDER	2/3	6061-T6	0.063	A1	3.4	1.0	2219-T87	0.080
ESA ENDCONE	2/3	6061-T6	0.063	A2	4.65	0.65	2219-T87	0.063
US NODE ENDCONE	2/3	6061-T6	0.032	B	5.81	4.81	2219-T87	0.150
US LAB ENDCONE	2/3	6061-T6	0.050	B	5.81	4.81	2219-T87	0.125
ENHANCED US LAB CYLINDER	2/3	6061-T6	0.050	C3	3.0	1.5	2219-T87	0.125
ENHANCED JEM CYLINDER	2/3	6061-T6	0.032	C3	3.0	1.5	2219-T87	0.080
JEM CYLINDER	F	6061-T6	0.050	B	4.5	2.25	2219-T87	0.125
FGB CYLINDER	F	5456-0	0.080	C2	4.0	2.0	5456-0	0.063
SERVICE CYLINDER	F	5456-0	0.040	B	2.0	0.0	5456-0	0.063
RESEARCH MODULE	F	6061-T6	0.040	B	2.2	0.0	5456-0	0.125
ENHANCED RESEARCH MODULE	F	6061-T6	0.040	C1	2.2	1.1	5456-0	0.125

Results from two test programs were used to develop empirical predictor equations for effective pressure wall hole diameter and maximum tip-to-tip crack length. The first test program was conducted at

NASA/MSFC. In this test program, 0.313, 0.375, and 0.438 in. diameter aluminum spheres were fired at multi-wall test specimens at a nominal velocity of 6.5 and at obliquities of 0, 45, and 65 degrees. A total of 126 shots were completed as part of this test program. The second test program was conducted at the White Sands Test Facility. In this test program, 0.375, 0.5, 0.625, and 0.688 in. diameter aluminum projectiles were fired at selected multi-wall test specimens at a nominal velocity of 6.5 and at obliquities of 0, 45, and 65 degrees. At total of 23 shots were completed as part of this test program.

EMPIRICAL PREDICTOR EQUATIONS

The empirical predictor equations for pressure wall hole diameter and maximum tip-to-tip crack length were all in the following format:

$$X = A \cos B \theta \left[1 - e^{-C(d_p/d_{BL} - 1)} \right] \quad (1)$$

where we can write, for example, $X=D_h$ for hole diameter and $X=L_{tt}$ for maximum tip-to-tip crack length, respectively. In equation (1), d_p and θ_p are the diameter and obliquity of the impacting projectile while d_{BL} is the ballistic limit diameter at 6.5 km/s for the particular system under consideration under a θ_p -degree impact. Ballistic limit diameters for the various systems considered in this study were obtained using the equations given in References [12,13].

The form given by equation (1) was chosen for the two reasons. First, the quantity X, is zero when the projectile diameter equals the ballistic limit diameter. Second, the form of equation (1) represents the phenomenology expected to occur as the projectile diameter is increased beyond the ballistic limit diameter. The values of the constants A, B, and C were obtained for each system considered using a simplex curve fitting algorithm; resultant values, as well as the correlation coefficients for each equation, are given in Table 2. As can be seen in this Table, the high correlation coefficients indicate a rather good fit to the experimental data. It is noted that since the left-hand-side of equation (1) is not non-dimensional, the units of D_h and L_{tt} as predicted by the constants in Table 2 will be the same as the constant A in those tables.

Table 2. Empirical Equation Information: Pressure Wall Hole Diameter

WALL TYPE	A (in)	B (--)	C (---)	R ²
US NODE	2.287	1.801	2.517	0.90
US LAB CYLINDER	2.740	0.859	2.424	0.95
ESA LAB CYLINDER	67.647	1.380	0.0958	0.98
ESA ENDCONE	7.796	1.634	1.165	0.97
US NODE ENDCONE	2.863	1.311	4.107	0.96
US LAB ENDCONE	7.585	1.970	0.873	0.95
ENHANCED US LAB CYLINDER	8.247	0.361	5.745	0.77
ENHANCED JEM CYLINDER	9.448	0.120	6.435	0.98
JEM CYLINDER	34.431	2.315	0.164	0.96
FGB CYLINDER	5.949	1.448	1.517	0.99
SERVICE CYLINDER (Center)	20.716	1.318	0.0427	0.95
SERVICE CYLINDER (On-rib)	23.092	0.694	0.0279	0.87
RESEARCH MODULE	1.702	0.416	1.474	0.83
ENHANCED RES. MODULE	7.475	0.758	3.031	0.99

Table 3. Empirical Equation Information: Maximum Tip-to-Tip Crack Length

WALL TYPE	A (in)	B (---)	C (---)	R ²
US NODE	3.476	1.603	4.933	0.87
US LAB CYLINDER	3.869	1.041	2.772	0.81
ESA LAB CYLINDER	13.325	1.771	3.349	0.97
ESA ENDCONE	10.779	1.655	7.031	0.96
US NODE ENDCONE	3.847	0.973	4.293	0.96
US LAB ENDCONE	13.609	3.67	1.908	0.99
ENHANCED US LAB CYLINDER	10.219	0.226	178.09	0.91
ENHANCED JEM CYLINDER	14.554	0.177	80.797	0.89
JEM CYLINDER	8.021	4.007	4.287	0.99
FGB CYLINDER	46.813	1.920	0.197	0.99
SERVICE CYLINDER (Center)	10.714	1.448	0.110	0.98
SERVICE CYLINDER (On-rib)	36.996	0.945	0.0248	0.87
RESEARCH MODULE	1.926	0.498	9.518	0.79
ENHANCED RES. MODULE	7.612	0.565	6.308	0.99

COMMENTS AND OBSERVATIONS

The empirical equations obtained through the curve fitting exercise were plotted against empirical data for an impact velocity of 6.5 km/s; the projectile diameter was varied between one and five times the ballistic limit diameter. A review of these plots revealed some interesting information regarding the nature of the penetration phenomena that take place in each of the multi-wall systems considered.

Most notably, the nature of the inner bumper had a profound effect on the damage sustained by the pressure wall. Systems such as the LAB Cylinder and the JEM Cylinder sustained significantly larger holes when the MLI inner bumper in the baseline configuration was replaced by a Nextel/Kevlar inner bumper to yield the "enhanced" configuration. Thus, whereas the use of Nextel/Kevlar inner bumpers can increase the ballistic limit of such systems [14], this benefit must be balanced in any survivability analysis with possible increases in crew vulnerability due to increased leak rates following module wall perforation. It was also observed that the mounting of the Nextel/Kevlar inner bumper may have had an effect on the effective hole diameters and the maximum tip-to-tip crack lengths. Additional tests are planned at NASA/MSFC to quantify this effect.

ACKNOWLEDGMENTS

The author is grateful for the support provided by the NASA/ASEE Summer Faculty Fellowship Program and the NASA/MSFC Structural Developments Branch. The author would also like to acknowledge the work of Angela Nolen, Melanie McCain, and Mary Hovater (EH15) in performing the high speed impact tests at NASA/MSFC that made this study possible. Finally, the author is grateful to Joel Williamsen (ED52) for his many helpful suggestions during the course of this investigation.

REFERENCES

1. Maiden, C.J., Gehring, J.W., and McMillan, A.R., Investigation of Fundamental Mechanism of Damage to Thin Targets by Hypervelocity Projectiles, GM-DRL-TR-63-225, Santa Barbara, California, 1963.
2. McMillan, A.R., Experimental Investigation of Simulated Meteoroid Damage to Various Spacecraft Structures, NASA-CR-915, Washington, D.C., 1965.
3. Burch, G.T., Multi-plate Damage Study, AFATL-TR-67-116, Eglin Air Force Base, Florida, 1967.
4. Lundeborg, J.F., Stern, P.H., and Bristow, J.R., Meteoroid Protection for Spacecraft Structures, NASA-TM-54201, Washington, D.C., 1965.
5. Schonberg, W.P., Bean, A.J., and Darzi, K., Hypervelocity Impact Physics, NASA-CR-4343, Washington, D.C., 1991.
6. Schonberg, W.P., Cracking Characteristics of a Habitable Module Pressure Wall Following Orbital Debris Penetration, Final Report, NASA/ASEE Summer Faculty Fellowship Program, Marshall Space Flight Center, Huntsville, Alabama, 1994.
7. Schonberg, W.P., "Aluminum 2219-T87 vs. 5456-H116: A Comparative Study of Pressure Wall Materials in Dual-Wall Structures Under Hypervelocity Impact", *Acta Astronautica*, Vol. 26, No. 11, 1992, pp. 799-812.
8. Common Module Shell Unzipping Due to Meteoroid/Orbital Debris Strikes, Space Station Freedom Program Office, Report No. GSS-40.05-RPT-6-001, Reston, Virginia, 1994.
9. Williamsen, J.E., Vulnerability of Manned Spacecraft to Crew Loss from Orbital Debris Penetration, NASA-TM-108452, Marshall Space Flight Center, Alabama, 1994.
10. Micrometeoroid and Orbital Debris Induced Catastrophic Failure Prediction Methods, Space Station Freedom Program Office, Report No. GSS-40.05-RPT-6-003, Reston, Virginia, 1994.
11. Kessler, D.J., Reynolds, R.C., and Anz-Meador, P.D., Orbital Debris Environment for Spacecraft Designed to Operate in Low Earth Orbit, NASA-TM-100471, Houston, Texas, 1988.
12. Christiansen, E.L., "Design and Performance Equations for Advanced Meteoroid and Debris Shields", *International Journal of Impact Engineering*, Vol. 14, pp. 145-156, 1992.
13. Christiansen, E.L., *Private Communication*, 1995.
14. Christiansen, E.L., Crews, J.L., Williamsen, J.E., Robinson, J.H., and Nolen, A.M., "Enhanced Meteoroid and Orbital Debris Shielding", *International Journal of Impact Engineering*, Vol. 17, 1995.

1995

NASA/ASEE SUMMER FACULTY FELLOWSHIP PROGRAM

**MARSHALL SPACE FLIGHT CENTER
THE UNIVERSITY OF ALABAMA IN HUNTSVILLE**

THE SHUTTLE MAIN ENGINE: A FIRST LOOK

Prepared By:	Barbara Schreur, Ph.D.
Academic Rank:	Associate Professor
Institution and Department:	Texas A&M University-Kingsville Department of Electrical Engineering and Computer Science

NASA/MSFC

Office:	Astrionics
Division:	Software
Branch:	Systems Engineering

MSFC Colleague:	Charles Nola
-----------------	--------------

Introduction

Anyone entering the Space Shuttle Main Engine (SSME) team attends a two week course to become familiar with the design and workings of the engine.

This course provides intensive coverage of the individual hardware items and their functions. Some individuals, particularly those involved with software maintenance and development, have felt overwhelmed by this volume of material and their lack of a logical framework in which to place it.

To provide this logical framework, it was decided that a brief self-taught introduction to the overall operation of the SSME should be designed. To aid the people or new team members with an interest in the software, this new course should also explain the structure and functioning of the controller and its software.

This paper presents a description of this presentation.

Development of the Presentation

Initially, this presentation was envisioned as a video tape, with diagrams, film clips, synchronized voice-over and text. Not only was this overly ambitious for the 10 week period, it was discovered that there is an extensive protocol at Marshall Space Flight Center for gaining approval for the production of video tapes. In part, the approval depended on a demonstration of need and cost effectiveness. It was decided, therefore, to utilize one of the computer accessible packages to produce a product accessible wholly by computer. Microsoft's PowerPoint, being available, was used.

To produce the presentation, it was necessary first, to learn the general function of the main engine systems. Then, to organize the presentation of the systems, acquire and prepare the necessary diagrams and assemble the text. This had to be done in spiral mode as the preparation of the presentation inevitably prompted technical questions which required clear answers which then required modification of the presentation.

The learning phase, itself, was spiral and lasted 5 to 6 weeks. Initially, written documentation was studied [1, 2 and 3]. Then various engineers were consulted. The consultations provided better understanding and perspective so that more could be gained from the documentation..

As knowledge was gained, the layout of the presentation was prepared, modified and eventually finalized.

Many of the images used were found in the written documentation. While they could have been scanned in from this documentation, improved quality was obtained in images provided by Rockwell International. The photographic

images were obtained from various Internet sources, including NASA's Spacelink, and from captured video tape images.

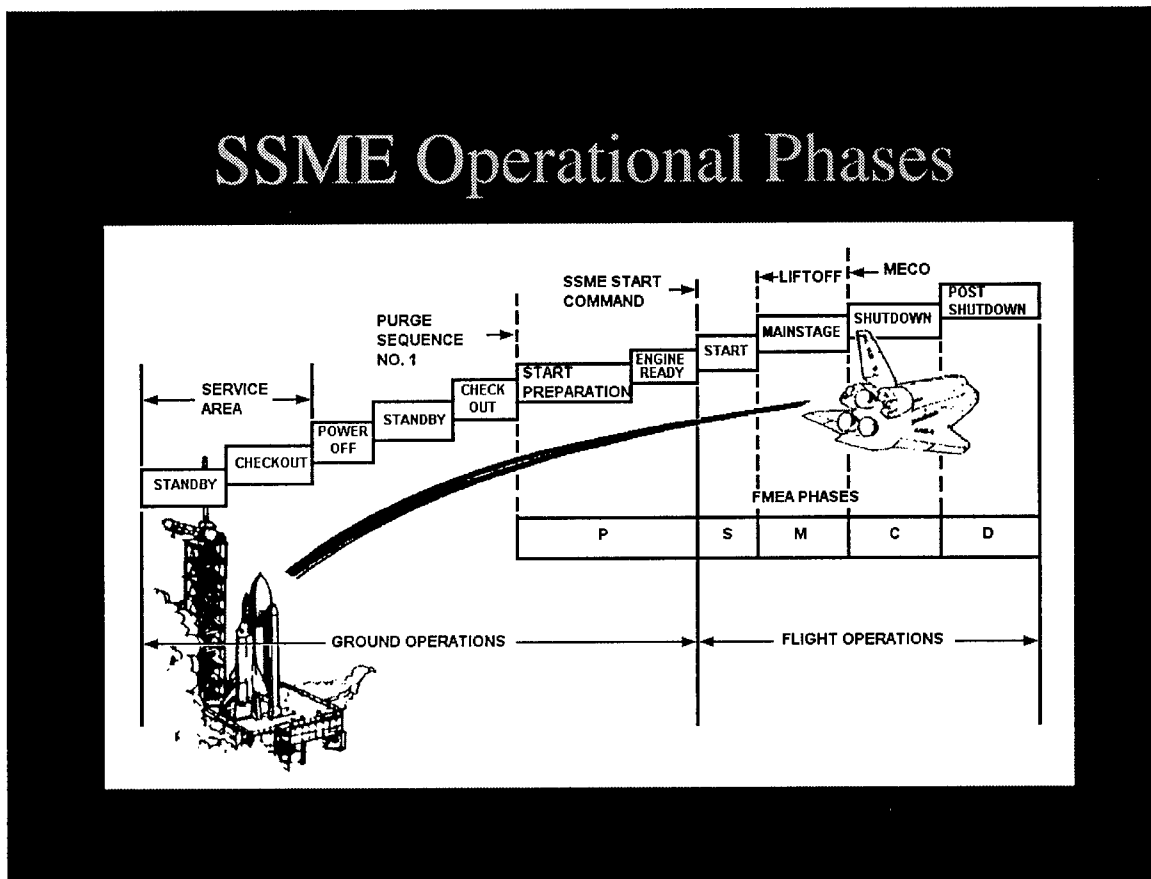


Figure 1. An image that was redrawn at the bit level for a clearer image.

The bit mapped line drawings, see Figure 1, were first cleaned up to sharpen lines and remove speckles. Color was then added to one of those diagrams to show various stages of the fluid flow, see Figures 2 and 3, and to highlight and identify the major parts being discussed. The PowerPoint package provided pleasing background color for the monochromatic images.

Text was added to the sequenced images, sometimes as text only slides, to provide explanation of the image being presented. This text is written largely in outline form, but, where necessary, additional discussion is provided, as shown in Figure 3.

Oxidizer Flow Cont'd

- A last branch
 - supplies LOX (11%) to the preburner oxidizer boost pump located at the bottom of the HPOTP.

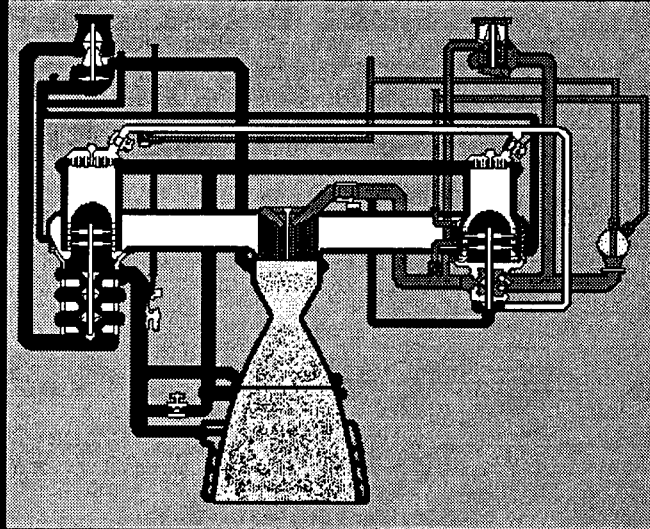


Figure 2. Shows flow of oxygen to the boost pump located at the bottom of the high pressure oxidizer turbopump.

Conclusion

The finished presentation comprises 118 computer screens or slides. Typically, while self-paced, it takes about 3 hours to view.

Extensions

It would be useful to add comments to a number of the slides, both as note pages and as audio. There is also a need for more extensive and detailed discussion of the software, which would in effect turn the presentation into a course which introduces the software.

The presentation could also be converted for inclusion as a section of the NASA homepage on the World Wide Web.

The presentation also demonstrates that a fully animated video tape showing the flow would be more meaningful.

Oxidizer Flow Cont'd

- With the added pressure from the boost pump, the oxidizer is injected into both preburners.
 - The flows into the preburners are controlled by the OPOV and the FPOV.
 - Used together, the valves establish the thrust level while the FPOV maintains a 6.026 to 1 ratio mixture in the MCC.

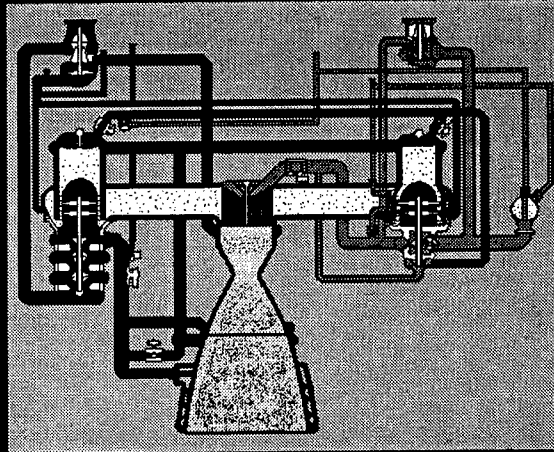


Figure 3. Shows the oxygen flow into the preburners.

Acknowledgements

Thanks to Charles Nola who presented me with this topic, Dave Wilson who spent time explaining the workings of the engine, Amy Hardy of Intergraph who helped me scan images and edit them, and the people at Rocketdyne in the HSL who helped with the details on the Controller software.

References

1. Space Shuttle Main Engine Block II Controller Software Design, Rockwell International Corporation, CP406R0022D Part II, February, 1994.
2. Space Transportation System Technical Manual, SSME Description and Operation, Rockwell International Corporation, E41000, RS-8559-1-1-1, August, 1991.
3. Consultations with engineers at MSFC on the software and hardware.

1995

NASA/ASEE SUMMER FACULTY FELLOWSHIP PROGRAM

**MARSHALL SPACE FLIGHT CENTER
THE UNIVERSITY OF ALABAMA IN HUNTSVILLE**

AN ANALYSES OF CD-ROM TECHNOLOGY FOR SPACELINK

Prepared By:	Willard A. Smith, Ph.D.
Academic Rank:	Associate Professor
Institution and Department	Tennessee State University Department of Physics, Mathematics and Computer Science
NASA/MSFC:	
Office:	Office of Education Programs
MSFC Colleague:	Jeff Ehmen

AN ANALYSIS OF CD-ROM TECHNOLOGY FOR SPACELINK

by

Willard A. Smith Ph.D.

This study first examined the possibility of placing NASA CD's in the Spacelink Public Electronic Library (SPEL). The goal of this task was to place these materials on the Internet. The second part of the study addressed the possibility of using CD's as storage for portions of SPEL. These files would also be on the Internet and available to the users of Spacelink.

CD technology was not designed with the Internet in mind. The original concept for CD Technology was to provide high volume, read only storage, for stand alone, high powered computer systems. This provides the user with data, processed images, sound, user interaction features or any combination of these features. Many CD-ROM's perform very well in this environment. For CD's to work, in this manner, on the Internet, a high speed connection (T1 or faster) is required. Many of the teachers served by Spacelink are on much slower connections. Many schools are slow to place phone lines in the classrooms. T1 connections for a classroom are an even larger issue and much less likely to be installed.

Current CD-ROM's present several issues related to their potential use, by the nature of the original design criteria of CD-ROM's. CD's also vary considerably by when and where they were produced. These issues fall into the following three broad categories.

Multi-Media CD-ROM's are the source of the current excitement in the public market. Multi-Media CD's feature the full array of data, graphics, sound, and interactive capabilities. These CD's come with descriptions of the hardware and software needed to run the disc. In most cases the CD-ROM is customized to a specified hardware and software platform. Different versions of each CD are produced for Macs, PCs, and UNIX based machines. These CD's are copyrighted and therefore can not be placed on Spacelink. The only known NASA CD of this type, "Welcome to the Planets," is already on the Internet.

Text and/or image CD-ROM's are more like the "free world atlas, dictionary and encyclopedia" provided with new computer systems. This is a greatly downgraded version of the multi-media CD-ROM's described above. The visual images are often of less quality. The interactive capabilities and sound, where they exist, are seriously limited. This group of CD's carries all the limitations related to the operating platform discussed above.

Some few NASA CD's are text and/or image CD's and come with text, images, and the "necessary executable software" to use the CD's. The visual quality of these CD's is excellent. The difficulty with these CD's is that the software provided is usually not executable. To solve this problem, source code of the software must be found and loaded onto the computer to be used in the process. This software must be recompiled, debugged and/or modified to correct the limiting conditions. In most cases this means doing this for each CD-ROM because no standard systems were used to develop the CD's or the software. This must be done for each platform to

be supported. If different versions of the operating system, or different hardware, from the "playing" system, were used to produce the CD, the discs may be unusable.

Compressed Raw Data CD's are raw data as captured from the acquisition platform. NASA has produced hundreds of CD's in this format. NASA CD's of this type are the data as received from Voyager, Mariner or other space crafts. Most are unprocessed data and are stored in compressed data format. On the CD is source code for the software needed to decompress and store the images on a hard drive in JPEG, gif, Raster, or other formats. This software, usually written in C or FORTRAN, must be compiled, link edited, and stored in executable form before beginning the processing of the images on the CD. The software in these CD's is not standardized. The success of the compilation, link editing, and development of an executable module depends, on the compatibility of the platforms of the original host and the user system. Software is also different for each of the NASA missions. Imaging viewing software is usually not included on the CD but must reside on the platform where the image is to be viewed.

The NASA CD's in this group are stored in compressed data format. Each CD contains approximately 2400 images (files). When decompressed, a file will often be 3+ times larger than in compressed mode. Many of the expanded files average 800k and range up to 9 meg of needed hard disc storage per image to allow for viewing of an image. That is a very large file to be transmitted over the Internet, especially if a slow link is in the path of the transmission. The receiving machine must have real memory large enough to capture the image.

These three types of CD's left several options related to placing CD's on Spacelink. One option was to place one CD on each of the ten drives now located on the SunSparc 1000 and leave them for some specified period. At the end of this period, rotate all or part of the ten CD's and replace them with new selections. The cost of additional equipment was minimal. Some disc storage space would be required. A major cost would be in programming time to compile, debug and modify the software to make the images available to Spacelink users. The ten drives would make only a fraction of the 500 plus CD's already produced by NASA available to users. Each time the CD's were changed the SPEL menus would have to be modified to reflect the changes. The cost of staff time and management problems of this option made it undesirable.

The Jet Propulsion Laboratory has placed some NASA CD's in a Jukebox for access over the Internet. Another option was to develop and place information about NASA CD's on the menus of Spacelink and point to the location providing the CD services. This eliminates the need to place the physical CD's of Spacelink at MSFC. Depending on the detail provided on the Spacelink menus the cost of this option was small. This option has several disadvantages. The indexes and menus on the host systems at other NASA sites are totally foreign to our teacher-student clientele. The JPL host system, where most of these CD's reside, consists of 7 nodes at this time. Access to complete services at JPL is restricted to NASA and NASA funded scientists. The help desk at JPL is staffed only part time. The service at the other nodes seems to be at this level or less. This is a new service at most sites and the questions of "how do we do this" are still under discussion. The NASA nodes providing CD's assume a level of expertise far beyond our "little old teacher" in Out Back, Iowa, and support for such individuals is minimal. The current load on some of the JPL nodes is such that a queue system is being discussed. This would require a request for the CD and the images needed and a wait for some time for the

process to be completed. This would tie up lines on Spacelink. This option was eliminated because it seemed to do little or nothing for our primary audience.

A third option was to purchase a large CD Jukebox or a series of smaller Jukeboxes, and integrate the NASA and other Educational CD's into SPEL. This would provide control of our services and support for the teachers and students. Changes and additions to the SPEL menus would have to be made only one time. This had several disadvantages. This option would require additional hardware and possibly some Hierarchical File Management (HFM) software. Integration of the files into the Spacelink menus would require up to a full person year. Backup procedures would have to be developed to prevent backing up the CD's on the readers. As the CD collection grows additional Jukeboxes would be needed to support this option. The approximate \$50,000 front end costs of hardware and software and continued staff cost made this option undesirable.

Another option was to combine the ten readers we now have with a 500 CD jukebox. Place the most popular CD's in the ten readers we now have and the remainder of the collection on the Jukebox. This makes full use of the current system hardware. This makes access to the most popular CD's virtually as quick as the files on the hard drives. This option provides a logical growth path as the collection of CD's grows. The cost of this option would be considerable in the new hardware needed. Some method of identifying the most popular CD's would have to be developed and monitored. This option brought with it the costs and limitations of the two options it combined. This option was also undesirable.

With the above options being undesirable or unrealistic, the issue of loading parts of SPEL onto CD's produced here at Marshall was examined. The technology of the CD-ROM has progressed to the point that it is possible to archive data files on to CD-ROM's, from a working database system, and have these files on the CD's continue to be an active part of the information system. This process involves the hardware of a Young Minds, Inc., CD Studio Intelligent Controller, and a Kodak CD recorder. The process is driven by MakeDisc Premastering Software using the ISO 9660/Rock Ridge processing format. (1)

The process discussed here was developed by Young Minds, Inc. of Redlands, California. This application does not require a separate workstation and can be directly linked to the SPARCServer 1000 now running Spacelink. The complete package of the MakeDisc Premastering Software; Young Minds, CD Studio Intelligent Controller; and a Kodak PCD Writer 225; has a federal price of \$14,329.80. This is also available on other hardware platforms.

ISO 9660 is the file system standard that has made CD-ROM technology so widely accepted and used. The ISO 9660/Rock Ridge is the most open of the file creation and access systems related to the ISO standards. UNIX, as the most open of the current operating systems, is best suited to take advantage of the ISO 9660/Rock Ridge standard for open file structures. The ISO 9660/Rock Ridge standard allows the implementation of the UNIX/POSIX (the file structure of SPEL) file structure as the file index and structure of the CD. This is designed to be directly accessible as a physical and logical extension of the UNIX/POSIX file structure of the on-line hard drives. (2)

The software to drive this process is MakeDisc Premastering Software from Young Minds, Inc. To develop a CD someone collects and identifies those files that are to be placed on the CD. This includes the necessary information for identification and technical definition of the needed details to identify the CD, what is stored on the CD, and how the files are stored on the platter.

After the files to be placed on the CD and necessary identification and processing information are collected, the MakeDisc software becomes a "fill in the blanks," and a "point and click" process. The GUI and instructions are designed to allow for unsophisticated file managers to develop the necessary information and expertise to complete this process with relative ease. The software stores the files, in CD format, on the disc, in the Young Minds Intelligent Controller. This allows for a preview of the CD before the disc is burned. This disc is fully editable and can be fully tested on the Young Minds CD Studio before the gold CD is burned.

The completed Studio work is transmitted to a Kodak PCD Writer 225 for processing. This is a dual speed "burner" and produces CD's at the speed needed for the CD drives now attached to the Sun SPARCServer 1000. This CD burning device does not require certified media and non-certified media are some less costly.

This newly produced CD is then ready to be placed on the CD drivers on the Spacelink system. At this time, with the deletion of the files now on the CD, from the Hard Drives, this makes the materials on the CD directly accessible to the users of Spacelink.

Updates to the SPEL that come after this CD is produced are added to this data set at the time of the production of the next CD. New Materials are integrated into the "new" CD, at the proper location, with the materials, on the current CD. The materials on the Current CD are saved on disc, or on tape, at the time of production of the "original CD" for future updates. The process described above of Premastering, testing, and burning are repeated and the new CD replaces the previous volume. This allows for dynamic growth of the files and directories and the addition of items that were not available when the previous CD volume was produced.

Several technical issues remain to be examined before transferring Spacelink files to CD's. Backup procedures remain to be tested. Documentation indicates that the backup tapes on the Spacelink System can be set to backup only the hard disc. This is the desirable option as the CD's would soon hold a very large volume of data. The nature of the CD is such that little or no need would exist for a backup. A simple inexpensive backup would be to burn a duplicate disc at the time of each production. This process would take only 15 minutes and cost approximately ten dollars. This backup CD could then be stored, off site with the backup tapes, as part of a good disaster recovery plan.

The directory interface and links with SPEL remain to be tested. Young Minds will supply references in the field using the system. Questions need to be formulated to take advantage of these contacts. The technical staff at Young Minds indicated that they supply systems to be tested and evaluated before purchase.

Speed of access and transfer of data are related technical issues yet to be fully tested. The directory search seems to be a bit slower. In testing this issue with CD's on line at JPL, the difference, between CD access delays, and the normal Internet delays for host contact and response, seems to be little if any. The transfer rate of a dual speed CD is approximately 300k bytes per second. Any one who has any network delays will see this as a good transfer rate. This would allow for the transmission of a good size gif much faster than many of our uses can receive, and store the data

The frequencies of production of "new" CD's and use of the equipment needs to be addressed. This is directly related to what data is to be placed on this media. A plan for what will trigger the production of the "next" CD needs to be developed. Is the production of the next CD time driven, volume driven, or ad hoc? A careful plan needs to be formulated before the testing of software and hardware and the questionings of references.

Some cost issues also remain. The price of this proposed hardware and software package is \$14,329.80. There would also be some additional costs for cabling and racks. The human cost of the initial set up of the system and learning to use the software and equipment must also be considered.

Outside production of the Archived CD's is an option. If the decision is made to use CD's on Spacelink, and to have them produced at a private company, like Disc Manufacturing here in Huntsville, each gold CD with a ten to fifteen day turnaround time would cost \$350.00+. The collection of the data to be placed on the CD and learning the technology well enough to do this would remain the responsibility of the Spacelink Staff. At this price, it would take little time and production of only a few CDs, to recover the cost of the proposed system.

An additional option to offset cost is to develop some slick CD's (The Best of Spacelink) for sale at the Space Museum or souvenir stores at the NASA Centers. With the gold master, the cost of a thousand CD order would be less than \$2.50 per CD. If a winner was produced, and more CD's were needed, an order of 5,000 CD copies would cost approximately \$1.50 per CD. CD's sell for about \$20 each. Profits of 12 to 15 dollars each would result in income of 60 to 75 thousand dollars profit on the sale on an order of 5000 CD's.

An important additional consideration is the relative cost of Hard Disc to CD's. Currently an 8 gigabyte Hard Drive costs approximately \$5000. With the \$14,000 plus cost of the identified system, 24 gigabytes of Hard Disc could be added to the Spacelink System.

This analysis did not identify an optimal solution to the use of CD's on Spacelink. Several options were analyzed that do not seem to be desirable at this time. Further study is needed to determine if CD's are a desirable addition to the Spacelink System.

-
1. Young Minds, Inc. "Documents and Sales Materials," Redlands, California, July 1995
 2. Clayton Summers "Introduction to ISO 9660," Wilmington, Delaware; Disc Manufacturing, Inc., 1993.

1995

NASA/ASEE SUMMER FACULTY FELLOWSHIP PROGRAM

**MARSHALL SPACE FLIGHT CENTER
THE UNIVERSITY OF ALABAMA IN HUNTSVILLE**

**A GEOMETRICAL RESULT REGARDING
TIME-OF-ARRIVAL LIGHTNING LOCATION**

Prepared by:	Richard Solakiewicz
Academic Rank:	Associate Professor
Institution and Department:	Chicago State University Department of Mathematics and Computer Science

NASA/MSFC

Laboratory:	Space Sciences
Division:	Earth System Science
Branch:	Observing Systems

MSFC Colleagues:	William Koshak, Ph.D. Richard Blakeslee, Ph.D. Hugh Christian, Ph.D.
------------------	--

One reason for investigating Lightning Detection And Ranging (LDAR) is to validate data from the Optical Transient Detector (OTD). A Time-Of-Arrival (TOA) procedure may be used with radio wave portions of lightning signatures. An antenna network is in place at KSC [1].

Algorithms are available [2,3] which provide the advantages of considerably simplifying the numerical estimation of source location and a clear error analysis. These algorithms involve judicious differencing of measurement data which allows information retrieval by performing a linear inversion. Other algorithms [4,5] require numerically finding intersections of hyperboloids. Such algorithms are more involved computationally, and the error analysis is not straightforward. The algorithm in [3] provides for a clearly defined error analysis as given in [6].

Efficiency in the retrieval of lightning location depends on the configuration of the antennas. Certain combinations of source locations and antenna configurations will result in the matrix of the linear system obtained using the algorithm in [3] having small eigenvalues. This will lead to a magnification of error. For example, a system of 4 antennas numbered from 1 to 4 sequentially around the perimeter of a rectangle yields eigenvalues which are proportional to $t_{12} + t_{34} = t_1 - t_2 + t_3 - t_4$, where t_j is the time of arrival of a signal from the lightning event to the j^{th} antenna. Letting R_j denote the distance from the source to the j^{th} antenna and c be the speed of light,

$$t_j = R_j/c. \quad (1)$$

Curved transit paths due to refractive effects in the atmosphere are not considered. For brevity, cable time delays have been neglected. Source locations on either of the 2 planes which are perpendicular to the plane of the rectangle and bisect any line segment connecting 2 consecutively numbered antennas yield $t_{12} + t_{34} = 0$. Such a configuration is "blind" to any sources on these planes.

A better configuration places antennas at the centroid and vertices of an equilateral triangle. The antenna at the centroid will be designated by the index 1; others are numbered 2 through 4. This configuration has been referred to as "ideal" in [7]. The eigenvalues for this configuration are proportional to $t_{12} + t_{13} + t_{14}$. This is equivalent to saying that the configuration is ineffective when the distance from the source to the antenna at the centroid is equal to the average of the distances from the source to the other 3 antennas. It turns out that this is never the case. The question of suitability of this particular arrangement of 4 coplanar antennas has been reduced to a problem in geometry. This report presents a solution.

The desired result is obtained by seeking the extrema of the sum of distances from the vertices to a point on a hemisphere of radius R centered at the centroid of the triangle. Full generality is recovered by allowing R to be arbitrary. We set up a Cartesian coordinate system, with points specified by (x, y, z) . Its origin is at the centroid. Vertices are located at

$$\mathbf{D}_2 = D\hat{\mathbf{y}}, \quad \mathbf{D}_3 = -D\left(\frac{\sqrt{3}}{2}\hat{\mathbf{x}} + \frac{1}{2}\hat{\mathbf{y}}\right), \quad \mathbf{D}_4 = D\left(\frac{\sqrt{3}}{2}\hat{\mathbf{x}} - \frac{1}{2}\hat{\mathbf{y}}\right); \quad (2)$$

the distance from the centroid to a vertex is D . For the present, assume $R \geq D$. It will be convenient to consider the distances from the vertices on an orthogonal coordinate system.

Vectors from antennas 1 through 4 to the source will be denoted by $\mathbf{R}, \mathbf{X}, \mathbf{Y}, \mathbf{Z}$ respectively. Let θ denote the angle between \mathbf{D}_2 and \mathbf{R} . Employing the law of cosines, it may be shown that

$$3R^2 = X^2 + Y^2 + Z^2 - 3D^2. \quad (3)$$

It will be necessary to extremize

$$F(X, Y, Z) = X + Y + Z \quad (4)$$

subject to (3).

Using Lagrange multipliers or any other suitable method, the only extremum in the first octant is $X = Y = Z = \sqrt{R^2 + D^2}$; $F = 3\sqrt{R^2 + D^2} > 3R$. This turns out to be a local maximum. Minima must be found by looking along boundaries. These are not necessarily in any coordinate plane. All of X, Y, Z must be greater than or equal to $R - D$. Eliminating Z reduces the problem;

$$f(X, Y) = X + Y + \sqrt{3(R^2 + D^2) - X^2 - Y^2} \quad (5)$$

must be minimized requiring that none of X, Y, Z be negative. An additional constraint is obtained from (3),

$$X^2 + Y^2 \leq 2(R^2 + D^2 + RD). \quad (6)$$

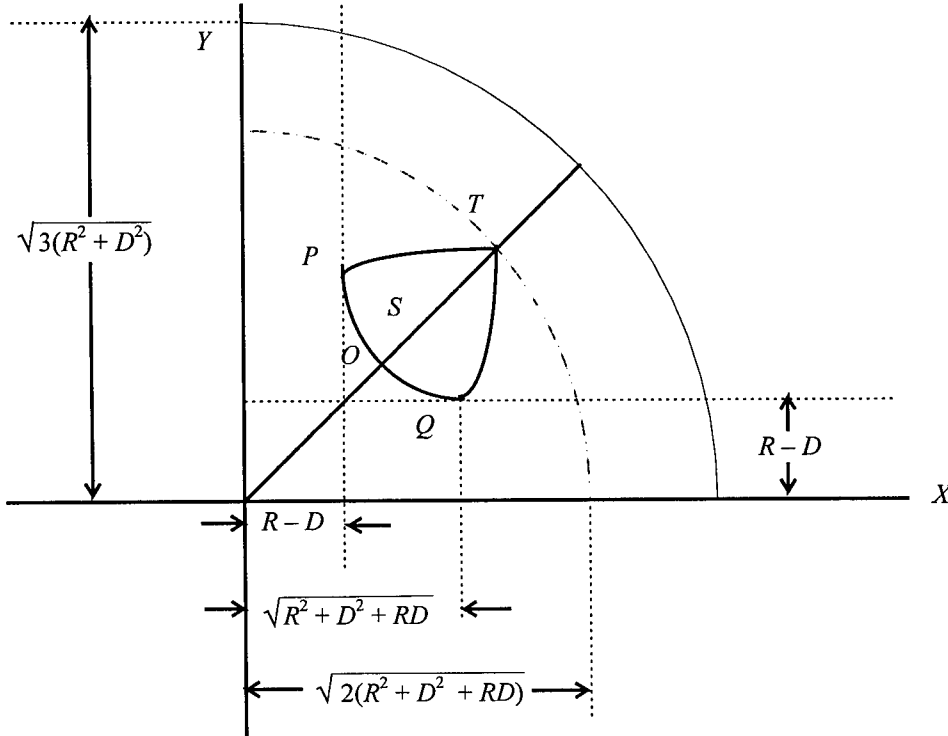


Fig. 1

This constraint does not sufficiently limit f ; X and Y cannot both attain their minimum values of $R - D$ at the same time. Boundaries are shown in Fig. 1. The smallest values of Y for a fixed X

occur when $z = 0$ (the lightning event is in the plane of the triangle). This may be demonstrated by writing

$$Y^2 = R^2 + D^2 - 2\mathbf{R} \cdot \mathbf{D}_3. \quad (7)$$

Elevating the lightning event from the plane of the triangle while keeping X and R constant is equivalent to rotating \mathbf{X} and \mathbf{R} about \mathbf{D}_2 . Here, \mathbf{D}_3 has no z component and y is constant. The value of Y is minimized when x is as small as possible (at $z = 0$).

The slope of a tangent to \overline{POQ} is given by

$$\frac{dY}{dX} = -\frac{\sin(2\pi/3 - \theta)}{\sin \theta} \frac{X}{Y}. \quad (8)$$

It is never positive and goes from 0 at $\left(\sqrt{R^2 + D^2 + RD}, R - D\right)$ to $-\infty$ at $\left(R - D, \sqrt{R^2 + D^2 + RD}\right)$. At the point O , $X = Y$, $\theta = \pi/3$, and $dY/dX = -1$. The coordinates of this point are $X = Y = \sqrt{R^2 + D^2 - RD}$.

The gradient

$$\nabla f(X, Y) = (1 - X/Z)\hat{\mathbf{X}} + (1 - Y/Z)\hat{\mathbf{Y}} \quad (9)$$

points in the direction of greatest increase of f . The region in Fig. 1 can be thought of as a mountain with its summit at $X = Y = \sqrt{R^2 + D^2}$ (the point labeled S). On the square region $0 \leq X \leq \sqrt{R^2 + D^2}$, $0 \leq Y \leq \sqrt{R^2 + D^2}$, we have $Z \geq X$ and $Z \geq Y$. Except at S , the inequality is strict. The gradient points up and to the right. Below the line segment \overline{OS} , $\pi/3 \leq \theta \leq 2\pi/3$, and $X > Y$. The opposite is true above \overline{OS} . The mountain has a ridge along this line segment. Below and to the left of S , it is clear that as X and Y decrease, Z increases (the components of the gradient remain positive). Values of f beneath or to the left of \overline{POQ} are smaller than values on this curve.

It will not be necessary to investigate the values of f along \overline{PT} or \overline{QT} . These curves can be mapped onto \overline{POQ} by a suitable relabeling of \mathbf{X} , \mathbf{Y} , \mathbf{Z} . Symmetry may be further exploited to reduce the effort. An interchange of \mathbf{X} and \mathbf{Y} will map \overline{OP} and \overline{OQ} onto each other.

It turns out to be difficult to parameterize Y in terms of X and obtain the minima along the bounding curve by differentiation. We will bound the values of f along \overline{OQ} by those on a simpler polygonal boundary below \overline{OQ} .

We begin at $Y = R - D$ and require

$$f(X, R - D) = X + (R - D) + Z(X, R - D) \geq 3R. \quad (10)$$

This leads to the inequalities

$$2X^2 - 2(2R + D)X + 2R^2 - D^2 + 2RD \leq 0, \quad R - \frac{\sqrt{3}-1}{2}D \leq X \leq R + \frac{\sqrt{3}+1}{2}D. \quad (11)$$

The largest value of X that needs to be considered is $\sqrt{R^2 + D^2 + RD}$. Extrema along this line segment, denoted by \overline{QB} (see Fig. 2), must be at the endpoints;

$$\begin{aligned} f\left(\sqrt{R^2 + D^2 + RD}, R - D\right) &= R - D + 2\sqrt{R^2 + D^2 + RD} > 3R, \\ f\left(R - (\sqrt{3}-1)D/2, R - D\right) &= 3R. \end{aligned} \quad (12)$$

The next portion of the bounding curve is drawn by leaving $X = R - (\sqrt{3}-1)D/2$ and increasing Y to some point below \overline{OQ} . The location of this point may be found by solving for $\cos \theta$ in $X^2 = R^2 + D^2 - 2RD \cos \theta$. We find that

$$\begin{aligned} \cos \theta &= \frac{\sqrt{3}-1}{2} + \frac{\sqrt{3}}{4} \frac{D}{R}, \\ \cos\left(\frac{2\pi}{3} - \theta\right) &= \frac{\sqrt{3}}{2} \sqrt{1 - \left[\frac{\sqrt{3}-1}{2} + \frac{\sqrt{3}D}{4R}\right]^2} - \frac{1}{2} \left[\frac{\sqrt{3}-1}{2} + \frac{\sqrt{3}D}{4R}\right] \\ &\leq \frac{3^{3/4}}{2^{3/2}} - \frac{\sqrt{3}-1}{4} < \frac{2}{3}. \end{aligned} \quad (13)$$

Using the law of cosines to write Y^2 in terms of R , D , and $\cos(2\pi/3 - \theta)$, we see that Y decreases as $\cos(2\pi/3 - \theta)$ increases. The smallest value of Y on \overline{POQ} for $X = R - (\sqrt{3}-1)D/2$ is bounded using (13);

$$Y \geq \sqrt{R^2 + D^2 - 4RD/3} > R - 2D/3. \quad (14)$$

We can proceed up to point C whose coordinates are $(R - (\sqrt{3}-1)D/2, R - 2D/3)$.

As for the first part of the polygonal bounding curve, the extrema are at the endpoints. The minimum value of f along \overline{BC} is $3R$ and occurs at B . The maximum is located at C and is given by

$$2R - \left[\left(\sqrt{3}-1\right)/2 + 2/3\right]D + \sqrt{R^2 + \left(14/9 + \sqrt{3}/2\right)D^2 + \left(\sqrt{3} + 1/3\right)RD} > 3R. \quad (15)$$

Proceeding as before, we fix $Y = R - 2D/3$ and see how far to the left we can go and still have $f \geq 3R$. This time we obtain the inequalities

$$R - \frac{\sqrt{42}/2 - 1}{3}D \leq X \leq R + \frac{\sqrt{42}/2 + 1}{3}D. \quad (16)$$

It will not be necessary to proceed from C all the way to the value indicated in (16). We can stop at a point E which has the same X -coordinate as O . From the estimate

$$\left(R - \frac{\sqrt{42}/2 - 1}{3}D\right)^2 < (R - 0.7D)^2 < R^2 + D^2 - RD, \quad (17)$$

we see that $f(X, Y) > 3R$ at every point of this portion of the boundary.

Finally, we proceed vertically from E to O . The derivative of f with respect to Y is positive everywhere along this line segment. The smallest value of f here is at E .

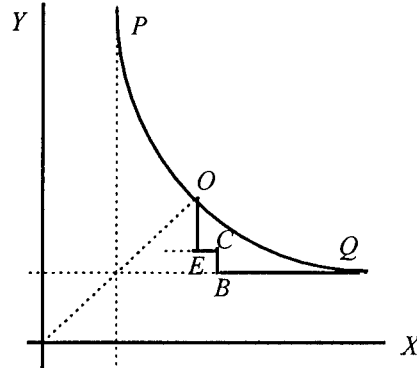


Fig. 2

Due to the relative positions of the actual and polygonal boundaries and the topography of the surface, the inequality is strict; $X + Y + Z > 3R$. When $R > 0$, the result for the case $R \leq D$ may be inferred by interchanging R and D in the preceding calculations and showing $X + Y + Z > 3D \geq 3R$. The case $R = 0$ is immediate.

The author would like to express his appreciation to W. Koshak, R. Blakeslee, H. Christian, and D. Phanord for their help and acknowledge the assistance of F. Six, G. Karr, L. Freeman, T. Shurtz, and S. Jefferson.

REFERENCES

1. Poehler, H. and C. Lennon, "Lightning detection and ranging system (LDAR), system description and performance objectives", NASA Technical Memorandum 74105 (1979).
2. Hager, W. and D. Wang, "An analysis of errors in the location, current, and velocity of lightning", being reviewed for publication in *J. Geophys. Res.* (1995).
3. Koshak, W., R. Solakiewicz, and H. Christian, "On the retrieval of lightning radio sources from time-of-arrival data", in preparation for submission to *J. Geophys. Res.* (1995).
4. Proctor, D., "A hyperbolic system for obtaining radio pictures of lightning", *J. Geophys. Res.* 76 (1971) 1478-1489.
5. MacClement, W. and R. Murty, "VHF direction finder studies of lightning", *J. Appl. Meteor.* 17 (1978) 786-795.
6. Twomey, S., *Introduction to the Mathematics of Inversion in Remote Sensing and Indirect Measurements*, Elsevier, New York, 1977.
7. Poehler, H., "An accuracy analysis of the LDAR system", NASA Contractor Report CR-154631 (1977).

1995

NASA/ASEE SUMMER FACULTY FELLOWSHIP PROGRAM

**MARSHALL SPACE FLIGHT CENTER
THE UNIVERSITY OF ALABAMA IN HUNTSVILLE**

WAS THE MSSTA II MISSION SUCCESSFUL?

Prepared By: Dwight C. Spencer

Academic Rank: Instructor

Institution and Department: Mississippi Delta Community College
Department of Science

NASA/MSFC:

Office: Space Sciences Laboratory
Division: Physics and Astronomy Division
Branch: Solar Physics Branch

MSFC Colleague: Richard B. Hoover

SCIENTIFIC OBJECTIVES

The Multi-Spectral Solar Telescope Array (MSSTA) is a rocket borne solar observatory designed to address a wide range of scientific questions relating to two aspects of the structure and dynamics of the solar atmosphere:¹¹

- (a) The heating and dynamics of chromospheric and coronal structures including spicules, coronal loops, bright points, and planes; and the role of the fine scale structure of the chromospheric network in the transport of mass and energy between these structures.
- (b) The large scale structures of the corona, including the interface of prominences and filaments with material at coronal temperatures, the transition region structure of coronal holes and plumes, and their relationship to the solar wind.

In order to address these fundamental scientific problems, the observational objective of the MSSTA is to obtain a set of high resolution spectroheliograms with the following properties:¹¹

- (i) Sufficiently broad spectral coverage and accurate photometry to allow modeling of structures covering the full range of temperatures observed in non-flaring chromosphere/corona, 10^4 K to 10^7 K.
- (ii) Sufficient spectral resolution ($\lambda / \Delta\lambda \sim 30-100$) in each spectroheliogram to allow isolation of the emission from lines excited over a narrow range of temperatures.
- (iii) To address objective (a), spatial resolution sufficient to resolve structures on the sun on a scale of 100-200 km (0.1-0.3 arc seconds); to address objective (b), images of the full disk and inner corona with resolution at least 1.0 arc second, and high sensitivity images of the extended corona (to $\sim 3-4$ solar radii above the limb) with resolution of ~ 3 arc seconds; for both objectives (c), direct measurements of the coronal magnetic field.
- (iv) To access the role of non-thermal phenomena in the heating and dynamics of the chromosphere/corona interface, high resolution ($\lambda / \Delta\lambda > 1000$) spectroheliograms with spatial resolution of 1-3 arc seconds.

The approach implemented, to address the observational objectives (i) and (ii), is to obtain very high resolution ($\sim 0.3-0.7$ arc seconds) spectroheliograms in lines excited over the full range of temperatures present in the non-flaring solar chromosphere, transition region, and corona by using an array of compact high resolution multilayer telescopes.¹¹

MSSTA II CONFIGURATION

The Multi-Spectral Solar Telescope Array (MSSTA)¹ is a sounding rocket borne observatory designed to image the sun at many spectral lines in soft X-Ray (XUV) [44.1-93.9Å], Extreme Ultraviolet (EUV) [150-335Å], and Far Ultraviolet (FUV) [1215.6-1550Å], wavelengths. MSSTA is a joint project of Stanford University NASA/Marshall Space Flight Center, and Lawrence Livermore National Laboratory. MSSTA II flown on November 3, 1994 at White Sands Missile Range consisted of nineteen telescopes; two Cassegrain telescopes, six Ritchey - Chrétien telescopes and eleven Herschellian telescopes (Figure 1).¹⁰

MSSTA Configuration ¹⁰

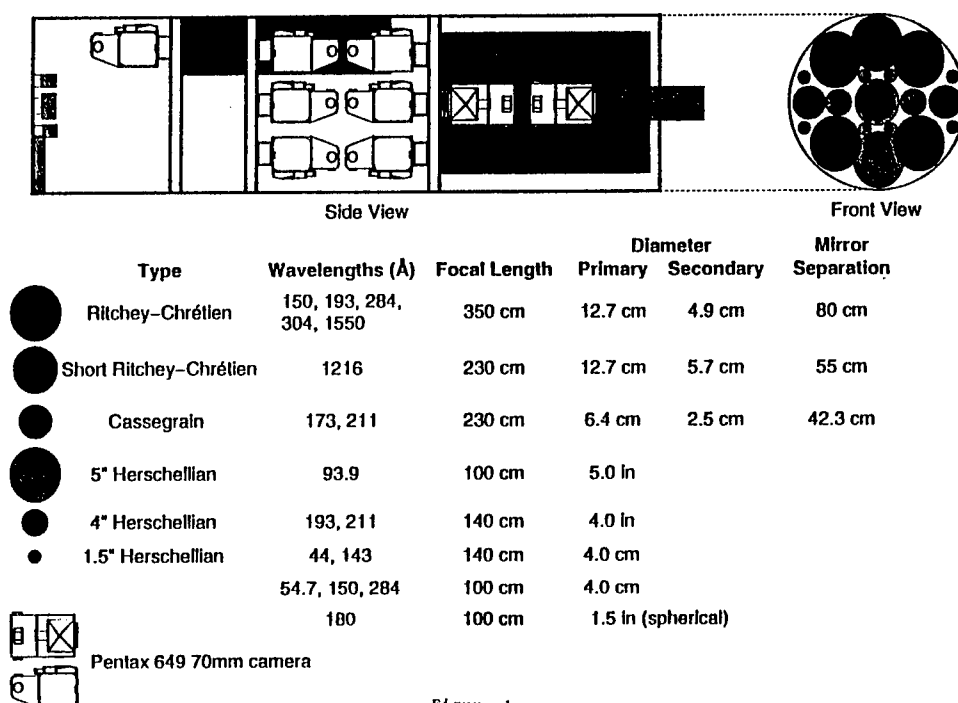


Figure 1

The two Cassegrain telescopes (with coated optics designed to reflect wavelengths of 173 and 211Å) were both flown on the first MSSTA payload on May 13, 1991. The 173 Å telescope was also flown on the Stanford-Marshall Space Flight Center Rocket Spectroheliograph sounding rocket payload on October 23, 1987. These Cassegrains are two-mirrored telescopes with spherical optical elements and were found to be defraction limited in visible wavelengths. The maximum resolution, however, is limited to 0.5 arc sec due to abberations.¹⁰

The six Ritchey-Chrétien telescopes are two mirrored telescopes with hyperbolic optical elements. These mirrors are held in place in their cells with a vacuum compatible Dow Corning Silastic RTV which also allows for slight motion during vibrational loading.¹⁰ To maximize changes in mirror separation, the optical benches were constructed of graphpic fiber in an epoxy resin.⁴ Earlier theoretical studies revealed that the Ritchey-Chrétien telescopes could obtain spatial resolutions of better than 0.3 arc sec over 48 arc min field of view at 1216Å (with the best

possible resolution of 0.03 arc sec occurring near the optical axis at a wavelengths of 173\AA).³ This flight carried five Ritchey-Chrétien telescopes with mirrors coated to image wavelengths of 150, 193, 284, 304, and 1550\AA . A Short Ritchey-Chrétien telescope was constructed and is capable of obtaining resolutions of 0.22 arc sec at its operating wavelength of 1216\AA .⁵

The eleven Herschellian telescopes flown were of five different types and designed to operate at 44.2, 54.7, 93.9, 143, 150, 180, 193, 211, and 284\AA . All were off-axis paraboloids except for the 180\AA telescope which was a General Optics 1.5 inch concave sphere with a 2 meter radius of curvature.¹⁰ The multilayer coating for this optic was deposited at MSFC by Palmer Peters a few weeks before launch.⁹

THE FLIGHT

The MSSTA II payload was launched aboard a Terrier-Black Brant VC Rocket from White Sands Missile Range at 1915 UT (1215 Local) November 3, 1994. The payload weighed 1072 lbs. The payload reached an altitude of 142.8 statute miles went down range approximately 52.0 statute miles (Figure 2).

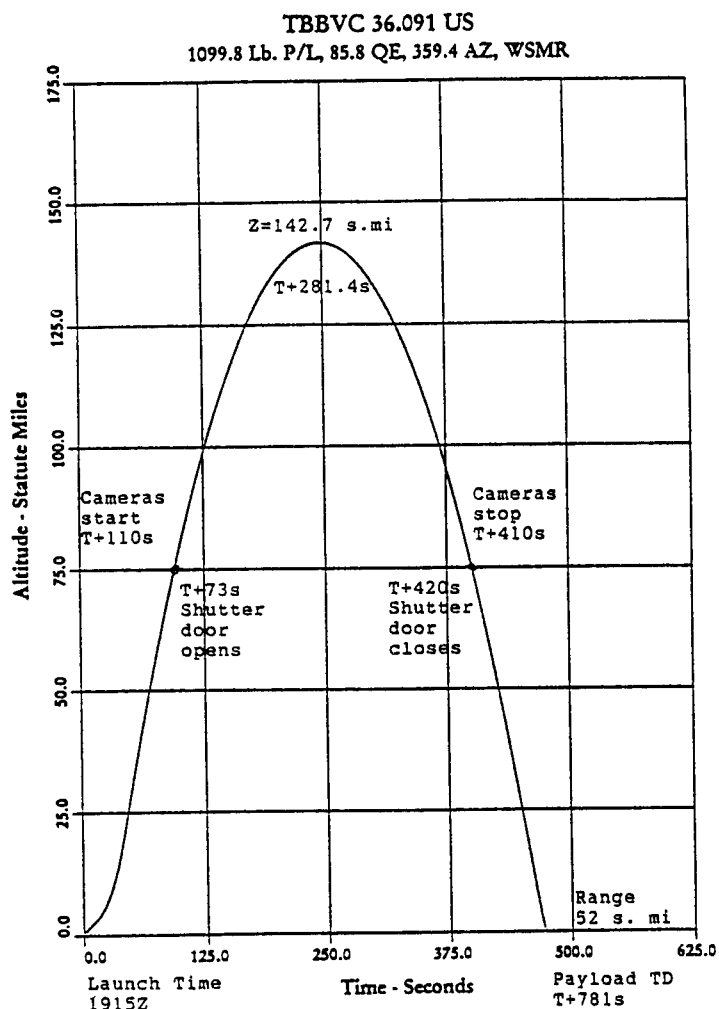


Figure 2 Altitude vs. Time¹²

At T+ 73 seconds into the flight the shutter door opened and at T+ 110 seconds (At an altitude of ~ 75 statute miles) the cameras began to operate (Figure 2). The cameras continued to operate for 300 seconds. Then at T+ 410 seconds (Again at an altitude of ~ 75 statute miles) the cameras shut down and at T+ 420 seconds the shutter door closed. The payload (MSSTA II) touched down at T+ 781 seconds.

MSSTA II RESULTS

MSSTA II obtained some outstanding solar images. In fact, it obtained the highest resolution images of the chromosphere ever photographed in the C IV line λ 1550Å.

The Cassegrain I telescope was able to image the corona in the Fe IX/X line at λ 173Å at a temperature of ~ 1,000,000 K (Photo 1). The fine lines in the photo are due to cracking of the XUV-100 film under vacuum. The image shows bright points, active regions, polar plumes and a coronal hole.

The Ritchey-Chrétien 2 telescope obtained the highest resolution images of the chromosphere ever photographed in the C IV line λ 1550Å at a temperature of ~ 100,000 K (Photo 2). The images show active regions, chromospheric network structure, spicules, small scale loops, and a coronal hole coincident with that observed in Photo 1.

The Short Ritchey-Chrétien yielded numerous images of the chromosphere in the H I Lyman α line at λ 1216Å at a temperature of ~ 20,000 K (Photo 3). The images also reveal active regions, chromospheric network, spicules, and small loops.



Photo 1. The corona at ~ 1,000,000 K
Fe IX/X λ 173Å



Photo 2. The chromosphere at ~100,000 K
C IV λ 1550Å

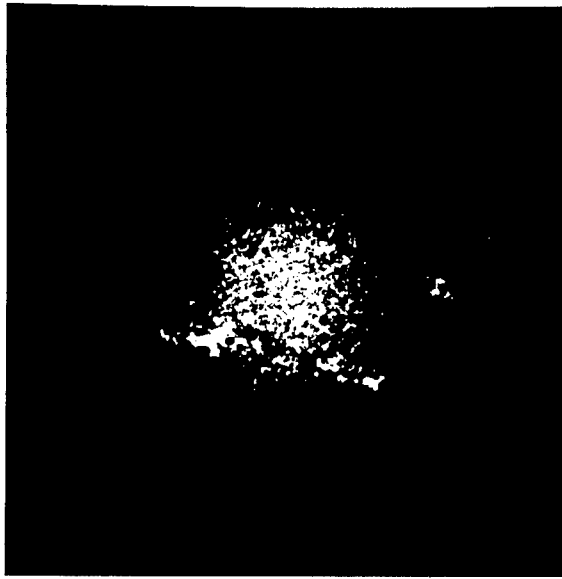


Photo 3. The chromosphere at $\sim 20,000$ K H I
Lyman α λ 1216Å

SUMMARY AND CONCLUSIONS

The MSSTA II payload with its compliment of nineteen telescopes was flown on November 3, 1994. The images obtained on this flight are still being analyzed. The 1550Å Ritchey-Chrétien yielded sub-arc second images of chromospheric fine structures which are correlated with coronal features shown in the 173Å Fe IX/X images. The MSSTA II payload was able to bring back images in wavelengths ranging from 173Å to 1550Å at temperatures ranging from 20,000K to 1,000,000K. The MSSTA II results were fully consistent with flight mission success criteria. Therefore, the mission was successful.

Detailed digitalization of all images obtained on this mission will be analyzed and compared with images obtained simultaneously or in close proximity with H- α , Ca K magnetograms and x-ray images from the Yohkoh Satellite. Subsequent research opportunities for these multilayer telescopes from a MIDEX Satellite, sounding rocket and the MIR Space Station are now being explored.

ACKNOWLEDGMENTS

This project was funded by NASA Grant NSG-5131 at Stanford University. Additional support has been received through the NASA/MSFC Center Director's Discretionary Fund. Dwight Spencer was supported by a NASA-ASEE Summer Faculty Fellowship Grant. I wish to thank Dr. Gerald R. Karr, MSFC NASA-ASEE Summer Faculty Fellowship Program Co-Director, Mr. Richard B. Hoover, Space Science Laboratory MSFC, Mr. David Gore Department of Physics UAB, Ms. Teresa Shurtz of Summer Programs Office at NASA/MSFC, and Ms. Jackie Bailey of Mississippi Delta Community College for their support.

REFERENCES

- [1] A.B.C. Walker, Jr., et al., "Multi-Spectral Solar Telescope Array," *Optical Engineering*, 29, pp. 581-591, 1990.
- [2] R.B. Hoover et al., "Solar Observations with the Multi-Spectral Solar Telescope Array," *SPIE Proc.*, 1546, pp. 175-187, 1991.
- [3] J.B. Hadaway, et al., "Design and Analysis of Optical Systems for the Stanford/MSFC Multi-Spectral Solar Telescope Array," *SPIE Proc.*, 1160, pp. 195-208, 1989.
- [4] R.B. Hoover, et al., "Performance of the Multi-Spectral Solar Telescope Array III. Optical Characteristics of the Ritchey-Chrétien and Cassegrain Telescopes," *SPIE Proc.*, 1343, pp. 189-202, 1990.
- [5] R.B. Hoover et al., "Design and Fabrication of the All-Reflecting H-Lyman α Coronagraph/Polarimeter," *SPIE Proc.*, 1742, pp. 439-451, 1992.
- [6] Arthur B.C. Walker, Center for Space Science and Astrophysics, Stanford University Stanford, CA 94305, Private Communication.
- [7] A.B.C. Walker, et al., "Soft X-Ray Images of the Solar Corona with a Normal-Incidence Cassegrain Multilayer Telescope," *Science*, 241, pp. 1725-1868, 30 Sep. 1998.
- [8] D.L. Shealy, R.B. Hoover, D.R. Gabardi, "Multilayer X-Ray Imaging Systems," *SPIE Proc.*, 691, pp. 83, 1986.
- [9] P.N. Peters, et al., "Fabrication of Multilayer Optics by Sputtering: Application to EUV Optics with Greater Than 30% Normal Reflectance," to appear in *SPIE Proc.*, 2515, 1995.

- [10] D.B. Gore, J.B. Hadaway, R.B. Hoover, A.B.C. Walker, "Optical Focusing and Alignment of the Multi-Spectral Solar Telescope Array II Payload," SPIE 1995.
- [11] A.B.C. Walker, Jr., et al., "Multi-Spectral Solar Telescope Array: Initial Results and Future Plans," SPIE Proc., 1742, pp. 500-514, 1992.
- [12] NASA, "Flight Requirements Plan for Terrier-Black Brant VC," pp. 6-18, 1992.

1995

NASA/ASEE SUMMER FACULTY FELLOWSHIP PROGRAM

MARSHALL SPACE FLIGHT CENTER
THE UNIVERSITY OF ALABAMA IN HUNTSVILLE

**ROLE OF THE MICRO/MACRO STRUCTURE OF WELDS IN CRACK
NUCLEATION AND PROPAGATION IN AEROSPACE ALUMINUM-LITHIUM
ALLOY**

Prepared by: George E. Talia, Ph.D.

Academic Rank: Associate Professor

Institution and Department: The Wichita State University
Department of Mechanical Engr.

MSFC Colleague: Arthur C. Nunes, Jr., Ph.D.

NASA/MSFC:

Office: Materials & Processes Laboratory
Division: Metallic Materials & Processes
Branch: Metallurgical Research

Introduction

Al-Li alloys offer the benefits of increased strength, elastic modulus and lower densities as compared to conventional aluminum alloys. Martin Marietta Laboratories has developed an Al-Li alloy designated 2195 which is designated for use in the cryogenic tanks of the space shuttle. The Variable Polarity Plasma Arc (VPPA) welding process is currently being used to produce these welds [1]. VPPA welding utilizes high temperature ionized gas (plasma) to transfer heat to the workpiece. An inert gas, such as Helium, is used to shield the active welding zone to prevent contamination of the molten base metal with surrounding reactive atmospheric gases. [1] In the Space Shuttle application, two passes of the arc are used to complete a butt-type weld. The pressure of the plasma stream is increased during the first pass to force the arc entirely through the material, a practice commonly referred to as keyholing. Molten metal forms on either side of the arc and surface tension draws this liquid together as the arc passes. 2319 Al alloy filler material may also be fed into the weld zone during this pass. During the second pass, the plasma stream pressure is reduced such that only partial penetration of the base material is obtained. Al 2319 filler material is added during this pass to yield a uniform, fully filled welded joint. This additional pass also acts to alter the grain structure of the weld zone to yield a higher strength joint.

Examinations of butt welds produced at the Marshall Space Flight Center in Al-Li 2195 has revealed cases of crack-like porosity in the weld fusion zone. Butt welds in 2195 Al-Li alloy with 2319 filler wire performed at Vanderbilt University under a range of welding conditions [20] exhibited secondary cracking along interdendritic boundaries in the fusion zone of fractured specimens in nearly all cases. Similar cracks were reported in the run-out portion of remaining unfractured samples. Two Vanderbilt samples displayed .06" interdendritic tears in the center of the fusion zone which were not involved in the fracture. Talia and Nunes found porosity in the first pass fusion zone in two pass weldments in the identical alloy. [3]

Cast aluminum alloys are particularly susceptible to interdendritic hot cracking due to their high coefficient of thermal expansion and high solidification shrinkage (approximately 6%). Chemical composition strongly influences the susceptibility to hot cracking among aluminum alloys. For example, a binary Al-Li alloy showed maximum susceptibility at 2.6 w/o Li, while binary Al-Mg alloys show maximum susceptibility at 1.4 w/o Mg. [4]

The present study focussed on the crack structures as potential flaws responsible for the premature fracture of cast fusion zone of 2195 Al-Li alloys, which would otherwise exhibit much greater strength.

Experimental Procedures

2195 Al-Li alloy plates were produced by the Reynolds Metals Company, two passes (root pass and cover pass) welds were performed at the Marshall Space Flight Center by Lockheed Martin-Manned Space Systems and Lockheed Martin Astronautics. Tensile samples were milled to obtain uniform cross-sections. Tensile tests at room temperature were employed to study the initiation and propagation of cracks and microcracks in the welding zone. Most of the tests were interrupted and transverse and longitudinal sections of the welds were examined by optical micrographic techniques.

Each metallographic sample was prepared for examination using standard polishing preparation techniques and etched with Keller's reagent. Observations were performed using a Nixon inverted microscope. Additional observations were performed using an scanning electron microscope.

Results and Discussion

The initial optical metallographic observations of the single pass weld revealed a well formed grain structure with a small amount of porosity. This porosity appear to compare with the initial porosity of the parent metal. However, Scanning Electron Micrographs revealed large porosity specially around the Cu-rich second phase (see Figure 1) and some of the pores take a crack-like shape as shown in Figure 2. The grain boundary integrity is by the porosity and the crack-like shape of the G.B. could reduce the fracture strength of the material.

Figure 3 exhibits sings of the influence of grain structure on the tensile behavior of a high-strength **2195 Al-Cu-Li** alloy. Crack nucleation can occur at slip-band grain boundary intersections and subsequent propagation can then occur along the slip bands or along grain boundaries. The welded zone has a central dendritic structure. Most of the long cracks seen in the microscope appear related to such dendritic structure and they are formed by a series of two to four narrow subcracks (see Figure 4). The number of subcracks increase as the deformation increases. A combined mechanism of G.B. cracking and metal yielding seems to govern the deformation.

Tensile tests at room temperature were employed to characterized the mechanical properties of the different alloys and to observe changes in the microstructure, especially in the welding zone. For comparison, 2219 samples were also tested. Additional tensile tests were performed to evaluate the welding zone strength after solution treatment (1 hr. at 485 degrees C) and aging (7 days at room temperature). Table 1 present a summary of the tensile data of the alloys. It is noteworthy that when cracking occurred corresponding serrations were observed in the stress-strain curves for both 2219 and 2195.

Table 1 - Tensile Data

	Y.S. (psi)	UTS (psi)	Max Def.*	Fracture Strength** (psi)	Max. True Strain*
2219 As Welded	13,342	42,692	31.2 %	55,618	0.27
2195 As Welded	30,864	43,866	5.8 %	46,410	0.06
2195 Thermal Treat.	27,120	51,112	22.8 %	61,508	0.20

* Assuming an strain gauge of 0.25 " - **Force divided by the fracture area

In general 2195 is a stronger material than 2219. The yield strength (Y.S.) of 2195 is much larger than the one presented for 2219. The UTS of both materials are similar but surprisingly, the fracture strength of 2219 is 20 % larger than of 2195. A possible explanation for the lower fracture strength may be the greater porosity of the G.B. of the 2195 as observed in Figure 1. Figure 5 illustrate the crack structure of 2195 as welded near the yielding (31,000 psi) at almost no

deformation. A very well defined crack is observed. For 2219 cracks appear at larger deformation. Figure 6 presents the initial of crack arrangement for a deformation of 13.2 % under true stresses of near 51,000 psi. Note the heavier deformation texture of 2219.

The thermally treated 2195 alloy increased in fracture strength from 20 % below to 10 % above that of 2219. Due to the thermal treatment, the G.B. segregation was eliminated (see Figure 7). Apparently, 2195 become much stronger if the interdendritic material is redissolved into the grains.

Conclusions and Recommendations

Initial results have led to the following tentative conclusions:

- a) The fracture strength of 2195 alloy welds is limited by the grain boundary integrity. G.B. porosity has a negative effect upon G.B. Integrity in 2195 alloy.
- b) The pattern of aligned dendrites at the center of both 2219 and 2195 welds is a source of initial cracks leading to fracture.
- c) Cracking produced serration in the stress-strain curve for both 2219 and 2195 alloys.
- d) In situ SEM observation of tensile tests at room temperature should be employed to characterize the structural features associated with the progressive phases of deformation.
- e) Hot tensile tests should be performed to evaluate the effect of the temperature variation on the integrity of the weldments.

Acknowledgments

The authors are extremely grateful to Dr. Sandeep Shah and Mrs Lynda Johnston (Lockheed Martin -Manned Space Systems) and Mr. Gerald Bjorkman for helpful discussions, experimental assistance, and welded material provided..

References

- 1) Nunes, A.C. "The Variable Polarity Plasma Arc Welding Process: It's Application to the Space Shuttle External Tank - First Interim Report", NASA Technical Memorandum TM-82532, June 1983.
- 2) Materials Science and Engineering Department - Vanderbilt University, "Analysis of the 2195 Aluminum-Lithium Alloy Weld Microstructure and Properties", Prepared for Martin Marietta Manned Space Systems, September 30, 1992.
- 3) Talia, G.E., Nunes, A.C., "Microstructural Analysis of the 2195 Aluminum-Lithium Alloy Welds", Prepared for the Marshall Space Flight Center, 1993.
- 4) Cross, C.E., Olson, D.L., Edwards, G.R., Capes, J.F., " Weldability of Aluminum - Lithium Alloys", Proceedings: Second International Aluminum-Lithium Conference, 1983

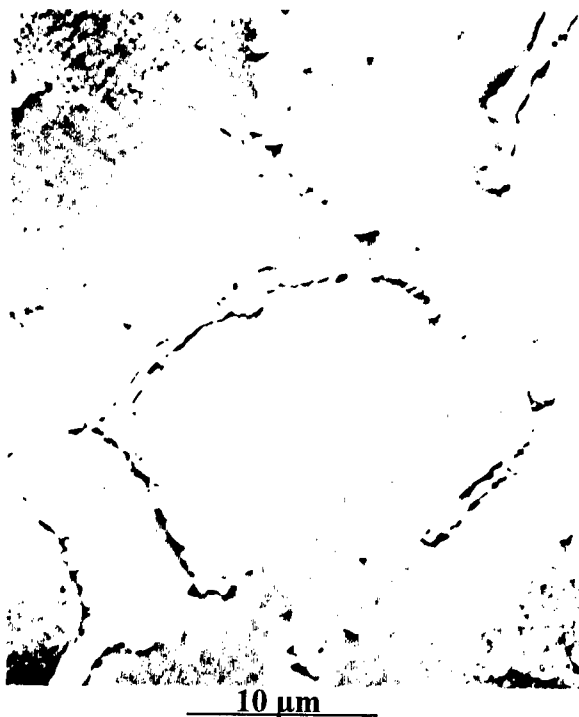


Figure 1.- Scanning Electron Micrograph presenting porosity special around the Cu-rich phase.



Figure 3.- Photograph presenting crack nucleation at slip band-grain boundary intersections.



Figure 2.- SEM micrographs showing G.B. with a crack-like shape.



Figure 4.- Optical micrographs of 2195 Al-Li alloy subjected to deformation.



Figure 5.- Crack structure of 2195 at almost no deformation.



Figure 7.- Micrographs showing the effect of the thermal treatment on the G.B. structure.



Figure 6.- Crack initiation in 2219 at deformation of 13 %.

1995

NASA/ASEE SUMMER FACULTY FELLOWSHIP PROGRAM

MARSHALL SPACE FLIGHT CENTER
THE UNIVERSITY OF ALABAMA IN HUNTSVILLE

MATHEMATICAL MODELING OF THE GAS AND POWDER FLOW IN THE
(HVOF) SYSTEMS TO OPTIMIZE THEIR COATINGS QUALITY

Prepared By:	Hazem H. Tawfik, Ph.D., P.E., CMfg.E.
Academic Rank	Professor and Director
Institution and Department	State University of New York at Farmingdale Manufacturing and Mechanical Research
NASA/MSFC:	
Laboratory:	Materials & Processes Laboratory
Division:	Metallic Materials Division
Branch:	Metals Processes Branch
MSFC Colleague:	Frank Zimmerman

1. INTRODUCTION

Thermally sprayed coatings have been extensively used to enhance materials properties and provide surface protection against their working environments in a number of industrial applications. Thermal barrier coatings (TBC) are used to reduce the thermal conductivity of aerospace turbine blades and improve the turbine overall thermal efficiency. TBC allows higher gas operating temperatures and lower blade material temperatures due to the thermal insulation provided by these ceramic coatings. In the automotive industry, coatings are currently applied to a number of moving parts that are subjected to friction and wear inside the engine such as pistons, cylinder liners, valves and crankshafts to enhance their wear resistance and prolong their useful operation and lifetime.

Recently, hexavalent chromium associated with hard chromium plating, was classified as a human carcinogen and environmental pollutant. Aerospace industry has traditionally used hard chrome plating as a corrosion protection material. Accordingly, NASA is developing thermal spray coatings to replace the hard chrome plating that is currently being utilized on the space shuttle main engine. These coatings are made of tungsten carbide and cobalt, chromium oxide, and FerroTic (iron based material with titanium carbide) to provide protection against wear, corrosion and hydrogen embrittlement of the low pressure liquid hydrogen carrying ducts on the shuttle main engine. One of these sections is the Low Pressure Fuel Turbo Pump (LPFTP) discharge duct used on the shuttle main engine. The duct carries liquid hydrogen fuel at temperature of -253°C (-423°F) to the High Pressure Fuel Turbopump from the (LPFTP) [1].

In addition to the extensive use of thermal spray in generating protective coatings, it has been used in the manufacturing of near-net shape parts with customized material and engineered properties. In these applications, thermal spray is used to build up material(s) to form the required part geometry. Moreover, thermal spray is used for the repair of worn or mis- machined mechanical parts.

Despite the considerable advancement in the thermal spray technology, the industry still faces strong challenges with the coatings quality in the following areas: 1) Delamination or debonding at the substrate/coating interface and intersplat boundaries - this usually occurs due to mechanical and thermal residual stresses caused by a mismatch in the thermal expansion coefficient combined with localized sharp temperature gradient due to a high cooling rate. 2) The occurrence of voids and porosity within the coatings - is usually caused by trapped gases and/or powder oxidation during spraying process. This will drastically weaken both the corrosion protection ability and the hardness of the thermally sprayed coatings. The porosity will allow the corrosive solution to penetrate the coating to the interface between the base material and the coating.

Thermally sprayed coatings are formed from the flattened consolidation and solidification of molten powder particles; thus, the properties of these coatings are highly dependent on the spraying process itself. Accordingly, the microstructure, porosity, hardness and bonding strength of the coatings are mainly controlled by the temperature and the

velocity of molten particles [2]. Critical review of the literature on thermal spray coatings, indicated that high velocity thermal spray processing conditions offer the best potential to minimize the occurrence of manufacturing related flaws and provide high quality coatings [3].

In recent years the High Velocity Oxygen Fuel (HVOF) system has been considered an asset to the family of thermal spraying processes Fig. (1). Especially, for spray materials with melting points below 3000 °K it has proven successful, since it shows economic advantages when compared to other coating processes that produce similar quality coatings [4]. In such systems that produce high velocity particles, the oxide content of the coatings did not correlate to the particle temperature or the excess oxygen in the lean fuel conditions, but it is related to high substrate temperatures [5]. It is believed that the primary mechanism for the formation oxide inclusions occurs after a particle splat, when the hot coating is exposed to the oxygen contained in the relatively low velocity boundary layer. The exposure times of a given splat to the boundary layer are on the order of seconds, a factor of 10^3 longer than during particle flight [6]. The usual evaluation of optimized spraying parameters, which include stand off distance, fuel and oxygen flow rates, powder size, and barrel length, are based on numerous, extensive, and expensive experiments laid out by trial-and-error or statistical design of experiments and Taguchi methods [4].

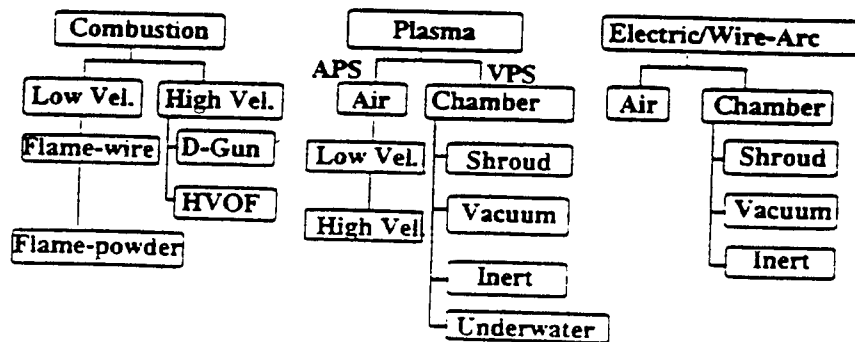


Figure 1. Thermal Spray processes

The application of simulation techniques to thermal spray processes has grown steadily over the past years because of the relatively inexpensive parametric analysis and operations. Once a model of the process is established and validated, system parameters become evident. The obtained fundamental understanding of the optimization process can be accomplished with a numerical computer model [4].

The objective of this investigation was to develop a computer model that simulates the thermal and gas dynamics of both gases and particles associated with the HVOF process to provide predictions of the particles velocities and temperatures. In the HVOF process oxygen and atomized kerosene are injected coaxially into the combustion chamber, Fig. (2), where they are mixed and ignited by a spark plug. The hot combustion gases are accelerated to supersonic conditions in a convergent-divergent nozzle. At the exit of the nozzle the

powder is transversely injected with an argon or nitrogen carrier gas. The powder is heated and accelerated in the gun barrel and jet region by the hot gas and eventually is deposited on the substrate. The model was partially validated against the very limited experimental data collected from Hobart Tafa using the JP-5000 gun and shown in Figure (2).

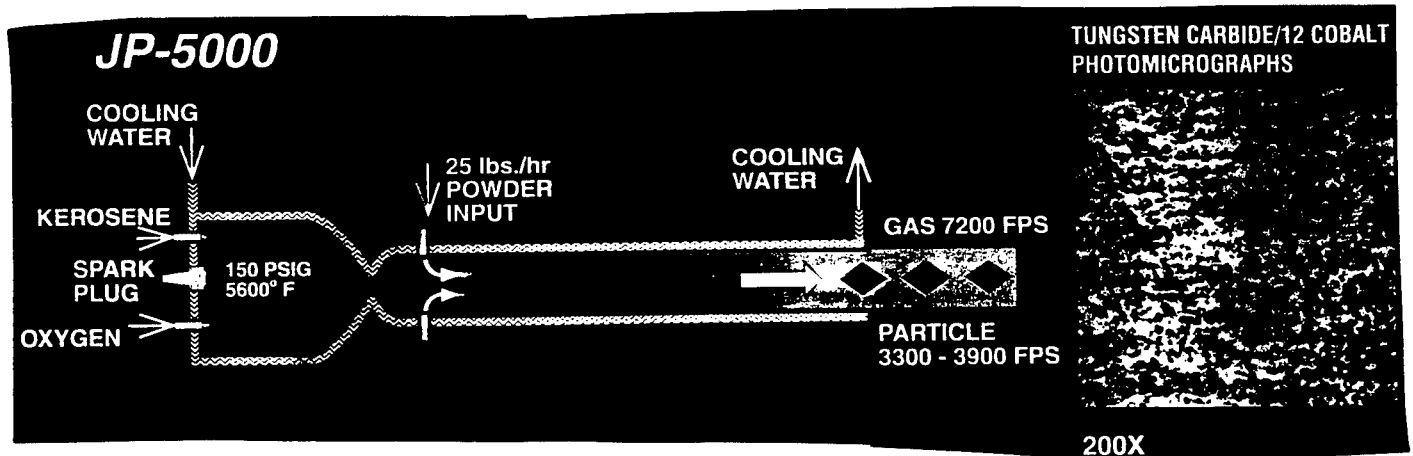


Fig.(2) Hobart Tafa HVOF/JP-5000 - with shown Numerical Values for Gas and Particle Velocity and Temperature

2. MATHEMATICAL MODEL

The current model development was accomplished in four main stages as described in the following :

First Stage: Modelling of the gases flow inside the HVOF system without initial consideration to the powder flow [7]:

The generalized flow equations with the influence parameters were used to model the gas flow in the HVOF system shown in Figure (2). The temperature and Mach Number equations (1), (2) were numerically integrated for a single phase non-adiabatic friction flow with variable specific heats [7].

$$\frac{dM^2}{M^2} = -2 \frac{(1 + \frac{k-1}{2} M^2)}{1 - M^2} \frac{dA}{A} + \frac{1 + kM^2}{1 - M^2} \frac{dQ}{c_p T} + \frac{kM^2(1 + \frac{k-1}{2} M^2)}{1 - M^2} 4f \frac{dx}{D} - \frac{dk}{k} \quad (1)$$

$$\frac{dT}{T} = \frac{(k-1) M^2}{(1 - M^2)} \frac{dA}{A} + \frac{(1 - kM^2)}{(1 - M^2)} \frac{dQ}{c_p T} - \frac{k(k-1)M^4}{2(1 - M^2)} 4f \frac{dx}{D} \quad (2)$$

Equations (1) and (2) above were solved by a numerical computer model and predictions of the gas velocity and temperature were obtained [7] at all the flow cross sections inside the

thermal spray system for the inlet conditions given in Fig. (1). Due to the appearance of the term $(1-M^2)$ in the denominator of equations (1) and (2), the numerical model experienced some degree of singularity in the vicinity of the throat section. The model quickly recovered as the solution propagated downstream of the throat area. However, this singularity problem could be completely rectified by the application of a Taylor series expansion on these terms in the throat proximity zone.

Second Stage: Empirical Correlation for the mean axial velocity and temperature decay of a free supersonic jet plume:

Visual studies such as Schlieren flow visualization showed a "potential core" with an embedded shock-diamond structure that is formed in the supersonic zone due to the underexpanded nature of the jet, Fig (3), [6]. Further down stream large turbulent eddies were generated by the large velocity and temperature gradients at the boundary layer between the jet and the ambient air. This mixing zone is further subjected to the effect of a large density difference between the hot jet core and the comparatively cold and slow ambient atmosphere. Small particles $5\text{ }\mu\text{m}$ or smaller will fully track the turbulent motion of the fluid, however, much larger particles, such as typical HVOF metal spray powders, are generally unaffected by the eddies and remain in the relatively high temperature, low density, and least motion resistance zone near the jet centerline.

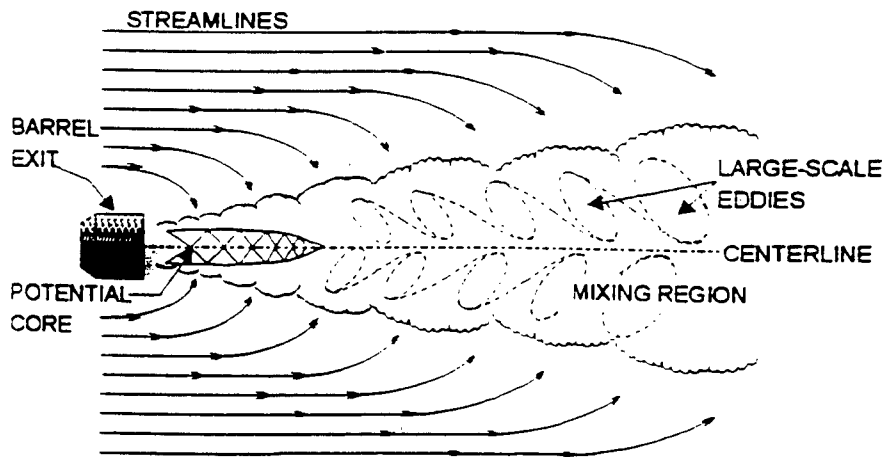


Fig. (3) Supersonic Jet Structure

In an attempt to better understand the noise generation mechanism in supersonic free jets, considerable investigation efforts have been devoted to the measurements of various flow parameters and the study of how these quantities vary with jet flow conditions [8]. Earlier mean velocity measurements [8] using laser velocimeter and hot-wire anemometer resulted in an empirical formula which gives the variation of the potential core length, Figure (3) with the Mach number for both heated and cooled jets, it read as follows:

$$\frac{x_c}{D} = 4.2 + 1.1 M_j^2 \text{ ----- (3)}$$

Another general empirical correlation for the supersonic axial mean velocity decay with range of validity between Mach Number 0.3 - 1.4., this correlation read as follows [8]:

$$\frac{U}{U_j} = 1 - \exp \left[\frac{1.35}{\left(1 - \frac{x}{x_c}\right)} \right] \text{ ----- (4)}$$

In the HVOF applications the jet mean axial velocity and temperature ranges are between (1.5 - 2.5 M) and (1500 - 3000° K) respectively. The recent study of the heated jets indicated that the potential core length decreased as the jet temperature increased [9]. Thus, correlations (3), and (4) were modified to expand their range of validity by correlating recent measurements of the mean axial decay velocity and temperature obtained from NASA/Langley [9] and University of Toronto [10]. Figures 4 and 4A show the mean velocity and temperatures correlations in relation to the measured values respectively. The comparison of these Figures 4, and 4A for free axisymmetrical jets indicated that the velocity decays faster than the temperature.

Third Stage: Momentum Transfer Mechanism Between Gas and Particle

The momentum equation, for either solid or liquid particles, are solved in a Lagrangian frame of reference moving with the particles. The equation of motion for the particle is written as [11]:

$$m_p \frac{dV_p}{dt} = \frac{1}{2} \rho_g A_p C_D (V_g - V_p) |V_g - V_p| - V_p \nabla p \text{ ----- (5)}$$

Where m_p is the mass of the particle and V_p is the velocity vector of the particle, C_D is the drag coefficient, and the particle motion in two-phase flows depends upon the gas properties, particle properties, and ρ_g , V_g , P are the density, velocity and pressure of the gas, respectively. A_p is the particle surface area and V_p is the particle volume. All particles are assumed to be spherical. This equation of motion for a particle accounts for the acceleration/deceleration of the droplet, due to the combined effects of drag from the gas flow, and local pressure gradients in the gas. Because the gas flow pressure change is small in the friction flow inside the gun barrel and the free jet plume, the gas pressure gradient effect on the particle motion is neglected in comparison to the drag force. A literature survey in the area of two-phase flows reveals that a number of drag coefficient equations have been used to calculate particle motion in supersonic flows [12]. Because the particles are initially injected into a supersonic flow, each particle will have a shock wave on the upstream side. The drag induced on these particles in this supersonic flow is calculated with the following

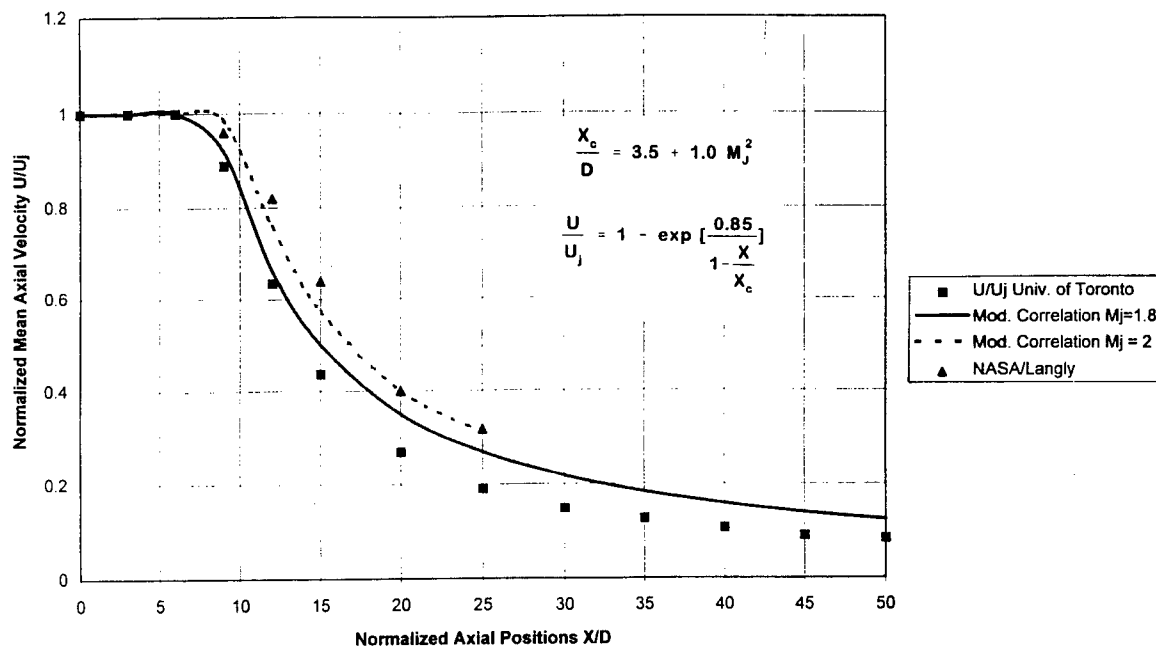


Figure (4) Modified Axial Decay Velocity in Supersonic Jet Plumes

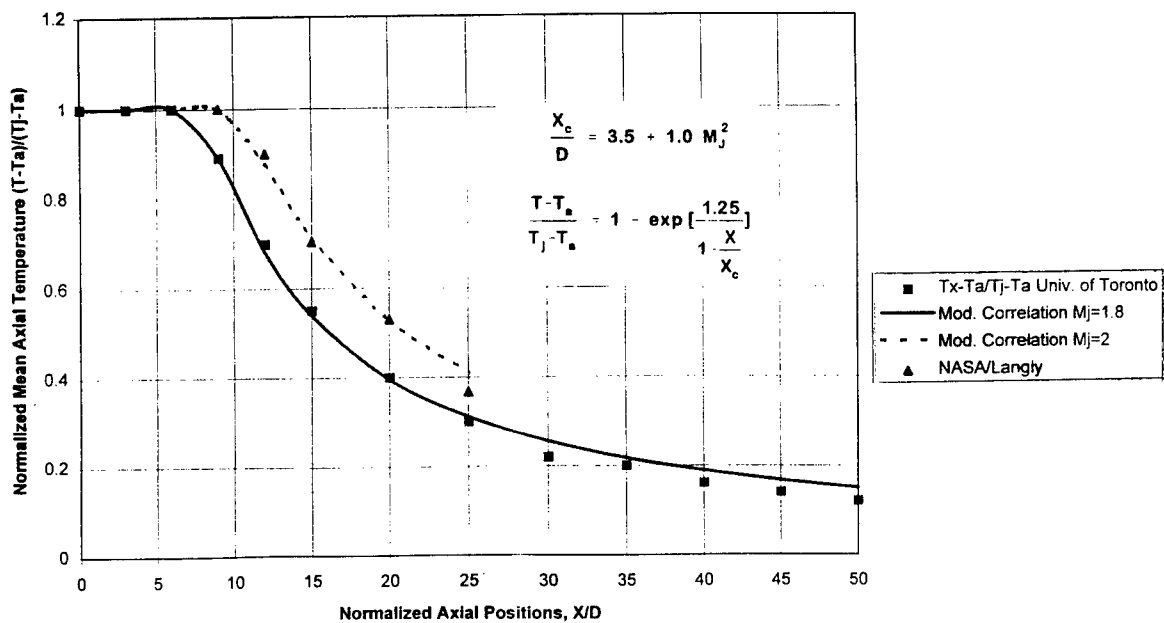


Figure (4) Modified Axial Decay Temperature For Supersonic Jet Plumes

empirical correlation:

$$\frac{dV_p}{dt} = \frac{3}{4} C_D \left(\frac{\rho_g}{\rho_p} \right) \frac{(V_g - V_p) |V_g - V_p|}{d} \text{----- (6)}$$

The drag coefficient for the particle is based on the local Reynolds number of the particle and is evaluated as:

$$R_e = \frac{\rho |V_g - V_p| d_p}{\mu}$$

here μ is the molecular viscosity of the gas. The variation of the gas viscosity was evaluated from the graph and empirical formula shown in Figure (5). The following correlations have been found to be valid for a wide range of Reynolds number [11]; it reads as follows:

$$C_D = \frac{24}{R_e} \quad \text{for } R_e < 1$$

$$C_D = \frac{24}{R_e} (1 + 0.15 R_e^{0.687}) \quad \text{for } 1 < R_e < 10^3$$

$$C_D = 0.44 \quad \text{for } R_e > 10^3$$

Fourth Stage: Heat Transfer Mechanism Between The Gas and The Powder:

The coefficient of heat transfer (h) between the particle and the gas can be determined from the following Ranz-Marshall semiempirical equation:

$$Nu = \frac{h d_p}{k_g} = 2 + 0.6 Re^{.5} Pr^{0.3333}, \quad Pr = \frac{c_p \mu_g}{k_g}$$

Where c_p is the specific heat of combustion gases given by correlations shown in table (1), d_p is particle diameter, and k_g is the coefficient of gases thermal conductivity - it was evaluated from a correlation as a function of the temperature as shown in Figure (6). Considering that the particle maintained its spherical configuration all through the process, the temperature of the particle was calculated from the following expression:

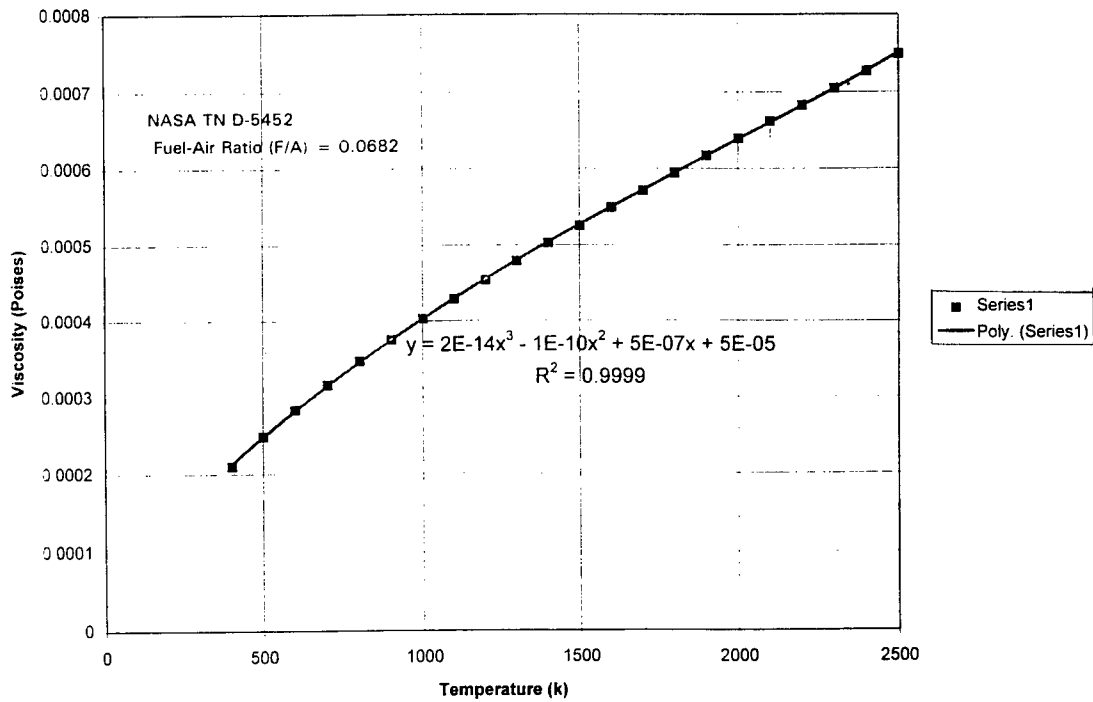


Fig. (5) Viscosity vs Temperature For Combustion Gases of ASTM-A-1 Burned in Air at 3 Atmospheres

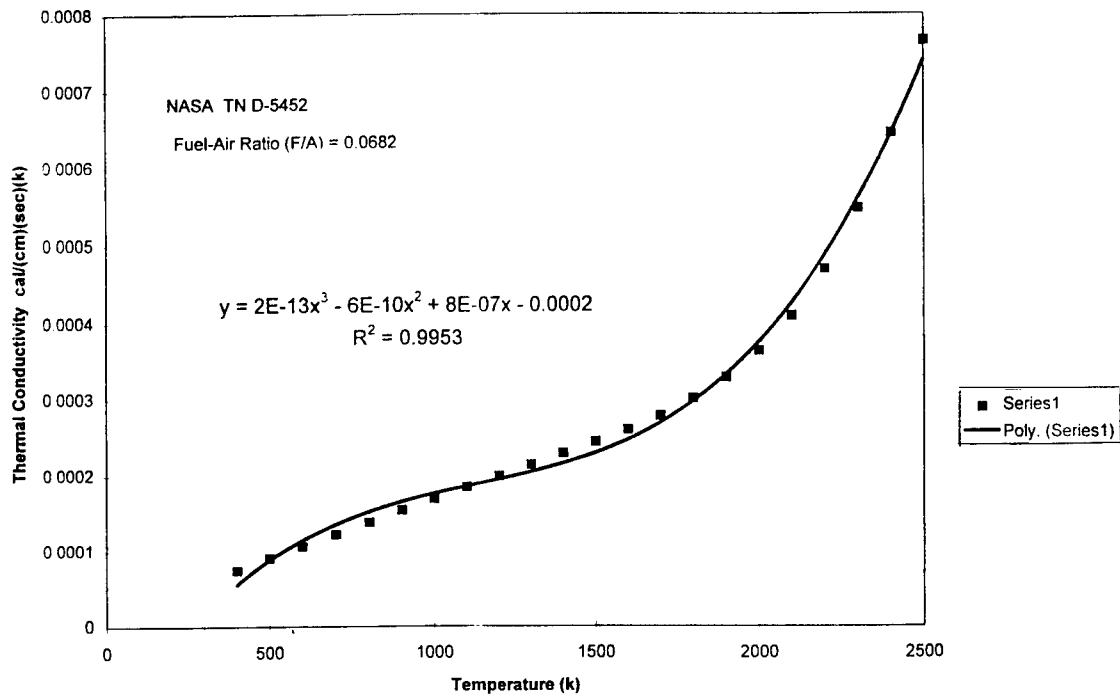


Fig.(6) Thermal Conductivity vs Temperature For Combustion Gases of ASTM-A-1 Burned in Air at 3 Atmospheres

$$T_p = \frac{\Delta t h T_g + \frac{1}{3} \rho_p R_p c_p T_{p_i}}{\Delta t h + \frac{1}{3} \rho_p R_p c_p}$$

3. RESULTS AND ANALYSIS

The model predictions showed an expected sharp increase in both of the particle velocity and temperature when the powder was initially injected in the barrel, Figures (7A) , and (8A). The particle velocity reached almost half the gas velocity at the end of the barrel. Meanwhile, the particle temperature closely approached the gas temperature at the same section. This indicates that the heat transfer mechanism between the gas and the particle is more efficient than the momentum transfer mechanism. The model predictions of particle and gas velocities and temperatures in the jet plume Figures (7B) and (8B) showed that the gas maintained its velocity and temperature over the potential core zone, that extends up to X/D approximately equals 8 to 10, due to a very small amount of ambient air entrainment. At the end of this zone, both the gas velocity and temperature experience rapid decrease as they cross below the particle velocity and temperature curves shown in Figures(7B) and (8B). This is attributed to large entrainment of a comparatively much cooler and slower surrounding atmosphere in the mixing turbulent region of the jet generated by the shear boundary layer and the density difference between the jet and the environment. The overall effect is that the jet is cooled , spread, and decelerated as depicted in Figures (7B) and (8B). Also, the same two Figures showed the velocity and temperature predictions of two different particles, Tugesten Carbide (WC) and Inconel 718. The predictions showed the expected trends as the lighter Inconel 718 particle with a density almost half that of the WC particle gained and lost both heat and momentum faster than the WC particle as clearly shown in Figures (7A), (7B), (8A), and (8B).

5. CONCLUSIONS

- (1) The model predictions showed the expected velocity and temperature trends for both particle and gas.
- (2) The model was partially validated against a very limited measurements provided by the manufacturer
- (3) After model validation, it could be used for parametric study and optimization of HVOF systems.
- (4) Singularity due to the $(1-M^2)$ term, very briefly affected the model prediction around the throat area but the model quickly recovered.

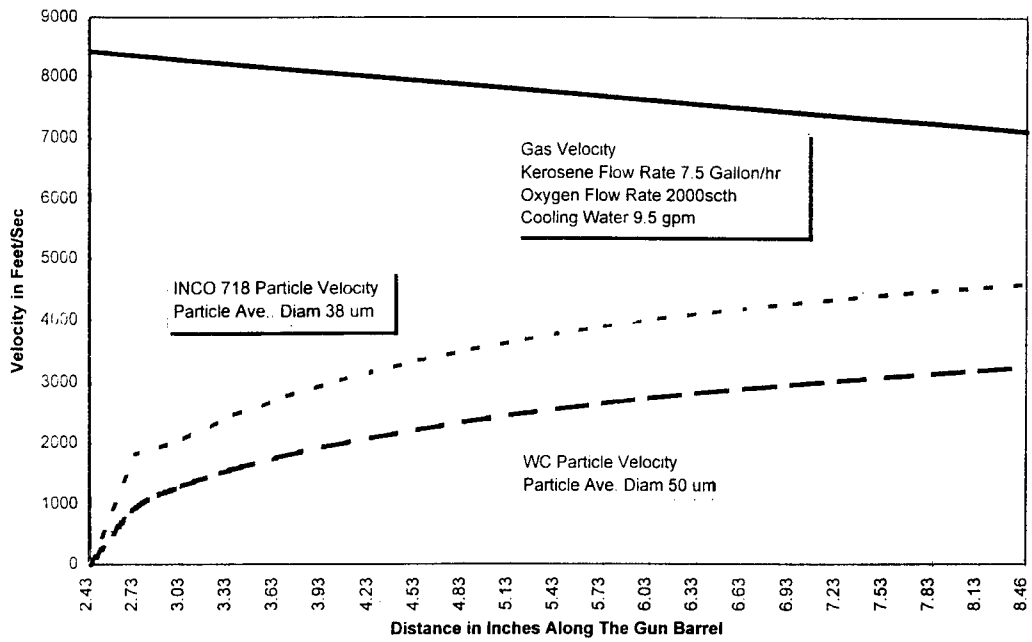


Fig.(7A) Predicted Gas and Particles Velocities Inside The JP-5000 Barrel

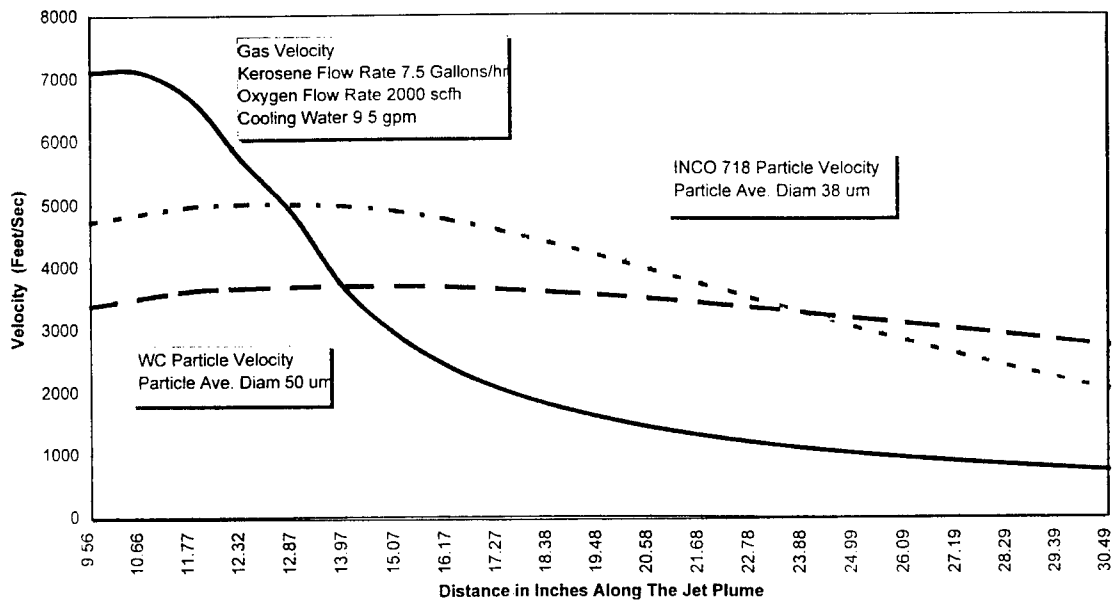


Fig. (7B) Predicted Gas and Particles Velocities In The Free Jet Plume of a HVOF System

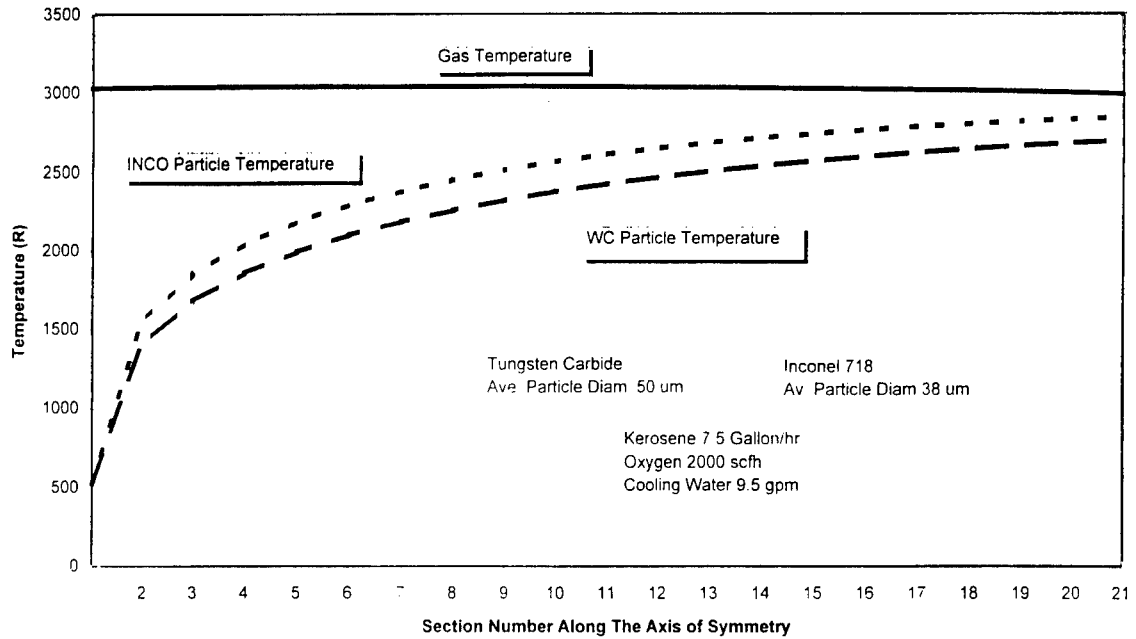


Fig.(8A) Predicted Gas and Powder Temperatures inside The JP-5000 Gun Barrel

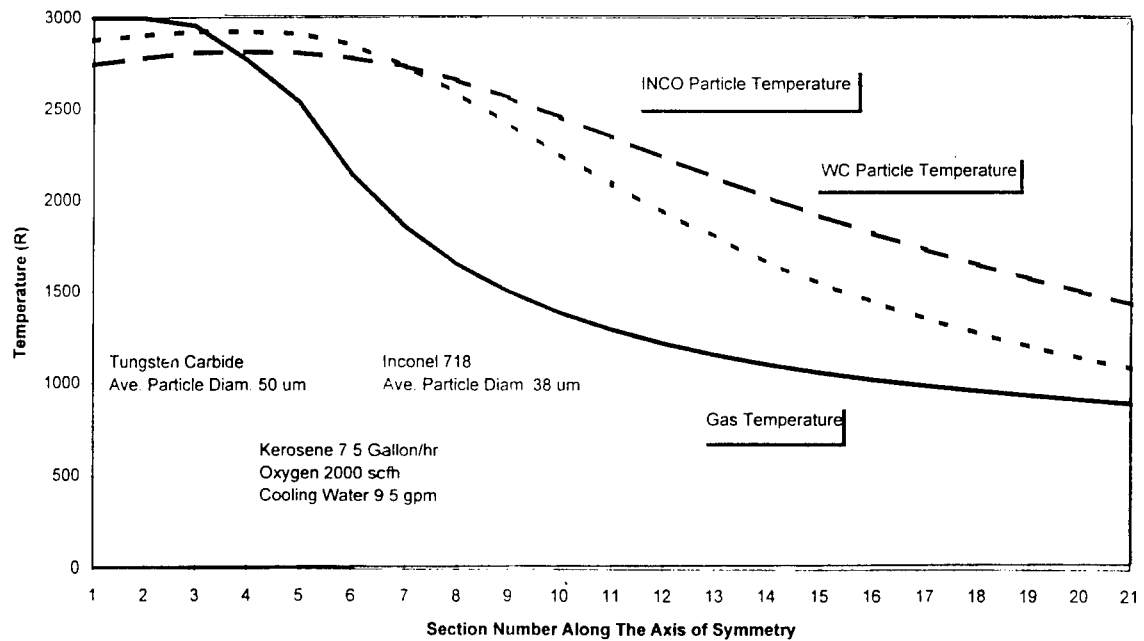


Fig. (8B) Predicted Gas and Powder Temperatures in The Jet Plume

6. RECOMMENDATIONS

- (1) Measurements of velocity and temperature of gas and particle are necessary for the model validation
- (2) The model should be used to perform parametric study and system optimization
- (3) Rectify the singularity problem due to the appearance of the term $(1-M^2)$ in the denominator - Use Taylor series expansion

7. REFERENCES

- [1] R.L.Daniel, H.L. Sanders, M.J. Mendrek, "Replacement of Environmentally Hazardous Corrosion Protection Paints on the Space Shuttle Main Engine Using Wire Arc Sprayed Aluminum", Proceedings of the 7th National Thermal Spray Conference 20-24 June 1994, Boston, Massachusetts.
- [2] P.Siitonen, T.Konos, P.Kettunen, "Corrosion Properties of Stainless Steel Coatings Made by Different Methods of Thermal Spraying", Proceedings of the 7th National Thermal Spray Conference 20-24 June 1994, Boston, Massachusetts.
- [3] R.Shah, K-C.Wang, K.Parthasaathi, J.Jo, E.Onesto, "Towards Manufacturing High-Quality Thermal Spray Coatings", Proceedings of the 7th National Thermal Spray Conference 20-24 June 1994, Boston, Massachusetts.
- [4] O.Knotek, E.Lugscheider, P.Jokiel, U.Schnaut, A.Wiemers, "Chromium Coatings by HVOF Thermal Spraying: Simulation and Practical Results, Proceedings of the 7th National Thermal Spray Conference 20-24 June 1994, Boston, Massachusetts.
- [5] W.D.Swank, J.R.Fincke, D.C.Haggard, G.Irons, R.Bullock, "HVOF Particle Flow Field Characteristics", Proceedings of the 7th National Thermal Spray Conference 20-24 June 1994, Boston, Massachusetts.
- [6] C.M.Hackett, G.S.Settles, "Turbulent Mixing of the HVOF Thermal Spray and Coating Oxidation", Proceedings of the 7th National Thermal Spray Conference 20-24 June 1994, Boston, Massachusetts.
- [7] H.Tawfik, F.Zimmerman, "Quality Optimization of Thermally Sprayed Coatings Produced by HVOF Systems Using Mathematical Modeling", 1994 NASA/ASEE Summer Faculty Fellowship Program, NASA Marshall Space Flight Center, AL.
- [8] J.C.Lau, P.J.Morris, "Measurements in subsonic and supersonic free jets using a laser velocimeter", J. Fluid Mech, (1979), vol. 93, part 1, pp.1-27

- [9] N.T.Lagen, J.M.Seiner,"Evaluation of Water Cooled Supersonic Temperature and Pressure Probes For Application to 2000°F Flows", NASA Technical Memorandum 102612.
- [10] L.Y.Jiang, J.P.Sislian, "LDV Measurements of Mean Velocity Components and Turbulence Intensities in Supersonic High-Temperature Exhaust Plumes", AIAA-93-3067.
- [11] W.L.Oberkampf, M.Talpallikar,"Analysis of a High Velocity Oxygen-Fuel (HVOF) Thermal Spray Torch-Part 1: Numerical Formulation", Proceedings of the 7th National Thermal Spray Conference 20-24 June 1994, Boston, Massachusetts.
- [12] M.L.Thorpe, and H.J.Richter,"A Pragmatic Analysis and Comparison of HVOF Processes", Journal of Thermal Spray Technology, Volume (12) June 1992-161.

1995

NASA/ASEE SUMMER FACULTY FELLOWSHIP PROGRAM

**MARSHALL SPACE FLIGHT CENTER
THE UNIVERSITY OF ALABAMA IN HUNTSVILLE**

ORBITAL DEBRIS REMOVAL USING GROUND-BASED LASERS

Prepared By: Charles R. Taylor, Ph.D.

Academic Rank: Assistant Professor

Institution and Department: Pacific University
Physics Department

NASA/MSFC:

Office: Program Development
Division: Advanced Systems and Payloads
Branch: Space Science & Applications Office

MSFC Colleague: Jonathan W. Campbell, Ph.D.

INTRODUCTION

Orbiting the Earth are spent rocket stages, non-functioning satellites, hardware from satellite deployment and staging, fragments of exploded spacecraft, and other relics of decades of space exploration: orbital debris. The United States Space Command tracks and maintains a catalog of the largest objects. The catalog contains over 7000 objects.

Recent studies^{1,2} have assessed the debris environment in an effort to estimate the number of smaller particles and the probability of a collision causing catastrophic damage to a functioning spacecraft. The results of the studies can be used to show, for example, that the likelihood of a collision of a particle larger than about one centimeter in diameter with the International Space Station during a 10-year period is a few percent, roughly in agreement with earlier estimates for Space Station Freedom.³ Particles greater than about one centimeter in diameter pose the greatest risk to shielded spacecraft. There are on the order of 10^5 such particles in low Earth orbit.

The United States National Space Policy, begun in 1988, is to minimize debris consistent with mission requirements. Measures such as venting unused fuel to prevent explosions, retaining staging and deployment hardware, and shielding against smaller debris have been taken by the U.S. and other space faring nations.^{4,5}

There is at present no program to remove debris from orbit. The natural tendency for upper atmospheric drag to remove objects from low Earth orbit is more than balanced by the increase in the number of debris objects from new launches and fragmentation of existing objects. In this paper I describe a concept under study by the Program Development Laboratory of Marshall Space Flight Center and others to remove debris with a ground-based laser.⁶ A longer version of this report, including figures, is available from the author.

LASER ENERGY/TARGET MOMENTUM COUPLING

At low intensity, laser radiation exerts a force on a target by the mechanism of radiation pressure. If the intensity is higher, vaporization occurs at the target surface, resulting in higher laser energy-target momentum coupling, and higher pressure on the target. The greatest coupling occurs when the intensity is high enough to form a plasma in the vapor. The pressure can be much higher than the radiation pressure. Experiments to determine the coupling coefficient have been done which demonstrate coupling on the order of 10 dyne/W.

The pressure exerted on a piece of orbital debris as a result of laser radiation from the ground alters the orbit. The laser should be fired under conditions that cause the perigee altitude to decrease. When this happens, the increased atmospheric drag at lower altitude causes the object to spiral into the atmosphere, where it is destroyed by frictional heating.

CONCENTRATION OF GROUND-BASED LASER ENERGY ON ORBITING TARGET

The feasibility of removing debris with a ground-based laser hinges on attaining a high intensity, on the order of 10^8 W/cm², on targets in orbit. Intensity can be increased by keeping the laser beam as narrow as possible. The angular sizes of the largest targets are on the order of 0.1 μ rad. A telescope operating at the diffraction limit can deliver a beam of this angular size at visible wavelengths if its aperture diameter is about 5 m. The angular size of the beam increases with increasing wavelength, and decreases with increasing aperture diameter.

Fluctuations in atmospheric density related to convective motion limit the angular size of the beam to about 5 μ rad or greater unless adaptive optics are used. With adaptive optics, a

pointing system with the phenomenal accuracy of $0.1 \mu\text{rad}$ is needed to keep the narrow beam on target.

In addition to minimizing the beam width on the target, intensity is maximized by using the highest available pulse energy and minimum pulse duration. If the intensity is too great within the atmosphere, the beam width will be degraded by stimulated rotational Raman scattering (SRS).^{7,8} For pulses longer than about 0.1 ns, SRS is a threshold phenomenon whose intensity threshold decreases with increasing zenith angle. In addition, Rayleigh scattering by the atmosphere reduces the energy reaching the target. Atmospheric extinction increases with decreasing wavelength, and increases with increasing zenith angle.

EFFECT OF LASER IMPULSE ON PERIGEE ALTITUDE

The effect of an impulse on the orbit of a piece of debris depends on the magnitude and direction of the impulse, the mass of the object, the geocentric distance and speed at the time of the impulse, and the angle at which the object is climbing with respect to the local horizontal. The effect is not linear, so that doubling the impulse does not necessarily double the effect on the perigee altitude. It is possible for multiple pulses to have an effect on the perigee altitude which is opposite to the effect the pulses would cause individually!

In order to investigate the effects of varying the many parameters, I wrote a spreadsheet, LASER2D. The laser/target geometry is assumed to be two-dimensional in this early work. The laser is assumed to be on the equator of the Earth, and the inclination of the orbit is assumed to be zero degrees.

The user specifies an initial orbit by entering the perigee and apogee altitudes and the time of transit as a fraction of the orbital period. The debris target is specified by its diameter and ballistic coefficient. The laser parameters which are entered are the pulse energy, frequency, diameter at launch, wavelength, and pulse duration. The user also enters the range of zenith angles over which pulses are to be fired. Zenith angles are entered as positive numbers for rising targets and negative numbers for setting targets. The mass of the target is calculated from the diameter and ballistic coefficient. The user may opt to use the ballistic coefficient of a Na sphere of the chosen diameter.

The beam diameter at launch, pulse energy, and maximum zenith angle are used to calculate a minimum pulse duration to prevent the onset of stimulated Raman scattering. The user will generally use this minimum pulse duration in order to maximize intensity. The spreadsheet does not perform any extinction calculations in its present version. The momentum coupling coefficient is calculated from Phipps's empirical formula for aluminum alloys with plasma ignition, which depends on the intensity on the target, wavelength, and pulse duration. It varies with zenith angle because of the intensity dependence.

It is assumed that adaptive optics corrects the beam for atmospheric density variations, and that 84% of the energy is concentrated in an angular radius given by $1.22 \lambda/D$, where D is the launch diameter. The spreadsheet does not check that the intensity is great enough for plasma ignition, but the user may view the intensity calculations.

The user may view a graph of the perigee change for single pulses as a function of zenith angle. Also available is a graph of the perigee change per zenith angle increment for multiple pulses. The spreadsheet calculates final orbital elements after a pass with continuous hits over the selected zenith angle range, but these numbers must be considered as estimates only. They don't take into account the changes in trajectory over the course of the bombardment.

RESULTS OF SPREADSHEET INVESTIGATIONS

Debris in circular orbits are considered first. A small target is one for which the laser always illuminates the entire target. A large target is one for which the laser only illuminates a portion of the target. A target which is entirely illuminated when near the laser and not entirely illuminated further from the laser is an intermediate case, acting as a large target at small zenith angles and as a small target at large zenith angles.

A single pulse is most effective in lowering the perigee of a small target when it is fired near a zenith angle of 30 degrees (altitude 60 degrees) as the target rises in the west. This is the angle at which the decrease in intensity with distance is balanced by the increase of the effectiveness of the impulse as it is applied more nearly opposite the velocity vector. At the zenith, a single small pulse has little effect, but a large pulse or many small pulses lower the perigee. At negative zenith angles, as the object is setting in the east, it is possible for small pulses to raise the perigee while large pulses lower it.

If the laser is pulsed steadily as the piece of debris makes its pass, the zenith angle changes most rapidly near the zenith, and more pulses are fired in equal zenith angle increments further from the zenith. The greatest perigee change per zenith angle increment is attained for zenith angles near 50 degrees.

A large piece of debris always intercepts the same fraction of the laser energy, and the effect of a single pulse increases toward larger zenith angles, until it is offset by the decrease in momentum coupling with decreasing intensity. The increase in effectiveness with zenith angle is even more pronounced when the effect of pulses is considered as a function of zenith angle increment. It is advantageous to use the largest possible zenith angles, limited by extinction.

The situation is somewhat more complicated when elliptical orbits are considered. The greatest reduction in perigee can be attained when the object is approaching apogee as it transits the zenith. Under these circumstances, laser shots over a wide range of zenith angles, including some negative angles, lower the perigee. These circumstances arise about once every fourth orbit. If it happens that the object has passed apogee as it transits the zenith, laser pulses at certain positive zenith angles can raise the perigee instead of lowering it. When the object is near perigee as it approaches the zenith, all pulses at positive zenith angles have a weak tendency to raise the perigee.

Since there is no range of zenith angles at which laser pulses are certain to lower perigee in all circumstances, it is necessary either to determine the orbital circumstances at the time a target is acquired, or adopt a strategy which tends to lower perigee on average but admits the possibility of raising perigee in a certain fraction of cases. In order to determine the orbital circumstances, one must measure the range, radial component of velocity, and rate of zenith angle change. The zenith angle interval required for this measurement needs to be studied.

For a common debris object of fixed composition and shape, namely a solid Na sphere, in an initially circular orbit, I have investigated the maximum size of object whose perigee can be lowered to 400 km in a single pass as a function of the altitude of the orbit. The maximum sizes estimated with LASER2D are listed in Table 1. Spheres of diameter 0.5 cm and 1.0 cm can be brought down to 400 km perigee in a single pass from orbits of 1400 km and 1100 km, respectively.

Larger pieces of debris are best characterized by total mass. As an example I considered an object of diameter 100 cm and mass 10 kg. The strategy for lowering its perigee from 1500 km to 400 km was to fire on it when its apogee was nearly overhead, at zenith angles from 75 degrees to zero degrees. The perigee and apogee altitudes after each pass estimated with

LASER2D are shown in Table 2. The perigee is lowered below 400 km in 13 passes, so that the entire process could be accomplished in as little as about four days.

Table 1. Maximum diameter of Na sphere whose perigee can be lowered to 400 km in a single pass. The initial orbit is circular. Laser pulses of 1000 J are fired at 20 Hz over the zenith angle range from 60 degrees (rising) to -1 degrees (setting). The launch diameter of the beam is 5 m and the wavelength is 530 nm. The pulse duration is 1.43 ns. The maximum momentum coupling is at the zenith, where the range is least and the intensity greatest, but the effect of a pulse in lowering perigee is greatest near 30 degrees.

<u>Initial altitude (km)</u>	<u>Max. diameter (cm)</u>	<u>Max. mass (g)</u>	<u>Max. Cm (dyne/W)</u>
1500	0.40	0.032	5.6
1400	0.50	0.064	5.8
1300	0.62	0.121	6.1
1200	0.77	0.23	6.4
1100	0.99	0.49	6.7
1000	1.31	1.14	7.1
900	1.83	3.1	7.6
800	2.7	10.2	8.2
700	4.4	45	8.8
600	8.5	310	9.6
500	18.1	3000	10.8

Table 2. Orbital history for 100 cm, 10 kg object in an initially circular orbit of altitude 1500 km. The laser is fired over the zenith angle range of 75 degrees (rising) to -1 degree (setting). It is fired only on passes when the piece of debris is near apogee at transit. The laser energy per pulse is 1000 J and it is fired at 20 Hz. The wavelength is 530 nm and the pulse duration is 2.73 ns. Because the target is larger than the beam for most of the pass, it is advantageous to fire at high zenith angles (low altitudes). The perigee can be brought below 400 km in thirteen favorable passes.

<u>Pass number</u>	<u>Perigee altitude (km)</u>	<u>Apogee altitude (km)</u>
0	1500	1501
1	1411	1495
2	1319	1493
3	1227	1492
4	1135	1492
5	1044	1492
6	954	1493
7	865	1494
8	777	1495
9	690	1496
10	604	1497
11	519	1498
12	435	1499
13	352	1500

CONCLUSIONS

The spreadsheet is an important tool for relating the many variables in the laser strategy. It would be a fairly simple matter to generalize to the three dimensional case, in which the laser is located at any latitude and the orbit may have any inclination. This would make it possible to

track changes in the inclination as well as the perigee. It would also be a simple matter to include extinction by the mechanism of Rayleigh scattering. If this were done, more realistic conclusions could be drawn about the best zenith angles at which to launch the laser pulses.

My studies indicate that several technical problems must be solved in order for the strategy to be feasible.

1. A detection scheme must be found which finds pieces of debris as they rise low above the horizon, and measures their ranges, radial velocities, and transverse velocities. These are to be used to calculate the orbital circumstances well enough to decide where in the pass it would be effective to hit the object with the laser. The system should operate day and night to be most effective. The system must be capable of recognizing targets such as working satellites which are not to be hit.
2. A large adaptive optics system must be built which compensates for the density fluctuations in the atmosphere, so that a near-diffraction limited beam can be concentrated on the target. This system should work at all zenith angles, day and night, and for a target which is moving rapidly with respect to the air mass.
3. A targeting system must be built with a pointing accuracy on the order of $0.1 \mu\text{rad}$ to place the beam on the target and keep it there. This must be done while the target is moving rapidly, and take into account that retardation causes the target to appear many beam widths behind its actual position at the time the pulse is to arrive. It must also be possible to follow the object as its path changes due to the cumulative effects of laser pulses.

REFERENCES

1. S.R. Maethner, A.E. Reinhardt, and L.O. Anderson, "Report on USAF space debris phase one study", Phillips Laboratory Technical Report, PL-TR--94-1042, June, 1994.
2. E.G. Stansbery, D.J. Kessler, and M.J. Matney, "Recent results of orbital debris measurements from the Haystack radar", AIAA 95-0664, AIAA 33rd Aerospace Sciences Meeting and Exhibit, Reno, NV, Jan. 9-12, 1995.
3. D.S. McKnight and M.L. Fudge, "Space station Freedom vulnerability study", SPIE Vol. 1951, Space Debris Detection and Mitigation, pp. 98-105, 1993.
4. W. Flury and D. McKnight, "Space debris: an international policy issue", *Advances in Space Research*, Vol. 13, No. 8, pp. 299-309, 1993.
5. J.P. Loftus Jr. and R. Reynolds, "Orbital debris mitigation: issues and options", SPIE Vol. 1951, Space Debris Detection and Mitigation, pp. 144-153, 1993.
6. C.R. Phipps and M.M. Michaelis, "NEO-LISP: deflecting near-Earth objects using high average power, repetitively pulsed lasers", LA-UR--94-3124, 23rd European Conference on Laser Interaction with Matter, St. John's College, Oxford, England, Sep. 19-23, 1994.
7. M.A. Henesian, C.D. Swift, and J.R. Murray, "Stimulated rotational Raman scattering in nitrogen in long air paths", *Optics Letters*, Vol. 10, No. 11, pp. 565-567, Nov. 1985.
8. M.D. Skeldon and R. Bahr, "Stimulated rotational Raman scattering in air with a high-power broadband laser", *Optics Letters*, Vol. 16, No. 6, pp. 366-368, Mar. 15, 1991.

1995

NASA/ASEE SUMMER FACULTY FELLOWSHIP PROGRAM

**MARSHALL SPACE FLIGHT CENTER
THE UNIVERSITY OF ALABAMA**

STATISTICAL OPTIMIZATION OF SHEAROGRAPHY INSPECTIONS

Prepared By:	Enoch C. Temple, Ph.D.
Academic Rank:	Associate Professor
Institution and Department:	Alabama A&M University Mathematics Department
NASA/MSFC:	
Laboratory:	Materials and Processes
Division:	Engineering Physics
Branch:	Nondestructive Evaluation
MSFC Colleague:	Sam Russell, Ph.D.

1. INTRODUCTION

The space industry has developed many composite materials that have been designed to have high durability in proportion to their weights. Many of these materials have a likelihood for flaws that is higher than in traditional metals. There are also material coverings (such as paint) that develop flaws that may adversely affect the performance of the system in which they are used. Therefore, there is a need to monitor the soundness of composite structures. To meet this monitoring need, many nondestructive evaluation (NDE) systems have been developed. An NDE system is designed to detect material flaws and make flaw measurements without destroying the inspected item. Also, the detection operation is expected to be performed in a rapid manner in a field or production environment.

Within the last few years, several video-based optical NDE methodologies have been introduced. Some of the most recent of these methodologies are shearography, holography, thermography, and video image correlation. A detailed description of these may be found in Chu et al. (1985), Hung (1982), and Russell and Sutton (1989).

This research focuses on a performance evaluation of shearography equipment. Users of this equipment realize that performance is a function of a set of control variables as well as a set of noise variables. However, there is a shortage of research that characterizes this relationship in model form. Hence, this project has four major objectives:

- (1) Identify the control and noise variables that are most likely to influence shearography performance.
- (2) Define a model that connects equipment output to control and noise variables.
- (3) Determine the control and noise variables and their interactions that have significant influence on shearograph performance.
- (4) Identify the setting for control variables that will optimize equipment performance. At this setting, compute a probability of detection (POD) curve.

Due to the necessary shortness of this research period, objective (1) is achieved through engineering judgment. The remainder of this paper addresses objectives (2) through (4).

In the following discussion, y is considered to be an output from an NDE inspection system. Output y is assumed to be a random variable with some probability distribution. Depending on the system, y is either continuous (eddy current is an example) or binary (shearography is an example). Berens and Hovey (1984) described an \hat{a} -hat analysis method for a continuous y and a hit/miss methodology for systems that produce binary output. For completeness, this report discusses a setup where the continuous y is expressed as a function of control and noise variables. A similar setup is discussed for binary y along with a prescription for achieving the above-mentioned objectives.

2. CONTINUOUS OUTPUT VARIABLE

Assume that y is the continuous output of an NDE inspection system with a normal probability distribution of mean μ . Further assume that control variables x_1, x_2, \dots, x_k and

noncontrollable noise variables z_1, z_2, \dots, z_m have an influence on output y . For compactness, let control vector $\underline{X} = (x_1, x_2, \dots, x_k)'$ and noise vector $\underline{Z} = (z_1, z_2, \dots, z_m)'$. A general equation that connects output y to \underline{X} and \underline{Z} is

$$y = \beta_0 + \underline{X}'\underline{\beta} + \underline{Z}'\underline{\delta} + \underline{X}'\underline{\Lambda}\underline{Z} + \varepsilon , \quad (2.1)$$

where $\underline{\beta}$ is a general parameter of vector coefficients of control variables, $\underline{\delta}$ is a coefficient vector of noise variables, $\underline{\Lambda}$ is a matrix which contains the coefficients of the interactions between noise and control variables, and ε is a random lack of fit component.

Model (2.1) generates two response surfaces that are of benefit to NDE performance evaluation. They are system output mean which is given by

$$E[y] = \mu = \beta_0 + \underline{X}'\underline{\beta} , \quad (2.2)$$

and system output variance

$$\text{Var}[y] = \sigma^2 = [\underline{\delta}' + \underline{X}'\underline{\Lambda}] V [\underline{\delta}' + \underline{X}'\underline{\Lambda}]' , \quad (2.3)$$

where V is the variance-covariance matrix for noise variables in \underline{Z} . Observed data on y , \underline{X} , and \underline{Z} may be used to estimate parameter values β_0 , $\underline{\beta}$, $\underline{\delta}$, and $\underline{\Lambda}$. Prior observations on z (perhaps field data) are used to estimate V . Once parameters are estimated, hypotheses tests may be performed to determine if control and/or noise variables have an influence on NDE performance. In particular, NDE evaluators are interested in variable interactions.

The reader may recognize components of the Taguchi methodology in this presentation. Actually, model (2.1) remedies some of the shortcomings in the Taguchi method. In fact, unlike Taguchi, model (2.1) provides for interaction analysis and allows a complete analysis of output behavior with respect to changes in control variables. Myers et al. (1992) give a description of model (2.1) and details its connection to the Taguchi method. In this paper, we apply model (2.1) to the evaluation of NDE equipment performance.

Application Example

To illustrate the usefulness of model (2.1) to NDE performance evaluation, we use an example constructed by Myers et al. (1992). For our case, we pretend that there are two control (x_1, x_2) and two noise (z_1, z_2) variables for which (2.1), (2.2), and (2.3) become (2.1)', (2.2)', and (2.3)', respectively.

$$Y = \beta_0 + x_1\beta_1 + x_2\beta_2 + \delta_1z_1 + \delta_2z_2 + \lambda_{11}x_1z_1 + \lambda_{12}x_1z_2 + \lambda_{21}x_2z_1 + \lambda_{22}x_2z_2 + \varepsilon , \quad (2.1)'$$

$$E[Y] = \beta_0 + x_1\beta_1 + x_2\beta_2 , \quad (2.2)'$$

$$\begin{aligned} \text{Var}(Y) = & \sum_{j=1}^2 \delta_j \sigma_j^2 + 2 X_1 (\delta_1 \lambda_{11} \sigma_1 + \delta_2 \lambda_{12} \sigma_2^2) + 2 X_2 (\delta_1 \lambda_{21} \sigma_1^2 + \delta_2 \lambda_{22} \sigma_2^2) \\ & + \sum_{j=1}^2 \sum_{i=1}^2 X_j^2 \lambda_{ji}^2 \sigma_i^2 + 2 X_1 X_2 (\lambda_{11} \lambda_{21} \sigma_1^2 + \lambda_{12} \lambda_{22} \sigma_2^2) + \sigma_\varepsilon^2 \end{aligned} \quad (2.3)'$$

In (2.2)' and (2.3)', $\Lambda = \begin{bmatrix} \lambda_{11} & \lambda_{12} \\ \lambda_{21} & \lambda_{22} \end{bmatrix}$, $\beta = (\beta_1, \beta_2)'$, $\underline{\delta} = (\delta_1, \delta_2)'$, $\text{var}(\underline{Z}) = V = \begin{bmatrix} \sigma_1^2 & 0 \\ 0 & \sigma_2^2 \end{bmatrix}$, and $\text{Var}(\varepsilon) = \sigma_\varepsilon^2$.

For the variables used to construct (2.1)' through (2.3)', if a statistical analysis shows that $\beta_2 = 0$ while all other parameters in (2.1)' are nonzero, then (2.2)' and (2.3)' show that an adjustment on control variable x_2 affects $\text{Var}[Y]$ and has no effect on mean $E[Y]$. Additional comments about this situation appear in the data analysis section.

3. BINARY OUTPUT VARIABLE

In many NDE systems, the output is 1 or 0 where 1 represents a flaw detection and 0 denotes a nondetection. This output variable y is said to be binary or hit/miss. For each single flaw inspection, it is assumed that p is the probability of flaw detection and thus y has a Bernoulli probability mass function $f(y) = p^y(1-p)^{y-1}$. The mean of y is given by

$$E[y] = \mu = p \quad (3.1)$$

It is desirable to devise a setup for output y that is similar to (2.1). One difficulty, among many, is that the variance $\text{Var}(y) = p(1-p)$ which is not constant over flaw size and model (2.1) requires a constant variance. However, the difficulties posed by the binary nature of y are remedied by using (3.1) to express mean μ (i.e., p) as a function of control variables \underline{X} and noise variables \underline{Z} . Such a remedy is offered by Beren and Hovey (1984) where they express p as a function of one variable (crack size). They also listed seven candidate relationships between crack size and probability of detection. Of their seven, this research uses their recommendation that the logistic relationship best describes the connection between p and crack size a . This research is also the first that we could find where p is expressed as a function of control vector \underline{X} and noise vector \underline{Z} for NDE equipment.

For variables a and p , as defined above, the logistic relationship is

$$p = \frac{e^{\beta_0 + \beta_1 a}}{1 + e^{\beta_0 + \beta_1 a}} \quad (3.2)$$

where β_0, β_1 are constants. A transformation of (3.2) gives

$$\ln \left(\frac{p}{1-p} \right) = \beta_0 + \beta_1 a \quad (3.3)$$

Cox (1970) showed that when $\bar{P} = \frac{s}{N}$, where s represents the number of successes (flow detections) out of N trials (flaws) at size α , then $\ln\left(\frac{P}{1-P}\right)$ has an approximate normal distribution provided p is replaced by \bar{p} and N is large.

Since $\ln\left(\frac{P}{1-P}\right)$ is near normal, we may let

$$\ln\left(\frac{P}{1-P}\right) = \beta_0 + \underline{X}'\underline{\beta} + \underline{Z}'\underline{\delta} + \underline{X}'\underline{\Lambda}\underline{Z} + \varepsilon, \quad (3.4)$$

and (3.4) is similar to (2.1) and will be used for a statistical evaluation of shearograph NDE equipment. In fact, the setup in (3.4) permits parameter estimation, statistical tests for model terms, identification of variable settings which will optimize variance in $\ln\left(\frac{P}{1-P}\right)$ and for construction of POD curves.

4. EXPERIMENTAL DESIGN MODEL

The engineers on this project initially identified 13 control and 4 noise variables. This number of variables generates a design that is too large for this research time period. Hence, using engineering judgment, their initial set was reduced to a short list which consisted of 3 control and 3 noise variables. On the short list, variables field of view (FOV), shear, and heat were classified as control while flaw size, flaw orientation, and lighting were treated as noise. Variables FOV, heat, lighting, and orientation contained 2 levels, flaw size and shear contained 3. The 6 variable combinations produced a total of 144 experimental design settings (cells). The experimental design model is

$$\ln\left(\frac{P}{1-P}\right) = \beta_0 + \beta X + P + Q + R + S + T + (\text{interactions}) + \varepsilon, \quad (4.1)$$

where P, Q, R are control, S, T are noise such that $E[S] = E[T] = 0$ and X is flaw size where $E[X] = a$, $\text{Var}(X) = \lambda_{11}$. That is, X is a variable with both a fixed but uncontrollable component and a noise component.

5. DATA COLLECTION AND ANALYSIS

To conduct experiments at the 144 settings for all 6 variables, a specimen panel was designed so that it contained flaws that are similar to those that the shearograph equipment would evaluate in an applied situation. The panel contained flows of 3 sizes, 2 orientations, and 2 of each size-orientation combination. Thus, the panel contained a total of 12 flaws. This single panel was inspected once by a single operator at each of all possible combination settings for variables heat, FOV, shear, and light. This gives 2 observations for each of the 144 cells. Thus, the experiment consisted of 288 observations.

Two observations per cell is too low to completely analyze the effects of all variables in a six factorial design. In fact, the literature on this subject suggests about 25 observations per cell. However, we judged that this preliminary study would give excellent insight on shearograph

performance even with the low cell counts provided we used an alternative to the full six-factorial design. Thus, we chose to analyze the collected data by using a two-factorial experiment to analyze each combination in the set of all possible two-variable subset combinations. The analysis is repeated for all possible three-variable subset combinations. Each analysis included a test of significance of at most two-variable interactions and a test for main affects. Of all the possible two-variable and three-variable analyses, Table 1 shows what variables showed at least one single significant main affect (row 1) or was involved in at least one significant interaction (row 2). Significance here means that the probability level of the estimated coefficient was 0.05 or less.

Table 1

	Size	Shear	Heat	Orient	FOV	Light
1	X	X		X		
2	X	X	X	X		

Since FOV and light are not checked in Table 1, we deleted them and performed a qualitative analysis with size (3,6,9), shear (0,2,4), heat (5,10), and orientation (-1,1) as independent variables. The significant terms from this analysis are as shown in equation (5.1).

$$\ln \left(\frac{p_i}{1-p_i} \right) = 0.6337 (a_i * h) + 0.8498 (a_i * s) - 4.09 (r) + 1.861 (a_i * r) + 0.2268 (h * r) \quad (5.1)$$

where $a_i \equiv$ flaw size, $h \equiv$ heat, $r \equiv$ orientation, $s \equiv$ shear, and $E[X] = a$, as discussed in section 4.

6. CONCLUSION

Table 1 shows that FOV and light were deleted from experimental models because they were judged to be insignificant. An inspection of (5.1) shows size and shear are not significant "stand alone" variables. However, they each are part of a significant interaction. These interactions suggest that heat and shear are control variables that influence the probability of detection for shearography. These control variables interact with size and orientation. A transformation of (5.1) to form (3.2) gives the average POD curve formula.

REFERENCES

1. Berens, A.P., and Hovey, P.W. (1984), "Flaw Detection Reliability Criteria," vol. 1, Method and Results, AFWAL-TR-84-4022, Air Force Aeronautical Labs.
2. Chu, T.C., Ranson, W.F., Sutton, M.A., and Peters, W.H. (1985), "Applications of Digital Image Correlation Techniques to Experimental Mechanics," *Experimental Mechanics*, pp. 232-244.
3. Cox, D.R (1970), *The Analysis of Binary Data*, Methuen and Co.
4. Myers, R.H., Khure, A.I., and Vining, G. (1992), "Response Surface Alternatives to the Taguchi Robust Parameter Design Approach," *The American Statistician*, pp. 131-139.
5. Russell, S.S., and Sutton, M.A. (1989), "Strain Field Analysis Acquired Through Correlation of X-Ray Radiographs of Fiber Reinforced Composite Laminates," *Experimental Mechanics*.

1995

NASA/ASEE SUMMER FACULTY FELLOWSHIP PROGRAM

**MARSHALL SPACE FLIGHT CENTER
THE UNIVERSITY OF ALABAMA IN HUNTSVILLE**

**ADAPTIVE GRID METHODS FOR RLV ENVIRONMENT ASSESSMENT AND
NOZZLE ANALYSIS**

Prepared By:	Hugh J. Thornburg, Ph.D.
Academic Rank:	Research Engineer I
Institute and Department:	Mississippi State University National Science Foundation Engineering Research Center
NASA/MSFC:	
Laboratory:	Structures and Dynamics
Division:	Fluid Dynamics
Branch:	Computational Fluid Dynamics
MSFC Colleague(s):	Paul McConnaughey, Ph.D. T.S. Wang, Ph.D. Joe Ruf

Adaptive Grid Method for RLV Environment Assessment and Nozzle Analysis

by

Hugh Thornburg
NSF Engineering Research Center for
Computational Field Simulation
Mississippi State University
Mississippi State, MS 39762

INTRODUCTION

Rapid access to highly accurate data about complex configurations is needed for multi-disciplinary optimization and design. In order to efficiently meet these requirements a closer coupling between the analysis algorithms and the discretization process is needed. In some cases, such as free surface, temporally varying geometries, and fluid structure interaction, the need is unavoidable. In other cases the need is to rapidly generate and modify high quality grids. Techniques such as unstructured and/or solution-adaptive methods can be used to speed the grid generation process and to automatically cluster mesh points in regions of interest. Global features of the flow can be significantly affected by isolated regions of inadequately resolved flow. These regions may not exhibit high gradients and can be difficult to detect. Thus excessive resolution in certain regions does not necessarily increase the accuracy of the overall solution.

Several approaches have been employed for both structured and unstructured grid adaption. The most widely used involve grid point redistribution, local grid point enrichment/derefinement or local modification of the actual flow solver. However, the success of any one of these methods ultimately depends on the feature detection algorithm used to determine solution domain regions which require a fine mesh for their accurate representation. Typically, weight functions are constructed to mimic the local truncation error and may require substantial user input. Most problems of engineering interest involve multi-block grids and widely disparate length scales. Hence, it is desirable that the adaptive grid feature detection algorithm be developed to recognize flow structures of different type as well as differing intensity, and adequately address scaling and normalization across blocks. These weight functions can then be used to construct blending functions for algebraic redistribution, interpolation functions for unstructured grid generation, forcing functions to attract/repel points in an elliptic system, or to trigger local refinement, based upon application of an equidistribution principle. The popularity of solution-adaptive techniques is growing in tandem with unstructured methods. The difficulty of precisely controlling mesh densities and orientations with current unstructured grid generation systems has driven the use of solution-adaptive meshing. Use of derivatives of density or pressure are widely used for construction of such weight functions, and have been proven very successful for inviscid flows with shocks[2,7,11]. However, less success has been realized for flowfields with viscous layers, vortices or shocks of disparate strength. It is difficult to maintain the appropriate mesh point spacing in the various regions which require a fine spacing for adequate resolution. Mesh points often migrate from important regions due to refinement of dominant features. An example of this is the well know tendency of adaptive methods to increase the resolution of shocks in the flowfield around airfoils, but in the incorrect location due to inadequate resolution of the stagnation region. This problem has been the motivation for this research.

In this research a NURBS representation is employed to define block surfaces for boundary point redistribution. The features described have been implemented into Adapt2D/3D. An adaptive grid

system capable of automatically resolving complex flows with shock waves, expansion waves, shear layers and complex vortex–vortex and vortex–surface interactions. An adaptive grid approach seems well suited for such problems in which the spatial distribution of length scales is not known a priori.

APPROACH TO ADAPTION

The elliptic generation system:

$$\sum_{i=1}^3 \sum_{j=1}^3 g^{ij} \hat{r}_{\xi^i \xi^j} + \sum_{k=1}^3 g^{kk} P_k \hat{r}_{\xi^k} = 0 \quad (1)$$

where \mathbf{r} : Position vector,
 g^{ij} : Contravariant metric tensor
 ξ^i : Curvilinear coordinate, and
 P_k : Control function.

is widely used for grid generation [1]. Control of the distribution and characteristics of a grid system can be achieved by varying the values of the control functions P_k in Equation 1 [1]. The application of the one dimensional form of Equation 1 combined with equidistribution of the weight function results in the definition of a set of control functions for three dimensions.

$$P_i = \frac{(W_i)_{\xi^i}}{W_i} \quad (i = 1, 2, 3) \quad (2)$$

These control functions were generalized by Eiseman [2] as:

$$P_i = \sum_{j=1}^3 \frac{g^{ij} (W_i)_{\xi^i}}{g^{ii} W_i} \quad (i = 1, 2, 3) \quad (3)$$

In order to conserve some of the geometrical characteristics of the original grid the definition of the control functions is extended as:

$$P_i = (P_{\text{initial geometry}}) + c_i (P_{wt}) \quad (i = 1, 2, 3) \quad (4)$$

where $P_{\text{initial geometry}}$: Control function based on initial geometry
 P_{wt} : Control function based on current solution
 c_i : Constant weight factor.

These control functions are evaluated based on the current grid at the adaption step. This can be formulated as:

$$P_i^{(n)} = P_i^{(n-1)} + c_i (P_{wt})^{(n-1)} \quad (i = 1, 2, 3) \quad (5)$$

where

$$P_i^{(1)} = P_i^{(0)} + c_i (P_{wt})^{(0)} \quad (i = 1, 2, 3) \quad (6)$$

A flow solution is first obtained with an initial grid. Then the control functions P_i are evaluated in accordance with Equations 2 and 5, which is based on a combination of the geometry of the current grid and the weight functions associated with the current flow solution[11].

Evaluation of the forcing functions corresponding to the grid input into the adaptation program has proven to be troublesome. Direct solution of Equation 1 for the forcing functions using the input grid coordinates via Cramer's rule or IMSL libraries was not successful. For some grids with very high aspect ratio cells and/or very rapid changes in cell size, the forcing functions became very large. The use of any differencing scheme other than the one used to evaluate the metrics, such as the hybrid upwind scheme[8], would result in very large mesh point movements. An alternative technique for evaluating the forcing functions based on derivatives of the metrics was implemented[3].

$$P_i = \frac{1}{2} \frac{(g_{11})_{\xi_i \xi_i}}{g_{11}} + \frac{1}{2} \frac{(g_{22})_{\xi_i \xi_i}}{g_{22}} + \frac{1}{2} \frac{(g_{33})_{\xi_i \xi_i}}{g_{33}} \quad (i = 1, 2, 3) \quad (7)$$

This technique has proven to be somewhat more robust, but research efforts are continuing in this area.

WEIGHT FUNCTIONS

Application of the equidistribution law results in grid spacing inversely proportional to the weight function, and hence, the weight function determines the grid point distribution. Ideally, the weight would be the local truncation error ensuring a uniform distribution of error. However, evaluation of the higher-order derivatives contained in the truncation error from the available discrete data is progressively less accurate as the order increases and is subject to noise. Determination of this function is one of the most challenging areas of adaptive grid generation. Lower-order derivatives must be non-zero in regions of wide variation of higher-order derivatives, and are proportional to the rate of variation. Therefore, lower-order derivatives are often used to construct a weight function as a proxy for the truncation error. Construction of these weight functions often requires the user to specify which derivatives and in what proportion they are to be used. This can be a time consuming process. Also, due to the disparate strength of flow features, important features can be lost in the noise of dominant features. The weight functions developed by Soni and Yang [7] and Thornburg and Soni [8] are examples of such efforts. The weight function of Thornburg and Soni [8] has the attractive feature of requiring no user specified inputs. Relative derivatives are used to detect features of varying intensity, so that weaker, but important structures such as vortices are accurately reflected in the weight function. In addition, each conservative flow variable is scaled independently. One-sided differences are used at boundaries, and no-slip boundaries require special treatment since the velocity is zero. This case is handled in the same manner as zero velocity regions in the field. A small value, epsilon in equation 8, is added to all normalizing quantities. In the present work this weight function has been modified using the Boolean sum construction method of Soni [7]. Also, several enhancements of an implementation nature have been employed. For example epsilon has been placed outside the absolute value operator. This eliminated the possibility of spurious gradients in the weight function in regions where epsilon was nearly equal and opposite in sign to the local normalizing flow variable. Also, the normalizing derivatives have been set to an initial or minimum value of ten percent of the freestream quantities. This alleviates problems encountered in flows without significant features to trigger adaption in one or more coordinate directions. Otherwise a few percent variation would be normalized to the same level as a shock or other strong feature. The current weight function is as follows:

$$W = \frac{W^1}{\max(W^1, W^2, W^3)} \oplus \frac{W^2}{\max(W^1, W^2, W^3)} \oplus \frac{W^3}{\max(W^1, W^2, W^3)}$$

Where,

$k=1,2,3,$

and

$$\begin{aligned}
 W^k = 1 + & \frac{\frac{|\varrho_{\xi k}|}{|\varrho| + \varepsilon}}{\left(\frac{|\varrho_{\xi k}|}{|\varrho| + \varepsilon}\right)_{\max}} \oplus \frac{\frac{|(\varrho u)_{\xi k}|}{|(\varrho u)| + \varepsilon}}{\left(\frac{|(\varrho u)_{\xi k}|}{|(\varrho u)| + \varepsilon}\right)_{\max}} \oplus \frac{\frac{|(\varrho v)_{\xi k}|}{|(\varrho v)| + \varepsilon}}{\left(\frac{|(\varrho v)_{\xi k}|}{|(\varrho v)| + \varepsilon}\right)_{\max}} \oplus \frac{\frac{|(\varrho w)_{\xi k}|}{|(\varrho w)| + \varepsilon}}{\left(\frac{|(\varrho w)_{\xi k}|}{|(\varrho w)| + \varepsilon}\right)_{\max}} \\
 & \oplus \frac{\frac{|\varrho_{\xi k \xi k}|}{|\varrho| + \varepsilon}}{\left(\frac{|\varrho_{\xi k \xi k}|}{|\varrho| + \varepsilon}\right)_{\max}} \oplus \frac{\frac{|(\varrho u)_{\xi k \xi k}|}{|(\varrho u)| + \varepsilon}}{\left(\frac{|(\varrho u)_{\xi k \xi k}|}{|(\varrho u)| + \varepsilon}\right)_{\max}} \oplus \frac{\frac{|(\varrho v)_{\xi k \xi k}|}{|(\varrho v)| + \varepsilon}}{\left(\frac{|(\varrho v)_{\xi k \xi k}|}{|(\varrho v)| + \varepsilon}\right)_{\max}} \oplus \frac{\frac{|(\varrho w)_{\xi k \xi k}|}{|(\varrho w)| + \varepsilon}}{\left(\frac{|(\varrho w)_{\xi k \xi k}|}{|(\varrho w)| + \varepsilon}\right)_{\max}} \quad (8)
 \end{aligned}$$

The symbol \oplus represents the Boolean sum. Note that the directional weight functions are scaled using a common maximum in order to maintain the relative strength. For the results shown, the weight function used is the sum of the weight function defined by Eq. 8 and the one defined in [8]. The weight function defined in [8] is Eq. 8 evaluated without using the Boolean sum.

Flow past a wedge at Mach = 2.0 is used to illustrate the enhanced detection capabilities of this newly developed weight function. Figure 1 presents weight functions evaluated using the previous procedure, lower half plane, as well as the current procedure, upper half plane.

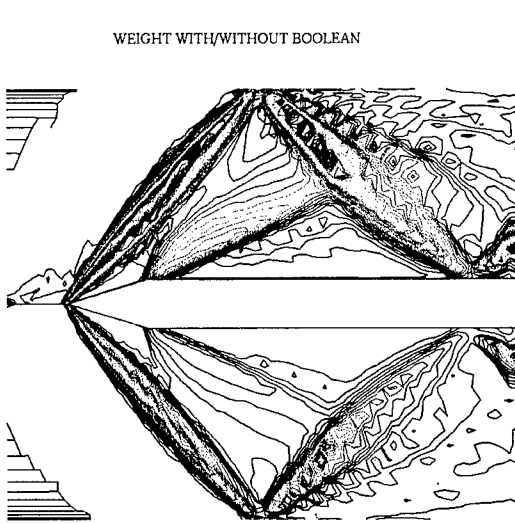


Figure 1. Comparison of Weight Functions.

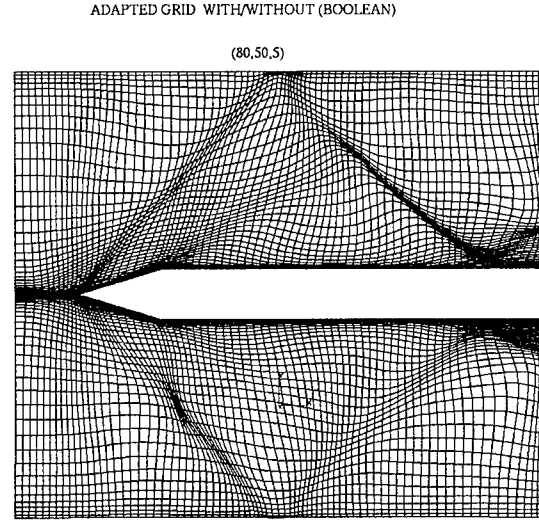


Figure 2. Comparison of Adapted Grids.

It can be observed that both weight functions clearly detected the primary shock. It can also be seen that the expansion fan, boundary layer, and the reflected shocks are much more clearly represented in the current weight function. Adapted grids using both weight function formulations are presented in Fig. 2. The high gradient regions of the expansion region are only reflected in the adapted grid using the new weight function. The reflected shock is also much sharper. Figure 3 compares the solution obtained using the current adaption procedure with that obtained using the original grid. The enhanced resolution is clearly evident.

ADAPTED/ORIGINAL SOLUTION (BOOLEAN)

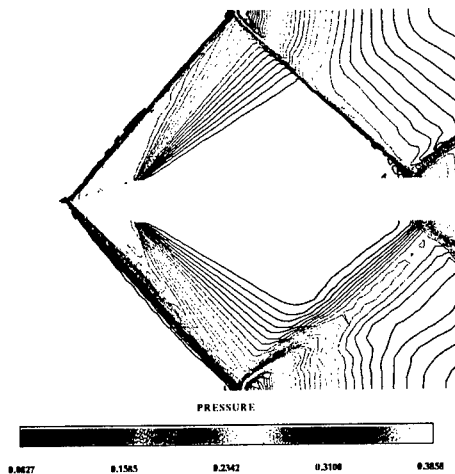


Figure 3. Comparison of Solutions Using Adapted Grid.

References

1. Thompson, J.F., Warsi, Z.U.A. and Mastin, C.W., Numerical Grid Generation: Foundations and Applications, North-Holland, Amsterdam. 1985.
2. Eiseman, P.R., "Alternating Direction Adaptive Grid Generation," AIAA Paper 83-1937, 1983.
3. Soni, B.K., "Structured Grid Generation in Computational Fluid Dynamics," Vichnevetsky, R., Knight, D., and Richter, G. (eds.), Advances in Computer Methods for Partial Differential Equations VII, Rutgers University, pp 689-695, June 1992.
4. Buning, P.G. and Steger, J.L., "Graphics and Flow Visualization in Computational Fluid Dynamics," AIAA Paper 85-1507-CP, Proceedings of the AIAA 7th Computational Fluid Dynamics Conference, 1985.
5. NASA LeRC and USAF AEDC, "NPARC 1.0 User Notes," June 1993.
6. Ghia, K.N., Ghia, U., Shin, C.T. and Reddy, D.R., "Multigrid Simulation of Asymptotic Curved-Duct Flows Using a Semi-Implicit Numerical Technique," Computers in Flow Prediction and Fluid Dynamics Experiments, ASME Publication, New York 1981.
7. Soni, B.K. and Yang, J.C., "General Purpose Adaptive Grid Generation System," AIAA-92-0664, 30th Aerospace Sciences Meeting, Reno, NV, Jan. 6-9, 1992.
8. Thornburg, H.J. and Soni, B.K., "Weight Functions in Grid Adaption," Proceedings of the 4th International Conference in Numerical Grid Generation in Computational Fluid Dynamics and Related Fields held at Swansea, Wales 6-8th April 1994.
9. Soni, B.K., Thompson, J.F., Stokes, M.L. and Shih, M.H., "GENIE++, EAGLEView and TIGER: General and Special Purpose Interactive Grid Systems," AIAA-92-0071, 30th Aerospace Sciences Meeting, Reno, NV, Jan. 6-9, 1992.
10. NASA LaRC, "User Document for CFL3D/CFL3DE (Version 1.0)", 1993.
11. Thompson, J.F., "A Survey of Dynamically-Adaptive Grids in Numerical Solution of Partial Differential Equations," Applied Numerical Mathematics, vol. 1, pp 3-27, 1985.

1995

NASA/ASEE SUMMER FACULTY FELLOWSHIP PROGRAM

MARSHALL SPACE FLIGHT CENTER
THE UNIVERSITY OF ALABAMA IN HUNTSVILLE

CREATING NEW OPPORTUNITIES FOR COMMUNICATING ABOUT
SPACE SCIENCE

Prepared By:	Debbie Treise, Ph.D.
Academic Rank:	Assistant Professor
Institution and Department:	University of Florida Department of Advertising College of Journalism and Communications
NASA/MSFC Office:	Public Affairs
MSFC Colleagues:	John Taylor Dr. Dom Amatore Dave Drachlis Ed Medal

Situation Analysis

Several unique conditions exist within and among NASA, Marshall Space Flight Center, the media, and society as a whole that present both competing problems and exciting opportunities for communicating about space science.

With the political and economic atmosphere changing so drastically, NASA has found it necessary to change its mission from one of exploration to that of accountability and application. These changes have made it difficult for NASA to assess how its roles and constituency groups have changed in response. Specifically, at the MSFC Space Sciences Lab, management must now decide the most appropriate communication objectives, strategies and target markets to direct messages reflecting these changes. Complicating the issue is that MSFC must walk a fine line between looking as though it is spending too much money and "marketing" themselves, which it is strictly prohibited from doing, and imparting the information in an exciting enough form to be picked up by the media.

Additionally, space scientists are being asked to become marketers and to "promote" their research findings to the public in an effort to provide "relevancy" to their existence. They are being forced into nontraditional and unfamiliar roles and must now identify "marketable" story ideas. At the same time, downsizing in the public affairs office has affected the amount of attention traditional PAOs are able to devote to promoting space science.

As a result, MSFC management and scientists have expressed mixed views on how best to meet the new demands. On one end of the continuum are those who believe MSFC should communicate about scientific achievements on the basis of technology transfer and economic benefit to the general public. Conversely, those on the other end think space science should be sold on the basis of knowledge generation to educators and children.

To complicate the dilemma, it appears that interest in the hard sciences is waning. Indeed, a recent Parade Magazine article (1995, June 4) discussed the media's role in contributing to young people's lack of appreciation for the "joys of science," "the delights in discovering how the universe is put together," and "the exhilaration in knowing a deep thing well." Additionally, the broadcast entertainment media were criticized for perpetuating a stereotype of "so-called scientists" as "moral cripples driven by a lust for power" communicating to young people that science is dangerous and that "scientists are worse than weird: they're crazed." For adults, according to the article, the problem is one of lack of attention to news features devoted to science except for medicine and technology.

From the perspective of the science writers interviewed, they are finding it increasingly more difficult to pinpoint solid science topics, particularly those originating from MSFC. For example, several of the writers believe that, "The technology transfer stories just take too long." "They're not direct enough, and it's getting harder and harder to run another protein crystal growth story without some more immediate benefit from doing that research." Science writers are being pressured by their editors to "dig deeper" to find different and more compelling angles and human interest stories.

Target Market Definition

Many of the problems discussed above can be sorted out by identifying the market(s) that SSL wishes to reach. By defining and prioritizing target markets, SSL will be able to more efficiently determine the value it can deliver to each. While several constituencies other than the general public have been designated by SSL (i.e., Congress, state and local government, etc.), specific segments *within* the general public can be used to reach these targets as well.

As mentioned, science is not an important topic to most Americans. For the majority of the public, the range of competing issues to attend to is so vast that only a small percentage of them will become salient. This concept of "issue attentiveness" refers to a process in which people focus their attention on a relatively small set of public affairs issues, keep up with those issues, and take an active citizenship role regarding that set of issues. The resulting "specialization" process affects the formulation of public policy about those issues (Miller, 1994).

The concept has recently been applied to space and science policy formation. Work by several researchers has outlined a pyramid structure (see Figure 1) that illustrates the outcome of the specialization process described above (Almond, 1950; Miller & Prewitt, 1979; Miller, 1982, 1994; NSB, 1981, 1990, 1994). The most important group for SSL are the attentive public (estimates run between 6-18% of the American public). This group is both interested in and knowledgeable about space and science and who receive the flow of appeals from those above through professional organizations, specialized journals and magazines and employment-related institutions. The attentives represent the strongest and steadiest source of support for the space program and related sciences in terms of their attitudes about cost/benefit analysis, attitudes toward the space station, general attitudes toward science and technology, risk/benefit assessment of scientific research, and attitudes toward spending for space exploration (It is important to note that this group is most strongly in favor of spending for other domestic programs as well.). Those in the attentive group are higher in SES as compared to other groups and are nearly twice as likely to institute letter-writing campaigns, make telephone calls and schedule personal visits with decision makers. For example, nearly one-third of this group contacted a public official or legislator on an issue during 1991.

Summary

It is clear from the research and interviews that there are valid and valuable short and long term goals that need to be addressed. Although the immediate danger has passed, it appears that SSL may be fighting an uphill battle to keep its accomplishments in the forefront to ensure its survival. In that case, it is extremely important for MSFC to immediately raise and maintain the awareness of SSL as a location conducting "world-class science" among that segment of the public who are the most influential and the most likely to take action -- the attentive public. According to Miller (1994), elections have little or no impact on issues such as science policy or space policy. Instead organized groups and informed, concerned citizens must maintain direct contact with agency officials and legislators to effect a change. In this case, the marketing "80/20 rule" would seem to apply. This concept postulates that 80 percent of a product is purchased by 20 percent of the population. Translated to space sciences, that 20 percent of the market is the attentive public. Additionally, most of the literature suggests that the current problems have little to do with labs or public perceptions. Instead it is politics. If this is the case, directing an effort toward a *mass* audience would be an error; it is the policy makers who need to be reached.

It is indeed a responsibility for all significant science and exploration institutions to educate the *general public* about their research. However, that is an ambitious, expensive and long-term objective. As the discussion on target markets indicates, the general or non-attentive public has competing and more important issues to consider. Attempts to *create* interest where there is currently little or none is counterproductive. Additionally, due to low science literacy rates among the general public, it would seem unwise to expect that the SSL could stimulate enough understanding about or attention to its efforts have a significant impact on policy. However, a good place to start to begin reaching this market is through their school-aged children and educators. Several of the proposed approaches detailed below address this important market.

In sum, it is clear that the immediate need for SSL is to target, through specialized channels, those attentives who are influential with policy makers and serve as opinion leaders for a more general audience. For a number of reasons, the *general* public does not have an interest in the more technical areas of science and space. And because mass media values dictate a bias for relevant, exciting and timely story ideas aimed at the non-specialized interests of many, *mass* media channels (network newscasts, for example) are not the most effective or appropriate vehicles to target with news about space science. Unless scientists in the SSL are producing results that are immediately applicable to the general public, network news and similar outlets will not, as a general rule, cover their stories.

Suggested Approaches

Before discussing strategies to reach the appropriate target markets, it is vitally important that both public affairs and SSL reconsider their respective missions and recognize the value of a solid communication mechanism to generate newsworthy stories. Although communication between the two areas appears to be improving, both must alter their respective mindsets to increase communication between and among each other, Marshall management and Headquarters.

Additionally, it would seem that public affairs must enlarge its charter beyond information disseminator to a more proactive approach directed toward more specialized media outlets. On the other hand, SSL will need to recognize that establishing an ongoing, workable communication link to public affairs is vital. It also appears that some science within SSL may be harder to make relevant and therefore will not attract network news coverage aimed at a *mass* market. Communicating about much of the science being conducted at SSL will require more discipline-specific outlets reaching those attentives who will, if needed, contact policy makers.

In addition, many of the reporters interviewed suggested strategies applicable to both members of the Space Sciences Lab and to the public affairs office. For example, as an overall approach, science writers suggested that both public affairs and scientists step back, be objective and select potential story ideas from the standpoint of the end user or receiver. They also believe that the best scientists are those who can reposition their research into a "What problem am I solving?" format and then relate those stories and story ideas in a manner understandable to the target market. The most effective PAOs, according to science writers, are those who have a high priority for prompt response.

Several overall themes could be used to address the specified adult target market discussed including: solving the mysteries we don't understand; uncovering unexpected mysteries; the value of probing new frontiers in keeping with the American culture and spirit; and the value of keeping ahead in technology and science global competition. Additionally, the need for and relevance of conducting this research could be illustrated by focusing on the predictions of some of the greatest minds throughout history. For example, in the 16th Century, Nostradamus predicted that the cure for a 20th Century plague (AIDS?) will be developed in a self-operating machine above the Earth (space station?)

In addition to the myriad media contact and programs the PAO currently has in place, based on the research conducted, several possible strategies are detailed below. They are listed in order from those most likely to provide the greatest payback.

Public Affairs Writer/Contractor

It is recommended that writer be hired who is skilled in both public affairs and science writing to work exclusively with SSL to accomplish several tasks. As previously discussed, it is vitally important that an internal communication mechanism be in place. A writer, assigned to public affairs (since all information dealing with the mass media must first go through the public affairs office), would be in an ideal place not only to establish contact with the media and to receive requests from various media representatives, but also to work closely with scientists from the different divisions to identify and develop "marketable" stories. In addition, a more proactive approach could be implemented if the writer is able to establish lead times for "breaking" stories to coordinate with media lead times.

After the internal communication mechanism is in place, the writer will need to develop and nurture solid, healthy relationships with the editors of various science media. To increase the chances of acceptance, it is a good idea to be in regular but selective contact with these outlets. These relationships are important to cultivate because the media have developed a hierarchy of how they deal with each source. That hierarchy is governed by 1) the status of the organization, 2) the media's perception of how savvy that organization's PAOs are, and 3) their relationship with public affairs. The contractor will need to cultivate the attitude that when the editors hear from SSL, it will be a good story. The same relationships will need to be developed for producers associated with the Learning Channel, "Discovery," "NOVA" and the Weather Channel -- all potential outlets for SSL stories.

Another important job for the writer would be to attend annual meetings such as the upcoming American Association for the Advancement of Science (AAAS) Convention in February. This meeting is widely attended by approximately 5,000 scientists, 500 science writers and numerous public affairs officers from across the country. It is expected that public affairs officers will attend to establish relationships with various writers. In fact, at last year's conference there were various sessions on the agenda that dealt with media coverage of science and public perceptions of science. Other duties for the contractor/writer would be to: interpret R&T reports for possible story ideas; research, develop and write human interest feature stories about the SSL scientists and their endeavors to be placed in the Marshall Star and to be distributed to NASA Headquarters.

Other suggestions include a rotating exhibit at the leading science and industry museums, a hands-on exhibit in the space station trailer, a speaker's bureau, public radio programming, Sci-Fi Channel talk shows, developing relationships with A&E, Discovery Channel, NOVA and editors of select children's magazines, high school student newspaper workshops, and a hands-on exhibit in the Space and Rocket Center.

Research Conducted

Interviews were conducted with MSFC personnel including:

Representatives from center management (7)
Space Sciences Lab Director
Chief Scientists from each of the three divisions
Scientists from the three divisions (19)
Public Affairs office (all)

In addition, interviews were conducted with:

National science writers (8)
Academics conducting research in the area of science writing (3)
News Directors or assignment editors from various ADI markets (30)
Public Affairs officers from Headquarters, JSL and Space Telescope Institute (3)

Representatives from NBC and CBS news assignment desks
Library literature search
Viewed mission and non-mission videotapes
Space and Rocket Center tours
Additional tours to the Space Station assembly building and the neutral buoyancy tank

Additional Work Completed

PSAs

Approximately one month before the release of the movie "Apollo 13," Headquarters, in conjunction with Universal and the stars of the movie, requested bulleted information regarding possible space science story ideas from which to develop public service announcements. Several SSL scientists put together some story ideas which were sent to Headquarters. They subsequently were returned with the request to make them more understandable. I researched and re-wrote them. The resulting information was transmitted to Headquarters.

DAAC

Representatives from the DAAC indicated that their primary markets were their IWG group, university researchers, students K-12 and commercial users. They believe that their IWG group is of paramount importance; however, they expressed concern that only about 10% of this group was accessing the available data.

It is suggested that projects, rather than individual researchers need to be targeted earlier at the RFP stage so that researchers could incorporate the availability of the global hydrology data into their proposals. Because researchers generally work in fairly large teams, and may be involved in several long-term projects at one time, perhaps DAAC is reaching a sufficient number of this target.

References

- Almond, G. 1950. *The American People and Foreign Policy*. New York: Harcourt, Brace and Co.
- Miller, J.D. 1980. Political and Issue Specialization: A Behavioral Imperative. Paper presented to the 1980 American Political Science Association.
- _____, 1982. *The Information Needs of the Public Concerning Space Exploration*. A special report to the National Aeronautics and Space Administration.
- _____, 1994. *The Information Needs of the Public Concerning Space Exploration*. A special report to the National Aeronautics and Space Administration.
- Miller, J.D. and K. Prewitt, 1979. *The Measurement of the Attitudes of the U.S. Public toward Organized Science*. Report submitted to the National Science Foundation in accordance with NSF contract SRS78-16839. Chicago: National Opinion Research.
- National Science Board, 1981 *Science Indicators -- 1980*. Washington, DC: U.S
- National Science Board, 1990. *Science and Engineering Indicators -- 1989*. Washington, DC: U.S
- National Science Board, 1994. *Science and Engineering Indicators -- 1993*. Washington, DC: U.S
- Sagan, C. 1995 (June 4). What TV Could Do for America. *Parade*.
- Schmidt, R., 1994 (June 8). Poor Stayed Home While Rich Voted in '94. *Huntsville Times*, A6.

1995
NASA/ASEE SUMMER FACULTY FELLOWSHIP PROGRAM

MARSHALL SPACE FLIGHT CENTER
THE UNIVERSITY OF ALABAMA IN HUNTSVILLE

“TECHNOLOGY TRANSFER METRICS: MEASUREMENT AND VERIFICATION
OF DATA/REUSABLE LAUNCH VEHICLE BUSINESS ANALYSIS”

Prepared By:	George W. Trivoli, Ph.D.
Academic Rank:	Professor of Finance/Eminent Scholar
Institution and Department:	Jacksonville State University Department of Finance and Statistics
NASA/MSFC:	
Office:	Technology Transfer Office Program Control & Management Support Office
MSFC Colleagues:	David W. Cockrell Timothy E. Tyson

"Technology Transfer Metrics: Measurement and Verification of Data/Reusable Launch Vehicle Business Analysis"

Introduction

Congress and the Executive Branch have mandated that all branches of the Federal Government exert a concentrated effort to transfer appropriate government and government contractor-developed technology to the industrial use in the U.S. economy. For many years, NASA has had a formal technology transfer program to transmit information about new technologies developed for space applications into the industrial or commercial sector. Marshall Space Flight Center (MSFC) has been in the forefront of the development of U.S. industrial assistance programs using technologies developed at the Center.

During 1992-93, MSFC initiated a technology transfer metrics study. The MSFC study was the first of its kind among the various NASA centers. The metrics study is a continuing process, with periodic updates that reflect on-going technology transfer activities.

Body

This researcher, working with NASA colleagues, David Cockrell and Timothy Tyson, has been engaged in a series of projects aimed at both measurement and verification of technology transfer metrics. One of the major tasks in which this research has been involved with is the development of metrics for the Small Business Innovation Research Program (SBIR).

Annually, NASA invites eligible small businesses to submit proposals for its SBIR program. The SBIR program objectives include stimulating technological innovation in the private sector, strengthening the role of small business concerns in meeting Federal (NASA) research and development needs, and increasing the commercial application of federally supported research results.

This researcher was involved in verifying SBIR recipients of MSFC for the years 1989-92 in order to develop a list to be surveyed. A questionnaire was developed in cooperation with Tech-Masters, Inc. (William Fieselman), David Cockrell, and Auburn University (Clint LeNoir, Jr.). The questionnaire is designed to elicit responses from past recipients of SBIR grants regarding the commercial and economic benefits of the research and development activities resulting from the SBIR's. The completed questionnaire was mailed on July 14th (see attached copy).

In developing the SBIR questionnaire, this researcher was part of a team that traveled to Auburn University to meet with Clint LeNoir and his team at the Auburn Technical

Assistance Center on June 13-14, 1995. From a detailed and complicated four-page questionnaire, the teams were able to reduce it to a single page with a cover letter in a very brief period of time.

This researcher also aided in developing an approach to measure the economic benefits of investments made by businesses utilizing NASA/MSFC technology. The original technology transfer metrics did not include benefits that accrued to businesses as a result of investments made. An accepted internal financial management practice generally includes depreciation on investments as part of cash flows (e.g., net income + depreciation). Therefore, once a firm has deducted depreciation from its sales revenue to derive Earning Before Taxes, the firm is able to determine its net income by deducting taxes.

Since depreciation expense can be thought of as a tax savings, managerial finance adds depreciation savings back in to the firm's net income to derive net cash flows from operations. We proposed that using an average allowable depreciation charge, which was determined by polling leading accounting firms regarding the average depreciation taken by its industrial-type clients. The average depreciation charge can then be used to adjust the total investment for business respondents to the NASA survey as follows:

$[\text{Total Investment by Firms}] [\text{Average Depreciation Percent}] = \text{Adjusted Cash Flow.}$

Suppose the average depreciation taken by industrial firms is 80 percent during the first two years of an investment. If the total investment is \$100 million, the following result occurs:

$[\$100 \text{ Million Investment}] [.80] = \$80 \text{ Million Adjusted Cash Flow.}$

By restating and recalculating the existing collected data in the above manner, it is possible to add many additional "jobs added or jobs saved" to those already calculated as a result of NASA/MSFC technology transfer.

This researcher writes a weekly column entitled "Your Investing" that is distributed by the New York Times regional newspapers wire desk. In addition, the column is internationally syndicated by United Press International. As a result of working with the Technology Transfer Office, a column has been written to appear on September 3, 1993, entitled, "NASA's Technology Transfer Program: Opportunities for Investment" (see attached). Each column will be coordinated with the Technology Transfer Office, MSFC.

In addition to working with external metrics, this researcher also aided in reviewing and suggesting changes to the MSFC Internal Metrics Project. The purpose of the MSFC Internal Metric Project is to develop a set of integrated metrics, which provide

quantifiable measures of MSFC's overall performance with respect to the five strategic goals detailed in the Center's Strategic Plan. The five strategic goals are related to space transportation and propulsion systems, scientific research/payload development, payload integration/operations, research technology and advanced development, and human and physical resources.

Working with a team composed of Larry E. Lechner, Don Whirley, Gene A. Olsen, and Tony Sharpe (Tech-Masters, Inc.), we developed a structure of sub-categories for objectives to measure the effectiveness of NASA/MSFC in meeting goal #1 in space transportation and propulsion systems. Specifically, four overall sets of metrics are set forth to measure safety, reliability, performance, and cost effectiveness for space shuttle main engine, solid rocket motor, solid rocket booster, external tank, and expendable launch vehicle. The overriding focus of this set of metrics is to provide sufficient information to determine both the overall efficiency of MSFC in meeting goal #1 and to provide management with a tool for tracking safety, reliability, performance, schedule, and cost-effectiveness.

This researcher was involved in analyzing and critiquing a draft Working Paper, "Measuring the Economic Benefits of Technology Transfer from a National Laboratory: A Primer," by R. B. Archibald, D. H. Finifter, and N. R. Smith, The College of William and Mary, July, 1995. The fatal flaw in their analysis is the classical assumption of "...technology know-how imbedded in machinery and the minds of the workers are held constant..." (pp. 2-3). This means that technology is frozen in their approach. The whole point of technology transfer is to actively advance technological commercialization so as to impact economic development positively.

The authors of this Working Paper agree that there are two basic outcomes of technology transfer, "... (1) a change in total output produced, and (2) a change in the mix of goods and services produced." (pp. 7-8). Yet, they totally ignore the first to concentrate their analysis on the second. Their conclusions fall directly out of their original assumption of fixed technology and concentrates only on changes in the mix of goods and services. Thus, their conclusion that "...on average technological progress increases the quality of jobs in the economy, not the quantity..." is totally false.

The authors defend their national approach to measurement of economic effects over a regional one, stating the "...defining a region is an arbitrary process..." (p. 16). This may be so, but once one defines a region, it is entirely feasible to develop metrics to measure economic factors within a specific region. Indeed, the U. S. Department of Commerce does this with virtually all of the economic data, including the RIMS II Regional Input-Output Modeling System, which sets forth regional economic multipliers based upon industry SIC codes. ("Regional Multipliers: A User Handbook for the Regional Input-Output Modeling System (RIMS II)," 2nd edition, U. S. Department of Commerce, Bureau of Economic Analysis, Washington, D. C., May, 1994).

Finally, twenty percent of this researcher's time has been devoted to working with a team from the MSFC Engineering Cost Office (Joseph Hamaker, Manager) on the Reusable Launch Vehicle (RLV) business analysis. This researcher participated on a high-level team involving NASA administrators (Ivan Bekey and Dandel Tam) in developing an internal report on the RLV for the NASA Administrator's Office.

In addition, this researcher has aided the MSFC Engineering Cost Office team in developing an approach to evaluating the feasibility of the RLV. Specifically, the RLV business analysis addresses the commercial feasibility of funding, developing, and operating an RLV.

Some of the issues addressed and suggestions made by this researcher include examining the basic assumptions of the analysis. These questions or suggestions include:

1. Suggested that the total development and production costs for RLV be increased to \$9 billion to bring it more in line with the assumptions of industry.

2. That the assumed interest rate on debt for industry be increased to 12 percent from 10 percent; again to bring it more in line with industry assumptions. The reason being that there is a difference between the interest rate on borrowed funds and both the weighted average cost of capital (includes debt + equity capital) and the actual assigned discount rate used to evaluate the project.

3. That the assumed prime lending rate charged by banks be increased from 8 percent to 8.75 percent to reflect the current prevailing rate charged by large banks.

4. Suggested that, in addition to calculating in IRR (internal rate of return) for the project, a payback (using discounted cash flows) and net present value be calculated.

5. That there be some treatment of accelerated depreciation in the calculation of annual cash inflows rather than simply straight-line depreciation. Most of the above mentioned suggestions have been adopted in the business analysis for the RLV. Of course, much work still needs to be done to develop useful criterion with which to adequately evaluate proposals submitted by industry.

Conclusions and Recommendations (will be limited to Technology Transfer External and Internal Metrics)

The Summer Faculty Fellowship has been both interesting and challenging. Most of the tasks and problems were quite different from both my academic environment and business consulting experience. New challenges and vistas have been opened for me which are quite interesting and exciting. A greater awareness of the vast diversity of the

various missions of NASA/MSFC has become apparent. In addition, a tremendous respect for the industriousness and dedication of the MSFC fellow staff has been gained.

Based upon limited exposure and experience in the Technology Transfer Office, several observations and/or suggestions are offered:

1. Having reviewed the technology transfer metrics measurement process, it is the view of this researcher that the adoption of the RIMS II economic multiplier used by the U.S. Department of Commerce to be both reasonable and widely accepted. Moreover, use of the RIMS II multipliers allows for easy comparison; thus should be adopted by the other NASA Centers similarly engaged in measurement of the benefits of technology transfer.

2. Regarding the actual application of the multipliers, the suggestion made is to include the value of depreciation in calculating the benefits of investments to both the business enterprise and the economy (see discussion above).

3. Regarding internal metrics, it appears that under the five categories of goals set forth in the overall strategic plan, there are too many strategic objectives specified. Moreover, there are difficulties in adequately measuring and/or generating data to determine if the objectives are being met. For instance, under goal 4, a strategic objective is to be the "agency lead" in promoting the timely introduction/application of scientific research and technology developments. This invites comparison with other Centers and government agencies without providing any means of measurement or comparison. Perhaps this goal could be reworded to read, "Be a leading Agency."

4. In addition, under goal 5, the overall goal is stated to be, "enhancement and sustaining of a highly skilled and motivated work force... supported by first-class facilities, equipment, and services." Who is to determine what is "first-class?" Perhaps this wording could be changed to "...supported by excellent state-of-the-art facilities...." Moreover, what measures are appropriate in determining if the Center has achieved the overall goal? Some attention must be devoted toward either rewriting, or reducing the number of strategic objectives.

5. A final recommendation is that the Technology Transfer Office issue at least one "tech-transfer" success story (news release) a month. The "story" should be brief, well-written, and contain a human interest or "rags-to-riches" element. This researcher is willing to devote one column a month of "Your Investing" to a NASA tech-transfer theme with an investment slant (see attached column).

6. In addition, there is a need to develop a measure of the value added resulting from a job-reducing process or innovation by a business. If a business is able to introduce a process or innovation as a result of NASA/MSFC technology transfer that enables it to

reduce jobs but increase output, productivity or efficiency, this is still a benefit. However, as currently counted, it tends to understate the "job creation" measure for the particular business. Suppose a firm installs a new process as a result of technology transfer from MSFC that increases output or productivity by \$1 million; but it results in the use of five fewer employees. Using the approach suggested by the RIMS II Regional Multipliers User Handbook, we can derive the following. Suppose each additional \$1 million of output from one firm results in the total (all industries) final demand multiplier for employment of 22 new jobs. Therefore, the net effect on all industry employment from one firm's job-reducing innovation is still a net increase of 17 jobs ($+22 - 5 = 17$).

This researcher will take back to the Jacksonville State University campus many experiences to share with fellow faculty, administrators, and students. As part of the Business Finance Course, numerous examples are given to students from the business world, now NASA/MSFC, examples will be presented ranging from measuring technology transfer to determining the projected cash flows from a future RLV. For instance, whenever capital budgeting for long-term investment by private industry is discussed in Business Finance, this researcher will provide a simplified procedure for estimating the cash flows from a proposed Reusable Launch Vehicle.

Commercial Benefits of the Small Business Innovative Research Program

Company Name:
Address:

Contact Person:
Phone Number:

SBIR Project Name and Phase:

1. Number of employees in firm: _____ 2. Standard Industrial Classification (SIC) Code _____

Please answer the following questions about the above listed SBIR project. Your participation in this survey is very important and greatly appreciated.

A. About this SBIR project: (Answer all questions that are appropriate to your firm)

1. Which of the following outcomes resulted from this SBIR project: (Check all that apply) _____ a. New product;
_____ b. Improved product; _____ c. New process; _____ d. Improved process; _____ e. New or Improved service _____ f. Other
2. What is the direct impact to your firm from this SBIR project (above the value of the SBIR funding provided)?
 - a. Revenue or sales: \$ _____
 - b. Cost savings: \$ _____
 - c. Number of jobs: # New jobs _____; # Saved jobs _____
 - d. Investment in the firm's operations: \$ _____
3. Did this SBIR result in your firm acquiring any of the following? (Check all that apply)
_____ a. Patent(s); _____ b. Copyright(s); _____ c. Licensing agreement(s)
4. Did this SBIR result in your firm "spinning off" another company or division? Yes _____ No _____
5. Would this project have been undertaken without the SBIR program? Yes _____ No _____

B. Indirect effects:

1. Beyond the above direct benefits of this SBIR project, did your firm experience any indirect benefits as a result of this SBIR?
Yes _____, No _____ What kind of indirect benefits? (Check all that apply)
_____ a. Investment in new or improved instruments, equipment, or software
_____ b. Improved staff training or utilization
_____ c. Related product / service development
_____ d. Related R & D
_____ e. Other (please specify): _____
2. Please estimate the value of the total indirect benefits to your firm resulting from the performance of the SBIR: \$ _____
3. In addition to your company did the outcomes from this SBIR project result in:
 - a. a technology advancement within your industry? Yes _____ No _____
 - b. a technology advancement in other industries? Yes _____ No _____

C. Summary:

1. Indicate the amount and source of any additional funding received for this project above the amount of the contract:
Internal Company Funding \$ _____; External Funding \$ _____
2. Rate your overall experience with the SBIR program on the following scale:
_____ Excellent; _____ Good; _____ Fair; _____ Poor.
3. The above company information is considered proprietary and confidential under the B4 exception to the Freedom of Information Act, and therefore cannot be released without permission of the originator. Yes _____ Initial _____

!!!!!!!

\$\$\$[September 3, 1995] ['NASA's Technology Transfer Program: Opportunities for Investment'] [Local]

This past summer, this writer had the opportunity to conduct research at NASA/Marshall Space Flight Center, Huntsville, AL. As part of the 1995 NASA Summer Faculty Fellowship Program jointly sponsored by NASA and the University of Alabama, this writer worked on several fascinating projects, including technology transfer.

Technology transfer is the process of moving new technology from government research and development to the private sector to benefit Americans generally, and U.S. businesses specifically. NASA has been actively engaged in technology transfer, virtually from its beginning back in the 1960's. Most people are well aware of numerous technological break-throughs as a direct result of NASA research and development related to the U.S. space program. Such things as miniaturization of computers, Teflon, Velcro, Corning-ware, that we use in our everyday lives, are commercial developments resulting from NASA research.

One of the research tasks involving this writer was helping to develop methods for measuring the economic impact on the U.S. economy of the continuing process of technology transfer in recent years. The problem with measurement is that economic impact to a great extent is beyond the control of NASA. Often most cooperative relationships with the Agency and private businesses end when a specific project is finished. NASA has begun to develop a large data-base on what happens to the technology down the road in terms of job creation and commercialization.

In the fall of 1994, NASA's Marshall Space Flight Center released a report on the Southeastern regional impact of its technology transfer activities, including industrial outreach, Space Act Agreements, and dual-use programs. Measuring the five-year impact, the results of an indepth survey revealed 665 new or saved jobs, 69 new products, \$10.2 million increased investment, \$11.5 million in production cost-savings, and \$47.2 million in increased sales.

Are there any good investment opportunities as a result of NASA's tech-transfer? You bet[EXCLAMATION MARK] One recent example is Waterjet Systems, Inc., a subsidiary of United Technologies Corporation. The project was created by NASA as cost effective and environmentally safe method for removing the thermal protective surface from the Shuttle Solid Rocket booster. NASA combined a powerful high pressure water pump with a robot-precision controlled nozzle.

Pratt & Whitney, a wholly-owned subsidiary of United Technologies Corporation in Huntsville AL., successfully transferred the waterjet processing technology from the manned spaced program to aviation and other industries. The Waterjet Blasting System is now used extensively to help clean and maintain aircraft bodies and engines. The process uses only recycled tap water and allows precise cleaning and decorating which is able to remove surface build-up of grim one layer at a time; this process leaves the surface of an engine, aircraft part or body unblemished.

There are literally thousands of technological transfers to private sector resulting in new products or services that are occurring throughout the United States. Many of the new products and services are being developed by small businesses that not only are the back bone of the U.S. economy; but also, many lead to good investment opportunities.

(George W. Trivoli, Eminent Scholar and Professor of Finance at Jacksonville (Ala.) State University, has written a book based upon his columns and other information, titled, [BEGIN BOLD] Your Investing: A Dollar and Sense Guide to Personal Investing[END BOLD]. (For copies of the book, please send \$17.50 per copy to Smart Ideas Publishing, P.O. Box 982, Jacksonville, AL 36265.)

1995

NASA/ASEE SUMMER FACULTY FELLOWSHIP PROGRAM

**MARSHALL SPACE FLIGHT CENTER
THE UNIVERSITY OF ALABAMA IN HUNTSVILLE**

**NON-LINEAR RESONANCE
OF FLUIDS
IN A CRYSTAL GROWTH CAVITY**

Prepared By:	Francis C. Wang, Ph.D.
Academic Rank:	Assistant Professor
Institution and Department:	Alabama A & M University Department of Engineering Technology
NASA/MSFC:	
Laboratory:	Space Sciences
Division:	Microgravity Science & Application
Branch:	Crystal Growth & Solidification
MSFC Colleague(s):	Charles R. Baugher, MSFC Colleague N. Ramachandran, Ph.D., USRA Colleague

NON-LINEAR RESONANCE OF FLUIDS IN A CRYSTAL GROWTH CAVITY

INTRODUCTION

In the microgravity environment, the effect of gravity on fluid motion is much reduced. Hence, secondary effects such as vibrations, jitters, surface tension, capillary effects, and electromagnetic forces become the dominant mechanism of fluid convection. Numerous studies have been conducted to investigate fluid behavior in microgravity with the ultimate goal of developing processes with minimal influence from convection. Industrial applications such as crystal growth from solidification of melt and protein growth for pharmaceutical application are just a few examples of the vast potential benefit that can be reaped from material processing in space.

However, a space laboratory is not immune from all undesirable disturbances and it is imperative that such disturbances be well understood, quantifiable, and controlled. Non-uniform and transient accelerations such as vibrations, g-jitters, and impulsive accelerations exist as a result of crew activities, space vehicle maneuvering, and the operations of on-board equipment. Measurements conducted on-board a U. S. Spacelab showed the existence of vibrations in the frequency range of 1 to 100 Hz,¹ with a dominant mode of 17 Hz and harmonics of 54 Hz. The observed vibration is not limited to any coordinate plane but exists in all directions. Similar situation exists on-board the Russian MIR space station. Due to the large structure of its design, the future International Space Station will have its own characteristic vibration spectrum.

It is well known that vibration can exert substantial influence on heat and mass transfer processes, thus hindering any attempts to achieve a diffusion-limited process. Experiments on vibration convection for a liquid-filled enclosure under one-g environment [2,3] showed the existence of different flow regimes as vibration frequency and intensity changes. Results showed the existence of a resonant frequency, near which the enhancement is the strongest, and the existence of a high frequency asymptote. Numerical simulations of vibration convection have been conducted by Yurkov⁴, Fu and Shieh⁵, and by Wang⁶. These analyses considered a two-dimensional air-filled cell under weightlessness condition and showed results similar to those of the experiments.

It is not yet known whether resonance convection can be triggered by g-jitter alone or whether it requires the interaction of g-jitter with other convective forces in low gravity. An order of magnitude analysis, however, can be used to show the dependence of the resonance frequency on the fluid Prandtl number. Even though the onset of resonance convection may depend on other factors, results indicate that fluids with low Prandtl numbers are more susceptible to resonance than those with high Prandtl numbers. The current study is aimed at gaining additional insights to this problem using germanium as working fluid. Germanium was chosen for this analysis because of its common usage in solidification process and its relatively low Prandtl number ($Pr = 0.02$).

ANALYTICAL MODEL

The Navier-Stokes equations for an incompressible fluid with Boussinesq approximation were used for this analysis. These equations can be non-dimensionalized using a characteristic velocity based on thermal diffusion, α , and the dimension of the cell, L . For a two-dimensional problem in which the sinusoidal vibration is along the same direction as the residual acceleration, the following equations can be used:

$$\frac{\partial U}{\partial X} + \frac{\partial V}{\partial Y} = 0 \quad (1)$$

$$\frac{\partial U}{\partial \tau} + U \frac{\partial U}{\partial X} + V \frac{\partial U}{\partial Y} = -\frac{\partial P}{\partial X} + \text{Pr} \nabla^2 U \quad (2)$$

$$\begin{aligned} \frac{\partial V}{\partial \tau} + U \frac{\partial V}{\partial X} + V \frac{\partial V}{\partial Y} = & -\frac{\partial P}{\partial Y} + \text{Pr} \nabla^2 V \\ & + \text{Pr}[Ra + G\omega \sin(\tau\omega)]\theta \end{aligned} \quad (3)$$

$$\frac{\partial \theta}{\partial \tau} + U \frac{\partial \theta}{\partial X} + V \frac{\partial \theta}{\partial Y} = \frac{\partial^2 \theta}{\partial X^2} + \frac{\partial^2 \theta}{\partial Y^2} \quad (4)$$

Here U and V are the non-dimensional velocity components, Pr the Prandtl Number, Ra the Rayleigh number, G the Grashof Number, and ω the non-dimensional circular frequency. Notice that the forcing term in equation (3) is proportional to the product of Prandtl number, the temperature differential, and the buoyancy effect of acceleration. The buoyancy term consists, in general, of two components, one due to the residual acceleration and one due to the oscillation force. The constant acceleration is expressed in terms of the Rayleigh number, and the applied oscillation is expressed in terms of the product of the Grashof number, the circular frequency and a time varying sine function.

NUMERICAL INVESTIGATION

Equations (1-4) were solved numerically using the NASA developed two-dimensional Finite Difference Navier-Stokes solver (FDNS2D) [Ref. 7]. The working fluid is germanium which is a representative fluid used in solidification from melts. The properties of germanium along with that of water and air are given in Table 1.

Property	Water	Air	Germanium
Kinematic Viscosity (m ² /s)	9.8260E-07	1.6000E-05	3.3160E-07
Density (kg/m ³)	9.9740E+02	1.1650E+00	6.1000E+03
Thermal Diffusivity (m ² /s)	1.4490E-07	2.2860E-05	1.5120E-05
Expansion Coefficient (1/K)	2.7720E-04	3.3000E-03	1.2600E-04
Prandtl number	7.00	0.70	0.02

Table 1. Summary of Fluid Properties

The calculation domain of the cavity is divided into a finite difference mesh of 31 by 31. The fluid was initially assumed in a quasi-static condition with a constant temperature difference of 100K maintained across two opposing surfaces. At time zero, a continuous vibration acceleration of constant amplitude is applied in the direction normal to the temperature gradient. Transient solutions were obtained for different vibration frequencies using a time marching technique. Iterations at each time step were used to ensure convergence. Figure 1 depicts the domain of calculations.

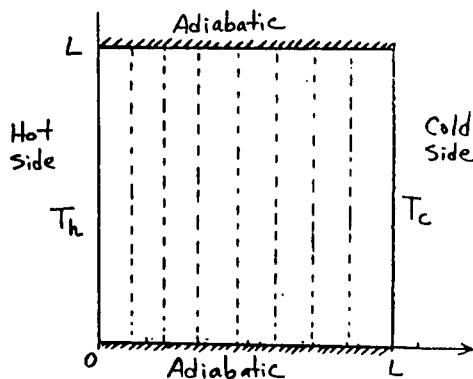


Figure 1. Geometry of Cavity

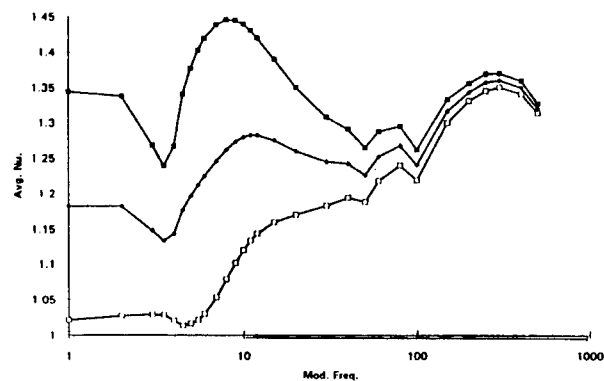


Figure 2. Average Nu Plot for Germanium

RESULTS & DISCUSSIONS

Numerical results for germanium ($Pr = 0.02$) in a cavity of 1 cm squared in a zero gravity environment will be reported. A Grashof number of 10^4 was used in the analysis. Figure 2 shows the existence of several different flow regimes as the vibration frequency increases. Expressed in terms of the averaged Nusselt number, the result indicated an increase of heat transfer from the hot wall to the cold wall at low vibration frequencies. This heat transfer rate peaks out near a resonance frequency, then went through a transition regime of instability. Finally it settles to an asymptote at very high frequencies. This trend is very similar to that of air, shown in Figure 3 from a previous study [Ref. 6]. However, the transition between the flow regimes occurs at much lower frequencies, and the enhancement of heat transfer rate is less prominent for germanium.

The resonance regime for germanium is found between the non-dimensional frequencies of 3 and 10, which translates to a frequency of 0.247 Hz for a cell of 1 cm. This frequency is much smaller than that of air which exists in the range of 10 to 30 Hz. This difference is due to the difference in fluid properties, especially due to the fluid viscosity and fluid Prandtl number. A plot of the steady state temperature at a point near the top of the mid-plane is shown in Figure 4. It shows that at lower vibration frequencies the temperature variation is high, and its mean value is close to the medium value between the two side walls. As the frequency increases, the temperature variation becomes smaller, and the mean value moves toward a lower value. A review of temperature data at several points along the mid-plane reveals that there exists a temperature gradient in the direction parallel

to the direction of vibration, with the top boundary always at higher temperature than the lower boundary. This has been attributed to the persistence of flow as a result of the initial impulse.

Time variation of the averaged Nusselt number and temperature at three points along the mid-plane for a few selected frequencies are given in Figures 5 and 6, respectively. The three frequencies selected $\omega = 3, 10$, and 100 represent regimes of transition, resonance, and high frequency vibration convection. Notice the existence of the double peaks in Nusselt number during each cycle of vibration for $\omega = 3$ in Figure 5. This is due to the complete reversal of the temperature about the mid-plane of the cavity during an oscillating cycle of vibration, as shown clearly in the top portion of Figure 6.

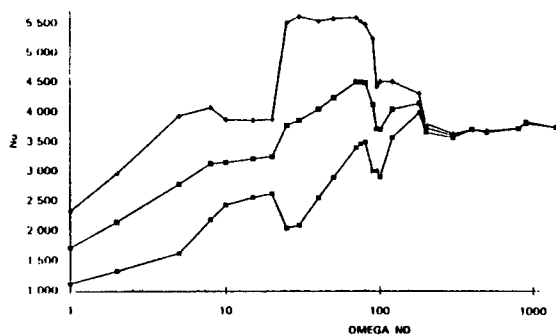


Figure 3. Average Nu Plot for Air

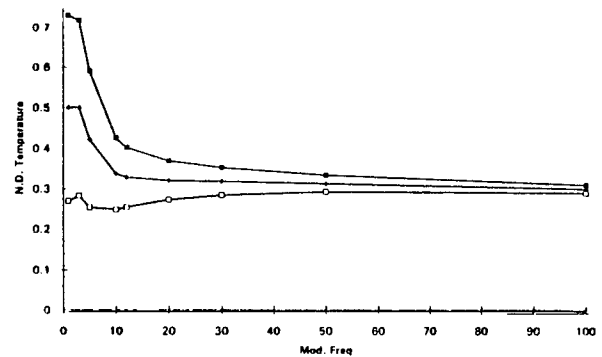


Figure 4. Temperature Plot for Mid-Plane

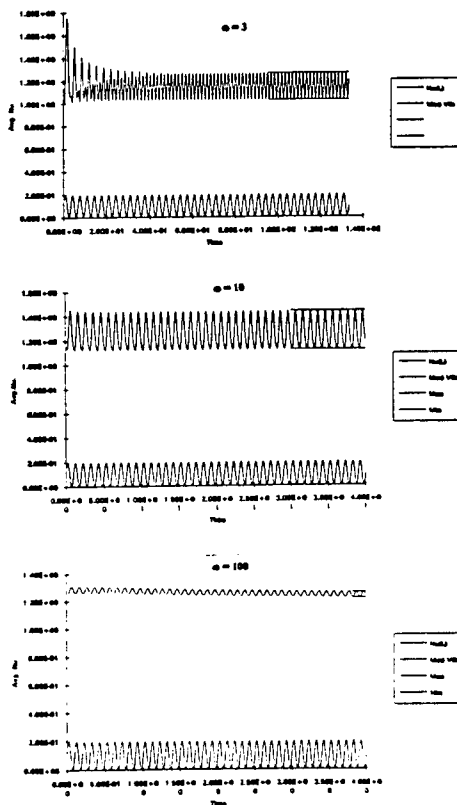


Figure 5. Variation of Nusselt Numbers for $\omega = 3$ (top), 10 (middle), and 100 (bottom)

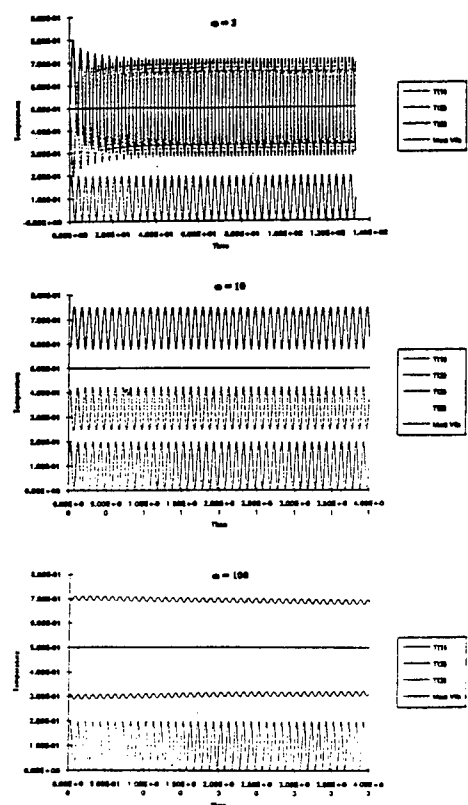


Figure 6. Variation of Temperature for $\omega = 3$ (top), 10 (middle), and 100 (bottom)

CONCLUSIONS & RECOMMENDATIONS

Results of a numerical simulation of vibration convection of a crystal growth cavity in zero gravity showed the existence of different flow regimes at different vibration frequencies. Results showed that the division of the flow regimes and the peak heat transfer rate dependent on the Prandtl number of the working fluid. A complete reversal of temperature profiles about the cavity mid-plane at low vibration frequencies leads to heat transfer rate which oscillates at twice the vibration frequency. At higher vibration frequencies, the fluid near the top portion of the cavity is consistently hotter than the fluid near the bottom, resulting in an internal heat flow in the direction normal to the applied temperature gradient. At very high frequencies, the flow reaches an asymptote, and the heat transfer rate becomes independent of the vibration frequency.

Additional analyses are needed to investigate the effects of cavity geometry, e.g. cylindrical shape, or one with different length to height ratios. Effects due to non-zero gravity also need to be considered. Experimental programs aimed at verifying the numerical results are under consideration. A flight experiment will eventually be needed to verify the results of vibration effects on fluid convection in micro-gravity conditions.

REFERENCES

1. Ramachandran, N., C. R. Baugher, and M. J. B. Rogers, "Acceleration Environment on the Space Shuttle and Its Impact On Thermo-Solutal Fluid Mechanics," *1993 ASME Winter Annual Meeting*.
2. Forbes, R.E., Carley, C.T., and Bell, C.J., "Vibration Effects on Convective Heat Transfer in Enclosures," *Journal of Heat Transfer*, **92**, Ser. C, 429-438, March 1970.
3. Ivanova, A.A., and Kozlov, V.G., "Vibrationally Gravitational Convection in a Horizontal Cylindrical Layer," *Heat Transfer-Sov. Res.* **20**, 235-247, 1988.
4. Yurkov, Yu. S., "Vibration-induced thermal convection in a square cavity in weightlessness (finite frequencies)," In *Konvektivnyye techeniya, Convective Perm Teachers' Institute*, Perm. pp. 36-37 (1981).
5. Fu, W.S., and Shieh, W.J., "A Study of Thermal Convection in an Enclosure Induced Simultaneously by Gravity and Vibration," *Intl. J. Heat Mass Transfer*, **35**, 7, 1695-1710, 1992.
6. Wang, F.C., "Effects of Vibration (G-Jitters) on Convection in Micro-gravity," In *1994 NASA/ASEE Summer Faculty Fellowship Program Report*, NASA Contract Report CR-196533, NASA MSFC, p. XLVI-1 to XLVI-8, 1994.
7. "FDNS, A General Purpose CFD Code, User's Guide," ESI-TR-93-01, Engineering Sciences, Inc., Huntsville, AL 35802 (1993).

1995

NASA/ASEE SUMMER FACULTY FELLOWSHIP PROGRAM

MARSHALL SPACE FLIGHT CENTER
THE UNIVERSITY OF ALABAMA IN HUNTSVILLE

Effect of Melt-Solid Interface Shape on Lateral Compositional
Distribution of Unidirectionally Solidified II-VI Semiconducting Alloys

Prepared By: Jai-Ching Wang, Ph.D.

Academic Rank: Associate Professor

Institution & Department: Alabama A&M University
Department of Physics

NASA/MSFC:

Office: Space Sciences Laboratory
Division: Microgravity Science & Application
Branch: Crystal Growth & Solidification Physics

MSFC Colleagues: S. L. Lehoczky, Ph.D.
C.-H. Su, Ph.D.
D. C. Gillies, Ph.D.
D. A. Watring
Y.-G. Sha, Ph.D.
F. R. Szofran, Ph.D.

INTRODUCTION

A computer code developed previously [1] has been used to simulate lateral compositional distributions for several II-VI semiconducting systems. The code is based on analytical results [2] obtained by following Coriell et al. formalism [3]. The system under study is an azimuthal symmetric cylindrical system with a curved melt-solid interface shape during an unidirectional solidification process. It is assumed that the system is under a steady state diffusion limited growth condition with a curved melt-solid interface and equation for the diffusion limited growth is

$$\nabla^2 C(r, z) + \beta \frac{\partial}{\partial z} C(r, z) = 0. \quad (1)$$

In terms of cylindrical coordinates explicitly, the equation is expressed as

$$\frac{\partial^2}{\partial r^2} C(r, z) + \frac{1}{r} \frac{\partial}{\partial r} C(r, z) + \frac{\partial^2}{\partial z^2} C(r, z) + \beta \frac{\partial}{\partial z} (C(r, z)) = 0, \quad (2)$$

where the dimensionless solute concentration, C , has been scaled by the bulk concentration C_0 , r and z are dimensionless axial and radial coordinates which have been scaled by the radius of the ampoule, R , and $\beta = VR/D$, in which V is the growth velocity, R is the sample radius and D the diffusion constant of the solute in the liquid.

The boundary conditions to be satisfied are

$$C(r, z \rightarrow \infty) = 1, \quad (3)$$

$$\frac{\partial}{\partial r} C(r, z) = 0 \text{ at } r=1 \text{ and } r=0, \quad (4)$$

$$\beta(k-1)C_I(r, z) = \frac{\partial}{\partial z} C_I(r, z) - \frac{\partial}{\partial r} C_I(r, z) \frac{\partial}{\partial r} W(r). \quad (5)$$

where k is the segregation constant, $W(r)$ the melt-solid interface and I denotes at the melt-solid interface location.

The melt-solid interface shape can be expressed as a series of Bessel's functions,

$$W(r) = \delta + \sum_{n=1}^{\infty} \delta(n) J_0(u_n r). \quad (6)$$

where δ is the planar interface location and $\delta(n)$'s are the coefficients for the Bessel's functions $J_0(u_n r)$ and u_n 's are the zeros of $J_1(\alpha)$.

The diffusion equation, equation (2), can be solved by the separation of variables method.

In the limit that dw/dr is small compared to $2k+p(n)-1$, where $p(n)$ denote $\sqrt{1 + \left(\frac{2u_n}{\beta}\right)^2}$ and have

large values for small β , the solution for solute concentration in the melt at coordinate (r, z) is

$$C(r, z) = 1 + \frac{1-k}{k} e^{-\beta(z-\delta)} + \sum_{n=1}^{\infty} \frac{2\beta(1-k)\delta(n)}{2k+p(n)-1} e^{-\frac{\beta}{2}[1+p(n)](z-W(r))}, \quad (7)$$

The solute concentration in the melt at the melt-solid interface is

$$C_I(r, z) = 1 + \frac{1-k}{k} e^{-\beta(W-\delta)} + \sum_{n=1}^{\infty} \frac{2\beta(1-k)\delta(n)}{2k+p(n)-1}. \quad (8)$$

The solute concentrations of the solid at the interface, $C_{SI}(r, z) = kC_I(r, z)$, is

$$C_{SI}(r, z) = k + (1-k) e^{-\beta(W-\delta)} + \sum_{n=1}^{\infty} \frac{2\beta k(1-k)\delta(n)}{2k+p(n)-1}. \quad (9)$$

For small β limit and $\beta(W-\delta)$ is small, we may expand the exponent term and obtain the solute concentration in the solid at the melt-solid interface as

$$C_{SI}(r, z) = 1 - \beta(1-k) \sum_{n=1}^{\infty} \frac{\delta(n) J_0(u_n r)}{1 + \frac{2k}{p(n)-1}}. \quad (10)$$

If $2k/[p(n)-1] \ll 1$, then equation (10) reduces to a simpler expression

$$C_{SI}(r, z) = 1 - \beta (1 - k) [W(r) - \delta], \quad (11)$$

i.e., the deviation of C_{SI} from unity is proportional to the deviation of interface shape from planarity. The proportional constant is the product of β and $(1-k)$.

NUMERICAL CALCULATIONS AND RESULTS

We use equations (9), (10), (11) to calculate compositional distribution at the melt-solid interface for a diffusion limited growth system with a curved melt-solid interface shape for small β values. The results in Figure 1 show that equations (9) and (10) give very close answers while equation (11) over estimates the results by a few percent. Calculated lateral compositional distributions by using equation (10) for four different melt-solid interface shapes are shown in Figure 2. Scaling these compositional distributions with their interface deflections yields curves with similar shapes as shown in Figure 3. By adjusting the scaled curves they all fall on one curve, indicating that the lateral compositional distribution is proportional to melt-solid interface shape for same β and k (see Figure 4). The results agree with the simple expression equation (11) because both the conditions, β is small and $2k/[p(n)-1] \ll 1$, are satisfied in this study. The experimental conditions for various systems under consideration are listed in Table 1 which have β equal to 0.1455, 0.16 or 0.2667 small enough such that the analytical and approximate expression obtained above apply. In the MZT USML-1 experiments [4], the interface shapes were not radially symmetrical, therefore, the deflections of the interfaces for the right and left handed sides were measured. Table 2 is a comparison of the calculated and experimental radial segregation on MZT USML-1 experiment. The results agree reasonably well. Figure 5 shows the simulated and experimental data for MCT D4 crystal grown under axial 50 kG magnetic field [5]. The experimental data agree quite well with the theoretical results indicating that the convection in the melt during the growth has been reduced by the magnetic field. Figure 6 gives the simulated and experimental data for MCT D6 crystal grown without magnetic field [5]. Due to larger convective fluid flow in the melt during crystal growth in D6 experiment compared to that of D4 experiment, D6 crystal has larger deflection of melt-solid interface shape. The simulated results show that the composition distribution scales with melt-solid interface shape, but with larger discrepancies between the two curves at the edges. This is due to the contribution from the convective fluid flow in the melt. The simulated data and the experimental data for MZT B16-4 crystal are shown in Figure 7. The disagreement between theory and experiment in MCT D6 and MZT B16-4 experiments are also believed to be due to contributions from convective fluid flow [6]. Figure 8 shows the simulated and experimental data for MCT USMP-2 space flight crystal [7] grown in space. The two curves have significant mismatches at the edges. Which was believed to be contributed by the residual transverse microgravity.

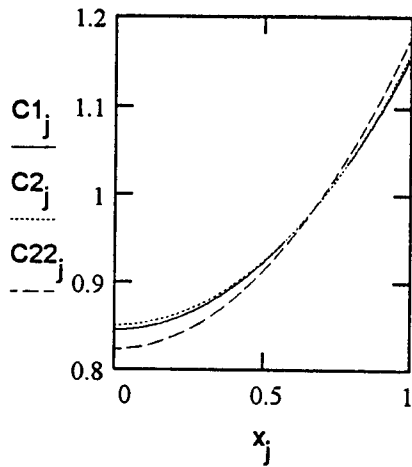


Figure 1. C_1, C_2 and C_{22} are calculated lateral composition distributions for an MCT sample with $k=4$, $\beta=0.1455$, and deflection= 0.8125 by using equation (9), (10) and (11) respectively

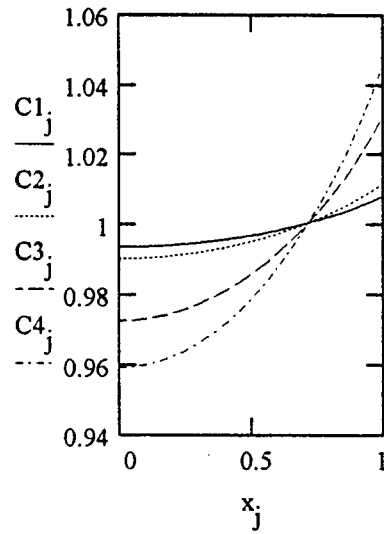


Figure 2. Composition distributions for various deflections. The radius of the sample is 0.4 cm. The deviation of the interfaces are 0.092mm, 0.136 mm, 0.368mm & 0.544 mm.

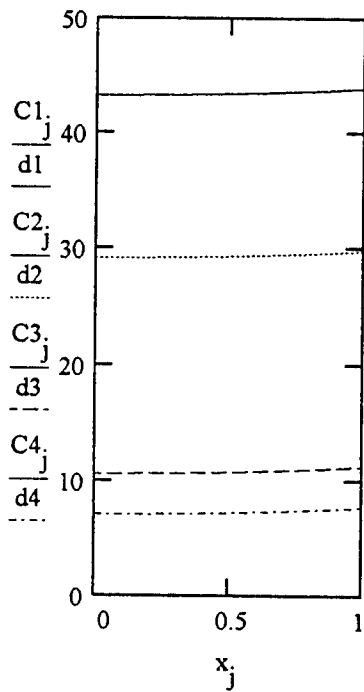


Figure 3. Deflection scaled composition distributions. The radius of the sample is 0.4 cm. The deviation of the interfaces are 0.092mm, 0.136 mm, 0.368mm & 0.544 mm.

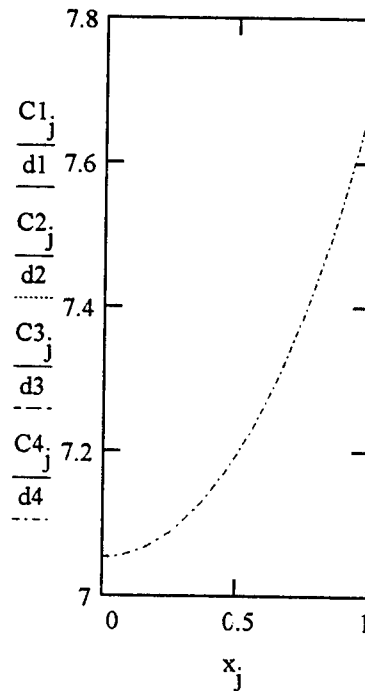


Figure 4. Adjusted deflection scaled composition distributions. The radius of the sample is 0.4 cm. The deviation of the interfaces are 0.092mm, 0.136 mm, 0.368mm & 0.544 mm. The results show the lateral composition deviation scale with the interface deviation.

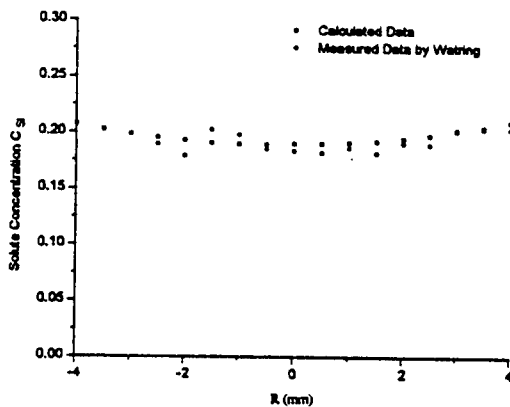


Figure 5. Calculated and measured data of MCT D4 crystal with 50 KG magnetic field

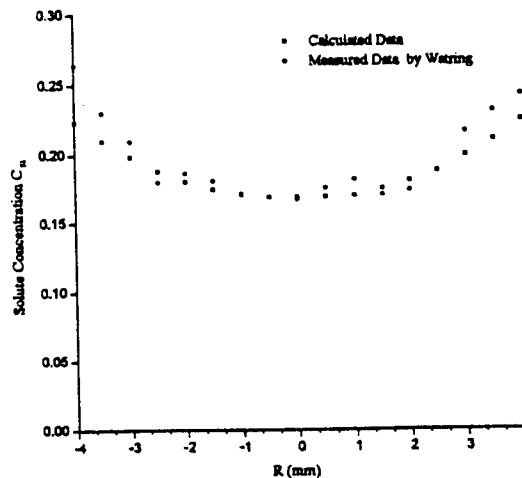


Figure 6. Calculated and measured data of MCT D6 crystal without magnetic field

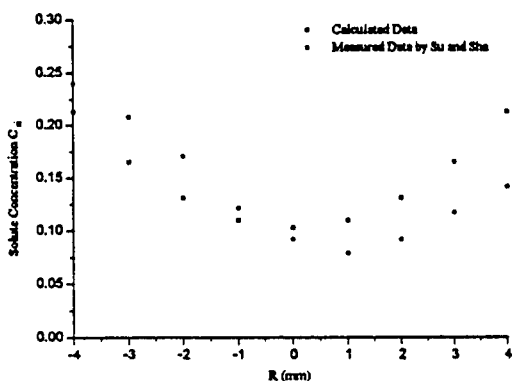


Figure 7. Calculated and measured data of MZT B6-4 ground based crystal. Deflections are 1.086 & 1.091 on left and right hand sides of the crystal.

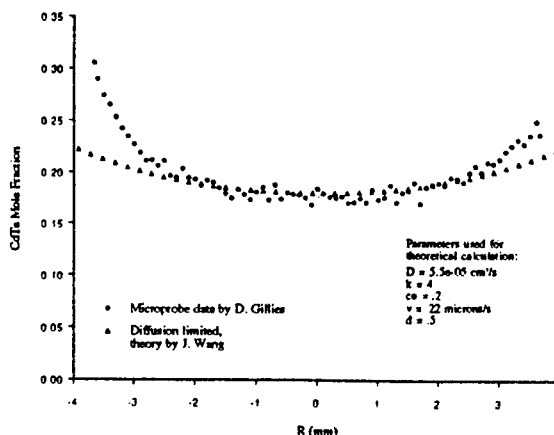


Figure 8. MCT-27Q, Flight Sample Composition across x-Diameter

Table 1: Ampoule Data

Ampoule I.D.	C_0	V (cm/s)	k	D (cm ² /s)	R (cm)	$\beta=VR/D$	Deflection Δ
MCT D4	0.2	2×10^{-5}	4	5.5×10^{-5}	0.4	0.1455	0.275
MCT D6	0.2	2×10^{-5}	4	5.5×10^{-5}	0.4	0.1455	0.8125
MZT USML-1	0.16	4×10^{-6}	4	6×10^{-6}	0.4	0.2667	R-0.5 L-0.225
MZT B16-4	0.16	4×10^{-6}	4	6×10^{-6}	0.4	0.2667	R-1.091 L-1.086
MCT USMP-2	0.2	2.2×10^{-5}	4	5.5×10^{-5}	0.4	0.16	0.5

Table 2: Measured and simulated lateral compositional deviations of MZT USML-1 space flight experimental data

Measured	Calculated
$\Delta C_1/C_0=0.40$	$\Delta C_1/C_0=0.375$
$\Delta C_2/C_0=0.18$	$\Delta C_2/C_0=0.153$

REFERENCES

- [1] Wang, J. C., "Numerical Formulation of compositional Segregation at Curved Solid-Liquid Interface during Steady State Solidification Process", NASA CR 196533, ed. by Freeman, M., Chappell, C. R., Six, F. and Karr, G. R., Oct. 1994
- [2] Wang, J. C., "Investigation of compositional Segregation During Unidirectional Solidification of Solid Solution Semiconducting Alloy", NASA CR 162051, ed. by Karr, G. R., Barfield J., and Kent, M., pXLI1-20, Aug. 1982
- [3] Coriell, S. R., F. Boisvert, R. G. Rehm, and R.F. Sekerka, "Lateral Solute Segregation During Unidirectional Solidification of a binary Alloy with a Curved Solid-Liquid Interface", Journal of Crystal Growth **54**, 167, 1981
- [4] Lehoczky, S. L., F. R. Szofran, D. C. Gillies, S. D. Cobb, C. H. Su, Y. G. Sha, R. N. Andrews, "Crystal Growth of Selected II-VI Semiconducting Alloys by Directional Solidification," NASA CP-3272 Volume I 163-222, May 1994
- [5] Waring, D. A., "The Effects of Vertical Magnetic Fields on Segregation in HgCdTe," Presented Second International Conference on Solidification and Gravity Miskole-Lillafured, Hungary, April 25-28, 1995
- [6] Capper, P., C. L. Jones, E. J. Pearce and M. J. T. Quelch, "Growth of $Cd_xHg_{1-x}Te$: Comparison of Some Properties with the Predictions of two Melt Growth Models", Journal of Crystal Growth **62**, 487, 1983
- [7] Lehoczky, S. L., F. R. Szofran, and D. C. Gillies, "Growth of Solid Solution Single Crystals", to be published in Launch+1 Year Science Review of USMP-2, 1995

1995

NASA/SEE SUMMER FACULTY FELLOWSHIP PROGRAM

**MARSHALL SPACE FLIGHT CENTER
THE UNIVERSITY OF ALABAMA IN HUNTSVILLE**

**A CONVERTOR AND USER INTERFACE TO IMPORT CAD FILES INTO
WORLDTOOLKIT VIRTUAL REALITY SYSTEMS**

Prepared By: Peter Hor-Ching Wang, Ph.D.

Academic Rank: Assistant Professor

Institution and Department: Alabama A & M University
Department of Computer Information Science

NASA/MSFC:

Office: Mission Operations Laboratory
Division: Operations Engineering
Branch: Crew Systems Engineering

MSFC Colleague: Joe Hale

INTRODUCTION

Virtual Reality (VR) is a rapidly developing human-to-computer interface technology. VR can be considered as a three-dimensional computer-generated Virtual World (VW) which can sense particular aspects of a user's behavior, allow the user to manipulate the objects interactively, and render the VW at real-time accordingly. The user is totally immersed in the virtual world and feel the sense of transforming into that VW.

NASA/MSFC Computer Application Virtual Environments (CAVE) has been developing the space-related VR applications since 1990. The VR systems in CAVE lab are based on VPL RB2 system which consists of a VPL RB2 control tower, an LX eyephone, an Isotrak polhemus sensor, two Fastrak polhemus sensors, a folk of Bird sensor, and two VPL DGII DataGloves. A dynamics animator called Body Electric from VPL is used as the control system to interface with all the input/output devices and to provide the network communications as well as VR programming environment. The RB2 Swivel 3D is used as the modelling program to construct the VWs. A severe limitation of the VPL VR system is the use of RB2 Swivel 3D, which restricts the files to a maximum of 1020 objects and doesn't have the advanced graphics texture mapping. The other limitation is that the VPL VR system is a turn-key system which does not provide the flexibility for user to add new sensors and C language interface.

Recently, NASA/MSFC CAVE lab provides VR systems built on Sense8 WorldToolKit (WTK) which is a C library for creating VR development environments. WTK provides device drivers for most of the sensors and eyephones available on the VR market. WTK accepts several CAD file formats, such as Sense8 Neutral File Format, AutoCAD DXF and 3D Studio file format, Wave Front OBJ file format, VideoScape GEO file format, Intergraph EMS stereolithographics and CATIA Stereolithographics STL file formats. WTK functions are object-oriented in their naming convention, are grouped into classes, and provide easy C language interface.

Using a CAD or modelling program to build a VW for WTK VR applications, we typically construct the stationary universe with all the geometric objects except the dynamic objects, and create each dynamic object in an individual file.

VWs, define the form, behavior and appearance of objects, are the core of a VR system. "From the standpoint of Virtual Environment (VE) construction, geometric modelling is a vital enabling technology whose limitations may impede progress. As a practical manner, the VE research community will benefit from a shared open modelling environment." (Nathaniel Durlach, Anne Mavor 1995)

One of the important aspects of a VR system is the modelling of VWs. At NASA/MSFC, there are lots of existing CAD files in different file formats for each project. It is very beneficial for the CAVE lab to have the capability to import these existing CAD files, such as AXAF CAD files in IDEAS or CATIA file formats, into the WTK VR system.

It is critical to provide a convertor and the user interface allowing the WTK VR systems to import VWs from existing files in various CAD file formats. A few existing VWs in different CAD file formats are being investigated and imported into the WTK VR system. A configured master file is used to organize all the dynamic objects in different CAD file formats and a user interface is provided for user to access all the existing WTK VR applications.

OBJECTIVES

The objectives of this effort are to find a path to import existing AXAF CAD files in IDEAS and CATIA file formats into WTK VR system, to provide a user interface for accessing multiple CAD files in different file formats, to integrate the Polhemus Fastrak sensors, Spaceball sensor and its associated button commands, and distributed network communications into a complete 3D VR environment for space-related VR applications.

APPROACH

In order to access existing CAD files in MSFC, several widely used CAD file formats are investigated. There are several CAD file formats supported by WTK. But, the IDEAS and CATIA CAD files used in AXAF are not supported by WTK directly, therefore they must be transformed before importing into the WTK environment. Fortunately, an IDEAS UNF to Sense8 NFF convertor is obtained from the WTK user's group. A convertor to tranform CATIA files into stereolithographics STL files is available. In order to generically import various CAD files into WTK VR system, a

converter is generated to transform CAD files in any WTK acceptable file formats into either DXF or NFF file formats. The WTK VR system normally deals with tremendous amount of data. Therefore, a friendly user interface is created to allow the users to access the CAD model files stored in different formats. These CAD files can be located in one single directory or specified in a configured master file. In a typical application, the universe will be constructed with static objects, while each dynamic object will be created in an individual CAD file. Once the AXAF CAD files in IDEAS and CATIA file formats can be imported into the WTK environments, an integrated 3D VR environment needs to be created for the user to study the experiments of AXAF project.

CONCLUSIONS

Several CAD file formats are studied and the path to import IDEAS UNF files and CATIA stereolithographics files into WTK VR Applications is identified. The WTK-based VR system is able to import VWs in different CAD file formats, such as Sense8 NFF, AutoCAD 3D Studio, AutoCAD DXF, Wave Front OBJ file format, VideoScape GEO file format, Intergraph EMS stereolithographics STL and CATIA Stereolithographics STL file formats. The CAD files can be imported as single file, multiple files located in a single directory, or multiple files specified in a configured master file. The Spaceball and its buttons are defined for the user to navigate through the VW and to issue several frequently used commands. They are also defined to allow the user to pitch, yaw and roll the user's viewpoint, to allow the user to modify the sensitivity of sensors, and to control the switch between ntsc and rgb modes. The network communications are created to achieve the synchronization and image rendering between two SGI machines. A complete networked immersive VR system with Fastrak sensors and Spaceball control is integrated to study the AXAF experiments in VR environment. One of the Fastrak sensors is attached to the eyephone to track the user's movement, while the other is attached to user's hand to interact with those dynamic objects. A predefined 10 locations can be specified in a file to allow the user to be repositioned during the experiments. A path can be loaded or created during the experiments, and replayed at a later time.

A set of IDEAS UNF files from IOWA State Visualization Lab are imported to WTK VR environment. Several CATIA stereolithographics STL files from AXAF and TRW are also imported into the WTK VR environment. An airlock in Intergraph EMS stereolithographics STL file format is also imported into the WTK VR environment. These experiments proves that

the WTK 3D VR environment is capable to process and review these CAD files and its simulations successfully.

RECOMMENDATIONS

Due to the high fidelity of the airlock file, the performance drops to less than one frame per second on the SGI 4D/310 with 24MB RAM system. It is recommended that a partition scheme be adopted to allow the VR system to import high fidelity VW as well as the real time performance. It is recommended that a hierarchical structure and the dynamic attributes of objects to be specified in a file to perform the reach envelope and human factor engineering studies. It is also recommended that higher performance hardware be used to provide the needed processing power on high fidelity VWs in the space-related applications.

ACKNOWLEDGEMENT

I would like to express my great appreciations to my MSFC Colleague Joe Hale for his creative ideas and guidance. I also like to thank Gina Klinzak of NTI , Mark Blasingame and Rick Moseley of Boeing for their time and help to provide the nice working environment. The financial support of the NASA/ASEE Summer Faculty Fellowship Program, Teresa Shurtz, Gerald Karr, and Fran Six are gratefully acknowledged.

REFERENCES

1. Benn, Karen P. The assessment of Virtual Reality for Human Anatomy Instruction. NASA Contractor Report. NASA CR-196533
2. Helsel, Sandra K. and Judith P. Roth. Virtual Reality Theory, Practice and Promise. Meckler Publishing, 1991.
3. Roy S. Kalawsky. The Science of Virtual Reality and Virtual Environments. Addison-Wesley. 1993
4. Lindsey, Patricia F. Development of Microgravity, Full Body Functional Reach Envelope Using 3-D Computer Graphic Models and Virtual Reality Technology. NASA Contractor Report.

NASA CR-196533

5. Nathaniel Durlach, Anne Mavor. Virtual Reality: Scientific and Technological Challenges. National Research Council. 1995
1995
6. Pimentel, Ken and Kevin Teixdeira. Virtual Reality: Through the New Looking Glass. McGraw-Hill, Inc. 1993.
7. Rheingold, Howard. Virtual Reality. Simon & Schuster, 1991.

1995
NASA/ASEE SUMMER FACULTY FELLOWSHIP PROGRAM

MARSHALL SPACE FLIGHT CENTER
THE UNIVERSITY OF ALABAMA IN HUNTSVILLE

**DEVELOPMENT OF THE COMMAND DATA SYSTEM AND GROUND
SOFTWARE FOR THE SEDSAT-1 MICROSATELLITE**

Prepared By:	B. Earl Wells, Ph.D.
Academic Rank:	Assistant Professor
Institution and Department:	The University of Alabama in Huntsville Department of Electrical and Computer Engineering
NASA/MSFC:	
Office:	Small Expendable Deployer Systems
Division:	Earth and Space Science Projects
Branch:	Science and Applications Projects
MSFC Colleagues:	Jim Harrison Pat Doty Tommy Harris Frayne Smith

Mission Objectives

SEDSAT-1 is designed to be a low cost scientific satellite which is to be used to perform a minimum of five tasks which include 1) the acquisition of a number of important parameters associated with the tethering processes from the payloads perspective (such as accelerations incurred and imaging data of the tether during deployment), 2) to act as a remote sensing platform for making measurements of the Earth's Atmosphere (allowing research to be performed in such areas as vertical lightning observation, visible light spectrography, and cloud cover studies, 3) to act as a general purpose amateur radio communication satellite relaying information back to earth, 4) to demonstrate the feasibility of the deployment in low-earth orbit of advanced technology such as the Gallium Arsenide Solar Cells, Nickel Metal Hydride batteries, and multi-chip module technology and, 5) to support student's active participation in applying the disciplines of engineering and science to space-based hardware platforms.

The project includes the Three-axis Accelerometer System, TAS, Experiment which is designed to report the accelerations that the satellite undergoes during the tethering operations and during the second phase of the mission when the free floating satellite comes in contact with orbit debris. The SEASIS (SEDS Earth, Atmosphere, and Space Imaging System) is another SEDSAT experiment designed to provide images of the tether during its deployment and the earth during the second phase of the mission. To control these experiments and virtually all other satellite operations the Command Data System, CDS is employed. This system utilizes a moderate complexity microcontroller controlled by tasks operating under a real-time operating system to dynamically monitor and control the satellite.

The scope of this researchers efforts has been in the general area of coordinating and assisting the student researchers with the development of the CDS and ground station interfaces. This included the low-level CDS hardware design and the formulization of a general software plan and schedule for both the CDS and ground station portions of the project.

Hardware Development

Figure 1 is a simplified view of the basic electrical subsystems which make up the SEDSAT-1 design as envisioned during the beginning of the fellowship period. Although concurrent engineering practices allowed for the simultaneous design and implementation of the CDS hardware while the software was being developed, the schedule illustrates that the design of the hardware is in the critical path and must be completed before the integration phases of the project.

A detailed description of each subsystem appears in the UAH Document Number 0100 entitled SEDSAT-1 Documentation and Drawing List (January 1995). The CDS hardware was partially designed and prototyped and inadequately documented at the time of the beginning of the fellowship. A detailed evaluation of this prototype and design revealed that there were three major problems. First, the EDAC (single-bit correct/multiple bit detect) protected memory region was not designed to be byte addressable. This was likely to cause extreme problems because the high-level-language compiler being used was very likely to produced object code which performed byte accesses and the external DMA was chosen previously to be an 8 bit device which by its very nature performed byte accesses. Second, there was found to be timing problems with the Transputer Interface IMSC011 chip which resulted in unreliable communications with the SEASIS Experiment. Third the DMA design was incomplete and needed modification.

To allow the EDAC protected memory region to perform individual byte access, circuitry had to be designed that would latch a byte into buffers, read the complete data word from memory, correct the complete data word when necessary, and insert the byte to be written into the data word, generate new check bits, and store the data word back into memory. The circuitry required for this task was not trivial and was implemented inside an FPGA. This implementation was performed in this matter as an aid to prototyping since it could be used to replace large numbers of MSI logic devices. (The actual flight hardware might employ discrete TTL logic if it is determined that the FPGA devices cannot be shielded sufficiently from radiation hazards.) At the end of the fellowship period, there still existed timing problems in this circuitry which were being resolved. The Transputer to CDS interface was redesigned to allow both the External 8037A DMA device and the 80186 to access its internal registers. This allowed the T805 Transputer in the SCC 100 to communicate with the 80186 via its high-speed data link. A paper design was also conducted to integrate the external DMA controller onto the CDS board to allow seamless transfer of image data from the SEASIS experiment. Implementation of the prototype circuitry was not performed due to problems with implementing the byte addressable memory. Analysis was also been performed to predict the performance implications of not including the external DMA. The analysis indicates that there is only a moderate performance penalty but the large number of unknowns present has lead to the suggestion that the DMA circuit be prototyped allowing experiments to be conducted to determine its usefulness.

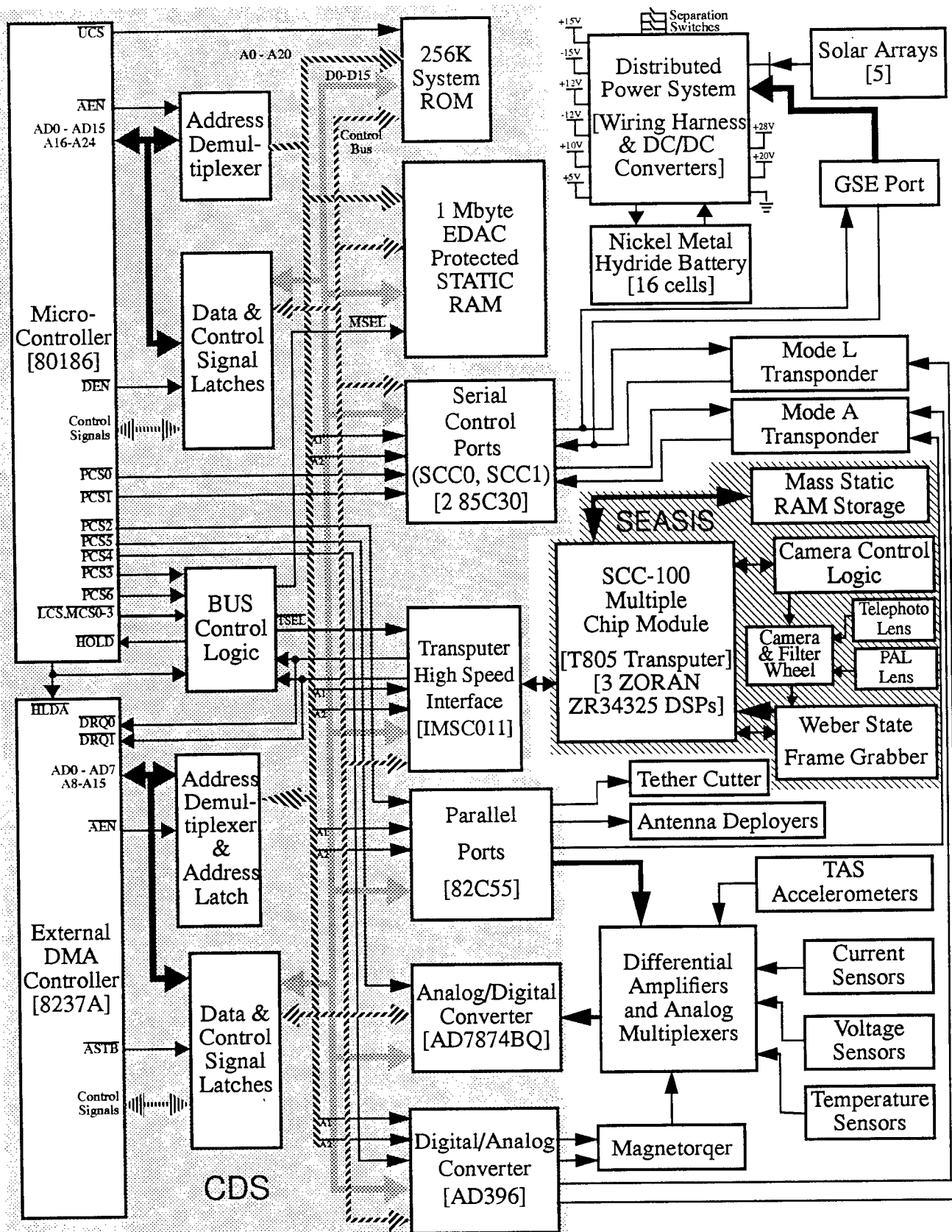


Figure 1: SIMPLIFIED FUNCTIONAL DIAGRAM OF SEDSAT-1 HARDWARE

Software Development

Figure 2 is a complete functional description of the software tasks associated with the CDS operation whose function were identified or refined during the fellowship period. These tasks are further subdivided in the detailed schedule which are included in the full report.

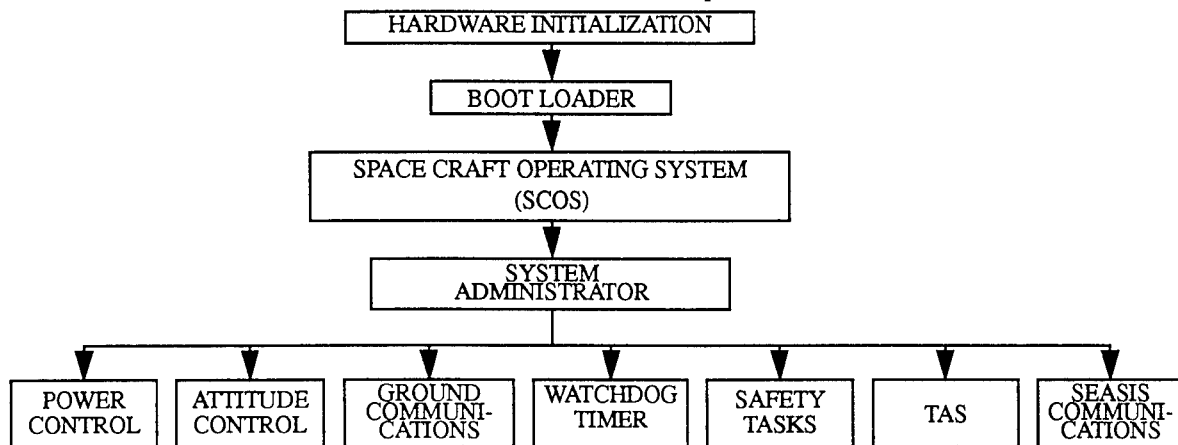


Figure 2: Functional Description of Software Tasks for Command and Control System

Hardware Initialization Routine

This routine is to initialize all the system hardware and includes the following functions:

- (1) Initialization of all CDS board external (80186) I/O and memory selects, (2) execution of a "memory wash" of the EDAC protected RAM, (3) initialize all external peripherals including 8037A DMA, 825230 Serial Communication Controllers, INMOS C011 Transputer Interface Chip, 80255 Parallel Port and, (4) upon initial start-up, copy ROM to RAM then pass control directly to SCOS for tether mission or upon cold start (i.e. external reset) transfer program control to the Boot Loader Routine.

Boot Loader

The boot loader task is a low-level task written in assembly language that is activated upon system start-up or reset. It is responsible for uploading the basic operating system into system RAM. The boot loader will be invoked each time the SCOS operating system is to be updated. To allow for the tether portion of the mission to occur, the boot load will allow the SCOS operating system and all necessary application tasks to be copied directly from the system ROM into RAM without requiring explicit commands being sent via the RF control links. This code must be very robust and extensively tested since it is mission critical.

Space Craft Operating System

For improved reliability a specialized real-time operating system for the SEDSAT-1 will be deployed that has over 80 operating years on LEO Satellites. This operating system incorporates a real-time multitasker which support the simplified concept of message streams for inter-task communication and has specialized AX.25 libraries to simplify the task of satellite/ground communications. The operating system allows for inexpensive DOS-based PC's to be used for system development and emulation.

System Administrator

A number of actual software tasks (not necessarily a one-to-one correspondence with the functional description in Figure 2) will have to be initialized and placed in the SCOS execution queue. This task is concerned with placing the initial tasks in the instruction queue and other initialization operations.

Power Control Task

To maintain an overall positive power margin, a periodic software task will be invoked that will monitor the current, voltage, and temperature associated with the main power system and the associated subsystems. An algorithm will be developed which will vary the power levels associated with the transponders based upon the calculated charge/discharge rate of the satellite's batteries. In the event of an energy emergency, the power control tasks contain separate software exceptions which will disable all experiments and the Mode A transponder. This is also the default mode which the satellite is placed upon system reset.

Attitude Control

This task uses information such as voltage/current readings from the solar arrays and imaging information from the SEASIS experiments to produce current pulses to the three axis magnetorquers to control in a closed-loop manner the attitude of the satellite.

Ground Communications

This task is concerned with the implementation of a high-level communication protocol to perform store-and-forward operations of data obtained from the on-board experiments. This task utilizes the Bek-TeK AX.25/University of Surey software routines which were provided as part of the SCOS operating system to accomplish this goal.

Safety Tasks

These two tasks control the safety critical operations of the satellite as they reflect on Space Shuttle Operations. They include the enabling of the tether cutter, and the 10 meter antenna deployer. These tasks are not uploaded until after the SEDSAT-1 is fully deployed.

Three-axis Accelerometer (TAS) Software

This task involves recording the accelerations that are undergone by the SEDSAT-1 along each of its three orthogonal axes. This information will be recorded for future downlink to the ground during the tether portion of the mission where it will be evaluated off-line to provide more information on tether dynamics. In the secondary portion of the mission this data will be made available for use as one of the inputs to control the attitude of the spacecraft.

SEASIS Communications

Communications with the SEASIS experiment will occur via the SCC-100 MCM's 20Mbit/sec Transputer link through the IMSC011 interface. The data transferred in this matter will be re-packetized and buffered to be transmitted to the ground station via the Ground Communication task. To improve the transmission speed this operation will in most likelihood require the use of the use of an external DMA.

Mission Milestones

The following represents a list and a short description of the set of milestones determined as part of this research, which will be used to measure the progress of the CDS/Ground Station Software portion of the SEDSAT-1 Mission. Note that the software version numbers have the following format Vx.x, where x.x represents the portion of functionality that the software component is expected to have when compared to its proposed function during flight. It does not necessarily indicate the amount of effort that is required to obtain this functionality. The milestones which are highlighted with an asterisk are key MSFC milestones agreed upon on July 6, 1995 as stated in a Memorandum for record from Rein Ise. A complete set of mission subtasks associated with software development are presented in the CDS Software Requirements Documented.

(i) Internal CDR (start date: 8/3/95)

The SEDSAT team will present their work for an internal critical design review. It is desirable that the team employ experts from outside their immediate group to participate in this process. All pertinent design issues will be considered.

(ii) Assembly of CDS PC, Mother Board and Mode L Transponder Flight Hardware (9/1/95)*

At this point the main motherboard, which distributes and routes the power to the daughter boards, and the CDS PC board should be designed, laid out, and fabricated.

(iii) Beginning of the NASA SEDSAT-1 CDR (start date: 9/15/95)*

This milestone is concerned with the initiation of the NASA Critical Design Review. The NASA design review will be centered around Space Shuttle safety concerns.

(iv) CDS V0.5 Software Release (11/30/95)

This software release will contain the tether cutting routines, power system software, bootloader, and functional test routines.

(v) CDS Hardware/Software Interface Verification (12/1/95)*

The CDS board will be tested utilizing the built-in functional test routines associated with CDS Software Release V0.5.

(vi) CDS V0.7 Software Release (1/31/96)

This software release will contain the watchdog software, antenna deployment software, and the CDS/SEASIS communication routines.

(vii) Complete Assembly of CDS Bus (2/1/96)*

The CDS board and portions of the motherboard will be verified using the functional test routines associated with CDS Software Release V0.7. Additionally, the fail-safe reset circuitry should be implemented and tested.

(viii) CDS V1.0 Software Release (4/1/96)

This represents the full flight versions of the CDS software which will be placed in CDS ROM. This will include all CDS V0.7 functionality with the addition of the complete CDS File System and the magnetic stabilization routines.

(ix) Delivery of SEDSAT-1 for Environmental Testing (6/15/96)*

The SEDSAT-1 hardware is to be delivered to MSFC to conduct a number of tests. This should be preceded by a verification of the CDS/SEASIS hardware/software interface and the combined functional test of all SEDSAT systems.

(x) Delivery to KSC (10/1/96)*

The SEDSAT-1 will be delivered to Kennedy Space Center for deployment.

(xi) Ground Acquisition V0.2 Software Release (10/15/95)

This release of the ground software will include the interface specification/demonstration of the icon to high-level language interface definition/demonstration, the basic ground station LABVIEW front panel/block diagram definition, and the low-level routines to fully support the ground station equipment, GSE, port that is used to communicate with the satellite during environmental testing.

(xii) Ground Acquisition V0.5 Software Release (1/31/96)

This software release is to include the basic telemetry monitoring software including all drivers and handlers that will be used to allow real-time data acquisition. Additionally, the protocol associated with the command/control operations will be fully defined and implemented; future revisions should not effect the basic function of the software only improve the ergonomics and improve efficiency.

(xiii) Ground Acquisition V0.7 Software Release (2/1/97)

In this release the flight versions of the command/control software, and the telemetry monitoring software will be fully developed, implemented, and tested.

(xiv) Ground Acquisition V1.0 Software Release (4/15/97)

The SEDSAT program will allow individual access via amateur radio to a restricted set of functions (satellite status, and imaging information) to interested parties. This software will be developed during this time period for both the PC and Macintosh environments.

Conclusions

During this fellowship period a viable team of capable students has been assembled, a significant number of problem areas have been identified and solutions proposed, constructive meetings have occurred with industry representatives, and feasible schedules have been created. Greater progress could have been made, however, if there were more care taken in the manner in which the students were assigned engineering tasks. This resulted in the secondary portions of the design being completed ahead of schedule and the most critical portion of the design, completion of the CDS hardware design, being delayed by several months. This is a natural by-product of placing too much responsibility upon a single individual to make high-level managerial decisions at the same time that same individual is expected to be designing low-level hardware. It appears, however, that there has been a refocusing of direction which is likely to correct this situation before it becomes critical to the overall schedule but it is unlikely that this will occur by the scheduled time of the first NASA milestone. It is believed by this researcher that the aforementioned problems and weakness can be overcome and that this unique project has a reasonable chance of being ready in time for its scheduled launch.

1995

NASA/ASEE SUMMER FACULTY FELLOWSHIP PROGRAM

**MARSHALL SPACE FLIGHT CENTER
THE UNIVERSITY OF ALABAMA IN HUNTSVILLE**

**CAPILLARY ELECTROPHORESIS: IMAGING OF ELECTROOSMOTIC AND
PRESSURE DRIVEN FLOW PROFILES IN FUSED SILICA CAPILLARIES**

Prepared By:	George O. Williams, Jr.
Academic Rank:	Instructor
Institution and Department:	Calhoun Community College Department of Natural Sciences
NASA/MSFC:	
Laboratory:	Space Science
Division:	Microgravity Science and Applications
Branch:	Biophysics
MSFC Colleagues:	Percy Rhodes Robert Snyder, Ph.D. David Donovan

Introduction

This study is a continuation of the summer of 1994 NASA/ASEE Summer Faculty Fellowship Program. This effort is a portion of the ongoing work by the Biophysics Branch of the Marshall Space Flight Center. The work has focused recently on the separation of macromolecules using capillary electrophoresis (CE). Two primary goals were established for the effort this summer. First, we wanted to use capillary electrophoresis to study the electrohydrodynamics of a sample stream. Secondly, there was a need to develop a methodology for using CE for separation of DNA molecules of various sizes.

In order to achieve these goals we needed to establish a procedure for detection of a sample plug under the influence of an electric field. Detection of the sample with the microscope and image analysis system would be helpful in studying the electrohydrodynamics of this stream under load. Videotaping this process under the influence of an electric field in real time would also be useful. Imaging and photography of the sample/background electrolyte interface would be vital to this study. Finally, detection and imaging of electroosmotic flow and pressure driven flow must be accomplished.

Experimental Section

Experiments to accomplish the following were designed and implemented this summer.

1. capillary electrophoresis chamber design and construction
2. sample materials selected and prepared for CE experiments
3. background electrolytes or buffer systems were prepared
4. experiments with sample injection methods
5. power requirements for CE were determined
6. systems interfacing, monitoring and safety requirements
7. methods for detection of sample
8. fluorescence and imaging in real time during CE runs
9. documentation by way of videotape
10. data analysis

A small CE chamber ~ 36 cm long was built using two pieces of fused silica with polyamide coating, O.D. = 356 μm , I.D. = 246 μm . Each was sealed with silicone adhesive sealant inside the ends of an uncoated square glass capillary, 400 μm I.D. Total volume for this system is ~ 163 μL . This assembly was placed on a small plastic block, 75 mm X 25 mm, and sealed into place with silicone adhesive sealant. The capillary ends of the chamber were placed into small 25 mL buffer wells of glass with copper bottoms for electrical connection. The inlet and outlet buffer wells were placed on to a small copper electrode attached to the top of a small lab jack with double sided tape.

This system allowed for the leveling of the background electrolytes and elimination of pressure driven flow.

Detection and imaging of the sample fluid required a material which could be seen with the light microscope. We decided to use a fluorescent sample material which could be intensified, videotaped, and analyzed using the Zeiss Axioplan and Hamamatsu image analysis system. The buffer of choice was a phosphate buffer with a conductivity of $\sim 320 \mu\text{mhos}$. This electrolyte was seeded with quinine bisulfate, $100 \mu\text{g/mL}$, and the sample material was a preparation of 0.1 N sulfuric acid with quinine bisulfate at a concentration of $100 \mu\text{g/ml}$ (1). A volume of $200 \mu\text{L}$ of dilute $5.4 \mu\text{m}$ diameter polystyrene latex microspheres was placed into the outlet and inlet buffer chambers. The leveling jacks were adjusted while viewing the movement of these particles until all particles had completely stopped moving in the square capillary. This was done to eliminate pressure driven flow within this CE system. Quinine bisulfate is excited by ultraviolet radiation at 360 nm , and since the background electrolyte and the sample both contained this compound these experiments were conducted in a darkened laboratory. The ultraviolet light was turned on and the emission was observed with the naked eye, brought into view on a tv monitor, and videotaped.

Samples were injected by electroosmotic flow for twenty seconds (2) and the inlet buffer capillary tip was replaced in the background electrolyte. Optimum power requirements were $\sim 2 \text{ kv}$, at $\sim 8.0 - 9.0 \mu\text{A}$. A dc power supply was used to provide power and an in-line meter was used for monitoring the current. The CE runs were accomplished with two persons for safety. Detection of the sample/buffer interface was easily achieved since the emission spectrum was slight for the buffer and much brighter for the sample. The tube assembly was placed on a Zeiss Axioplan research microscope and the fluid observed and videotaped using the Hamamatsu/Argus-10 system. Averaging of the raw image of four frames per second provided optimum image enhancement.

Another test chamber was constructed with a longer square glass capillary in the center. This unit was placed on top of a $75\text{mm} \times 25 \text{ mm}$ copper block which was covered with black electrical tape. This unit allowed us to place it on a specially designed and custom built motorized stage which has a speed control on the horizontal axis as viewed in the microscope. After the image was seen on the tv monitor the CE unit was set to the speed synchronized to the electroosmotic flow of materials inside the capillary. This system enabled us to observe and videotape the sample/buffer interface for several minutes.

Results and Discussion

The CE system was ideal for observing the interface. The fluorescent material provides good visibility, and the image analysis system with image enhancement provides a smooth, stable sample image for observation and online experimentation such as the changing of parameters during CE runs under load. Time requirements for movement of this sample materials vary with voltage. We used much higher voltages, about 55.5 v/cm, for sample injection and movement to the detection area on the capillary. Once the sample stream was in view, voltages were reduced to ~ 12 v/cm and the electroosmotic flow was drastically reduced.

Electroosmotic flow (EOF) was first identified in the late 1800's when Helmholtz worked with an applied electric field in a horizontal glass tube containing an aqueous salt solution. He pointed out that the silica imparts a layer of negative charge to the inner surface of the tube, which, under an electric field, led to the net movement of fluid toward the cathode (3). EOF or bulk flow acts as a pumping mechanism to propel all molecules (cationic, neutral, and anionic) toward the detector with separation ultimately being determined by differences in the electrophoretic migration of the individual analytes. The magnitude of EOF is dependent on a number of parameters including pH and ionic strength of the analytes. The inclusion of EOF in the calculation of velocity is essential (4).

During some of our experiments we were able to induce movement of the sample slug by reversing the polarity during the run. This resulted in a flow in the opposite direction. Also, pressure driven flow profiles were easily induced by either elevating or lowering buffer wells located beside the microscope stage on lab jacks. Overall, this portion of the summer work went extremely well and we are pleased with our results.

We are also working with a fluorescent material which binds to cells. We would like to be able to detect and videotape the separation of proteins using CE. Finally, we are continuing the work with DNA using fluorescence, gels for sieving, and capillary electrophoresis for the separation of various sizes of these macromolecules.

Acknowledgments

Appreciation is expressed to Dr. Frank Six, NASA, MSFC, Dr. Gerald Karr, University of Alabama Huntsville, and Dr. Mike Freeman, University of Alabama, Tuscaloosa, for administration of the NASA/ASEE Summer Faculty Fellowship Program. I also want to express sincere thanks to Dr. Robert Snyder, Mr. Percy Rhodes, and Mr. David Donovan of the Biophysics Branch, Space Sciences Laboratory, for their assistance with the work for the summer.

References

1. Parker, C.A. Photoluminescence of Solutions. Elsevier Publishing Co., New York. 544 p. 1968.
2. Guzman, Norberto, A., Hernandez, Luis, and Hoebel, Bartley G., "Capillary Electrophoresis: A New Era in Microseparation," BioPharm. pp 22-37, 1989.
3. Helmholtz, H.Z. About electrical interfaces (translated title), Ann. Phys. Chem. 7,337, 1879.
4. Landers, James (editor). Handbook of Capillary Electrophoresis. CRC Press. Ann Arbor. 644 p. 1994.

1995

NASA/ASEE SUMMER FACULTY FELLOWSHIP PROGRAM

**MARSHALL SPACE FLIGHT CENTER
THE UNIVERSITY OF ALABAMA**

**A TECHNIQUE FOR DETERMINING CLOUD FREE VS CLOUD CONTAMINATED
PIXELS IN SATELLITE IMAGERY**

Prepared By:

Richard A. Wohlman

Academic Rank:

Instructor

Institution and Department:

Western Carolina University

Department of Mathematics and Computer Science

NASA/MSFC:

Laboratory:

Earth Sciences

Division:

Earth System Science

Branch:

Observing Systems

MSFC Colleagues:

Gary J. Jedlovec, PhD.

Anthony R. Guillory

INTRODUCTION

Since the first earth orbiting satellite sent pictures of the earth back to them, atmospheric scientists have been focused on the possibilities of using that information as both a forecasting tool and as a meteorological research tool. With the latest generation of Geostationary Operational Environmental Satellites (GOES) now entering service, that view of the earth yields views at a frequency and resolution never before available. These satellites have imagers with a five band multi-spectral capability with high spatial resolution. In addition, the sounder has eighteen thermal infrared (IR) channels plus one low-resolution visible band. With a resolution as small as one kilometer, GOES provides scientists with a powerful eye on the atmosphere. Menzel and Purdom (1994) detail both the imager and sounder capability as well as other systems on the GOES satellites.

Immediately apparent in the visible channel are the patterns of clouds swirling over both oceans and continents. These clouds range in size from huge planetary systems covering thousands of kilometers to puffy fair weather cumulus clouds on the order of half a kilometer in size. With the IR sensors temperature patterns are observed. High clouds appear very cold, while low stratus field show temperatures near that of the surface. The surface, in turn, generally appears warmer than the clouds. It would seem then a simple manner to determine cloud and surface temperature from the imagery, but such is not the case. While most of the atmospheric constituents are well mixed and homogeneous, water vapor is not. The water molecule, because of its unique structure and vibration modes, affects the transmittance of the atmosphere most notably in the infrared regions. There are regions of the IR spectrum where water vapor acts as a strong absorber, and at others it is nearly transparent. The transparent wavelengths are called windows, and one such window occurs at $11.2\mu\text{m}$. Adjacent to this window at $12.7\mu\text{m}$ which is strongly absorbed by water vapor.

These two wavelengths form what is known as a split window, the utility of which was first used by Chesters et al. (1983). Using the linearized form of the radiative transfer equation, they were able to use the split window to determine the amount of water vapor present in the atmosphere. Jedlovec (1987) developed the physical split-window (PSW) technique which determines the integrated water content (IWC). Guillory et al. (1993) used the PSW method using Visible Infrared Spin Scan Radiometer (VISSR) Atmospheric Sounder (VAS) found on the older versions of the GOES satellites. Recently, Jedlovec and colleagues have been attempting to apply the PSW method using full disk IR imagery obtained by the new generation of GOES satellites. IWC is essential for improved analysis and prediction of convective storms which have been observed to develop in regions of both strong and rapidly evolving moisture gradients (Miller 1972). It has also been used in the prediction of clouds and precipitation (Perkey 1976).

CLOUD CLEARING VS. CLOUD FILTERING

Full disk IWC retrievals pose several significant problems. One of these is the requirement for the image pixel be cloud free. Since the method uses upwelling surface radiation

in the PSW, it appeared obvious that any cloud contamination would modify the 11.2 μ m and/or the 12.7 μ m brightness temperature which would then make IWC retrievals inaccurate. Thus, a method was needed to eliminate the cloudy pixels from the data. There are two approaches to doing this, one called cloud clearing, the other cloud filtering.

Cloud clearing generally employs statistical methods by which clouds are eliminated (cleared). The goal is to modify measured radiances to the 'clear column' values which would be observed from the same atmospheric profile with no cloud contamination. Eyre and Watts (1987) present a fairly comprehensive review of several cloud clearing methods to which the interested reader is invited. This method tends to average the radiances over a partially cloudy area to a significant extent, so to moisture gradients would also be spread over larger areas. Since we are interested in the gradients themselves, modification by the cloud clearing method is not desirable.

Cloud filtering, on the other hand, does not affect the moisture gradient as the cloud clearing method can. Cloud filtering is simply a method by which cloud contaminated pixels are eliminated entirely from the image so that the retrieval method uses only clear pixels. While cloud filtering might be simple in concept, in practice it is another thing entirely. Again, several methods exist. McMillin (1978) details a method which uses spatial comparisons between a given pixel and its neighbors. McMillin and Dean (1982) describes an operational scheme which makes use of a multi-spectral, multi-step series of tests to determine cloud contamination.

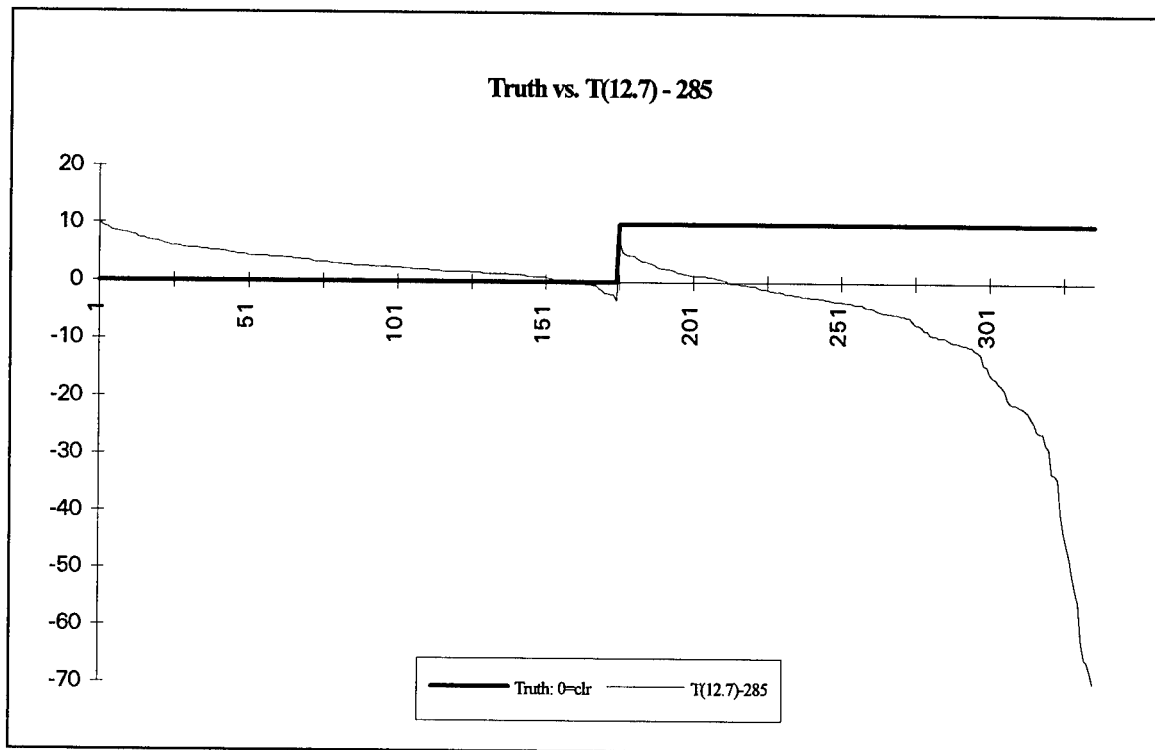
Pieces and parts of each of numerous methods for cloud clearing or filtering were considered for our cloud filtering scheme. But, with the charge of making the scheme as simple, fast and accurate as possible so that ultimately real time GOES data might be used, many were eliminated as being too complicated, computationally difficult and time consuming. We took a new approach in trying to find a simple cloud filtering method.

DATA COLLECTION AND ANALYSIS

GOES pathfinder data was used to gather radiance information from three sources: 12.7 μ m and 11.2 μ m brightness temperatures, and visible brightness counts. The pathfinder dataset provides eight kilometer resolution in all of these wavelengths which are all temporally and spatially correlated. Data was gathered from the odd dates from 19 through 27 August 1988 at both 1500Z and 1800Z using a locally produced program running in the McIDAS environment. Each dataset was comprised of an array of pixel information which contained pixel location in both image coordinates and earth coordinates, 11.2 μ m and 12.7 μ m radiance, and visible brightness count. There were between 325 and 350 datapoints selected from an image which extended from 18°N to 45°N, and from 70°W to 105°W. These data were then imported to a spreadsheet for manipulation, and study.

Of first concern was the generation of a 'truth' value for each pixel, that is, a binary type value which described the pixel as clear or cloudy. This was done in a gross manner in the selection program run under McIDAS, and fine tuned by individually examining pixels in all three wavelengths for final determination of their clear or cloudy status. This examination considered

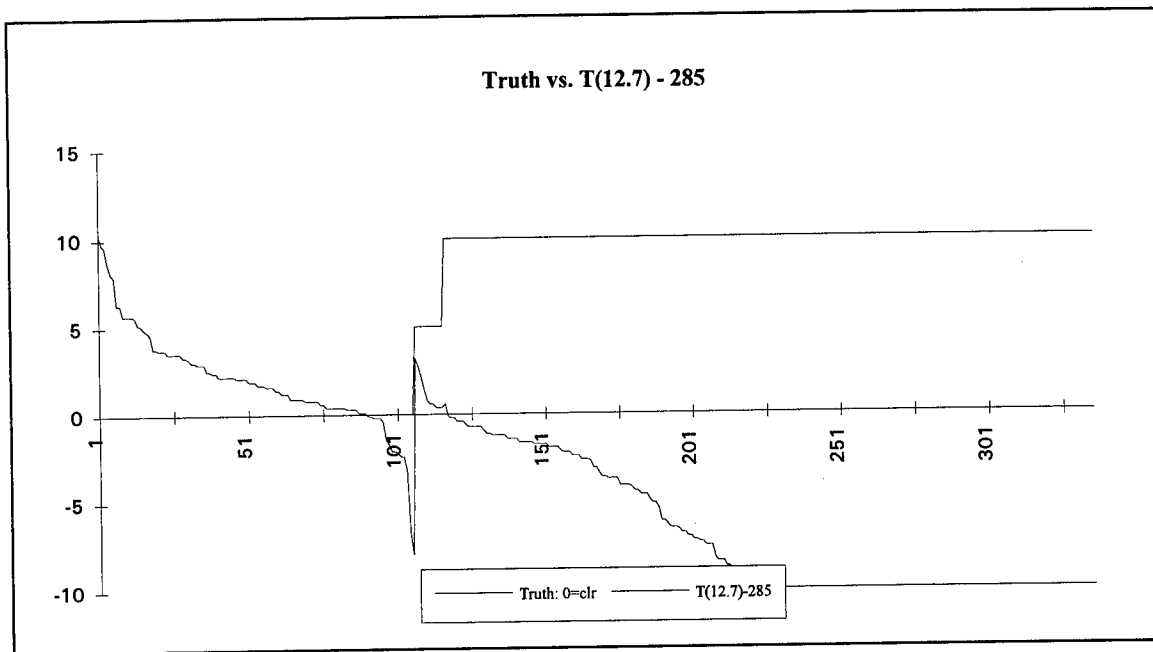
the relationship of the individual pixel value to neighboring values. For example, if a visible brightness count was 65 (a rather low value) it might indicate a clear pixel if over land, but could show a cloud contaminated pixel over water. By comparing it to the adjacent pixels, it can usually be determined to be clear or cloudy. If the pixel was determined to be clear, it was assigned a truth value of 0, if cloudy, 10. Once 'truth' was determined with a high degree of certainty, a data manipulation was performed. The data were sorted by 'truth' (from low to high) and secondarily sorted by the 12.7 μ m brightness temperature. Additionally, 285 was subtracted from the 12.7 μ m brightness temperature to lower the curve to the y-axis for plotting, as shown below. The number 285 was chosen after careful consideration of many data sets, as it provided a good first guess at determining clear versus cloudy.



It is apparent that there are four categories of pixels in this chart. The first are pixels which are identified as clear (true clear), and that where the T(12.7)-285 line is above the heavy 'Truth' line. Second are false cloudy- those pixels which are colder than 285 which indicates cloudy, but are actually clear. Next are those pixels whose temperature is greater than 285, but are in fact cloudy (false clear) and finally are the true cloudy pixels. The statistics for this data, 15Z 25 Aug. 1988, show that of 336 pixels total, 175 were clear, and 161 were cloudy. The selection method found 158 of the clear and 128 of the cloudy which are 90.29% and 79.5% respectively. There were 17 false cloudy and 33 false clear (9.71% and 20.5%).

A close examination of the tabular data showed that for all cases, the false clear pixels were due to one major factor, that being the small cumuliform clouds over warm gulf water. False cloudy results were made for several reasons: cold water, mountain tops, and pixels near the limb. If it were possible to somehow reduce the false clear pixels, then the result would be to

increase the correct selection of cloudy pixels while losing the pixels which yielded false cloudy results. Another day was examined with the thought of accepting the cumulus over water, and initial results seem to indicate that while these clouds show up very brightly in the visible spectrum because of the very dark background of the ocean, they are almost nonexistent in the IR channels because they are both shallow, small in horizontal extent, and very nearly ocean temperature. Re-evaluating the data for the 19th at 15Z, and changing the 'truth' value from 10 to 5 and resorting as above, we found that almost all of the false clear pixels were eliminated. This, once again, assumes that the small cumulus over water may be treated as clear pixels. The results are as follows:



The false clear values all appear below the 'step' in the 'truth' line, and the statistics for the dataset bear out the fact that 99.55% of the cloudy pixels are selected correctly using this simple algorithm. In fact, this selection process, using the $12.7\mu\text{m}$ channel is more successful than the more commonly used $11.2\mu\text{m}$ channel under conditions limited to the constraints of these data sets as mentioned above. The success comes at no expense to the true clear pixels, but it does not save those points which were deemed cloudy by the cutoff temperature, so the percentage of all clear pixels correct does not greatly improve, only (on this date) increasing from 84.91% to 86.21% with 13.79% still false cloudy. Data from the remaining days has yet to be analyzed, but following an initial evaluation it is anticipated that the by accepting the small cumuliiform clouds over the ocean as clear (given that the assumption of no contamination in the IR channels under these conditions is substantiated) an increase in correct cloudy pixels will increase to the 95% level or above.

CONCLUSION

It has been rather surprising to find that a first cut scheme for discriminating between clear and cloudy pixels should be so effective. That method being to set a threshold of 285K in

the 12.7 μ m channel as a cloud/no cloud cutoff. Integrating 11.2 μ m and even visible data does not appreciably affect the results.

RECOMMENDATIONS

Continued exploration of the cumuliform clouds over the gulf is highly recommended in light of the promising developments in that area. As these data sets are very restricted in latitude, an analysis of latitude dependence is needed, with expectations being that there be some modification to the threshold cutoff varying with latitude. Similarly, seasonal effects are anticipated for constant times, as well as variations due to the solar angle. These might be accurately modeled as some sinusoidal function of time of day and day of year once information from datasets for the entire year are developed. Limb effects were examined in a very cursory manner in this study, but once again, a mathematical relationship between satellite zenith angle and limb darkening/brightening should be possible.

REFERENCES

- Chesters, D., L. W. Uccellini and W. D. Robinson, 1983: Low-level water vapor fields from the VISSR Atmospheric Sounder (VAS) split window channels. *J. Climate Appl. Meteor.*, **22**, 725-743.
- Eyre, J. R., P. D. Watts, 1987: A Sequential Estimation Approach to Cloud-Clearing for Satellite Temperature Sounding. *Q. J. R. Meteorol. Soc.*, **113**, 1349-1376.
- Guillory, A. R., G. J. Jedlovec, 1993: A Technique for Deriving Column-integrated Water Content Using VAS Split-Window Data. *J. App. Meteor.*, **32**, 1226-1241.
- Jedlovec, G. J., 1985: An evaluation and comparison of vertical profile data from the VISSR Atmospheric Sounder (VAS). *J. Atmos. Oceanic Technol.*, **2**, 559-581.
- McMillin, L. M., 1978: An Improved Technique for Obtaining Clear Radiances From Cloud-Contaminated Radiances. *Mon. Wea. Rev.*, **106**, 1590-1597.
- McMillin, L. M., C. Dean, 1982: Evaluation of a new Operational Technique for Producing Clear Radiances. *J. App. Meteor.*, **21**, 1005-1014.
- Menzel, W. P., J. F. W. Purdom, 1994: Introducing GOES-I: The First of a New Generation of Geostationary Operational Environmental Satellites. *Bull. Amer. Meteor. Soc.*, **75**, 757-781.
- Miller, R. C., 1972: Notes on analysis and severe storm forecasting procedures of the Air Force Global Weather Central. AWS Tech. Rep. 200 (Rev.), Air Weather Service, Scott AFB, 190 pp. [Available from Headquarters, AWS, Scott, AFB, IL 62225.]
- Perkey, D. J., 1976: A description and preliminary results from a fine-mesh model for forecasting quantitative precipitation. *Mon. Wea. Rev.*, **104**, 1513-1526.

1995

NASA/ASEE SUMMER FACULTY FELLOWSHIP PROGRAM

**MARSHALL SPACE FLIGHT CENTER
THE UNIVERSITY OF ALABAMA IN HUNTSVILLE**

**THERMAL ANALYSIS OF HGFQ USING FIDAP™:
SOLIDIFICATION FRONT MOTION**

Prepared by:	Keith A. Woodbury, P.E., Ph.D.
Academic Rank:	Associate Professor
Institution and Department:	University of Alabama Department of Mechanical Engineering
NASA/MSFC:	
Division:	Thermal Analysis & Life Support
Branch:	Environmental Control
MSFC Colleague:	William C. Patterson

INTRODUCTION

The High Gradient Furnace with Quench (HGFQ) is being designed by NASA/MSFC for flight on the International Space Station. The furnace is being designed specifically for solidification experiments in metal and metallic alloy systems. The HGFQ Product development Team (PDT) has been active since January 1994 and their effort is now in early Phase B.

Thermal models have been developed both by NASA and Sverdrup (support contractor) to assist in the HGFQ design effort. Both these models use SINDA as a solution engine, but the NASA model was developed using PATRAN and includes more detail than the Sverdrup model. These models have been used to guide design decisions and have been validated through experimentation on a prototypical "Breadboard" furnace at MSFC.

One facet of the furnace operation of interest to the designers is the sensitivity of the solidification interface location to changes in the furnace setpoint. Specifically of interest is the motion (position and velocity) of the solidification front due to a small perturbation in the furnace temperature.

FIDAPTM is a commercially available finite element program for analysis of heat transfer and fluid flow processes. Its strength is in solution of the Navier-Stokes equations for incompressible flow, but among its capabilities is the analysis of transient processes involving radiation and solidification.

The models presently available from NASA and Sverdrup are steady-state models and are incapable of computing the motion of the solidification front. The objective of this investigation is to use FIDAPTM to compute the motion of the solidification interface due to a perturbation in the furnace setpoint.

ANALYTIC MODEL

A precursor to the numerical model is the development of a comparable analytic model. This model is not capable of providing information about solidification, but is useful for comparing numerically computed temperature distributions and gradients in a solid rod.

A Green's function approach [1] was used. It is assumed that heat is added uniformly over discrete sections along the length of the rod. Furthermore, it was assumed that the rod had constant thermal properties and had an axisymmetric temperature distribution. For a uniform heat addition over a zone from z_1 to z_2 , the temperature at any point in the rod is

$$\begin{aligned}
T^+(r^+, z^+, t^+) = & 2 \frac{q^+}{\gamma} \left\{ \Delta z^+ t^+ + \gamma^2 \Delta z^+ \sum_{n=1}^{\infty} \frac{1}{\beta_n^2} \left[1 - e^{-\beta_n^2 t^+ / \gamma^2} \right] \frac{J_0(\beta_n r^*)}{J_0(\beta_n)} \right. \\
& + \frac{2}{\pi^3} \sum_{m=1}^{\infty} \frac{1}{m^3} \left[1 - e^{-m^2 \pi^2 t^+} \right] \cos(m\pi z^+) \left[\sin(m\pi z_2^+) - \sin(m\pi z_1^+) \right] \\
& + \frac{2}{\pi} \sum_{n=1}^{\infty} \sum_{m=1}^{\infty} \frac{\gamma^2}{\beta_n^2 + \gamma^2 m^2 \pi^2} \frac{1}{m} \left[1 - e^{-t^+ (\beta_n^2 + \gamma^2 m^2 \pi^2) / \gamma^2} \right] \frac{J_0(\beta_n r^*)}{J_0(\beta_n)} \\
& \left. \times \cos(m\pi z^+) \left[\sin(m\pi z_2^+) - \sin(m\pi z_1^+) \right] \right\}
\end{aligned}$$

Here the characteristic values are the roots of $J_1(\beta_n)=0$, and the '+' notation denotes dimensionless quantities ($r^+ = r/L$, $z^+ = z/L$, $t^+ = \alpha t/L^2$, $r^* = r/r_0$, $\gamma = r_0/L$ and $q^+ = q/q_{ref}$).

NUMERICAL MODEL

A schematic showing the relevant section of HGFQ to be modeled is shown in Figure 1. The FIDAP™ model is axisymmetric and includes the SACA detail but not the quench. The SACA representation includes the Aluminum sample, the graphite ampoule, the gas gap, and the stainless steel cartridge. Hot and cold loads are not modeled separately but are considered part of the sample. The baseline configuration is the SACA in a Helium atmosphere, with a furnace setpoint temperature of 1100 C.

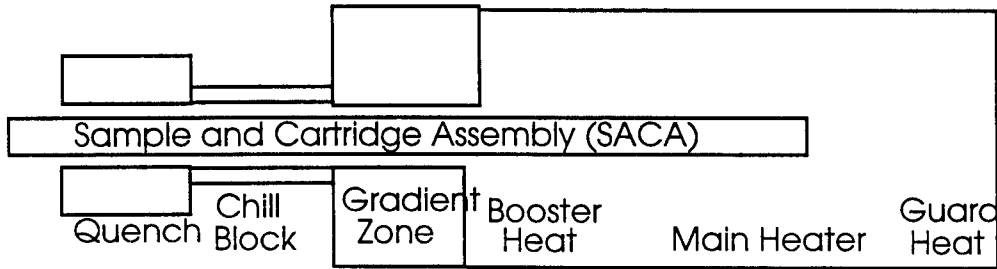


FIGURE 1. Schematic of HGFQ



FIGURE 2. Depiction of Computational Mesh

Grid. Several computational meshes have been used in this study, but the latest one is depicted in Figure 2. This mesh has 2431 nodal points and contains 2682 elements and is identical to the one used previously except for the addition of a finer grid in the gradient zone. This fine grid is designed to capture the phase change interface to facilitate good resolution of its location at any time step.

Thermal Properties. The required thermal properties for Helium gas, 304 stainless steel, Graphite, and Aluminum were obtained from NASA [2]. These properties are consistent with those used in both the NASA and Sverdrup models.

Boundary Conditions. The only specified boundary conditions are the constant furnace wall temperature (taken as 1100 C in the baseline case) and a constant heat transfer coefficient and water temperature on the back of the chill block (take as $h=750 \text{ W/m}^2/\text{K}$ and 22 C). All other surfaces are assumed adiabatic. However, all surfaces in the cavity bounded by the SACA and the outer wall are assumed to participate in grey-body radiative exchange. Radiation within the SACA (between the cartridge and the ampoule) is neglected.

Modeling Solidification. FIDAP™ provides two means for accounting for phase change in a transient calculation. The first is an Explicit Front-Tracking method in which the location of the interface is added as an unknown in the system of equations. Once the location is determined, the mesh is regenerated so that a prespecified group of elements is always adjacent to the interface. The second technique is an Enthalpy-based method where the solidification is accounted for by a variable specific heat. In this case, the solidification front is found by locating the isotherm associated with the phase change temperature.

The enthalpy-based method was chosen for the computations for two reasons associated with the moving mesh. The mesh update algorithm is somewhat primitive and does not allow specification of "meshable" and "unmeshable" regions within the solid phase. This means that the ampoule, gas gap, and cartridge might be remeshed in the process. Secondly, the movement of nodes on the boundaries associated with remeshing will invalidate the previously computed radiation view factors.

Computations. The computational procedure is a two step process. First, FIDAP™ is used to solve the steady-state problem associated with the SACA at a fixed position (the 50% processed position was used). The output temperature field for this condition is saved in the output file. Second, a transient calculation is performed which uses the steady-state solution as initial condition data. The solution was obtained using a trapezoidal rule (Crank-Nicholson) integration with $\Delta t = 1.0$ second over a 120 second period.

Post-Processing: Position. Once the transient temperature field was obtained, the position and velocity of the interface were still to be determined. The basis for the location of the interface at any time was taken to be the intersection of the 660 C isotherm with the centerline of the sample. The history of this location was determined by using the "MOVIE" command of the FIDAP™ post processor, and relying on the fact that the data from any "LINE" plot is echoed to a file. By plotting the centerline temperature distribution at all times using the "MOVIE" feature, all the centerline $T(x)$ information at each time interval was captured in an ASCII file. This file was processed with a simple "C"-program which used linear interpolation to find the x -location of the 660 temperature level at each time step.

Post-Processing: Velocity. Once the $X_{front}(t)$ information is known, the velocity of the front is found as the derivative (slope) of this function. Unfortunately, the information is available discretely with finite precision, and the challenge of differentiating a “noisy” function is faced. The differentiation was achieved by three means: 1) finite-differencing on the $X_{front}(t)$ data, 2) differentiating a polynomial curve fit to the data, and 3) finite-differencing the 5-point average of the data.

RESULTS

The results were obtained for a +2 C step in the furnace temperature. Although this is larger than a perturbation that likely will be seen on the furnace, it will demonstrate the effect. The position and velocity results are shown in Figures 3 and 4, respectively.

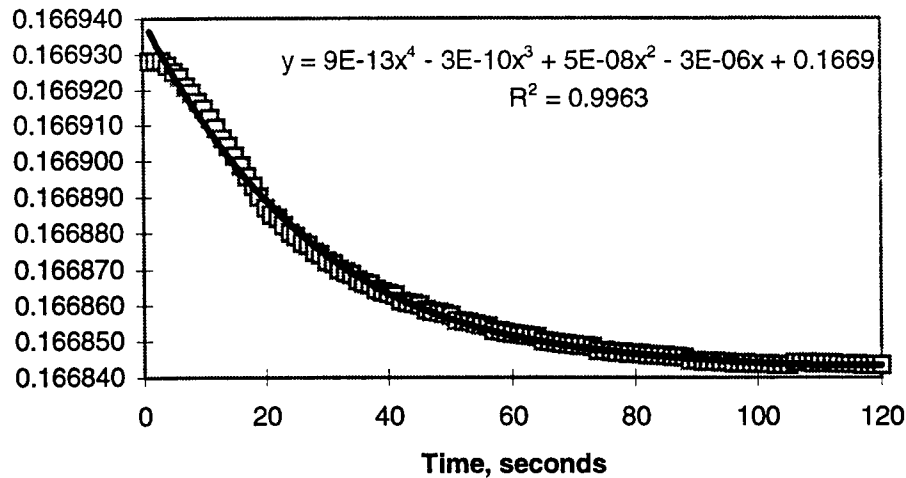


Figure 3. Front location versus time for +2 C furnace step

A more typical variation in furnace temperature is a +0.2 C step. The results for this case (both position and velocity) are seen in Figure 5. The effects of limited precision, associated primarily with the 5-digit accuracy from the FIDAP™ post processor printout, is evident.

Conclusions

Based on the present results, it is clear that front velocities of 2-3 $\mu\text{m/s}$ may be possible due to a furnace instability of +2 C. It is less certain but apparent that for a +0.2 C furnace step that front velocities of 0.2-0.3 $\mu\text{m/s}$ may be possible. For each of these cases, the present analysis indicates a transient associated with the front motion lasting at least 2 minutes.

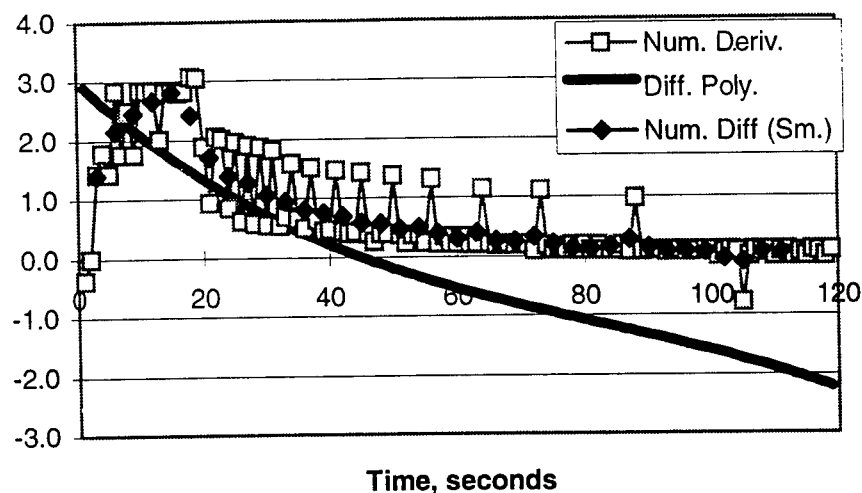


Figure 4. Front velocity versus time for +2 C furnace step

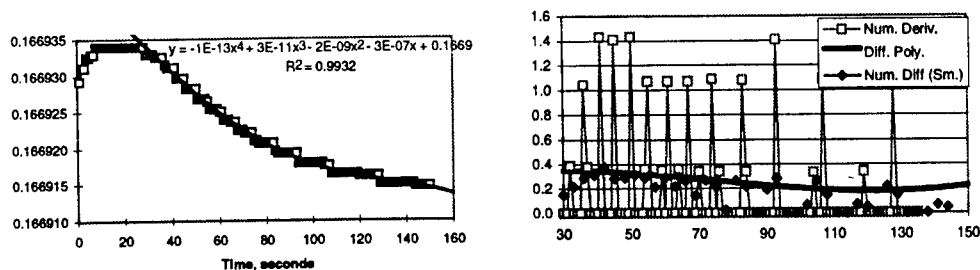


Figure 5. Position(left) and velocity (right) for +0.2 C furnace step

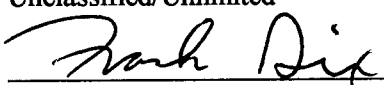
REFERENCES

- [1] Beck, J. V., Cole, K. D., Haji-Sheikh, A., and Litkouhi, B., *Heat Conduction Using Green's Functions*, Hemisphere Publishing Co., 1992.
- [2] Westra, D., ED63 Branch MSFC, Private Communication, July, 1995.

REPORT DOCUMENTATION PAGE

Form Approved
OMB No. 0704-0188

Public reporting burden for this collection of information is estimated to average 1 hour per response, including the time for reviewing instructions, searching existing data sources, gathering and maintaining the data needed, and completing and reviewing the collection of information. Send comments regarding this burden estimate or any other aspect of this collection of information, including suggestions for reducing this burden, to Washington Headquarters Services, Directorate for Information Operations and Reports, 1215 Jefferson Davis Highway, Suite 1204, Arlington, VA 22202-4302, and to the Office of Management and Budget, Paperwork Reduction Project (0704-0188), Washington, DC 20503.

1. AGENCY USE ONLY (Leave blank)		2. REPORT DATE February 1996	3. REPORT TYPE AND DATES COVERED Contractor Report (Final Report)	
4. TITLE AND SUBTITLE Research Reports - 1995 NASA/ASEE Summer Faculty Fellowship Program			5. FUNDING NUMBERS NGT-01-008-021	
6. AUTHOR(S) G. Karr, R. Chappell, F. Six, M. Freeman, Editors				
7. PERFORMING ORGANIZATION NAME(S) AND ADDRESS(ES) The University of Alabama in Huntsville and The University of Alabama, Tuscaloosa, Alabama			8. PERFORMING ORGANIZATION REPORT NUMBER	
9. SPONSORING / MONITORING AGENCY NAME(S) AND ADDRESS(ES) National Aeronautics and Space Administration Washington, D.C. 20546			10. SPONSORING / MONITORING AGENCY REPORT NUMBER NASA CR-199830	
11. SUPPLEMENTARY NOTES				
12a. DISTRIBUTION / AVAILABILITY STATEMENT Unclassified/Unlimited  Date: 2/23/96 Dr. Frank Six, University Affairs Officer			12b. DISTRIBUTION CODE	
13. ABSTRACT (Maximum 200 words) For the 31st consecutive year, a NASA/ASEE Summer Faculty Fellowship Program was conducted at the Marshall Space Flight Center (MSFC). The program was conducted by the University of Alabama in Huntsville and MSFC during the period May 15, 1995 through August 4, 1995. Operated under the auspices of the American Society for Engineering Education, the MSFC program, as well as those at other NASA centers, was sponsored by the Higher Education Branch, Education Division, NASA Headquarters, Washington, D.C. The basic objectives of the programs, which are in the 32nd year of operation nationally, are (1) to further the professional knowledge of qualified engineering and science faculty members; (2) to stimulate an exchange of ideas between participants and NASA; (3) to enrich and refresh the research and teaching activities of the participants' institutions; and (4) to contribute to the research objectives of the NASA centers. The Faculty Fellows spent 10 weeks at MSFC engaged in a research project compatible with their interests and background and worked in collaboration with a NASA/MSFC colleague. This document is a compilation of Fellows' reports on their research during the summer of 1995. The University of Alabama in Huntsville presents the Co-Directors' report on the administrative operations of the program. Further information can be obtained by contacting any of the editors.				
14. SUBJECT TERMS Astrionics; structures and dynamics; materials and processes; systems analysis and integration; propulsion; space sciences; mission operations; information systems; advanced spacecraft and payload systems; preliminary design; and technology transfer.			15. NUMBER OF PAGES 494	
			16. PRICE CODE NTIS	
17. SECURITY CLASSIFICATION OF REPORT Unclassified	18. SECURITY CLASSIFICATION OF THIS PAGE Unclassified	19. SECURITY CLASSIFICATION OF ABSTRACT Unclassified	20. LIMITATION OF ABSTRACT Unlimited	

National Aeronautics and
Space Administration
Code JTT
Washington, DC
20546-0001

Official Business
Penalty for Private Use, \$300

Postmaster: If Undeliverable (Section 158 Postal Manual), Do Not Return
